Marine carbon isotopes, carbonate mineralogy and indices of chemical weathering during the Tonian and Cryogenian periods: examples from North and South China

Steven J Robinson

University College London
Department of Earth Sciences

A thesis submitted in fulfilment of the requirements for the degree of Doctor of Philosophy

August 2016

Declaration

I, Steven Robinson, confirm that the work presented in this thesis is my own. Where information has been derived from other sources, I confirm that this has been indicated.

Use of colour

The printed version of the thesis is in black and white. Most diagrams are in colour, so make more sense in the digital version.

A personal note

I began to take a serious interest in geology in the 1990s. Over time this became a consuming passion, until in 2008 I gave up paid employment and formally studied for a second degree. There are advantages, I console myself, in becoming exposed to the state of the art/science relatively late in life. Perhaps one then has a better ability to understand that much of what is known is not known. I began the research project straight after graduation, and write these final words early in 2017. To get to this stage has been a long journey.

Abstract

In the mid to late Neoproterozoic, Earth is thought to have experienced climate change more extreme than at any other time in history, swinging from warm to globally freezing conditions and back again twice, possibly as many as four times. Yet life in the late Neoproterozoic flourished as never before. Not much later, phylogenetically disparate and morphologically complex animals appeared as if from nowhere, their descendants having survived millions of years of temperatures below zero. The thesis examines this scenario.

Shallow-marine carbonate chemistry in the Neoproterozoic is characterised by a predisposition toward dolomite and huge variability in carbon-isotope composition. Carbonate rocks terminating the putative 'snowball' glaciations manifest both characteristics, but why ^{13}C-depleted dolomites immediately followed is not well understood. The first part of the thesis considers the carbonate system in the light of two early-Neoproterozoic (Tonian) successions from North China: a mixed-clastic-carbonate succession that abruptly switched from calcite to dolomite, and another, not previously described, in which carbonate $\delta^{13}C$ went from +4‰ to -6‰ and back to 0‰.

The second part focuses on weathering. The carbonate strontium isotope record from the mid Tonian onward suggests that silicate weathering – a function of temperature – was intense, even during the Cryogenian. Siliciclastic sediments reflect weathering more directly. The continuous record of such sediments from South China analysed here, spanning the late Tonian to the start of the Ediacaran, enable silicate weathering to be tracked through the critical transitions when temperatures supposedly plunged. They show no abatement in weathering. However, even in the period before the formations analysed, most of the chemical alteration took place after deposition.

Conclusions include the following. (1) Carbonate and siliciclastic chemistry were interrelated via the common factor of high atmospheric CO_2. Seas were alkaline, and silicate dissolution took place under water as well as on land. Dolomite, inhibited today by kinetic barriers and low activities of Mg^{2+} and CO_3^{2-}, was favoured by high temperatures and high concentrations of these ions, in many cases precipitating direct from seawater. (2) Calcium carbonate was mostly aragonite or vaterite, and primarily authigenic. (3) Carbon isotope ratios were controlled by water depth, varying from around -6‰ in deep water to high positive values in evaporitic settings. (4) While the ocean subsurface appears to have been anoxic through the Precambrian, modern levels of carbon isotope fractionation and organic carbon burial do not support the view that atmospheric oxygen was low. (5) Faulting of the continental crust during the Neoproterozoic produced hydrothermal enrichments of ^{87}Sr, Fe, Mn and Mg (among other elements), and cap carbonates exemplify such enrichment. They were depleted in ^{13}C, initially, because sea-level in their respective rift settings was high. Temperatures did not fall in the approach to the Sturtian and Marinoan intervals, and epicontinental water bodies in the Cryogenian were never frozen.

Contents

1. The sedimentological, geochemical and philosophical background 8

1.1 Diamictites, striations, dropstones 8
1.2 Phenomena that require explanation 10
1.3 Snowball Earth as a scientific paradigm 22
1.4 Geochemical aspects 25
1.4.1 The dolomite problem 25
1.4.2 Variation in the marine carbon-isotope signal 28
1.4.3 Chemical weathering 28

CARBONATE SYSTEMS

2. The Jiuliqiao and Sidingshan Formations, Anhui Province, North China: a model system of marine Mg-Ca carbonate and siliciclastic sedimentation in the early Neoproterozoic 37

2.1 Introduction 38
2.2 Geological setting 41
2.3 Methods 46
2.4 Results
2.4.1 Element relationships 48
2.4.2 Carbon isotopes 54
2.4.3 Carbonate crystallinity 54
2.4.4 Feldspar and quartz analyses 57
2.5 Silicate and carbonate dissolution as a function of pH 59
2.6 Controls on dolomitisation
2.6.1 Phase discontinuities 61
2.6.2 Dolomitisation via dissolution and re-crystallisation 64
2.6.3 Abiotic controls on dolomitisation 65
2.6.4 Sulphate, pyrite, sulphur isotopes and organic carbon 66
2.7 Evidence for direct precipitation of dolomite
2.7.1 Diagenesis requires implausible volumes of fluid throughput 69
2.7.2 Small, uniform crystal size 70
2.7.3 No remnants of primary calcite in the dolostones 71
2.7.4 Non-depletion of $\delta^{13}C_{carb}$, enrichment of $\delta^{18}O$ 72
2.7.5 Crypto-dolomite within the quartz and feldspar 73
2.7.7 Implications for the interpretation of other ancient dolomites 74
2.7 Conclusions 76

3. A large-amplitude negative carbon-isotope excursion through the early Neoproterozoic Majiatun Formation of Liaoning Province, North China 84

3.1 Introduction 85
3.2 Regional setting and chronostratigraphy 86
3.2.1 Yingchenzi Formation 87
3.2.2 Shisanlitai Formation 92
3.2.3 Majiatun Formation 92
3.3 Methods 94
3.4 Results

3.4.1 Carbonate carbon and oxygen isotopes 97
3.4.2 Organic carbon 97
3.4.3 Other elements 99
3.4.4 Microscopy 103
3.4.5 Re-crystallisation, silica and pH (Luhai) 104
3.4.6 Was the original carbonate mineralogy aragonite or calcite? 106
3.5 Controls on carbon and oxygen isotope ratios
3.5.1 Carbon isotope mass balance 108
3.5.2 Negative carbon isotopes and organic carbon remineralisation 109
3.5.3 Carbonate alkalinity, pH and organic carbon fractionation 111
3.5.4 The cause of the $\delta^{13}C$ kink 112
3.5.5 Oxygen isotope variation 114
3.6 Sedimentation rates 115
3.7 Other Tonian excursions 116
3.7.1 Shorikha Formation, Siberia 117
3.7.2 Bitter Springs Formation, Australia 117
3.7.3 Upper Grusdievbreen and Lower Svanbergfjellet Formations, East Svalbard 118
3.7.4 Shaler Supergroup, Victoria Island, northwestern Canada 118
3.7.5 Fifteenmile Group, Ogilvie Mountains, northwestern Canada 118
3.7.6 Little Dal Group, Mackenzie Mountains, northwestern Canada 119
3.7.7 Beck Spring Dolomite, Death Valley, California 119
3.7.8 Tambien Group, northern Ethiopia 119
3.8 Implications for the carbon isotope cycle 121
3.9 Conclusions 122

4. Carbon and oxygen isotope variation in Proterozoic carbonates – a function of sea-level 129

4.1 Introduction 130
4.2 Isotopic variation with depth 133
4.3 Isotopic variation of organic carbon 139
4.3.1 Overviews of the aggregated data 140
4.3.2 TOC variation over time 142
4.4 What controls organic fractionation? 143
4.5 What controls inorganic fractionation? 145
4.6 TOC and the organic carbon burial flux 146
4.7 Towards a depth-dependent model 148
4.8 Negative excursions
4.8.1 Upwelling in the context of deglaciation 153
4.8.2 Systematic variation in $\delta^{18}O$ through negative excursions 154
4.9 Implications
4.9.1 $\delta^{13}C$ as a proxy for sea-level 157
4.9.2 Carbonate $\delta^{13}C$ earlier in the Precambrian 159
4.9.3 Implications for the history of atmospheric oxygen 161
4.10 Conclusions 163

SILICICLASTIC SYSTEMS

5. Silicate weathering in the Neoproterozoic as evidenced by strontium isotopes 176

5.1 Introduction 176

5.2 Seawater $^{87}Sr/^{86}Sr$ in the Precambrian 177
5.3 Strontium isotope variation in the Neoproterozoic 180
5.4 Atmospheric pCO_2 in the Neoproterozoic 184
5.5 Strontium isotopes and dolomite 190
5.6 Correlations based on the new strontium isotope stratigraphy 190
5.7 Conclusions 191

6. Causes of sedimentation in the Nanhua Rift Basin, South China, during the mid Neoproterozoic: a critical review 196

6.1 The formation of the South China Block 196
6.2 Rifting in relation to sediment generation 201
6.3 Lithological change through the Cryogenian Period 209
6.4 Regional sea-level change 214
6.5 The evidence for glaciation 216
6.6 Magmatism and lithospheric extension as evidenced by zircons 220
6.7 Chemical deposits 223
6.8 Summary 224

7. The chemical index of alteration: issues of interpretation, and secular differences in weathering style 232

7.1 Major element composition as a function of weathering 233
7.2 Sedimentation rates 234
7.3 Grain size 234
7.4 The composition of the precursor rock 235
7.5 Recycling 236
7.6 Non-silicate CaO 239
7.7 The possibility of K metasomatism 240
7.8 Conclusions 249

8. Major and trace element analysis of sedimentary rocks of the Nanhua Rift Basin in the period 820–620 Ma 255

8.1 The geological context 255
8.2 Analytical method 256
8.3 Geochemical results and associated lithologies
8.3.1 The extent of recycling 256
8.3.2 Composition of the source rocks 257
8.3.3 Grain size 258
8.3.4 Loss on ignition and carbonate content 259
8.3.5 Loss on ignition and organic carbon 260
8.4 Geochemical results and associated sedimentology 261
8.5 Iron as an index of hydrothermal input 267
8.6 Secular trends
8.6.1 Data integration 269
8.6.2 ANK variation 820–630 Ma 270
8.6.3 Fe variation 820–630 Ma 272
8.6.4 Trace elements 730–620 Ma 272
8.7 Evaluation of CIA 275
8.8 Mg, Ca, Na and K through time 277
8.9 Mg v. Fe 280
8.10 Precambrian ice ages or catastrophic rifting? 281

8.11 Conclusions 286

THE ATMOSPHERE

9. Sedimentary systems under high atmospheric CO_2 292

9.1 Carbon dioxide, marine carbon isotope ratios and carbonate mineral formation 293
9.2 Great oxygenation events 296
9.3 Silicate weathering, outgassing, seafloor spreading rates, ocean pH, degree of carbonate saturation, dolomite 306
9.4 Climate change in the Neoproterozoic – an alternative view 311

Acknowledgements 328
Appendix 1. Data for Jiuliqiao, Sidingshan and Zhaowei Formations 329
Appendix 2. Data for Yingchenzi, Shisanlitai and Majiatun Formations 333
Appendix 3. XRF data, South China 336
Appendix 4. Backscattered electron photomicrographs of samples from the Jiuliqiao and Sidingshan Formations 343
Appendix 5. Transmitted light photomicrographs of samples from the Jiuliqiao and Sidingshan Formations 349

CHAPTER ONE

The sedimentological, geochemical and philosophical background: Snowball Earth from outside the paradigm

1.1. Diamictites, striations, dropstones

Outside the circle of researchers who specialise in the Neoproterozoic, the idea of Snowball Earth is not well known. On at least two occasions, not far apart, and for millions of years, Earth was locked from the poles to the equator in a state of deep-freeze: the greatest and longest-lived environmental crisis in Earth history. Eventually, overcoming the planet's high albedo and low surface temperature, carbon dioxide built up to levels unprecedented even in the Archaean, at which point the ice melted within a few thousand years (Hoffman et al. 1998). The idea is audacious, indeed stupendous. But while some of the evidence may seem clear-cut, other evidence is less so. In an effort to account for much flowing water at the time, some sedimentologists speak of a 'slushball' state. One or two explain the facts by large-scale rifting (Eyles & Januszczak 2004), though even they accept that glaciers were eroding material at high altitudes and latitudes.

The earlier of the two worldwide glaciations is dubbed the 'Sturtian', the later the 'Marinoan'. Together they bracket the approximately 85-million-year 'Cryogenian' period – etymologically referring to ice production – of which only 20% was interglacial. Former ice sheets are attested by thick accumulations of diamictite, by the faceted and striated clasts they sometimes contain, by striated pavements and dropstones (outsize clasts deflecting the laminae of fine-grained sediments).

The attribution of such deposits to the action of ice has its roots in the 19th century, but the belief that they formed at low latitudes developed in response to the plate tectonics revolution. If glaciation was the agent, it must have been 'sufficiently extreme to form marine tillites in the tropics' (Harland 1964). The proposal was scarcely less startling than plate tectonics itself. One point favouring plate tectonics had been the existence of 'undoubted moraines' in India, at a latitude of only 20–22° N (Wegener 1912). The deposits were Permian, but if India then lay at that latitude, almost no part of the Earth's surface would have been ice-free – an indigestible notion. With Wegener's re-arrangement of the continents all the glaciated areas were centred round southern Africa, and the difficulty disappeared. In the Precambrian, however, the difficulty persisted.

With the stakes so high, a great deal of thought was given to what criteria might distinguish glacial from non-glacial diamictites. Among those who weighed up the Neoproterozoic evidence was Brian Harland. He found the areal extent of the tillites and the size of their clasts persuasive (Harland & Rudwick 1964). Even more decisive was the way individual pebbles and boulders had distorted the layers of the finer sediment around and below them: the only adequate explanation was that these stones had dropped from icebergs.

His argument, published in *Scientific American*, was skilfully constructed, and since the reasoning remains current, it is worth examining. It began with the reminder that there were at least two series of glaciations prior to the Pleistocene ice age, of comparable or even greater scale: one during the Late Carboniferous and Permian, the other not long before the Cambrian. The reality of the most recent episode was beyond doubt. Also well established was the glacial origin of the Permo-Carboniferous tillites, even if, puzzlingly, they were confined to the southern hemisphere; indeed there might have been several glaciations during that time. The Precambrian episode was attested by phenomena of the same kind, for example the tillite and underlying striated pavement at Varanger Fjord in Norway.

The glacial origin of the Precambrian tillites was not entirely unambiguous. Tillite-like rocks, it was recognised, could also form in other ways – for example, as a result of submarine earth tremors or gravity slides. On re-examination, the Varanger tillite, for example, appeared to be a slumped lens-shaped deposit resting on sandstone that was grooved by the submarine slumping of the till itself. Nonetheless, in most cases the extent of the tillites and the size of the boulders in them pointed to a glacial origin. By the same token, their distribution was so widespread that the ice sheets could not have been restricted to high latitudes.

Then this statement: ‘It is necessary to confine the argument to tillites laid down in water’, implying that many more straightforward but climatologically less informative cases could have been cited, for ‘mountain glacial tillites might have been deposited in any latitude’. ‘Tillite’ was to be defined so as to include water-laid deposits (Harland et al. 1966). Others have objected to this confounding of distinct sedimentary processes (Boulton & Deynoux 1981), but if the manoeuvre made the association with the presumed agent even less direct, it also purchased the advantage of rendering the rejection of a glacial origin more difficult. As is well known, gravity flow deposits – notably turbidites and diamictites – are a common component of glaciomarine environments. So are conglomerates, breccias, mudstones and sandstones, which occur also in non-glacial contexts. If very few facies are unique to ice action, it is equally true that very few are incompatible with it.

Neogene sequences of undoubtedly glaciomarine origin are extraordinarily diverse. Since all these facies commonly occurred in the Cryogenian, might these not also be glaciomarine? Even cold-based glaciers can entrain, transport, deform and deposit eroded material.

The admission of aqueous environments also enabled a potentially extreme view to be mitigated. The wide extent of these deposits did

> not mean that the entire earth was covered with ice; indeed, that would be most unlikely. During an intense glacial period increasing cold would extend the total area of sea ice, although large areas of ocean at low latitudes probably would remain open. On land the ice sheets might develop mostly at middle latitudes. Whatever the exact distribution of ice, the water-deposited tillites clearly indicate that icebergs or sea ice transported material from the land or shallow seas into warmer waters.

Dropstones, while evidence of glaciers and floating ice, were also evidence of oceans not covered by ice, of ongoing rain-out of fine material. Over the last two decades, much of the critical discussion has turned on the same question: was the Earth entirely frozen over, or were parts of the ocean and land ice-free (Kerr 2010)? In climate models the most stable state is a global freeze-over, with sea ice thickening towards the equator (Goddéris et al. 2011).

1.2. Phenomena that require explanation

A comprehensive review of the underpinning evidence is beyond the scope of this thesis, but we can take a little time to look at the problems – problems that the interpretation creates rather than confronts from an independent standpoint. Many of them, in one form or another, are well known.

1. *The Earth receives much more solar radiation at low than at high latitudes, making low-latitude glaciation inherently unlikely*. Very little land during the Cryogenian appears to have lain at latitudes higher than 60° (Fig. 1.1c, Evans & Raub 2011, Li et al. 2013). Land area was concentrated where the Earth was warmest. The paradox places a heavy burden of proof on those who champion the proposal. Models can simulate a snowball state under certain conditions of sea-ice albedo and greenhouse gas depletion, but they have to take the geological case on trust. They are exercises in 'what if', and in the absence of evidence that carbon dioxide levels did plunge to the modelled levels, they remain speculative. An extraordinary cause or combination of causes is required to push equatorial temperatures far below their norm. No such cause has been identified.

2. *Worldwide glaciation implies an overall sea-level fall of at least 500 m*. Terrestrial ice-sheets draw off water that previously lay in the ocean. During the Last Glacial Maximum, sea-level is estimated to have been around 130 m lower than today (Clark et al. 2009). During the postulated

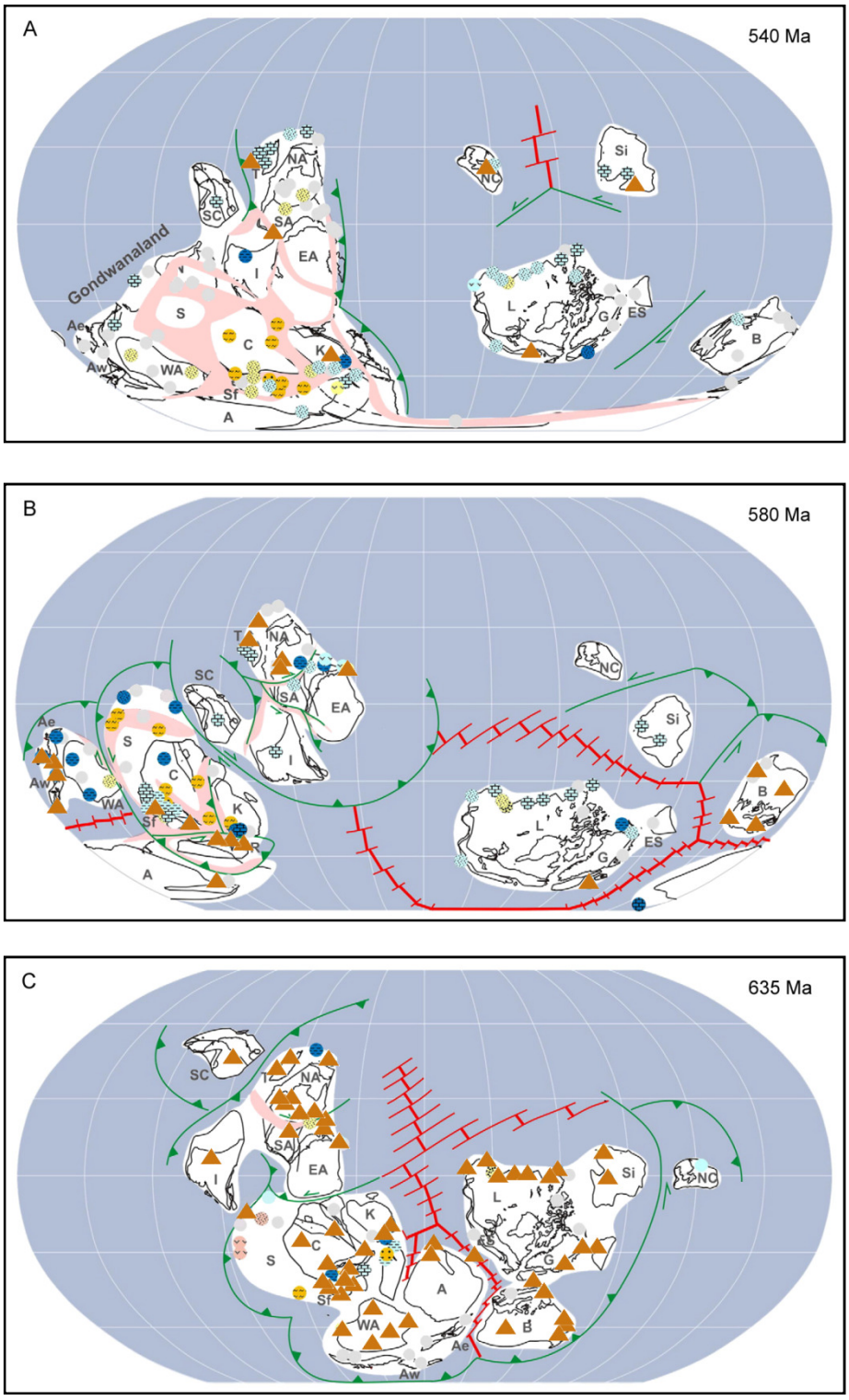

Figure 1.1. Palaeogeographic maps for rocks interpreted as glaciogenic (brown triangles) and dated to the (**a**) terminal Ediacaran, c. 545 Ma, (**b**) mid Ediacaran, c. 585 Ma, and (**c**) Marinoan, 635 Ma. Adapted from Li et al. (2013), to which readers are referred for a key to facies and geographical units. Some place North China (NC) between South China (SC), Australia (NA, SA) and India (I) (Myrow et al. 2015). Note that carbonates (brick symbol) formed c. 540 Ma at latitudes up to 60° S. Penecontemporaneous evidence of glaciation extends to below 30° N and S, implying that glaciation was ubiquitous, notwithstanding the carbonates.

Cryogenian glaciations, the fall would have been greater: modelling suggests a drop of ~525 m in the Sturtian and ~710 m in the Marinoan (Liu & Peltier 2013). The estimates are conservative, taking into account the rebound of ocean floor as mass was shifted to the continents but not the sinking of ocean floor as ocean lithosphere cooled. There are other uncertainties. As glaciation proceeds, the mass of ice on the continent exerts a gravitational attraction on the ocean, drawing it nearer and higher (Andrews 1978). However, sea-level overall is falling, so the ocean tends to be further away and its surface eventually recedes below that of the now emergent shelf. There is also the question whether ice spread landward from the ocean or oceanward from the land. At a minimum, platform seas would have been completely frozen; glaciomarine sediments should not occur in epicontinental settings. If the ice spread oceanward, sediment eroded from the coast and shelf would have been dumped in the ocean beyond the shelf, along with material released from the ice sheets as they melted and withdrew. Little of this would have been preserved. If the ice spread landward, the erosion may have been less severe, and such deposits as there were – it is difficult to visualise turbidites and debrites – would have been washed away in the subsequent transgression. Most problematic of all are the dropstones. They can occur at any level in a diamictite-bearing succession, not necessarily towards the end. If they dropped from icebergs and sea-level was 100s of metres lower, the icebergs were floating on land.

L. J. G. Schermerhorn put the question more than 30 years ago:

> Erosion of underlying strata [means] that fall of sea level … occurred before the mixtites [= diamictites] were laid down in the basins, presumably due to an advance of land ice. In that case, how to explain the formation of *marine* tillites … overlying eroded strata? For if these strata were eroded because of emergence due to sealevel drop, then necessarily the sea must have again invaded the basin to deposit marine tillites. This would mean a transgression at the height of glaciation.

Few researchers have attempted to test the predicted changes in sea-level against the stratigraphic record, and few localities offer an incentive to do so. Consider this summary of the situation in western Scotland: ‘The bedded sediments beneath, in and above the Port Askaig Tillite were deposited in shallow waters, probably in a shelf sea’ (Spencer 1985): sea-level before, during and after glaciation remained much the same. Nonetheless, there are supposed to have been at least 17 glacial advances and thaws during the period. One location that has been studied with sea-level in mind is the palaeo-continental margin of northwest Namibia. The build-up of an extensive shallow carbonate platform created a gradient towards deeper water in the south, with a height difference between platform and lower slope of 0.5 km (Hoffman et al. 2007), even perhaps, at the deglaciation stage, 1.8 km (Domack & Hoffman 2011). On the distal slope the Franni-aus Member

of the carbonate Ombaatjie Formation preserves a ‘glacioeustatic falling-stand wedge’, while the 40–100 m of diamictite immediately above it mark the ice grounding-line. A sea-level fall of over 1.3 km is inferred. However, the Franni-aus Member consists of turbidites and debrites. It is not in origin a shallow-water deposit, it does not suggest a fall in sea-level, and there is no evidence that the whole platform and most of the slope then stood above water. A sea-level drop of more than a kilometre would have exposed ‘not only the carbonate platforms surrounding the continents but also the youngest parts of the ocean crust’: any ‘carbonates would have been deposited far from the continents’ (Fairchild 2016). Even on the platform, the uppermost Ombaatjie Formation deepens, truncated at the top by deeper-water deposits that, overall, shallow upward (Fig. 3 in Prave et al. 2016).

3. *Most of the deposits interpreted to be glacial formed under water*. By definition, a snowball state is one where all continents are under ice (aside from the point that the ocean has retreated beyond the continental shelf). While subglacial lakes are conceivable, proglacial expanses of open sea are not. Epicontinental seas are frozen and ice sheets grounded, preventing aqueous sedimentation. By contrast, the great majority of diamictites interpreted to indicate the presence of ice are water-laid and surrounded by other aqueous deposits, including vertically settling ash beds (Prave et al. 2016). In order to get round the paradox, cartoons of the environment depict a marginal zone where an ice sheet terminates against open sea and icebergs float in front of it, just as in many a non-snowball environment today (Mustard & Donaldson 1987, Wang & Li 2003, Le Heron et al. 2012, Benn et al. 2016). Wherever glacial deposits are identified – and one location might be 160 km inland of another, both of them epicontinental (Le Heron et al. 2014, Busfield & Le Heron 2014) – water and ice are thus reconciled, albeit at the cost of begging the question how ice was continually caught in the act of melting.

4. *The causes mooted to have ‘triggered’ snowball conditions explain nothing.* One scenario is massive consumption of atmospheric CO_2 by weathering of freshly erupted basalt (Goddéris et al. 2003, Cox et al. 2016). Basalt is much more susceptible to weathering and dissolution than felsic rock. However, modelling produces a snowball state only if the pre-glacial pCO_2 was below 280 ppm. To put this in context, pCO_2 in the late Archaean is modelled at 60,000 ppm (Wolf & Toon 2013) for a mean surface temperature of only 15° C, in the early Cambrian, 5000 ppm (Berner 2006). When the lower solar radiation of the time is factored in, 280 ppm is equivalent to a global air temperature of 0.8 °C. Close to freezing conditions are postulated at the outset and leave unaddressed the problem how pCO_2 came to fall to that starting level. The carbonate $\delta^{18}O$ record indicates warm climates throughout the Neoproterozoic. Cooler temperatures would have resulted

in lower weathering rates (Dessert et al. 2003) and hence a feedback limiting any fall in atmospheric CO_2.

One might look to later times for evidence that large effusions of basalt led to catastrophic cooling. Possibly the largest known is the Central Atlantic Magmatic Province, of late Triassic age. Large amounts of CO_2 were injected into the atmosphere, with the release of methane possibly a knock-on effect, and global temperatures rose (Ruhl et al. 2011). Immediately pre-CAMP CO_2 levels are estimated at 2000 ppm, increasing during magmatism to 4500 ±1200 ppm until settling back to levels similar to or slightly lower than before (Schaller et al. 2012). Most, possibly all, the effect of increased weathering was cancelled out by the CO_2 injected. Although several times larger in extent than the Franklin Large Igneous Province of 725–712 Ma, the largest and latest of the pre-Sturtian LIPs and likewise straddling the humid palaeo-equator, the Triassic analogue – cited by Cox et al. (2016) in support of a link between weathering and the start of the Sturtian – did not lead to catastrophic cooling. In any case, the Franklin basalts were still weathering, according to Kunzmann et al. (2015), in the interglacial period.

In order to ameliorate the initial conditions, it has been suggested that disaggregation of the Rodinia supercontinent promoted additional weathering and consumption of CO_2 (Donnadieu et al. 2004). In reality, the break-up would have been accompanied by an increase in volcanism and associated degassing as rifts evolved into spreading centres. Degassing of CO_2 from the present East African Rift system is estimated to be comparable to emissions from all the mid-ocean ridges put together (Lee et al. 2016). Along with the rise in atmospheric CO_2, younger and therefore warmer ocean crust would have raised marine temperatures. For these reasons, there were no ice sheets during the break-up of Pangaea in the Triassic and Jurassic periods: CO_2 did not plummet to icehouse levels.

Another scenario postulates runaway ice-albedo feedback as ice advanced past a critical latitude (Schrag et al. 2002). As with the presupposition of pre-glacial temperatures around 1° C, this presupposes that such ice sheets existed (mostly sea-ice, given that most land was within tropical latitudes). It does not explain how climate cooled sufficiently for ice to form at the outset. The shift of Rodinia's geographical centre towards the equator would have had only a minor effect on albedo (Charnay et al. 2013).

A third scenario – devised to account for the descent of carbon-isotope ratios down to -6‰ before the diamictite-rich Ghaub Formation – postulates methane slowly leaking from hydrates buried by the voluminous discharge of tropical rivers (Schrag et al. 2002). Thus one climate paradox is

substituted for another, for hydrates are ice crystals and form when temperatures are cold; they give up their gases when temperatures rise (hence the suggestion from Kennedy et al. (2001b) that they were involved in ice-sheet melting). The discovery that carbon-isotope values recovered to at least -2‰ before the diamictite (Hoffman 2011) has since undermined the proposal.

5. *Whether glaciation occurred at any time prior to the Cryogenian – or indeed later, in the Ediacaran and Palaeozoic – depends on the same sedimentological interpretations that underpin the reality of Cryogenian glaciations: the case cannot be based on precedent.* Compelling geochemical evidence of cold temperatures earlier is lacking. Diamictites, striated clasts and dropstones, followed by ^{13}C-depleted cap carbonates, occur in Late Mesoproterozoic Brazil (Geboy et al. 2013), coinciding with a time of heightened magmatism and intracontinental rifting (Kumar et al. 2007). Those aside, there is no earlier evidence of glaciation for 1600 million years – and again it is sedimentological.

In the Neoproterozoic, diamictite-forming episodes abound. In Namibia three are known, the earliest dating to some time before 720 Ma (Hofmann et al. 2015), plus a fourth dated to c. 547 Ma, the same age as seemingly glacial deposits in many other parts of the world (Baode et al. 1986, Stoker et al. 1999, Chumakov 2011, Jenkins 2011) (Fig. 1.1a). Four such horizons are known on the Tarim Craton, NW China (Xu et al. 2009, He et al. 2014), the first dating to before 720 and after 740 Ma, the latest to terminal Ediacaran. The Gaskiers and putatively correlative glaciations dated to c. 585–580 Ma (Xiao et al. 2004, Carto & Eyles 2011, McGee et al. 2013, Pu et al. 2016) constitute, elsewhere, a fifth horizon (Fig. 1.1b) and a 'Fauquier' glaciation dated to 572 Ma

Figure 1.2. Grooved and striated surface beneath the pebbly Luoquan Formation, a deposit dated to the latest Ediacaran and thought to have been formed by glaciers; near Shangxuma village, Henan Province. A second such surface occurs 20 cm above the one shown. Were the striations made by clasts within moving ice or by the movement of the overlying diamictite?

Figure 1.3a. Striated, faceted clast ~70 cm above the striated pavement and presumably plucked from it.

Figure 1.3b. Dropstone pair, apparently broken in two post deposition, Luoquan. The pebbly matrix is laminated below the impact level (red mark, left), amorphous through the middle layer (ending at white mark), laminated through the upper layer. The draping pattern of the upper laminae suggests flow from left to right after an interval of rainout.

(Hebert et al. 2010) a sixth, so that it might fairly be said that glaciations were a regular occurrence from 750 Ma to the end of the Neoproterozoic (Chumakhov 2011). In the Middle Urals, three episodes are attested, all Ediacaran (Maslov et al. 2013). Some of the mid- and late-Ediacaran diamictites, striated surfaces and dropstones accumulated at equatorial palaeo-latitudes (Figs. 1.1–1.3). Current sedimentological interpretation absolutely requires that the mid- and late-Ediacaran glaciations be global, for unlike other facies, which reflect environments limited in space, 'glacial diamictites', be they few (Fig. 1.1a) or many (Fig. 1.1c), override all environments, ultimately even the ocean. If ice sheets existed in one place at low altitude and latitude, they existed (with the possible exception of arid areas) everywhere – notwithstanding the apparently contemporaneous precipitation of shallow-marine carbonates (Fig. 1.1), or the contemporaneous habitation of the shoreface by *Cloudina*, small shelly fauna, sponges, motile trace-makers and the numerous lineages that, although they left no fossils, must likewise have been adapted to tropical temperatures. Is it really conceivable that a multimillion-year deep-freeze might have had a positive effect on evolution (Hoffman & Schrag 2000)?

6. *In some regions the expected diamictites are simply missing.* This is not to suggest that diamictite should be expected: if sea-level fell by 500 m, the glaciations should be marked by unconformities without overlying diamictites. On the Otavi platform in northern Namibia, however, carbonate sedimentation continues through the Marinoan interval almost uninterrupted (Fig. 1.4, Hoffman & Schrag 2002 Fig. 9, Hoffman 2011). In some sections there is, at best, a disconformity and the isotopic record is continuous. Variation in carbonate $\delta^{18}O$ leading up to the hiatus is relatively minor, becoming more negative (arguably warmer) as $\delta^{13}C$ declines. Much the same is true in the Sadlerochit Mountains of Alaska (Fig. 1.4): sedimentation across the Cryogenian/ Ediacaran boundary is continuous and diamictite absent, the absence being ascribed to an imaginary glacio-eustatic drop in sea-level which left the carbonate platform exposed until an equally imaginary postglacial transgression. Diamictite of Marinoan age is also missing in Utah and Idaho (Yonkee et al. 2014). South-east California presents almost the opposite situation, for the coarse-grained Kingston Peak Formation appears to span the entire Cryogenian and lacks any clear interglacial interval (Mrofka & Kennedy 2011). So does the Broken Hill area, New South Wales, where glaciogenic-appearing deposits reach a maximum thickness of 5000 m (Young 1992). The Middle Urals region has three Ediacaran diamictite-bearing units, each separated by other

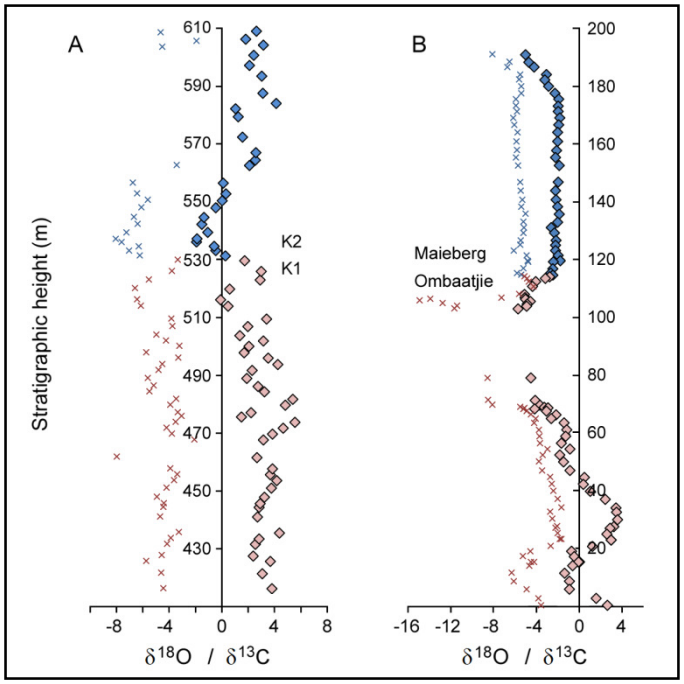

Figure 1.4. The late Cryogenian 'pre-glacial' to 'post-glacial' successions at (**a**) Sadlerochit Mountains, Alaska (section F705, Macdonald et al. 2009) and (**b**) Danube, Namibia (section P6005, Fig. 1.6, data courtesy of P. Hoffman). Crosses denote $\delta^{18}O$, diamonds $\delta^{13}C$. The signals are continuous, $\delta^{18}O$ shows no rising trend indicative of ocean cooling, and the most negative $\delta^{13}C$ values do not occur at the inferred disconformity between the lower and upper formations. At Duurwater, Namibia, the missing Ghaub Formation below the Maieberg shows mostly positive $\delta^{13}C$ (to +3.3, Kennedy et al. 2001a).

formations, but no Sturtian and Marinoan diamictites (Chumakhov 2011, Maslov et al. 2013). The Baikal region of southern Siberia apparently lacks any diamictites (Pokrovsky & Bujakaite 2016).

7. *Iron formations immediately precede or coincide with the diamictites*. Iron formations are a recurrent feature of the Archaean and late Palaeoproterozoic from 3.5 to 1.8 Ga, after which they disappear, despite the persistence of ferruginous conditions in the ocean (Planavsky et al. 2011). Much of the gap is filled by iron oxide copper-gold deposits (Hitzman et al. 1992, Groves et al. 2010), which are chemically distinct and rare in the Neoproterozoic. In the period 2.0 to 1.8 Ga iron formations coincide with a global peak in the growth of continental crust, mafic-ultramafic magmatism and volcanogenic massive sulphide deposits (Rasmussen 2012). When they re-appear, from c. 750 Ma, they are invariably associated with diamictites, and indeed diamictite may occur within the iron formations (Stern et al. 2013, Cox et al. 2013). Occasionally, they contain dropstones, up to 2.5 m across (Klein & Beukes 1993, Lottermoser & Ashley 2000, Macdonald et al. 2010a, Freitas et al. 2011), even pseudomorphs of evaporite minerals (Young 1976). In most cases the iron oxide was deposited in rift-basins, following massive leaking of hydrothermal iron through faults (e.g. Baldwin et al. 2016). As often as not, the formations immediately precede the Sturtian diamictites (as in Alaska, northwest Canada, Namibia), contrary to the original formulation of the Snowball Earth hypothesis (Kirschvink 1992). Few, if any, date to the Marinoan interval; one is known from the late Ediacaran (Frei et al. 2013). While there is a fairly obvious and direct link with crustal extension, there is no obvious link with glaciation.

8. *Carbonates show no evidence of cooling in the lead-up to the Cryogenian glaciations.* The Plio-Pleistocene, which saw northern-hemisphere ice sheets extend down to 40° (in some regions not as far as 60°), was preceded by an irregular 45-million-year record of overall cooling, traceable through deep-sea cores. In benthic foraminifera oxygen-isotope ratios rose from 0 to 4.5‰, equivalent to a temperature fall of 19° C (Mudelsee et al. 2014). By contrast, shallow-water carbonates in the approach to the Sturtian and Marinoan intervals, when surface temperatures must have fallen from high modern-equatorial (30–40° C) to subzero, reveal no hint of such a rise. Not surprisingly, most of the diamictites are preceded by erosional unconformities, and some of the unconformities could span millions of years. Examples of conformable transitions include the Coppercap Formation of northwestern Canada, which at the hinge-end of a half-graben passes gradationally into the Sayunei Formation (Eisbacher 1981), and the Sturtian-age Matheos Formation of northern Ethiopia. In both cases, limestone underlies the transition and $\delta^{18}O$ falls as $\delta^{13}C$ becomes negative (Macdonald et al. 2010b, Miller et al. 2003, Swanson-Hysell et al. 2015). Similarly, the Sturtian-age Port Askaig Formation of western Scotland in places conformably overlies and continues the

dolomite sedimentation of the Lossit Limestone Formation. The transition into the Marinoan-age Namaskluft Formation (Macdonald et al. 2010a), Namibia, is also conformable in places and shows no evidence of cooling in its carbonate $\delta^{18}O$.

Formation	Age	Max t (m)	Location	Reference
Australia				
Elatina	M	1500	South Flinders Range	Preiss 1999
Appila Tillite	S	1500	South Flinders Range	Preiss et al. 2011
Bolla Bollana	S	2500	North Flinders Range	Coats 1981
Fitton	S	1560	North Flinders Range	Coats & Preiss 1987
PualcoTillite	S	3300	South Flinders Range	Coats & Preiss 1987
Yancowinna Subgroup	S/M	5000	Adelaide Geosyncline	Young 1992
Canada				
Vreeland	?	2000	NE British Columbia	McMechan 2000
Toby	S	2500	Southern Cordillera	Smith et al. 2011
China				
Nantuo	M	2800	S China	Liao et al. 1981
Tereeken		2000	Heishan-Zhaobishan area, Tianshan	Xiao et al. 2004
Chang'an	S	1900	Guizhou Province, S China	Zhang et al. 2011
Namibia				
Blaubeker	S	1000	Gobabis-Witvlei area	Prave et al. 2011
Numees	S	>1000	Kaigas River	Macdonald et al. 2010a
Oman				
Fiq	M	1500	Jebel Akhdar	Leather et al. 2002
Siberia				
Bol'shoy Patom	M	1100	Lena River	Chumakov et al. 2011
USA				
Kingston Peak	S/M	3200	Death Valley, Ca	Mrofka & Kennedy 2011
Perry Canyon	S	3800	Utah	
W Svalbard				
Haaken	M	3000	Oscar II Land	Hambrey 1983
Kapp Lyell seq.	M	3000	Wedel Jarlsberg Land	Bjørnerud 2010
Trondheimfjellet	S	1300	Oscar II Land	Hambrey 1983

Table 1.1. Diamictite-bearing formations with a maximum thickness t >1000 m. Age: 'S', Sturtian, or 'M', Marinoan. The majority are Sturtian.

9. *The thickest diamictite-bearing units formed in and, by implication, as a result of rifts*. The great majority of Cryogenian diamictite-rich deposits were laid down in water, and many attain thicknesses of 1000–3000 m, even greater when successive formations are considered (Table 1.1). Thick glaciomarine deposits of Plio-Pleistocene age fringe the continental margins today, notably

the trough-mouth fans left by ice streams (Dowdeswell et al. 2002). Diamictites constitute a large part of these accumulations, resulting from debris flows triggered by small earthquakes as ice loading and oversteepening destabilised the sediment. Sediment extends over long distances, from the continental slope to the abyssal plain, and tends to be thickest around base of slope (O'Grady & Syvitski 2002). The two largest fans in the North Atlantic are the Bear Island and North Sea Fans. They begin at present water depths of around 500 m and extend to beyond 3000 m – sea-level at the time of deposition being, on average, 130 m lower. By contrast, the thick Neoproterozoic accumulations are located on the shelf or inland, where in non-glacial times water depth would typically have been 0–200 m. In glacial times, there would have been no water.

Most Neoproterozoic environments interpreted as glacially influenced are associated with rifting. The Sturtian deposits of the Adelaide Rift Basin are dominated by debrites and turbidites unconformably preceded by shallow-marine siltstones and dolomites (Hore et al. 2015). The grabens accommodating them cut into the shelf at the same time as deposition (Preiss 2000). In the southern Canadian Cordillera faulting and volcanism exactly coincide with the presumed glaciation (Smith et al. 2011). In Oman the Cryogenian Abu Mahara Group lies in a graben within which the oldest deposits are 'glacial rainout' diamictites of the Ghubrah Formation (Fig. 1.5). Alternating diamictites and dropstone-bearing turbidites are interpreted as reflecting glacial advances and retreats, but 'some diamictites are only locally developed and indicate a source from one flank of the basin while nonglacial deposition proceeded at the other' (Leather et al. 2002). An angular unconformity of 20–30° separates the Ghubrah Formation from the overlying mass flow deposits

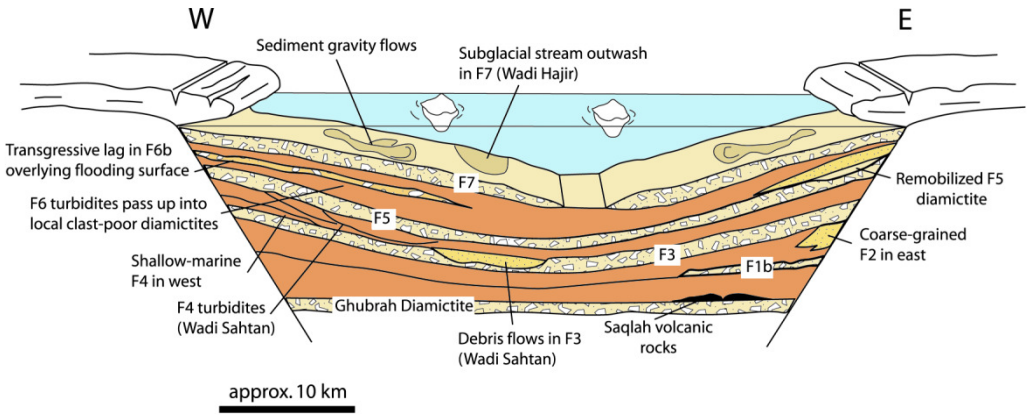

Figure 1.5. Rifts in the Neoproterozoic provided space for thick accumulations of sediment but are not acknowledged to have been significant producers of sediment: the grabens, but for the glaciers, would have remained empty. In reality, fault movements, earthquakes and rapid increases in gradient could have generated the full range of 'glaciomarine' deposits. Unlike the rifts, ice sheets are not directly attested, and causally superfluous. Diagram from Leather et al. (2002) illustrating a rift basin in Oman. Angular unconformity between Ghubrah Formation and lower turbidites not shown.

without any effect on sedimentological interpretation: the succeeding diamict still rains out of the water (Le Guerroué et al. 2005). Along the Fransfontein Ridge of northern Namibia deposition of the 'glaciogenic' Chuos Formation occurred at the same time as the opening of two canyons more than 1000 m deep. Only thin diamictites along the outer walls of the canyons remain to tell the tale (Fig. 1.6): the debris which tore through the basement had too much energy to be deposited. Grainstone turbidites filled the canyons during the 'interglacial' period. Further south there is a similar story: diamictites less than 30 m thick line the base of a palaeo-canyon 1 km deep and 8 km wide, subsequently filled by redeposited limestone, sandstone turbidites, dropstones and debrites (Macdonald et al. 2010a).

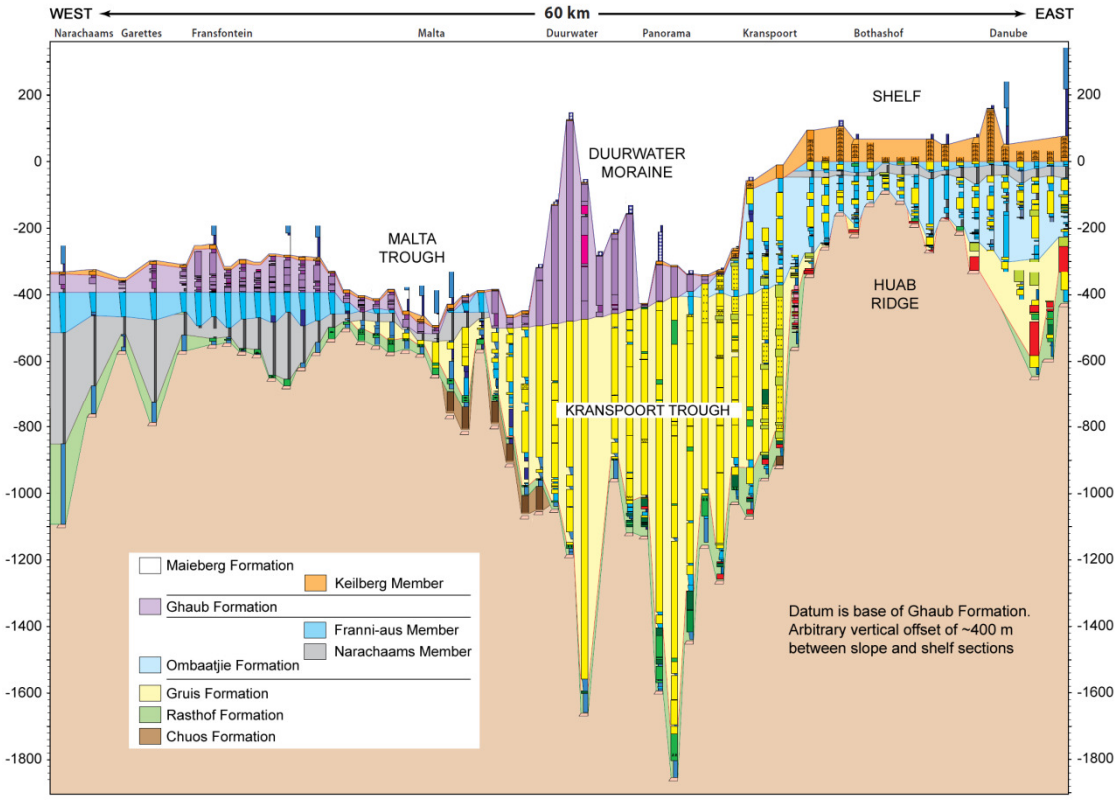

Figure 1.6. Reconstruction of topography at Fransfontein Ridge, northern Namibia, at the start of the Ediacaran period (updated from Hoffman 2011 and simplified). The up-to-1300-m deep Kranspoort Trough is filled mostly by grainstone turbidites (yellow). The Chuos Formation, the older of the diamictite horizons, occurs only on the trough walls. The Ghaub Formation, the younger diamictite horizon, is thickest above the trough.

10. *The Sturtian and Marinoan sequences are immediately and abruptly followed by* ^{12}*C-rich carbonates, mostly dolostone*. How these should be understood remains unresolved. The problem begins with the diamictite-rich intervals themselves: do these represent the full span of time during which the Earth was ice-bound, any number of successive freezes and thaws, or just the melting phase? Opinions differ, for 'an unambiguous sedimentary record of hydrological shutdown during

a prolonged global glaciation appears to be lacking' (Etienne et al. 2007). The record is dominantly aqueous, whether the region was close to the equator (e.g. Laurentia) or 30° distant from it (e.g. South Australia, Namibia). Melting should not have been triggered until atmospheric CO_2 reached the critical threshold (300,000 ppm according to Goddéris et al. 2011). Clastic sediments deposited in water hundreds of metres deep (as turbidites indicate) were then succeeded by dolostones and limestones, interpreted as the product of an almost instantaneous shift to Bahamian temperatures or hotter (300,000 ppm equates to a mean surface temperature of 60° C) as sea-level rose hundreds of metres higher. Another puzzling feature is the diversity and instability of their carbon-isotope signals: in the Sturtian, $\delta^{13}C$ generally becomes heavier, in the Marinoan, lighter (Kennedy et al. 1998, Hoffman & Schrag 2002). Oxygen isotopes through the cap carbonates (e.g. Fig. 1.4) do not support even a 30° C rise in sea-surface temperature.

1.3. Snowball Earth as a scientific paradigm

More than fifty years on from Thomas Kuhn's *The Structure of Scientific Revolutions* (1962) the concept of a scientific paradigm is common currency. Even if we have not read the book or were not around when it came out and provoked excited discussion, we know what a paradigm is. It is a high-level theoretical framework, an explanation accepted almost universally by experts in the field, which makes sense of the world and permits the carrying on of 'normal science'.

> Normal science consists in ... extending the knowledge of those facts that the paradigm displays as particularly revealing, by increasing the extent of the match between those facts and the paradigm's predictions, and by further articulation of the paradigm itself. ... During the period when the paradigm is successful, the profession will have solved problems that its members could scarcely have imagined and would never have undertaken without commitment to the paradigm. And at least part of that achievement always proves to be permanent. ... Acquisition of a paradigm and of the more esoteric type of research it permits is a sign of maturity in the development of any given scientific field.

Examples include Copernicus's proposal that the Earth and planets revolved around the Sun and Newton's interpretation of light as a stream of particles. Many of the examples are explanations whose imperfect or even incorrect nature was later revealed through their being superseded. However, it is not a matter of definition that scientific paradigms are imperfect or incorrect, though one might argue that they are all conditional (Popper 1959, 1965).

A paradigm begins life as a hypothesis. If it proves successful in dealing with criticism and new discovery, modifying itself as necessary, it becomes a theory. A classic example is Alfred Wegener's hypothesis of continental drift. In its modern form the theory of plate tectonics seems so

secure one can hardly imagine its ever being superseded. Equally secure is the idea that ice caps covered large parts of the northern and southern hemispheres in the Pleistocene. 'Snowball Earth' is both a paradigm and a hypothesis. It is a hypothesis inasmuch as no one knows what caused the glaciation and it is beset by problems; it is a paradigm inasmuch as the idea of a snowball glaciation itself is unquestioned. Even the most sceptical of critics accept that, in many cases, deposits were 'glacially influenced' (Schermerhorn 1974, Eyles & Januszczak 2004). The only discussed alternative is a 'slushball' state, as advocated by sedimentologists who take a less absolute, more *ad-hoc* approach.

Some all-embracing explanations deserve being committed to, including, in their time, imperfect ones; others may not. Based on the considerations above, my judgment is that Snowball Earth is a bad paradigm. It survives, not because it successfully accounts for phenomena, but because, as with all totalitarian schemes, it tolerates no rivals and allows only subsidiary questions, such as how many glaciations there were, or whether the snowball was hard or soft. It is not the servant of those who subscribe to it, but their master. As discussion sections in countless papers attest, a glaciation scenario is advanced first and explanations spun to accord with it. The idea is entrenched in the very name of the period. That the 'Cryogenian' was icy cold is as indubitable as that coal formed in the Carboniferous or chalk in the Cretaceous.

Michael Polanyi (1958) illustrated the immovability of belief systems by recalling the Azande belief in the powers of the poison-oracle. When the oracle failed, the failure was rationalised by supposing that tribesmen had committed a breach of taboo or gathered the wrong variety of poison. Reasons for doubt were met one by one, and the refutations confirmed by circularity. Scientific paradigms exhibit the same logical structure:

> Any contradiction between a particular scientific notion and the facts of experience will be explained by other scientific notions; there is a ready reserve of possible scientific hypotheses available to explain any conceivable event. ... The stability of theories against experience is maintained by epicyclical reserves which suppress alternative conceptions in the germ; a procedure which in retrospect will appear right in some instances and wrong in others.

Lee Smolin (2006, p. 69) provides another example from his experience as a theoretical physicist:

> Someone posits a new unification. There are big consequences for experiment. Unfortunately, experiment disagrees. Scientists then complicate the theory, in a way that incorporates several adjustable constants. Finally, they adjust those constants to hide the

missing predicted phenomena, thus explaining why the unification, if true, has not resulted in any observations.

In the present case, the unification consists in interpreting all diamictite-bearing deposits that contain striated clasts and/or dropstones as glaciogenic. Experiment consists of the geological record and of attempts to model glaciations under assumptions compatible with that record. Objections are met by scenarios compatible with the paradigm. For example, extensive evidence of open water in diamictite-bearing deposits is countered by the possibility that 'most glacial deposits ... formed while the ice was in its final retreat' (www.snowballearth.org/against); the implausibility of striations withstanding abrasion within debris flows is obviated by having the striated stones drop from icebergs (Le Heron 2015); the algae and unicellular protozoa that, 100 Ma later, transformed themselves into arthropods and fish survived the sudden descent into the deep-freeze, 55 Ma of continuing deep-freeze, a sudden ascent into the post-glacial super-greenhouse, another descent into the deep-freeze and another ascent into the post-glacial super-greenhouse by retreating

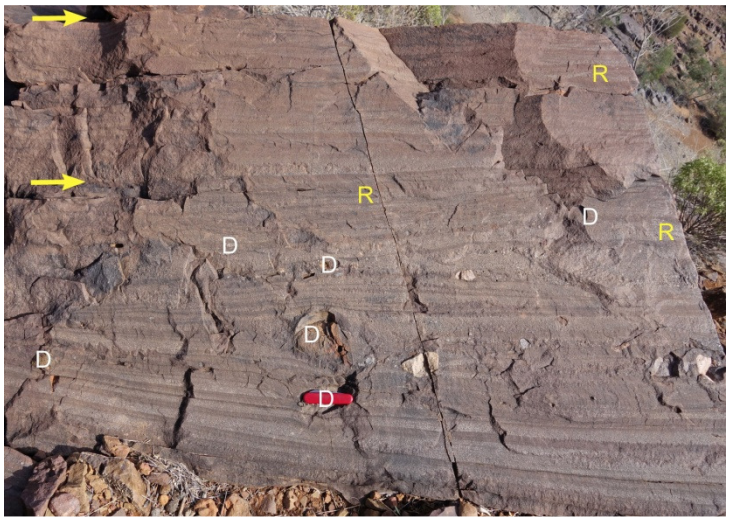

Figure 1.7a. Iron-rich **t**urbidite-like beds in the Merinjina Tillite of the Northern Flinders Ranges, Australia. Inconspicuous dropstones are indicated by 'D', ripples by 'R'. Arrows indicate bedding planes. The above these planes corresponds to Bouma division T_b, while the part-rippled, part -laminated upper parts of each bed correspond to divisions T_c and T_d. There is no hemipelagic T_e. The later bed may consist of several amalgamated fining-up units. Flow is L to R.

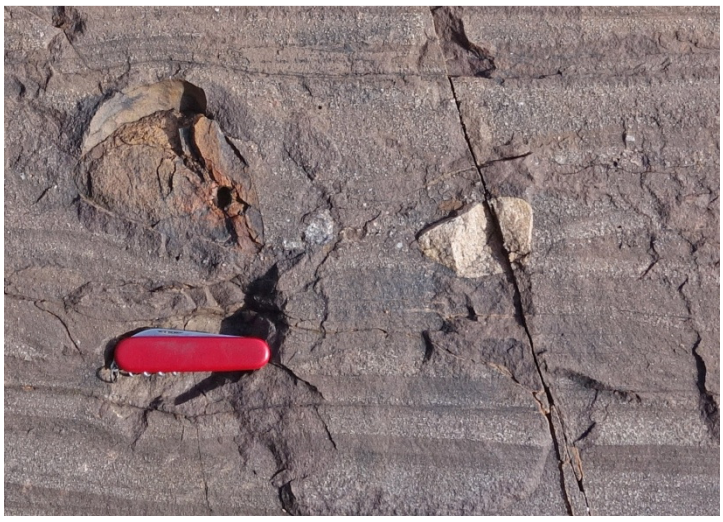

Figure 1.7b. Close-up of dropstones in Fig. 1.7a. Note the two quartz-granule laminae dipping beneath the largest, now vacated dropstone and the deflection of the upper lamina behind the smaller pinkish-white dropstone, indicating current flow from L to R. A similar deflection is seen to the R of the vacancy occupied by the penknife.

to hot volcanic springs on the seafloor and ice near the surface where photosynthesis could be maintained (Hoffman & Schrag 2000); the sea-level problem, if acknowledged at all, is muddied by the possibility that ice-sheets exercised a gravitational attraction on nearby water. Perhaps the most precarious circularity is to assume that all dropstones found among turbidites and debrites in thick Pleistocene successsions were transported by icebergs. The Cryogenian record has many examples of dropstones within turbidites (Wehr 1986, Alvarenga & Trompette 1992, Kellerhals & Matter 2003, Bjørnerud 2010, Domack & Hoffman 2011, Mrofka & Kennedy 2011, Balgord et al. 2013, Le Heron et al. 2014), whether or not the turbidites are formally identified as such (Arnaud & Eyles 2002, Leather et al. 2002, Hoffmann et al. 2004, Giddings & Wallace 2009). The obvious inference is that the dropstones were introduced laterally, by the same flow as dropped the enclosing sand. The laminae deflected by them are those characteristic of turbidites (Fig. 1.7). It is hardly satisfactory to suppose that icebergs were releasing clasts just at the moment a turbidity flow passed underneath, millennia after the last one.

A scientific proposal must be capable of being falsified. Some studies cast doubt on the hard snowball version while conveying the impression that a 'slushball' version remains viable; as such, they remain safely within the paradigm. The root problem is the interpretation of the striated clasts, striated pavements, and dropstones, not the problems which arise if, and only if, one accepts a glacial interpretation. If one does, the testimony of the clasts and striations closes the door on more fundamental doubt. Normal styles of sedimentation are perforce interpreted as reflecting 'interglacials', 'ice-free oases', 'open-water refugia' and the like (Le Heron et al. 2012, Ye et al. 2015), and the hypothesis becomes sedimentologically unfalsifiable.

1.4. Geochemical aspects

Striated clasts, striated pavements and dropstones are discussed in chapter 6. However, the thesis primarily addresses the geochemical evidence bearing on climates in the Neoproterozoic. Arguably the Tonian and Cryogenian periods had more aspects in common than is generally supposed and did not undergo extreme climate change. Three aspects are treated.

1.4.1. *The dolomite problem*

Silicate weathering consumes CO_2 and produces carbonate, bicarbonate, Mg and Ca ions, thereby maintaining the dolomite saturation state of the seawater receiving them. If pCO_2 and silicate weathering decrease, the saturation state decreases, except to the extent that carbonate mineral precipitation also decreases and balance is maintained. In the Precambrian world, the oceans were supersaturated to a greater extent than now (Grotzinger & James 2000) and dolomite formed in

Formation/unit	Age	Details	Reference
Scotland			
Port Askaig Fm	S	Beds of recrystallised dolomite up to 11m thick at 4 horizons. Detrital origin discounted.	Spencer 1971
Australia			
Bolla Bollana Tillite	S	(i) 42 m of alternating calcareous and non-calcareous tillite, yellow dolomite and bouldery dolomite. 'Primary.'	Coats 1981
		(ii) Two stromatolitic bioherms 80 m from base of 600m-thick glaciogenic unit, largest mound 10 x 2.5 m.	Young & Gostin 1988
		(iii) Buff, parallel-laminated, bedded dolomite	Le Heron et al. 2014
Braemar Ironstone	S	Dolomite within and above ironstones and ferruginous siltstones. 'Sedimentary in origin.'	Lottermoser & Ashley 2000
Warcowie Dolomite	S	Yellow dolomite matrix, clasts at some levels.	Le Heron et al. 2011
Olympic Fm	M	Laterally persistent intervals of stromatolitic, oolitic and oncolitic dolomite and dolomicrite overlying, underlying and in places interbedded with boulder conglomerate.	Kennedy et al. 2001a
Julius River Mb	M	Fine-grained microsparitic limestone with minor black shale interbeds.	Calver 1998
Areyonga Fm	S	(Table 13)	Walter et al. 2000
Oman			
Fiq Fm	S	Unit F2: thin, interbedded with laminated tufaceous siltstones. Unit F6: laterally extensive, graded, overlying diamictite/conglomerate, suggesting reworked 'carbonate precipitation'. Depleted $\delta^{13}C$.	Allen et al. 2004
China			
Tereeken Fm	M	Thin carbonate laminae, <1 cm thick, within silty rhythmites; 12 m of bedded homogeneous dolomicrite and dolomicrosparite.	Xiao et al. 2004
Sizhoushan Fm	S	~1 m bed in lower part of formation above diamictite	Feng & Zhang 2016
Namibia			
Ghaub Fm	M	Dolomicrite; peloidal aggregates with fine-grained (>10 mm) clotted fabric . 'Primary.'	Kennedy et al. 2001a
Chuos Fm	S	One or two laterally continuous dolomicrite layers 1-2 m thick, pebble-free, 'enigmatic.' (Bethanis area:) locally autochthonous carbonate rocks with stromatolites.	Miller et al. 2010, Nascimento et al. 2016
Svalbard			
Wilsonbreen Fm	M	(Ormen:) 0.5m-thick silty, dolomitic microbial laminae; (Dracoisen:) limestone stromatolites within sandstone; (Ditlovtoppen:) 1.5 m of dolomite and limestone ribbonites and rhythmites. 'Primary, evaporitic.'	Fairchild et al. 1989, Halverson et al. 2004, Bao et al. 2009, Benn et al. 2015
Canada			
Toby Fm	S	Planar-tabular carbonate beds cms to ms thick, patchy	Smith et al. 2011
Ethiopia			
Matheos Fm	S	Black dolomite.	Miller et al. 2003
Urals			
Churochnaya Fm	M?	18m of brecciated dolomite, lower contact gradational.	Chumakov 1981

Table 1.2. Instances of dolomite (occasionally calcite) within diamictite-bearing sequences. The question whether the dolomite precipitated directly from seawater or was a product of calcite diagenesis is not addressed; 'primary' here means non-detrital.

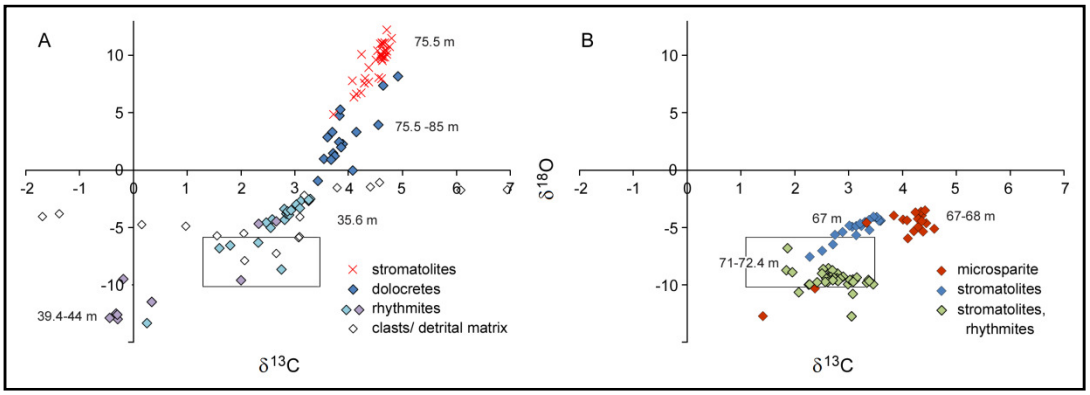

Figure 1.8. (a) Systematic stable-isotope variation in lacustrine dolomites from the Wilsonbreen Formation (data from Bao et al. 2009). Oxygen isotope values, the heaviest ever reported for carbonates, are adjusted downward by 2.7‰ to equate with calcite fractionation. (b) Limestone samples not far in stratigraphic height from the stromatolitic dolomites show similar $\delta^{13}C$ but different $\delta^{18}O$. Boxes indicate isotope values typical of Neoproterozoic marine carbonates. The strong trend in (a) suggests loss of the lighter isotopes as a result of very high temperatures, consistent with the dolomite mineralogy. The extreme conditions are largely confined to the 75-85 m interval.

much greater volumes, over a greater range of environments. Even as late as the Cambrian, over 40% of carbonate rock is estimated to be dolomite (Given & Wilkinson 1987).

In the absence of biomineralising organisms, kinetic barriers prevent calcium carbonate from precipitating until the degree of supersaturation tips them over. Dolomite will not normally precipitate at all without the mediation of microbes – in most cases sulphate-reducing bacteria – and these require warmth and light (the latter indirectly, via organic matter produced by cyano-bacteria and algae). Owing to the cessation of silicate weathering during Snowball Earth and the consequent build-up of CO_2, seas are predicted to have been acidic (Hoffman et al. 1998). Even in modern proglacial environments the solute flux is dominated by carbonate dissolution (Anderson et al. 2000). Beds of limestone and dolostone are therefore not expected among Cryogenian glaciogenic deposits.

However, carbonate minerals do occur in such contexts, the most common being dolomite, often fine-grained and bedded (Table 1.2). Among the better known examples are horizons from Neoproterozoic Svalbard. The within-paradigm response has been to argue that dolomite cannot have formed in warm conditions because the sequences containing them are glaciogenic (Fairchild et al. 1989). Moreover, 'although dolomitization is undoubtedly favoured by increasing temperatures, we now know from modern examples that dolomite can form under cool conditions' (Fairchild 1993). The examples adduced come from Neogene slope sediments north of Little Bahama Bank (Mullins et al. 1985), where the dolomite is a minor (up to 15%) secondary product of aragonite dissolution and Mg addition from interstitial seawater and/or high-Mg calcite. Pore-water temperatures of 5–

10° C are suggested. The surface waters from which the original minerals precipitated would almost certainly have been warmer. Whether the examples from Svalbard formed diagenetically is debatable. What is clear is that, unlike the suggested analogues, they formed in shallow water, not ice, and some were evaporitic (Fig. 1.8). The rise in both $\delta^{13}C$ and $\delta^{18}O$ is the effect of a shallow restricted body progressively losing the lighter molecules, ^{12}C and ^{16}O, over a period too short for the water to be replenished. It is evidence that conditions at the horizons where clastic sedimentation diminished were favourable to dolomite formation and at times extremely warm. This is, after all, the interpretation placed on dolomites precipitated immediately after the diamictites. Although evaporation can occur where the air is dry and cold, as on Antarctica, strong sequential enrichment has yet to be documented and dolomite does not form on Antarctica (Fairchild et al. 2015).

Sampling of a shallow-marine carbonate succession in Anhui Province has provided an opportunity to investigate some of the conditions in which dolomite formed. After 100 m of calcium carbonate the mineralogy abruptly switched to dolomite. What caused the switch? What overcame the kinetic barriers? How alkaline were the waters? Was the dolomite a product of diagenesis or a direct precipitate? These questions are considered in Chapter 2.

1.4.2. *Variation in the marine carbon-isotope signal*

If one considers the carbon-isotope record of the Neoproterozoic as a whole (e.g. Halverson 2010), its most striking aspect is its jaggedness. Values after ~820 Ma are rarely stable for long: they go through excursions positive and negative, and some of the latter appear to be associated with glaciogenic deposits – causally as well as chronologically. The cap carbonates following diamictite successions are invariably depleted. Climate change is therefore attributed, at least in part, to ocean-driven changes in the carbon cycle (Kaufman et al. 1997). More recently, the causality has been complicated by the discovery of two multi-regional, large-scale negative excursions well before the Sturtian episode, dubbed the Bitter Springs and Islay anomalies. Neither coincides with glaciations. The largest of all such excursions, the Shuram anomaly (Le Guerroué et al. 2006), is late Ediacaran, very close in time to the last of the Neoproterozoic diamictites (§1.2). Was this too a global event? Majority opinion is that it was, although synchroneity is difficult to establish and there is no obvious link with climate. Later still, in the Phanerozoic, nearly all negative excursions are associated with global warming, not cooling (Stanley 2010), a common scenario being massive injection of mantle-derived carbon dioxide (e.g. Clarkson et al. 2015).

Clearly a better understanding of the Neoproterozoic carbon-isotope system is needed. An opportunity to investigate the controls on isotopic variability came when samples collected before this project turned out to record an exceptionally early and systematic negative excursion. Chapter

3 reports the work on those samples. Chapter 4 goes on to offer a general explanation of carbon-isotope instability in the Neoproterozoic.

1.4.3. *Chemical weathering*

Earth without an atmosphere would be some 33° C colder and the oceans frozen. That the oceans have always been liquid, even before the Archaean, is due to the greenhouse effect, and apart from water itself the gas doing most to keep the planet warm is carbon dioxide. Since solar radiation was lower in the past, levels of carbon dioxide must have been higher. How much higher is difficult to quantify.

In the absence of direct records of pCO_2, a proxy is needed. The most obvious link is with silicate weathering, and since cooling as a result of falling CO_2 exerts a negative feedback on weathering, the link may be regarded as quite tight. The strongest proxy for silicate weathering, in turn, is the seawater strontium isotope ratio preserved in marine carbonates. There are now many hundreds of strontium isotope measurements for the mid to late Neoproterozoic. Chapter 5 interrogates the data to determine whether ratios dropped as temperatures fell in the approach to the glaciations and rose in their aftermath.

A suite of late-Tonian and Cryogenian rock samples were also collected from the Nanhua Rift Basin of South China. The basin constitutes one of the world's most complete Neoproterozoic records. Before the Ediacaran, the record is almost entirely siliciclastic. Chapter 6 presents an overview of the tectonic context and considers to what extent rifting – beginning around 815 Ma – contributed to sediment generation. During the Tonian, mass flow deposits were dominant: did this pattern suddenly change in the approach to the Cryogenian? Did sea-level show the expected dip as ice sheets sucked water out of the ocean or the expected rise as ice sheets melted? How should one make of the various chemical deposits that punctuated the Neoproterozoic?

Hot, humid climates are conducive to silicate weathering, cold, arid climates are not. As they weather, the principal minerals of igneous rocks change into clay minerals. The 'chemical index of alteration' is a measurement of such weathering, devised specifically to track climate change before, during and after glaciation. Chapter 7 discusses the pitfalls, including the inference that Precambrian rocks were almost ubiquitously affected by potassium metasomatism. Analysis of the South China samples is presented in Chapter 8.

Chapter 9 offers some summarising thoughts about why ocean chemistry in the Proterozoic was different from today. Sustained by high rates of outgassing, seafloor spreading and subduction, atmospheric pCO_2 had a profound effect on geological systems: on weathering intensity, clay

mineral formation, alkalinity, saturation state, dolomite formation and carbon isotope ratios. What may not have been very different is atmospheric O_2. Oxygen, a product of photosynthesis, enters the atmosphere only to the extent that sedimentary burial prevents organic matter – the other product – from being oxidised. Over secular timescales the burial flux has been more or less constant. How tenable, then, is the current view that atmospheric levels in the early Precambrian were negligible, rose in great steps, and did not approach modern levels until after the appearance of animals? The final section considers Neoproterozoic climate change in the light of the terrestrial record. Rodinia was under stress. The first major episode of crustal extension occurred 990–980 Ma, the second 840–820 Ma. The third began in the late Tonian, c. 745 Ma, and continued into the Cryogenian, when rifting climaxed and the supercontinent came apart. As faults released the tension, rift basins widened and sank, and coarse sediment filled them from the crumbling sidewalls. The disturbances, it is proposed, were tectonic rather than climatic.

References

Allen, P.A., Leather, J., Brasier, M.D., 2004. The Neoproterozoic Fiq glaciation and its aftermath, Huqf supergroup of Oman. *Basin Res.* 16, 507–534.

Alvarenga, C.J.S., Trompette, R., 1992. Glacially influenced sedimentation in the later Proterozoic of the Paraguay belt (Mato Grosso, Brazil). *Palaeogeogr. Palaeocl*. 92, 85–105.

Anderson, S.P., Drever, J.I., Frost, C.D., Holden, P., 2000. Chemical weathering in the foreland of a retreating glacier. *Geochim. Cosmochim. Acta* 64, 1173–1189.

Arnaud, E., Eyles, C.H., 2002. Glacial influence on Neoproterozoic sedimentation: the Smalfjord Formation, northern Norway. *Sedimentology* 49, 765–788.

Balgord, E.A., Yonkee, W.A., Link, P.K., Fanning, C.M., 2013. Stratigraphic, geochronologic, and geochemical record of the Cryogenian Perry Canyon Formation, northern Utah: Implications for Rodinia rifting and snowball Earth glaciation. *GSA Bull.* 125, 1442–1467.

Baldwin, G.J., Turner, E.C., Kamber, B.S., 2016. Tectonic controls on distribution and stratigraphy of the Cryogenian Rapitan iron formation, northwestern Canada. *Precambrian Res.* 278, 303–322.

Bao, H., Fairchild, I.J., Wynn, P.M., Spötl, C., 2009. Stretching the envelope of past surface environments: Neoproterozoic glacial lakes from Svalbard. *Science* 323, 119–122.

Baode, G., Ruitang, W., Hambrey, M.J., Wuchen, G., 1986. Glacial sediments and erosional pavements near the Cambrian-Precambrian boundary in western Henan Province, China. *J. Geol. Soc. Lond.* 143, 311–323.

Benn, D.I. et al., 2015. Orbitally forced ice sheet fluctuations during the Marinoan Snowball Earth glaciation. *Nature Geosci.* 8, 704–708.

Berner, R.A., 2006. Inclusion of the weathering of volcanic rocks in the GEOCARBSULF model. *Am. J. Sci*. 306, 295–302.

Bjørnerud, M.G., 2010. Stratigraphic record of Neoproterozoic ice sheet collapse: the Kapp Lyell diamictite sequence, SW Spitsbergen, Svalbard. *Geol. Mag.* 147, 380–390.

Boulton, G.S., Deynoux, M., 1981. Sedimentation in glacial environments and the identification of tills and tillites in ancient sedimentary sequences. *Precambrian Res.* 15, 397–422.

Busfield, M.E., Le Heron, D.P., 2014. Sequencing the Sturtian icehouse: dynamic ice behaviour in South Australia. *J. Geol. Soc. Lond.* 171, 443–456.

Calver, C.R. 1998. Isotope stratigraphy of the Neoproterozoic Togari Group, Tasmania. *Aust. J. Earth Sci.* 45, 865–874.

Carto, S.L., Eyles, N., 2011. The deep-marine glaciogenic Gaskiers Formation, Newfoundland, Canada. In: E. Arnaud, G.P. Halverson, G. Shields-Zhou (eds), *The Geological Record of Neoproterozoic Glaciations*, Geol. Soc. Lond. Mem. 36, 467–473.

Charnay, B. et al., 2013. Exploring the faint young Sun problem and the possible climates of the Archean Earth with a 3-D GCM. *J. Geophys. Res. Atmos.* 118, 1–18.

Chumakov, N.M., 1981. Late Precambrian Churochnaya tillites of the Polyudov Ridge, U.S.S.R. In: M.J. Hambrey, W.B. Harland (eds), *Earth's Pre-Pleistocene Glacial Record*, Cambridge University Press, Cambridge, pp 666–669.

Chumakov, N.M., 2011. Late Proterozoic African glacial era. *Stratigr. Geo. Correl.* 19, 1-20.

Chumakov, N.M., Pokrovsky, B.G., Melezhik, V.A., 2011. The glaciogenic Bol'shoy Patom Formation, Lena River, central Siberia. In: E. Arnaud, G.P. Halverson, G. Shields-Zhou (eds), *The Geological Record of Neoproterozoic Glaciations*, Geol. Soc. Lond. Mem. 36, 309–316.

Clark, P.U. et al., 2009. The Last Glacial Maximum. *Science* 325, 710–714.

Coats, R.P., 1981. Late Proterozoic (Adelaidean) tillites of the Adelaide Geosyncline. In: M.J. Hambrey, W.B. Harland (eds), *Earth's Pre-Pleistocene Glacial Record*, Cambridge University Press, Cambridge, pp 537–547.

Coats, R.P., Preiss, W.V., 1987. Stratigraphy of the Umberatana Group. In: W.V. Preiss (compiler), *The Adelaide Geosyncline*, Bull. Geol. Surv. S. Aust. 53, 125–210.

Cox, G.M. et al., 2013. Neoproterozoic iron formation: An evaluation of its temporal, environmental and tectonic significance. *Chem. Geol.* 362, 232–249.

Cox, G.M. et al., 2016. Continental flood basalt weathering as a trigger for Neoproterozoic Snowball Earth. *Earth Planet. Sci. Lett.* 446, 89–99.

Dessert, C., Dupré, B., Gaillardet, J., François, L.M., Allègre, C.J., 2003. Basalt weathering laws and the impact of basalt weathering on the global carbon cycle. *Chem. Geol*. 202, 257–273.

Domack, E.W., Hoffman, P.H., 2011. An ice grounding-line wedge from the Ghaub glaciation (635 Ma) on the distal foreslope of the Otavi carbonate platform, Namibia, and its bearing on the snowball Earth hypothesis. *GSA Bull.* 123, 1448–1477.

Donnadieu, Y., Godderis, Y., Ramstein, G., Nedelec, A., Meert, J., 2004. A 'snowball Earth' climate triggered by continental break-up through changes in runoff. *Nature* 428, 303–306.

Dowdeswell, J.A. et al., 2002. On the architecture of high-latitude continental margins: the influence of ice-sheet and sea-ice processes in the Polar North Atlantic. In: J.A. Dowdeswell, C.Ó Cofaigh (eds), *Glacier-Influenced Sedimentation on High-Latitude Continental Margins*, Geol. Soc. Lond. Spec. Pub. 203, 33–54.

Etienne, J.L., Allen, P.A., Rieu, R., Le Guerroué, E., 2007. Neoproterozoic glaciated basins: a critical review of the Snowball Earth hypothesis by comparison with Phanerozoic glaciations. In M.J. Hambrey et al. (eds), *Glacial Sedimentary Processes and Products*, IAS Spec. Pub., Wiley-Blackwell, pp 343–399.

Evans, D.A.D., Raub, T.D., 2011. Neoproterozoic glacial palaeolatitudes: a global update. In: E. Arnaud, G.P. Halverson, G. Shields-Zhou (eds), *The Geological Record of Neoproterozoic Glaciations*, Geological Society, London, Memoir 36, 93–112.

Eyles, N., Januszczak, N. 2004. 'Zipper-rift': a tectonic model for Neoproterozoic glaciations during the breakup of Rodinia after 750 Ma. *Earth-Sci. Rev.* 65, 1–73.

Fairchild, I.J., 1993. Balmy shores and icy wastes: The paradox of carbonates associated with glacial deposits in Neoproterozoic times. *Sedimentology Review* 1, 1–16.

Fairchild, I.J., 2016. Neoproterozoic glass-bleeding. *Nature Geosci.* 9, 192–193.

Fairchild, I.J., Hambrey, M.J., Spiro, B., Jefferson, T.H., 1989. Late Proterozoic glacial carbonates in northeast Spitsbergen new insights into the carbonate-tillite association. *Geol. Mag.* 126, 469–490.

Fairchild, I.J. et al., 2016. Continental carbonate facies of a Neoproterozoic panglaciation, north-east Svalbard. *Sedimentology* 63, 443–497.

Feng, L., Zhang, Q., 2016. The pre-Sturtian negative $\delta^{13}C$ excursion of the Dajiangbian Formation deposited on the western margin of Cathaysia Block in South China. *J. Earth Sci.* 27, 225–232.

Frei, R., Gaucher, C., Stolper, D., Canfield, D.E., 2013. Fluctuations in late Neoproterozoic atmospheric oxidation — Cr isotope chemostratigraphy and iron speciation of the late Ediacaran lower Arroyo del Soldado Group (Uruguay). *Gondwana Res*. 23, 797–811.

Freitas, B.T., Warren, L.V., Boggiani, P.C., De Almeida, R.P., Piacentini, T., 2011. Tectono-sedimentary evolution of the Neoproterozoic BIF-bearing Jacadigo Group, SW-Brazil. *Sediment. Geol.* 238, 48–70.

Geboy, N.J. et al., 2013. Re–Os age constraints and new observations of Proterozoic glacial deposits in the Vazante Group, Brazil. *Precambrian Res.* 238, 199–213.

Giddings, J.A., Wallace, M.W., 2009. Sedimentology and C-isotope geochemistry of the 'Sturtian' cap carbonate, South Australia. *Sediment. Geol.* 216, 1–14.

Given, R.K., Wilkinson, B.H., 1987. Dolomite abundance and stratigraphic age: constraints on rates and mechanisms of Phanerozoic dolostone formation. *J. Sed. Petrol.* 57, 1068–1078.

Goddéris, Y. et al., 2003. The Sturtian 'snowball' glaciation: fire and ice. *Earth Planet. Sci. Lett.* 211, 1–12.

Goddéris, Y., Le Hir, G., Donnadieu, Y., 2011. Modelling the Snowball Earth. In: E. Arnaud, G.P. Halverson, G. Shields-Zhou (eds), *The Geological Record of Neoproterozoic Glaciations*, Geol. Soc. Lond. Mem. 36, 151–161.

Grotzinger, J.P., James, N.P., 2000. Precambrian carbonates: evolution of understanding. In: N.P. James (ed.), *Carbonate Sedimentation and Diagenesis in the Evolving Precambrian World*, SEPM Spec. Pub. 67, 3-20.

Groves, D.I., Bierlein, F.P., Meinert, L.D., Hitzman, M.W., 2010. Iron oxide copper-gold (IOCG) deposits through Earth history: Implications for origin, lithospheric setting, and distinction from other epigenetic iron oxide deposits. *Econ. Geol.* 105, 641–654.

Halverson, G.P., Maloof, A.C., Hoffman, P.F., 2004. The Marinoan glaciation (Neoproterozoic) in northeast Svalbard. *Basin Res.* 16, 297–324.

Halverson, G.P., Wade, B.P., Hurtgen, M.T., Barovich, K.M. 2010. Neoproterozoic chemostratigraphy. *Precambrian Res*. 182, 337–350.

Hambrey, M.J., 1983. Correlation of Late Proterozoic tillites in the North Atlantic region and Europe. *Geol. Mag*. 120, 209--232.

Harland, W.B. 1964. Critical evidence for a great infra-Cambrian glaciation. *Geol. Rundsch*. 54, 45-61.

Harland, W.B., Herod, K.N., Krinsley, D.H., 1966. The definition and identification of tills and tillites. *Earth-Sci. Rev.* 2, 225–256.

Harland, W.B., Rudwick, M. J. S. 1964. The great infra-Cambrian ice age. *Sci. Am*., August, 42–49.

He, J., Zhu, W., Ge, R., 2014. New age constraints on Neoproterozoic diamicites in Kuruktag, NW China and Precambrian crustal evolution of the Tarim Craton. *Precambrian Res.* 241, 44–60.

Hebert, C.L., Kaufman, A.J., Penniston-Dorland, S.C., Martin, A.J., 2010. Radiometric and stratigraphic constraints on terminal Ediacaran (post-Gaskiers) glaciation and metazoan evolution. *Precambrian Res.* 182, 402–412.

Hitzman, M.W., Oreskes, N., Einaudi, M.T., 1992. Geological characteristics and tectonic setting of Proterozoic iron oxide (Cu-U-Au-REE) deposits. *Precambrian Res.* 58, 241–287.

Hoffman, P.F., 2011. Strange bedfellows: glacial diamictite and cap carbonate from the Marinoan (635 Ma) glaciation in Namibia. *Sedimentology* 58, 57–119.

Hoffman, P., 2011. A history of Neoproterozoic glacial geology, 1871-1997. In: E. Arnaud, G.P. Halverson, G. Shields-Zhou (eds), *The Geological Record of Neoproterozoic Glaciations*, Geol. Soc. Lond. Mem. 36, 17–37.

Hoffman, P.F., Kaufman, A.J., Halverson, G.P., Schrag, D.P., 1998. A Neoproterozoic Snowball Earth. *Science* 281, 1342–1346.

Hoffman, P.F., Schrag, D.P., 2000. Snowball Earth, *Sci. Am.*, January, 68–75.

Hoffman, P.F., Schrag, D.P., 2002. The snowball Earth hypothesis: testing the limits of global change. *Terra Nova* 14, 129–155.

Hoffman, P.F. et al., 2007. Are basal Ediacaran (635 Ma) post-glacial "cap dolostones" diachronous? *Earth Planet. Sci. Lett*. 258, 114–131.

Hoffmann, K.H., Condon, D.J., Bowring, S.A., Crowley, J.L., 2004. U-Pb zircon date from the Neoproterozoic Ghaub Formation, Namibia: Constraints on Marinoan glaciation. *Geology* 3, 817–820.

Hofmann, M. et al., 2015. The four Neoproterozoic glaciations of southern Namibia and their detrital zircon record: The fingerprints of four crustal growth events during two supercontinent cycles. *Precambrian Res.* 259, 176–188.

Hore, S. (cartographer and compiler), 2015. *Mount Painter Region*, Adelaide Geological Survey of South Australia.

Jenkins, R.J.F., 2011. Billy Springs glaciation, South Australia. In: E. Arnaud, G.P. Halverson, G. Shields-Zhou (eds), *The Geological Record of Neoproterozoic Glaciations*, Geol. Soc. Lond. Mem. 36, 693–699.

Kaufman, A.J., Knoll, A.H., Narbonne, G.M., 1997. Isotopes, ice ages, and terminal Proterozoic earth history. *Proc. Nat. Acad. Sci. USA* 94, 6600–6605.

Kellerhals, P., Matter, A., 2003. Facies analysis of a glaciomarine sequence, the Neoproterozoic Mirbat Sandstone Formation, Sultanate of Oman. *Eclogae Geol. Helv.* 96, 49–70.

Kennedy, M.J., Christie-Blick, N., Prave, A.R., 2001a. Carbon isotopic composition of Neoproterozoic glacial carbonates as a test of paleoceanographic models for snowball Earth phenomena. *Geology* 29, 1135–1138.

Kennedy, M.J., Christie-Blick, N., Sohl, L.E., 2001b. Are Proterozoic cap carbonates and isotopic excursions a record of gas hydrate destabilization following Earth's coldest intervals? *Geology* 29, 443–446.

Kennedy, M.J., Runnegar, B., Prave, A.R., Hoffmann, K.-H., Arthur, M.A., 1998. Two or four Neoproterozoic glaciations? *Geology* 26, 1059–1063.

Kerr, R.A., 2010. Snowball Earth has melted back to a profound wintry mix. *Science* 327, 1186.

Kirschvink, J.L., 1992. Late Proterozoic low-latitude global glaciation: the Snowball Earth. In: J.W. Schopf, C. Klein (eds),*The Proterozoic Biosphere: A Multidisciplinary Study*, Cambridge University Press, Cambridge, pp 51-52.

Klein, C., Beukes, N.J., 1993. Sedimentology and geochemistry of the glacigenic Late Proterozoic Rapitan iron-formation in Canada. *Econ. Geol.* 88, 542–565.

Kumar, A., Heaman, L.M., Manikyamba, C., 2007. Mesoproterozoic kimberlites in south India: A possible link to ~1.1 Ga global magmatism. *Precambrian Res.* 154, 192–204.

Kunzmann, M., Halverson, G.P., Scott, C., Minarik, W.G., Wing, B.A., 2015. Geochemistry of Neoproterozoic black shales from Svalbard: Implications for oceanic redox conditions spanning Cryogenian glaciations. *Chem. Geol.* 147, 383–393.

Leather, J., Allen, P.A., Brasier, M.D., Cozzi, A., 2002. Neoproterozoic snowball earth under scrutiny: evidence from the Fiq glaciation of Oman. *Geology* 30, 891–894.

Le Guerroué, E., Allen, P.A., Cozzi, A., 2005. Two distinct glacial successions in the Neoproterozoic of Oman. *GeoArabia* 10, 17–34.

Le Guerroué, E., Allen, P.A., Cozzi, A., 2006. Chemostratigraphic and sedimentological framework of the largest negative carbon isotopic excursion in Earth history: The Neoproterozoic Shuram Formation (Nafun Group, Oman). *Precambrian Res.* 146, 68–92.

Le Heron, D.P., 2015. The significance of ice-rafted debris in Sturtian glacial successions. *Sed. Geol.* 322, 19–33.

Le Heron, D.P., Busfield, M.E., Collins, A.S., 2014. Bolla Bollana boulder beds: A Neoproterozoic trough mouth fan in South Australia? *Sedimentology* 61, 978–995.

Le Heron, D.P., Busfield, M.E., Kamona, F., 2012. An interglacial on snowball Earth? Dynamic ice behaviour revealed in the Chuos Formation, Namibia. *Sedimentology* 60, 411-427.

Le Heron, D.P., Cox, G., Trundley, A., Collins. A.S., 2011.Two Cryogenian glacial successions compared: Aspects of the Sturt and Elatina sediment records of South Australia. *Precambrian Res.* 186, 147–168.

Lee, H. et al., 2016. Massive and prolonged deep carbon emissions associated with continental rifting. *Nature Geosci.* 9, 145–150.

Li, Z.X., Evans, D.A.D., Halverson, G.P., 2013. Neoproterozoic glaciations in a revised global palaeogeography from the breakup of Rodinia to the assembly of Gondwanaland. *Sed. Geol.* 294, 219–232.

Liao, S.F., 1981. Sinian glacial deposits of Guizhou Province, China. *In*: M.J. Hambrey, W.B. Harland (eds), *Earth's Pre-Pleistocene Glacial Record,* Cambridge University Press, Cambridge, pp 414–423.

Liu, Y., Peltier, W.R., 2013. Sea level variations during snowball Earth formation: 1. A preliminary analysis. *J. Geophys. Res. Solid Earth* 118, 4410–4425.

Lottermoser, B.G., Ashley, P.M., 2000. Geochemistry, petrology and origin of Neoproterozoic ironstones in the eastern part of the Adelaide Geosyncline, South Australia. *Precambrian Res*. 101, 49– 67.

Macdonald, F.A., McClelland, W.C., Schrag, D.P., Macdonald, W.P., 2009. Neoproterozoic glaciation on a carbonate platform margin in Arctic Alaska and the origin of the North Slope subterrane. *GSA Bull.* 121, 448–473.

Macdonald, F.A., Strauss, J.V., Rose, C.V., Dudas, F.O., Schrag, D.P., 2010a. Stratigraphy of the Port Nolloth Group of Namibia and South Africa and implications for the age of Neoproterozoic iron formations. *Am. J. Sci.* 310, 862–888.

Macdonald, F.A. et al., 2010b. Calibrating the Cryogenian. *Science* 327, 1241–1243.

Maslov, A.V. et al., 2013. New constraints for the age of Vendian glacial deposits (Middle Urals). *Doklady Earth Sciences* 449, 303–308.

McGee, B., Collins, A.S., Trindale, R.I.F., 2013. Glacially incised canyon in Brazil: further evidence for mid-Ediacaran glaciation? *J. Geol.* 121, 275–287.

McMechan, M.E., 2000. Vreeland diamictites – Neoproterozoic glaciogenic slope deposits, Rocky Mountains, Northeast British Columbia. *Bull. Can. Petrol. Geol*. 48, 246–261.

Miller, N.R. et al., 2003. Significance of the Tambien Group (Tigrai, N. Ethiopia) for Snowball Earth events in the Arabian–Nubian Shield. *Precambrian Res.* 121, 263–283.

Miller, R.M., Frimmel, H.E., Halverson, G., 2010. Passive continental margin evolution. In: C. Gaucher et al. (eds), *Neoproterozoic-Cambrian Tectonics, Global Change and Evolution, A Focus on Southwestern Gondwana*, Elsevier, Amsterdam, pp 161-181.

Mrofka, D., Kennedy, M., 2011. The Kingston Peak Formation in the eastern Death Valley region. In: E. Arnaud, G.P. Halverson, G. Shields-Zhou (eds), *The Geological Record of Neoproterozoic Glaciations*, Geol. Soc. Lond. Mem. 36, 449–458.

Mudelsee, M., Bickert, T., Lear, C.H., Lohmann G., 2014. Cenozoic climate changes: A review based on time series analysis of marine benthic $\delta^{18}O$ records. *Rev. Geophys. 52*, 333–374.

Mullins, H.T. et al., 1985. Authigenic dolomite in Bahamian peri-platform slope sediment. *Geology* 13, 292–295.

Mustard, P.S., Donaldson, J.A., 1987. Early Proterozoic ice-proximal glaciomarine deposition: The lower Gowganda Formation at Cobalt, Ontario, Canada. *GSA Bull.* 98, 373–387.

Myrow, P.M. et al., 2015. Depositional history, tectonics, and provenance of the Cambrian-Ordovician boundary interval in the western margin of the North China block. *GSA Bull.* 127, 1174–1193.

Nascimento, D.B., Ribeiro, A., Trouw, R.A.J., Schmitt, R.S., Passchier, C.W., 2016. Stratigraphy of the Neoproterozoic Damara Sequence in northwest Namibia: Slope to basin sub-marine mass-transport deposits and olistolith fields. *Precambrian Res.* 278, 108–125.

O'Grady, D.B., Syvitski, J.P.M., 2002. Large-scale morphology of Arctic continental slopes: the influence of sediment delivery on slope form. In: J.A. Dowdeswell, C. Ó Cofaigh (eds), *Glacier-Influenced Sedimentation on High-Latitude Continental Margins*, Geol. Soc. Lond. Spec. Pub. 203, 11–31.

Planavsky, N.J. et al., 2011. Widespread iron-rich conditions in the mid-Proterozoic ocean. *Nature* 477, 448–452.

Pokrovsky, B.G., Bujakaite, M.I., 2016. Isotopic compositions of C, O, Sr, and S and problem of ages of the Katera and Uakit Groups, Western Transbaikal Region. *Lithol. Miner. Resour.* 51, 262–282.

Polanyi, M., 1958. *Personal Knowledge*, Routledge & Kegan Paul, London.

Popper, K., 1965. *Conjectures and Refutations: The Growth of Scientific Knowledge*, Routledge, London.

Popper, K., 1959. *The Logic of Scientific Discovery,* Hutchinson & Co, New York. Originally published in 1935 as *Logik der Forschung*.

Prave, A.R., Condon, D.J., Hoffmann, K.H., Tapster, S., Fallick, A.E., 2016. Duration and nature of the end-Cryogenian (Marinoan) glaciation. *Geology* doi:10.1130/G38089.1.

Prave, A.R., Hoffmann, K.H.,Hegenberger, W., 2011. The Witvlei Group of East-Central Namibia. In: E. Arnaud, G.P. Halverson, G. Shields-Zhou (eds), *The Geological Record of Neoproterozoic Glaciations*, Geol. Soc. Lond. Mem. 36, 211–216.

Preiss, W.V., 1999. Parachilna Sheet SH54-13. 1:250 000 scale Geological Map and Explanatory Notes, 2nd edn. Primary Industries and Resources, South Australia.

Preiss, W.V., 2000. The Adelaide Geosyncline of South Australia and its significance in Neoproterozoic continental reconstruction. *Precambrian Res.* 100, 21–63.

Preiss, W.V. et al., 2011. The glacial succession of Sturtian age in South Australia: the Yudnamutana Subgroup. In: E. Arnaud, G.P. Halverson, G. Shields-Zhou (eds), *The Geological Record of Neoproterozoic Glaciations*, Geol. Soc. Lond. Mem 36, 701–712.

Pu, J.P. et al., 2016. Dodging snowballs: Geochronology of the Gaskiers glaciation and the first appearance of the Ediacaran. *Geology* doi:10.1130/G38284.1.

Rasmussen, B. et al., 2012. Deposition of 1.88-billion-year-old iron formations as a consequence of rapid crustal growth. *Nature* 484, 498–501.

Ruhl, M., Bonis, N.R., Reichart, G.-J., Sinninghe Damsté, J.S., Kürschner, W.M., 2011. Atmospheric carbon injection linked to end-Triassic mass extinction. *Science* 333, 430–434.

Schaller, M.F., Wright, J.D., Kent, D.V., Olsen, P.E., 2012. Rapid emplacement of the Central Atlantic Magmatic Province as a net sink for CO_2. *Earth Planet. Sci. Lett.* 323–324, 27–39.

Schermerhorn, L.J.G., 1974. Late Precambrian mixtites: glacial and/or nonglacial? *Am. J. Sci*. 274, 673–824.

Schrag, D.P., Berner, R.A., Hoffman, P.F., Halverson, G.P., 2002. On the initiation of a snowball Earth. *Geochem. Geophys. Geosyst*. 3, 10.1029/2001GC000219.

Smith, M.D., Arnaud, E., Arnott, R.W.C., Ross, G.M., 2011. The record of Neoproterozoic glaciation in the Windermere Supergroup, southern Canadian Cordillera. In: In: E. Arnaud, G.P. Halverson, G. Shields-Zhou (eds), *The Geological Record of Neoproterozoic Glaciations*, Geol. Soc. Lond. Mem. 36, 413–423.

Smolin, L., 2007. *The Trouble with Physics*, Allen Lane, London.

Spencer, A.M. 1971. *Late Precambrian Glaciation in Scotland*. Mem. Geol. Soc., Lond., 6.

Spencer, A.M., 1985. Mechanisms and environments of deposition of Late Precambrian geosynclinal tillites: Scotland and East Greenland. *Palaeogeogr. Palaeocl*. 51, 143–157.

Stanley, S.M., 2010. Relation of Phanerozoic stable isotope excursions to climate, bacterial metabolism, and major extinctions. *Proc. Natl. Acad. Sci. USA* 107, 19185–19189.

Stern, R.J., Mukherjee, S.K., Miller, N.R., Ali, K., Johnson, P.R., 2013. ~750 Ma banded iron formation from the Arabian-Nubian Shield—Implications for understanding Neoproterozoic tectonics, volcanism, and climate change. *Precambrian Res.* 239, 79–94.

Stoker, M.S., Howe, J.A., Stoker, S.J., 1999. Late Vendian–?Cambrian glacially influenced deep-water sedimentation, Macduff Slate Formation (Dalradian), NE Scotland. *J. Geol. Soc. Lond.* 156, 55–61.

Swanson-Hysell, N.L. et al., 2015. Stratigraphy and geochronology of the Tambien Group, Ethiopia: Evidence for globally synchronous carbon isotope change in the Neoproterozoic. *Geology* 43, 323–326.

Walter, M.R., Veevers, J.J., Calver, C.R., Gorjan, P., Hill, A.C., 2000. Dating the 840–544 Ma Neoproterozoic interval by isotopes of strontium, carbon, and sulfur in seawater, and some interpretative models. *Precambrian Res.* 100, 371–433.

Wang, J., Li, Z.X., 2003. History of Neoproterozoic rift basins in South China: implications for Rodinia break-up. *Precambrian Res*. 122, 141–158.

Wegener, A., 1912. Die Entstehung der Kontinente. *Geol. Rundsch*. 3, 276–292. Eng. trans. R. von Huene, 2002. The origins of continents. *Int. J. Earth. Sci*. 91, S4–S17.

Wehr, F., 1986. A proglacial origin for the upper Proterozoic Rockfish Conglomerate, central Virginia, U.S.A. *Precambrian Res*. 34, 157–174.

Wolf, E.T., Toon, O.B., 2013. Hospitable Archean climates simulated by a general circulation model. *Astrobiology* 13, 656–674.

Xiao, S. et al., 2004. The Neoproterozoic Quruqtagh Group in eastern Chinese Tianshan: evidence for a post-Marinoan glaciation. *Precambrian Res.* 130, 1–26.

Xu, B. et al., 2009. SHRIMP zircon U–Pb age constraints on Neoproterozoic Quruqtagh diamictites in NW China. *Precambrian Res.* 168, 247–258.

Ye, Q. et al., 2015. The survival of benthic macroscopic phototrophs on a Neoproterozoic snowball Earth. *Geology* 53, 507–510.

Yonkee, W.A. et al. 2014. Tectono-stratigraphic framework of Neoproterozoic to Cambrian strata, west-central U.S.: Protracted rifting, glaciation, and evolution of the North American Cordilleran margin. *Earth-Sci. Rev.* 136, 59–95.

Young, G.M. 1973. Late Precambrian mixtites: glacial and/or non-glacial? *Am. J. Sci.* 276, 366–370.

Young, G.M., 1992. Neoproterozoic glaciation in the Broken Hill area, New South Wales, Australia. *GSA Bull*. 104, 840–850.

Young, G.M., Gostin, V.A., 1988. Stratigraphy and sedimentology of Sturtian glacigenic deposits in the western part of the North Flinders Basin, South Australia. *Precambrian Res.* 39, 151–170.

Zhang, Q.R. Chu, X.L., Feng, L.J., 2011. Neoproterozoic glacial records in the Yangtze Region, China. In: E. Arnaud, G.P. Halverson, G. Shields-Zhou (eds), *The Geological Record of Neoproterozoic Glaciations*, Geol. Soc. Lond. Mem. 36, 357–366.

CHAPTER TWO

The Jiuliqiao and Sidingshan Formations, Anhui Province, North China: a model system of marine Mg-Ca carbonate and siliciclastic sedimentation in the early Neoproterozoic

Abstract

Dolomite, $CaMgCO_3$, is a common mineral in the marine geological record, especially in the Precambrian, but its precipitation from seawater is ordinarily prevented by kinetic barriers. Instead, the mineral forms from already precipitated calcium carbonate and the barriers are overcome via sulphate-reducing microbes (SRM). Although calcium carbonate and dolomite are end-members of a solid-solution series, rock compositions tend to be bimodal: either Mg-poor or Mg-rich. On the other hand, experiments at high temperature (> 100° C) indicate that dolomitisation proceeds via an intermediate phase. How the findings relate to dolomite formation at Earth-surface temperatures is not well understood, nor why the barriers to formation were more easily overcome in the Precambrian than today.

The Neoproterozoic sequence investigated here went through an abrupt switch from limestone to dolostone at the formation boundary half way through its 200 m thickness and provides an ideal opportunity to investigate these questions. Carbonate minerals are surprisingly heterogeneous. The most common phases are magnesian calcite (molar $MgCO_3$ 3–11%), very high magnesian calcite (VHMC, 24–40%), and dolomite (44–51%). Far fewer compositions lie outside these ranges. Most limestones include patches of VHMC. Mg-enrichment began soon after deposition, involved dissolution of the precursor, and continued until recrystallisation and compaction closed up pore space, leaving the metastable intermediate phases preserved.

Although also not homogeneous, the dolostones are less variable. Several lines of evidence indicate that the dolomite was primary, notably absence of remnant calcite, small crystal size, and carbon and oxygen isotope values differing from those of the limestones by the margin expected if dolomite was an independent mineral. Lower concentrations of sulphur and a large rise in sulphate-pyrite $\delta^{34}S$ fractionation suggest that SRM were instrumental in liberating Mg ions from their bonds with sulphate.

The Jiuliqiao and lower Sidingshan Formations may be fairly described as a mineralogical Lagerstätte, affording unparalleled insight into the nature of early Neoproterozoic carbonate production. Unlike the dolomite, the calcium carbonate formed *in situ*, amongst synsedimentary K-feldspar, quartz and illite. The squashed spherical form of the carbonate grains suggests that the original phase may have been vaterite. Feldspar is often fossilised in a state of partial dissolution, with sharp reaction fronts between largely unaltered feldspar and remnant quartz. Leaching of potassium ions increased the already elevated ambient alkalinity and vaterite precipitated in response, even within the feldspar. Alkalinity in the Sidingshan waters was lower, but still sufficient to dissolve feldspar. There the replacing carbonate was calcitic dolomite.

TOC correlates with the silicate fraction in the limestones but not the dolostones, reflecting different ecologies. In the one, organic production was controlled by nutrient supply. In the other, the clastic flux was lower and nutrients had to be recycled; arguably, gross production was dominated by species adapted to oligotrophic conditions. Petrographic evidence suggests a switch from a bacteria- to a microalgae-dominated ecology. Sulphate originated from the oxidation of oceanic sulphide, and was also continually recycled. Below the uppermost layer, the shallow dolomite-forming waters appear to have been anoxic.

2.1. Introduction

Nearly all marine carbonates forming today consist of calcium carbonate, with little or no magnesium. Some form as aragonite ooze in tropical and equatorial shallows; most are residues of zooplankton whose calcite shells have settled on the deep-sea floor. Although the upper 100 m of the ocean are supersaturated in respect of calcium and magnesium carbonate, kinetic factors inhibit spontaneous precipitation (Wright & Oren 2005). Carbonate sediment mostly consists of skeletal fragments because organisms that synthesise aragonite, low-Mg calcite or high-Mg calcite ($MgCO_3$ > 4%) are able to overcome the kinetic barriers. Cements, being secondary precipitates, are typically richer in Mg (11–13% Morse et al. 2006, up to 19% Mucci 1987). Dolomite proper tends to be restricted to evaporitic settings, where it is promoted by high temperatures and high concentrations of Mg. High temperatures need not be critical. Dolomite, possibly directly precipitated, occurs in the organic-rich sediments of Canadian lakes (Last & Last 2012). Secondary dolomite (Kelts & McKenzie 1982) and VHMC (Mullins et al. 1985) have been found in organic-rich sediments of the deep sea. The molar $MgCO_3$ content of most deep-sea calcium carbonate is < 0.1% (Mackenzie & Garrels 1966).

In the Precambrian, levels of atmospheric CO_2, silicate weathering (which generates bicarbonate) and carbonate saturation state were all higher. Strictly abiotic precipitation of calcium carbonate (evidenced, for example, by aragonite seafloor fans, herring-bone calcite and marine tufas) was much more common, declining through the Proterozoic as saturation state declined (Grotzinger & James 2000). Accompanying the decline, microbially mediated precipitation played a proportionally greater role, as photosynthesisers on the seafloor (microbial mats) consumed CO_2 and increased alkalinity. Most carbonate production took place in epicontinental settings. As a proportion of total carbonate, dolomite was much more common than now (Ronov 1964, Tucker 1992), and formed over a wider range of depths.

Seawater is supersaturated in respect of carbonate minerals chiefly because the thermodynamic factors that favour precipitation are counteracted by the covalent bonding of Ca and Mg ions with water molecules, hydroxyl ions and sulphate ions. Ca and Mg both have high hydration energies compared to Na and Cl (the most abundant elements dissolved in seawater); they hydrate more readily and their activities are correspondingly reduced. The hydration bond of Mg, which is especially strong, is the main reason for dolomite's high activation energy (Arvidson & Mackenzie 1999). Complexing also occurs between the cations and the carbonate and bicarbonate anions; the activity of CO_3^{2-} may be reduced by 90% or more, and again, Mg ions are more prone to complexing than Ca ions. Direct precipitation of dolomite by the ionic bonding of Ca^{2+} and Mg^{2+} with CO_3^{2-} is thus prevented. In the absence of organic mediation dolomite cannot be synthesised under normal-salinity Earth-surface conditions.

Dolomite precipitation is most commonly mediated by sulphate-reducing microbes (Deng et al. 2010). In the sediment these anaerobes decompose organic carbon and cycle it back into inorganic carbon. The products are bicarbonate and hydrogen sulphide:

$$2CH_2O + MgSO_4^0 \rightarrow H_2S + 2HCO_3^- + Mg^{2+} \quad (1)$$

Only 10% of seawater Mg^{2+} is complexed with SO_4 (Pytkowicz & Hawley 1974). However, hydrogen sulphide promotes the dehydration of the remaining Mg^{2+} (Zhang et al. 2012b), and dissociation of bicarbonate promotes the production of calcium carbonate:

$$2HCO_3^- \rightarrow CO_3^{2-} + H_2O + CO_2 \quad (2)$$

$$Ca^{2+} + CO_3^{2-} \rightarrow CaCO_3 \quad (3)$$

Bicarbonate from reaction (1) promotes the formation of Mg-carbonate indirectly, as calcium carbonate at the crystal–water interface dissolves, then combines with newly liberated magnesium and carbonate from the reversal of reaction (3):

$$1{+}xCa^{2+} + 1{-}xMg^{2+} + 2CO_3 \rightarrow Ca_{1+x}Mg_{1-x}(CO_3)_2 \qquad (4)$$

Although preceded by the dissolution of calcium carbonate, equation (4) also describes the direct precipitation of dolomite. Direct precipitation mediated by SRM has been documented in hypersaline lakes and lagoons (Wright & Wacey 2005, Vasconcelos et al. 2005). However, in most environments dolomite forms from intermediate Mg-Ca phases, as it does during high-temperature synthesis of the mineral (Katz & Matthews 1977). Compelling evidence of primary growth except as cement (Mitchell et al. 1987, Hood & Wallace 2011) has rarely been adduced from the marine geological record. Instances include microbial carbonates from the Late Triassic (Mastandrea et al. 2006, Preto et al. 2015). The original mineral of carbonate formed by biomineralising organisms is necessarily calcite or aragonite.

In addition to increasing the activity of Mg^{2+}, SRM promote dolomite nucleation by electronegative attraction of Mg and Ca ions onto their cell walls (van Lith et al. 2003, Roberts et al. 2013). Most organic matter in Proterozoic seas was probably cyanobacterial and would have had the same effect (Bontognali et al. 2008, Krause et al. 2012, Zhang et al. 2012a). Decayed cyanobacterial sheaths and mucilage contain high amounts of these elements (Gebelein & Hoffman 1973, Dupraz et al. 2004, Baumgartner et al. 2006). On remineralisation (the decomposition of solid organic carbon back into dissolved inorganic carbon) the ions return to the water, thereby increasing local salinity. Finally, ammonia from the enzymatic break-down of bacterial and algal protein reacts with water to raise alkalinity and pH (Slaughter & Hill 1991).

In small amounts dolomite, along with magnesian calcite, can be synthesised without organic mediation if calcium sulphate is absent and seawater salinity (not including carbonate ions) at least three times normal (Liebermann 1967). Hypersalinity militates against dolomite precipitation (Folk & Land 1975). In the case of calcium carbonate, degree of saturation may be defined as:

$$\Omega = \frac{[Ca^{2+}] \,.\, [CO_3^{2-}]}{K_{sp}} \qquad (5)$$

where square brackets refer to effective concentrations (activities) and K_{sp} is the solubility product for the specified temperature, salinity and pressure. A system is saturated where $\Omega = 1$, over-saturated where $\Omega > 1$. Although calcite solubility increases as a function of seawater Mg/Ca (Tyrrell & Zeebe 2004), fluid inclusion data suggest that Mg and Ca concentrations, currently around 53.3 and 10.5 mmol/L respectively, have varied by no more than a factor of 3.5. Carbonate concentration, on the other hand, varies with atmospheric pCO_2. Now around 200 μmol/L, in the Precambrian seawater $[CO_3^{2-}]$ may have been similar to $[Ca^{2+}]$ (Grotzinger & Kasting 1993). In

such circumstances, saturation state in respect of calcium carbonate and dolomite would have been higher and the minerals have precipitated much more easily.

Magnesium ions in seawater can substitute for calcium in varying proportions, from pure calcium carbonate, $CaCO_3$, to pure dolomite, $Ca_{0.5}Mg_{0.5}CO_3$, normally via dissolution of one phase and recrystallisation of another richer in Mg. However, the resultant Mg/Ca ratios do not form a continuous series (Chave 1954, Sperber et al. 1984). Most Palaeozoic rocks consist either of low-Mg calcite (up to 4% mole $MgCO_3$) or dolomite close to stoichiometric (45–50%). Proterozoic rocks show a similar dichotomy (Veizer 1978, Sochava & Podkovyrov 1995). The end-members are the most stable, least soluble phases. Intermediate phases over time may have progressed to the one or reverted to the other; or they may never have been common. With regard to Palaeozoic examples, Sperber et al. (1984) attributed the dichotomy to two different types of diagenetic environment, one closed to further Mg input (restricting development of the mineral), the other open (allowing calcium carbonate over time to be fully dolomitised). In the Proterozoic, the diagenetic environment was less conducive to progressive dolomitisation, since carbonate sediment, being non-bioclastic, was generally less porous. It also lithified more rapidly (Knoll et al. 1993, Shields 2002), possibly within weeks (Bartley 1996). Contrary to models requiring millions of years (as reviewed in Warren 2000, Machel 2004), in many cases dolomite formation preceded lithification.

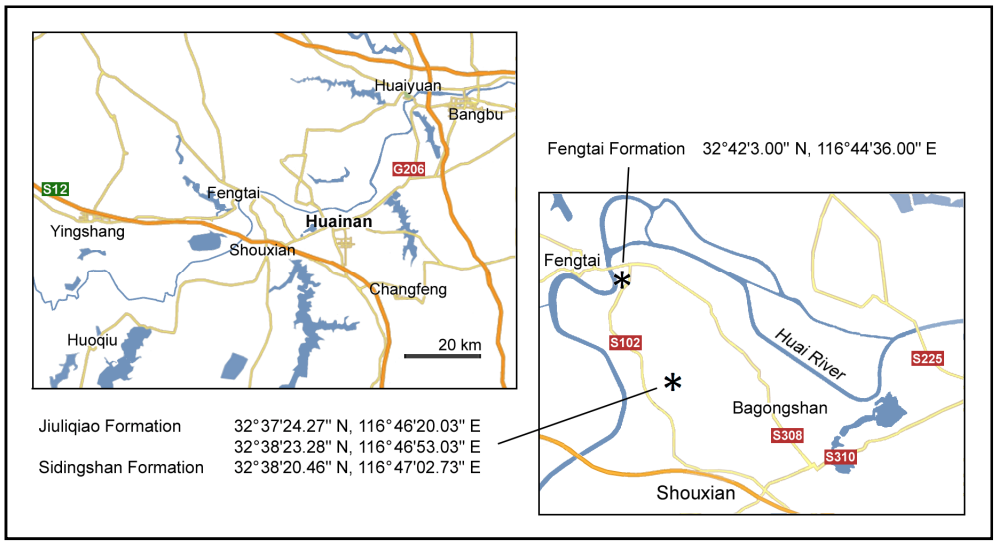

Figure 2.1. Outcrop locations relative to the city of Huianan, northern Anhui Province, China.

2.2. Geological setting

The main section studied was a quarry and hillside 5 km west of Bagongshan, Anhui Province, China (Fig. 2.1), here named the Xishantao section. It encompasses all the Juiliqiao Formation and all but the topmost part of the Sidingshan Formation. Together with the underlying Shouxian

Dates (Ma)	LIAONING *East*	E of HUAIBEI *East*	HUAINAN *South*	HUOQIU *South*
510	Jianchang	Houjiashan	Houjiashan	Houjiashan
520	*unconformity*	Gouhou	*unconformity*	Yutaishan
		disconformity		Longxian Mb
<711	Dalinzi			*unconformity*
<733	Getun			
≤820	*disconformity*	Jinshanzhai		
		disconformity	Fengtai Mb	Fengtai Mb
~925	Xingmincun	Wangshan	Sidingshan	Sidingshan
≤955	Cuijiatun	Shijia	Jiuliqiao	
~980?	Majiatun	'Weiji'	Shouxian	
	Shisanlitai	Weiji	Liulaobei	
	Yingchenzi	Zhangqu		
	Ganjingzi	Jiudingshan		
	Nanguanling	Niyuan		
		Zhaowei		

Table 2.1. Correlation scheme for Neoproterozoic formations on the North China craton. The scheme is constrained by detrital zircon ages and supported by similarities in lithology and biofacies between the Cuijiatun–Yingchenzi sequence and the Shijia–Zhangqu sequence. The diamictites of the Longxian 'Member' invite correlation with the terminal Ediacaran Luoquan Formation, Henan Province (Fig. 1.1). The radically different facies of the Fengtai 'Member' and the unconformity above it suggest that the Fengtai is much older.

Formation, these comprise the Feishui Group. For comparative purposes the study also includes a few samples of the Zhaowei Formation, taken from a quarry 30 km south-east of Xuzhou, Jiangsu Province, 180 km south of the other locality.

Summaries of the regional stratigraphy are given in Zang & Walter (1992) and Dong et al. (2008), an overview of the chemostratigraphy in Xiao et al. (2014). Correlations between regions are uncertain. Dolerite dikes and sills intruding the Zhaowei, Niyuan, Jiudingshan, Shijia, Wangshan and Jinshanzhai Formations as well as correlative formations in Liaoning Province have consistently yielded magmatic zircon U–Pb ages around 925 and 890 Ma (Liu et al. 2006, ages recalculated by Fu et al. 2015, Wang et al. 2012), a chronology strengthened by Pb–Pb dating of baddeleyite grains (Zhang et al. 2016) and U-Pb dating of detrital zircons (He et al. 2016). Most of the Precambrian sequence is therefore Tonian in age. Cherts in the Sidingshan Formation have yielded a Sm-Nd age of 801±46 Ma (Yang et al. 2004) – the only constraint available for the Huainan sequence. The Jiuliqiao Formation is younger than the Zhaowei.

Where it was sampled the Jiuliqiao Formation is approximately 90 metres thick. It is preceded by calcareous arkosic (quartz and feldspar) sandstones of the Shouxian Formation, 35–90 m thick,

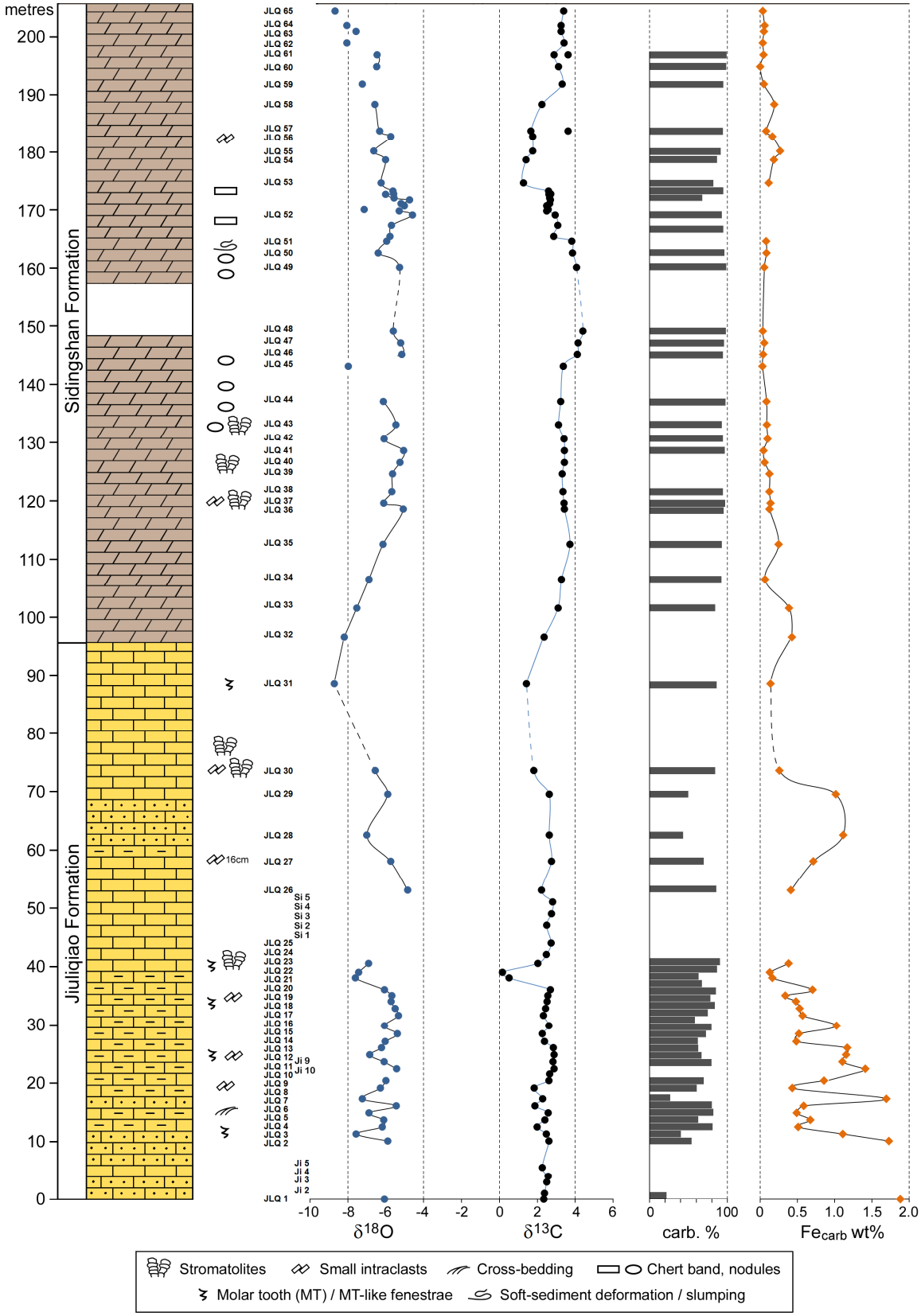

Figure 2.2. Log of the Jiuliqiao and Sidingshan Formations with respective carbon and oxygen isotope data. Outcrops being sporadic, the sedimentary features noted may also be present in other parts of the section. Grain size discussed in text. Dolomite oxygen isotope ratios adjusted on the basis that stoiochiometric dolomite was -2.7‰ lighter; Ji 2-5 and Si 1-5 from Guilbaud et al. 2015; Fe concentrations normalised to carbonate fraction.

Figure 2.3. (**a**) Overview of middle Jiuliqiao Formation – orange colour from subaerial oxidation of iron. (**b**) Columnar stromatolites at 40 m. (**c**) Small disused quarry around 170 m. A fault has raised the more distant beds on the right. Arrows point to the continuous chert band shown in (f). (**d**). Chert nodule in lower quarry face. The dolomite is finely laminated and at some levels intraclastic (top). Laminae are faintly visible through the nodule but deflection is also evident. (**e**) Laterally and vertically displaced, broken chert band (centre) and laminar chert horizon (top), located on far left of quarry in (c); 20p coin centre left for scale. (**f**) Continuous chert band, upper part brecciated and filled with Fe-oxide-rich marl.

some containing ripples and large-scale trough and tabular cross-bedding. Beds in the Jiuliqiao are generally thinner and finer-grained, beginning with calcareous siltstone and fine sandstone, laminated near the base, wavy on top. Swaley beds with cross-stratification and shaley interbeds appear about 13 m into the formation, stacked, microbial mats after about 20 m. The remainder of the formation consists mostly of silty limestones, with columnar stromatolites (dense concentric

structures 2–4 cm wide) appearing intermittently from about 40 m. These forms are typical of shallow-subtidal water depths (Altermann 2008); their appearance in the Jiuliqiao appears to be linked with low Fe, high carbonate content (Fig. 2.2). Carbonate proportions through the formation vary from about 25% at the base to about 80% at the top. In thin section, fabrics include tiny intraclasts, fine quartz and feldspar laminae alternating with fine calcite-rich laminae, and densely stacked diffuse microbial laminae or organic-rich stylolitic partings (App. 5). Carbonate Mg/Ca ranges from 0.01 to 0.12 (weight ratio).

The overlying Sidingshan Formation, about 160 m thick, consists entirely of dolostone (Mg/Ca 0.50–56). Exposure is sporadic and the lower boundary was not seen, but samples bracketing the transition to dolostone suggest it was abrupt. In thin section, fabrics include biolaminae, small stromatolites, and intraclasts. Stromatolites are visible at several horizons, both microdigitate and domal, the latter up to 65 cm tall. Biomass appears to have been dominantly algal (App. 5). As elsewhere (Tucker 1992, Frank et al. 1997, McKirdy et al. 2001), intraclastic breccias appear to have arisen from the disruption of incipient, subaqueous hardgrounds rather than desiccation of intertidal or supratidal muds. No ooids were observed (mentioned by Zang & Walter 1992) and no karstified horizons: sediments remained submerged. Intraclasts within the dolomite are also dolomitic. Chert nodules are frequent around the middle of the formation.

The 10 m leading up to a prominent sequence boundary at 173 m are fully exposed in a small disused quarry (Fig. 2.3c) and were sampled at high resolution. The dolostone is almost white, striped with darker microbial mm-to-cm-thick laminae and studded with chert nodules (Fig. 2.3d). Carbonate content irregularly decreases towards this boundary. Two continuous bands of dark-grey chert up to 10 cm thick occur at 167 m and 173 m. The upper band is brecciated towards the top and blanketed by iron-rich marl. Emergence at this point cannot be ruled out, although the preceding beds exhibit frequent disruption and slumping. The succeeding carbonates, their $\delta^{13}C$ falling from 2.6 to 1.3‰, are interpreted as significantly deeper-water.

The Sidingshan is unconformably overlain by the Fengtai Formation, a diamictite of variable thickness (up to 200 m). Clasts are derived from the Sidingshan. The contact is not extant at the logged locality but was seen in Bagongshan National Park, a few km distant, where it is planar (Fig. 2.4c). The Fengtai Formation and the upper 24 m of the Sidingshan were also logged and sampled at Yangdengshan (Fig. 2.1). Carbon-isotope values from the Sidingshan here are identical to those at Xishantao. The diamictite contains striated clasts and in places overlies a striated surface; accordingly it has been interpreted as glaciogenic (Zang & Walter 1992). The overall trend

of the preceding carbonates is one of upward shallowing, from storm wave base in the lower Jiuliqiao to depths of probably < 5 m towards the top of the Sidingshan.

The Zhaowei Formation consists mainly of limestone, with interleaved calcareous shale. Dolostone of sub-stoichiometric composition occurs at one horizon (sample ZW 51). The contact with the underlying Jiayuan Formation is not visible at the locality.

Issues of diagenesis were discussed in Xiao et al. (2014). As commonly in the Precambrian (Veizer & Hoefs 1976), the carbonate is fine-grained, and lithification – discussed below (§2.4.3) – was early. Preservation of fine sedimentary features, low variability in oxygen isotope ratios and preservation of oxygen-isotope differences between calcite and dolomite (Fig. 2.2) suggest that diagenetic alteration was minor. Microgranular textures in the Jiuliqiao Formation appear original; some samples show varying degrees of recrystallisation. Dolostones range from those showing little if any recrystallisation, with sedimentary texture, algal matter and laminations still visible, to those where recrystallisation was extensive (Appendices 4 and 5). The latter coincide with anomalously low $\delta^{18}O$, mostly at the top of the formation (JLQ 45, 59, 62–65).

2.3. Methods

Hand samples were washed, weathered surfaces cut away, and clean surfaces drilled for powder. To ascertain the ratios of oxygen and inorganic carbon isotopes, aliquots of 200–500 μg were analysed at Bloomsbury Environmental Isotope Facility (BEIF), University College London, on a ThermoFinnigan Delta^{PLUS} XP stable isotope mass spectrometer coupled to a ThermoScientific Gas Bench II. Prior to analysis, vials were flushed with He, then acidified with 100% phosphoric acid. BDH (Carrara marble internal lab standard) was used to correct for temporal changes in isotopic composition during each run. Precision of BDH analyses greater than 1000 mv was ±0.03 for $\delta^{13}C$, ±0.08 for $\delta^{18}O$. All values are reported in the Vienna Pee Dee Belemnite notation (VPDB) relative to NBS19.

The carbonate fraction was also calculated by reacting 1.0–1.5 g of whole-rock powder with 10% HCl until all carbonate was dissolved. The supernatant was centrifuged, drained and replaced with de-ionised water. After drying, the residue was broken up and more HCl added, left for a minimum 6 hours, centrifuged, rinsed three more times and dried. Total organic carbon was obtained from the de-carbonated samples by combustion in a LECO C/S Analyser.

The insoluble residue was analysed at the BEIF for organic carbon isotope ratios. Aliquots of 6–40 mg were combusted in a Thermo Electron 1112 series Flash EA, with a gas chromatographic

separation column linked via a CONFLO IV interface to a continuous flow IR-mass spectrometer. Carbon isotope ratios were measured against internal and external standards with a reproducibility of ~0.1‰.

Carbonate-associated Mn, Sr, K and Fe in the Jiuliqiao Formation were measured by dissolving the carbonate fraction of 4–10 mg aliquots at room temperature in 10% acetic acid for 24–48 hours. Solutions were centrifuged and analysed on a Varian 720 ICP-ES optical emission spectrometer at the Wolfson Laboratory for Environmental Geochemistry, University College London, then diluted ten-fold to obtain concentrations of Fe, Mg and Ca. Results of the two operations were cross-checked with the Fe data. Percentage carbonate calculated stoichiometrically from Mg, Ca, Mn and Sr concentrations was used as a further check on credibility, since totals should not exceed 100%. Carbonate content so calculated ranged from 31 to 88%. Results were reproducible to within 12% for K, 2–6% for the other elements. Trace-element data represent weight fractions of the total sample but relate solely to the carbonate content.

Thin sections were prepared for all samples. In addition to optical microscopy, these were examined under a Jeol JSM-6480LV scanning electron microscope (SEM) and microprobe EDS calibrated to cobalt. Samples were bound in carbon tape and examined under low vacuum (25–75 Pa) and low accelerating voltage (15 keV). Spatial resolution is around 2 μm. Areas for element analysis were selected at random from different parts of the thin section, with field of view ranging from 220 x 165 to 320 x 240 μm. Spot analyses per sample averaged 33, with up to 20 spot analyses, each run for 50 seconds, taken from a single area. Boundaries between one crystal and another were avoided. Element maps of 1600 x 1200 μm areas (run time 9 minutes) were made from 2–5 different parts of the slide to determine bulk composition and element ratios, and cross-checked against ICP results.

Elements below Z = 11, such as carbon, are not accurately detected by the microprobe, and although the detection limit is given as 0.01%, error margins for elements occurring at low concentration are commensurately high. The silicate-forming elements Ca, Mg, Fe, Si, Al and K encompassed the range of most minerals present. In addition, Na, Mn, Ti, Ba, S, F, Cl and P (amongst others) were present in trace amounts. Carbon was excluded from analysis except when focusing on organic carbon. The instrument reported constituents as either weight or molar % to the second decimal place, normalising one or the other to 100%. The option of normalising to molar % was chosen. Weights of individual elements in spot carbonate analyses were subsequently normal-ised to the stoichiometry of calcite, magnesite and silica, the calcite fraction being calculated as:

$$Ca\% + Ca\% \times 60/40.08$$

the magnesite fraction as:

$$Mg\% + Mg\% \times 60/24.3 + Fe\% + Fe\% \times 60/55.845$$

and the silicate fraction as:

$$Si\% + Si\% \times 32/28.086 + K\% + Al\%$$

Weights were normalised on the basis that the three fractions totalled 100%. Weights of individual elements in spot quartz and feldspar analyses were normalised to 100% divided by the sum of the Si, Al and K oxides.

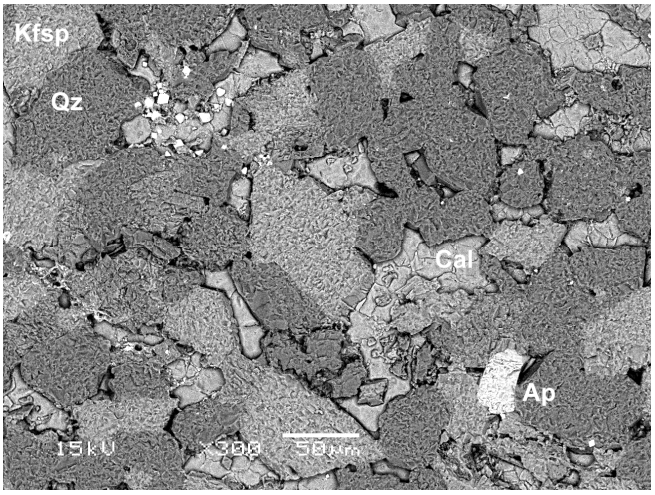

Figure 2.5. SEM image of JLQ 8, showing K-feldspar crystals interlinked by partial dissolution and partly altered to quartz. The still visible boundaries of the Si-rich calcite grains authigenically filling the holes of this network suggest that the calcite is not recrystallised. The bright crystals top left are pyrite.

2.4. Results

2.4.1. *Element relationships*

The main silicate mineral in both the Jiuliqiao and Sidingshan Formations is K-feldspar, followed by quartz and illite. Feldspar crystals are small (< 150 μm), corroded and presumably detrital. Most of the quartz appears to have arisen from dissolution of the feldspar (Fig. 2.5). Under low pH, as would have characterised subaerial weathering in CO_2-rich water, the reaction, given time, would have been:

$$KAlSi_3O_8 + 2H_2O + 2CO_2 \rightarrow K^+ + Al^{3+} + 3SiO_2 + 2HCO_3^- + 2OH^- \qquad (6)$$

Under the high pH that might have characterised coastal waters in the wake of such weathering the reaction would have been:

$$KAlSi_3O_8 + 4HCO_3^- \rightarrow K^+ + Al^{3+} + 3SiO_2 + 4CO_3^{2-} + 2H_2O \qquad (7)$$

Or in the case of illite, a clay mineral with much lower potassium:

$$KAl_3Si_3O_{10}(OH)_2 + HCO_3^- + 3H^+ \rightarrow K^+ + 3Al^{3+} + 3SiO_2 + CO_3^{2-} + 6OH^- \qquad (8)$$

Accordingly, varying amounts of K^+ and Al^{3+} ions, generally in proportion to each other, appear as substantial background elements in the carbonate analyses. Silica was both a solid residual phase and an aqueous phase ($Si(OH)_4$) within precipitating carbonate.

Concentrations can be extremely high. In spot analyses of what is ostensibly calcite, silicon can approach or even exceed the weight of calcium. Analyses are included in the carbonate dataset only if Si is < Ca and cation proportions are consistent with calcite stoichiometry. Averaged for each sample, the carbonate silica content correlates with the bulk silica fraction (Fig. 2.6b). Dissolved element concentrations were intimately related to the proportion of siliciclastic sediment available for dissolution. Aluminium can be up to 2.8%. Ranges among the five Zhaowei Formation samples are lower, up to 3% for Si and 1% for Al. Co-variation between Si, Al and K in the Jiuliqiao and Zhaowei Formations is so close that most of the carbonate-included silica can be attributed to feldspar dissolution. After JLQ 49 correlations between these elements are weaker.

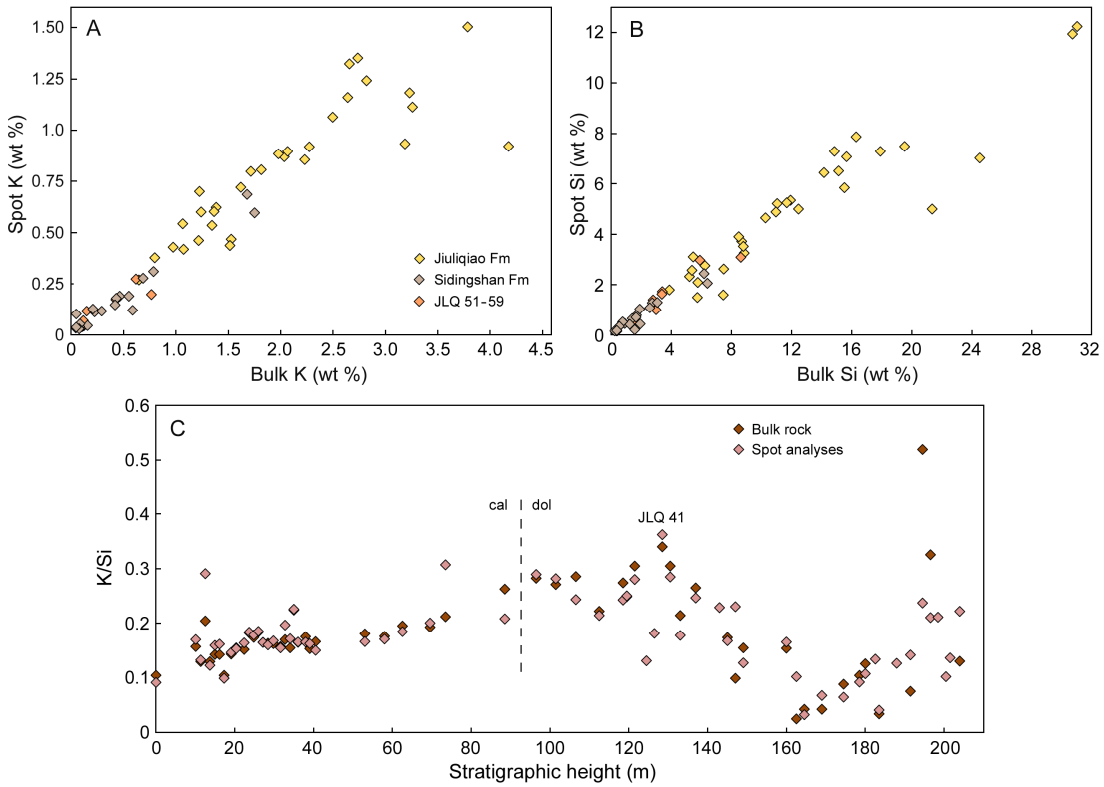

Figure 2.6. Average **(a)** potassium and **(b)** silicon content of bulk rock, compared with spot carbonate analyses. This is essentially the same relation as spot carbonate Si or K v bulk clastic content. **(c)** Average K/Si through the stratigraphic sequence.

The siliciclastic fraction through the Jiuliqiao fluctuates erratically, generally in the range 15–40%, with steeper rises at 17 m (JLQ 8) and 53–63 m (JLQ 26–28) (Fig. 2.2). It is lower through the Sidingshan Formation, after JLQ 33 generally less than 8%. It rises to a maximum of 18% around the sequence boundary at 174 m (Fig. 2.6c).

Bulk K, Al and Si all correlate closely with the respective quantities in spot carbonate analyses, with dolostones showing the same trend as limestones (Fig. 2.6). The only exceptions are rocks with carbonate content < 50%. Even though bulk silica includes discrete, fine crystals of quartz, through most of the sequence bulk and spot K/Si ratios are very similar. Potassium proportionally increases through the Jiuliqiao Formation and peaks in the lower Sidingshan (Fig. 6c), reflecting the mix between K-feldspar and illite; ratios are lowest around 170 m. Silica also crystallised as chert nodules and as polycrystalline quartz in some veins and microcavities. Some of the nodules characterising the middle Sidingshan deflect the laminae below and above them (Fig. 2.3d); in other cases the laminae pass undeflected through the nodules, suggesting co-precipitation of chert and carbonate. Polycrystalline quartz inclusions, sometimes forming rosettes, occur in JLQ 51–59, coincident with the dip in bulk and spot K/Si and a dip in $\delta^{13}C$.

Iron is abundant only in the Jiuliqiao Formation. The dominance of K-feldspar in the clastic sediment suggests a granitic source; mafic minerals are rare. Thus most of the Fe in the seawater from which the carbonate minerals precipitated probably derived from oceanic sources. The same applies to Mn, which covaries with Fe through the formation. Being soluble in anoxic seawater, Fe increased in abundance with depth and serves here as a proxy for depth.

Adjusted for carbonate content, Fe values obtained by ICP tend to be at least 20% lower than spot microprobe values, suggesting that the latter include a proportion of insoluble, interstitial iron. Having a radius between those of Mg and Ca, and the same charge, Fe^{2+} substitutes well for Ca in the calcite lattice, increasingly with temperature (Dromgoole & Walter 1990). Spot analyses for carbonate-rich samples show a strong correlation between Fe and Ca. Hence the stoichiometry of magnesian calcite seems best represented by the ratio (Mg+Fe)/Ca (hereafter Mg*/Ca). Correlation between the elements in VHMC is much weaker and starts afresh from Mg*/Ca = Mg/Ca (Mg/Ca ≈ 0.18, Fe = 0), reflecting addition of Mg and Fe to a previous phase from which the Fe dissolved out. Dolomite has a different crystal structure, in which Ca and Mg are ordered into alternating layers. Dolostones contain little Fe^{2+} (Figs. 2.2, 2.7a). Fe substitution in the dolomite is not systematic and again starts from Mg*/Ca = Mg/Ca. Like the 13LH samples from Dalian, the Zhaowei Formation samples are best modelled on the basis that Fe did not substitute for Ca or Mg

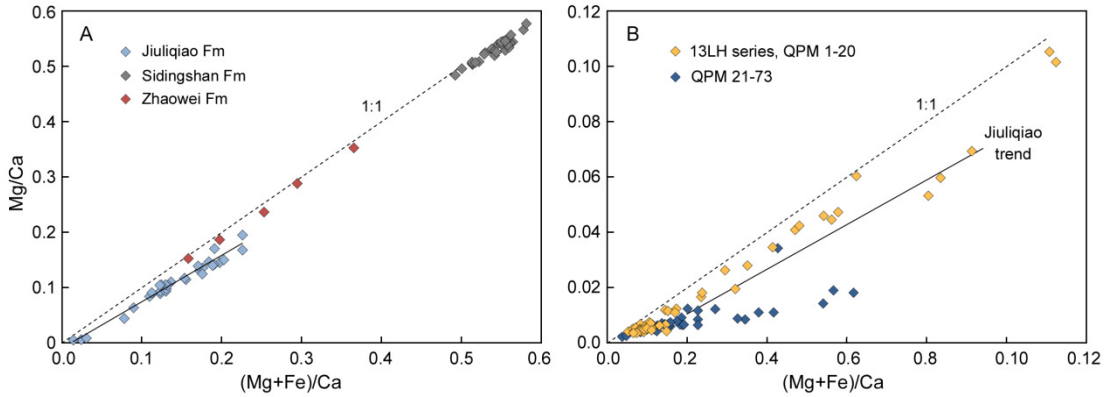

Figure 2.7. (a) Averaged spot analyses suggest that Fe substituted readily in the Jiuliqiao carbonates but not significantly in the dolomites or in the Zhaowei Formation. **(b)** ICP-OES analyses of carbonates in the Dalian area: the Fe in samples QPM 21-73 is interpreted to be mostly interstitial.

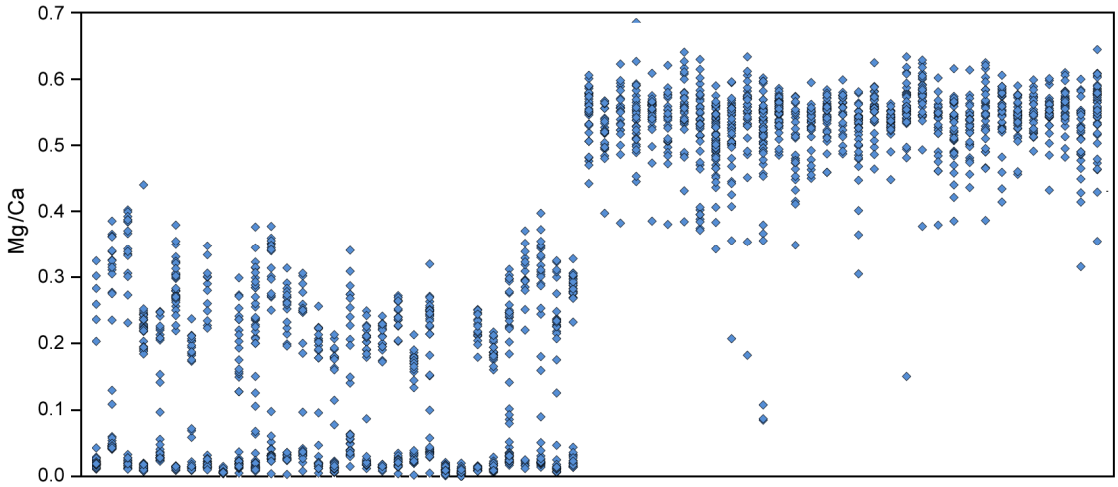

Figure 2.8. Spot Mg/Ca ratios of carbonates through the Jiuliqiao and Sidingshan Formations. The mineralogy of JLQ 9, 23 and 24 is entirely LMC.

significantly. Thus, even where Fe^{2+} is abundant, substitution appears to have been controlled by factors other than structural compatibility.

Until the application of electron microprobes, dolomitic carbonate rocks were analysed in bulk and assumed to be homogeneous in composition. In reality, as with some invertebrate organisms (Moberly 1968, Schroeder et al. 1970), single dolomite samples encompass a range of Mg/Ca ratios (Searl 1994, Jones et al. 2001). The present study shows that Mg-rich calcites too can be heterogeneous: on a microscopic scale patches of VHMC occur through most of the pre-dolomite sequence. Composition is bimodal, with ratios clustering either side of a hiatus (Fig. 2.8). The range of these clusters is highly variable but seems influenced by the flux of siliciclastic material. Samples JLQ 9, 23 and 24 exhibit only LMC compositions (Mg/Ca < 0.02). Dolomite samples are unimodal and less wide-ranging in composition, but also not homogeneous, and none in aggregate attains the

Sample	Cryst.	Min.	Height	FeS_x	$(Fe,Ca)CO_3$	Fe_3O_4	Fe_2O_3	Ank.
JLQ 1	1	H	0	Y				
JLQ 2	2	H	10.1	Y				
JLQ 3	1	H	11.3	Y				
JLQ 4	2	H	12.5	Y				
JLQ 5	1	H	13.7	Y				
JLQ 6	2	H	14.9	Y				
JLQ 7	2	H	16.1	Y				
JLQ 8	1	H	17.3	Y				
JLQ 9	1	L	19.1		Y			
JLQ 10	1	H	20.4	Y				
JLQ 11	1–2	H	22.4					
JLQ 12	2	H	23.6	Y				
JLQ 13	1	H	24.8	Y				
JLQ 14	1	H	26	Y				
JLQ 15	1–2	H	27.1	Y				
JLQ 16	1	H	28.4	Y	Y			
JLQ 17	1	H	29.8	Y				
JLQ 18	1–2	H	31.6					
JLQ 19	2–3	H	32.8	Y				
JLQ 20	3	H	34	Y				
JLQ 21	1–2	H	35	Y				
JLQ 22	1	H	48	Y				
JLQ 23	1	L	38		Y			
JLQ 24	1	L	39		Y			
JLQ 25	3	H	41	Y				
JLQ 26	2	H	53	Y				
JLQ 27	2–3	H	58	Y				
JLQ 28	1	H	57.5	Y				
JLQ 29	2	H	64.5		Y			
JLQ 30	2	H	68.5		Y			Y
JLQ 31	2–3	H	83.5		Y	Y	Y	
JLQ 32		D	96.5			Y		Y
JLQ 33		D	96.5				Y	Y
JLQ 34		D	101.5					Y
JLQ 35		D	112.5					Y
JLQ 36		D	118.5					Y
JLQ 37		D	119.5					Y
JLQ 38		D	121.5					Y
JLQ 39		D	124.5					Y
JLQ 40		D	126.5					
JLQ 41		D	128.5					Y
JLQ 42		D	130.5					Y
JLQ 43		D	133					
JLQ 44		D	137					Y
JLQ 45		D	143	Y				Y
JLQ 46		D	145	Y				Y
JLQ 48		D	149					Y
JLQ 49		D	160					Y
JLQ 52		D	169				Y	Y
JLQ 53		D	174.5					
JLQ 54		D	178.5					Y
JLQ 55		D	180					Y
JLQ 58		D	188					Y
JLQ 59		D	191.5	Y				Y
JLQ 60		D	194.5	Y				
JLQ 61		D	196.5					
JLQ 62		D	198.5			Y		
JLQ 63		D	200.5					Y
JLQ 65		D	204					Y

Table 2.2. Crystallinity (coded as in Table 2.3), carbonate mineralogy and characteristic iron-rich minerals of the Jiuliqiao and Sidingshan Formations (JLQ 1–31 and 32–64 respectively). Ank. = ankerite, $(Ca,Fe,Mg)CO_3$. JLQ 32 may also include FeO. H = HMC, L = LMC, D = dolomite.

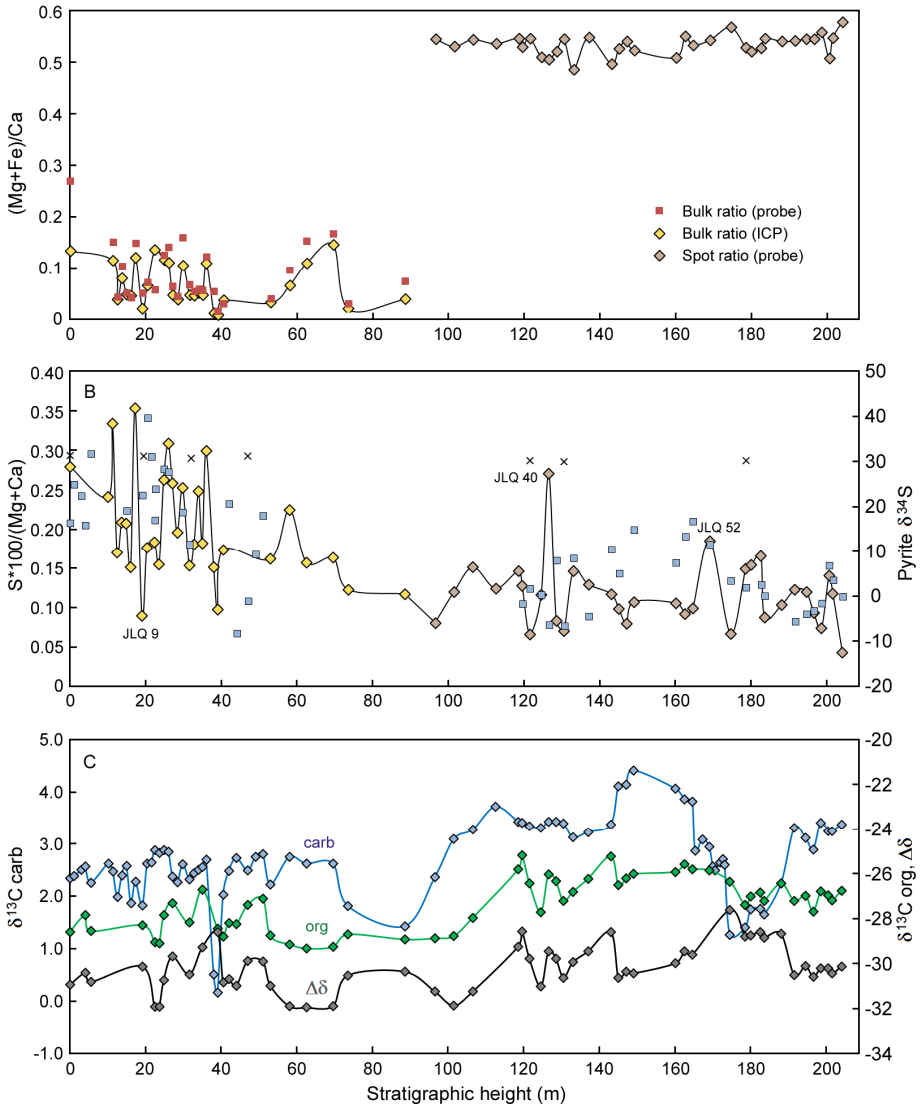

Figure 2.9. (a) Mg*/Ca through the Jiuliqiao (yellow) and Sidingshan Formations. **(b)** Carbonate-associated sulphur concentrations (CAS) through the sequence; sulphur averaging 0.4% in stromatolitic layers of JLQ 43 not shown. Squares denote pyrite $\delta^{34}S$, crosses carbonate-associated sulphate $\delta^{34}S$. **(c)** Carbon isotope ratios of organic carbon are shown as negative in order to utilise the same scale as for organic $\delta^{13}C$; thus the lowest degree of fractionation between organic and inorganic carbon is at 174 m. Sulphur isotope data and some of the organic carbon data are from R. Guilbaud et al. (2015).

proportions of stoichiometric dolomite, though individual crystals may. One dolomite sample from the Zhaowei formation, ZW 51, includes patches of Mg-rich calcite (Mg*/Ca 0.15–0.20). The bimodal distribution in the range 43–48% $MgCO_3$ reported from 'bulk' analysis of other dolostones (Sperber et al. 1984) and in the range 43–51% $MgCO_3$ as analysed by EDS (Searl et al. 1994) is not observed.

In addition to its presence in the calcites and dolomites, iron also occurs in tiny amounts (< 0.1%) as pyrite, ankerite, magnetite and haematite (Table 2.2). Pyrite occurs mostly in the Jiuliqiao

Formation and is non-detrital (e.g. App 4, Figs. 7, 11), occasionally in the form of framboids. In the Sidingshan Formation it is rare; ankerite is the characteristic species. Among the limestones, Mg-poor ferroan ankerite, $(Fe,Ca)CO_3$, coincides with the incidence of LMC, with low carbonate Fe, and with falls in $\delta^{13}C$ at 38 m and before the Jiuliqiao/ Sidingshan boundary. Occurring in the Jiuliqiao within feldspar and as a precipitate between grains, it is authigenic. Iron oxides are rare throughout; the ferric phase occurs at the Jiuliqiao/Sidingshan boundary and at 169 m (JLQ 52). Through most of the succession conditions in the substrate were reducing.

Spot analyses also pick up trace amounts of sulphur. As previously noted, error margins are high, so little reliance can be placed on single figures, which vary greatly, but averaged concentrations show systematic trends. Fluctuations through JLQ 3–25 (11–41 m) closely correspond with fluctuations in Mg/Ca (Fig. 2.9). Through the Jiuliqiao Formation averages trend downwards from 0.08 to 0.04%, after which they vary mostly between 0.02 and 0.06%. Levels in the dolostones are mostly lower than in the limestones. High concentrations in the dolostones are associated with stromatolites, possibly because these were oases of oxygen production and dissolved sulphur in the water column was captured as sulphate.

2.4.2. *Carbon isotopes*

Inorganic carbon isotopes are steady around 2.5‰ through most of the Jiuliqiao Formation but take a brief dive at 38 m – evidently a local, not global signal (Fig. 2.9). There is also a gentler drop to 1.4‰ towards the end of the unit. Ratios rise to around 3.3‰ in the dolostones. Values rise further to 4.4‰ at 149 m, then drop rapidly to 1.3‰ immediately after the sea-level lowstand at 174 m, another instance of local control. From there they recover to levels typical of the earlier Sidingshan. Organic carbon isotopes are somewhat erratic, ranging from -29.3 to -25.2‰. Of greater significance is the difference between the organic and inorganic signal, i.e. the extent to which metabolising organisms fractionated the dissolved carbon. Again the signal is erratic, with three peaks around 32‰ at 23 m (JLQ 11–12), 62 m (JLQ 27–29) and 101 m (JLQ 33) and a minimum of 27.6‰ at 174 m (JLQ 53). Organic and inorganic carbon isotopes weakly co-vary ($R^2 = 0.26$).

2.4.3. *Carbonate crystallinity*

Since its precipitation did not involve calcifying algae or animals, carbonate sediment in the Precambrian had a different texture from that forming today, and terms such as ‘micrite’, ‘microspar’ and ‘grainstone’ are either not applicable or need to be re-defined. In the Folk classification ‘micrite’ refers to fine-grained carbonate whose constituents are less than 4 μm across, consisting of broken skeletal material and inorganic crystals. In the present sample suite the best preserved

Index	Details
1	K-feldspar crystals part-eroded/dissolved and altered to quartz. Outlines of calcite grains visible. VHMC mostly euhedral if present, sometimes surrounding calcite grains.
2	K-feldspar crystals part-eroded/dissolved and altered to quartz. Calcite partially recrystallised. VHMC patchy to euhedral.
3	K-feldspar amorphously semi-dissolved. Calcite recrystallised. Calcite grains at centre of some VHMC patches. VHMC patchy to euhedral.

Table 2.3. Main stages of recrystallisation in the Jiuliqiao Formation distinguishable from scanning electron and transmitted light microscopy (Table 2.2). See Appendices 4 and 5 for examples. The granular morphology of least-altered matrix calcite is identical to that of molar-tooth structure, suggesting that the mineral precipitated *in situ*.

calcite has a granular form. The smallest grains are 5–10 μm across, and occur in fenestrae and molar-tooth structure (Fig. 2.10a, App. 4 Fig. 5, App. 5 Figs. 1, 8). The granular morphology is typical of molar-tooth precipitates, possibly arising from precipitation in early-formed, gaseous cavities (Furniss et al. 1998). The cavity-filling calcite is necessarily authigenic. Matrix calcite has the same morphology, but the grains are slightly larger (Figs. 2.5, 2.10b, App. 4 Fig. 9). In both cases rims are enriched in Mg and Fe (brighter under SEM), produced by a veneer of cement, thickest at corners, that subsequently merged with the grains; the extant boundaries are uncemented. The original grains were spherical, modified into larger polyhedra by cementation and compaction. The non-crystalline form suggests a primary origin; since the term ‘microspar’ implies neomorphism, it is avoided.

In contrast to the granular, relatively low-Mg calcite, Mg-rich calcite is mostly amorphous and appears to have arisen via dissolution. Boundaries between primary and secondary crystals are sharp. Mg content away from the boundaries, while variable, is not markedly greater than next to them. Some patches enclose solitary grains of calcite that resisted dissolution (Fig. 2.10, App. 4 Figs. 3, 6, 9). Also in contrast to the granular calcite, some instances of Mg-rich calcite are crystalline and rhombohedral (e.g. App. 4 Figs. 3, 14, 17). The distinction suggests the rhombs precipitated directly from the water column.

The spherical form of the grains suggests a vaterite precursor – as, with regard to molar tooth structure, has been suggested before (Pollock et al. 2006). Vaterite is a metastable calcium carbonate polymorph, less soluble than either aragonite or calcite. Experiments indicate that dissolved organic molecules promote its precipitation, consistent with the idea that gas from the decomposition of organic matter produced the molar tooth cavities. Since the matrix grains are

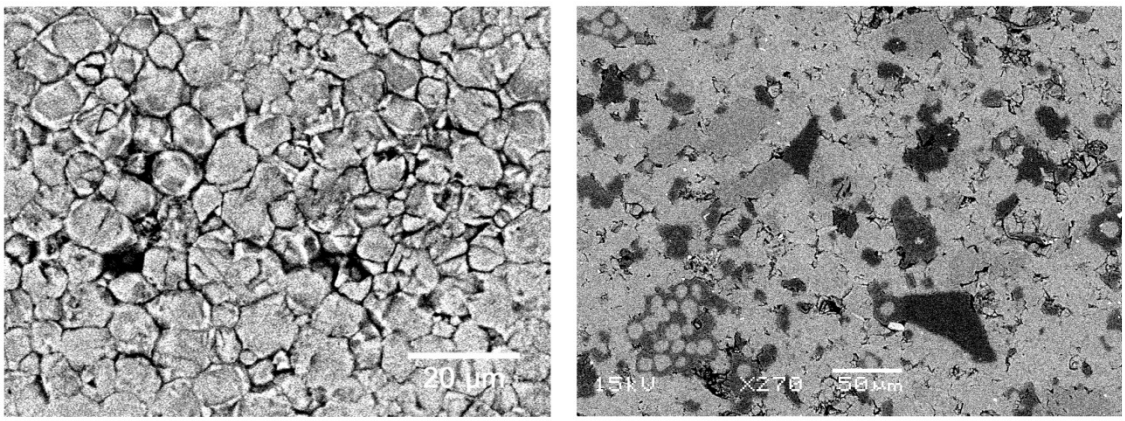

Figure 2.10. Backscattered electron images. **(a)** JLQ 4: calcite grains within 'molar tooth' structure. The x-ray-bright rims are richer in Fe and Mg than the cores. **(b)** JLQ 20: light grey material = calcite, including the spherical forms of original grains; medium grey = feldspar; dark grey = VHMC (Mg*/Ca ~0.3); grey-black = silica.

morphologically identical, the implication is that these too were originally vaterite, their larger size being due to higher concentrations. Vaterite is also promoted by high alkalinity (pH > 9) (Spanos & Koutsoukos 1998) and high [DIC] (Dickinson et al. 2002); relations with temperature are more equivocal (Weiss et al. 2014). With regard to magnesium substitution, which vaterite tolerates, if anything, more easily than calcite does (Sawada et al. 1990), it is here assumed to behave similarly to calcite.

Porosity through the Jiuliqiao Formation is low. Where dissolution destroyed the original grains, recrystallisation consumed the space created, accelerating lithification. Fluids introduced by subsequent fracturing were confined to the fractures themselves, as illustrated by JLQ 32 (App. 4 Fig. 23, App. 5 Fig. 9), where a fracture 0.7 mm thick includes fragments of matrix dolomite but is itself filled with high-Mg calcite (Mg/Ca 0.04). Dolomite formation appears to have preceded lithification, since the fluid penetrating solid rock was depleted in Mg. Thinner fractures and networks of fluid penetration, some developing before the sediment lithified, were rich in Fe^{2+} and organic matter.

In JLQ 32, just after the boundary between limestone and dolostone, blobs of microgranular dolomite derived from thin stromatolite crusts occur in a matrix of coarser crystals (App. 5 Fig. 10). Similar textures characterise the intact stromatolites, where darker, finer-grained layers alternate with lighter, coarser layers. Coarser dolomite crystals tend to be localised at intraclast boundaries or in the spaces between stromatolite growths (App. 5 Figs. 11–13). They are more pervasive in the upper half of the formation (e.g. JLQ 59), along with inclusions of comparatively large (< 250 μm) dolomite crystals and microcrystalline quartz (App. 5 Figs. 20–22). In the lower half of the formation, most crystals are small (4–20 μm), subhedral to anhedral with straight, compromise

boundaries and many crystal-face junctions, consistent with rapid formation at low temperature (< 50°C) and high saturation (Sibley & Gregg 1987). Thin, sometimes densely stacked, microbial laminae, both in intraclasts and matrix, tend to be finer-grained than intervening matrix.

2.4.4. *Feldspar and quartz analyses*

Three explanations can be conceived for the extraordinarily high concentrations of Si, Al and K in spot carbonate analyses. One is that they represent inclusions of very fine undissolved siliciclastic material in the carbonate. Such inclusions are not evidenced in images of the carbonate, however, even at high magnification, and it would be difficult to account for the occurrence of detrital sub-

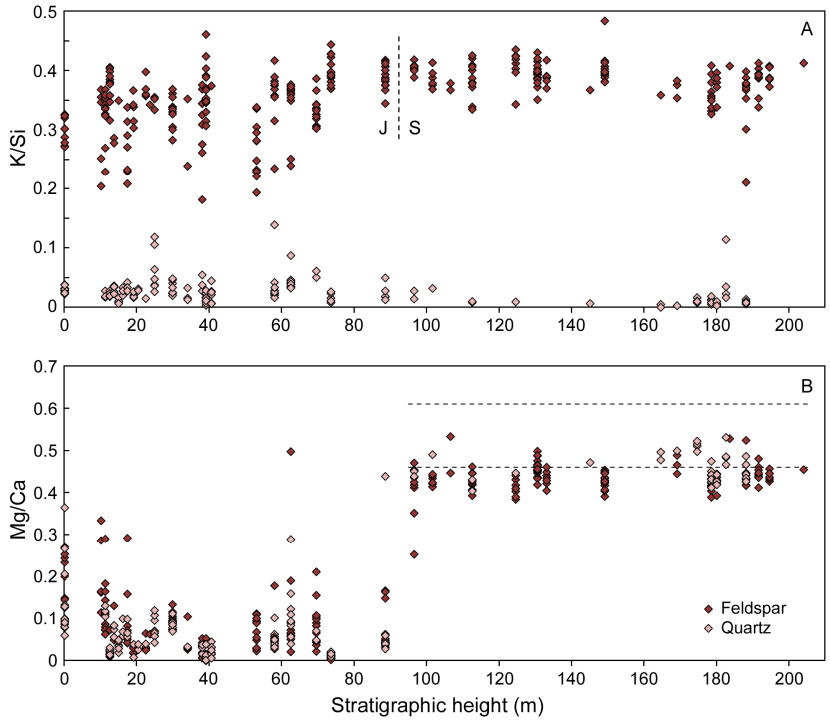

Figure 2.11. (**a**) K/Si and (**b**) Mg/Ca proportions within detrital silicate through the Jiuliqiao (J) and Sidingshan (S) Formations. Dotted lines in (b) delineate the range of Mg/Ca in the dolomite.

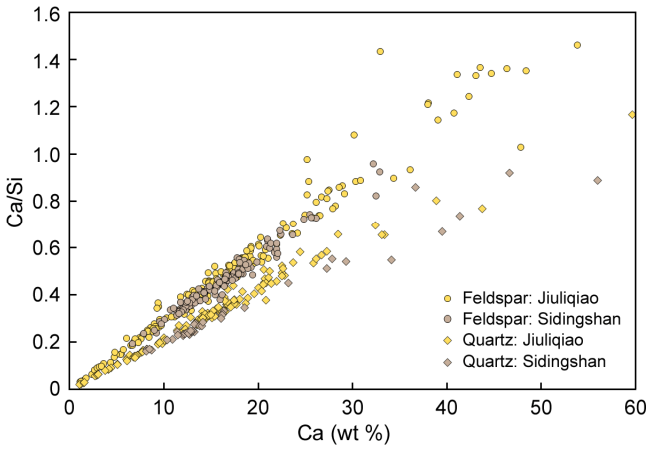

Figure 2.12. Ca composition of feldspar/illite and quartz in relation to Si. A few values plot beyond the two axes. Feldspar and illite follow the upper trend, less soluble quartz the lower.

micron or nanoscale particles alongside others typically 10–100 microns across. Feldspar dissolution such as that illustrated in Appendix 4 (Figs. 1, 2, 4, 6–8, 10, 13 and 21) is ubiquitous, and smaller fragments would have been more susceptible to dissolution than larger ones. Another possibility is that the elements are present as interstitial ions within the lattice. This is also discounted: the stoichiometry of EDS analyses requires that Si be present as SiO_2, which could not have been accommodated in the lattice structure, and the amounts of Si, Al and K are too high. The remaining possibility is that the elements were dissolution products captured between lattice structures. McIntire (1963) characterises occlusion as a process whereby

> Impurities adsorbed at the surface during the growth of the mineral become trapped as subsequent layers are added. In addition to adsorbed ions, the impurities may even include mechanically admixed inclusions of the fluid from which the mineral grew, or minute crystals of a distinctly different solid phase. Occlusion is especially great in cases where the mineral has grown rapidly.

In the present instance the impurities were chiefly SiO_2, Al^{3+} and K^+, as per reactions (7) and (8). Sodium was only a very minor component.

Dissolution can be further quantified by analysing the silicates. Through most of the Jiuliqiao Formation K-feldspar and illite both occur, and the range of the K/Si ratio is broad; in the Sidingshan almost the only detectible mineral is K-feldspar and the ratio accordingly less variable (Fig. 2.11a). Quartz, most of it deriving from these minerals, also contains significant amounts of K. Most remarkable are the Mg/Ca ratios (Fig. 2.11b). In the Jiuliqiao Formation these broadly correspond 1:1 with the Mg/Ca of the respective carbonates. In the Sidingshan Formation the ratios are consistently lower. Nonetheless Mg/Ca jumps dramatically at the limestone/dolostone boundary and nearly all ratios exceed 0.40, both in the feldspar and the quartz. Absolute concentrations are also high. Calcium can exceed 50% of the weight total and even exceed Si (Fig. 2.12). The trends of the quartz and non-quartz minerals are systematic and distinct.

Calcium, a component of calcium carbonate, increases along the trajectories of dissolution as K and Al are lost (Fig. 2.13). Initially, K-feldspar loses K and illite loses Al. Thereafter the respective minerals become unstable and the cations dissolve out proportionally and en masse towards the stoichiometry of quartz. Nonetheless, substantial amounts of K and Al remain in the lattice. As seen also in Fig. 2.11a, illite – a product of K-feldspar weathering under high pCO_2 – is essentially absent from the Sidingshan Formation, and there is no evidence of aluminium hydroxide in either formation. Calcium carbonate replacement in the course of K-feldspar dissolution has been observed in other contexts (Milliken 2003).

The proportions of K and Al in the silicates can be compared with those in the carbonates. Normalised to Si, calcites and dolomites are both enriched in K. By contrast, while the dolomites are strongly enriched in Al relative to Si, nearly all calcites are depleted (by 0–15%). Arguably, some Al escaped into the water column complexed with CO_3^{2-} and was there captured by dolomite.

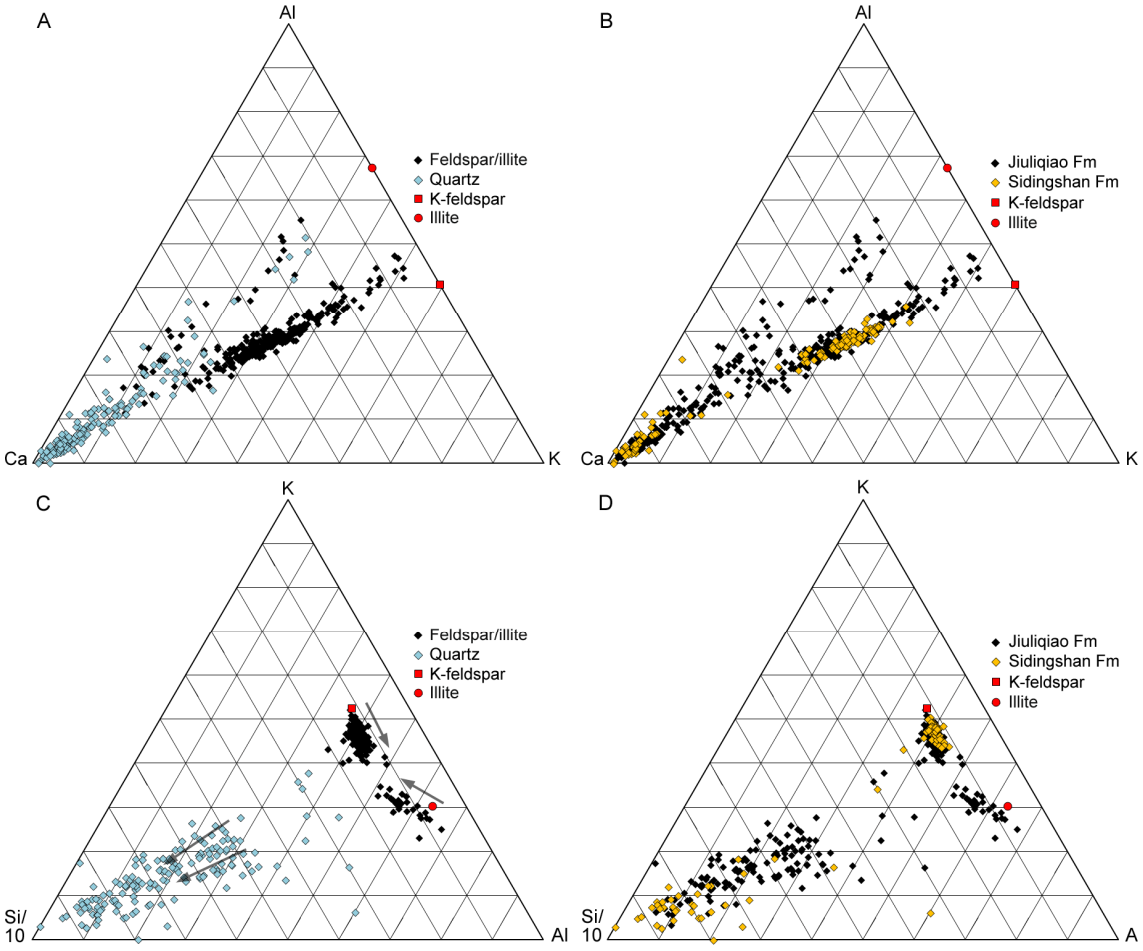

Figure 2.13. (**a**, **b**) Trilateral relations of molar Al, Ca and K in the silicates. Ca increased as feldspar and illite dissolved to quartz. (**c**, **d**) Trilateral relations of molar K, Si and Al, showing that illite and its quartz derivative occur only in the limestones. The square and circle symbols denote ideal K-feldspar and illite respectively.

2.5. Silicate and carbonate dissolution as a function of pH

It is a common misconception that in a world of high atmospheric pCO_2 ocean pH must have been lower. In fact, over timescales sufficient for fluctuations in pCO_2 to be buffered, the balance of the dissolved carbon species remains the same and pH is unaffected. Salinity has a major effect on alkalinity, and thereby pH, for two reasons. First, greater salinity reduces the solubility of CO_2 and increases the concentration of CO_3^{2-} proportional to HCO_3^- (Slaughter & Hill 1991). Second, the cations released to the ocean by more intense silicate weathering (e.g. reaction 6) neutralise the anions Cl^- and SO_4^{2-} that would otherwise combine with H^+ to form strong acids (Deffeyes 1965).

Silicate weathering can take place in marine settings, at rates comparable to those on land (Wallmann et al. 2008). In both situations, the chief products are clay minerals. Clay minerals may result also from 'reverse weathering', whereby silica, dissolved cations and bicarbonate recombine and liberate CO_2. In the present case, clay-mineral fragments are rare and detrital; there is no sign of reverse weathering. Plagioclase dissolved completely, while the less soluble K-feldspar underwent partial dissolution. The strong correlation between bulk silicate content and the Al and K entering precipitated carbonate (Fig. 2.6) suggests that the alkalinity produced by subaerial weathering, driven by high atmospheric pCO_2, was locally intensified by submarine weathering. Most calcium carbonate precipitated within the pore spaces of the partly dissolving silicates and thereby occluded (*sensu* McIntire) concentrations of the dissolution products proportional to the bulk silicate/carbonate ratio.

As with other feldspars, K-feldspar and illite solubility are lowest around pH 6–8 and increase exponentially in both the acidic and basic directions (Blum & Stillings 1995, Köhler et al. 2003). Quartz is more soluble at high pH (also high temperature and salinity) than at low pH (Brady & Walther 1990). Calcium carbonate has the opposite profile, precipitating at high pH and dissolving at low pH. It follows that conditions in the Jiuliqiao substrate were basic, not acidic. Calcium carbonate took the place of the dissolved K^+, Al^{3+} and SiO_2. In combination, therefore, the reactions may be written:

$$KAlSi_3O_8 + 4Ca^{2+} + 4HCO_3^- \rightarrow K^+ + Al^{3+} + 3SiO_2 + 4CaCO_3 + 2H_2O \qquad (9)$$

In this way the increase in alkalinity generated by silicate dissolution was counterbalanced by the decrease consequent on carbonate precipitation, which simultaneously incorporated K^+, Al^{3+} and aqueous silica. The consumption of bicarbonate by authigenic calcite has also been inferred from modern settings (Wallmann et al. 2008). Calcitic dolomite appears to have replaced dissolved K^+, Al^{3+} and SiO_2 in feldspar in the same manner.

Where alkalinity fell, vaterite underwent patchy dissolution, re-precipitating as VHMC as alkalinity recovered. Correlation between Mg/Ca and carbonate-associated sulphur (CAS) suggests that sulphate reduction was involved in VHMC formation. Sulphate reduction initially led to a decrease in pH, as the weak acid H_2S (reaction 1) dissociated into HS^- and H^+ (Meister 2013). Thereby pH dropped below the vaterite saturation threshold and caused the mineral to dissolve. The consequent addition of carbonate to the fluid, coupled with the generation of organic-derived bicarbonate, then began to restore alkalinity. In theory, the removal of sulphide as pyrite would also have helped to restore pH, although pyrite does not noticeably occur close to VHMC in the Jiuliqiao. Since

carbonate Mg/Ca broadly correlates with silicate Mg/Ca (Fig. 2.11b), pore water must have been enriched in Mg at the levels where high Mg/Ca is recorded. Cyanobacterial matter may have concentrated Mg, but again this is not evident from extant TOC. More probably, Mg^{2+} activity was enhanced by the dehydrating effect of the H_2S (Zhang et al. 2012b). Most of the sulphur captured in the Mg-enriched carbonates (forestalling reaction with Fe^{2+}) is inferred to be free sulphur produced by microbial oxidation of H_2S.

Mg-rich collars around calcite grains can be thinner than 2 microns, yet without evidence of diffusion from one phase to the other. As with the dissolution fronts in K-feldspar crystals or Fe-rich rims around calcite grains (App. 4 Fig. 5), compositional differences are preserved on a microscopic scale. The sharpness of the dissolution fronts shows that kinetics were controlled by the activation energy of dissolution, hence by pH, rather than by the much lower activation energy of diffusion. Consequently, diffusion is not a feasible explanation for high Si, Al and K in calcite or high Ca in feldspar. Diagenesis, reducing chemical disequilibrium between sedimentary phases and their environment, was to that extent limited.

Note that although Neoproterozoic carbonates are often described as ‘silicified’, the diagenetic nature of the process needs to be demonstrated. Here silica was incorporated mostly during primary crystallisation. Patchy silicification (e.g. Fig. 2.3d) implies a fall in pH but also high concentrations of silica in the seawater generally and a probability that high concentrations were incorporated when the carbonates precipitated.

2.6. Controls on dolomitisation

2.6.1. *Phase discontinuities*

Discontinuities in Mg*/Ca composition exist because the bypassed phases are more soluble. Solubility is in part a function of crystal structure. In the case of ideally ordered dolomite, layers of Ca^{2+} octahedra perpendicular to the *c*-axis alternate with layers of CO_3^{2-} groups and Mg^{2+} octahedra (Chang et al. 1998). Instabilities in calcite arise because cation replacement affects inter-atomic bond lengths and angles. Diminished shielding of the cations allows them to vibrate more, rendering inter-atomic bonds weaker. In dolomite the octahedra are less distorted and provide better shielding (Althoff 1977). Lattice distortion appears to be the main reason why magnesian calcites are more soluble than the calcite and dolomite end-members.

High-temperature experiments in which dolomite has been abiotically synthesised show that Mg is incorporated into the lattice via dissolution and recrystallisation rather than solid diffusion. Where calcite is the reactant and the solution has a Mg/Ca ratio < 1.0, the first phase to form is VHMC,

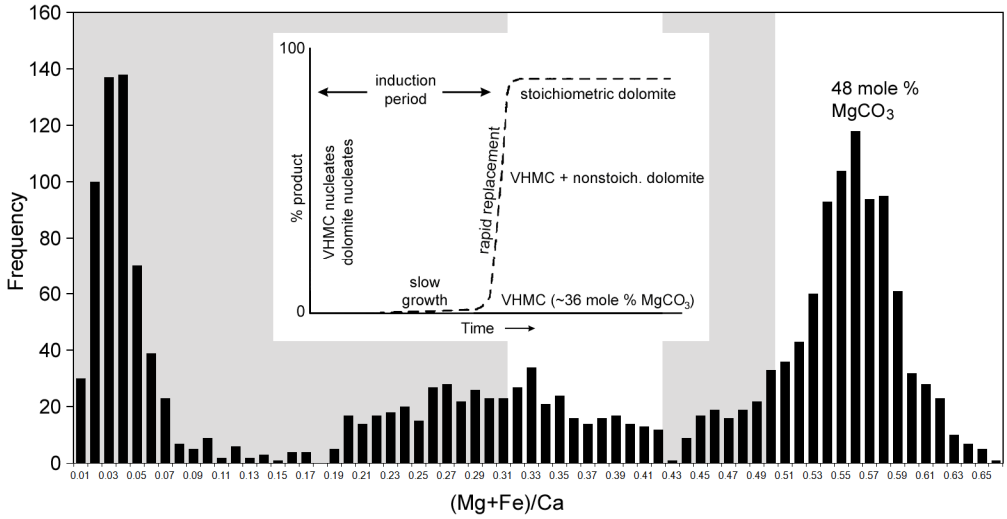

Figure 2.14. Histogram of solid-solution phase frequency in the Jiuliqiao (0.01–0.43 Mg*/Ca) and Sidingshan (0.42–0.65 Mg*/Ca) Formations. Inset diagram from Sibley et al. (1994). Shaded areas encompass compositions bypassed in the experiments. Frequency of the end-members is influenced by SEM-operator selection of what crystals to analyse.

with a $MgCO_3$ composition of 34–40% (Mg/Ca 0.31–0.40), slightly higher if the solution is richer in Mg (Sibley et al. 1994). Having reached that stage, dolomitisation proceeds rapidly to completion, in the course of which VHMC may co-exist with sub-stoichiometric dolomite. The phase inbetween (41–45% $MgCO_3$, Mg/Ca 0.42–0.50) is bypassed. Although it is not entirely clear how stoichiometric proportions are attained, the process is thought to involve cation replacement, crystal overgrowth and the nucleation of new crystals (Sibley 1990). The co-existence of different phases implies incomplete, arrested reaction. If the reactant is aragonite, dolomitisation occurs more quickly and fine-grained crystals may convert to dolomite directly. From coarser-grained aragonite the first phase to form is low-Mg calcite (5.6% $MgCO_3$, Mg/Ca 0.036) followed by VHMC (39.6%, 0.40) (Katz & Matthews 1977).

Broadly speaking, these findings concur with the distribution of Mg*/Ca in the present dataset. Compositions fall into three clusters, with ranges of 0.00–0.08, 0.19–0.41 and 0.43-0.63 (Fig. 2.14). The ranges are wider than those indicated in the experiments, presumably because the barriers to VHMC and dolomite formation in the natural environment were weaker. The emergence of calcitic dolomite at Mg*/Ca = 0.43 marks a distinct threshold, indicating a degree of ordering. Other experiments show that Mg/Ca = 0.40 represents the maximum amount of Mg which the calcite lattice can sustain without ordering (Hong et al. 2016). This is also, conversely, the lowest ratio (Mg/Ca = 0.39 ±1) seen in naturally occurring dolomite (Land 1998). At this point, in contrast to their random distribution in the VHMC lattice, Ca and Mg begin to segregate into

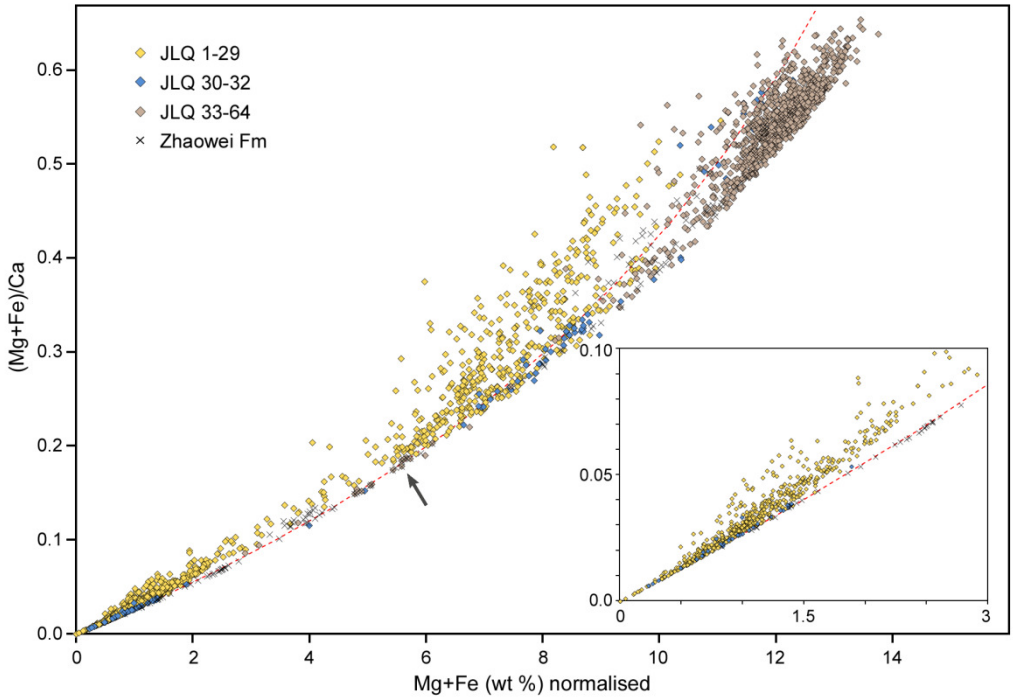

Figure 2.15. Distribution of Mg*/Ca as a function of Mg and Fe. The dotted line represents the ideal distribution of phases on an iron-free basis (e.g. Mg in stoichiometric dolomite = 50% x 24.3 wt %). Data plot to the left of this line because actual compositions include Fe, which is heavier than Mg. Iron-poor compositions plot increasingly to the right of the line because normalisation assumes an atomic weight of 100 for all phases whereas stoichiometric dolomite is 92.2. Arrow indicates the Mg/Ca composition at which Fe substitution for Mg begins *de novo*.

distinct layers. As with many synsedimentary or early-formed dolomites, peak frequency, at 0.55, falls short of stoichiometric dolomite, 0.606.

It is instructive to plot changing Mg*/Ca as a function of Mg* (Fig. 2.15). There are two distinct trends of Fe substitution. One begins at Mg*/Ca 0.01, continuing to 0.07 and beyond (as seen in the inset); the other begins around 0.19 and continues, in the limestones, to dolomitic proportions of 0.50 or more. In the intermediate phases (mainly VHMC) of the second trend, Fe can constitute 25% or more of the Mg* content, though some of this is likely to be interstitial (incorporated during re-precipitation) and 0.50 Mg*/Ca therefore not commensurate with true dolomite.

Clustering in the Zhaowei samples is less regular (but the dataset is smaller). Mg/Ca peaks at 0.06–0.07 and, after a hiatus, again at 0.11–0.13. The interval 0.19–0.27 is almost vacant. VHMC is irregularly distributed but most frequent around 0.38. Thereafter there is no clear hiatus in the run-up to dolomite, but frequency is lowest around 0.44–0.47, i.e. slightly further along than in the Jiuliqiao and Sidingshan samples (possibly because interstitial Fe in the Jiuliqiao samples exaggerates Mg*/Ca at this point).

2.6.2. *Dolomitisation via dissolution and recrystallisation*

Dolomite can form in a variety of settings, by a variety of processes, as mineral composition responds to changes in burial depth and thereby pore-water composition, pH, temperature and pressure. Generally, inchoate and/or partial dolomitisation can be attributed to insufficient concentrations of free Mg in the pore water, on the basis that dolomitisation would not occur at all if carbonate alkalinity and temperature were the critical factors. Sufficient Mg supply requires that the rock be accessible to Mg-rich fluids. Once the rock is sealed off by compaction and cementation, further dolomitisation ceases to be possible unless permeability is re-established through pervasive fracturing. In that case, complete dolomitisation may be only a matter of time.

The process of Mg-enrichment in the Jiuliqiao Formation began while the sediment was still open to fluid-mediated diagenesis. Oxygen-isotope values lie within the range typical of Neoproterozoic carbonates and *prima facie* reflect the temperatures accompanying precipitation. It is therefore significant that the phases are, broadly considered, the same as those documented in high-temperature experiments. At whatever temperature, and regardless of the role played by bacteria, incorporation of Mg involved the quantum transformation of one stable state to another. Although the phases comprise an array (Fig. 2.15) and the range defining the discontinuities varies from sample to sample (Fig. 2.8), it was not a process of continuous enrichment.

Dissolution occurs because, even with the most stable phases, ions at the surface constantly interchange with those in the surrounding fluid, and above 3 mol% $MgCO_3$ calcite solubility increases with Mg content, up to a maximum of ~19 mol% $MgCO_3$, the limit for naturally occurring marine calcites (Fig. 2.16). Where a Mg ion is adsorbed or incorporated in place of a Ca ion, a critical imbalance may be reached where the fluid is no longer effectively saturated for the magnesian calcite phase and the phase dissolves. Further Mg input restores saturation. Incipient dissolution of this kind appears to be the cause of Mg-enrichment in grain rims (Fig. 2.8a), as in

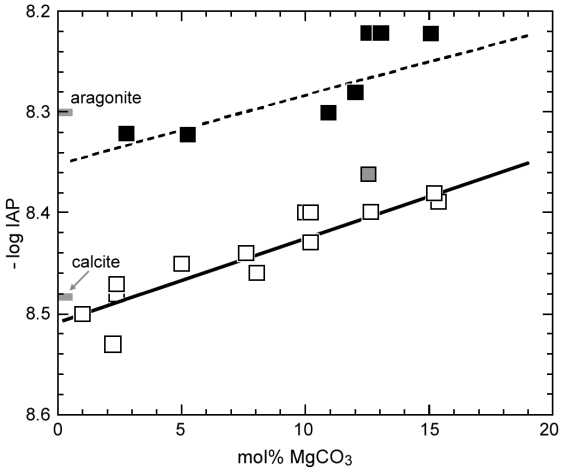

Figure 2.16. Increasing solubility with Mg content (redrawn from Morse et al. 2006). Filled squares: biogenic calcite. Unfilled: synthetic calcite. Grey: excluded from biogenic best fit.

cements generally. Any phase that subsequently precipitates has to be less soluble in the enriched fluid than that which previously dissolved. The main control on solubility being ambient pH, potentially the most critical factor promoting calcite dissolution is the reduction of sulphate by SRM, as discussed above.

At the other extreme, ordered, stoichiometric dolomite is less soluble even than Mg-free calcite; the disordered form has about the same solubility. Very-high magnesium calcite is the first, but transitory, phase to nucleate in experiments because it is less soluble than preceding phases but more soluble than close-to-stoichiometric dolomite. The final step, whereby Mg approaches molar parity with Ca, is kinetically easier (Sibley et al. 1987). Thus, in addition to the problem of how the Sidingshan Formation came to be pervasively dolomitised, if that was the process, there is the question why crystals with Mg*/Ca of 0.20–0.43 in the Jiuliqiao Formation did not undergo the same process.

2.6.3 *Abiotic controls on dolomitisation*

The principal abiotic controls on growth of dolomite are temperature, solution Mg/Ca and saturation state (Machel & Mountjoy 1986). Temperature affects whether dolomitisation takes place at all without bacterial mediation; if it does take place, temperature also affects the rate of reaction and precipitation (Burton & Walter 1987, Arvidson & Mackenzie 2000). Higher temperature favours Mg uptake, a relation which, along with the mesophilic nature of most SRM, explains why dolomite generally occurs at shallow water depths and low latitudes. In the case of Lagoa Vermelha (where SRM are involved) both calcite and high-Mg calcite precipitate at temperatures up to 40° C, only dolomite (stoichiometric but disordered) at 45° C (Vasconcelos et al. 2005).

Rising temperature as a consequence of shallowing may be one factor that promoted dolomite in the Sidingshan Formation, and in principle may be tracked through $\delta^{18}O$ (after a 2.7‰ correction for the larger carbonate-water fractionation compared to calcite, but ignoring a -0.8‰ difference due to phosphoric acid fractionation; Rosenbaum & Sheppard 1986). However, while a rise in temperature would cause a fall in $\delta^{18}O$, by about 0.20–0.25 ‰ per degree C, greater evaporation would cause a rise in $\delta^{18}O$. Because of these contrary effects, a change in temperature as a result of shallowing is impossible to establish.

For a given concentration, solutions with lower Mg/Ca will yield products poorer in Mg (Kaczmarek & Sibley 2011, Xu et al. 2013) – the same effect as lower temperature at the same Mg/Ca (Mucci 1987, Burton & Walter 1987). At high solution ratios the Mg/Ca of the precipitate in abiotic experiments will not exceed 0.07 (De Choudens-Sánchez & González 2009). HMC among

the Jiuliqiao samples extends as far as 0.07 and a few attain higher ratios (Fig. 2.15). Thus Mg does not appear to have been in short supply. In abiotic experiments Mg concentration appears to be less important than temperature (Arvidson & Mackenzie 1999). Modern seawater is many times more supersaturated in respect of dolomite than calcite, but even if supersaturation is further increased, for example by evaporation, precipitation will not occur. Microbes increase effective saturation primarily by promoting dehydration of the ions.

2.6.4. *Sulphate, pyrite, sulphur isotopes and organic carbon*

Apart from aerosols, sulphur enters the ocean from two directions: through outgassing of SO_2 and H_2S at mid-ocean spreading centres, where it is oxidised to sulphate, and via rivers, following the oxidation of pyrite and other sulphides by subaerial weathering (Canfield 2004). In the Proterozoic, most of the mantle-derived sulphur would have remained as H_2S or $FeHS^+$ (Saito et al. 2003), since the subsurface ocean was anoxic. Some sulphate would have been generated by oxidation of H_2S at the surface and reaction of atmospheric SO_2 with water. The extent to which crustal sulphide was oxidised by subaerial weathering is unknown.

Carbonate sulphur concentrations through most of the Jiuliqiao Formation are relatively high, declining through the last 30 m (Fig. 2.9b). Most of the sulphur is inferred to have been involved in reduction of sulphate (§2.5). Microbes preferentially extracted the lighter isotope, ^{32}S, leaving the sulphide end-product depleted. Sulphate $\delta^{34}S$ through the sequence is remarkably stable, declining slightly from an average 31.2‰ in the Jiuliqiao to 30.2‰ in the Sidingshan. Through the first 40 m pyrite $\delta^{34}S$, by contrast, is erratic, ranging from not depleted at all to 20‰ lighter than the sulphate. In the Sidingshan, carbonate sulphur concentrations are mostly similar to those of the later Jiuliqiao. The scant pyrite is markedly depleted, with an average sulphate-pyrite fractionation of 27‰ (Jiuliqiao Formation, 12‰).

Sulphur isotope systematics are complex and beyond the scope of this study. Nonetheless a few points may be made. Minimal variation in sulphate $\delta^{34}S$ suggests that isotopic values were locally buffered by high concentrations. In absolute terms the values themselves are high, though within the range of the much more variable (+5 to +40‰) Mesoproterozoic record (Guo et al. 2015). Isotopic enrichment, with an overall rising trend through the Precambrian, results from the burial of ^{34}S-depleted pyrite.

On the assumption that sulphate levels were low, some researchers postulate a ‘reservoir effect’ whereby $\delta^{34}S$ rose as sulphide formed from an increasingly enriched sulphate pool lower in the water column (Gomes & Hurtgen 2015). In this scenario the apparent sulphate-pyrite fractionation

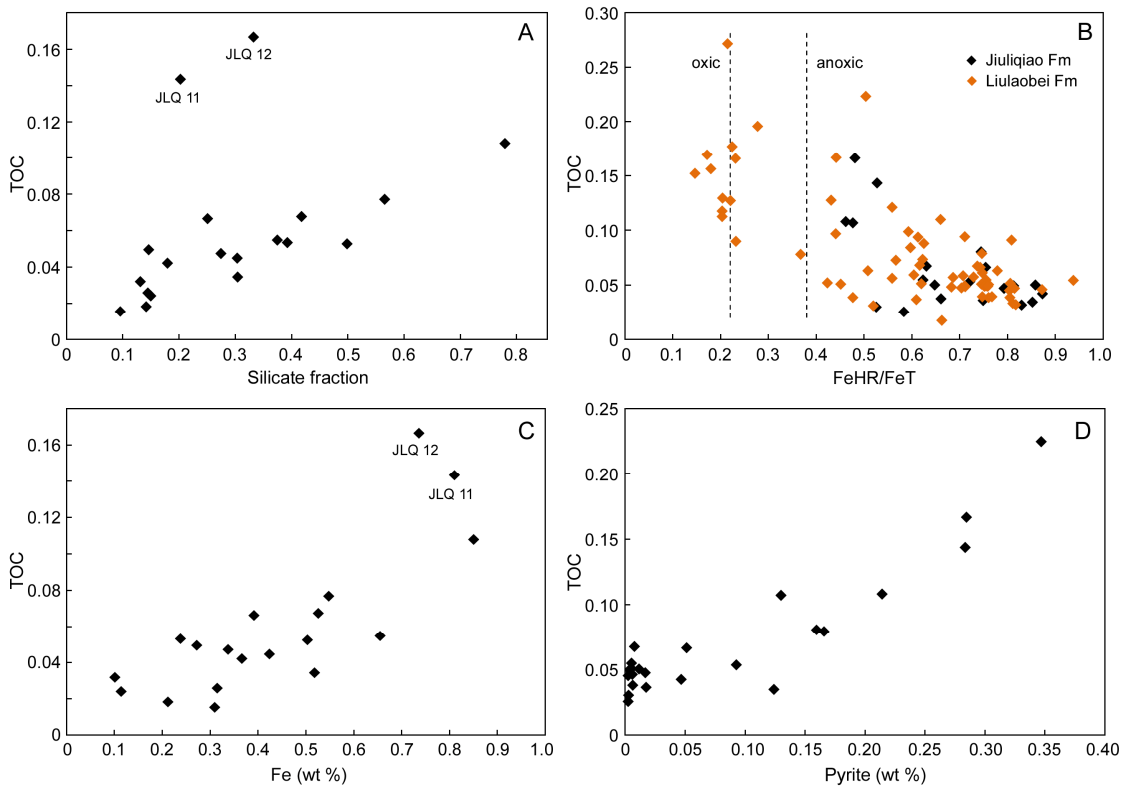

Figure 2.17. Preserved organic C is meaningfully related to other local signals: (**a**) as a function of silicate fraction, Jiuliqao Formation; (**b**) as a function of redox; (**c**) as a function of carbonate Fe, measured by ICP-OES; and (**d**) as a function of FeS_2. Data in (b) and (d) mostly from Guilbaud et al. (2015).

is depressed because the sulphate signal comes from carbonate precipitated at the surface whereas the pyrite signal averages the whole subsurface water column. However, in the present case both calcium carbonate and pyrite appear to have formed at or below the seafloor. Low fractionation cannot be attributed to a reservoir effect. More probably it arises from the reaction of Fe^{2+} with dissolved mantle-derived H_2S or HS^- that had not gone through a cycle of sulphate reduction.

Sulphate-reducing microbes require organic carbon. Strong correlation between TOC – the refractory residue after remineralisation – and the silicate fraction in the Jiuliqiao (Fig. 2.17a), as also between TOC and Fe (Fig. 2.17c, d), suggests that production was driven by nutrient supply. There are no such correlations in the dolostones, which contain less TOC and relatively little siliciclastic material. In Phanerozoic environments the frequent correlation of pyrite and TOC is attributed to the dependence of sulphate reduction on the availability of OC (Berner 1989, Ohmoto & Goldhaber 1997); correlation is weak when the environment is euxinic and OC-limited. The evidence from microscopy (App. 5) is that production in the Sidingshan did not decrease markedly. Did perhaps a change in ecology modify the relationship?

An alternative, or additional, explanation of the large increase in average sulphate–pyrite fractionation is that sulphate reduction shifted from the substrate to the water column. Pyrite was no longer forming from H_2S (Table 2.2). Unburied, sulphide mixed with the oxygen-producing surface and reverted back to sulphate. Anoxia enhanced the recycling of nutrients such as sulphur and phosphorus and thus far stimulated production, which led to higher rates of aerobic remineralisation, the perpetuation of water-column anoxia and – completing the feedback loop – the efficient recycling of benthic phosphorus (Ingall & Jahnke 1997, Kraal et al. 2010). After JLQ 31 microalgae appear to have been the dominant phytoplankton (App. 5). In the oligotrophic conditions accompanying the fall in siliciclastic sedimentation and dissolved Fe and Mn (important nutrients), microalgae gained a competitive advantage (Agawin 2000, Nagy et al. 2009). Once established, their dominance became difficult to reverse (Scheffer et al. 1997, Butterfield 2009), even when waters temporarily deepened.

The principal technique for inferring the redox state of ancient marine environments is iron speciation. Highly reactive Fe (i.e., pyrite and phases reactive enough to form pyrite, either in the water column or during early diagenesis) is measured proportional to total Fe, with enrichment in pyrite occurring where sulphide is abundant in the water column. In modern settings the iron derives from continental weathering and is remobilised from the oxic shelf to deeper sulphidic waters, where it rains out as pyrite. A ratio above 0.38 indicates that the subsurface water column is anoxic. So quantified, the redox state above Jiuliqiao sediments was anoxic but highly variable. The most systematic trend was a steady rise in FeHR/FeT through the first 15 m, from 0.46 to 0.87 (Guilbaud et al. 2015).

In the upper Liulaobei Formation preceding the Feishui Group, where the environment appears to have been slightly deeper, several samples fall well below the 0.38 threshold (Fig. 2.17b). The oxic states are attributed to storms, but the clearest association is with organic carbon. Dissolved iron and other nutrients stimulated photosynthesis, the oxygen so generated oxidised the iron (cf. Fralick & Pufahl 2006), and the iron hydroxides turned to pyrite (Fig. 2.17d). In this way photosynthetic oxygen could stimulate pyrite formation. The results of iron speciation must therefore be interpreted with caution. Although anoxic, Liulaobei environments produced very little pyrite.

Although it contributed little to FeHR, pyrite, mostly varying from $FeS_{1.4}$ to FeS_2, was the main iron mineral in the Jiuliqiao environments. Haematite and magnetite occurred in the interval straddling the limestone-dolostone transition (Table 2.2, Fig. 2.18), indicating that the substrate briefly touched the oxycline. Either the water deepened thereafter – something the subsequent

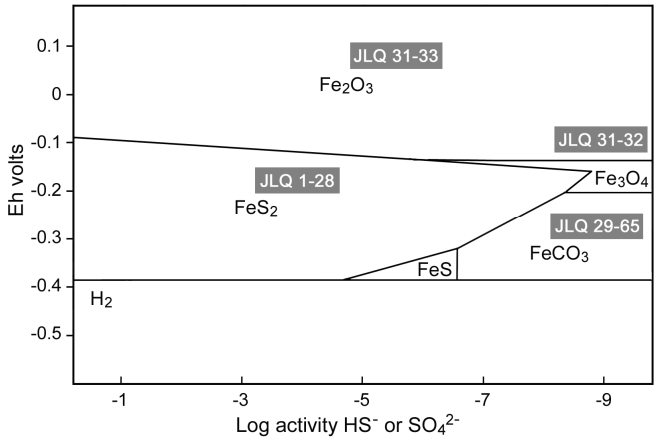

Figure 2.18. Mineral stability fields of Fe minerals as a function of Eh and dissolved S (Curtis & Spears 1968), assuming pH 7, activity of HCO_3^- $10^{-2.5}$ and solids stable where activity of Fe^{2+} $<10^{-3}$. The figure is illustrative: both pH and $aHCO_3^-$ were in fact probably much higher.

switch to dolomite and low concentrations of Fe^{2+} do not indicate – or the oxic zone withdrew to a still shallower level. Oxidation is also reflected in the reaction of barium with sulphate in the feldspar (App. 4 Figs. 23, 24), apparently only in JLQ 32. BaAl commonly substitutes for KSi in feldspar.

In the Sidingshan, $(Fe,Ca)CO_3$ was the main iron mineral (Table 2.2). Since there was no shortage of H_2S in the water, the explanation seems to be that sulphate reduction was primarily taking place above the zone where Fe^{2+} was most available – what little was available – and that this was above the substrate. Ankerite formed lower down, where sulphur was in short supply (Curtis & Spears 1968), perhaps via microbial iron respiration; very little pyrite formed. A corollary is that dolomite was forming above the substrate.

2.7. Evidence for direct precipitation of dolomite

2.7.1. *Diagenesis requires implausible volumes of fluid throughput*

Whatever the rate of sedimentation, rates of lithification were not slow, as shown by the frequency of intraclasts in the sediments (Fig. 2.3d, 2.4b; App. 5 Figs. 4, 5, 15, 18). Alteration of calcite to dolomite requires large water/rock ratios, so that rapid lithification and concurrent occlusion of pore space (enabling metastable phases to be preserved) only exacerbate the 'dolomite problem'. Starting, say, with limestone of 40% porosity at 25° C, the replacement of calcium in accordance with the reaction

$$2CaCO_3 + Mg^{2+} \rightarrow CaMg(CO_3)_2 + Ca^{2+} \qquad (10)$$

would require a volume of seawater 650 times that of the rock to pass through the sediment (Land 1985), and this on the unrealistic assumption that all oversaturated Mg went into dolomite and conditions were kinetically ideal. The ratio can be reduced if dolomitisation proceeded in accordance with reaction (4) rather than reaction (10), so that the final rock volume increased, or if

the temperature was higher, but in substance the problem remains (Machel 2004) – especially with lithification being rapid (an increase in rock volume would have consumed pore space more rapidly). The fluid circulation or ion diffusion required for dolomite to have formed through diagenesis is consequently difficult to visualise (*ibid*.).

Could, then, the dolomite have precipitated directly from the water column? The immediate advantage of this scenario is that availability of Mg ceases to be problematic. Calcium and magnesium would have been extracted from the circulating water body in equal measure. It would also explain why seawater passing through fractures in lithified dolomite crystallised as calcite (App. 5 Fig. 9): the substrate environment was depleted in Mg, and evidently this later seawater was not a dolomitising fluid. As discussed below, other lines of evidence point in the same direction.

2.7.2. *Small, uniform crystal size*

Recrystallisation usually results in larger crystals (Malone et al. 1996, Machel 1997), by a process known as 'aggrading neomorphism'. In a closed or restricted solution crystallisation tends to proceed more slowly, and small crystals act as nucleation seeds for the growth of larger ones. The typical crystal size of primary dolomite, whether cement (Mitchell et al. 1987) or matrix (Mastandrea et al. 2006, Preto et al. 2015), is 5–10 μm, possibly up to 60 μm. Dolomite in the Sidingshan varies in size. In sections through stromatolites (App. 5 Figs. 12, 13, 17) organic-rich laminae consist of small crystals 5–20 μm in diameter. Whether or not they arose from microbially induced dolomite at the stromatolite surface, there is no evidence of dissolution and recrystallisation of earlier phases. Organic-poor laminae inbetween comprise regularly-sized, mostly subhedral microcrystals 20–40 μm in diameter, consistent with precipitation from the overlying water and limited recrystallisation. The intervals between stromatolite columns are much coarser, of mixed crystal size and include appreciable amounts of microcrystalline silica. Similar contrasts may be seen at boundaries between intraclasts and matrix. Some samples, with slightly lower $\delta^{18}O$, appear coarser-crystalline throughout (App. 5 Fig. 21). In contrast to the inferred association between organic matter and dissolution in the Jiuliqiao, organic-rich patches in the Sidingshan have smaller crystals. The coarse dolomite fabrics suggest recrystallisation linked to the dissolution of finer dolomite crystals, and in several recrystallised samples microcrystalline dolomite still persists. Coarse recrystallisation is not accompanied by higher Mg/Ca.

Primary growth of dolomite in and above stromatolites suggests that sulphate-reducing anaerobes worked in the same micro-environment as cyanobacteria. Indeed, some SRM can tolerate oxygen, and they are a common component in microbial mat systems (Baumgartner et al. 2006). At night,

when photosynthesis stops, microbial mats are typically anoxic and SRM remineralise mucilage within hours, promoting the precipitation of carbonate. In the same systems other organisms re-oxidise sulphide and cause carbonate minerals to dissolve. The anomalously high sulphur recorded in some spot analyses (up to 0.48 %) may have been due to sulphide-oxidising activity, as may the high $\delta^{34}S$ pyrite values through JLQ 45–52.

2.7.3. *No remnants of primary calcite in the dolostones*

If the dolostones originated via dissolution of precursor calcite, one would expect to find enclaves, if not entire horizons, of remnant calcite that was not at all, or only partially, dolomitised. Dolomitisation tends to occur around horizons associated with previous porosity, around tectonic faults and fractures or around compaction features such as stylolites (Carnell & Wilson 2004). Here one looks for non-dolomitised residues in vain. Calcite occurs only as a very occasional spar within tiny voids in partially recrystallised dolomite – as a late, not early, mineral (App. 5 Fig. 16).

Why, then, did calcium carbonate not precipitate at the same time as dolomite? Ultimately it is a matter of solubility. Dolomite is intrinsically less soluble than calcium carbonate, but is inhibited by Mg complexes with H_2O and CO_3^{2-}. SRM facilitate precipitation by generating hydrogen sulphide, which dehydrates Mg. If Fe^{2+} is scarce, the sulphide rises into the upper water column, where it is re-oxidised, microbially or inorganically, to sulphuric acid (Stoessel 1992, Ku et al. 1999, Moreira et al. 2004):

$$H_2S + 2O_2 \rightarrow H_2SO_4 \qquad (11)$$

$$CaCO_3 + H_2SO_4 \rightarrow CaSO_4^0 + H_2O + CO_2 \qquad (12)$$

The process that promoted dolomite lower down, in anoxic organic-rich waters, also worked against the precipitation of calcium carbonate higher up.

ZW 51, a sample surrounded either side by limestones, offers an interesting contrast, being a dolostone with non-negligible occurrences of magnesian calcite (App. 4 Fig. 32). The HMC appears to occupy former spaces between dolomite crystals, suggesting growth of HMC after deposition but before compaction.

Alkalinity was also a factor. As we have seen, calcium carbonate precipitation was promoted not so much by photosynthetic consumption of CO_2 as by dissolution of alkali feldspar; it therefore precipitated at or within the substrate. On the other hand, because Mg complexes with CO_3^{2-} more readily than Ca does, and with CO_3^{2-} much more than with HCO_3^- (Garrels & Thompson 1962),

the higher carbonate/ bicarbonate ratio of high pH waters would have disadvantaged dolomite. Dolomite would have been favoured by only moderate alkalinity.

The proportion of silicon captured in the carbonate minerals follows that of silicates in the bulk sediment. The higher the rate of silicate deposition relative to carbonate precipitation, the higher was the concentration of K^+ and CO_3^{2-} resulting from silicate dissolution. Net alkalinity can therefore be parameterised by multiplying the averaged carbonate-normalised weight % of silicon associated with the calcite or dolomite component by the 'bulk' carbonate percentage. Thus gauged, pH fell as $\delta^{13}C$ increased and conditions favoured dolomite (Fig. 2.19). The calcite samples clearly fall in a different domain from most of the dolomite samples, either because the same zone of precipitation underwent a change in alkalinity or because (the preferred explanation) the zone from which dolomite precipitated was less alkaline and, by implication, well above the substrate. That water depth itself had an effect on alkalinity may be seen from the higher values of JLQ 51–58, when $\delta^{13}C$ fell and sea-level temporarily rose.

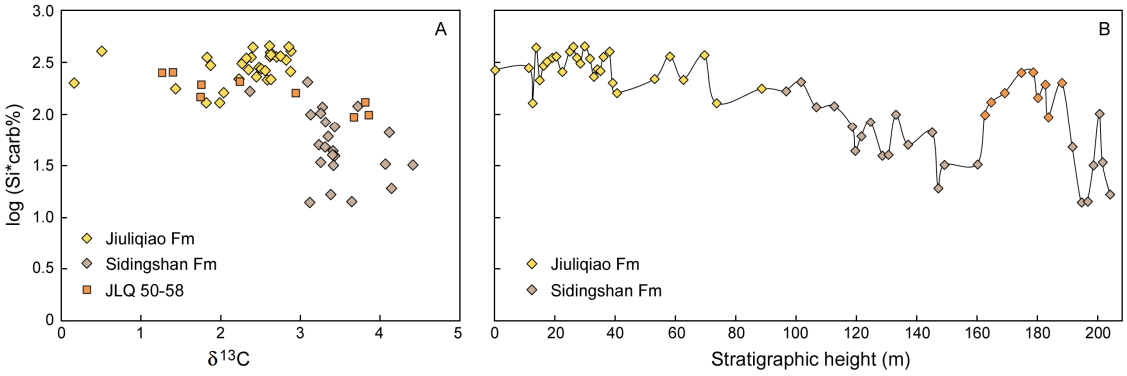

Figure 2.19. Carbonate-included silica concentration normalised to carbonate fraction (estimated via ICP) as it varied with **(a)** $\delta^{13}C$, **(b)** stratigraphy. The water in which most dolomite formed was less alkaline than that in which calcite formed. JLQ 50–58 represent an episode of deepening.

2.7.4. *Non-depletion of $\delta^{13}C_{carb}$, enrichment of $\delta^{18}O$*

If the dolomite formed within the sediment, catalysed by remineralisation of organic matter, a proportion of the carbonate carbon should have derived from organic matter, depending on how much organic matter remained to be remineralised and how much of the carbon recycled was lost to the water above. Consequently the isotopic ratio of the dolomite should have been several per mil lighter than the ratio of the calcite from which it also derived some of its carbon. Isotopic depletion is seen in modern dolomite forming in such conditions (e.g. Irwin et al. 1977, Vasconcelos & McKenzie 1997, Budd 1997, Meister et al. 2007). That the dolomite of the Sidingshan Formation is apparently not depleted implies that it did not form in such conditions.

Similar considerations apply to the Jiuliqiao Formation. Since the calcium carbonate is authigenic and apparently also not depleted to any great extent, remineralisation must have been largely completed before the residue reached the sediment. Moreover, the dissolved inorganic carbon (DIC) from which it precipitated must have been isotopically well mixed.

Dolomite incorporates more ^{18}O from seawater than does calcite. The difference in fractionation decreases as water temperature increases, but the decrease is so slight as to be immaterial for temperatures in the range 0–60° C (Chacko & Deines 2008). In their experiments with lagoon water Vasconcelos et al. (2005) derived the following correlation:

$$1000 \ln \alpha_{\text{dolomite-water}} = 2.73 \times 10^{6} T^{-2} + 0.26 \qquad (13)$$

Since the corresponding equation for calcite-water fractionation (Friedman & O'Neil 1977) has an almost identical slope and an intercept of -2.89, the difference in fractionation is effectively 2.6‰ at all temperatures. Some studies suggest a higher figure (Horita 2014). The equation for dolomite assumes that it precipitates, like calcite, directly from the water. The 2.2‰ average difference between the calcites (JLQ 1–31) and dolomites (JLQ 32–58) of the present dataset (relating to an average Mg*/Ca difference of 0.47, as against 0.61 for pure calcite) is thus consistent with direct precipitation. Proterozoic dolostones generally are heavier than coeval limestones (Prokoph et al. 2008). The fine-grained dolomite beds in Baffin Bay, Texas, enriched by approximately 3‰ over co-existing aragonite and Mg-calcite, appear to be a modern example of direct precipitation (Ehrens & Land 1972). That most dolostones in the Phanerozoic have oxygen isotope ratios similar to coeval limestones (Veizer & Hoefs et al. 1976) suggests that they were not directly precipitated.

2.7.5. *Crypto-dolomite within the quartz and feldspar*

As we have seen, carbonate minerals filled the spaces within silicate minerals vacated by partial dissolution – a direct and immediate response to the increase in alkalinity. The composition of the precipitated minerals was therefore controlled by the ambient conditions at the time of dissolution. In the Jiuliqiao Formation feldspar dissolution, precipitation of calcium carbonate within the feldspar and precipitation of vaterite grains between feldspar crystals all took place at the same time. Consequently the Mg*/Ca ratio of the feldspar carbonate approximates that of the granular carbonate (Fig. 2.11). In the Sidingshan the Mg*/Ca ratio of the feldspar is lower than that of the precipitated dolomite, but still dolomitic (> 0.40) and still distinct from that of the Mg-rich calcite which filled voids. The differences suggest that the dolomite crystals precipitated first, the feldspar dolomite precipitated from water from which some Mg had been extracted, and the calcite

precipitated after the pore water had been thereby further depleted. None of the feldspars have a Mg*/Ca ratio lower than 0.40.

2.7.6. *Implications for the interpretation of other ancient dolomites*

Tucker (1982) was among the first to postulate primary dolomite formation, and to ask whether it was not the norm in the Proterozoic. One example adduced was the Beck Spring Dolomite underlying the Cryogenian Kingston Peak Formation of south-eastern California. Preservation of detail was so impressive that 'unless one knew, from staining, X-ray diffraction, or some other technique, that the rock was a dolomite, one would believe it to be an undolomitized Phanerozoic limestone'. The different components – pisolites, micrite, fibrous and sparry cements – were likewise isotopically distinct, a finding incompatible with whole-rock diagenesis.

The dolomitic Leba Formation of south-western Angola is Mesoproterozoic in age (Heydari 2013). Internal textures of all grains and cements, including micrite, ooids, oncoids and seafloor cements, are perfectly preserved. Heydari himself suggests that the dolomite precipitated directly from seawater. The Denault Formation of north-eastern Canada is Palaeoproterozoic (Zentmyer et al. 2011). Shales in the outer-ramp facies include silt- to micrite-sized crystals of dolomite. Laminites in the middle-ramp facies comprise alternating crinkled biofilms and layers of dolomite crystals 2–10 μm in size; some crystals contain gypsum-pseudomorph cores, indicating evaporitic sulphate precipitation at the same time as the carbonate. Pyrite is absent. Dolomites are reported to be 49 mol% $MgCO_3$ (0.58 Mg/Ca) and their depositional fabric, including dolomite intraclasts, is well-preserved. In the light of the present study, it is difficult to see why the microcrystalline, fabric-preserving dolomite should not be regarded as primary rather than mimetic.

In Australia most early-to-mid-Neoproterozoic carbonates are dolomites. In summarising their features Hill and Walter (2000) state that they were either uniformly recrystallised or recrystallised in two stages, one retaining the microstructure, the other destroying it. In the common case where the fabric is preserved, crystal size is 1–10 μm. No reason is given for interpreting the micrite as secondary. In the Flinders Range the dolomite crystals in the post-Sturtian Oodnaminta Reef Complex are often less than 8 μm. Sedimentary fabric remains visible, in contrast to the coarsely crystalline replacement dolomite of many Phanerozoic dolomites (Hood et al. 2011). Limestone occurs only in slope facies, where debrites include blocks in which dolomite partially replaced the micrite (Hood & Wallace 2012); it does not follow that all dolomite was originally limestone. On the platform most dolomite ooids show no dissolution or recrystallisation textures, and while it may be that 'the occurrence of micritic laminae, and lack of radial fabrics within mimetically

dolomitised ooids is consistent with an originally aragonitic mineralogy', such features may also be consistent with an originally dolomitic mineralogy: the description of the ooids as 'mimetic' and dolomitised begs the question.

The Rasthof Formation of northern Namibia is a 220-m-thick post-Sturtian carbonate, consisting almost entirely of dolomite. The first 14 m pass from below fair-weather base to shallower-water stromatolites. Near the bottom, laminae of light (presumably organic-poor) dolomite alternate with darker calcite (Tojo et al. 2007). Rip-up clasts display the same lamination, showing that the dolomite formed before the clasts and before the carbonate was consolidated. Direct precipitation is implied. Similar alternations of dolomite and calcite are reported from the Bitter Springs Formation (Hill et al. 2000), the dolomite being 0.5‰ to 1.1‰ heavier than the calcite (cf. Sheppard & Schwarcz 1970). They also occur at certain horizons in the diamictite-rich Ghaub Formation, although here a detrital origin is possible (Hoffman 2011).

The cap carbonates at the end of the Cryogenian are nearly all dolostone. After a few metres there is typically a switch to limestone, for example at the end of the Mirassol d'Oeste Formation, Brazil. Preservation of laminae, primary fenestral porosity, peloids and micritic textures suggest a primary origin (Sansjofre et al. 2011). Although calcite sometimes occurs within the dolomite, it is either secondary (large blocky crystals) or post-depositional (veins) (e.g. Wang et al. 2008).

The Polanco Formation, Uruguay, is a mixed siliciclastic-carbonate unit of late Ediacaran age (Gaucher et al. 2000). Rhythmites consist of alternating calcarenite/calcisiltite and dolosiltite/ dololutite. The authors interpret the dolomite as primary on the grounds that it is very fine-grained, distinct from the calcite on a millimetre scale, organic-rich and often pyritic, consistent with an origin via sulphate reduction. Dolosiltite also occurs as rip-up intraclasts in overlying calcarenites, showing that the dolomite formed about the same time as the calcite.

The same question arises in relation to examples from the Palaeozoic, when, in general, platform seas were more oxygenated and conditions less favourable for primary dolomite. In the Lower Ordovician Ellenburger Group of west Texas multiple generations of dolomite can be identified (Kupecz & Land 1994). The earliest, and most voluminous, predates karstification and brecciation and consists of fine to very fine crystals (13–59 μm) with planar boundaries, distinct from a later, larger group of crystals (95–167 μm) with non-planar boundaries. Carbon isotope values of the two groups are virtually indistinguishable but the karstified samples display a wider and lower range of $\delta^{18}O$ (-2.4 to -8.8 ‰ as against -2.4 to -6.2 ‰). By analogy with less altered stratigraphic correlatives, the earlier dolomites may have been direct precipitates from seawater.

In the Lower Carboniferous carbonates of the Williston Basin, southern Canada (Rott & Qing 2013), dolomite is pervasive. Most of it is fine (20–30 μm) to very fine (4–20 μm), the former probably a recrystallisation of the latter. Most ooids consist of dolomite cores (originally organic-rich) and calcite outer layers. Dolomite formation is inferred to have been very early. It predates the medium to coarsely crystalline calcite cement that overlies and in parts replaces the dolomite ooid rims, predates the medium crystalline dolomite cement that commonly lines vugs and pores in the dolomite host rock, and predates the anhydrite (originally gypsum) that filled some spaces. There is no evidence of a calcitic phase earlier than the very fine dolomite. Inorganic $\delta^{13}C$ ranges from about 2.3 to 3.4‰.

As a final example, I mention the Lower Carboniferous dolomites of the Dunvegan Gas Field, Alberta. Machel (1997) cites them as a clear-cut example of dolostones that have not been obviously recrystallised. Crystal size is in the range 1–20 μm, average Mg/Ca 0.44, $\delta^{13}C$ 1.4–4.3 ‰ and $^{87}Sr/^{86}Sr$ the same as contemporaneous seawater (Al-Aasm 2000). If dissolution-reprecipitation occurred, it did not change the original crystal size, stoichiometry or geochemical composition outside of the range of original dolomite formation.

2.8. Conclusions

The Jiuliqiao Formation is a mixed deposit of magnesian calcite and siliciclastics, mainly K-feldspar. Much of the feldspar is altered to quartz, a residue of partial dissolution under high pH. The succeeding Sidingshan Formation is silicate- and iron-poor dolomite. Carbon-isotope ratios are typical of the mid Tonian: just over 2‰ in the Jiuliqiao, rising to between 3 and 4‰ in the Sidingshan, briefly interrupted by an episode of deepening where they fall to 1‰. The link with sea-level suggests that $\delta^{13}C$ was controlled by local conditions. The unconformably overlying Fengtai Formation consists of carbonate-rich diamictite, with features inviting comparison with Cryogenian diamictites.

The almost pristine state of preservation and wide range of mineralogies in the Jiuliqiao and Sidingshan Formations afford unprecedented insight into the conditions governing the composition and precipitation of carbonate minerals in the mid Neoproterozoic. Geochemical and petrographic evidence demonstrate that most, possibly all, calcium carbonate was authigenic, precipitating as vaterite within sediment dominated by alkali feldspar. Silicate weathering under an atmosphere rich in CO_2 generated high levels of bicarbonate runoff, which promoted further silicate dissolution in seawater and further raised alkalinity. Carbonate precipitated in response. Siliciclastic sediment was thus part of the carbonate factory.

In both formations the $\delta^{13}C$ of residual organic carbon is 28–32‰ lighter than carbonate carbon. Since the calcite precipitated *in situ*, from DIC that was not to any great extent isotopically depleted, remineralisation must have taken placed largely above the seafloor and the shallow-sea water column must have been isotopically well mixed.

Dolomite rarely forms in modern coastal environments and is almost impossible to synthesise in solutions that mimic seawater. The greatest limiting factor appears to be the supply of Mg. Complexing with water molecules and carbonate and sulphate ions prevents Mg from forming ionic bonds with carbonate, while the ordered layering of Mg and Ca in the dolomite lattice presents an energy barrier. Occurring around Mg/Ca = 0.40 (ignoring Fe), the barrier is reflected in the Mg/Ca compositions of the Jiuliqiao Formation. Mg enrichment via dissolution and recrystallisation – the process that characterises dolomitisation today – failed to produce dolomite.

In the Sidingshan environment dolomite appears to have been favoured by (i) intermediate alkalinity, associated with low siliciclastic input, (ii) de-complexing and dehydration of Mg ions in the course of anaerobic sulphate reduction, and (iii) low nutrient levels, promoting an increase in nutrient (S, Mn, Fe, P) recycling and raising the oxycline. Again, since dolomite formation was intimately associated with the remineralisation of organic matter but did not result in any obvious isotopic depletion, remineralisation must have taken place largely above the seafloor. The mineral precipitated from the water column, where in evaporative settings Mg was not limited. A brief survey of other instances of dolomite in the Proterozoic and early Palaeozoic suggests that direct precipitation was not unusual. Dolomite formation was more common in the Precambrian because anoxia was more common. High seawater temperature was probably also a factor, though difficult to isolate, as was high saturation state, owing to high levels of atmospheric CO_2.

References

Agawin, N.S.R., Duarte, C.M., Agustí, S., 2000. Nutrient and temperature control of the contribution of picoplankton to phytoplankton biomass and production. *Limnol. Oceanogr.* 45, 591–600.

Al-Aasm, I.S., 2000. Chemical and isotopic constraints for recrystallisation of sedimentary dolomites from the Western Canada sedimentary basin. *Aquat. Geochem.* 6, 227–248.

Altermann, W., 2008. Accretion, trapping and binding of sediment in Archean stromatolites – morphological expression of the antiquity of life. *Space Sci. Rev.* 135, 55–79.

Althoff, P.L., 1977. Structural refinements of dolomite and a magnesian calcite and implications for dolomite formation in the marine environment. *Am. Mineral.* 62, 772–783.

Arvidson, R.S., Mackenzie, F.T., 1999. The dolomite problem: control of precipitation kinetics by temperature and saturation state. *Am. J. Sci*. 299, 257–288.

Arvidson, R.S., Mackenzie, F.T., 2000. Temperature dependence of mineral precipitation rates along the $CaCO_3$–$MgCO_3$ join. *Aquat. Geochem.* 6, 249–256.

Bartley, J.K., 1996. Actualistic taphonomy of cyanobacteria: implications for the Precambrian fossil record. *Palaios* 11, 571–586.

Baumgartner, L.K. et al., 2006. Sulfate reducing bacteria in microbial mats: Changing paradigms, new discoveries. *Sediment. Geol.* 185, 131–145.

Berner, R.A., 1989. Biogeochemical cycles of carbon and sulfur and their effect on atmospheric oxygen over Phanerozoic time. *Palaeogeogr. Palaeocl*. 75, 97–122.

Blum, A.E., Stillings, L.L., 1995. Feldspar dissolution kinetics. *Rev. Miner.* 31, 291–351.

Bontognali, T.R.R. et al., 2008. Microbes produce nanobacteria-like structures, avoiding cell entombment. *Geology* 36, 663–666.

Brady, P.V., Walther, J.V., 1990. Kinetics of quartz dissolution at low temperatures. *Chem. Geol*. 82, 253–264.

Budd, D.A., 1997. Cenozoic dolomites of carbonate islands: their attributes and origin. *Earth Sci. Rev*. 42, 1–47.

Burton, E.A., Walter, L.M., 1987. Relative precipitation rates of aragonite and Mg calcite from seawater; temperature or carbonate ion control? *Geology* 15, 111–114.

Butterfield, N.J., 2009. Macroevolutionary turnover through the Ediacaran transition: ecological and biogeochemical implications. *Geol. Soc. Lond. Spec. Pub.* 326, 55–66.

Canfield, D.E., 2004. The evolution of the Earth surface sulfur reservoir. *Am. J. Sci.* 304, 839–861.

Carnell, A.J.H., Wilson, M.E.J., 2004. Dolomites in Southeast Asia – varied origins and implications for hydrocarbon exploration. In: C.J.R. Braithwaite, G. Rizzi, G. Darke (eds), *The Geometry and Petrogenesis of Dolomite Hydrocarbon Reservoirs,* Geol. Soc. London Spec. Publ. 235, 255–300.

Chacko, T., Deines, P., 2008. Theoretical calculation of oxygen isotope fractionation factors in carbonate systems. *Geochim. Cosmochim. Acta* 72, 3642–3660.

Chang, L.L.Y., Howie, R.A., Zussman, J., 1998. *Rock-Forming Minerals, Volume 5B, Non-silicates: sulphates, carbonates, phosphates, halides*, 2nd edn., Geological Society, London.

Chave, K., 1954. Aspects of the biogeochemistry of magnesium, 2. Calcareous sediments and rocks. *J. Geol*. 62, 587–599.

Curtis, C.D., Spears, D.A., 1968. The formation of sedimentary iron minerals. *Econ. Geol.* 63, 257–270.

De Choudens-Sánchez, V., González, L.A., 2009. Calcite and aragonite precipitation under controlled instantaneous supersaturation: elucidating the role of $CaCO_3$ saturation state and Mg/Ca ratio on calcium carbonate polymorphism. *J. Sed. Res.* 29, 363–376.

Deffeyes, K.S., 1965. Carbonate equilibria: a graphic and algebraic approach. *Limnol. Oceanog.* 10, 412–426.

Deng, S. et al., 2010. Microbial dolomite precipitation using sulfate reducing and halophilic bacteria: Results from Qinghai Lake, Tibetan Plateau, NW China. *Chem. Geol.* 278, 151–159.

Dickinson, S.R., Henderson, G.E., McGrath, K.M., 2002. Controlling the kinetic versus thermodynamic crystallisation of calcium carbonate. *J. Cryst. Growth* 44, 369–378.

Dong, L. et al., 2008. Restudy of the worm-like carbonaceous compression fossils *Protoarenicola*, *Pararenicola*, and *Sinosabellidites* from early Neoproterozoic successions in North China. *Palaeogeogr. Palaeocl*. 258, 138–161.

Dromgoole, E.L., Walter, L.M., 1990. Iron and manganese incorporation into calcite: Effects of growth kinetics, temperature and solution chemistry. *Chem. Geol*. 81, 311–336.

Dupraz, C., Visscher, P.T., Baumgartner, L.K., Reid, R.P., 2004. Microbe–mineral interactions: early carbonate precipitation in a hypersaline lake (Eleuthera Island, Bahamas). *Sedimentology* 51, 745–765.

Ehrens, E.W., Land, L.S., 1972. Subtidal Holocene dolomite, Baffin Bay, Texas. *J. Sed. Petrol.* 42, 155–161.

Folk, R.L., Land, L.S., 1975. Mg/Ca ratio and salinity: two controls on crystallization of dolomite. *AAPG Bull.* 59, 60–68.

Fralick, P., Pufahl, P.K., 2006. Iron formation in Neoarchean deltaic successions and the microbially mediated deposition of transgressive systems tracts. *J. Sed. Res.* 76, 1057–1066.

Frank, T.D., Lyons, T.W., Lohmann, K.C., 1997. Isotopic evidence for the paleoenvironmental evolution of the Mesoproterozoic Helena Formation, Belt Supergroup, Montana, USA. *Geochim. Cosmochim. Acta* 61, 5023–5041.

Friedman, I., O'Neil, J.R., 1977. Compilation of stable isotope fractionation factors of geochemical interest. U.S. Geological Survey Professional Paper 440-KK.

Fu, X. et al., 2015. New paleomagnetic results from the Huaibei Group and Neoproterozoic mafic sills in the North China Craton and their paleogeographic implications. *Precambrian Res.* 269, 90 – 106.

Furniss, G., Rittel, J.F., Winston, D., 1998. Gas bubble and expansion crack origin of "molar-tooth" calcite structures in the Middle Proterozoic Belt Supergroup, Western Montana. *J. Sed. Res.* 68, 104–11.

Garrels, R.M., Thompson, M.E., 1962. A chemical model for seawater at 25°C and one atmosphere total pressure. *Am. J. Sci.* 260, 57–66.

Gaucher, C., Sial, A.N., Blanco, G., Sprechmann, P., 2004. Chemostratigraphy of the Lower Arroyo del Soldado Group (Vendian, Uruguay) and palaeoclimatic implications. *Gondwana Res.* 7, 715–730.

Gebelein, C.D., Hoffman, P., 1973. Algal origin of dolomite laminations in stromatolitic limestone. *J. Sed. Petrol. 43*, 603–613.

Gomes, M.L., Hurtgen, M.T., 2015. Sulfur isotope fractionation in modern euxinic systems: Implications for paleoenvironmental reconstructions of paired sulfate–sulfide isotope records. *Geochim. Cosmochim. Acta* 157, 39–55.

Grotzinger, J.P., James, N.P., 2000. Precambrian carbonates: evolution of understanding. In: N.P. James (ed.), *Carbonate Sedimentation and Diagenesis in the Evolving Precambrian World*, SEPM Spec. Pub. 67, 3–20.

Grotzinger, J.P., Kasting, J.F., 1993. New constraints on Precambrian ocean composition. *J. Geol.* 151, 235–243.

Guilbaud, R., Poulton, S.W., Butterfield, N.J., Zhu, M., Shields-Zhou, G.A., 2015. A global transition to ferruginous conditions in the early Neoproterozoic oceans. *Nature Geosci.* 8, 466–470.

Guo, H. et al., 2015. Sulfur isotope composition of carbonate-associated sulfate from the Mesoproterozoic Jixian Group, North China: Implications for the marine sulfur cycle. *Precambrian Res.* 266, 319–336.

He, T. et al., 2016. Measuring the 'Great Unconformity' on the North China Craton using new detrital zircon age data. In: A.T. Brasier, D. McIlroy, N. McLoughlin (eds), *Earth System Evolution and Early Life: a Celebration of the Work of Martin Brasier*. Geol. Soc. Lond. Spec. Pub. 448, doi.org/ 10.1144/SP448.14.

Heydari, E., 2013. Direct precipitation of dolomite from seawater in the Mesoproterozoic Leba Formation of Angola, Africa. GSA *Abstracts with Programs* 45, 819.

Hill, A.C., Walter, M.R., 2000. Mid-Neoproterozoic (~830–750 Ma) isotope stratigraphy of Australia and global correlation. *Precambrian Res.* 100, 181–211.

Hill, A.C., Arouri, K., Gorjan, P., Walter, M.R., 2000. Geochemistry of marine and non-marine environments of a Neoproterozoic cratonic carbonate/evaporite: the Bitter Springs Formation, Central Australia. In: J.P. Grotzinger, N.P. James (eds), *Carbonate Sedimentation and Diagenesis in an Evolving Precambrian World*, SEPM Special Publications 67, 327–344.

Hoffman, P.F., 2011. Strange bedfellows: glacial diamictite and cap carbonate from the Marinoan (635 Ma) glaciation in Namibia. *Sedimentology* 58, 57–119.

Hong, M., Xu, J., Teng, H.H., 2016. Evolution of calcite growth morphology in the presence of magnesium: Implications for the dolomite problem. *Chem. Geol.* 172, 55–64.

Hood, A.v.S., Wallace, M.W, 2012. Synsedimentary diagenesis in a Cryogenian reef complex: Ubiquitous marine dolomite precipitation. *Sediment*. *Geol.* 255-256, 56–71.

Hood, A.v.S., Wallace, M.W., Drysdale, R.N., 2011. Neoproterozoic aragonite–dolomite seas? Widespread marine dolomite precipitation in Cryogenian reef complexes. *Geology* 39, 871–874.

Horita, J., 2014. Oxygen and carbon isotope fractionation in the system dolomite–water–CO_2 to elevated temperatures. *Geochim. Cosmochim. Acta*, 129, 111–124.

Ingall, E., Jahnke, R., 1997. Influence of water-column anoxia on the elemental fractionation of carbon and phosphorus during sediment diagenesis. *Marine Geol.* 139, 219–229.

Irwin, H., Curtis, C., Coleman, M., 1977. Isotopic evidence for source of diagenetic carbonates formed during burial of organic rich sediments. *Nature* 269, 209–-213.

Jones, B., Luth, R.W., MacNeil, A.J., 2001. Powder X-ray diffraction analysis of homogeneous and heterogeneous sedimentary dolostones. *J. Sed. Res.* 71, 790–799.

Kaczmarek, S.E., Sibley, D.F., 2011. On the evolution of dolomite stoichiometry and cation order during high-temperature synthesis experiments: An alternative model for the geochemical evolution of natural dolomites. *Sediment. Geol.* 240, 30–40.

Katz, A., Matthews, A., 1977. The dolomitization of $CaCO_3$: an experimental study at 252-295° C. *Geochim. Cosmochim. Acta* 41, 297–308.

Kelts, K., McKenzie, J., 1982. Diagenetic dolomite formation in Quaternary anoxic diatomaceous muds of Deep Sea Drilling Project Leg 64, Gulf of California. In: J.R. Curray et al. (eds), *Initial Reports of the Deep Sea Drilling Project 64*, U.S. Government Printing Office, Washington, pp 553-569.

Knoll, A.H., Fairchild, I.J., Swett, K., 1993. Calcified microbes in Neoproterozoic carbonates: implications for our understanding of the Proterozoic/Cambrian transition. *Palaios* 8, 512–525.

Köhler, S.J., Dufaud, F., Oelkers, E.H., 2003. An experimental study of illite dissolution kinetics as a function of pH from 1.4 to 12.4 and temperature from 5 to 50°C. *Geochim. Cosmochim. Acta* 67, 3583–3594.

Kraal, P., Slomp, C.P., Forster, A., Kuypers, M.M.M., 2010. Phosphorus cycling from the margin to abyssal depths in the proto-Atlantic during oceanic anoxic event 2. *Palaeogeogr. Palaeocl.* 295, 42–54.

Krause, S. et al., 2012. Microbial nucleation of Mg-rich dolomite in exopolymeric substances under anoxic modern seawater salinity: New insight into an old enigma. *Geology* 40, 587–590.

Ku, T.C.W., Walter, L.M., Coleman, M.L., Blake, R.E., Martini, A.M., 1999. Coupling between sulfur recycling and syndepositional carbonate dissolution: Evidence from oxygen and sulfur isotope composition of pore water sulfate, South Florida Platform, U.S.A. *Geochim. Cosmochim. Acta* 63, 2529–2546.

Kupecz, J.A., Land, L.S., 1994. Progressive recrystallization and stabilization of early-stage dolomite: Lower Ordovician Ellenburger Group, west Texas. In: B. Purser, M. Tucker, D. Zenger (eds), *Dolomites: A Volume in Honour of Dolomieu*, Blackwell Scientific Publications, Oxford, pp 255–279.

Land, L.S., 1985. The origin of massive dolomite. *J. Geol. Educ.* 33, 112–125.

Land, L.S., 1989. Failure to precipitate dolomite at 25 °C from dilute solution despite 1000-fold oversaturation after 32 years. *Aquat. Geochem.* 4, 361–368.

Last, F.M., Last, W.M., 2012. Lacustrine carbonates of the northern Great Plains of Canada. *Sed. Geol.* 277–278, 1–31.

Liebermann, O., 1967. Synthesis of dolomite. *Nature* 213, 241–245.

Liu, Y., Gao, L., Liu, Y., Song, B., Wang, Z., 2006. Zircon U–Pb dating for the earliest Neoproterozoic mafic magmatism in the southern margin of the North China Block. *Chin. Sci. Bull*. 22, 2375-2382.

Machel, H., 1997. Recrystallization versus neomorphism, and the concept of 'significant recrystallization' in dolomite research. *Sed. Geol*. 113, 161–168.

Machel, H.G., 2004. Concepts and models of dolomitization: a critical reappraisal. In: C.J.R. Braithwaite, G. Rizzl, G. Darke (eds), *The Geometry and Petrogenesis of Dolomite Hydrocarbon Reservoirs*. Geol. Soc. Lond. Spec. Pub. 235, 7–63.

Machel, H., Mountjoy, E.W., 1986. Chemistry and environments of dolomitization – a reappraisal. *Earth Sci. Rev*. 23, 175–222.

Mackenzie, F.T., Garrels, R.M., 1966. Chemical mass balance between rivers and oceans. *Am. J. Sci.* 264, 507–525.

Malone, M.J., Baker, P.A., Burns, S.J., 1996, Recrystallization of dolomite: an experimental study from 50–200°C. *Geochim. Cosmochim. Acta* 60, 2189–2207.

Mastandrea, A., Perri, E., Russo, F., Spadafora, A., Tucker, M., 2006. Microbial primary dolomite from a Norian carbonate platform: northern Calabria, southern Italy. *Sedimentology* 53, 465–480.

McIntire, W.L., 1963. Trace element partition coefficients—a review of theory and applications to geology. *Geochim. Cosmochim. Acta* 27, 1209–1264.

McKirdy, D.M. et al., 2001. A chemostratigraphic overview of the late Cryogenian interglacial sequence in the Adelaide Fold-Thrust Belt, South Australia. *Precambrian Res.* 106, 149-186.

Meister, P., 2013. Two opposing effects of sulfate reduction on carbonate precipitation in normal marine, hypersaline, and alkaline environments. *Geology* 41, 499-502.

Meister, P., et al., 2007. Dolomite formation in the dynamic deep biosphere: results from the Peru Margin. *Sedimentology* 54, 1007–1031.

Milliken, K.L., 2003. Late diagenesis and mass transfer in sandstone shale sequences. In: F.T. Mackenzie (ed.), *Treatise on Geochemistry, Volume 7*, Elsevier, Amsterdam, pp 159–190.

Mitchell, J.T., Land, L.S., Miser, D.E., 1987. Modern marine dolomite cement in a north Jamaican fringing reef. *Geology* 15, 557–560.

Moberly, R., 1968. Composition of magnesian calcites of algae and pelecypods by electron microprobe analysis. *Sedimentology* 11, 61–82.

Moreira, N.F., Walter, L.M., Vasconcelos, C., McKenzie, J.A., McCall, P.J., 2004. Role of sulphide oxidation in dolomitization: Sediment and pore-water geochemistry of lagoon system. *Geology* 32, 701–704.

Morse, J.W., Andersson, A.J., Mackenzie, F.T., 2006. Initial responses of carbonate-rich shelf sediments to rising atmospheric pCO_2 and "ocean acidification": Role of high Mg-calcites. *Geochim. Cosmochim. Acta* 70, 5814–5830.

Mucci, A., 1987. Influence of temperature on the composition of magnesian calcite overgrowths precipitated from seawater. *Geochim. Cosmochim. Acta* 51, 1977–1984.

Mullins, H.T. et al., 1985. Authigenic dolomite in Bahamian peri-platform slope sediment. *Geology* 13, 292–295.

Nagy, R.M., Porter, S.M., Dehler, C.M., Shen, Y., 2009. Biotic turnover driven by eutrophication before the Sturtian low-latitude glaciation. *Nature Geosci.* 2, 415–418.

Ohmoto, H., Goldhaber, M.B., 1997. Sulfur and carbon isotopes. In: H.L. Barnes (ed.), *Geochemistry of Hydrothermal Ore Deposits*, Wiley, New York, pp 517–611.

Pollock, M.D., Kah, L.C., Bartley, J.K., 2006. Morphology of molar-tooth structures in Precambrian carbonates: Influence of substrate rheology and implications for genesis. *J. Sed. Res*. 76, 310–323.

Preto, N. et al., 2015. Primary dolomite in the Late Triassic Travenanzes Formation, Dolomites, Northern Italy: Facies control and possible bacterial influence. *Sedimentology* 62, 697–716.

Prokoph, A., Shields, G.A., Veizer, J., 2008. Compilation and time-series analysis of a marine carbonate $\delta^{18}O$, $\delta^{13}C$, $^{87}Sr/^{86}Sr$ and $\delta^{34}S$ database through Earth history. *Earth-Sci. Rev.* 87, 113–133.

Pytkowicz, R.M., Hawley, J.E., 1974. Bicarbonate and ion-pairs and model of seawater at 25°C. *Limnol. Oceanogr.* 19, 223–234.

Roberts, J.A. et al., 2013. Surface chemistry allows for abiotic precipitation of dolomite at low temperature. *Proc. Nat. Acad. Sci. USA* 110, 14540–14545.

Ronov, A.B., 1964. Common tendencies in the chemical evolution of the Earth's crust, ocean and atmosphere. *Geochim. Intern.* 4, 713–737.

Rosenbaum, J., Sheppard S.M.F., 1986. An isotopic study of siderites, dolomites and ankerites at high temperatures. *Geochim. Cosmochim. Acta* 50, 1147–1150.

Rott, C.M., Qing, H., 2013. Early dolomitization and recrystallization in shallow marine carbonates, Mississippian Alida Beds, Williston Basin (Canada): evidence from petrography and isotope geochemistry. *J. Sed. Res.* 83, 928–941.

Saito, M.A., Sigman, D.M., Morel, F.M.M., 2003. The bioinorganic chemistry of the ancient ocean: the co-evolution of cyanobacterial metal requirements and biogeochemical cycles at the Archean–Proterozoic boundary? *Inorg. Chim. Acta* 356, 308–318.

Sansjofre, P. et al., 2011. A carbon isotope challenge to the snowball Earth. *Nature* 478, 93–97.

Sawada, K., Ogino, T., Suzuki, T., 1990. The distribution coefficients of Mg^{2+} ion between $CaCO_3$ polymorphs and solution and the effects on the formation and transformation of $CaCO_3$ in water. *J. Cryst. Growth* 106, 393–399.

Scheffer, M., Rinaldi, S., Gragnani, A., Mur, L.R., van Nes, E.H., 1997. On the dominance of filamentous cyanobacteria in shallow, turbid lakes. *Ecology* 78, 272–282.

Schroeder, J.H., Dwornik, E.J., Papike, J.J., 1970. Primary protodolomite in echinoid skeletons, *GSA Bull*. 80, 1613–1616.

Searl, A., 1994. Discontinuous sold-solution in Ca-rich dolomites: the evidence and implications for the interpretation of dolomite petrographic and geochemical data. In: B. Purser, M. Tucker, D. Zenger (eds), *Dolomites: A Volume in Honour of Dolomieu*, Blackwell Scientific, Oxford, pp 361-–376.

Sheppard, S.M.F., Schwarcz, H.P., 1970. Fractionation of carbon and oxygen isotopes and magnesium between coexisting metamorphic calcite and dolomite. *Contrib. Mineral. Petrol*. 26, 161–198.

Shields, G.A., 2002. 'Molar-tooth microspar': a chemical explanation for its disappearance ~ 750 Ma. *Terra Nova* 14, 108–113.

Sibley, D.F., 1990. Unstable to stable transformations during dolomitisation. *J. Geol.* 98, 739–748.

Sibley, D.F., Dedoes, R.E., Bartlett, T.R., 1987. Kinetics of dolomitisation. *Geology* 15, 1112–1114.

Sibley, D.F., Gregg, J.M., 1987. Classification of dolomite rock textures. *J. Sed. Petrol.* 57, 967–975.

Sibley, D.F., Nordeng, S.H., Borkowski, M.L., 1994. Dolomitization kinetics in hydrothermal bombs and natural settings. *J. Sed. Res.* A64, 630–637.

Slaughter, M., Hill, R.J., 1991. The influence of organic matter in organogenic dolomitization. *J. Sed. Petrol.* 61, 296–303.

Sochava, A.V., Podkovyrov, V.N., 1995. The compositional evolution of Meso- and Neoproterozoic carbonate rocks. *Precambrian Res.* 73, 283–289.

Sperber, C.M., Wilkinson, B.H., Peacor, D.R., 1984. Rock composition, dolomite stoichiometry, and rock/water reactions in dolomitic carbonate. *J. Geol.* 92, 609–622.

Spanos, N., Koutsoukos, P.G., 1998. Kinetics of precipitation of calcium carbonate in alkaline pH at constant supersaturation. spontaneous and seeded growth. *J. Phys. Chem. B* 102, 6679–6684.

Stoessel, R.K., 1992. Effects of sulphate reduction on $CaCO_3$ dissolution and precipitation in mixing-zone fluids. *J. Sed. Petrol.* 62, 873–880.

Tojo, B., Katsuta, N., Takano, M., Kawakami, S., Ohno, T., 2007. In: P. Vickers-Rich, P. Komarower (eds), *The Rise and Fall of the Ediacaran Biota*, Geol. Soc. Lond. Spec. Pub. 286, 103–113.

Tucker, M.E., 1982. Precambrian dolomites: petrographic and isotopic evidence that they differ from Phanerozoic dolomites. *Geology* 10, 7–12.

Tucker, M.E., 1992. The Precambrian-Cambrian boundary: seawater chemistry, ocean circulation and nutrient supply in metazoan evolution, extinction and biomineralization. *J. Geol. Soc. Lond*. 149, 655–668.

Tyrrell, T., Zeebe, R.E., 2004. History of carbonate ion concentration over the last 100 million years. *Geochim. Cosmochim. Acta* 68, 3521–3530.

Van Lith, Y., Warthmann, R., Vasconcelos, C., McKenzie, J.A., 2003. Microbial fossilization in carbonate sediments: a result of the bacterial surface involvement in carbonate precipitation. *Sedimentology* 50, 237–245.

Vasconcelos, C., McKenzie, J.A., 1997. Microbial mediation of modern dolomite precipitation and diagenesis under anoxic conditions (Lagoa Vermelha, Rio de Janeiro, Brazil). *J. Sed. Res.* 67, 378–390.

Vasconcelos, C., McKenzie, J.A., Warthmann, R., Bernasconi, S.M., 2005. Calibration of the $\delta^{18}O$ paleothermometer for dolomite precipitated in microbial cultures and natural environments. *Geology* 33, 317–320.

Veizer, J., Hoefs, J., 1976. The nature of O^{18}/O^{16} and C^{13}/C^{12} secular trends in sedimentary carbonate rocks. *Geochim. Cosmochim. Acta* 40, 1387–1395.

Veizer, J., 1978. Secular variations in the composition of sedimentary carbonate rocks, II. Fe, Mn, Ca, Mg, Si and minor constituents. *Precambrian Res*. 6, 381–413.

Wallmann, K. et al., 2008. Silicate weathering in anoxic marine sediments. *Geochim. Cosmochim. Acta* 72, 3067–3090.

Wang, J., Jiang, J., Xiao, S., Li, Q., Wei, Q., 2008. Carbon isotope evidence for widespread methane seeps in the ca. 635 Ma Doushantuo cap carbonate in south China. *Geology* 36, 347–350.

Wang, Q.H., Yang, D.B., Xu, W.L., 2012. Neoproterozoic basic magmatism in the southeast margin of North China Craton: Evidence from whole-rock geochemistry, U-Pb and Hf isotopic study of zircons from diabase swarms in the Xuzhou-Huaibei area of China. *Sci. China Earth Sci*. 55, 1461–1479.

Warren, J., 2000. Dolomite: occurrence, evolution and economically important associations. *Earth-Sci. Rev.* 52, 1–81.

Weiss, C.A. et al., 2014. Influence of temperature on calcium carbonate polymorph formed from ammonium carbonate and calcium acetate. *J. Nanotech. Smart Mater*. 1, 1–6.

Wright, D.T., Oren, A., 2005. Nonphotosynthetic bacteria and the formation of carbonates and evaporites through time. *Geomicrobiol. J.* 22, 27–53.

Wright, D.T., Wacey, D., 2005. Precipitation of dolomite using sulphate-reducing bacteria from the Coorong Region, South Australia: significance and implications. *Sedimentology* 52, 987–1008.

Xiao, S. et al., 2014. Biostratigraphic and chemostratigraphic constraints on the age of early Neoproterozoic carbonate successions in North China. *Precambrian Res.* 246, 208–225.

Xu, J. et al., 2013. Testing the cation-hydration effect on the crystallization of Ca-Mg-CO_3 systems. *Proc. Nat. Acad. Sci. USA* 110, 17750–17755.

Yang, J., Zheng, W., Tao, X., Wang, Z., 2004. The Sm–Nd age of cherts from Sidingshan Formation of the Huainan Group of Anhui Province. *Geol. Rev*. 50, 413–417.

Zang, W., Walter, M.R., 1992. Late Proterozoic and Early Cambrian microfossils and biostratigraphy, northern Anhui and Jiangsu, central-eastern China. *Precambrian Res.* 57, 243–323.

Zentmyer, R.A., Pufahl, P.K., James, N.P., Hiatt, E.E., 2011. Dolomitization on an evaporitic Paleoproterozoic ramp: Widespread synsedimentary dolomite in the Denault Formation, Labrador Trough, Canada. *Sed. Geol.* 238, 116–131.

Zhang, F. et al., 2012a. Polysaccharide-catalyzed nucleation and growth of disordered dolomite: a potential precursor of sedimentary dolomite. *Am. Mineral.* 97, 556–567.

Zhang, S.H., Zhao, Y., Ye, H., Hu, G.H., 2016. Early Neoproterozoic emplacement of the diabase sill swarms in the Liaodong Peninsula and pre-magmatic uplift of the southeastern North China Craton. *Precambrian Res*. 272, 203–225.

Zhang, F., Xu, H., Konishi, H., Kemp, J.M., Roden, E.E., 2012b. Dissolved sulfide-catalyzed precipitation of disordered dolomite: implications for the formation mechanism of sedimentary dolomite. *Geochim. Cosmochim. Acta* 97, 148–165.

CHAPTER THREE

A large-amplitude negative carbon-isotope excursion through the early Neoproterozoic Majiatun Formation of Liaoning Province, North China

Abstract

The Neoproterozoic carbonate record is punctuated by several large-scale (amplitude > 5‰) carbon-isotope excursions, greater and more frequent than at any other time in Earth history. Here I report on a 9‰ positive-to-negative $\delta^{13}C$ anomaly in the Majiatun Formation of North China. Plunging to at least -5.4‰, it is the only excursion below -2‰ known from the Sino-Korean craton. Concentrations of major and trace elements in the carbonates are also reported. The minimum age of the formation is c. 940 Ma, while potential correlations with negative excursions in India and Siberia suggest an age near the start of the Neoproterozoic.

Organic carbon content in the succession is low and declines in step with carbonate $\delta^{13}C$. As currently understood, a fall in $\delta^{13}C$ to the value of unfractionated, mantle carbon implies a complete shutdown of global organic production. However, facies and geochemistry indicate that the excursion accompanied an increase in water depth and that the rise in sea-level was an effect of subsidence and faulting. Other excursions in the Tonian Period, here briefly reviewed, show a similar link with sea-level. Major differences in the stratigraphic profile of those considered contemporaneous are consistent with such a control.

3.1. Introduction

The Tonian (1000–c.720 Ma) is the earliest and least well known of the three periods into which the Neoproterozoic is divided. At its start, most of the continents were aggregated. By its end, the assembled supercontinent, known as Rodinia, had undergone extensive rifting and was breaking up, as it continued to do in the Cryogenian and Ediacaran periods. The era is also marked by increasingly errant swings in the carbon-isotope stratigraphy of its epicontinental carbonates. Average $\delta^{13}C$ values in the late Mesoproterozoic were around 2–4‰, slightly higher in the Tonian and becoming more wayward as time went on (Halverson et al. 2010). Prior to that, as far back as 2000 Ma, perturbations of the carbon cycle appear to have been minor.

A paucity of reliable dates makes it difficult to say just when carbon-isotope systems became less stable. If we define a large excursion as anything over 5‰ in amplitude, potentially the oldest Neoproterozoic event was that recorded in Unit I-4 of the Atar Group, Mauritania, extending from -6 to +2 (Kah et al. 2012). A second excursion in Unit 1-6, 140 m higher, goes from +4.8 to -2.2‰, immediately above a transgressive surface; a rapid, transient return to evaporitic conditions conceals the return phase but a subsequent dip can be traced in the Adrar region down to -2.5‰ (Shields et al. 2007). While the chronological clues are ambiguous, a Re-Os age of 1107 ±12 Ma for Unit I-5 does not seem unreasonable, and is supported by chemostratographic correlation with two negative excursions (the earlier one down to -8, the upper down to -4‰) in the Late Mesoproterozoic Lapa Formation (Azmy et al. 2009, Geboy et al. 2013). The oldest excursion assigned to the Tonian, from +3 to -5‰, occurs in the cherty dolomites of the upper Shorikha Formation of Siberia, Turukhansk area (Knoll et al. 1995). On the basis of correlations between the Turukhansk and Uchur-Maya regions (e.g. Priyatkina et al. 2016) this probably dates to soon after 1000 Ma. Values beginning at -2.3‰ have been reported from carbonates of broadly the same age in northwest India, descending to -4‰ and climbing eventually to +4.7‰ (Purohit et al. 2012, Roy & Purohit 2015).

Much later in the Tonian is the anomaly associated with the Bitter Springs Group, from the Amadeus Basin of Central Australia, which descends from +6 to -4‰ and back again (Hill et al. 2000, Swanson-Hysell et al. 2010). Excursions thought to reflect the same episode have been documented from NE Svalbard (Maloof et al. 2006, Halverson et al. 2007) and from various parts of NW Canada (Thomson et al. 2015). The three regions may have been contiguous, with Australia adjoining Laurentia to its north (rotated so that western Canada lay to the north) and Svalbard adjoining Laurentia to its east (Swanson-Hysell et al. 2012). If the correlations are correct, a maximum age of 811 ±0.25 Ma is provided by a tuff in the Ogilvie Mountains, NW Canada (Macdonald et al. 2010). Correlative sections record an excursion down to -6‰ shortly above this marker (Macdonald et al. 2012). Elsewhere, in the Ballachulish Subgroup of western Scotland (southern Laurentia), a potentially coeval excursion goes from +5 to -7 (Prave et al. 2009). A Tonian age is supported by $^{87}Sr/^{86}Sr$ values (Sawaki et al. 2010), but a date younger than 730 Ma has also been suggested (Rooney et al. 2011, Stephenson et al. 2013). In Ethiopia a comparable excursion is bracketed by tuffs possibly before and definitely after the event, dated to 815 ±0.32 Ma and 789 ±0.24 Ma respectively (Swanson-Hysell et al. 2015).

The last major negative excursion of the Tonian is the ‘Islay anomaly’, named after the Islay Limestone. It goes down to -7‰ (Prave et al. 2009). It is also well defined in the Mackenzie

Mountains of NW Canada, where at the Moose Horn section it briefly touches -6 before a steady recovery to +1.5‰ (Macdonald et al. 2010). In a much thicker drill-core the recovery reaches +7 (Rooney et al. 2014), a difference of 5.5‰. Re-Os dating fixes the point where $\delta^{13}C$ values become positive at 732 ±4 Ma, some 15 Ma before the oldest diamictites (Rooney et al. 2014). In the Ogilvie Mountains, the end of an earlier, much briefer, but equally negative fall, is dated to 740 ±6 Ma (Strauss et al. 2014). Both excursions touch -7‰. In NE Svalbard carbon-isotope values fall to -6 but the subsequent rise is truncated by diamictite (Hoffman et al. 2012); correlative shales during the excursion indicate a shift from suboxic to anoxic waters, consistent with deepening (Kunzmann et al. 2015). Owing to a regional unconformity, no carbonates are known from the equivalent horizon in Australia. The same is broadly true in Namibia, although there are hints of a truncated excursion below the diamictites (Halverson et al. 2005).

3.2. Regional setting and chronostratigraphy

Here I report a major negative carbon-isotope excursion of early Tonian age from North China. According to one authoritative scheme (Li et al. 2008), at that time the Sino-Korean craton was situated on the edge of Rodinia quite close to Svalbard and Siberia. The geological record around Dalian, a city in the south of Liaoning Province, encompasses the late Mesoproterozoic and early Tonian down to c. 925 Ma. In order of deposition the Jinxian Group comprises the carbonate-dominated Yingchenzi, Shisanlitai and Majiatun Formations, and the siliciclastic-dominated Cuijiatun, Xingmincun and Getun Formations. A disconformity separates the Xingmincun from the Getun, which has a maximum age of c. 733 Ma (He et al. 2016).

A large number of zircon ages from dolerite dikes and sills across the region cluster around 925 and 900 Ma respectively (Peng et al. 2011a, Liu et al. 2012). The igneous province produced by the swarms is estimated to have been 1000 km across. Zircons from quartz sandstone of the Xingmincun Formation, two formations up from the Majiatun, give a maximum age of 926 ±18 Ma (Yang et al. 2012). Magmatic zircons from a sill intruding the Xingmincun yield a crystallisation age of 900 ±34 Ma (Zhang et al. 2016), while baddeleyite grains yield ages of 924 ±5 and 886 ±5 Ma. Much the same ages have been obtained for dikes and sills in northern Jiangsu and Anhui Provinces (Peng et al. 2011b, Wang et al. 2012, Fu et al. 2015). Overall the data suggest a minimum age around 925 Ma for the Xingmincun and perhaps 940 Ma for the Majiatun Formation. The dikes imply that the disconformity after the Xingmincun was occupied by flood basalt, which was weathered away in the interval before deposition of the Getun Formation (Table 2.1). The iron formation of the lower Xingmincun can be seen as a prelude to the later magmatism.

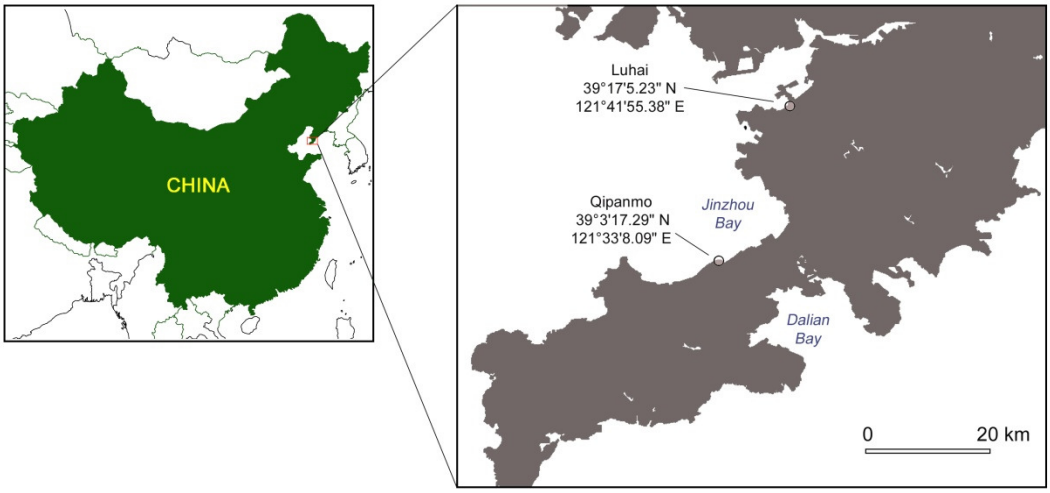

Figure 3.1. Location of the two studied sections north of Dalian city in Liaoning Province, China.

The Majiatun Formation records the negative carbon-isotope excursion. In 2010 the upper Shisanlitai, lower Majiatun, two carbonate horizons in the succeeding Cuijiatun Formation and most of the upper Xingmincun Formation were sampled at Luhai village (Fig. 3.1, samples labelled LH) by way of reconnaissance. In 2013 the area was revisited, by which time the Majiatun and Xingmincun sections had been quarried out. However, an overlapping section on the other side of the road preserved the lower part of the excursion and the uppermost Yingchenzi and Shisanlitai Formations leading up to it (13LH series). The entire Majiatun was also sampled at the coastal section near Qipanmo (pronounced *Cheepanmaw*), 30 km to the SSE (QPM series).

3.2.1. *Yingchenzi Formation*

The Luhai section (Fig. 3.2) preserves the uppermost 15 m of the Yingchenzi. These consist of medium dark-grey tan-weathering limestones, becoming marly and dolomitic towards the top with shaly interbeds. Sub-vertical calcite-filled fractures penetrate beds that appear to have undergone folding during deposition (Fig. 3.4a). Near the top the limestones are composed mostly of ooids, cemented, without compaction, in coarse-crystalline spar (Fig. 3.5a). Most ooids are spheroid, 0.1–0.5 mm in diameter; some show layering suggestive of an originally aragonite mineralogy; a smaller number are ovoid or asymmetric; many have organic-dark cores. In one sample many of the ooids are recrystallised, with organic-dark rims (Fig. 3.5b). The co-existence of sparry and non-recrystallised ooids indicates that re-crystallisation occurred early and was arrested by early cementation. Molar-tooth structure is common at a few horizons. A microbial mat is well preserved at 9 m.

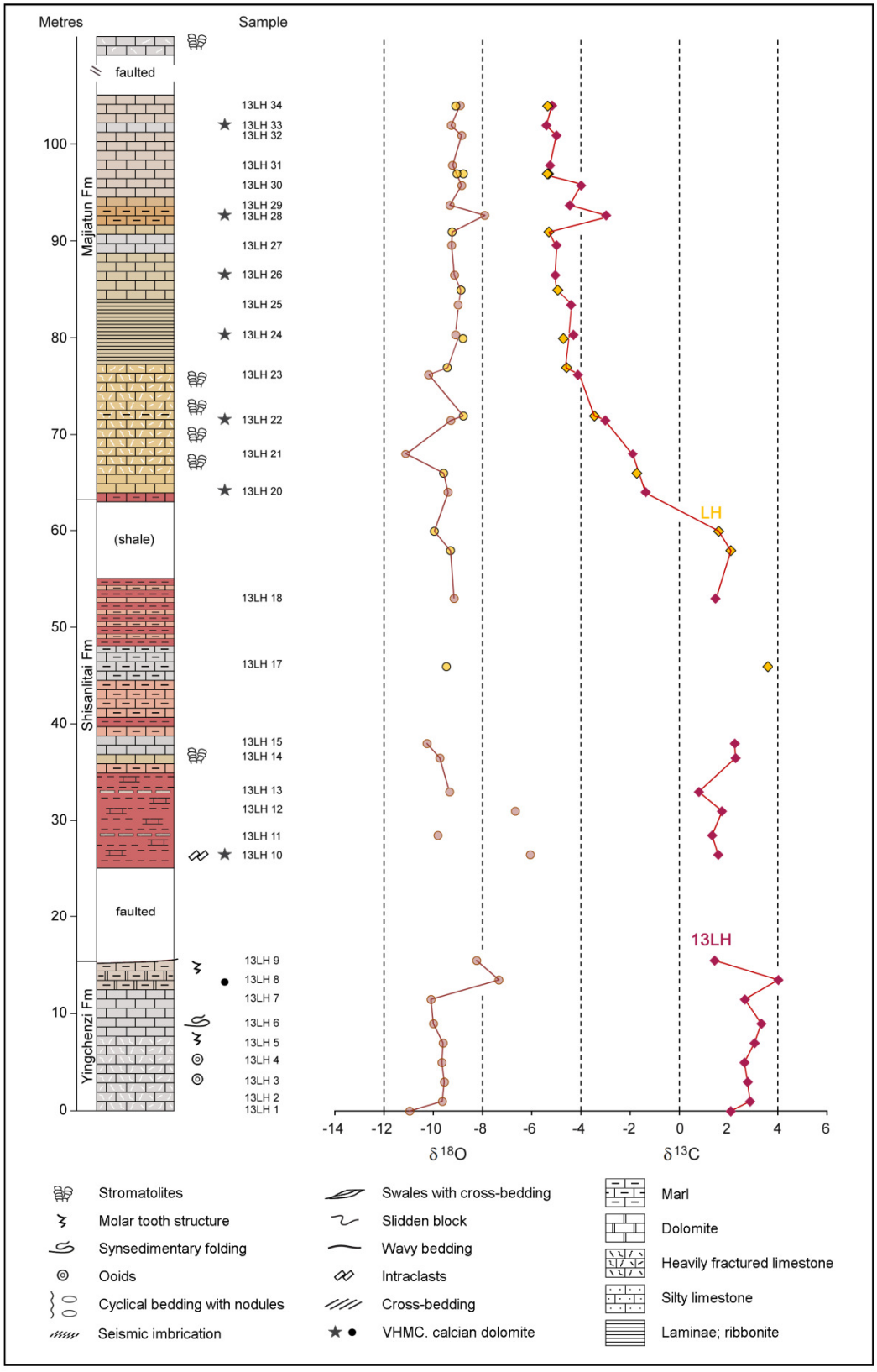

Figure 3.2. Chemostratigraphy of the Luhai section sampled in 2013 (13LH series), correlated with samples taken in 2010 (LH series). In contrast to the correlative facies logged in 2013, the LH samples from around 60 m are >80% carbonate, suggesting there maybe another fault at this level. Colours schematically approximate those observed in the field. The hiatus at 15-25 m is estimated.

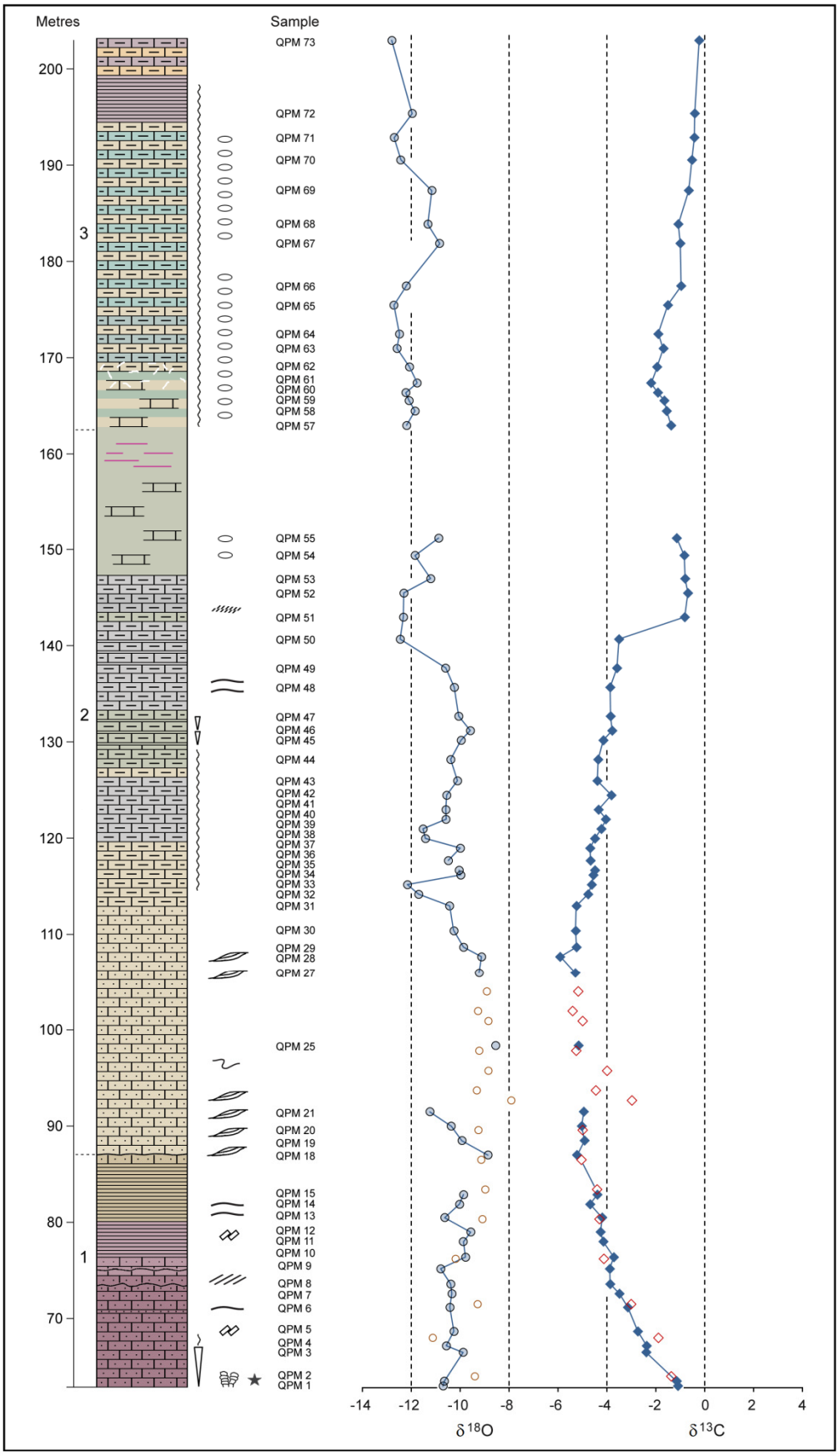

Figure 3.3. Chemostratigraphy of the Qipanmo section (QPM series). Values of the overlapping Luhai section shown with open symbols, scales as in Fig. 3.2.

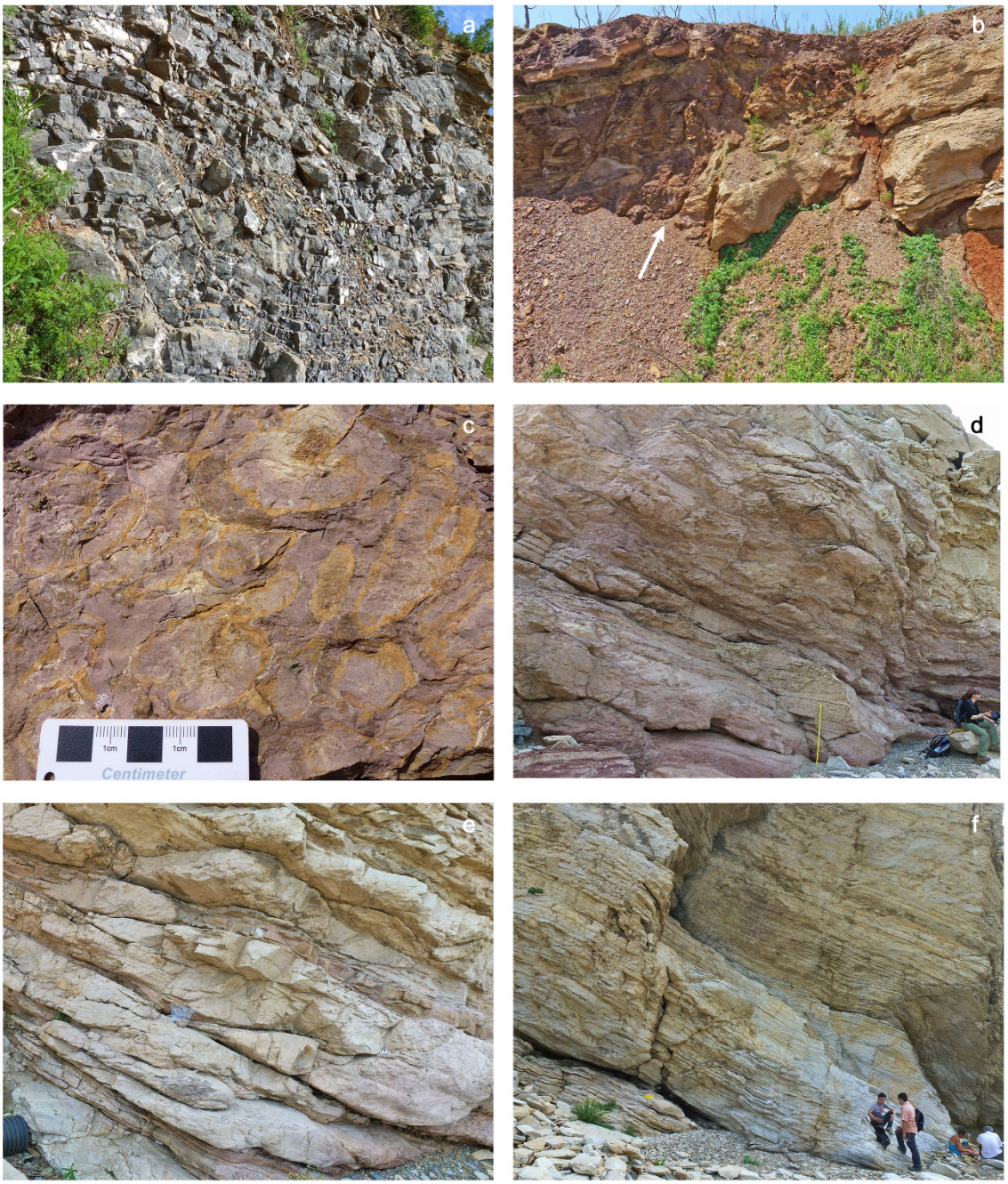

Figure 3.4. (a) Slump folding of strata in upper Yingchenzi Formation. **(b)** Faulting between shales of the Shisanlitai Formation (left) and marls of the uppermost Yingchenzi Formation (right). Listric fault marked with arrow. Going up, the transition appears conformable. **(c)** Oblique section through iron-oxide-rimmed stromatolites near base of the Majiatun Formation, Qipanmo. **(d)** Prominent erosion surfaces at base of metre stick in lower Majiatun and ~1.5 m higher, followed by incipient swaley bedding. **(e)** Well-developed swaley, partly cross-stratified bedding at QPM 18. **(f)** Thin beds from 115 m onwards, becoming progressively more cyclical.

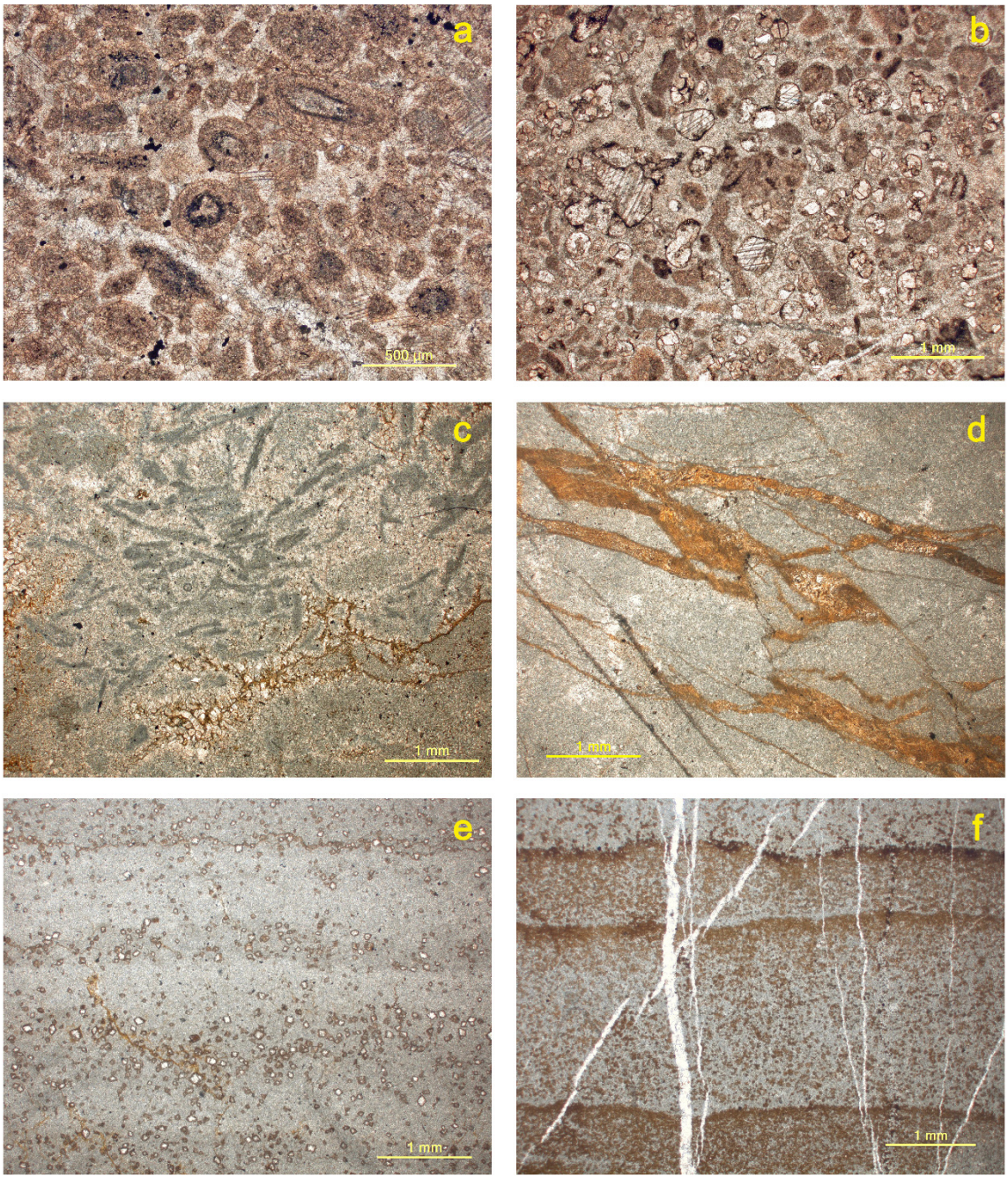

Figure 3.5. Thin-section micrographs. **(a)** Concentric-layered ooids, 13LH 3. **(b)** Partly recrystallised ooids, 13LH 4. **(c)** Filamentous algal organic matter in dark calcite microspar, 13LH 11. The lighter, organic-poor calcite is more evidently recrystallised. The brown cement filling the cracks suggests iron-rich bottom water. **(d)** Iron-rich cement fills pull-apart fractures, hinting at early cementation, 13LH 14. **(e)** Discrete iron-oxide-rimmed crystals of VHMC in microspar matrix, with faint lamination produced by variation in organic matter, 13LH 26. **(f)** Dense laminae of sedimented iron-oxide-rimmed crystals of VHMC, 13LH 25.

3.2.2. *Shisanlitai Formation*

The boundary with the Shisanlitai is an abrupt but apparently conformable transition into dark-red calcareous shale (Fig. 3.4b). Multiple faults truncate the limestones; the sharp drop in $\delta^{13}C$ between 13LH 8 and 9 crosses a fault with an estimated downthrow of 10 m shortly after the boundary. After about 10 m the carbonate component asserts itself, forming harder purplish brown marls, some of which host colonies of domal or closely-packed columnar stromatolites. Samples 13LH 13 and 14 show microscopic iron-rich veining (Fig. 3.5d). The top part of the Shisanlitai, not exposed on this side of the road, is shaly, with the return to competent limestones marking the approximate boundary with the Majiatun. Samples from below the Majiatun in the quarried-out section (Fig. 3.2, samples LH 2 and 3) come from bioherms within the shale.

3.2.3. *Majiatun Formation*

Overall, the Majiatun has higher carbonate content than the Shisanlitai, and is more carbonate-rich at Luhai (average 83%) than at Qipanmo (73%). The carbonates at Luhai also contain more Mg (average 0.04 Mg/Ca as against 0.01), as might be expected of a more proximal setting. Stromatolites are abundant here in the lowest part of the formation; at Qipanmo they were observed only in the lowermost part. At Luhai, from 78 m onwards, the faintly laminar limestone includes layered, thinly distributed rhombs of very high magnesium calcite (VHMC), up to 80 μm in size and coated with iron (Fig. 3.5e).

The sedimentology is best studied at Qipanmo. In the lowest part of the formation the carbonate is purple and/or orange-brown. Orange-brown staining of stromatolite rims (Fig. 3.4c) suggests penecontemporaneous, possibly bacterial, oxidation of ferrous iron in the carbonate; the strong purple coloration of the infill reflects a somewhat lower degree of oxidation. A cycle of increasing silt content is followed by a smaller, second fining-up cycle. Conditions were shallow enough for wave action to produce rip-up mudstone clasts and brecciation. The last expression of cyclicity is the alternation of 5–10 cm calcareous siltstone and sandstone interbeds around the 8 m level. Two wavy erosion surfaces 1.5 m apart (Fig. 3.4d) are followed by thinner, laminar and generally more planar beds as depth increased to below fair-weather wave base. At 77 m the laminae thicken briefly into ribbonites. Occasional scouring and pods of intraclasts are seen. The purplish hue fades into orange-brown and subsequently greyer rocks from around 80 m.

Thicker, swaley-sigmoidal or trough-like, partly cross-stratified beds, often with erosionally planed tops, supervene above an extensive erosion surface at 87 m and signify further deepening and high-energy flow (Fig. 3.4d, e). Intraclast breccia near the base of this interval derives from more

Figure 3.6. Exposures at Qipanmo. **(a)** Possibly seismic imbrication at 144 m. **(b)** Renewal of cyclicity in nodular marly limestones from 163 m onwards. **(c)** Intermittently continuous nodular ribbons in marly matrix, all densely fractured, around QPM 61. Thickness and density of ribbons are greatest towards the middle of each cycle, which comprises ~14 such layers. **(d)** Similar facies at QPM 72, but matrix is more purple and cycles comprise ~28 layers.

Figure 3.7. Panorama of upper Majiatun and lower Cuijiatun Formations. Arrows mark faults, that on the right being the boundary between the units. The Majiatun Formation here consists of ribbonites similar to those shown in Fig. 5.

Figure 3.8. The faulted boundary between the Majiatun and Cuijiatun Formations. Dotted white lines pick out the lamination of the shales: strongly folded lower down, almost horizontal higher up, suggesting that the fault developed during deposition of the lower Cuijiatun, closely followed by compression.

proximal ribbonites. Beds thin upsection, calcareous shale partings become more pronounced and the angle of stratification decreases. By 113 m the partings are minimal and the beds, now only 1–10 cm thick, are planar. Faint cyclicity becomes apparent in sub-metre-scale intervals of variable iron-oxide weathering (Fig. 3.4f), possibly marking a gradual return to shallower conditions; threesmall carbonate-increasing cycles are apparent at 130–133 m, after which bedding remains thin (< 5 cm) with thin shale partings. The shale component increases, roughly equalling carbonate proportions by 148 m. At that juncture the beds become studded with small calcareous nodules.

A change in colour from grey-green to brownish at 163 m marks a transition from reduced to partly oxidised iron, coincident with the onset of marked sub-metre-scale cyclicity similar to that between 51 and 67 m (Fig. 3.6b). In the more calcareous part of each cycle the nodules tend to merge into continuous ribbons (Fig. 3.6c). Towards the top of the section the matrix becomes purplish, still enclosing rhythmic bundles of ribbon-like layers. A complete cycle here consists of 28–30 such ribbons (Fig. 3.6d). Similar but more continuous ribbonites are also seen at the top of the Majiatun at Luhai. There they are cut by two faults, the second fault down-throwing the Cuijiatun against the Majiatun (Fig. 3.7). Rucking of the bedding against the fault surface suggests that the fracture occurred during deposition of the shale (Fig. 3.8).

3.3. Methods

Hand samples were washed, weathered surfaces cut away, and clean surfaces drilled for powder. To obtain the ratios of oxygen and inorganic carbon isotopes, aliquots of 200–500 μg were analysed at Bloomsbury Environmental Isotope Facility (BEIF), University College London, on a

ThermoFinnigan Delta^{PLUS} XP stable isotope mass spectrometer coupled to a ThermoScientific Gas Bench II. Prior to analysis, vials were flushed with He, then acidified with 100% phosphoric acid. BDH (Carrara marble internal lab standard) was used to correct for temporal changes in isotopic composition during each run. Precision of BDH analyses greater than 1000mv was ±0.03 for $\delta^{13}C$, ±0.08 for $\delta^{18}O$. All values are reported in the Vienna Pee Dee Belemnite notation (VPDB) relative to NBS19.

Carbonate-associated Mn, Sr, K and Fe were measured by dissolving the carbonate fraction of 4–10 mg aliquots at room temperature in 10% acetic acid for 24–48 hours. These were then centrifuged and analysed on a Varian 720 ICP-ES optical emission spectrometer at the Wolfson Laboratory for Environmental Geochemistry, University College London. Solutions were diluted ten-fold to obtain concentrations of Fe, Mg and Ca. Results of the two operations were cross-checked by reference to the Fe data. Percentage carbonate calculated stoichiometrically from Mg, Ca, Mn and Sr concentrations was used as a further check on credibility, since totals should not exceed 100%. Carbonate content so calculated ranged from 1 to 96%. Results were reproducible to within 12% for K, 2–6% for the other elements. Trace-element data so obtained represent weight fractions of the total sample but relate solely to the carbonate content. Herein they are normalised to 100% carbonate (denoted by subscript ‘n’).

The carbonate fraction was also calculated by reacting 1.0–1.5 g of whole-rock powder with 10% HCl until all carbonate was dissolved. The supernatant was centrifuged, drained and replaced with de-ionised water. After drying, the residue was broken up and more HCl added, left for a minimum 6 hours, centrifuged, rinsed three more times and dried. As expected, the carbonate fraction was significantly higher than that calculated from the ICP-ES data. Whole-rock samples (0.5 g) were also dissolved in acetic acid and subjected to the same protocol. Differences between the whole-rock and stoichiometrically calculated carbonate fraction are attributed to HCl being a strong acid and/or samples not being compositionally homogeneous, especially where the fraction is low. The ICP-derived number is used only for normalising data derived by that method. Total organic carbon was obtained from the same de-carbonated samples by combustion in a LECO C/S Analyser. Some samples were at the limit of detectibility.

The insoluble residue was also analysed at the BEIF for organic carbon isotope ratios. Aliquots of 6–40 mg were combusted in a Thermo Electron 1112 series Flash EA, with a gas chromatographic separation column linked via a CONFLO IV interface to a continuous flow IR-mass spectrometer. Carbon-isotope ratios were measured against internal and external standards with a reproducibility of ~0.1‰.

Finally, 27 samples from the LH and 13LH series and 7 from the QPM series were selected for study under SEM and microprobe EDS to generate backscattered electron images and quantitative element analyses (spot size 50 nm). Polished samples were bound in carbon tape and examined under low vacuum (25–75 Pa) and low accelerating voltage (15 keV). Spot analyses were run for 60 seconds. Elements specified for analysis were Ca, Mg, K, Al, Si, Fe, Mn and S. Upwards of 30 determinations of mineral carbonate composition per sample were taken in total from at least three areas, at which point the averages of the trace elements (Mn and S) began to stabilise. While the probe reports to only 0.01% and becomes less accurate as the concentration decreases, experience suggests that averaging produces an adequate approximation. As a cross-check, K and Mn were compared with the ICP results. Generally, data were congruent, although EDS tended to report higher values (Fig. 3.9); with ICP a proportion of the elements tends to be leached out.

Non-normalised weight values reported by EDS were normalised to the stoichiometry of calcite and dolomite, proportional to the Mg/Ca ratio. The calcite fraction was calculated as:

$$Ca\% + Ca\% \times 60/40.08$$

the magnesite fraction as:

$$Mg\% + Mg\% \times 60/24.3 \; [+ Fe\% + Fe\% \times 60/55.845]$$

(including Fe in the case of 13LH 8) and the non-carbonate fraction as:

$$Si\% + Si\% \times 32/28.086 + K\% + Al\%$$

The weights of individual elements were then normalised on the basis that the three fractions totalled 100%.

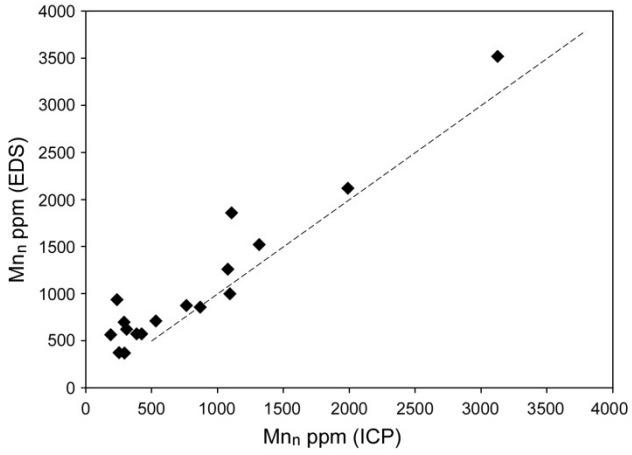

Figure 3.9. Concentrations of Mn in the carbonates from Luhai analysed by ICP-OES and EDS.

3.4. Results

3.4.1. *Carbonate carbon and oxygen isotopes*

Carbon isotope ratios in the upper Yingchenzi Formation range from 2.0 to 3.3‰, jumping at the top from 2.6 to 4.0‰ (Fig. 3.2). The first sample from the Shisanlitai Formation drops to 1.4, after which values vary between 0.8 and 2.3. The first negative value occurs at the base of the Majiatun. Through the stratigraphic overlap of 40 m the isotope curves of the two sections are almost identical, reaching a nadir of -5.25; at Qipanmo one sample touches -5.9. An aberration above 92 m at Luhai represents a disturbance of a trend that is otherwise remarkably regular. It is not seen at Qipanmo, possibly because of a sampling gap. Incongruent values at the end of the LH and 13LH series (not shown in Fig. 3.2) are due to faulting. A kink at 141 m abruptly deflects the curve 2.5‰ towards the positive, after which the trend immediately begins to recover; within 30 m $\delta^{13}C$ is back to where it would have been had the disturbance not occurred.

Oxygen isotope ratios at Luhai are mostly around -8.8 to -10‰. At Qipanmo they are similar through the overlapping section. As the carbon isotope excursion reverses, they fall even further to a minimum of -12.8. Two samples from carbonate-rich horizons in the Cuijiatun Formation (not shown) yield values similar to those of the upper Majiatun ($\delta^{13}C \sim 0.4$, $\delta^{18}O \sim -11.5$). Through the second half of the negative excursion, carbon and oxygen isotope ratios co-vary inversely; preceding data show no co-variation (Fig. 3.3).

3.4.2. *Organic carbon*

Organic carbon is dispersed within the matrix as irregular spots. As a proportion of total weight, it correlates with the silicate fraction (Fig. 3.10). Except for QPM 57–65 and samples where $\delta^{13}C$ is less than -5‰, TOC decreases in the descent phase of the excursion and rises in the ascent phase (Fig. 3.11). QPM 57–65 have anomalously high TOC, inversely correlating with carbonate $\delta^{13}C$ ($R^2 = 0.59$); QPM 61, 63 and 64 have very low carbonate.

Ranging from -29 to -22‰, organic carbon isotope values through the QPM series are heavy compared to associated inorganic values, though not untypical in relation to the low level of organic carbon. The degree to which organisms preferentially synthesised ^{12}C ($\delta^{13}C_{carb}$ -$\delta^{13}C_{org}$) is depressed, the fractionation decreasing as $\delta^{13}C_{carb}$ becomes more negative. Values vary in step with this parameter along two trends, one before the kink in $\delta^{13}C_{carb}$, the other after (Fig. 3.12). Through QPM 6–50, there is no co-variation between $\delta^{13}C_{carb}$ and $\delta^{13}C_{org}$: that is, $\delta^{13}C_{carb}$ rises or falls while $\delta^{13}C_{org}$ varies little (mostly between -25 and -27). Through QPM 1–5 and 51–73 the parameters anticorrelate: as $\delta^{13}C_{carb}$ rises, organic fractionation ($\Delta\delta$) generally increases more.

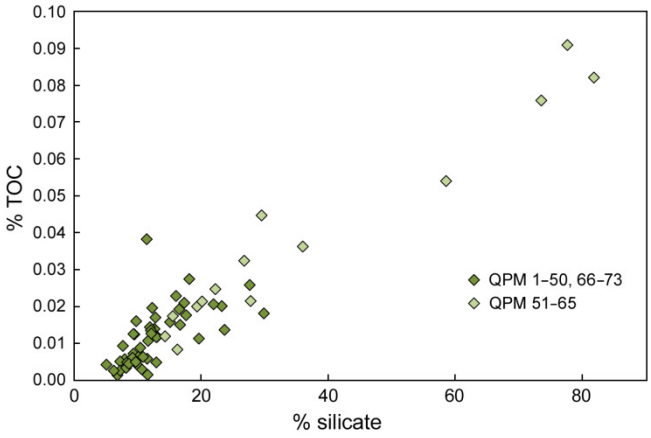

Figure 3.10. Organic carbon as a function of silicate (non-carbonate) content, Majiatun Formation.

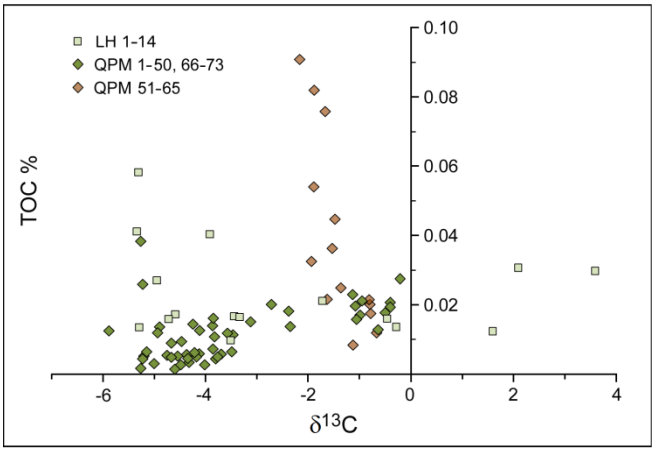

Figure 3.11. Organic carbon content as a function of $\delta^{13}C$, upper Yingchenzi, Shisanlitai and Majiatun Formations.

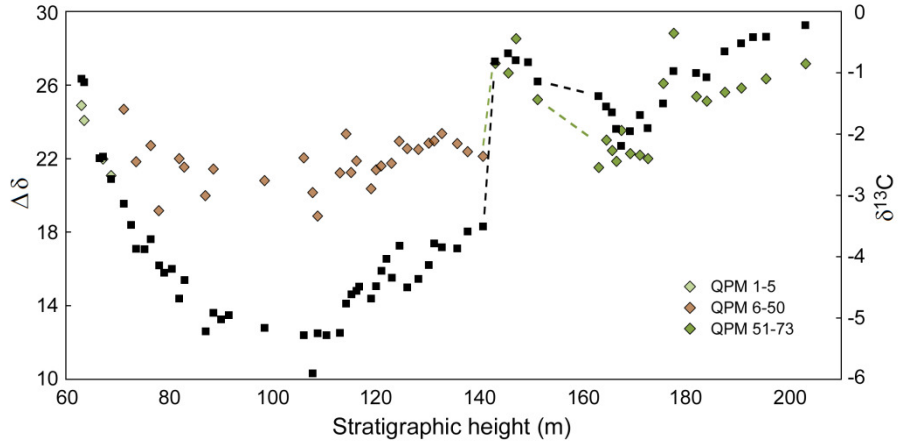

Figure 3.12. Organic carbon-isotope fractionation (diamonds) versus $\delta^{13}C_{carb}$ (squares). Note the instantaneous response of $\delta^{13}C_{carb}$ to the fall in $\delta^{13}C_{org}$.

3.4.3. *Other elements*

Apart from O, the main silicate-forming elements are Si, Al, K, Fe and Mg. These exist principally as optically indistinguishable components of the carbonate rather than as discrete silicate crystals. The dominant component is Si, discussed in section 3.4.5. Al and K correlate strongly with Si. Al is

anomalously high in 13LH 3. Fe correlates less strongly with Si, since the source of Fe was partly marine.

Physical erosion breaks down basement rock into its constituent crystals; chemical weathering leads to the formation of clays. Taking orthoclase as a representative primary mineral:

$$\underset{\text{K-feldspar}}{2KAlSi_3O_8} + 3H_2O + 2CO_2 \rightarrow 2K^+ + \underset{\text{silica}}{4SiO_2} + \underset{\text{kaolinite}}{Al_2Si_2O_5(OH)_4} + \underset{\text{bicarbonate}}{2HCO_3^-} \qquad (1)$$

Clays are enriched in Al relative to the reactant, leaving a proportion of aqueous K and SiO_2 to be washed seaward. Under low or high pH clay minerals themselves break down into their constituent ions, including Al^{3+} (Köhler et al. 2003). Under high pH and pCO_2, the chemical weathering of feldspar can ultimately be expressed as:

$$KAlSi_3O_8 + 4HCO_3^- \rightarrow K^+ + Al^{3+} + 3SiO_2 + 4CO_3^{2-} + 2H_2O \qquad (2)$$

As discussed in Chapter 2, the upshot is that high concentrations of K^+, SiO_2 and the immobile ion Al^{3+} in seawater imply intense chemical weathering, whether on land or in the sea.

Neither Al nor K substitutes easily for Ca in the calcium carbonate lattice. High concentrations are attributed primarily to ions in interstitial lattice sites. Concentrations are highest in the Shisanlitai Formation and in QPM 54–65, the latter coincident with high TOC. Except in the Shisanlitai, K is generally more abundant where $\delta^{13}C$ is negative (Fig. 3.13a) and somewhat higher at Luhai than at Qipanmo, consistent with Luhai being more proximal to the terrestrial source.

Iron in seawater may derive either from hydrothermal sources or from the dissolution of continental silicates. In oxygenated water iron precipitates as ferric (hydr)oxide, leaving only miniscule concentrations in solution (ppb). In the Precambrian the subsurface ocean was anoxic and concentrations of the soluble, divalent ion consequently much higher. To a first order, Fe^{2+} substitution in calcite is therefore an index of local anoxia. At both Luhai and Qipanmo it correlates negatively with Ca, and positively with Mg/Ca below Mg/Ca = 0.01. Correlation with K and Si shows that, at Luhai, the source of Fe was primarily terrestrial; at more distally located Qipanmo the correlation with K and Si is weaker. Systematic variation is also seen when Fe is plotted against $\delta^{13}C$ (Fig. 3.13b). Abundance is relatively low where $\delta^{13}C$ is positive, rising to > 1000 ppm as $\delta^{13}C$ becomes negative. In terms of stratigraphy, a few spikes (not evident in the SEM data) occur at Luhai around 83–96 m. At Qipanmo there is a rising trend beginning at the $\delta^{13}C$ nadir, from values of ~ 1500 to ~ 3000 ppm. The overlying Cuijiatun Formation is rich both in ferric oxide and carbonate-included Fe (> 10000 ppm).

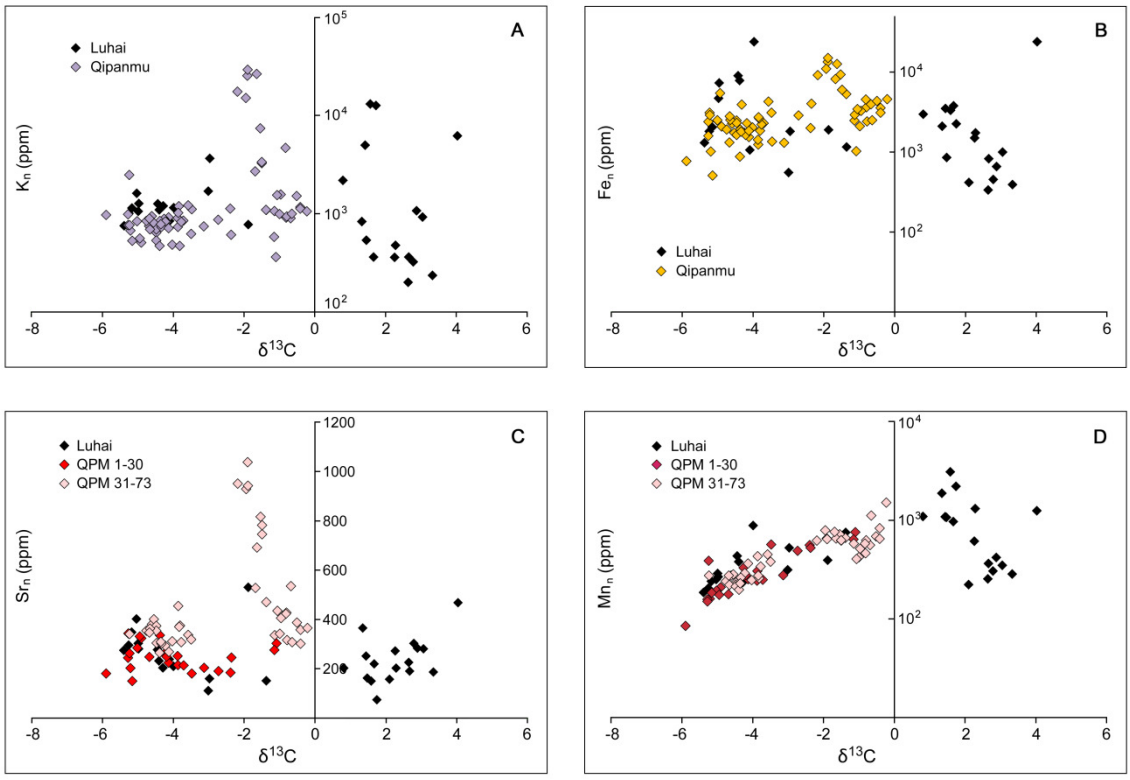

Figure 3.13. Relationship between $\delta^{13}C$ and trace elements. Apart from the anomalous interval between $\delta^{13}C$ -1 and -2.5‰ (discussed in the text), concentrations rise sharply at the beginning of the excursion to a maximum around +1‰. Except for Sr, vertical scales are logarithmic.

Since ICP analyses bulk composition and thereby averages out the Mg/Ca ratios of individual crystals, high-Mg minerals are manifest only under SEM. Two modes of crystallisation are seen. In the first, in parts of the Yingchenzi Formation (e.g. 13LH 2, 3, 6), VHMC appears as dark irregular patches amidst the calcite. These patches are interpreted as re-precipitated calcium carbonate that dissolved in the presence of organic carbon. Calcite veins in these samples are Mg-poor, indicating that re-crystallisation took place early. In the second mode, seen in the Shisanlitai and lower Majiatun Formations, inferred dolomite (13LH 8) or former dolomite (continuously from 13LH 20) appears as discrete, usually dark, subhedral to euhedral crystals, often Fe-poor and conspicuously rimmed by ankerite. Possibly the least altered though not the most Mg-rich examples are the subhedral crystals in LH 2. They are rich in Fe and unrimmed, suggesting that the (Mg-poor) ankerite rims formed during diffusive loss of Fe. Morphologically identical VHMC/former dolomite crystals have been observed in the Elbobreen Formation, NE Svalbard (Fairchild et al. 2016), in a matrix of recrystallised silicate and calcite. The regular, sometimes large (80 μm or more), unconstrained form of these crystals suggests direct precipitation from open water. The 13LH series clusters dominantly within the ranges 0–0.03 for the calcite matrix and 0.20–0.43 for VHMC. The higher range becomes narrower and less Mg-rich as $\delta^{13}C$ falls (Fig. 3.14). VHMC is

present at Qipanmo in the lowermost Majiatun. Decreasing with distance from land, Mg concentration appears to have been a major control on VHMC precipitation and composition. Except in 13LH 8, Fe substitution for Mg is considered to have been minor (Fig. 2.5 and §3.4.6).

	sea-water	samples	D_c	D_a
Si	3	20000		
K	400	3000	0.002	
Al	0.003	10000		
S	900	400		
Mn	0.004	350	20	0.86
Sr	8	230	0.07	1
Fe	0.003	2400	28	-
Mg	1290	5000	0.02	0.001

Table 3.1. Average ppm concentrations of elements analysed in this paper (Si, K, Al and S sample measurements as measured by EDS). Distribution coefficient for calcite, D_c, from Rimstidt et al. (1998), that for aragonite, D_a, from Veizer (1983).

Strontium, which is not redox-sensitive, occurs in seawater at relatively low concentrations – higher where waters are saline. Strontium is a significant trace element in feldspar, adsorbs on clay minerals and readily substitutes for Ca in aragonite but not calcite. At Luhai, and at Qipanmo through the downward phase of the excursion, Sr slightly increased as $\delta^{13}C$ became more negative; concentrations through the return phase were generally higher (Fig. 3.13c), much higher in the low-carbonate interval between 163 and 176 m.

Manganese, where abundant, indicates a hydrothermal source, marine or terrestrial. In the Neoproterozoic its concentration normally increases with depth (Hood & Wallace 2015), subsurface

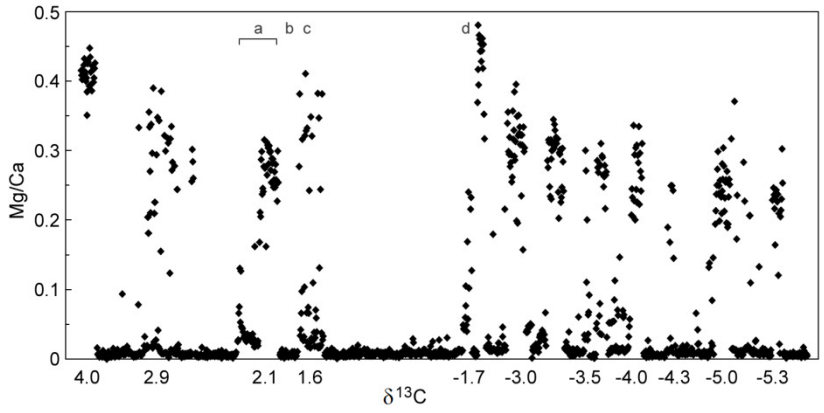

Figure 3.14. Spot analyses of Mg/Ca composition through the 13LH series (upper Yingchenzi to Lower Majiatun Formations) showing a progressive decline in as $\delta^{13}C$ becomes more negative. Dolomite is characterised by Mg/Ca > 0.40. Samples a–d are LH 2, LH 3, 13LH 10, 13LH 21 respectively.

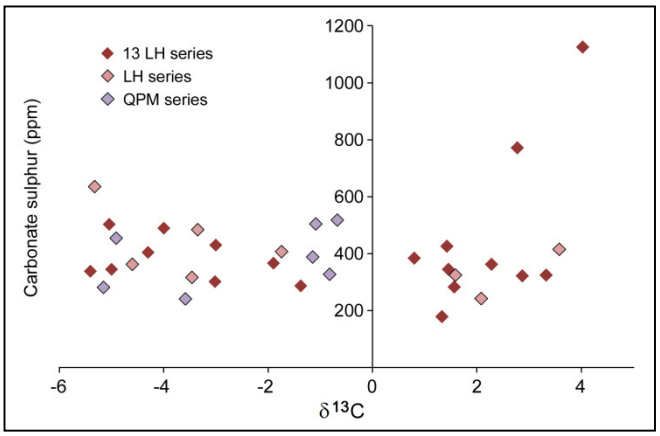

Figure 3.15. Carbonate-included S concentrations versus $\delta^{13}C$ through the Shisanlitai and lower Majiatun Formations.

chemistry being dominated by volcanic emanations of the mid ocean. Occurrence is likely to be of the reduced form, since oxidation to MnO_2 is kinetically inhibited (Diem & Stumm 1984). The ion substitutes for Ca^{2+} preferentially in calcite, quite well in aragonite (Table 3.1). Through the last 3 m of the Yingchenzi Formation concentrations rose from 350 to 1350 ppm, jumped to 3200 ppm above the contact with the Shisanlitai, then fell back through the rest of the formation and the lowermost Majiatun to < 400 ppm. The surge at the base of the Shisanlitai points to a fault-mediated influx of hydrothermal fluid, with the subsequent decline reflecting dilution as water depth increased. Manganese closely follows $\delta^{13}C$ (Fig. 3.13d): that is, fell through the downward phase of the negative excursion and, except for brief lapses after 171 and 187 m, rose through the return phase, suggesting that hydrothermal fluids were entering seawater throughout the Majiatun. Although the elements are chemically similar, co-variation between Mn and Fe through the Yingchenzi to Majiatun Formations is weak.

Microprobe data indicate sulphur concentrations of 230–1130 ppm (Fig. 3.15). The sulphur is inferred to be a mixture of free sulphur and sulphate, occluded in the lattice (*sensu* McIntire 1963). Both sample series show a rising trend as $\delta^{13}C$ becomes more negative; concentrations are more variable where $\delta^{13}C$ is positive. Levels in the Jiuliqiao and Sidingshan Formations are of the same order (Fig. 2.7b). The highest value is recorded by an entirely dolomitic sample, coincident with the most positive $\delta^{13}C$ and probably shallowest water depth. Iron sulphide (FeS_{1-2}, Table 3.2) is uncommon.

Sulphur enters the ocean through submarine volcanism and the oxidative weathering of continental sulphides. Most sulphur in the Precambrian ocean existed as dissolved H_2S (or HS^-). Sulphate concentrations were controlled by the balance between bacterial oxidation of sulphide, oxidation of sulphide by mixing at the oxic surface and microbial reduction of sulphate. The high concentrations of sulphur in the shallow-water samples 13LH 3 and 8 suggest that, at least in this environment, the occluded phase was principally sulphate.

Non-carbonate sulphur data collected by the LECO analyser suggest that pyrite content through the first 50 m of the Qipanmo section was minimal. Peaks occur around 116 m (QPM 32–34: 120–190 ppm), 125 m (QPM 42:100 ppm), 140 m (QPM 50: 430 ppm) and 168 m (QPM 60–61: 300 ppm).

	$\delta^{13}C$	FeS	FeS_{1-2}	Ankerite	VHMC
13LH 2	2.9			x	
13LH 3	2.8		x		
13LH 6	3.3	x			
13LH 8	4.0		x		x
13LH 9	1.4			x	
13LH10	1.5		x		x
13LH 11	1.3			x	
13LH 20	-1.4			x	x
13LH 22	-3.0			x	x
13LH 24	-4.3			x	x
13LH 26	-5.0			x	x
13LH 28	-3.0		x		x
13LH 33	-5.4	x		x	x

Table 3.2. Occurrence of Fe sulphide and carbonate as identified by SEM/EDS microscopy. Ankerite here is $(Ca,Fe)CO_3$. VHMC includes inferred dolomite (13LH 8) and evidence of former VHMC. Note that not all samples are analysed.

3.4.4. *Microscopy*

The following observations are considered representative of the thin sections studied.

Sample 13LH 8 (upper Yingchenzi): dark, organic-rich dolostone with calcite veins, crystals mostly discrete subhedral rhombs or rectangles, typically 12–22 μm in size, with Fe-rich rims, set in a recrystallised silicate matrix (Fig. 3.17a). Mg*/Ca of the crystals mostly ranges from 0.43 to 0.52 (Fig. 3.16); the carbonate-poor matrix ranges from 0.48 to 0.88. High levels of S (~0.12 wt %) and Fe (~1.5 wt %) occur in both crystals and matrix; the matrix also contains sporadic grains of Fe_2S_3 and non-cubic, sub-stoichiometric pyrite. Silicate shows strong correlation between Al and K in a molar ratio of approximately 3:1. Mg, Fe, Al and K show negative correlations with Si, i.e. silica precipitated in preference to metal compounds.

Sample 13LH 20 (lowermost Majiatun): orange-brown, laminated limestone, close-packed subhedral rhombic or rectangular crystals of sulphate-poor low-Mg calcite (dominantly Mg/Ca < 0.012), typically 20–60 μm in size. Some crystals rimmed by Ca-rich ankerite, others not (Fig. 3.17b). The remaining matrix is mostly amorphous silica, apparently filling spaces vacated by

dissolution. Iron-rich ankerite, $(Fe,Ca)CO_3$, also occurs occasionally as discrete grains, evidence that the substrate was reducing but not sulphidic (Table 3.2).

Sample 13LH 24 (lower Majiatun): grey recrystallised limestone including dispersed and inter-layered calcite crystals with ankerite rims. Mg/Ca dominantly < 0.015. Recrystallised calcite is punctured by small pockets of dissolution subsequently filled with silica. In 13LH 25, where layering is conspicuous, the rimmed crystals become more frequent upwards, climaxing in dense Fe-rich mats 0.5–2.0 mm apart (Fig. 3.4f). Precipitation of these crystals from the water column was rhythmic. Grains of ankerite also occur.

Sample 13LH 26: similar to 13LH 24, i.e. grey limestone enclosing dispersed and interlayered calcite crystals with ankerite rims (Fig. 3.5). Matrix Mg/Ca predominantly < 0.02, crystal Mg/Ca 0.06–0.32. Metastable VHMC crystals have partly lost Mg. Between the remnants of ankerite rims the boundaries between matrix and former crystal are diffuse (Fig. 3.17c). Under SEM, Mg-rich-patches within the crystals show up dark. Mg was lost from the outside in, before the process was arrested by pore-space occlusion.

Sample 13LH 33 (middle Majiatun): grey limestone with veins, recrystallised, Fe-poor, Mg/Ca 0.005. Fractures mostly filled with coarse-crystalline calcite, but some of the precipitate is variably, in places exceedingly, rich in Al, Si, Fe and organic C. A few Mg-depleted formerly VHMC euhedral rhombs are outlined against the surrounding matrix by their ankerite rims.

3.4.5 *Re-crystallisation, silica and pH (Luhai)*

With the exception of some ooids and occasional small lithic fragments in the deeper-water sediments, all calcite and silicate is recrystallised. Under SEM, silica-rich calcite is optically indistinguishable from silica-poor, and there is a continuum of compositions from negligible silicon to silicon >> calcium. In many places the element ratios suggest complete *in-situ* dissolution of the precursor mineral. Silica also occurs as re-precipitated fill in veins and voids within the recrystallised amalgam (Fig. 3.17) and as detrital grains of quartz.

Concentrations of silicon are low in modern waters (< 4 ppm), partly because of extraction by silica-secreting organisms such as diatoms and sponges, partly because tectosilicate minerals are almost insoluble at normal pH. At temperatures and pH higher than those characteristic of the modern ocean, solubility increases (Fleming and Crerar 1982, Blum & Stillings 1995, Köhler et al. 2003). In conformity with the Bowen reaction series, quartz is less soluble than illite, illite less than feldspar (Brady & Walther 1989). Proterozoic sea-water appears to have been supersaturated in

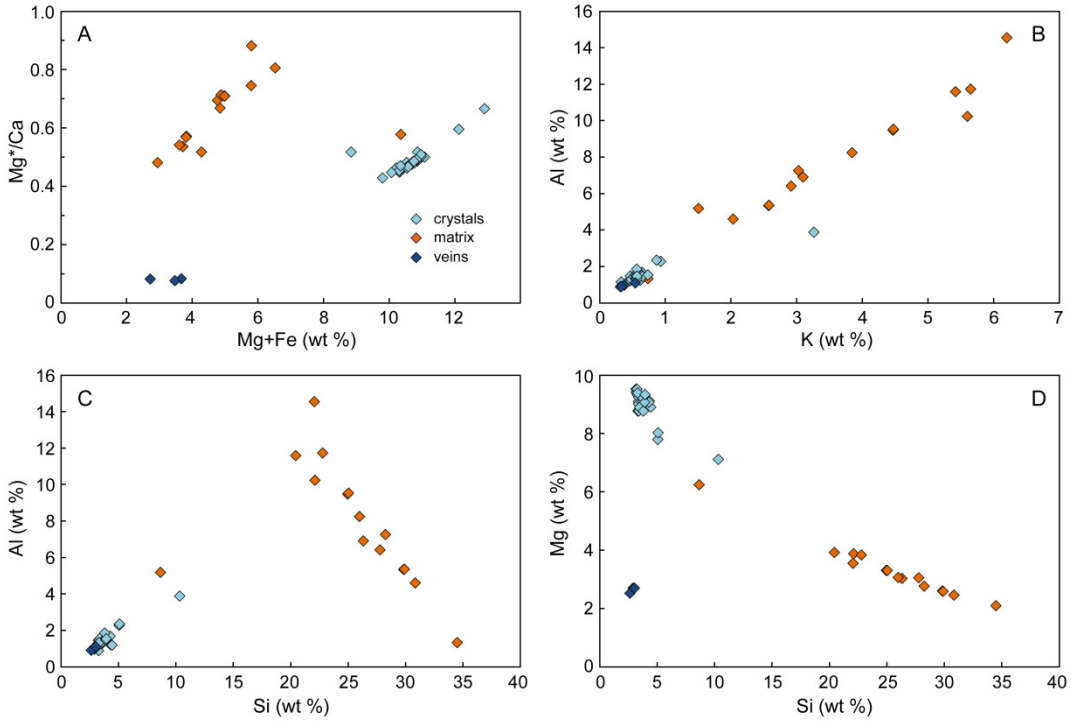

Figure 3.16. Microprobe spot analyses of 13LH 8. Dolomite crystals are mostly sub-stoichiometric (Mg*/Ca <0.606). Veins crystallised from fluid depleted in the analysed elements.

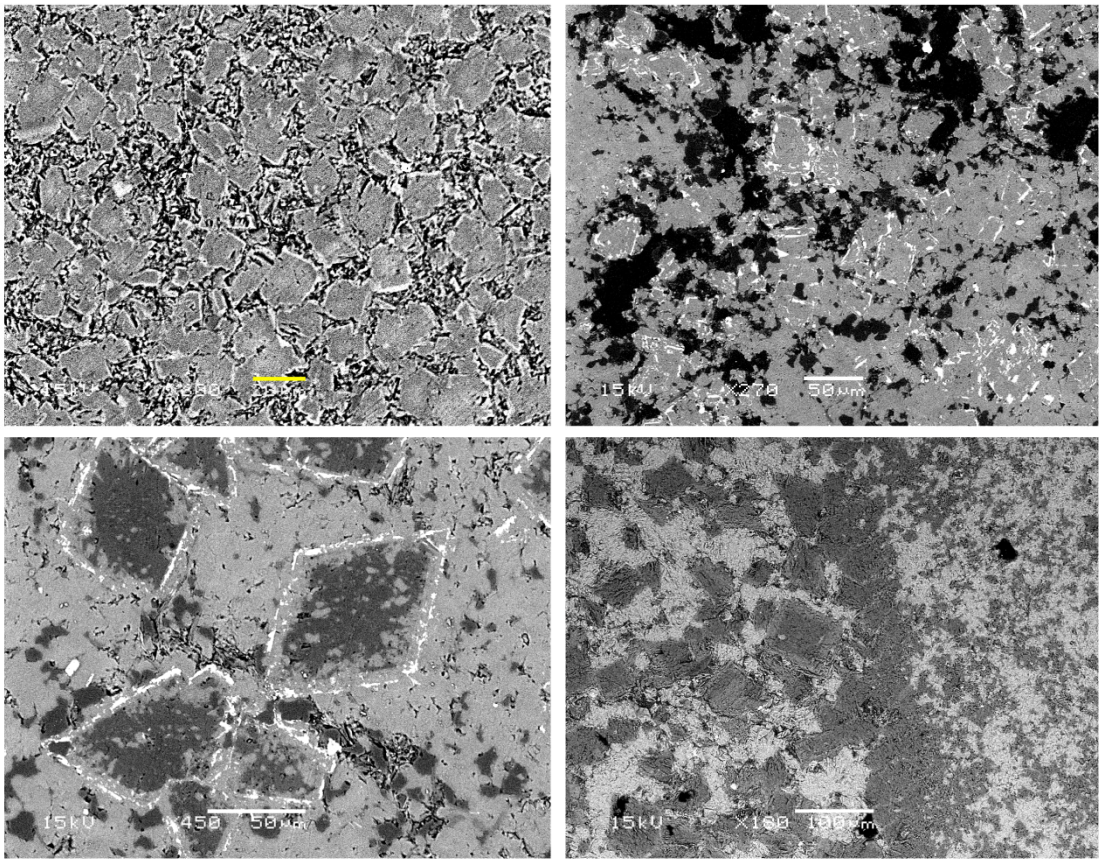

Figure 3.17 (previous page). Backscatter SEM images and related EDS reveal detail that the bulk data mask, if not muddy. **(a)** 13LH 8 (scale bar 20 μm) – discrete subhedral dolomite crystals in re-precipitated silicate matrix. **(b)** 13LH 20 – relict ankerite-rimmed, Mg-poor, formerly VHMC crystals. Grey matrix is calcite, dark patches amorphous silica, white blobs ankerite. **(c)** 13LH 26 – partially Mg-depleted rhombs (dark patches Mg-rich) in calcite matrix. (**d**) QPM 2, stromatolite – primary VHMC rhombs, individual (left) and vertically merged (centre), and disseminated secondary VHMC (right), all within recrystallised LMC.

respect of silica (Maliva et al. 2005). Although silicon does not substitute in the calcium carbonate lattice, concentrations within the mineral are high: up to 10% (wt).

As indicated by variable and strongly correlating K and Al (e.g. Fig. 3.16b), most of the Si derived from adjacent silicate minerals on the seafloor rather than from open sea-water. The elements were incorporated into the calcite as it crystallised on or just below the seafloor. High concentrations in some of the close-to-pristine VHMC crystals (13LH 22) suggest that the water above the sediment was also supersaturated in the respective minerals. The pH of the water column and uppermost substrate appears to have been well above that of modern seawater.

The order in which minerals crystallised is inferred to be: primary VHMC/ dolomite, carbonate and silicate matrix, secondary (Si-poor) VHMC, (low-Mg, high-Fe) ankerite, calcite veins. Silicate minerals dissolved at the same time as the calcite precipitated, and their Mg/Ca composition is broadly the same. Calcite precipitated while there was abundant Fe in the porewater (Fig. 2.7b). Metastable VHMC began to dissolve as burial pressure and hence solubility increased.

3.4.6. *Was the original carbonate mineralogy aragonite or calcite?*

Calcium carbonate has two commonly occurring phases, aragonite and calcite. The former is metastable and eventually morphs into the latter, so that now all Precambrian limestones are calcite. High-temperature burial is sufficient to effect the phase change, in which case the $\delta^{18}O$ remains unaltered (Bathurst 1975 p 239, Zhou & Zheng 2005). Where, much more commonly, diagenesis involves dissolution and re-precipitation, the $\delta^{18}O$ will re-equilibrate with the ambient fluid (Tucker 1986). High amounts of Si in some of the calcite crystals show that diagenesis involved dissolution in the presence of dissolving silicate. Trace-element heterogeneity at the microscale suggests that the water-rock ratio was low.

Two criteria help to determine the original mineralogy: Mg/Ca ratio and Sr content.

(1) In modern marine carbonates, inorganically precipitated calcite rarely contains less than 5% mol $MgCO_3$ (Berner 1975), whereas Mg is not readily incorporated in the

aragonite lattice. Ostensibly, Precambrian carbonates with a Mg/Ca weight ratio of < 0.03 therefore originated as aragonite. The Mg/Ca of the great majority of the samples is < 0.02. In context, the few samples with higher Mg/Ca (13LH 9, 10 and 12) are best interpreted as former calcite.

(2) Because Sr more easily fits in the aragonite lattice, aragonite often has elevated Sr concentrations, though some Sr may be lost on dissolution. Strontium correlates with Mg/Ca up to 0.01 Mg/Ca in the present sample set (Fig. 3.18). While Sr and Mg tend to correlate anyway in proximal environments because both derive from terrestrial runoff, the restriction of the correlation to very low levels of Mg suggests that small amounts of Mg can substitute for Ca in the aragonite lattice without difficulty. After Mg/Ca = 0.01, Sr falls off, consistent with random loss of Sr and gain of Mg during dissolution.

Accordingly, it is suggested that the calcite of the upper Yingchenzi, Shisanlitai and Majiatun Formations is recrystallised because it was originally aragonite.

That aragonite was the main phase precipitated through the sequence – and that the co-precipitating phase was calcian dolomite rather than merely HMC – affects interpretation of controlling parameters such as temperature (Mucci 1987), seawater Mg/Ca (Balthasar & Cusack 2014) and saturation state (De Choudens-Sánchez & González 2009). Of immediate relevance is the difference in ^{13}C fractionation, since aragonite tends to be heavier than calcite. Calculations of the difference vary: measurements of co-occurring phases in modern molluscs (Lécuyer et al. 2012) and Permian reef cements (Given & Lohmann 1985) suggest ~1‰, experiments ~1.7‰ (Romanek et al. 1992).

In the Phanerozoic there is some basis for characterising the ocean at any one time as disposed towards either low-Mg calcite or aragonite and high-Mg calcite, depending on the above controls and, ultimately, the overall rate of seafloor spreading (Stanley & Hardie 1999). Today the ocean is well-mixed and has a molar Mg/Ca ratio of 5.2, so that aragonite tends to precipitate even where the sea is quite cold. Whether Neoproterozoic seas can be meaningfully conceived in such terms is doubtful. Under high pCO_2 the pH of fluids effecting subaerial weathering would have been lower, while the concentration of bicarbonate and base cations in runoff and coastal seawater would have been higher. Strong nearshore-offshore gradients in Mg/Ca may have cut across the aragonite/ calcite divide (cf. Fig. 3.14). The phase precipitated in the Jiuliqiao and Liulaobei environments a little earlier in the Tonian was not aragonite or calcite, but vaterite.

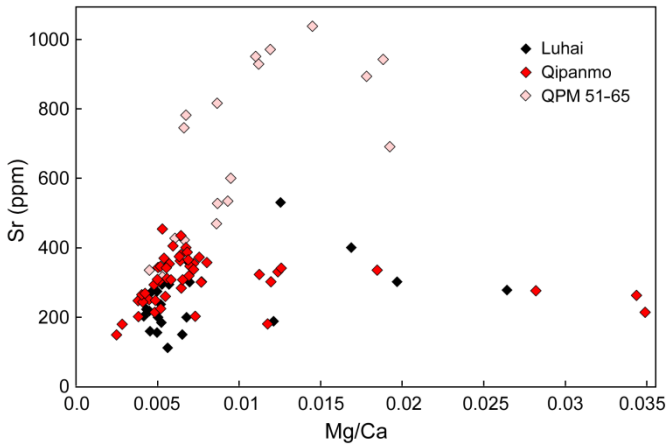

Figure 3.18. The degree to which Sr substituted for Ca in low- and high-Mg calcite.

The coincidence of vaterite precipitation and exceptional mineralogical preservation in the Jiuliqiao may not be accidental. Presumably the vaterite spheres retained their morphology when recrystallising to calcite. Where the original polymorph was aragonite, recrystallisation would have destroyed its morphology.

3.5. Controls on carbon and oxygen isotope ratios

3.5.1. *Carbon isotope mass balance*

The Proterozoic ocean is generally thought to have had a carbon-isotope structure similar to that of the ocean today: the open ocean was homogeneous and its composition faithfully reflected in the carbonates on epicontinental platforms. On that basis, a composite carbon-isotope record for the Neoproterozoic should facilitate stratigraphic correlation across all continents (Halverson et al. 2005): there was but one system, inputs were balanced by outputs and fractionation occurred to the extent that ^{12}C-enriched organic carbon was removed by sedimentary burial. Omitting the refinements of Hayes & Waldbauer (2006),

$$\delta^{13}C_{DIC} = \delta^{13}C_{in} + f\,\varepsilon \qquad (3)$$

where $\delta^{13}C_{in}$ is the isotopic ratio of the carbon entering the system, f the organic carbon removed as a fraction of total carbon and ε the average difference between carbonate and inorganic carbon ($\delta^{13}C_{DIC}$ less $\delta^{13}C_{org}$). Carbon entered chiefly through volcanic outgassing at plate boundaries and left the system by burial and ultimately subduction.

In the modern ocean dissolved inorganic carbon, or DIC, comprising CO_2(aq), HCO_3^- and CO_3^{2-}, ranges from 0.5 to 1.5‰, depending on latitude, with pre-industrial values 0.5‰ higher (Kroopnick 1985). At greater depths, DIC falls by up to 3‰, as ^{12}C-rich organic matter (OM) sinks through the water column, becomes oxidised and returns to the inorganic pool, initially as CO_2. At shallow

depths, most OM is remineralised after it has reached the sea-floor, by anaerobic bacteria in the substrate (Jørgensen 1982). Here the main product of oxidation is HCO_3^-, and because there is little re-circulation of the pore-water, the isotopic environment is considerably more depleted (Irwin et al. 1977). In either case, the organic residue finally buried is only a small fraction of the OM originally produced; as a fraction of the total sediment, usually less than 1%.

Carbon-isotope values much below 0‰ are difficult to model on the basis of mass balance. Values around -1‰ could arise if organic fractionation (ε) dropped below 20‰. There is also scope for varying the burial flux. Tectonic cycles may have had an effect on *f* through increasing the supply of nutrients and rates of sedimentation. On the other hand, it is not clear whether the flux would have been greatest during orogenesis (e.g. Kaufman et al. 1993, Barley et al. 2005), during subsequent denudation, or during rifting and supercontinent break-up (Knoll 1992, Des Marais et al. 1992), rendering such explanations somewhat *ad hoc*. If rocks were most likely to be preserved at the end of the orogenic cycle (Hawkesworth et al. 2009), this implies a higher flux during rifting. Possibly all these scenarios have some validity, in which case *f* may not have varied greatly and certainly not as wildly as has been supposed (e.g. by Hayes et al. 1999, Krissansen-Totton et al. 2015). Even if it did, an inferred minimum of around 0.1 would still not bring $\delta^{13}C_{carb}$ below -4‰. Organic production virtually had to cease before $\delta^{13}C_{carb}$ could have reached the mantle value.

3.5.2. *Negative carbon isotopes and organic carbon remineralisation*

A possible clue to what controlled $\delta^{13}C$ through the Yingchenzi, Shisanlitai and Majiatun Formations is provided by parallel changes in water depth. The ooids and dolomitic mineralogy of the upper Yingchenzi indicate very shallow conditions, coincident with the heaviest values. Concentrations of the redox-sensitive elements Mn and Fe were low. Faulting, subsidence and an influx of siliciclastic sediment during Shisanlitai deposition were accompanied by a steep rise in carbonate-associated Mn^{2+} in response to the injection of fluids rich in metals. Fe concentrations rose as the environment deepened, because carbonate precipitated close to or even below the seafloor, which was increasingly anoxic and ferruginous with depth. At the beginning of the Majiatun carbon isotope ratios fell steeply. ZnS and Cu_3S among the SEM-bright grains in QPM 1, along with grains of $Ti(CO_3)_2$ and directly precipitated calcian dolomite crystals at the same point in the Luhai sequence, suggest hydrothermal influence. Depths increased to subtidal, shallow enough for the expression of coarsening-up cycles, then reached close to storm wave-base, where swaley bed structures developed. Mn decreased as a result of dilution and distance from source (Fig. 3.13d); Fe remained steady (Fig. 3.13b). Maximum depth was attained shortly before the resumption of cyclical bedding at 115 m. Carbon isotope ratios were lowest around 108 m. The

return to shallower water and higher values was gentler. Facies evolution shows a degree of symmetry: medium-thick purple beds at the base become thinner and brownish up-section, laminar or ribbon-like, and re-appear in reverse order through the upper 30 m.

Inorganic carbon-isotope values might fall below 0‰ if OM were oxidised back into the DIC reservoir ('re-mineralised') and carbonate precipitated from the reservoir before the lighter carbon was diluted by vertical mixing. In the modern ocean remineralisation is primarily an aerobic process. The resultant isotopic gradient is small and vertically long, typically 1–2‰ over 1000 m. In shallow seas remineralisation mostly occurs within the sediment and the gradient above the seafloor is negligible. In the Proterozoic ocean, only the surface layer, where photosynthesis took place, was oxygenated. The subsurface was anoxic (Planavsky et al. 2011), so that sinking OM was oxidised primarily by anaerobic bacteria in the water column. Levels of TOC were consequently no higher than in modern and Cenozoic deep-sea settings (Martin et al. 2008). Factors aiding recycling may have included slower descent of OM through the water, exposing it to microbial reworking for longer (Logan et al. 1995), and higher temperatures, raising the metabolic rates of remineralising organisms proportionally higher than those of primary producers (Stanley 2010, Regaudie-de-Gioux & Duarte 2012). In the warm Eocene, off Tanzania, most remineralisation took place within the upper 150 m (John et al. 2014).

Steeper remineralisation gradients have been proposed to explain negative carbon-isotope excursions, particularly those seen above Cryogenian diamictites. As glaciation came to an end, anoxic, alkaline, ^{13}C-depleted deep water welled to the surface and triggered the rapid precipitation of similarly depleted carbonate minerals (Grotzinger & Knoll 1995). The idea has been rejected on the grounds that vertical circulation is normal and arresting it for any length of time all but impossible (Hoffman and Schrag 2002), with advocates and critics alike interpreting the excursions in relation to whole-ocean dynamics. In a context of epicontinental platforms where water depth was typically less than 100 m, and as a general explanation for negative excursions, overturn of deep ocean stratification is hardly in point, however. In epicontinental shelf settings the existence of a remineralisation gradient would have depended on the degree of wave and vertical mixing by storms, currents and convection. With temperature suppressing vertical mixing (de Boyer Montégut et al. 2004), the base of the mixed layer could have been much shallower.

3.5.3. *Carbonate alkalinity, pH and organic carbon fractionation*

Seawater is oversaturated in respect of calcium carbonate, because precipitation is inhibited by ion pairing and cation hydration. Today, marine carbonates consist primarily of solids synthesised by planktonic and benthic organisms. While direct precipitation from surface water is not unknown

(e.g. Swart et al. 2014), biomineralising organisms generally maintain saturation state below the level at which abiotic precipitation is possible.

In the Proterozoic, saturation state was controlled by abiotic precipitation. Because of high pCO_2, hence high DIC, photosynthesis is unlikely to have materially increased surface alkalinity (Arp et al. 2001), and its consumption of CO_2 would have been counteracted by non-equilibrium mixing with atmospheric CO_2. For this reason precipitation must have taken place lower in the water column, where, by implication, alkalinity was higher. Stromatolite build-ups show that at least some precipitation took place at the seafloor.

Today, marine alkalinity is principally generated by silicate weathering, which converts carbonic acid to bicarbonate. Under an atmosphere much richer in CO_2 the weathering of basement rock would have been intense. By charge balance, alkalinity arising from subaqueous silicate weathering was the sum of the major ion concentrations (Deffeyes 1965, Spivack & Staudigel 1994):

$$Alk = [Na] + [K] + 2[Mg] + 2[Ca] - [Cl] - 2[SO_4] \qquad (4)$$

On or near the seafloor, cation equivalents were released from silicates in excess of strong acid anion equivalents: silicate dissolution increased alkalinity, which was consumed (precluding endless positive feedback) by authigenic calcium carbonate. Although the recrystallised state of the carbonate reduces the quality of the petrographic evidence, precipitation in or close to the sediment is evident in the high amounts of Ca within the silicate. Ca weight % can be more than twice the Si, reflecting the nanoscale precipitation of calcium carbonate within dissolving silicate voids. Precipitation below the oxic zone is also indicated by the susceptibility of calcium carbonate to increases in concentrations of Fe^{2+} and Mn^{2+}. It is difficult to see why incorporation of these ions should have increased with depth if precipitation was from the surface.

The lower water column being generally anoxic, the low levels of $[SO_4^{2-}]$ maintained by sulphate-reducing bacteria also contributed to alkalinity (reaction 4). Although the reduction of sulphate produced H_2S, which was liable to dissociate into bisulphide and protons and thereby lower pH (Meister 2013), oxidation of OM increased alkalinity by generating bicarbonate. Net alkalinity increases if H_2S reacts with iron to produce FeS and ultimately FeS_2, which are precipitated, or if H_2S degasses into the atmosphere. Under SEM only four of the examined 13LH samples exhibited iron sulphide, three of them shallow-water (13LH 3, 6 and 8; Table 3.2). If sulphate reduction took place mainly in the lower water column, most H_2S would have risen into the oxic layer and been re-oxidised there, with or without assistance from sulphide-oxidising bacteria. This would have resulted in a vertical gradient whereby alkalinity increased downward through the water.

Variation in relative pH may be gauged by plotting the degree of *in-situ* silicate dissolution as recorded in the carbonate fraction against $\delta^{13}C$, here hypothesised to be a proxy for water depth. Silicate dissolution can be parameterised as log (Si_n x F_c), where Si_n is the averaged carbonate-normalised weight % silicon included in $(Ca,Mg)CO_3$ and F_c is the 'bulk' carbonate percentage. Multiplying by F_c reverses out co-variation attributable to the amount of silicate available (cf. Little et al. 2015). Thus gauged, pH markedly increases as $\delta^{13}C$ falls towards 0‰, and remains high throughout the negative excursion, slipping a little only between -5 and -6‰ (Fig. 3.19). As previously discussed (§2.4.1), the inferred pH increase with depth is attributed to a combination of sulphate reduction and subaqueous silicate dissolution.

Most organic production in the Proterozoic was by cyanobacteria and microalgae, the $\delta^{13}C$ of which depended on the carbon species utilised in photosynthesis. With distance from shore, supersaturation in respect of dissolved CO_2 would have decreased, owing to lessening wave action, and phototrophs would have become concentrated somewhat lower in the water column in order to maximise access to the nutrients released from silicate dissolution (Cullen 2015). With rising pH, CO_2 would have dwindled towards zero and cyanobacteria have had to manufacture their own CO_2 from HCO_3^- (Price 2011), a species 9‰ heavier than dissolved CO_2 (Mook et al. 1974, Zhang et al. 1995). Accordingly, $\Delta\delta$ would have decreased with depth as surface pH increased. Such a relationship helps to explain isotopic variation in the Majiatun Formation. Apart from the disturbance reflected in samples QPM 51–66, the decrease in organic fraction follows the decrease in carbonate $\delta^{13}C$ quite closely (Fig. 3.20). Inorganic $\delta^{13}C$ would have fallen in response to both the greater enrichment of buried organic carbon and the decrease in amount buried.

3.5.4. *The cause of the $\delta^{13}C$ kink*

The abrupt rise in $\delta^{13}C$ at 141 m from -3.5 to -0.8‰ reflects an event of some kind and suggests local control. Some explanations can be discounted. The evidence of seismic activity (Fig. 3.6a), although stratigraphically close, comes after the jump, and sediment can have been imbricated only after lithification some distance below the seafloor, which was therefore further above the hiatus. An injection of magmatic CO_2 would have caused $\delta^{13}C$ to fall, not rise. There is no unconformity or other obvious evidence of a drop in sea-level.

Two signals shift at this point. One is the difference in fractionation between organic and inorganic $\delta^{13}C$, jumping from 22 to 27‰ (Fig. 3.12): phytoplankton was suddenly extracting more ^{12}C from the system, and inorganic carbon was consequently heavier. The response was immediate: there was no significant lag between synthesis of the organic carbon and precipitation of the correlative

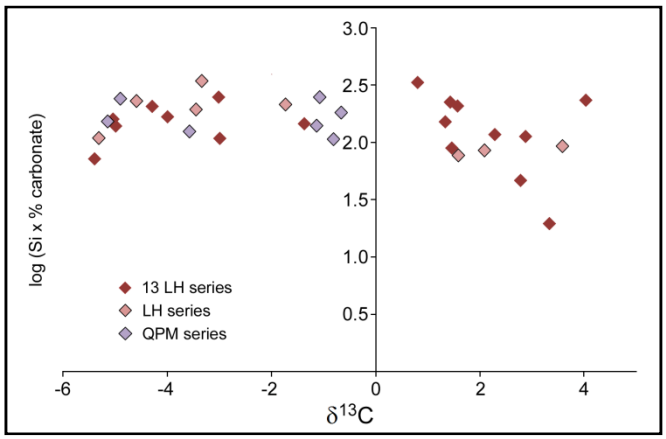

Figure 3.19. Carbonate-included silica concentration normalised to carbonate fraction (as estimated via ICP) versus $\delta^{13}C$, Shisanlitai and Majiatun Formations, Luhai. The two samples at $\delta^{13}C$ -0.7 and -0.8 are QPM 52 and 54.

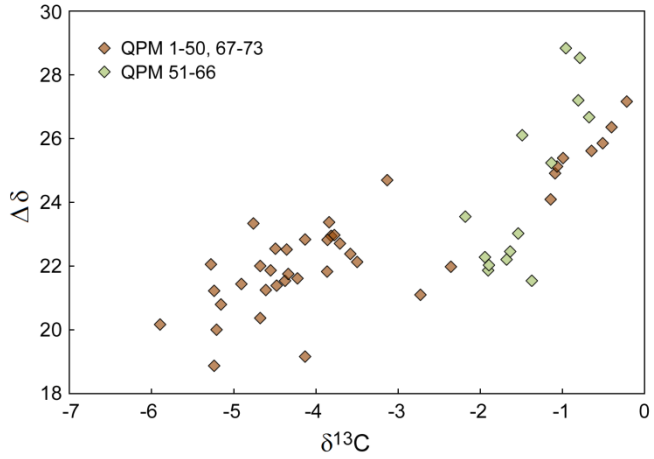

Figure 3.20. Organic matter through the Majiatun Formation fractionated dissolved inorganic carbon decreasingly as carbonate $\delta^{13}C$ decreased.

carbonate. Thereafter Δδ fell. The other signal is a surge in clastic sediment (QPM 51–64). As we have seen (Fig. 3.10), siliciclastic sediment appears to have stimulated organic production. Since there is no evidence that pH was low (Fig. 3.19), the signal reflects a rise in the clastic component rather than a fall in the carbonate. Stimulated by the rise in nutrients, organic production rose, and because of the higher sedimentation rate, more organic carbon was buried. TOC surged through the interval (Fig. 3.10, 11). In accordance with equation (3), $\delta^{13}C_{carb}$ rose in response to an increase in both *f* and ε. Apparently the erosive episode that increased the supply of siliciclastic material also brought in a flux of dissolved ^{12}C-rich carbon: a mix, perhaps, of HCO_3^- around -6‰ (the mantle value) and dissolved organic matter at the eroded source (cf. Wellman & Strother 2015). Organic fractionation decreased as the extraneous source of ^{12}C-rich carbon waned.

3.5.5. *Oxygen isotope variation*

Lastly, there is the question of how to interpret oxygen isotope variation. Although commonly disregarded in Neoproterozoic studies, carbonate $\delta^{18}O$ can carry significant information. Relevant controls on $\delta^{18}O$ include carbonate phase, evaporation, temperature and seawater $\delta^{18}O$.

Calcite is enriched in ^{18}O relative to aragonite. Much the same applies to dolomite, which at stoichiometric composition is some 2.7‰ heavier than calcite (Zhou & Zheng 2006). Oxygen isotopes in a sample with bulk Mg/Ca = 0.4 would therefore be at least 3‰ heavier than the equivalent aragonite. Only one sample has an entirely dolomitic carbonate fraction, and this only at ~0.4 Mg/Ca: 13LH 8, with an oxygen-isotope value about 4‰ heavier than preceding non-dolomitic samples. Thus most of the difference can be explained by mineralogy. The heavier values of 13LH 9, 10 and 12 correspond with the slightly elevated Mg/Ca of phases that were once more magnesian. The preservation of the difference in carbonate-water fractionation between dolomite and calcite even in cases where Mg was subsequently lost shows that values were not reset and homogenised post-burial.

Although the carbonates of the Yingchenzi and Shisanlitai Formations are shallow-water, their oxygen isotope values are low, similar to those of the deeper-water lower Majiatun Formation. Evaporative enrichment appears to have been minor, possibly because isotopically light water vapour returned as rain to the same area. A humid equatorial or sub-equatorial location would accord with palaeo-magnetic evidence for North China in the early Neoproterozoic (Fu et al. 2015).

Carbonate-water isotope fractionation decreases with temperature and $\delta^{18}O$ becomes lighter. If seawater $\delta^{18}O_{SMOW}$ was 0, as today, then aragonite $\delta^{18}O_{PDB}$ of around -10‰ would imply temperatures of around 60° C (Kim et al. 2007). Eukaryotic forms of life could not have survived such conditions and primary production would have been minimal. Thus seawater $\delta^{18}O$ must have been substantially lower than 0 (Kasting et al. 2006). Nonetheless, coupled with the equatorial location, the prevalence of aragonite at all depths and by implication over a large range of seawater Mg/Ca suggests that temperatures were high (Balthasar & Cusack 2014).

Oxygen isotope ratios fell markedly at 108 m, 138 m and 188 m. Each of these events is associated with inferred seismic activity. The first coincides with evidence of a fault at Luhai that truncates the $\delta^{13}C$ signal and may be linked to the initiation of crustal rebound (Fig. 3.2); the second immediately precedes the $\delta^{13}C$ kink at Qipanmo (Fig. 3.3) and the steep rise in siliciclastic content; the third is associated with renewed faulting at Luhai (Fig. 3.7). Since there was no change in carbonate mineralogy, these events might reflect increases in temperature brought about by mixing with fault-mediated fluids from deep in the crust.

The fall at 108 m also coincides with pivotal moments in two other geochemical signals, the lowest point in the $\delta^{13}C$ curve and the start of a rising trend in carbonate-included Fe. Given that relative sea-level began to drop at this juncture, faulting must have resulted in continental uplift rather than

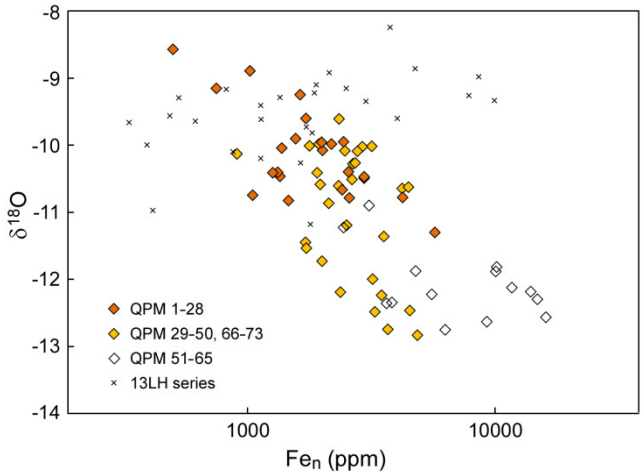

Figure 3.21. Increasing calcite-included Fe as $\delta^{18}O$ falls, Qipanmo section. Luhai shows no such correlation.

subsidence. Fluids released from deeper in the crust than those evidenced in the Shisanlitai were hot and replete in iron. While correlation does not prove causation, there is some co-variation between $\delta^{18}O$ and iron (Fig. 3.21). Qipanmo appears to have been closer than Luhai to the source.

Tectonic dislocations are a common feature of the Dalian succession. In addition to those just mentioned, penecontemporaneous faulting, folding and fracturing are apparent around the base of the Shisanlitai (Fig. 3.4a,b), associated with the dramatic change in facies; tremors produced more fracturing around 167–169 m (Fig. 3.6c); and a synsedimentary fault divides the Majiatun from the Cuijiatun Formation (Fig. 3.8). The shales of the Cuijiatun also contain deformation features. Unadjusted oxygen-isotope ratios in the Cuijiatun are mostly in the range -9.3 to -12‰.

3.6. Sedimentation rates

As a result of the tectonism, sedimentation rates may have been considerably faster than those normally implied by carbonate deposition. Throughout the descent phase of the excursion bedforms indicate high-energy processes. The relatively steep trajectory of the isotope curve reflects rapid subsidence rather than low sediment supply. On the other hand, siliciclastic input, and by implication erosion, was proportionally minor during this interval. The ascent phase occupied a thickness twice that of the descent phase. From around 140 m siliciclastic input increased but the overall trajectory of the isotope curve remained unaffected. The tectonic rebound being slower, higher rates of siliciclastic sedimentation were balanced by lower rates of carbonate sedimentation. Nonetheless, timescales may have been short enough for hot crustal fluids to have raised local sea temperature by several degrees, despite dilution.

Ribbonites are alternations of silt- and carbonate-rich layers, up to ~3 cm thick. Typically they formed in subtidal, low-energy conditions (Halverson et al. 2002), a setting consistent with their occurrence at Luhai and Qipanmo (Figs. 3.2, 3.6). The rhythmicity of such couplets is striking. One

possibility is that they relate to diurnal cycles, whereby marine photosynthesis during the day consumed CO_2 and pH rose, favouring carbonate production (Schmalz & Swanson 1969), whereas respiration during the night inhibited carbonate production and deposition of silt predominated. A higher-order cycle of 28–30 such ribbons suggests that there was also a monthly rhythm. The two orders of cyclicity are apparent from 163 m onward, with carbonate layers becoming thicker and less nodular as the environment shallowed. Diagenetic separation may have accentuated the contrasts in carbonate content.

Although the rates of sedimentation entailed are rapid, they are not unprecedented. Tidal beds displaying rhythmicity on the same scale (diurnal or semi-diurnal couplets, mm to cm thick) are documented in rocks of diverse age, including the Neoproterozoic (Chan et al. 1994, Alvarez 1995, Williams 1999). Examples from the Miocene expose sequences of aggradational tidal bedding up to 50 m thick (Tessier & Gigot 1989, Couëffé et al. 2005). The preservation of metastable carbonate phases in some instances (Figs. 3.14, 3.17), accentuated by the loss of Mg in others, also suggests comparatively rapid deposition.

3.7. Other Tonian excursions

The patterns of element abundance as a function of carbonate $\delta^{13}C$ (Fig. 3.13) suggest that $\delta^{13}C$ was closely linked to regional environment. Environment was controlled by sea-level, whereby waters became more anoxic and isotopically depleted with depth. The transition from positive to negative marks the descent through the redoxcline, below which Fe^{2+} became much more abundant. Sourced from near-shore fault systems, Mn^{2+} decreased as it became diluted seaward. Silicon (Fig. 3.19), potassium and aluminium increased as a consequence of silicate dissolution in conditions of high pH, promoted by the alkalinity generated by anaerobic bacteria. Sulphur increased with depth because anoxic waters were rich in sulphide (Fig. 3.15). The sudden rise in inorganic $\delta^{13}C$ and fall in organic $\delta^{13}C$ at 141 m likewise point to local/regional causes.

So was the Dalian event the only isotopic excursion in the Tonian period accompanied by a rise in relative sea-level? To address this question, other relevant sections are briefly reviewed.

3.7.1. *Shorikha Formation, Siberia*

Through most of this 800-m-thick formation, consisting of stromatolitic, sometimes intraclastic dolomite, $\delta^{13}C$ is positive. Negative values begin with the appearance of columnar stromatolites (*Katavia*), after which the dolomites become cherty and the stromatolites disappear. Positive values return with the appearance of argillaceous limestone (Knoll et al. 1995). Petrov and Semikhatov (2009) provide a detailed description of the facies but no geochemical data, referring the stromato-

lites at the base of the excursion to *Sacculia*. A sharp erosional surface marks the beginning of a deep, outer-ramp setting. The uppermost beds are interpreted as tidal flat.

3.7.2. *Sirohi Group, northwest India*

Unfortunately, the sedimentology is barely described. The mainly calcitic rocks follow metamorphosed shale near the base of a sequence that presumably shallows upward. Carbon isotopes ratios start at -2.3‰ 6 m into the carbonate, reach -4.1 at 24 m, then progressively rise to +4.7, where the last section ends. Oxygen isotope ratios progressively rise.

3.7.3. *Loves Creek Formation, Bitter Springs Group, Australia*

The negative excursion starts with oolites and intraclastic breccia at the base of the Loves Creek Formation (formerly Member), at which point the facies pass from red beds into a series of rapidly deepening, upward-shallowing mudstone-dominated stromatolite cycles (Southgate 1989, Hill et al. 2000). In their high-resolution isotopic study Swanson-Hysell et al. (2010) exclusively sampled dolostones, which tend to be slightly heavier than limestones. The stromatolite cycles continue to the end of the unit, by which time $\delta^{13}C$ had climbed back from -4.1 to -1.8‰. The rest of the excursion is lost in dolomitic siltstone. In short, the excursion starts with transgression and ends with regression (Swanson-Hysell et al. 2012). Another study has also noted a facies relationship, the evaporative environments being associated with heavy values and the microbial carbonates of deeper waters with depleted values (Klaebe et al. 2014).

Cycles are mostly 2–4 m thick, with some up to 12 m. They begin with domal, columnar, bulbous or stratiform stromatolites that expand upwards and outwards into large single domes. The domes are abruptly succeeded by thin columns that branch into successively smaller ones. These grade into a second set of stratiform stromatolites. The cycles end with erosion surfaces, discontinuous beds of intraclastic peloidal grainstone and evidence of emergence. Subsequent carbonates, red siltstones and shales indicate non-marine environments.

The Amadeus Basin containing the carbonates was a subsidence-prone intracratonic depression with periodic connection to the open sea. Although the cycles are stratigraphically small-scale, each progresses through almost the whole range of stromatolite forms and may reflect relatively large-amplitude sea-level change, though still within the photic zone. Among possible causes of the oscillations, the most likely is tectonic (cf. Bosence et al. 2009, Lovell 2010).

3.7.3. *Upper Grusdievbreen and Lower Svanbergfjellet Formations, East Svalbard*

An excursion probably related to the Bitter Springs event starts with an eroded surface of dolomitic packstone or conglomerate; in some places the surface is karst (Halverson et al. 2007). Within a

few metres the facies becomes red silt with hummocky cross-stratification and carbonate lenses, marking an abrupt descent into deeper water; the fall in $\delta^{13}C$ to -1.5‰ is also abrupt. Up-section, ribbonites form as the carbonate proportion increases, parallel with an upward-shallowing sequence and rising $\delta^{13}C$. Limestone switches to dolomite and shallower-water facies as $\delta^{13}C$ reaches zero, after which biolaminites and small stromatolites possibly reflect another rise in sea-level and $\delta^{13}C$ falls to -3‰. A second regionally extensive erosion surface marks the end of the excursion.

3.7.4. *Shaler Supergroup, Victoria Island, northwest Canada*

The older of two excursions occurs in the middle of the Wynniatt Formation, spanning about 60 m. The log provided in the initial report (Jones et al. 2010) is schematic but shows a deepening sequence in which grainstone passes into ribbonite couplets of silt-dolomite; $\delta^{13}C$ drops to -5‰. In another location the signal drops systematically to -11‰ as shallow-marine calcilutite gives way to calcareous black shale, the latter plunging to below storm-wave base (Thomson et al. 2015); all the negative values are in the shale, which is exceptionally rich in organic C, V, Mo and U; one sample reaches -14‰. The erosional unconformity separating the shale from the calcilutite suggests that sea-level rose rapidly. The rebound was immediate and almost as rapid. The younger excursion, in the upper Kilian Formation, drops to -4‰. A series of grainstone/ribbonite parasequences ends abruptly with a flooding surface, followed by a deepening sequence of siltstone, 6–11 m of purple silty debrite, then several meters of siltstone and limestone breccias (Jones et al. 2010). In another section the excursion zigzags back to -1‰ before carbonates are superseded by evaporites. As with the Bitter Springs Formation, the basin is intracratonic.

3.7.5. *Fifteenmile Group, Ogilvie Mountains, northwest Canada*

An excursion correlated with the Bitter Springs event (Macdonald et al. 2012) occurs at the base of the sixth of nine successive sequences that make up the ‘Reefal Assemblage’. These NNW-prograding stromatolite-cored reef tracts grade distally into shale-dominated basinal deposits; thus at any one locality each such sequence shallows up, from shales to dolomitic stromatolites or grainstones. Downward faulting parallels the direction of progradation, with reefs growing on footwalls while carbonate breccia, olistoliths and turbidites accumulated in the basin below. Two debrites above and below a tuff dated to 811 Ma herald the onset of the excursion at +6‰. In the shale, values turn negative, climbing back as facies change to ribbonite and lagoonal/supratidal biolaminite. A further descent to negative values occurs at the base of the ninth transgressive sequence. Here values remain negative as shales pass into grainstones and ribbonites, before recovering in the stromatolites. Throughout the region, maximum regression surfaces mostly occur close to peaks in $\delta^{13}C$.

3.7.6. *Little Dal Group, Mackenzie Mountains, northwest Canada*

A sustained negative excursion occurs in the Upper Carbonate Formation, east of the Ogilvie Mountains. The published log is schematic (Macdonald et al. 2010) but negative values begin abruptly at a flooding surface just above ribbonites. Reaching -2.5‰, they remain negative as facies pass through rhythmites, grainstones (re-deposited?), more rhythmites and stromatolites before climbing to positive values as the stromatolites shallow up.

3.7.7. *Beck Spring Dolomite, Death Valley, California*

A negative excursion in the upper 160 m of this unit goes from +5 to -3‰. The carbonate is dolomitic except for a transient limestone interval when $\delta^{13}C$ surges to +9–11‰ (Macdonald et al. 2013). Values of 3– 5‰ are associated with broken microbial mats and rip-up clasts, lower values, down to -1, with chip stones. After the limestone there is a gradual transgression (Smith et al. 2016), where interbedded pisoid grainstone and microbialite are succeeded by red shale, stromatolites characteristic of subtidal depths and bedded black chert. Black, oolitic limestone beds are present near the top. Above the formation boundary the carbonate passes gradationally into dolomitic siltstone. The excursion invites comparison with others elsewhere grouped together as the 'Islay anomaly', although in these places, as reviewed above (§3.1), it does down to -6 or lower.

3.7.8. *Tambien Group, northern Ethiopia*

The beginning of the excursion cannot be traced, as the oldest carbonates start at -6‰. In the west Tsedia section (T20) they are preceded by 300 m of extrusive basalts, volcaniclastics, sandstones and, towards the top, diamictites (Fig. 3.22). Over the next 100 m the environment deepens, as evidenced by scour, trough and swaley cross-stratification (cf. Fig. 3.4d, 4e) and progressively finer grain size. Through the following 500 m siltstone and shale preponderate. Pumice fragments through much of this interval show that volcanic activity had not entirely abated. Carbonates in the east Tsedia section (T18) appear about the level where the other section ends, accompanied by swaley cross-stratification and soft-sediment folds. Carbon-isotope values meander between -2.5 and -6.5. In the parallel section at west Chehmit (T16) ribbonites embody somewhat heavier values. The end of the excursion is patchily recorded at west Mai Kenetal (T1), where shallow-water intraclast breccias yield positive values of 1.7–2.7. Consistent with the depth difference, carbonates at west Mai Kenetal can be up to 5‰ heavier than the correlative sequence at east Tsedia. Carbon isotopes show the same depth dependence as in other regions, and it seems reasonable to infer that the excursion began – or would have begun had conditions favoured carbonate precipitation – some 500 m before its first manifestation, at the point where sea-level began to rise. Since the rocks at this point date to older than 815 Ma, the excursion in Ethiopia may

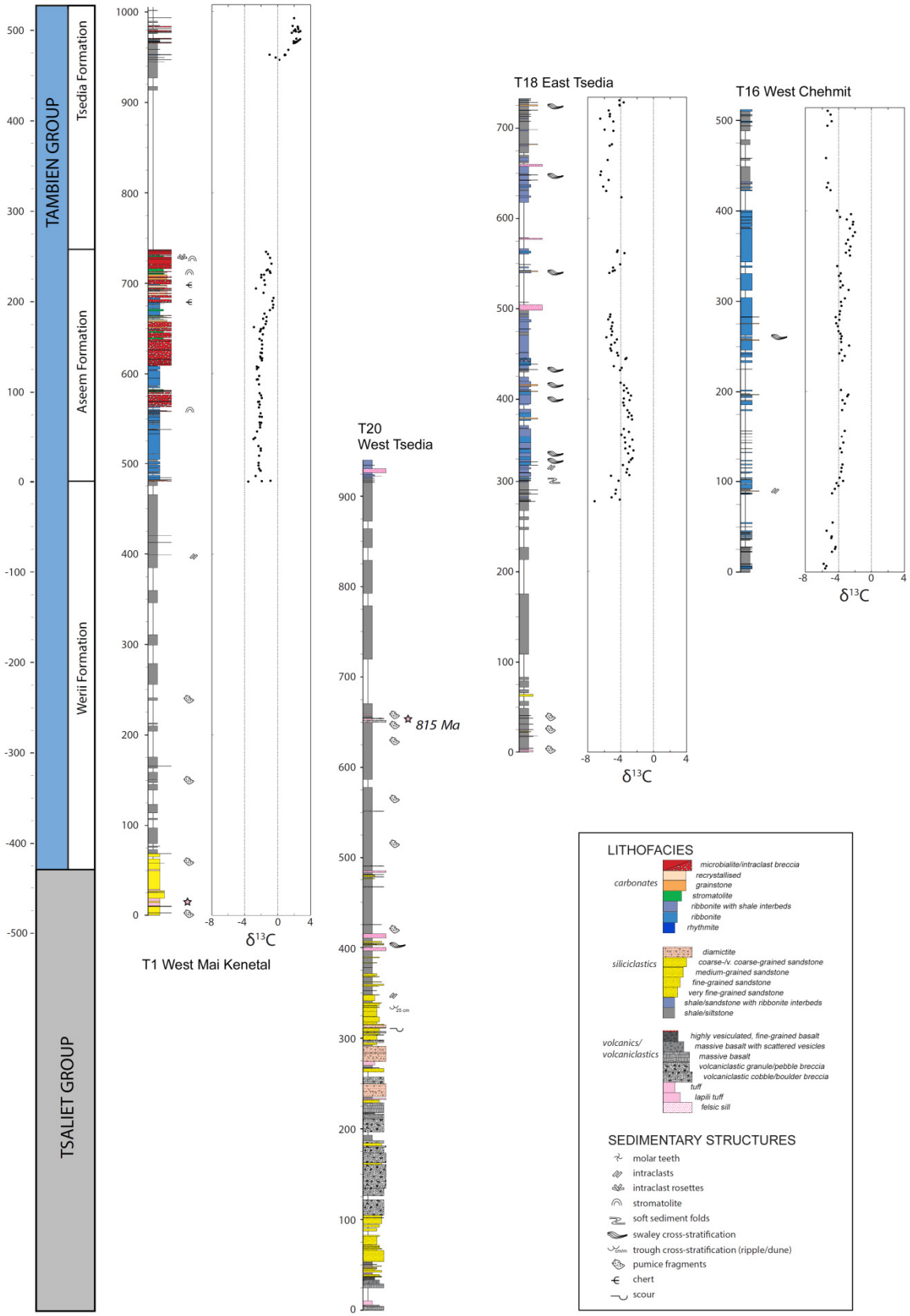

Figure 3.22. Chemostratigraphy of the lower Tambien Group, Ethiopia (based on Swanson-Hyell et al. 2015).

have begun before that in northwest Canada. By the same token, it appears to have been the longest-lived of the Bitter Springs excursions.

3.8. Implications for the carbon isotope cycle

Potentially correlatable isotopic excursions can be understood as reflecting changes in the global ocean only if they satisfy three conditions:

1. They have the same overall shape.
2. They start from approximately the same value and attain the same minimum.
3. They are independent of facies.

Figure 3.23 compares the excursions from six of the discussed regions. In order to maximise the degree of correspondence, sedimentation rates at Svalbard are assumed to be more than two times higher than through the other sections. The profiles are diverse. The Scotland excursion, which touches -7‰, is the most negative of the six. The Bitter Springs excursion is less negative and has a different beginning. The Svalbard excursion is much less negative, half-way through turns briefly positive and reaches its minimum only towards the end; again, it has a similar ending but a different beginning. The profile of the Ogilvie Mountains is difficult to match at all, since the excursion consists of two ephemeral spikes. In Ethiopia different sections show different profiles even in the same area. Varying rates cannot explain the differences in shape and absolute values.

The excursions are also not independent of facies. As we have seen, the negative excursions broadly coincide with cycles of transgression and regression.

Whether or not the excursions were coeval, the isotopic system was governed by conditions specific to the locality. Immediately before the excursions disparities between one locality and another are up to 6‰ – more if one includes the Victoria Island shales – and marked disparities persist during the excursions. There is also the difficulty of explaining how carbonate $\delta^{13}C$ could have reached unfractionated values. The Svalbard excursion has been attributed to a fall in ε from 0.40 to 0.14, on the basis that the carbon isotope record should be globally uniform (Maloof et al. 2006). But it is not uniform. In the absence of regional factors, a value of -6‰ implies that no organic carbon was being buried. If we were to assume that this was the value all along the platform, and on every craton, it would also imply that none was being produced – an ultra-catastrophic scenario that would have left fossil evidence of mass extinctions across the globe. In reality, the post-excursion part of the Bitter Springs Formation hosts some of the most diverse assemblages of micro-organisms known for the period (Schopf & Blacic 1971, Hill et al. 2000).

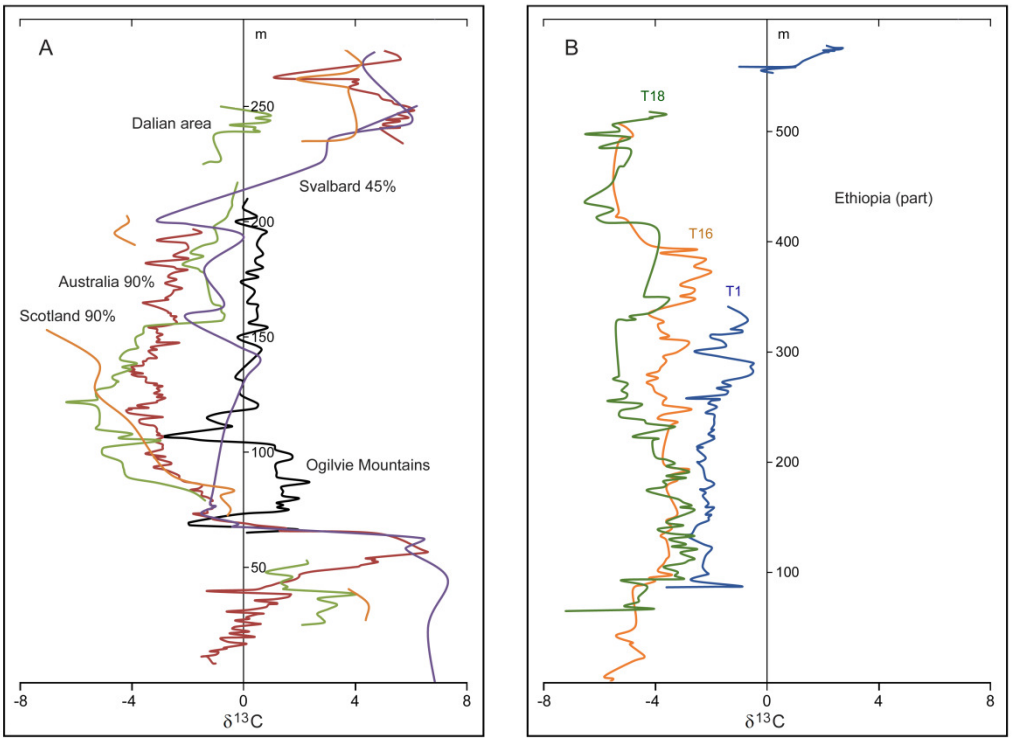

Figure 3.23. (a) Carbon-isotope profiles of negative excursions potentially correlatable with that of the Dalian area. Percentages denote the extent to which the stratigraphic interval has been expanded or contracted to maximise the overall fit, which is nonetheless minimal. **(b)** Isotope profiles of sections T1, T16 and T18 (Fig. 3.22) through the lower Tambien Group, Ethiopia. Note the much thicker stratigraphy and that the profiles record only the ascent phase of the excursion.

The exceptionally low values of the Wynniatt Formation are due to high TOC (up to 12%), remineralisation of which caused the porewater to be highly depleted; much of the carbonate is visibly authigenic (Thomson et al. 2015).

3.9. Conclusions

The upper Shishanlitai and Majiatun Formations record one of the best-preserved examples of a negative carbon-isotope excursion in the geological record. Both geochemistry and sedimentology show a strong link with water depth: variation in $\delta^{13}C$ was spatial rather than temporal, whereby DIC became isotopically lighter as the vertical distance between the production and remineralisation of organic matter increased. Seawater pH can be gauged by reference to the non-substituting elements Si, Al and K incorporated in the carbonate. Derived from the subaqueous dissolution of detrital silicates, their extraordinarily high concentrations indicate a pH well above that of modern seawater. Calcium carbonate precipitated close to the sea bottom in response to the alkalinity generated by silicate dissolution.

The amount of organic matter buried was a function of productivity, itself a function of water depth and, by implication, nutrient supply. A temporary kink in the upper part of the $\delta^{13}C$ curve was caused by an influx of freshwater rich in nutrients and dissolved organic carbon. Decreasing fractionation between organic and inorganic carbon and decreasing burial flux with depth also served to lower carbonate $\delta^{13}C$. Overall, $\delta^{13}C$ variation can be modelled on the basis that the relevant outputs were those recorded in the rocks themselves.

The coincidence of calcian dolomite with inferred faulting and the descent into negative $\delta^{13}C$ suggests that much of the Mg – along with elevated Mn, Zn, Cu and DIC – came from hydrothermal fluids. Mg-poor carbonate precipitated as aragonite. Taken together, the elevated solubility of silicates, the precipitation of primary dolomite, the low carbonate $\delta^{18}O$ ratio and the efficiency of organic carbon remineralisation indicate that waters were very warm.

The negative carbon-isotope excursion of the Majiatun Formation is older than that of the Loves Creek Formation and older than any so far documented from the Neoproterozoic, save that of the potentially coeval Shorikha Formation. Negative excursions reflect penecontemporaneous movements in relative epicontinental sea-level, not, as hitherto assumed, extreme swings in ocean chemistry. Excursions approximately coeval with the Bitter Springs event differ from each other both in shape and magnitude. Water bodies were not isotopically homogeneous, either laterally or vertically, and global correlations made on the contrary assumption are best avoided. While cratons underwent tectonic and isotopic upheaval, the global ocean may have remained largely unaffected.

References

Alvarez, P., 1995. Evidence for a Neoproterozoic carbonate ramp on the northern edge of the Central African craton: relations with Late Proterozoic intracratonic troughs. *Geol. Rundsch.* 84, 636–648.

Arp, G., Reimer, A., Reitner, J., 2001. Photosynthesis-induced biofilm calcification and calcium concentrations in Phanerozoic oceans. *Science* 292, 1701–1704.

Azmy, K. et al., 2009. Oceanic redox conditions in the Late Mesoproterozoic recorded in the upper Vazante Group carbonates of São Francisco Basin, Brazil: Evidence from stable isotopes and REEs. *Precambrian Res.* 168, 259–270.

Balthasar, U., Cusack, M., 2014. Aragonite-calcite seas – quantifying the gray area. *Geology* 43, 99–102.

Barley, M.E., Bekker, A., Krapež, B., 2005. Late Archean to Early Paleoproterozoic global tectonics, environmental change and the rise of atmospheric oxygen. *Earth Planet. Sci. Lett.* 238, 156–171.

Bathurst, R.G.C., 1975. *Carbonate Sediments and their Diagenesis*, 2nd edn, Elsevier, Amsterdam.

Berner, R.A., 1975. The role of magnesium in the crystal growth of calcite and aragonite from sea water. *Geochim. Cosmochim. Acta* 39, 489–504.

Blum, A.E., Stillings, L.L., 1995. Feldspar dissolution kinetics. *Rev. Miner.* 31, 291–351.

Bosence, D. et al., 2009. A dominant tectonic signal in high-frequency, peritidal carbonate cycles? A regional analysis of Liassic platforms from western Tethys. *J. Sediment. Res.* 79, 389–415.

Brady, P.V., Walther, J.V., 1989. Controls on silicate dissolution rates in neutral and basic pH solutions at 25°C. *Geochim. Cosmochim. Acta* 53, 2823–2830.

Castanier, S., Le Métayer-Levrel, G., Perthuisot, J.P., 1999. Ca-carbonates precipitation and limestone genesis – the microbiogeologist point of view. *Sed. Geol.* 126, 9–23.

Chan, M.A., Kvale, E.P., Archer, A.W., Sonett, C.P., 1994. Oldest direct evidence of lunar-solar tidal forcing encoded in sedimentary rhythmites, Proterozoic Big Cottonwood Formation, central Utah. *Geology* 22, 791–794.

Couëffé, R., Tessier, B., Gigot, P., Beaudoin, B., 2005. Tidal rhythmites as possible indicators of very rapid subsidence in a foreland basin: an example from the Miocene Marine Molasse Formation of the Digne foreland basin, SE France. *J. Sed. Res.* 74, 746–759.

Cullen, J.J., 2015. Subsurface chlorophyll maximum layers: enduring enigma or mystery solved? *Annu. Rev. Mar. Sci.* 7, 207–239.

De Boyer Montégut, C., Madec, G., Fischer, A.S., Lazar, *A.,* Ludicone, D., 2004. Mixed layer depth over the global ocean: An examination of profile data and a profile-based climatology. *J. Geophys. Res.,* 109*, C12003.*

De Choudens-Sánchez, V., González, L.A., 2009. Calcite and aragonite precipitation under controlled instantaneous supersaturation: elucidating the role of $CaCO_3$ saturation state and Mg/Ca ratio on calcium carbonate polymorphism. *J. Sediment. Res.* 29, 363–376.

Deffeyes, K.S., 1965. Carbonate equilibria: a graphic and algebraic approach. *Limnol. Oceanog.* 10, 412–426.

Des Marais, D.J., Strauss, H., Summons, R.E., Hayes, J.M., 1992. Carbon isotope evidence for the stepwise oxidation of the Proterozoic environment. *Nature* 359, 605–609.

Diem, D., Stumm, W., 1984. Is dissolved Mn^{2+} being oxidized by O_2 in absence of Mn-bacteria or surface catalysts? *Geochim. Cosmochim. Acta* 48, 1571–1573.

Fairchild, I.J. et al., 2016. The Late Cryogenian Warm Interval, NE Svalbard: Chemostratigraphy and genesis. *Precambrian Res.* 281, 128–154.

Fleming, B.A., Crerar, D.A., 1982. Silicic acid ionization and calculation of silica solubility at elevated temperature and pH. *Geothermics* 11, 15–29.

Fu, X. et al., 2015. New paleomagnetic results from the Huaibei Group and Neoproterozoic mafic sills in the North China Craton and their paleogeographic implications. *Precambrian Res.* 269, 90–106.

Geboy, N.J. et al., 2013. Re–Os age constraints and new observations of Proterozoic glacial deposits in the Vazante Group, Brazil. *Precambrian Res.* 238, 199–213.

Given, R.K., Lohmann, K.C., 1985. *Derivation* of the original isotopic composition of Permian marine cements. *J. Sediment. Petrol.* 55, 430–439.

Grotzinger, J.P., Knoll, A.H., 1995. Anomalous carbonate precipitates: is the Precambrian the key to the Permian? *Palaios* 10, 578–596.

Halverson, G.P., Hoffman, P.F., Schrag, D.P., Kaufman, A.J., 2002. A major perturbation of the carbon cycle before the Ghaub glaciation (Neoproterozoic) in Namibia: Prelude to snowball Earth? *Geochem., Geophys., Geosyst.* 3, 10.1029/2001GC000244.

Halverson, G.P., Hoffman, P.F., Schrag, D.P., Maloof, A.C., Rice, A.H.N., 2005. Toward a Neoproterozoic composite carbon-isotope record. *GSA* 117, 1181–1207.

Halverson, G.P., Maloof, A.C., Schrag, D.P., Dudas, F.O., Hurtgen, M., 2007. Stratigraphy and geochemistry of a ca 800 Ma negative carbon isotope interval in northeastern Svalbard. *Chem. Geol*. 237, 23–45.

Halverson, G.P., Wade, B.P., Hurtgen, M.T., Barovich, K.M. 2010. Neoproterozoic chemostratigraphy. *Precambrian Res*. 182, 337–350.

Hawkesworth, C., Cawood, P., Kemp, A., Storey, C., Dhuime, B., 2009. A matter of preservation. *Science* 323, 49–50.

Hayes, J.M., Strauss, H., Kaufmann, A.J., 1999. The abundance of ^{13}C in marine organic matter and isotopic fractionation in the global biogeochemical cycle of carbon during the past 800 Ma. *Chem. Geol.* 161, 103–125.

Hayes, J.M., Waldbauer, J.R., 2006. The carbon cycle and associated redox processes through time. *Phil. Trans. R. Soc. B* 361, 931–950.

He, T. et al., 2016. Measuring the 'Great Unconformity' on the North China Craton using new detrital zircon age data. In: A.T. Brasier, D. McIlroy, N. McLoughlin (eds), *Earth System Evolution and Early Life: a Celebration of the Work of Martin Brasier*. Geol. Soc. Lond. Spec. Pub. 448, doi.org/ 10.1144/SP448.14.

Hill, A.C., Arouri, K., Gorjan, P., Walter, M.R., 2000. Geochemistry of marine and non-marine environments of a Neoproterozoic cratonic carbonate/evaporite: the Bitter Springs Formation, Central Australia. In: J.P. Grotzinger & N.P. James (eds), *Carbonate Sedimentation and Diagenesis in an Evolving Precambrian World*, SEPM Spec. Pub. 67, 327–344.

Hoffman, P.F., Schrag, D.P., 2002. The Snowball Earth hypothesis: testing the limits of global change. *Terra Nova* 14, 129–155.

Hoffman, P.F. et al., 2012. Cryogenian glaciations on the southern tropical paleomargin of Laurentia (NE Svalbard and East Greenland), and a primary origin for the upper Russøya (Islay) carbon isotope excursion. *Precambrian Res.* 206–207, 137–158.

Hood, A.v.S., Wallace, M.W., 2015. Extreme ocean anoxia during the Late Cryogenian recorded in reefal carbonates of Southern Australia. *Precambrian Res.* 261, 96–111.

Irwin, H., Curtis, C., Coleman, M., 1977. Isotopic evidence for source of diagenetic carbonates formed during burial of organic rich sediments. *Nature* 269, 209–213.

Jaffrés, J.B.D., Shields, G.A., Wallmann, K., 2007. The oxygen isotope evolution of seawater: A critical review of a long-standing controversy and an improved geological water cycle model for the past 3.4 billion years. *Earth Sci. Rev.* 83, 83–122.

John, E. H., Wilson, J.D., Pearson, P.N., Ridgwell, A., 2014. Temperature-dependent remineralization and carbon cycling in the warm Eocene oceans. *Palaeogeogr., Palaeocl.* 413, 158–166.

Jones, D.S., Maloof, A.C., Hurtgen, M.T., Rainbird, R.H., Schrag, D.P., 2010. Regional and global chemostratigraphic correlation of the early Neoproterozoic Shaler Supergroup, Victoria Island, Northwestern Canada. *Precambrian Res.* 181, 43–63.

Jørgensen, B.B., 1982. Mineralization of organic matter in the sea bed – the role of sulphate reduction. *Nature* 296, 643–645.

Kah, L.C., Bartley, J.K., Teal, D.A., 2012. Chemostratigraphy of the Late Mesoproterozoic Atar Group, Taoudeni Basin, Mauritania: Muted isotopic variability, facies correlation, and global isotopic trends. *Precambrian Res*. 200–203, 82–103.

Kasting, J.F. et al.., 2006. Paleoclimates, ocean depth, and the oxygen isotopic composition of seawater. *Earth Planet. Sci. Lett.* 252, 82–93.

Kaufman, A.J., Jacobsen, S.B., Knoll, A.H. 1993. The Vendian record of Sr and C isotopic variations in seawater: Implications for tectonics and paleoclimate. *Earth Planet. Sci. Lett.* 120, 409–30.

Kim, S.T., O'Neil, J.R., Hillaire-Marcel, C., Mucci, A., 2007. Oxygen isotope fractionation between synthetic aragonite and water: Influence of temperature and Mg^{2+} concentration. *Geochim. Cosmochim. Acta* 71, 4704–4715.

Klaebe, R.M., Kennedy, M.J., Corrick, A.J., Brocks, J.J., Jarrett, A.J.M., 2014. Sedimentological constraints on the Bitter Springs delta13C anomaly. *Goldschmidt Abstracts* 1274.

Knoll, A.H., 1992. Biological and biogeochemical preludes to the Ediacaran radiation. In: J.H. Lipps, P.W. Signor (eds), *Origin and Early evolution of the Metazoa*, Topics in Geobiology 10, Plenum, New York, 53–84.

Knoll, A.H., Kaufman, A.J., Semikhatov, M.A., 1995. The carbon isotopic composition of Proterozoic carbonates: Riphean successions from northwestern Siberia (Anabar Massif, Turukhansk uplift). *Am. J. Sci.* 295, 823–850.

Köhler, S.J., Dufaud, F., Oelkers, E.H., 2003. An experimental study of illite dissolution kinetics as a function of pH from 1.4 to 12.4 and temperature from 5 to 50°C. *Geochim. Cosmochim. Acta* 67, 3583–3594.

Krissansen-Totton, J., Buick, R., Catling, D.C., 2015. A statistical analysis of the carbon isotope record from the Archean to Phanerozoic and implications for the rise of oxygen. *Am. J. Sci.* 315, 275–316.

Kroopnick, P.M., 1985. The distribution of $\delta^{13}C$ in ΣCO_2 in the world oceans: *Deep Sea Res.* 32, 57–77.

Kunzmann, M., Halverson, G.P., Scott, C., Minarik, W.G., Wing, B.A., 2015. Geochemistry of Neoproterozoic black shales from Svalbard: Implications for oceanic redox conditions spanning Cryogenian glaciations. *Chem. Geol.* 147, 383–393.

Lécuyer, C. et al., 2012. Carbon and oxygen isotope fractionations between aragonite and calcite of shells from modern molluscs. *Chem. Geol.* 332-333, 92–101.

Li, Z.X. et al., 2008. Assembly, configuration, and break-up history of Rodinia: a synthesis. *Precambrian Res*. 160, 179–210.

Little, S.H., Vance, D., Lyons, T.W., McManus, J., 2015. Controls on trace metal authigenic enrichment in reducing sediments: Insights from modern oxygen-deficient settings. *Am. J. Sci.* 315, 77–119.

Liu, S. et al., 2012. U–Pb zircon age, geochemical and Sr–Nd isotopic data as constraints on the petrogenesis and emplacement time of the Precambrian mafic dyke swarms in the North China Craton (NCC). *Lithos* 140–141, 38–52.

Logan, G.A., Hayes, J.M., Hieshima, G.B., Summons, R.E., 1995. Terminal Proterozoic reorganization of biogeochemical cycles. *Nature* 376, 53–56.

Lovell, B., 2010. A pulse in the planet: regional control of high-frequency changes in relative sea by mantle convection. *J. Geol. Soc. Lond*. 167, 637–648.

Macdonald, F.A., et al., 2010. Calibrating the Cryogenian. *Science* 327, 1241–1243.

Macdonald, F.A. et al., 2012. Early Neoproterozoic Basin Formation in Yukon, Canada: Implications for the make-up and break-up of Rodinia. *Geoscience Canada* 39, 77–99.

Macdonald, F.A. et al., 2013. The Laurentian record of Neoproterozoic glaciation, tectonism, and eukaryotic evolution in Death Valley, California. *GSA Bull.* 125, 1203–1223.

Maliva, R.G., Knoll, A.H., Simonson, B.M., 2005. Secular change in the Precambrian silica cycle: Insights from chert petrology. *GSA* 117, 835–845.

Maloof, A.C. et al., 2006. Combined paleomagnetic, isotopic, and stratigraphic evidence for true polar wander from the Neoproterozoic Akademikerbreen Group, Svalbard, Norway. *GSA Bull.* 118, 1099–1124.

Martin, R.E., Quigg, A., Podkovyrov, V., 2008. Marine biodiversification in response to evolving phytoplankton stoichiometry. *Palaeogeogr. Palaeocl*. 258, 277–291.

McIntire, W.L., 1963. Trace element partition coefficients—a review of theory and applications to geology. *Geochim. Cosmochim. Acta* 27, 1209–1264.

Meister, P., 2013. Two opposing effects of sulfate reduction on carbonate precipitation in normal marine, hypersaline, and alkaline environments. *Geology* 41, 499–502.

Mook, W.G., Bommerson, J.C., Staverman, W.H., 1974. Carbon isotope fractionation between dissolved bicarbonate and gaseous carbon dioxide. *Earth Planet. Sci. Lett.* 22, 169–172.

Mucci, A., 1987. Influence of temperature on the composition of magnesian calcite overgrowths precipitated from seawater. *Geochim. Cosmochim. Acta* 51, 1977–1984.

Peng, P. et al., 2011a. Neoproterozoic (~900 Ma) Sariwon sills in North Korea: Geochronology, geochemistry and implications for the evolution of the south-eastern margin of the North China Craton. *Gondwana Res*. 20, 243–254.

Peng, P. et al., 2011b. U–Pb baddeleyite ages, distribution and geochemistry of 925 Ma mafic dykes and 900 Ma sills in the North China craton: Evidence for a Neoproterozoic mantle plume. *Lithos* 127, 210–221.

Petrov, P.Y., Semikhatov, M.A., 2009. Platforms: Shorikha Formation of the Turukhansk Uplift, Siberia. *Stratigr. Geol. Correl.* 17, 461–475.

Planavsky, N.J. et al., 2011. Widespread iron-rich conditions in the mid-Proterozoic ocean. *Nature* 477, 448–552.

Prave, A.R., Fallick, A.E., Thomas, C.W., Graham, C.M., 2009. A composite C-isotope profile for the Neoproterozoic Dalradian Supergroup of Scotland and Ireland. *J. Geol. Soc. Lond.* 166, 845–857.

Price, G.D., 2011. Inorganic carbon transporters of the cyanobacterial CO_2-concentrating mechanism. *Photosynth Res*. 109, 47–57.

Priyatkina, N., Khudoley, A.K., Collins, W.J., Kuznetsov, N.B., Huang, H.Q., 2016. Detrital zircon record of Meso- and Neoproterozoic sedimentary basins in northern part of the Siberian Craton: Characterizing buried crust of the basement. *Precambrian Res.* 285, 21–38.

Purohit, R., Papineau, D., Kröner, A., Sharma, K.K., Roy, A.B., 2012. Carbon isotope geochemistry and geochronological constraints of the Neoproterozoic Sirohi Group from northwest India. *Precambrian Res*. 220–221, 80–90.

Regaudie-de-Gioux, A*.,* Duarte, C.M., 2012. Temperature dependence of planktonic metabolism in the ocean. *Global Biogeochem. Cycles* 26*,* GB1015.

Rimstidt, J.D., Balog, A., Webb, J., 1998. Distribution of trace elements between carbonate minerals and aqueous solutions. *Geochim. Cosmochim. Acta* 62, 1851–1863.

Romanek, C.S., Grossman, E.L., Morse, J.W., 1992. Carbon isotopic fractionation in synthetic aragonite and calcite: Effects of temperature and precipitation rate. *Geochim. Cosmochim. Acta* 56, 419–430.

Rooney, A.D., Chew, D.M., Selby, D., 2011. Re–Os geochronology of the Neoproterozoic–Cambrian Dalradian Supergroup of Scotland and Ireland: Implications for Neoproterozoic stratigraphy, glaciations and Re–Os systematic. *Precambrian Res.* 185, 202–214.

Rooney, A.D. et al., 2014. Re-Os geochronology and coupled Os-Sr isotope constraints on the Sturtian snowball. *Proc. Nat. Acad. Sci.* 111, 51–56.

Roy, A.B., Purohit, R., 2015. Lithostratigraphic, geochronological and depositional framework of the Precambrian basins of the Aravalli Mountains and adjoining areas, Rajasthan, India. In: R. Mazumder, P G. Eriksson (eds), *Precambrian Basins of India: Stratigraphic and Tectonic Context*, Geol. Soc. Lond. Mem. 43, 55–65.

Sawaki, Y. et al., 2010. $^{87}Sr/^{86}Sr$ chemostratigraphy of Neoproterozoic Dalradian carbonates below the Port Askaig glaciogenic formation, Scotland. *Precambrian Res.* 179, 150–164.

Schmalz, R.F., Swanson, F.J., 1969. Diurnal variations in the carbonate saturation of seawater. *J. Sediment. Petrol.* 39, 255–267.

Schopf, J.W., Blacic, J.M., 1971. New microorganisms from the Bitter Springs Formation (Late Precambrian) of the North-Central Amadeus Basin, Australia. *J. Paleontol.* 45, 925–960.

Schrag, D.P., Higgins, J.A., Macdonald, F.A., Johnston, D.T., 2013. Authigenic carbonate and the history of the global carbon cycle. *Science* 339, 540–543.

Shields, G.A., Deynoux, M., Strauss, H., Paquet, H., Nahon, D., 2007. Barite-bearing cap dolostones of the Taoudéni Basin, northwest Africa: Sedimentary and isotopic evidence for methane seepage after a Neoproterozoic glaciation. *Precambrian Res.* 153, 209–235.

Smith, E.F., Macdonald, F.A., Crowley, J.L., Hodgin, E.B., Schrag, D.P., 2016. Tectonostratigraphic evolution of the c. 780–730 Ma Beck Spring Dolomite: Basin Formation in the core of Rodinia. In: Z. Li et al. (eds), *Supercontinent Cycles Through Earth History*, Geol. Soc. Lond. Spec. Pub. 424, 213–239.

Southgate, P.N., 1989. Relationships between cyclicity and stromatolite form in the Late Proterozoic Bitter Springs Formation Australia. *Sedimentology* 36, 323–339.

Spivack, A.J., Staudigel, H., 1994. Low-temperature alteration of the upper oceanic crust and the alkalinity budget of seawater. *Chem. Geol.* 115, 239–247.

Stanley, S.M., 2010. Relation of Phanerozoic stable isotope excursions to climate, bacterial metabolism, and major extinctions. *Proc. Natl. Acad. Sci. USA* 107, 19185–19189.

Stanley, S.M., Hardie, L.A., 1999. Hypercalcification: paleontology links plate tectonics and geochemistry to sedimentology. *GSA Today* 9, 1–7.

Stephenson, D., Mendum, J.R., Fettes, D.J., Leslie, A.G., 2013. The Dalradian rocks of Scotland: an introduction. *Proc. Geol. Assoc.* 124, 3–82.

Strauss, J.V., Rooney, A.D., Macdonald, F.A., Brandon, A.D., Knoll, A.H., 2014. 740 Ma vase-shaped microfossils from Yukon, Canada: Implications for Neoproterozoic chronology and biostratigraphy. *Geology* 42, 659–662.

Swanson-Hysell, N.L. et al., 2010. Cryogenian glaciation and the onset of carbon-isotope decoupling. *Science* 328, 608–610.

Swanson-Hysell, N.L. et al., 2012. Constraints on Neoproterozoic paleogeography and Paleozoic orogenesis from paleomagnetic records of the Bitter Springs Formation, Amadeus Basin, central Australia. *Am. J. Sci.* 312, 817–884.

Swanson-Hysell, N.L. et al., 2015. Stratigraphy and geochronology of the Tambien Group, Ethiopia: Evidence for globally synchronous carbon isotope change in the Neoproterozoic. *Geology* 43, 323-326.

Swart, P.K., Oehlert, A.M., Mackenzie, G.J., Eberli, G.P., Reijmer, J.J.G., 2014. The fertilization of the Bahamas by Saharan dust: A trigger for carbonate precipitation? *Geology* 42, 671–674.

Tessier, B., Gigot, P., 1989. A vertical record of different tidal cyclicities: an example from the Miocene Molasse of Digne. *Sedimentology* 36, 767–776.

Thomson, D., Rainbird, R.H., Planavsky, N., Lyons, T.W., Bekker, A., 2015. Chemostratigraphy of the Shaler Supergroup, Victoria Island, NW Canada: A record of ocean composition prior to the Cryogenian glaciations. *Precambrian Res.* 263, 232–245.

Tucker, M.E., 1986. Formerly aragonitic limestones associated with tillites in the late Proterozoic of Death Valley, California. *J. of Sed. Petrol.* 56, 818–830.

Veizer, J., 1983. Chemical diagenesis of carbonates: theory and application of trace element technique. In: M.A. Arthur et al. (eds), *Stable Isotopes in Sedimentary Geology*, SEPM Short Course Notes 10.

Wang, Q.H., Yang, D.B., Xu, W.L., 2012. Neoproterozoic basic magmatism in the southeast margin of North China Craton: Evidence from whole-rock geochemistry, U-Pb and Hf isotopic study of zircons from diabase swarms in the Xuzhou-Huaibei area of China. *Sci. China Earth Sci*. 55, 1461–1479.

Wellman, C.H., Strother, P.K., 2015. The terrestrial biota prior to the origin of land plants (embryophytes): a review of the evidence. *Palaeontology* 58, 601–627.

Williams, G.E., 1999. Late Precambrian tidal rhythmites in South Australia and the history of the Earth's rotation. *J. Geol. Soc. Lond.* 146, 97-111.

Yang, D.B. et al., 2012. U–Pb ages and Hf isotope data from detrital zircons in the Neoproterozoic sandstones of northern Jiangsu and southern Liaoning Provinces, China: implications for the late Precambrian evolution of the southeastern North China Craton. *Precambrian Res*. 216–219, 162–176.

Zhang, J., Quay, P.D., Wilbur, D.O., 1995. Carbon isotope fractionation during gas–water exchange and dissolution of CO_2. *Geochem. Cosmochem. Acta* 59, 107–114.

Zhang, S.H., Zhao, Y., Ye, H., Hu, G.H., 2016. Early Neoproterozoic emplacement of the diabase sill swarms in the Liaodong Peninsula and pre-magmatic uplift of the southeastern North China Craton. *Precambrian Res*. 272, 203–225.

Zhang, X., Hua, H., Reitner, J., 2006. A new type of Precambrian megascopic fossils: the Jinxian biota from northeastern China. *Facies* 52, 169–181.

Zhou, G.T., Zheng, Y.F., 2005. Effect of polymorphic transition on oxygen isotope fractionation between aragonite, calcite, and water: A low-temperature experimental study. *Am. Mineral.* 90, 1121–1130.

Zhou, G.T., Zheng, Y.F., 2006. On the direction and magnitude of oxygen isotope fractionation between calcite and aragonite at thermodynamic equilibrium. *Aquat. Geochem*. 12, 239–268.

CHAPTER FOUR

Carbon and oxygen isotope variation in Proterozoic carbonates – a function of sea-level

Abstract

In contrast to the Mesoproterozoic, in the Neoproterozoic the carbon-isotope ratios of marine carbonate varied dramatically. Deviations both in the negative and positive directions were frequent and large-scale, and continued into the Cambrian. Commonly the anomalies are attributed to fluctuations in the burial of organic carbon, an increasing flux giving rise to positive excursions, and vice versa. By implication, there were times when organic production completely shut down, while at other times some 40% of deposited carbon was organic. TOC percentages do not support such extremes.

The review of isotopic shifts in the Tonian Period (Chapter 3) is here extended to the Cryogenian and Ediacaran. Descriptions of facies change accompanying the shifts at particular localities again indicate a systematic link with sea-level, such that carbonate $\delta^{13}C$ went negative as waters deepened and positive as waters shallowed. Organic carbon in relation to carbonate carbon was correspondingly enriched. The 'excursions' represent excursions of relative sea-level, not ocean chemistry. Beneath the photic zone, the water column was anoxic, alkaline and enriched in ^{12}C. Shore-to-basin gradients were similar: water bodies became more anoxic, alkaline and ^{12}C-rich as depth increased. Beyond the shelf the subsurface ocean may have been close to unfractionated. The marine system appears to have been isotopically stratified also during the Neoarchaean and most of the Palaeoproterozoic. Carbon isotope variation diminished in the Cambrian and, on the negative side, ceased to correlate clearly with sea-level in the Ordovician.

This being so, (1) negative excursions provide no support for hypothesised glaciations in the Neoproterozoic, when sea-level should have fallen, not risen; (2) excursions, negative or positive, are no basis for inferring Proterozoic 'oxygenation events'; (3) carbonate $\delta^{13}C$ may, with due caution, serve as an index of regional sea-level change; and (4) broadly similar chemostratigraphic profiles on different cratons reflect global-scale tectonic processes, which may or may not have been absolutely synchronous.

4.1. Introduction

The modern ocean differs from the Neoproterozoic as currently understood in several ways. In the modern ocean, most carbonate sediment consists of the skeletal remains of algae, foraminifera, corals and so on, and at least half accumulates in deep water (Milliman 1993). At the surface the isotopic values of dissolved inorganic carbon (DIC, comprising CO_2, HCO_3^- and CO_3^{2-}) ranges from 0.5‰ to 1.5‰, depending on latitude, with pre-industrial values 0.5‰ higher (Kroopnick 1985). Carbonate precipitating from the dissolved pool is around 1‰ higher (Romanek et al. 1992). At greater depths, isotopic composition falls, as ^{12}C-rich organic matter (OM) sinking through the water column – if not consumed by other organisms – is oxidised by microbes and photochemical reactions (Gieskes et al. 2015) and returned to the inorganic pool; the maximum difference is about 3‰. While most organic carbon (OC) is remineralised within decades, in the deep ocean very dilute concentrations can persist for millennia (Jiao et al. 2010, Arietta et al. 2015). Carbonate deposited on shallow-marine platforms tends to be heavier than deep-sea carbonate (Swart 2008, Gischler et al. 2009, Oehlert et al. 2011), and much of the OM is oxidised anaerobically in the sediment.

By contrast, below the mixed surface the Precambrian ocean was predominantly anoxic. Potential causes of such stratification include a greater inflow of dissolved Fe, greater salinity and higher ocean temperatures (Knauth 2005), these last two rendering oxygen less soluble and suppressing thermohaline circulation. Carbonate precipitation – inhibited, as always, by kinetic factors – was promoted by higher levels of supersaturation (Higgins et al. 2009) and in epicontinental settings by alkalinity (chapter 2). As water depth on the shelf increased, the rate of carbonate production and the proportion of carbonate to siliciclastic sediment declined. Further out, a large proportion of carbonate was taken up by ocean crust.

The oxygen-producing photic zone was thinner than today because seas were dominated by pico-plankton and contained higher amounts of OM in suspension (Butterfield 2009a). In the absence of grazing zooplankton, OM sank more slowly through the water column, in the course of which it was oxidised by bacteria to CO_2 and HCO_3^-. Anaerobic remineralisation was at least as efficient as aerobic (Calvert et al.1991, Lee 1992, Logan et al. 1995, Pawlowska et al. 2013). Epicontinental seas were probably warmer than Phanerozoic counterparts; they were certainly warmer than the modern deep ocean. Amongst the ecological consequences, picoplankton, including cyanobacteria, would have been prolific (Agawin et al. 2000), while higher metabolic rates in the remineralising bacteria would have made for more efficient recycling of OM and hence steeper $\delta^{13}C_{DIC}$ gradients in the water column (Rivkin & Legendre 2001, Stanley 2010, John et al. 2014). The depth of the

thermocline and pycnocline that approximate the base of the mixed layer would also have been much shallower (de Boyer Montégut et al. 2004).

As today, the marine, atmospheric, terrestrial and mantle systems were intimately connected. Carbon entered the ocean-atmosphere system through volcanic and non-eruptive outgassing, metamorphic reactions, acid weathering of silicate and carbonate, and oxidative weathering of organic carbon. It left the system in sediments which were added to the continental crust or in the sediments and secondary carbonate of oceanic crust. Average carbonate $\delta^{13}C$ rose or fell according to the proportion of OC buried – buried in carbonates, siliciclastic river deltas and deeper-water shales (e.g. Des Marais et al. 1992, Kaufman & Knoll 1995).

If we ignore the 1‰ calcite-DIC fractionation, the mass balance of the isotopic carbon cycle is represented as:

$$\delta^{13}C_{in} = f.\delta^{13}C_{org} + (1-f).\delta^{13}C_{carb} \quad (1)$$

Or in recast form:

$$\delta^{13}C_{carb} = \delta^{13}C_{in} + f(\delta^{13}C_{carb} - \delta^{13}C_{org}) \quad (2)$$

where $\delta^{13}C_{in}$ is the isotopic ratio of the carbon entering the system and f the OC removed as a fraction of all buried carbon (Hayes et al. 1999, Rothman et al. 2003). Entering by various routes, input carbon is assumed to have an isotopic ratio approximating that of the upper mantle (Hayes et al. 1999). The primitive upper mantle, best represented by MORB, typically ranges between -4.2 and -7.5‰ (Mattey et al. 1984). The values are from vesicles, inclusive of the fractionation effect whereby CO_2 is enriched on degassing and the residual carbon depleted (Cartigny et al. 2001). Mantle xenoliths peak bimodally at -5 and -25‰ (Deines 2002). Organic fractionation ($\delta^{13}C_{carb}$ minus $\delta^{13}C_{org}$) is commonly denoted as ε, a positive number. Also to be taken into account are the fractionation between solid and dissolved carbonate (Δ_{cw}), the fraction of carbonate buried in ocean crust (λ) and the isotopic difference between that carbonate and carbonate sedimented from the surface (Δ_m). A fuller equation is then (following Hayes & Waldbauer 2006):

$$\delta^{13}C_{carb} = \delta^{13}C_{in} + f(\varepsilon + \Delta_{cw}) + \lambda(1 - f)(\Delta_m - \Delta_{cw}) \quad (3)$$

Over time the fraction of carbonate buried in ocean crust has decreased, from perhaps close to 1.0 in the early Archaean to an estimated 0.35 or less at the end of the Proterozoic (Bjerrum & Canfield 2004). Still not taken into account is an unquantified, but probably small, amount of OC in ocean crust (Santelli et al. 2008).

The mass balance model assumes a steady state (or succession of steady states). However, not everything that leaves the system re-enters the system. Over time the volume of continental crust grows, and part of that growth consists of island-arc accretion whereby organic and inorganic carbon is trapped in the crust rather than cycled back into the mantle. Even where ocean crust and sediment are subducted, not all the carbon returns to the exosphere as carbon dioxide vapour. Some remains in the mantle, with a ratio significantly higher (at -1‰) than what is input (Coltice et al. 2004). Some of it degasses back into the atmosphere, with sometimes elevated ratios that suggest enrichment from the subducted sediment (Fischer & Lopez 2016), much of which is biogenic ooze. Values vary in time as well as in space: the $\delta^{13}C$ of CO_2 from Mount Etna, for example, has increased in just three decades from -4‰ to -1‰ (Chiodini et al. 2011).

In principle, the Precambrian should be easier to model than the Phanerozoic, because little OC was captured on or in the ocean crust, there were no calcareous plankton, and the terrestrial crust, to the extent above water, was largely unvegetated. Burial of OC was confined almost entirely to the continental shelf and margins. Moreover, assuming that life did not originate until after 3.9 Ga, initial ocean DIC should have been unfractionated, i.e. around -6‰.

This last prediction is not well substantiated. Sedimentary carbonates in Archaean greenstone belts (metamorphosed cratonic seafloor basalt), some as old as 3.5 Ga, record $\delta^{13}C$ of 1.5 ±1.5‰ (Veizer et al. 1989a); carbonate produced by hydrothermal alteration of the basalt was somewhat lower, at -1 ±1‰ (Veizer et al. 1989b, Nakamura & Kato 2004). With mantle degassing and pCO_2 probably at a maximum in the early Archaean and total carbonate production several times higher than today (Nakamura & Kato 2004), fractionation would have required correspondingly higher amounts of OC to be produced and buried, making it difficult to see how ocean DIC could have risen from -6‰ to ~0‰ in less than 0.5 Ga. If a high proportion of carbon was buried as organic carbon, the idea that there was little free oxygen in the Archaean is also difficult.

In the Neoproterozoic, the greatest challenge to the model is the occurrence of negative isotope anomalies (‘excursions’) down to -6‰ and beyond (Bristow & Kennedy 2008). At this point, equation (3) is satisfied only if f is zero, indicating that no OC was being sequestered and none, by implication, produced. During Snowball Earth episodes this is indeed postulated: screened from sunlight by ice and inhibited by near-zero temperatures, most biological production ceased (Hoffman & Schrag 2002). However, in Namibia as in other places, levels of -6‰ or lower were reached well before any such glaciation. During the glaciations themselves some of the deposited carbonate was depleted, some not (Kennedy et al. 2001). Carbonates deposited during deglaciation also record extreme depletion, albeit briefly.

Arguably the most questionable concept relating to isotopic mass balance is the assumption that the $\delta^{13}C$ of carbonates on the platforms was representative of the global ocean. As noted above, Neogene sequences sometimes show discrepancies between platform and open-marine carbonates, so that globally synchronous changes in $\delta^{13}C$ can be completely unrelated to variations in the global carbon cycle (Swart 2008). Discrepancies further back in time have also suggested that circulation between epicontinental seas and bordering oceans may have been restricted (e.g. Beauchamp et al. 1987, Holmden et al. 1998, Preto et al. 2015). Doubts of this nature extend back to the Neoproterozoic (Jiang et al. 2007, Giddings & Wallace 2009a, 2009b, Ader et al. 2009, Frimmel 2010), the Mesoproterozoic (Kah et al. 2012) and even the Palaeoproterozoic (Melezhik et al. 1999). Here I consider two aspects of the problem: the lateral variability of $\delta^{13}C_{carb}$ and the variability of $\delta^{13}C_{org}$ in relation to $\delta^{13}C_{carb}$.

4.2. Isotopic variation with depth

A number of studies have hinted at the possibility that carbon-isotope variation in the Neoproterozoic was related to water depth. As palaeo-environment is not always easy to interpret, such a gradient is most clearly demonstrated where $\delta^{13}C$ at the same locality changes with facies. The mid Neoproterozoic has several such examples. Most of the Akademikerbreen Group, NE Svalbard, consisting of ribbonites, grainstones and stromatolites, ranges from 5 to 8‰; a 200-m-thick stack of stromatolites climaxes with emergent microbially laminated dolomite around 8‰ and ends with a major flooding surface (Halverson et al. 2004). Higher up, in the lower Elbobreen Formation (Russøya Member), $\delta^{13}C$ plunges from +5 to -6 as the sequence reverses, going from microbially laminated dolomite to columnar stromatolites to dolomitic ribbonites (Hoffman et al. 2012). The same sea-level changes occur still more clearly in East Greenland, through the correlative Andrée Land Group (Fairchild & Hambrey 1995). Through the Etina Formation, South Australia, limestone intervals ranging between 7 and 9‰ alternate with shales. Conglomerates and layers of intraclastic limestone suggest very shallow-water conditions, while temporary falls in $\delta^{13}C$ to 2–4‰ coincide with cyclical deepening (McKirdy et al. 2001). In the Keele Formation, northwest Canada (Stoneknife section), $\delta^{13}C$ falls from more than 8‰ in the 'intertidal' lower part to less than -7‰ in the tempestites of the mid-to-outer-ramp upper part (Hoffman & Schrag 2002, Day et al. 2004). In Mongolia, the shallow-water and ^{13}C-enriched Taishir Formation (formerly Member) reverses an excursion down to -7.4 (at section F704), the negative values coinciding with rhythmites, marls and debris flows (Johnston et al. 2012). Elsewhere (section F949) the excursion bottoms out at -4.4, confirming, if nothing else, that the magnitude of the shift varies according to

location. Although positive and negative carbon-isotope excursions appear to be correlatable across the globe, maxima and minima differ.

The possibility that $\delta^{13}C$ is related to environment can be further assessed where carbonate facies are systematically analysed (Fig. 4.1 and Table 4.1). A useful example is the Tsagaan Olom Group (Macdonald et al. 2009). Here the shallowest facies type are biolaminites – they can also form at greater depths (Halverson et al. 2005, Schieber et al. 2007) – which are almost entirely restricted to $\delta^{13}C > 5‰$. The $\delta^{18}O$ gradient can be ascribed to a combination of evaporation, which raises $\delta^{18}O$, and dilution by river-water (Walker & Lohmann 1989) and/or rain-water, which, depending on latitude, tends to lower $\delta^{18}O$, the gradient increasing with nearness to the shoreline. Stromatolites typically occur in the middle zone, with $\delta^{13}C$ up to 4‰. Giant ooids – spherical grains that formed microbially on the shallow seafloor – occupy the same zones as biolaminites and stromatolites, and in the shallowest zone show the same diagenetic trend. Grainstones, forming in shallow environments (Table 4.1), show a distribution similar to ooids. In both cases, dolomite and limestone occupy distinct zones. Unusually, some of the grainstones are ^{13}C-depleted, but they occur at the end of a negative excursion from +10 to -6‰ that reflects a phase of rapid deepening (Fig. 4.2): are the grains in fact ^{13}C-enriched but re-deposited in a depleted matrix (cf. Husson et al. 2012), as their offset from the preceding rhythmites suggests? Through the excursion, facies pass from giant ooids to grainstones, to diamictite (a 20-m-thick continuation rather than an interruption

Facies	Lithology/ sedimentary features	Environment
Microbialaminite	Microbially laminated, thin (<1 cm) and laterally discontinuous beds. Often contain tepee structures, breccias and intraclasts.	Supra- to intertidal flats, subject to frequent exposure and evaporitic conditions.
Grainstone	Arenites, packstones, conglomerates. Clasts include ooids, reworked intraclasts, granules and rounded mud pellets. Trough cross-beds common. Sharp and scoured bases.	Shoals and shallow shelf.
Stromatolite	Branching, columnar, and conical stromatolites.	Mid to outer ramp and slope break.
Ribbonite	Fine sands and silts in alternating mm- to cm-scale beds. Hummocky cross-stratification and pinch-and-swell structures common.	Subtidal, low energy, but storm influenced.
Rhythmite	Fine-grained, rhythmic laminae, fining upward and typically continuous on the outcrop scale. Interbedded mm- to cm-scale allodapic beds the only indication of traction currents	Offshore (outer ramp or slope), deep, quiet environments.

Table 4.1. Definition of terms used to describe facies in the Tsagaan Olom Group and their interpretation in order of increasing water depth (from Halverson et al. 2002). In other circumstances the facies types may require different interpretations – even grainstones and ooids can be deep-water if re-deposited.

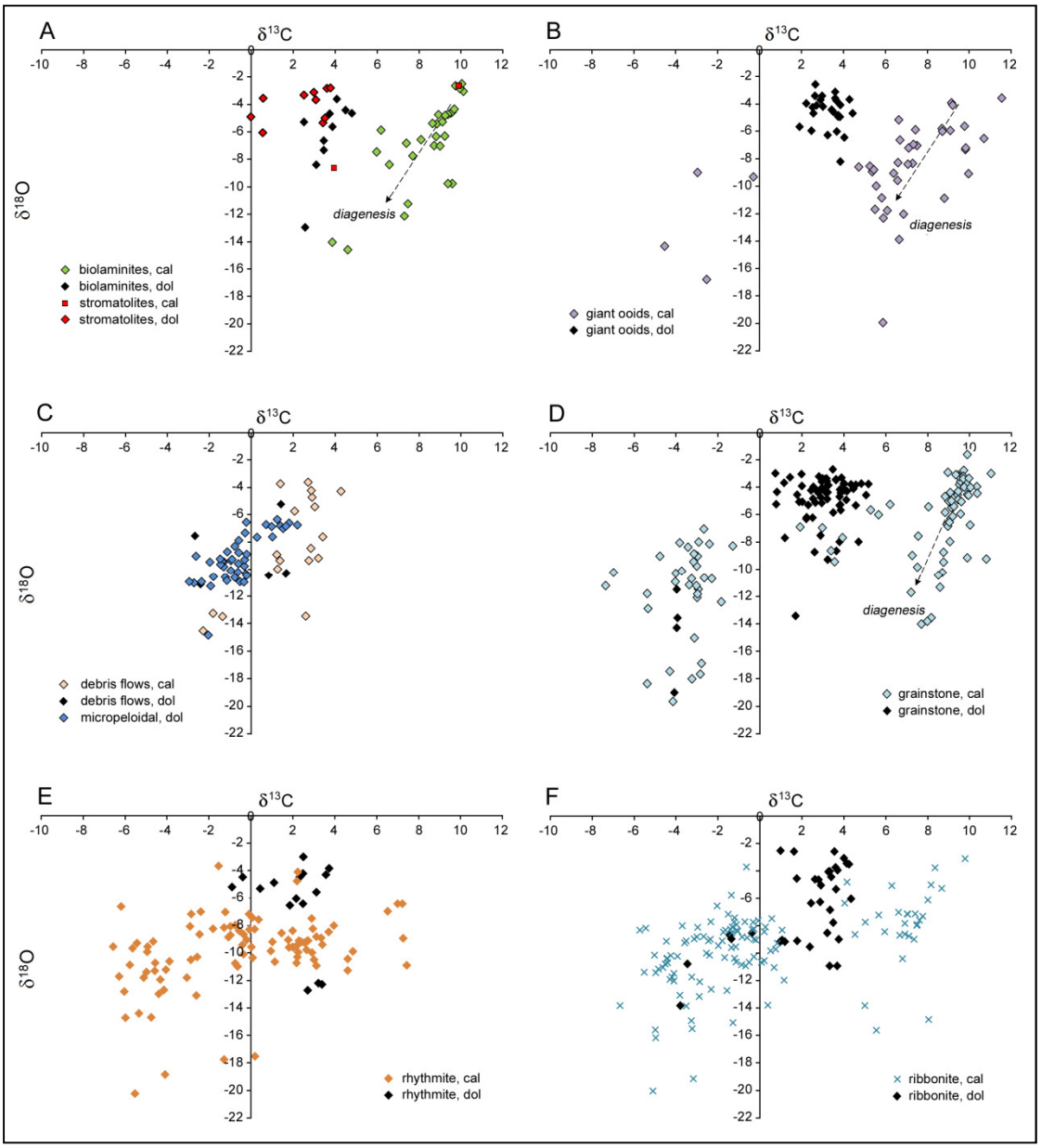

Figure 4.1. Distribution of carbonate facies in the Cryogenian-age Tsagaan Olom Group in relation to carbonate $\delta^{13}C$. Dolomite $\delta^{18}O$ normalised to calcite. There is evidence here that dolomite $\delta^{13}C$ was significantly depleted.

of this progression), to micropeloids, to ribbonites, to rhythmites at the base of the excursion. Most of the ribbonites in the formation show negative $\delta^{13}C$, consistent with their usually reflecting subtidal conditions, though they can occur in shallow-water settings. Similarly, rhythmites are broadly distributed, being sparse only above 4‰. Although generally interpreted as suspension deposits that formed below storm-wave base, they also occur in tidal settings and in the deeper-water high-energy upper flow regime. They are not, without further characterisation, indicative of water depth.

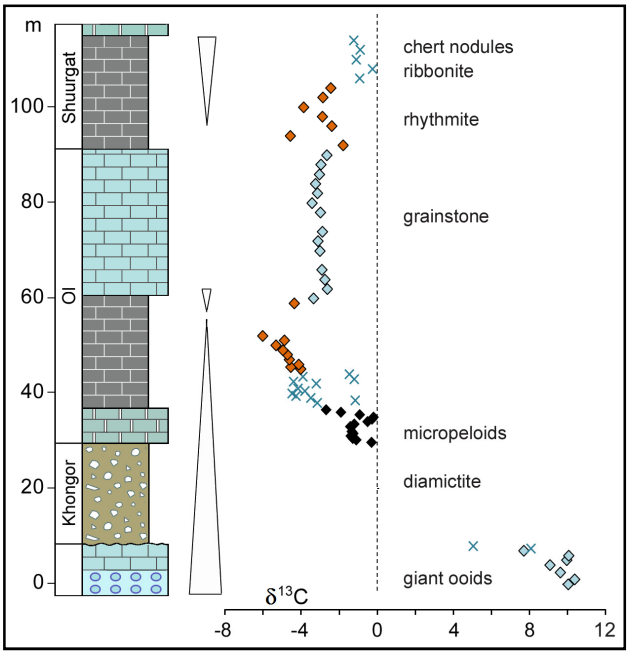

Figure 4.2. Chemostratigraphy of the first 114 m of section F708, Tsagaan Olom Group, Mongolia. Data, stratigraphic log and interpretation of sea-level change from Macdonald et al. (2009), except that the non-sampled diamictite is interpreted as a continuation of the deepening apparent below it, consistent with the falling trend of $\delta^{13}C$. The diamictite is believed to represent the Marinoan interval.

Finally, an isotopic gradient can also be evident where facies are traceable laterally from shelf to basin. In South Australia, for example, the shallowest facies (peloidal dolomite) of the relatively deep-water cap above the Sturtian-age Merinjina Tillite has $\delta^{13}C$ values between -3.6 and -0.3‰, in contrast to the laminated limestones further out where they range between -5.5 and -3.5‰. Equivalent calcareous shales deposited at basinal depths are even more depleted, between -6.7‰ and -3.7‰ (Giddings & Wallace 2009a). Upsection, the back-reef sediments of the Balcanoona Formation are enriched, averaging around 6‰, while contemporary basinal sediments average less than 1‰ (Giddings & Wallace 2009b). Blocks that tumbled from the platform into the calcareous shales of the basin retain their heavy signature.

In Namibia the isotope ratios of the Abenab Subgroup, spanning the entire Cryogenian, also vary laterally, with inner-shelf carbonates enriched by 1–2‰ compared to middle and outer shelf carbonates (Halverson et al. 2005). The oldest unit in the subgroup, the Rasthof Formation, goes from deep-water turbiditic rhythmites to stromatolites to grainstones to shallow-water biolaminites, in the course of which $\delta^{13}C$ rises from -4 to +4; at Ongongo it rises to +6.6 (Pruss et al. 2010). Outcrops of the middle unit, the Gruis Formation, are diverse, in both facies and carbon isotope ratios (Fig. 4.3). On the Northern Platform, section P1659 consists mostly of dolomite biolaminites, and its isotope profile is correspondingly low-amplitude: sea-level change is muted. P1012, by

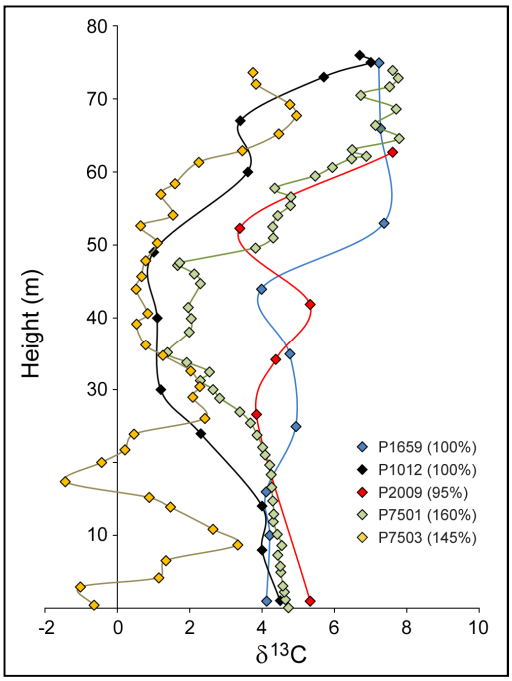

Figure 4.3. The $\delta^{13}C$ profiles of the mid-Cryogenian Gruis Formation, Namibia, through five sections. Dimensions of P2009, P7501 and P7503 normalised to those of P1659 and P1012, data as in Halverson et al. (2005), Hoffman & Halverson (2008) and Hoffman (2011).

contrast, deepens from grainstone into ribbonite and siliciclastic units, a movement mirrored by a 3.5‰ fall in $\delta^{13}C$, before the sequence is reversed. The lowest values are reached by P7503 on the distal foreslope, down to -1.5. Towards the top of the formation all profiles converge on highly enriched values around +7, coincident with subaerial exposure. On the inner platform the upper unit, the Ombaatjie Formation, is dominantly grainstone through the first two-thirds and again highly enriched (7–9‰), after which there is a rapid descent to -7, as facies pass through a series of ribbonite/biolaminite cycles (Hoffman 2011). On the dip-slopes water depths were sufficient to host a variety of stromatolites, including *Conophyton* (Hoffman & Halverson 2008). In many places uppermost carbonates continue stratigraphically and isotopically into the overlying cap carbonate (Fig. 1.3). Deep-water carbonate deposition went on at the same time as diamictite deposition elsewhere.

The uppermost cycle of the Ombaatjie draws back from -7 to -3‰, possibly reflecting a degree of uplift. The Keilberg Member cap at the base of the subsequent Maieberg Formation resumes a negative trajectory, in keeping with independently inferred transgression. The lowest value occurs at the top of the cap, but dolostones of the upper foreslope are less depleted than those of the lower foreslope and outer platform (Hoffman 2011). Through the remainder of the Maieberg, pyritic, shaly carbonates gradually shallow towards the cross-bedded grainstones of the upper member, and isotopic ratios rise from -5 to 0.5. The outer platform through this interval is lighter than the inner platform by some 2‰ (*ibid.*).

In northwest China the cap carbonate above the Ediacaran-age Hankalchough diamictite, sampled at four sections, represents a nearshore-offshore transect (Shen et al. 2011). In the offshore direction the diamictite becomes thicker and the carbonate thinner while carbon-isotope ratios decrease from -1‰ to as low as -16‰. An analogous, though less pronounced shift towards lighter values offshore is seen in the Doushantuo cap carbonate of South China (Huang et al. 2013).

The Hankalchough episode excepted (though it could be of the same age), the most negative excursion in the entire geological record is the Shuram-Wonoka excursion, an event documented from several cratons and most completely recorded in the Shuram Formation of Oman (Le Guerroué et al. 2006). A steep decline in $\delta^{13}C$ coincides with rapid deepening at the top of the preceding Khufai Formation, reaching -12‰ at the flooding surface that climaxes the lowest member of the Shuram. From there the isotope signal slowly rises through the mainly siliciclastic middle and upper members of the Shuram and the mainly dolomitic deposits of the Buah Formation. Positive values are not reached until the top. Storm-like conditions dominated the basin. The Wonoka Formation of South Australia records the same excursion, attaining -11‰ just after outer-shelf turbidites and eventually climbing to +2 as facies shallow into red siliciclastics and 'peritidal' oolitic and stromatolitic limestone (Calver 2000). Submarine canyons partly filled with conglomerates and turbidites formed synchronously with the lowest values (Giddings et al. 2010, Husson et al. 2012). A similar excursion in northwestern Canada's Gametrail Formation goes down to -8‰. Throughout the 800 m of Ediacaran stratigraphy high $\delta^{13}C$ coincides with lowstand facies and low $\delta^{13}C$ with highstand (Macdonald et al. 2013). A negative excursion through the upper part of the Doushantuo Formation goes down to -10 and further (depending on section). Along with the recovery to positive values it is said to be independent of lithofacies (Lu et al. 2013), but interpretation is complicated by re-deposition of ooids from upslope. Most shallow-shelf successions lack the excursion. Slump blocks in the middle of the basin reveal their shallow-shelf origin by their heavier isotopic signature. The most negative values occur in shales and laminated carbonate, at the most distal location reaching -14. Cerium anomalies track increasingly reducing conditions as $\delta^{13}C$ falls (Cui et al. 2015). The Johnnie Formation in California also records the excursion. Apparently the downward phase mostly occurred within the span of a 1- to 2-m-thick oolite unit, the base of which is interpreted as a diachronous surface left by high-energy transgression (Verdel et al. 2011, Bergmann et al. 2011). Isotope ratios reach their nadir of -11.6 in micritic limestones just above the oolite. The much slower recovery through the succeeding 500-m-thick limey argillite member turns positive only at the top, with the breccia horizon.

Negative $\delta^{13}C$ down to -12 is also reported from southern Middle Siberia at the relevant time. The ^{13}C-depleted succession consists of three formations totalling 1000 m or more. The key unit is the Nikol'skoe (Nikol'skaya) Formation, recording initiation of the excursion. Lithology varies, but in the Zhuya section it consists of cherry-red, pink, lilac and green marls and calcareous siltstones, consistent with deepening into anoxic water. Negative values continue into the Chencha Formation, the lower part of which is monotonous light-grey limestone; the upper part is more stromatolitic and algal. The Zherba Formation is characterised, at the Nokhtuisk section, by hummocky cross-stratification and turbidites (Pelechaty 1998). Towards the top it becomes richer in carbonate, mostly grainstone, and passes from calcite to dolomite, at which point the isotope values become positive. The upper boundary is a karst surface. The same strongly negative values occur in the Torgo Formation, correlative with the Nikol'skoe and Chencha Formations. As dolostones pass into variegated marls, $\delta^{13}C$ plummets to -10, where it remains throughout the succeeding light grey and red limestones. Values become positive again when the lithology returns to dolostone (Pokrovskii et al. 2006).

Such evidence that in basinal settings $\delta^{13}C_{carb}$ (hereinafter δ_{carb}) was significantly lower than on the platform, increasing upslope, suggests that the DIC from which deeper-water carbonate formed remained isotopically and physically distinct from that of shallow environments. Isotopic excursions are not evidence of wild fluctuations in open-marine chemistry but of epicratonic variation in sea-level.

4.3. Isotopic variation of organic carbon

According to equations 1–3, δ_{carb} varies chiefly as a function of δ_{org} and the burial flux, *f*. The belief is that $\Delta\delta$ (= δ_{carb} minus δ_{org}) varies little at any one time and average $\Delta\delta$ (= ε) varies through time only within narrow bounds. The principal variable is *f*, so that δ_{carb} and δ_{org} are expected to co-vary. Arising from the synthesis of dissolved inorganic carbon, organic carbon should follow inorganic carbon, as it does in Svalbard and East Greenland (Knoll et al. 1986), and this at a global level: the controls acting on δ_{carb} are changes in global *f* and δ_{org}. Co-variation is taken as evidence that the signals are not diagenetically compromised, while absence of co-variation is considered to require special explanation (e.g. Fike et al. 2006, McFadden et al. 2008).

To determine how closely these parameters are interlinked, Neoproterozoic carbonate datasets are here compiled that include both organic and inorganic carbon data. As most also include details of TOC (the insoluble residue as a proportion of the total sample), this parameter is also analysed. For the sake of maximising coverage, no attempt is made to filter TOC data for H/C ratios, which are not usually reported.

4.3.1. *Overviews of the aggregated data*

Firstly, does δ_{org}, as expected, vary with δ_{carb}? Some degree of correlation is apparent (Fig. 4.4a), but also some deviation from the expected trend: there is no simple and consistent bivariate linearity. The overall slope is shallower than that of a simple 1:1 relationship, and organic carbon almost ceases to track inorganic carbon as the latter goes negative. Overall, the data distribution has a stepped appearance. Defined by the δ_{carb} axis, three main zones suggest themselves: an outer zone between -6 and 0, a middle zone between 0 and +5, and an inner zone between +5 and +11. Within these zones the arrays appear mainly horizontal rather than oblique, without obvious correlation.

Does δ_{org} vary with $\Delta\delta$? Again, three zones are apparent, within which the parameters seem to follow a broadly 1:1 relationship, implying that δ_{org} varies greatly while δ_{carb} changes little (Figs. 4.4b, 4.5). The same trend appears in a fourth array of highly enriched δ_{org} and δ_{carb} values. Fractionation range is greatest in the outer zone, about equal in the middle and inner zones. Most values are stacked in the range 26–33‰, the upper value (= CH_2O-CO_2 fractionation of 25‰ plus CO_2-CO_3 fractionation of ~7‰ plus CO_3-$CaCO_3$ fractionation of 1‰) being the maximum fractionation observed in modern phytoplankton at room temperature (Popp et al. 1998). This is also the normal range for the pre-Pliocene Phanerozoic (Hayes et al. 1999). Nonetheless, $\Delta\delta$ varies enormously, from 36‰ down to at least 10‰. If δ_{org} and δ_{carb} perfectly co-varied, the data would be vertically distributed within a narrow $\Delta\delta$ band; δ_{org} would vary but $\Delta\delta$ would not. The plot for $\Delta\delta$ versus δ_{carb} in Figure 4.4b is the obverse of the δ_{org} relationship, i.e. where subsets of the latter show a steep slope, subsets of the former show no slope.

Although TOC values in the Neoproterozoic rarely display systematic variability, they may be informative if sampling is sufficiently comprehensive to outweigh natural vagaries (e.g. differing sedimentation rates) and discrepancies relating to analytical method (Könitzer et al. 2012). TOC tends to increase as δ_{org} becomes lighter (Fig. 4.4c), a pattern observed also in Mesoproterozoic carbonates and Archaean, Palaeoproterozoic and Mesoproterozoic shales (Strauss & Beukes 1996, Yamaguchi 2002, Luo et al. 2014). TOC is highest in the normal $\Delta\delta$ range of 26–33‰, the range where most δ_{carb} values fall, peaking around 29‰ (Fig. 4.4d). In relation to δ_{carb}, average TOC shows a rising trend from positive to negative, except through the interval +1 to +3 (n = 127) (Fig. 4.6). The trend (sharply contrasting with that of the Majiatun Formation) suggests that δ_{carb} models based on isotopic mass balance are misconceived. According to equation (2), TOC – assuming some relationship with *f* – is expected to rise from negative to positive.

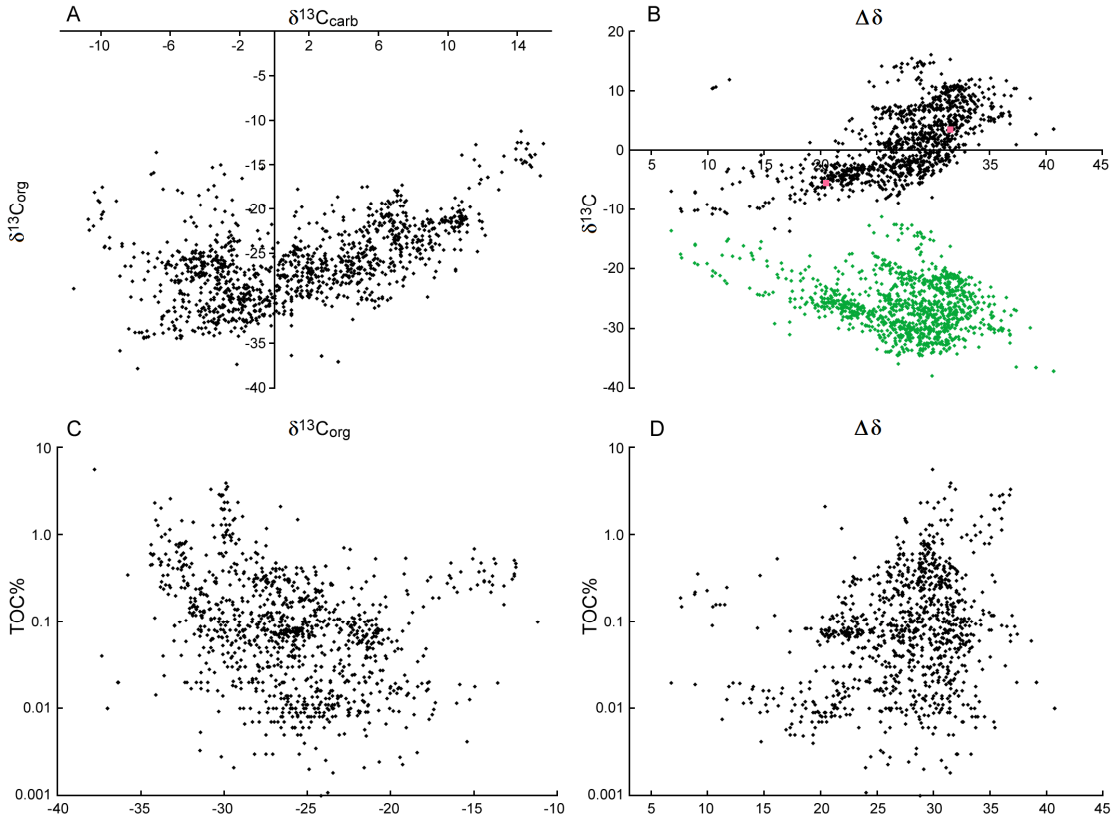

Figure 4.4. Compilations of Neoproterozoic organic carbon data: **(a)** carbonate v. organic $\delta^{13}C$; **(b)** organic fractionation, $\Delta\delta$, v. carbonate $\delta^{13}C$ (black) and organic $\delta^{13}C$ (green); **(c)** organic $\delta^{13}C$ v. TOC in weight % (logarithmic scale); and **(d)** organic fractionation v. TOC. Squares in (b) mark dotted line of Fig. 4.10.

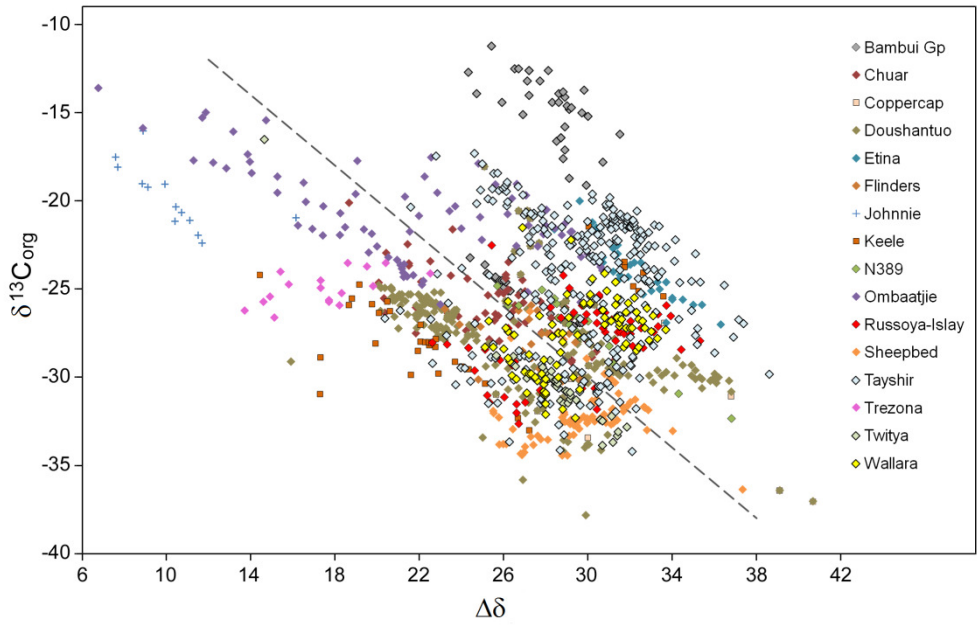

Figure 4.5. Organic fractionation v. organic $\delta^{13}C$ (Fig. 4.4b), colour-coded by formation. Most arrays are sub-parallel to the slope (dotted line) whereby $\delta^{13}C$ is invariant and only $\delta^{13}C_{org}$ varies. Perfect co-variation would be a vertical line whereby $\Delta\delta$ was constant.

Overall, δ_{carb} varies almost as much as δ_{org} does (Fig. 4.4a–d). However, in particular cases, δ_{org} can vary much more than δ_{carb}. To take an extreme example, in the Gametrail Formation δ_{org} ranges from -34 down to as high as -6 whereas δ_{carb} varies only from -5.1 to -7.7 (Macdonald et al. 2013). The example also shows that, at times, organic carbon fractionation can be very small – much lower than the ~28‰ considered normal for primary producers.

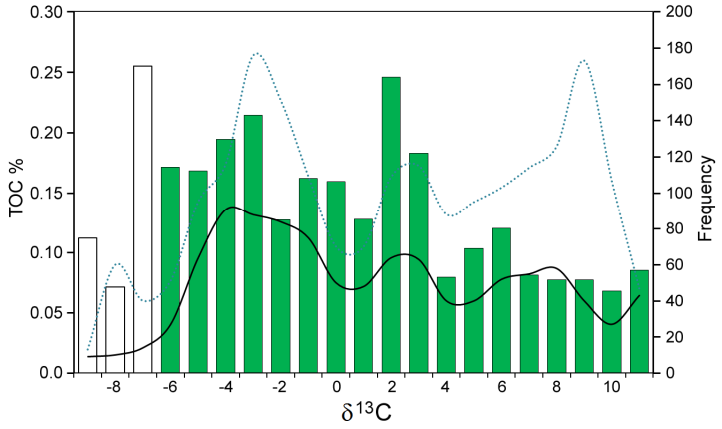

Figure 4.6. Average TOC % (columns) as a function of carbonate $\delta^{13}C$, Tonian and Cryogenian periods. Continuous line indicates number of analysed carbonate samples per 1‰ interval (right axis), dotted line total number of samples. Data from Jiuliqiao and Majiatun Formations not included. Data for negative $\delta^{13}C$ come partly from cap carbonates, when conditions may have been abnormal, and below -6‰ averages are statistically weak.

4.3.2. *TOC variation over time*

Figure 4.7 summarises a compilation of over 2400 TOC measurements from the mid to late Neoproterozoic. With the exception of samples from diamictite intervals, the data are restricted to limestone and dolostone. Shales – which tend to be richer – are excluded. So are the organic-rich manganese carbonates of the Datangpo Formation following South China's lower diamictite interval (715–660 Ma) and the anomalously high TOC in the Doushantuo Formation (Jiulongwan section) following South China's upper diamictite interval (640–635 Ma), though data from other sections are included. Too few data have as yet been reported for the early Cambrian to trace what happens to TOC through the crucial Ediacaran-Cambrian transition. Shales show a trend of increasing TOC throughout the Ediacaran.

Overall, average TOC rises from levels below 0.05% in the later Tonian to around 0.25% near the end of the Ediacaran (Fig. 4.7). TOC values from the Tonian-age Jiuliqiao (0.06%) and Sidingshan (0.03%) Formations are not included but are consistent with ages of 850–800 Ma. There also appears to be a second-order trend of rising TOC in the approach to each of the two main diamictite intervals. Chronological assignments are complicated by the fact that the stratigraphic intervals

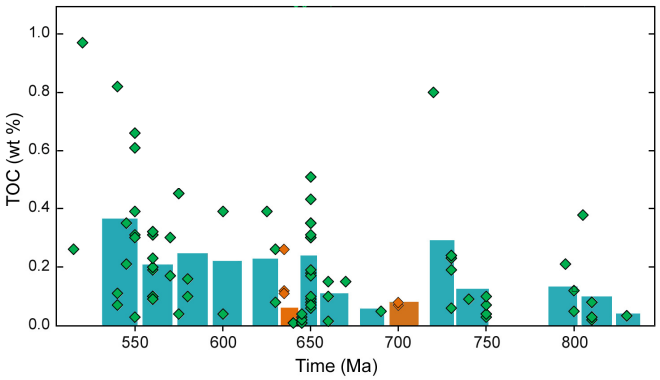

Figure 4.7. Carbonate-hosted total organic carbon through time. Diamond symbols represent averages per formation, columns these averages averaged over time bins. The Ombaatjie and Trezona Formations (645–640 Ma) are put in the same time interval as the diamictites (brown). The anomalously high TOC reported for the Doushantuo Formation by Macfadden et al. (2006) is omitted; however, the formation is represented by other studies (Ader et al. 2009, Jiang et al. 2010, Kano et al. 2011). The Jiuliqiao and Sidingshan Formations are also omitted.

represented by the diamictites may not be of equal duration. For example, the Ombaatjie and Trezona Formations lie stratigraphically below the diamictites, but the diamictites are thin, if present at all (Fig. 1.3), and their TOC content low; it seems probable that the formations were contemporaneous with thicker diamictites elsewhere. Whatever view is taken, the average TOC content of the diamictite-rich Nantuo, Nuccaleena and Ghaub Formations, generally seen as evidence of 'Snowball Earth' conditions, is no lower than that of most formations in the non-glacial Tonian period. There is also no support for the notion that the OC burial flux declined 800–600 Ma (Des Marais et al. 1992).

4.4. What controls organic fractionation?

Marine biomass fractionation, $\Delta\delta$, is the result of photosynthesis by primary producers. Zooplankton and organisms higher in the food chain reproduce the $\delta^{13}C$ of the food they eat (Deuser et al. 1968). The value is affected by several factors, notably growth rate, species composition, the proportion of *n*-alkyl lipids in the OM (Pawlowska et al. 2013), temperature, pH and dissolved CO_2. In nature these are often interrelated and in the laboratory difficult to isolate. Not all are amenable to geological investigation. Here I focus on temperature, pH, CO_2 and growth rate.

Temperature, although difficult to separate from CO_2, may exert some control over $\Delta\delta$. Experiments with the diatom *Skeletonema costatum* and coccolithophore *Emiliania huxleyi* suggest that between 9° and 30° C fractionation rises by 5‰ (Hinga et al. 1994). Be that as it may, the temperature range of surface water from proximal to distal across Neoproterozoic carbonate platforms is likely to have been small. Latitudinal differences may have been slightly more material. Through

the Cenozoic, a fall in ocean temperature is the most obvious explanation for the fall in ε (Hayes et al. 1999). As has long been recognised (Towe 1982, Lewan 1986, Popp et al. 1989), the δ_{org} of Proterozoic, Palaeozoic and Mesozoic phytoplankton was several per mil lower than that of modern phytoplankton, beginning to rise only in the Oligocene when global climate cooled (Hayes et al. 1999). The association of Phanerozoic black shales with greenhouse conditions and isotopically light carbon could also be interpreted to support a temperature effect (Meyers 2010).

Probably the most influential variable is dissolved CO_2 (Rau et al. 1997). Organic fractionation tends to be highest where the concentration is high, allowing algae and cyanobacteria to rely simply on diffusion for uptake of the gas – as, for example, in the stromatolites of Yellowstone National Park, analogous in form to Proterozoic conophytons (Estep 1984). Where concentrations are low and pH correspondingly high, cyanobacteria compensate by actively pumping HCO_3^- into the cell and converting it into CO_2 (Price 2011). The intracellular concentration of inorganic carbon can be raised up to 1000-fold by this mechanism. The synthesised organic carbon is enriched in ^{13}C because, depending on temperature, HCO_3^- at equilibrium is some 9‰ heavier than dissolved CO_2 (Mook et al. 1974, Zhang et al. 1995). Where concentrations are very low, Δδ can fall to as little as 6‰ (Deuser et al. 1968) or even lower (Hinga et al. 1994). At a given pH, $[CO_2]_{aq}$ is related to atmospheric pCO_2, although atmosphere and surface ocean are often not in equilibrium, particularly not in regions of low $[CO_2]_{aq}$ (Patterson et al. 1994). The relationship has been successfully used to quantify CO_2 drawdown during the Oceanic Anoxic Event at the end of the Cenomanian (Jarvis et al. 2011).

Phytoplankton growth rate tends to increase with $[CO_2]_{aq}$ (Wolf-Gladrow et al. 1999, Fu et al. 2008), nutrient availability, and temperature (Bissinger et al. 2008), leading to isotopic enrichment of the biomass. During a nutrient-induced algal bloom in the equatorial Pacific, OM was enriched by up to 7‰ (Bidigare et al. 1999). In the much colder waters of the Ross Sea, isotopic enrichment attributable to natural blooms was found to be of similar magnitude (Villinski et al. 2000). Because rapid consumption of dissolved CO_2 causes disequilibrium between the oceanic and atmospheric carbon pools, $\delta^{13}C_{DIC}$ is also enriched, though to a lesser extent: the consequent fall in Δδ accounts for less than half of the organic enrichment.

Recycling of OC back into the DIC pool entails a lowering of $\delta^{13}C$. In water bodies of sufficient depth, remineralisation below the level at which OC is produced will result in isotopic stratification, especially if the water body is restricted. In the subsurface waters of redox-stratified modern lake and fjord systems $\delta^{13}C_{DIC}$ down to -23‰ has been recorded (Pimenov et al. 2008, van Breugel et al. 2005). In epicontinental Proterozoic settings, where anaerobic remineralisation took

place at shallow depths, the gradient could also have been substantial, depending on the degree of vertical mixing and degree of remineralisation. Moreover, to the extent that the OM consisted of the chemoautotrophs themselves, organic fractionation would have been compounded, for biomass from chemoautotrophic and methanotrophic microbes is depleted relative to photoautotrophs, typically by -15 to -40‰ (e.g. Hollander & Smith 2001). That said, as $\Delta\delta$ rarely exceeds 35‰ in Neoproterozoic carbonates, this factor was probably not material on a gross scale. In the deeper environments where anaerobic respiration was more prevalent, $\Delta\delta$ is substantially smaller.

4.5. What controls inorganic fractionation?

In principle, δ_{carb} and δ_{org} are expected to co-vary because the preferential extraction of ^{12}C by organisms results in enrichment of ^{13}C. It has been argued that δ_{carb} and δ_{org} co-varied through the early Neoproterozoic but decoupled when the build-up of a large DOC reservoir – associated somehow with glacial events in the Cryogenian – began to overwhelm the δ_{org} signal from contemporaneous OM (Swanson-Hysell et al. 2010). This picture of secular isotopic change – based on four formations from Australia, the Doushantuo Formation from South China and the Shuram Formation from Oman – is not correct. Through at least part of the Wonoka Formation and parts of the Trezona Formation (δ_{carb} -9.8 to -7.0), the Shuram Formation ($\delta_{carb} \leq 0$) and the Doushantuo Formation (dolostone $\delta_{carb} > 5$, Xiao et al. 2012), the signals were coupled. Through many Tonian and Cryogenian formations they were not strongly coupled (Fig. 4.5). They were also not coupled in the Majiatun Formation. There is a weak correlation through the Juiliqiao and Sidingshan Formations, though not if they are considered separately.

Another variable known to affect DIC and therefore δ_{carb} is CO_2 gas exchange at the air-sea interface (Quay & Stutsman 2003). Atmospheric CO_2, with a pre-industrial value of -6.5‰, undergoes fractionation of around 8‰ in exchange with the ocean (at 23° C, Zhang et al. 1995). Disequilibrium in this exchange may have a modest effect on DIC of up to +2.2‰ (Quay et al. 2009). In addition, and perhaps more significantly, $\delta^{13}C_{DIC}$ in hot, evaporitic environments can be enriched as a result of preferential loss of CO_2 with the lighter isotope. A small effect has been recorded in the equatorial Pacific (Lynch-Stieglitz et al. 1995), a large effect (up to +16‰) in the brines of the Dead Sea (Stiller et al. 1985). A similar mechanism is invoked to explain δ_{carb} of 5–7‰ in Late Palaeozoic carbonates of the Sverdrup Basin (Beauchamp et al. 1987), increasingly heavy δ_{carb} in the profile of a Permian Zechstein evaporite (Potter et al. 2004) and, in conjunction with other factors, values of up to 17‰ in Palaeoproterozoic carbonates (Melezhik et al. 1999). The heavy $\delta^{18}O$ commonly associated with high δ_{carb} (e.g. Fig. 1.8) is consistent with high rates of evaporation.

Finally, the mineralogy of the carbonate phase also has an effect on $\delta^{13}C$. Aragonite tends to be heavier than low-Mg calcite: modern molluscs (Lécuyer et al. 2012) and Permian reef cements (Given & Lohmann 1985) suggest a difference of ~1‰, experiments a somewhat greater difference of ~1.7‰ (Romanek et al. 1992). Aragonite and high-Mg calcite tend to form in warm, low-Mg environments. Dolomite fractionation may be up to 2‰ greater than calcite (Sheppard & Schwarcz 1970, Horita 2014). While these differences are not negligible, they can have contributed little to secular δ_{carb} variation of up to 20‰.

4.6. TOC and the organic carbon burial flux

Most marine burial of OC takes place on continental shelves and margins, where productivity is high and the OC buried includes terrestrial carbon brought down by rivers. Compared to the amount produced, very little ends up permanently buried; most is recycled by aerobic and anaerobic oxidation back into the water. In recent deltaic-shelf sediments the initial, surficial proportion is typically less than 3% (Berner 1982). Measurements of TOC in recent deep-sea sediments rarely yield more than 7% and with age dwindle exponentially to less than 0.5% (Anderson et al. 2001).

Total organic carbon content is generally a measurement of the acid-insoluble carbon weight as a proportion of total sediment weight. It is very variable, but tends to be substantially higher in shales and clays than in carbonates, for reasons that continue to be debated (Arndt et al. 2013). The Jiuliqiao and Majiatun Formations also show this relationship (Figs. 2.18, 3.10). Possible factors include nutrient abundance, mineral surface area, and binding of OC to reactive iron. Apart from coals, the rocks with the highest content are black shales, defined as containing at least 1% OM; some contain more than 20%. Because of their inordinately high OM, coals and black shales had a major impact on the carbon cycle, as reflected by δ_{carb} maxima in the Silurian, the Permo-Carboniferous, the later Jurassic and the mid Cretaceous (Klemme & Ulmishek 1991, Prokoph et al. 2008). A link between δ_{carb} and burial flux is thus clear. On the other hand, black shales are of irregular occurrence and constitute only a minor proportion of total sedimentary rocks. Based on data from the Russian Platform, average shale TOC is around 0.63% (Green 1959), close to the average for all sediment types.

Inventories of organic and inorganic carbon in the terrestrial crust can be used to estimate *f* (Table 4.2). The ratio of preserved marine shales and claystones to marine sandstones and carbonates through the Phanerozoic ranges from 36% to 93%: highest in the Miocene, lowest in the early Cambrian (Ronov 1993). The same source suggests 80% for the late Neoproterozoic, but the figure

does not include ocean-crust carbonate (Gillis & Coogan 2011), here conservatively estimated at 5%. TOC is as calculated by Hunt (1972), who considered there was about three times as much OC in shales and claystones as in carbonates and sandstones. With these parameters *f* comes out at 0.21 (equivalent to average δ_{org} = 28‰, based on equation 2). The main point is that *f* is much more sensitive to the shale component than to the carbonate, because shale is richer in OC.

	A	B	C	D	E	
	Rock ratio (%)	**Inorganic C (wt%)**	**Organic C (TOC wt%)**	**Inorganic C A x B**	**Organic C A x C**	**Org C/total E/D+E**
(a)						
Shales & clays	52.4	0.8	0.75	0.419	0.393	
Sandstones	25.6	0.8	0.25	0.205	0.064	
Carbonates	22.0	8.4	0.25	1.848	0.055	
				2.472	0.512	0.17
(b)						
Shales & clays	75.0	0.8	0.75	0.60	0.563	
Sandstones	5.0	0.8	0.25	0.04	0.013	
Carbonates	20.0	8.4	0.25	1.68	0.050	
				2.32	0.625	0.21

Table 4.2. Calculations of organic-to-total-carbon ratios based on: **(a)** rock type proportions in the terrestrial crust as per Ronov (1968), inorganic C proportions as per Ronov & Yaroshevsky (1969) and organic C proportions as per Hunt (1972); **(b)** as for (a) but rock type proportions as estimated for the mid to late Neoproterozoic, i.e. a higher proportion of shale. Carbonates assumed to be 70% carbonate.

Average TOC % (Figs. 4.7, 4.8) rose through the Tonian and Cryogenian, remained fairly steady through most of the Ediacaran and rose steeply just before the Cambrian. If δ_{carb} was controlled by the burial flux, it should have followed a contrary path, falling through the Tonian and Cryogenian, remaining steady through the Ediacaran and falling steeply just before the Cambrian. In fact, according to a recent composite of single-region curves (Cox et al. 2016), it rose through the mid Tonian and was lower through most of the Ediacaran than through the late Cryogenian. Carbonates in south Siberia, at 3–7‰, remained enriched through most of the Ediacaran (Melezhik et al. 2009), once more challenging the idea that the global ocean can be represented by single values. Indeed, multi-region curves show variability of up to 8‰ or more (e.g. Bold et al. 2016).

The Ediacaran was when marine diversity, if not also biomass, was beginning to take off (Butterfield 2007). Standing marine biomass multiplied by several orders of magnitude through the Phanerozoic (Bambach 1993, Allmon & Martin 2014), facilitated by the oxygenation of depths below the photic zone. Organisms at different trophic levels now had space in which to expand

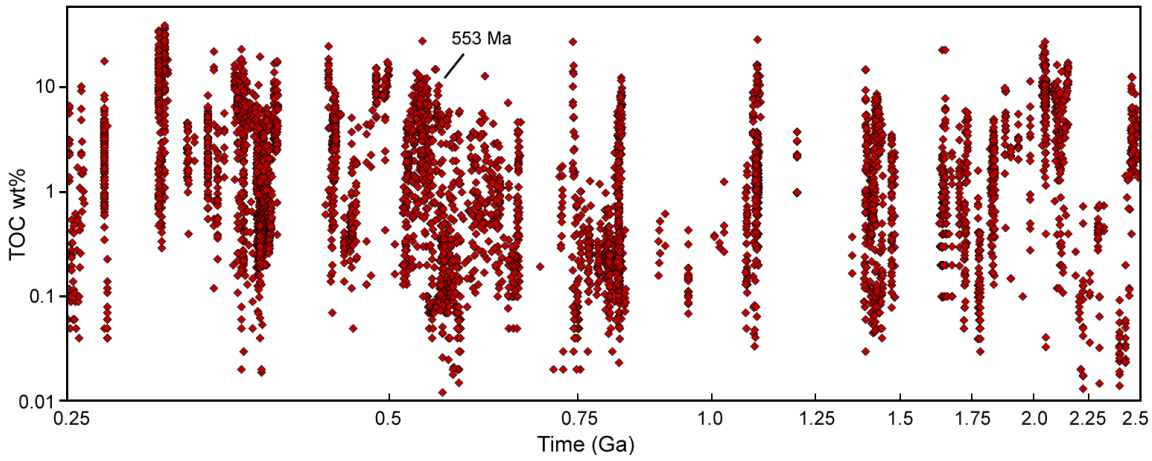

Figure 4.8. Shale TOC content through the earlier Palaeozoic and Proterozoic (compilation of published data).

numerically as well as diversify. If TOC did not increase correspondingly, this was mainly because it was the residue of primary producers, which rapidly ceased to dominate ocean ecology.

4.7. Towards a depth-dependent model

Variation of $\Delta\delta$ is more than 14‰ when δ_{carb} is positive, more than 20‰ when it is negative, and in the latter case $\Delta\delta$ is invariably lower (Fig. 4.4b). As reviewed above, the only factor capable of generating variability in organic fractionation is the response of oxygenic photosynthesisers to the availability of dissolved CO_2. By inference, concentrations of the gas were high when δ_{carb} was positive and low when δ_{carb} was negative.

At first sight, the trend of increasing $\Delta\delta$ with δ_{carb} does not accord with the parallel trend of decreasing water depth. Other factors being equal, CO_2 solubility increases with depth, so that CO_2 concentrations increase, not decrease. Moreover, the waters nearshore would presumably have been warmer than offshore, and this too would have reduced solubility. At the equator, for example, where temperatures are 25° C higher than in the Antarctic, dissolved CO_2 concentrations are about half. Organic $\delta^{13}C$, correspondingly, is at least 6‰ heavier (Goericke & Fry 1994).

However, the differences of pressure and temperature relating to depth gradients of a few hundred metres are small. DIC concentrations in the Pacific Ocean increase through the first 300 m from 1960 to 2080 µmol/kg (Quay & Stutsman 2003), and most of this is an effect of photosynthesis, not pressure. Whether temperature decreased seaward at the depth pertinent to carbonate precipitation is unknown; the $\delta^{18}O$ profile as negative $\delta^{13}C$ decreases suggests not (Fig. 4.12). In any case, there is no simple linear relationship between temperature and $[CO_2]_{aq}$ because shallow water bodies can be saturated (Liang et al. 2013) or even supersaturated with the gas (Estep 1984), just as they can with calcium carbonate (Opdyke & Wilkinson 1993). Breaking waves fold air bubbles down into

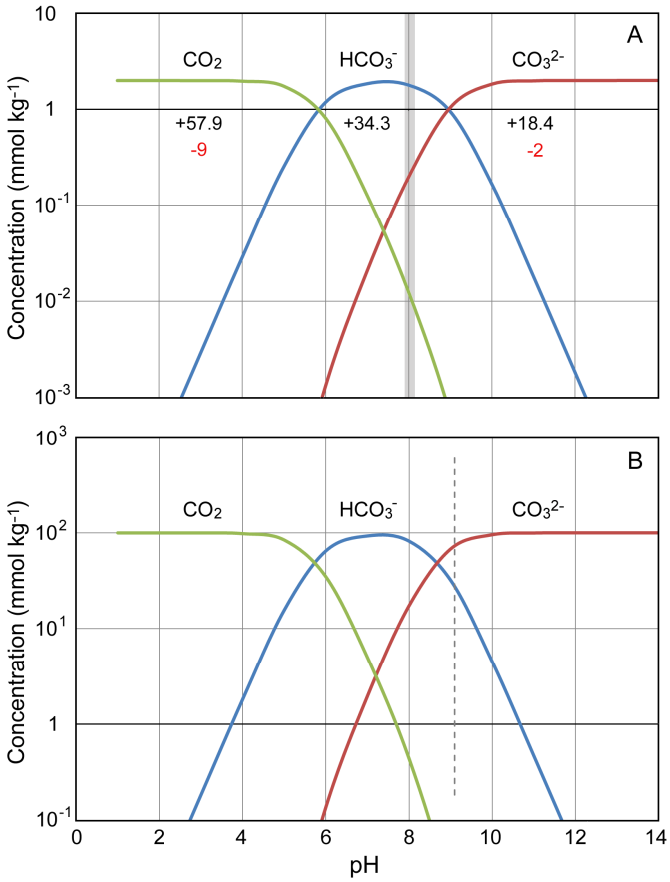

Figure 4.9. Concentration of dissolved carbonate species in seawater as a function of pH. (**a**) Modern conditions (T = 25° C, DIC = 2 mmol kg^{-1}, S = 35), normal range of pH shaded grey. Black numbers indicate the extent of positive $\delta^{18}O$ fractionation with respect to H_2O, red numbers the negative $\delta^{13}C$ fractionation with respect to HCO_3^-. (**b**) Conditions considered more relevant to the Neoproterozoic (T = 35° C, DIC = 100 mmol kg^{-1}, S = 50). Dotted line marks the pH at which $[CO_2]$ is the same as in (a). Graphs produced using CO2Sys v2.1. Note that, because of complexing, the total activity of HCO_3^- at pH 8.1 is 68 times greater than that of CO_3^{2-} (Garrels & Thompson 1962). Slight shift in pH due to higher T and S, not DIC.

the water where the hydrostatic pressure causes some of its gases to dissolve. Higher Δδ in shallow settings in all periods prior to the Oligocene, including the Cryogenian, suggests that atmospheric CO_2 never fell below 1000 ppm – the point at which Δδ in the Cenozoic began to fall. Concentrations in the early Eocene are independently estimated at 1400 ppm (Anagnostou et al. 2016).

The main controls on $[CO_2]_{aq}$ are pH and atmospheric concentration. As pH increases from 7 to 9, carbonate alkalinity – the proportion of CO_3^{2-} to HCO_3^- – in seawater increases, with $[CO_2]$ decreasing by more than two orders of magnitude (Fig. 4.9). Atmospheric pCO_2 in the Proterozoic would have been many times higher than today and alkalinity at a given pH much the same. However, the decrease in Δδ and hence $[CO_2]$ with water depth shows that shallow-marine $[CO_2]$ was at a critical level for phytoplankton. Seawater pH must therefore have been considerably

higher than today. In the modern ocean, [CO_2] increases with depth, owing to aerobic remineralisation, and $\Delta\delta_{DIC\text{-}DOC}$ shows no such decrease.

In anoxic settings organic carbon can decompose by a variety of microbially mediated pathways. In order of Gibbs free energy yield, these are denitrification, manganese reduction, iron reduction and sulphate reduction. This also tends to be the order in which they are stratified, whether through the water column (Wakeham et al. 2007) or in sediments below oxic water bodies (Froelich et al. 1979, Canfield et al. 1993). Denitrification occurs around the base of the suboxic zone, closely followed by manganese and iron reduction, while sulphate reduction is characteristic of fully anoxic conditions. Potentially, all these processes increase DIC and carbonate alkalinity:

$$5CH_2O + 4NO_3^- \rightarrow 2N_2 + 5HCO_3^- + H^+ + 2H_2O \quad (4)$$

$$CH_2O + 4Fe(OH)_3 + 8H^+ \rightarrow CO_2 + 4Fe^{2+} + 11H_2O \quad (5a)$$

$$CH_2O + 4Fe(OH)_3 + 7CO_2 \rightarrow 4Fe^{2+} + 8HCO_3^- + 3H_2O \quad (5b)$$

$$2CH_2O + SO_4^{2-} \rightarrow H_2S + 2HCO_3^- \quad (6)$$

How much each reaction contributes to the redox budget depends on the abundance of the respective oxidants. In the Precambrian ocean reduced Fe and S were not in short supply. Remineralisation via these elements depended on re-oxidation of Fe and S by diffusion and reaction with oxygen in the photic zone, and by microbial photosynthesis at the base of that zone (Konhauser et al. 2011, Johnston et al. 2009). If the ocean was sulphate-poor relative to the modern ocean, this was because the sulphate generated in the surface layer was continually being reduced in the anoxic subsurface, regardless of atmospheric oxygen levels. The evidence for sometimes high levels of OC extraction implies a well-oxygenated surface layer.

In addition to the effect of anaerobic remineralisation, the dissolution of detrital feldspar and illite also raised subsurface alkalinity (§2.4.1). Calcium carbonate therefore precipitated mostly in or on the seafloor. While some OM was produced at this level, for example as microbial mats, oxidation of which would have depleted ambient DIC, most would have been produced in the upper water column. As waters deepened, nutrients released from silicates at the bottom would have become less accessible to phytoplankton, which therefore tended to concentrate somewhat lower in the water column (Cullen 2015) where alkalinity was higher. Starved of CO_2, they were forced to photosynthesise using the isotopically heavier HCO_3^-. This could account for up to 9‰ of the seaward decrease in $\Delta\delta$, essentially representing the difference in alkalinity between the zone of carbonate precipitation, dominated by CO_3^{2-}, and the zone of photosynthesis, dominated by CO_2 in shallow localities and by HCO_3^- in deeper localities. As [CO_2] dwindled to negligible levels, other physiological effects might have kicked in to cause organic $\delta^{13}C$ to be even less depleted.

In very shallow environments, organic fractionation was high because so was aqueous [CO_2]. Supersaturation of CO_2 resulted from high evaporation, at a time when seas appear to have been warmer than today (Meng et al. 2011, Tartèse et al. 2016). Lower $CaCO_3$ solubility and consequently higher levels of precipitation as the water shallowed released more CO_2 into the water and thereby lowered surface alkalinity. Greater extraction of isotopically light CO_2 into the biomass and preferential evasion of lighter CO_2 caused DIC to be enriched. Beyond a certain threshold (~2000 μatm pCO_2 for *S. costatum*, Hinga et al. 1994) the rise in $\Delta\delta$ levelled off, as the amount of bicarbonate available tailed off (Fig. 4.4b). Organic fractionation was limited for physiological reasons to a maximum of ~36‰. Thus while δ_{carb} might continue to rise as the environment approached Dead Sea rates of evaporation, $\Delta\delta$ tended to remain within the range 26–33‰.

Since water depth was at a maximum when negative excursions were at their nadir, so was the degree of exchange with the open ocean. Beyond continental margins, anaerobic OC remineralisation is likely to have diminished, simply because OC was less abundant. Production depended on nutrient availability, and the most limiting nutrient, phosphorus, came primarily from the land. Although phosphate concentrations may have been higher than in the modern ocean (Planavsky et al. 2010), production oceanward would still have decreased, with consequences for $\delta^{13}C_{DIC}$.

In terms of mass balance, the main control on δ_{DIC} was the fraction of carbon buried as organic carbon. To judge from the carbonate $\delta^{18}O$ record, ocean temperatures in the Neoproterozoic were at least as high as in the Eocene and with metabolic rates correspondingly elevated, anaerobic remineralisation would have disposed of whatever OM was produced and not circulated back to the oxidising surface. Thus it is unlikely that ocean water would have been rich in organic carbon, as sometimes postulated (e.g. Rothman et al. 2003). Even if non-negligible OM did reach the ocean floor, the low level of other sedimentation (volcanic ash, aeolian dust) would have exposed it to continuing degradation. Even today the organic fraction of ocean-crust carbon is only around 0.05 (Coltice et al. 2004), with most OC burial (~96%) taking place near the coast (Berner 1982). By contrast, the fraction of carbonate buried in ocean crust may have been as high as 0.35 (Bjerrum & Canfield 2004). The fraction of carbon buried as OC in the ocean environment is likely to have been minimal and δ_{DIC} close to the mantle value. On the platforms, lateral mixing with the ocean may have meant that -6‰ tended to be the lower limit of δ_{carb} (Figs. 4.1, 4.2, 4.4a). More negative values could arise if carbonate precipitated from DIC rich in remineralised OC, as in redox-stratified modern lakes and fjords.

Carbon enters the exosphere mainly as CO_2. Allowing for fractionation on degassing of 2.2–4.5‰, divided between melt and vesicles (Cartigny et al. 2001), and for ocean-atmosphere fractionation of say -8.5‰ (at 19° C), atmospheric CO_2 would have been around -13‰ – considerably lighter than today because terrestrial OC sequestration was minimal in the Proterozoic. Reaction of $CO_{2(g)}$ with rainwater in the course of carbonate and silicate weathering would have reversed the fractionation because of the 8‰ difference between $CO_{2(g)}$ and HCO_3^-. Direct atmosphere-to-ocean transfer would have re-introduced the gas at -2‰ fractionation (Siegenthaler & Münnich 1981, Zhang et al. 1995), leading to HCO_3^- so derived of around -7‰. All told, a value of -7 to -5‰ seems a reasonable baseline for all marine environments.

Given that δ_{carb} in the Neoproterozoic was a function of water depth, the controls on δ_{carb} were necessarily local. What mattered was where the local system was located along the gradient between the open ocean, where *f* was negligible and DIC around -5‰, and the nearshore, where *f* was significant, and DIC around 2–4‰. An increasing remineralisation gradient with depth accentuated the lateral gradient. Carbonate reflected these differences because it precipitated close to the seafloor, as indicated by petrographic (§2.4.3), chemical (Fig. 4.11, §3.5.3) and isotopic (§2.7.4) evidence. Above +4‰ an additional control was temperature (degree of evaporation). The concept of global δ_{DIC} is barely meaningful. The ocean was not isotopically homogeneous either vertically or laterally, and we have no way of determining what the global value was except on the basis of platform-sea averages. Open-ocean δ_{DIC} may have remained fairly constant through the Proterozoic, exercising little influence on epicontinental δ_{DIC}.

The two carbonate sequences described in this thesis extend across a wide range of δ_{carb} and water depths. Corrected for the differing fractionations of aragonite, calcite and dolomite, δ_{carb} co-varied with $\Delta\delta$ (Fig. 4.10) – the consequence of concomitantly decreasing organic fractionation at the surface and decreasing δ_{DIC} in bottom waters as environments deepened. A similar slope of co-variation characterises the global picture (Fig. 4.4b).

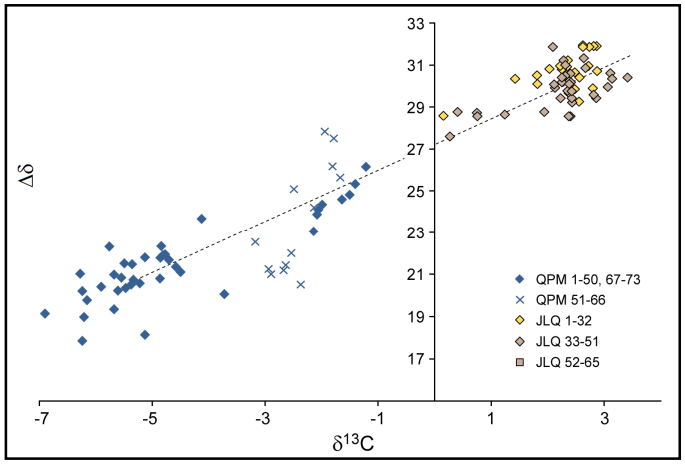

Figure 4.10. Organic fractionation as a function of carbonate $\delta^{13}C$ (normalised to calcite) in the Majiatun, Jiuliqiao and Sidingshan Formations. Dotted line traces 11‰ such fractionation in the course of 9‰ δ_{carb} enrichment.

4.8. Negative 'excursions'

4.8.1. *Upwelling in the context of deglaciation*

Excursions in platform carbonate down to -5‰ or lower are unknown after the Early Cambrian. At least two exceed -4 in the later Cambrian (Zhu et al. 2006). After the Palaeozoic, excursions barely go below -2, are short-lived, and usually attributed to massive injections of carbon dioxide enriched in ^{12}C (e.g. Sluijs & Dickens 2010). Anything lower than -6 cannot be accounted for by a change in global mass balance because the value of mantle carbon imposes a lower limit on possible values of open-marine DIC, at which point either *f* or ε is reduced to zero.

The 'conventional' explanation for negative excursions (as characterised by Hoffman & Schrag 2002) postulates that anaerobic remineralisation of OM beneath the surface layer created a large reservoir of ^{12}C-enriched alkalinity. As deglaciation got underway, upwelling stimulated the precipitation of carbonates which were isotopically light (Kaufman et al. 1991, Grotzinger & Knoll 1995, Kaufman et al. 1997). The proposal has its problems. Since the excursions occurred on epicratonic platforms at some remove from the open ocean, upwelling – in a context of world-wide glaciation and massive sea-level fall – is difficult to visualise, as well as document. Snowball glaciation would have lowered sea-level by at least 500 m (Liu & Peltier 2013), pushing the shoreline to the edge of the cratons and thus beyond where most 'glaciomarine' records occur. Buoyant melt-water pouring over dense saline water would have worked against upwelling (Shields 2005). And the sudden exposure of the ocean to 120,000–300,000 ppm CO_2 in the atmosphere (§1.3) would have caused massive acidification. Although the introduction of bicarbonate from silicate weathering would have ameliorated the effect, it is clear both from the present rise in pCO_2 and from catastrophic injections of CO_2 in the past (e.g. Rigo et al. 2007, Clarkson et al. 2015) that pH would have fallen. In any case, negative excursions are not restricted to cap carbonates.

If, on the other hand, the 'upwelling' was simply a rise in sea-level – the excursions reflecting a shift in shoreline, not ocean chemistry – these problems disappear. At times, transgressions were comparatively tranquil, at others, marked by intracratonic rifting and mass-flow deposits (diamictites and turbidites) that denoted chaotic episodes of local deepening, not eustatic sea-level falls. Faulting introduced fluids rich in Ca, Mg, Fe, Mn and other trace metals into waters that were already ferruginous. Enhanced nutrient release stimulated cyanobacterial production (Bidigare et al. 1999, Fig. 4.6), which increased the level of sulphate reduction and bicarbonate production, and this, along with the raised concentrations of the ions that made up aragonite and dolomite, stimulated the precipitation of carbonates that rarely formed in quantity this far from shore.

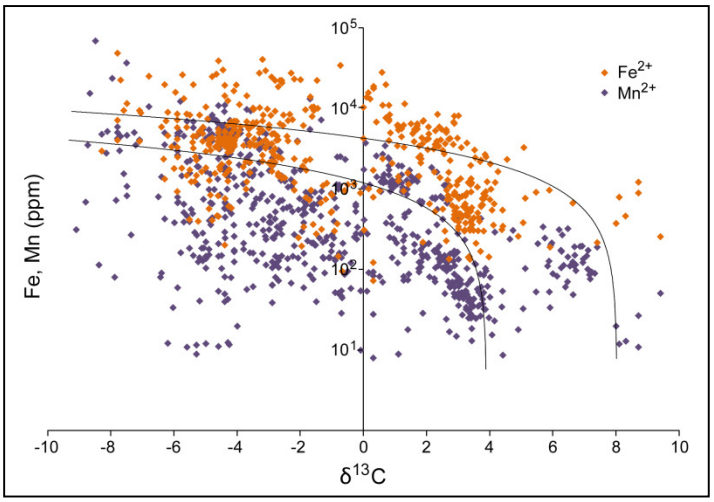

Figure 4.11. Compilation of carbonate-associated Fe^{2+} and Mn^{2+} (logarithmic scale, linear trend-lines) in Neoproterozoic samples. The increase in concentration towards negative $\delta^{13}C$ indicates increasing anoxia in that direction. As in other figures, relatively few samples plot around $\delta^{13}C$ = 0, which seems to represent a transitory hinge zone.

Precipitating from the anoxic subsurface, carbonates were consequently rich in Mg, Fe and Mn as well as ^{12}C (Fig. 4.11).

4.8.2. *Systematic variation in $\delta^{18}O$ through negative excursions*

Systematic decreases in $\delta^{18}O$ as δ_{carb} became more negative – or increases as δ_{carb} became less negative – are one of the most puzzling features of the Neoproterozoic and early Cambrian (Fig. 4.12). Examples include the Ombaatjie Formation (Johnston et al. 2012; Fig. 1.3), the Maieberg Formation (Halverson et al. 2007), the Wilyerpa Formation and overlying Tindelpina Shale (McKirdy et al. 2001), the Tsagaan Olom Group (Macdonald et al. 2009; Fig. 4.1), several of the cap carbonates (e.g. Yashioka et al. 2003, Porter et al. 2004, Shen et al. 2008), the Shuram Formation (Fike et al. 2006), the Gametrail Formation and Unit PH4 in the Ogilvie Mountains (Macdonald et al. 2013), the Dreigratberg Formation (F539 and F547 in Macdonald et al. 2010), the Wonoka Formation (Calver 2000), the Nikol'skoe and Chencha Formations (Melezhik et al. 2009), the Doushantuo Formation (Tahata et al. 2012), and the Cambrian-age Yu'anshan Formation (Peters & Gaines 2012) (some shown in Fig. 4.13).

That diagenesis caused systematic co-variation of $\delta^{13}C$ and $\delta^{18}O$ is a possibility routinely discussed in the reporting literature, in places extensively (e.g. Grotzinger et al. 2011, Husson et al. 2012); it has also been advanced on more general grounds (Derry 2010). The arguments are not rehearsed here. Suffice to say that the conclusion usually reached is that diagenesis was minor and does not explain the phenomenon. Other points to be made include: (1) Most Precambrian limestones were originally aragonite (or vaterite) and in the course of recrystallisation to calcite lithified early.

Being non-biogenic, they were generally less porous than their Phanerozoic counterparts, and the precipitation of additional carbonate during recrystallisation (calcite being less soluble than aragonite) further reduced pore space. The opportunity for late diagenetic fluids to enter the system was thus minimised. (2) Diagenesis fails to explain the particulars of even the most extreme excursions (Le Guerroué & Cozzi 2010, Husson et al. 2015), let alone lesser ones. (3) Since the $\delta^{18}O$ signal was more susceptible to alteration than the $\delta^{13}C$ signal, it is striking that the latter overall shows more variation than the former. (4) It is not demonstrated how co-variation could have resulted from alteration of only one signal. And (5) scenarios such as dissolution and reprecipitation through exposure to ^{18}O-depleted rainwater (Fig. 4.1 has likely examples, all in the

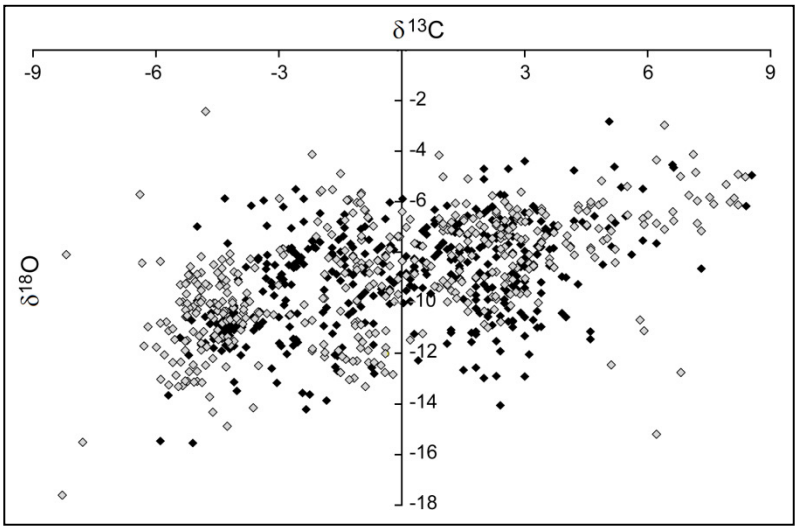

Figure 4.12. Compilation of Tonian and Cryogenian stable-isotope data for which there are also Mg/Ca data. Grey symbols: limestones. Black symbols: dolostones. $\delta^{18}O$ normalised to calcite (-2.7‰ x Mg/Ca ÷ 0.6). Most negative $\delta^{13}C$ samples come from carbonates that cap Cryogenian diamictites.

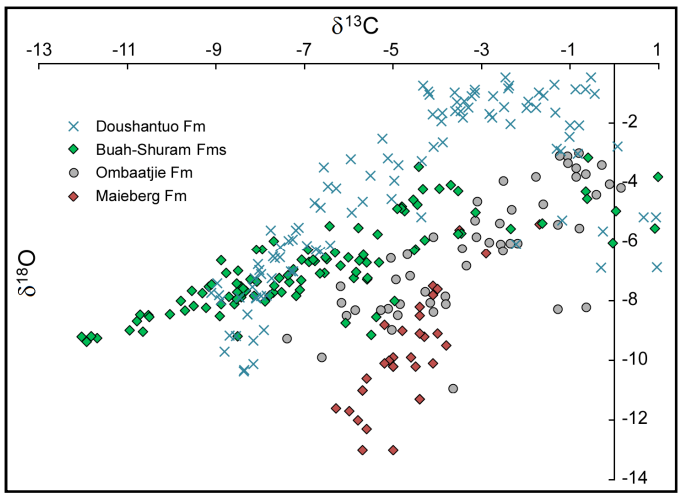

Figure 4.13. Instances of systematic co-variation between $\delta^{13}C$ and $\delta^{18}O$ (the latter normalised to calcite) as $\delta^{13}C$ becomes more negative. Formations range from latest Cryogenian to Ediacaran (650–550 Ma).

positive δ_{carb} range) or through exposure to high-temperature fluids after burial cannot explain why only deeper-water deposits were affected. In this respect, the proposed link between $\delta^{13}C$ and sea-level adds something new to the debate.

Oxygen-isotope ratios are also affected by alkalinity. At intermediate pH DIC consists mainly of HCO_3^-, which has a higher $\delta^{18}O$ than CO_3^{2-}; at higher pH CO_3^{2-} is the dominant species (Zeebe 2007, Fig. 4.9). Provided that the precipitate forms from carbonate and bicarbonate in the same proportion as they occur in the DIC, the oxygen isotopic composition of the precipitate will decrease as pH increases. Alkalinity and $\delta^{18}O$ inversely correlate.

Increasing alkalinity as δ_{carb} became more negative can be ruled out, because the zone most characteristic of carbonate precipitation was the shallow zone, where δ_{carb} was 1–3‰. Likewise, the index based on within-carbonate Si (§2.7.3, §3.5.3) suggests that alkalinity was almost as high at δ_{carb} -5‰ as at +2‰. Since evaporation and meteoric contamination can also be ruled out, the only remaining possibility among known controls is that the decrease in $\delta^{18}O$ reflected an increase in temperature. Large concentrations of dissolved Fe in the subsurface created a strong density contrast whereby warmer water was less buoyant than cooler water. Owing to higher rates of ocean crust production – a necessary corollary of the more vigorous outgassing underlying higher pCO_2 – the deeper ocean was thermally stratified (cf. Blake et al. 2010 for the Archaean).

The archetypal profile of the oxygen-isotope system can then be interpreted as passing through three zones: (1) the outer shelf ($\delta^{13}C$ < -3‰), where the $\delta^{18}O$ signal was dominated by temperature, (2) a middle zone (($\delta^{13}C$ > -3, < +3‰), where the signal overall was flat, and (3) an inner zone ($\delta^{13}C$ > +3‰), where the predominant control on $\delta^{18}O$ was evaporation. In some situations, hydrothermal input (Fig. 4.14) could depress middle-zone values, and meteoric diagenesis (Fig. 4.1) overwrite the inner zone's enriched values.

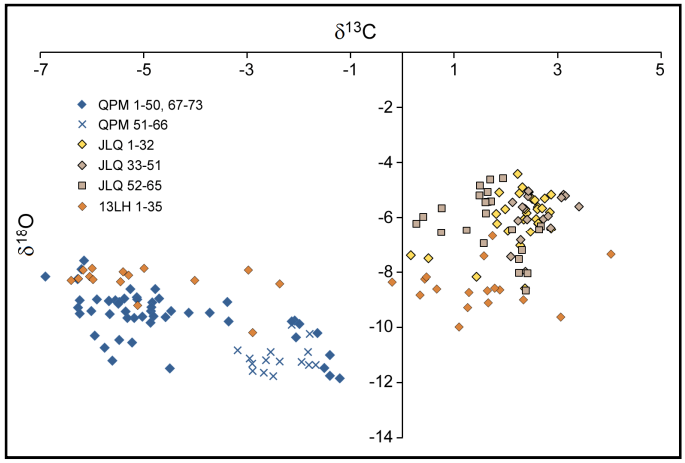

Figure 4.14. $\delta^{18}O$ (normalised to calcite) as a function of carbonate $\delta^{13}C$ in the Yingchenzi, Shisanlitai, Majiatun, Jiuliqiao and Sidingshan Formations. Carbonate precipitating in deeper water was depleted in ^{18}O.

4.9. Implications

4.9.1. *$\delta^{13}C$ as a proxy for sea-level*

Arguably there is no such thing as a stable continental platform (Moucha et al. 2008). In a world without ice, sea-level change is driven by tectonics, and the recurrent shallowing-up cycles that characterise long-term stratigraphic sequences reflect fluctuations in the buoyancy of the continental lithosphere. Few major negative excursions of $\delta^{13}C$ and $\delta^{18}O$ occurred on Mesoproterozoic platforms because, in most parts of the world, the tectonic regime was then relatively quiescent and fluctuations in sea-level minor. Deep-water shales were rarely preserved because few rift basins formed in which to preserve them and, because of low levels of erosion and nutrient supply, little OC was buried. As cratons came together in the later part of the Mesoproterozoic, the situation began to change: crustal thickening and buoyancy lowered sea-levels, carbonate platforms shrank and δ_{carb} shifted to higher values. Deep-water shales remained uncommon until the Neoproterozoic.

In the mid Neoproterozoic the supercontinent began to rift, and episodes of deepening led to dramatic expansions of the δ_{carb} range. The amplitude of excursions increased as nearshore carbonate platforms extracted more ^{13}C and topographic gradients became more pronounced. Sequences far apart had similar $\delta^{13}C$ profiles because such fluctuations were occurring synchronously across more than one craton. Asymmetric second- and third-order cycles, commonly starting with conglomerates or pronounced flooding surfaces, each reflected a build-up of heat and pressure in the mantle which elevated the continental lithosphere until pressure was released by faulting or flood volcanism. Pulsatory flow in mantle convection cells may also have contributed (Lovell 2010).

Major sea-level fall can be caused by glaciation. However, the catastrophic episodes of glaciation posited in the Neoproterozoic were associated with subsidence sufficient to generate large-scale debrites and turbidites, the latter deep-water in character (e.g. Feather et al. 2002). Sedimentation did not retreat to the continental margins. Carbon-isotope values straight after the Sturtian episode, as well as straight after the Marinoan, are mostly negative (e.g. Hoffman & Schrag 2002; Fig. 1.3). The rest of the interval between the Sturtian and Marinoan is characterised by high δ_{carb} and relatively low sea-level. There is no evidence that at the end of the Sturtian sea-level eustatically rose by 500 m, or that at the threshold of the Marinoan it fell by 700 m, as the glaciation hypothesis requires (Liu & Peltier 2013). In the Ediacaran, average δ_{carb} was lower than in the Tonian and Cryogenian. Part of the difference may have been due to a greater proportion of carbonate carbon deriving from recycled organic carbon.

The largest negative excursion of all, the Shuram-Wonoka, occurred near the end of the Neoproterozoic. Like the others, it was associated with sea-level rise. Although the tectonic dislocations associated with it were not as large as in previous such events, the Ediacaran continued to generate substantial mass flow deposits, dropstones, striated clasts and striated pavements, including some at low latitude (Baode et al. 1986, Corkeron & George 2001, Xiao et al. 2004, Alvarenga et al. 2007, Carto & Eyles 2011, Chumakov 2011, Jenkins 2011). The fall in δ_{carb}, the pseudo-glaciations and the 'Cambrian transgresssion' (Algeo & Seslavinsky 1995) were geochemical, sedimentological and stratigraphic aspects of the selfsame revolution. Nonetheless, sea-level change was not globally uniform. While some landmasses continued to disaggregate, others underwent collisions. Not all continents went under water. Those not flooded left only a poor carbonate record, if any (Squire et al. 2006).

The Cambrian was a period of transition. Negative excursions were still, in the main, associated with transgression (Montañez et al. 2000), positive excursions with regression (Saltzman et al. 2000, 2004). The seven successive oscillations in the Sukharikha Formation (Kouchinsky et al. 2007) are almost certainly linked to sea-level, as reflected in matching $\delta^{18}O$ and limestone-dolostone cycles. Overall, on Laurentia at least, also South China, the trend was one of transgression. The greater distance from the ocean isolated nearshore environments from dissolved H_2S and Fe, the principal consumers of oxygen. In the Ordovician, the link with sea-level was weaker than in earlier periods, the water column being largely oxygenated. Only now did animal diversity rise exponentially. The redox structure of the oceans beyond the shelf changed more slowly. Deep-sea oxygenation had to await the rise of terrestrial vegetation (Dahl et al. 2010).

Most Palaeozoic excursions after the mid Ordovician were positive, and isotopic variation from shore to outer shelf probably minor. After the mid Permian δ_{carb} went negative on six occasions. All were associated with ocean warming and with episodes of continental flood volcanism, namely the Emeishan Traps, the Siberian Traps, the Central Atlantic Magmatic Province, the Karoo-Ferrar Province, the Parana-Etendeka Province and the Ontong-Java Plateau. Later falls from positive values to 0‰ also involved massive injection of isotopically light carbon into the exosphere (e.g. Wright & Schaller 2013). In these instances at least, the system was not in balance: δ_{carb} was driven down by an excess of input over output carbon.

4.9.2. *Carbonate $\delta^{13}C$ earlier in the Precambrian*

The high fractionation of average epicratonic ocean DIC in the early Archaean (around 0.5‰ allowing for 1‰ fractionation during precipitation, §4.1) is unlikely to have been representative of the ocean as a whole. The open ocean would have been less ^{13}C-enriched. Data before 2.8 Ga, the

age of the oldest carbonate platforms, are sparse, and complicated by hydrothermal input of mantle CO_2 (Veizer et al. 1989a,b). Fe-poor carbonates in the Isua Supracrustal Belt, possibly forming from shallow water, record $\delta^{13}C$ between -2 and 0‰, contrasting with -6 to -4‰ in Fe-rich carbonates; the same pattern is seen in late Archaean BIFs (Craddock & Dauphas 2011). The Fe-poor, presumably shallow-water crystal fans of the Mosher Carbonate Formation, central Canada, dated to 2.8 Ga, are 2‰ richer (at 2.5‰) than the Fe-rich columnar stromatolites (Fralick & Riding 2015) – nearer 3‰ richer if the dolomite is normalised to calcite. A deep-water siderite sample had a value of -5.6‰. Limestone stromatolites from the Cheshire and Manjeri Formations, Zimbabwe, dated to 2.7 Ga, range from -1.2 to +0.6‰ (Abell et al. 1985), in contrast to calcareous black shales from the Cheshire Formation, deposited in deeper water, which range from -10.2 to -5.1‰ (Hofmann et al. 2001, Thomazo et al. 2013).

The oldest carbonates in the Transvaal Supergroup (~2.6 Ga) embody two shallowing-up cycles separated by a flooding surface and deeper-water shales (Fischer et al. 2009): the first cycle records a rise in $\delta^{13}C$ from -4 to +1‰, the other a rise from -3 to +0.5. At the top of the formation another flooding surface precedes organic-rich pyritic shales and occasional interbeds of carbonate grainstones, interpreted as mass flow deposits. Again, $\delta^{13}C$ rises from -3 to -1‰. Thereafter values fall back to just below 0‰ and remain fairly steady in the following aggradational package. A deepening episode marked by fenestral microbialites and iron formation sees $\delta^{13}C$ once again fall to -3, then return to just below 0‰. The correspondence between sea-level and isotopic change suggests a minimum of -5‰ for open-ocean DIC and 0‰ for the upper water column. Carbonate precipitated mainly at the seafloor. In the later part of the Transvaal succession, facies pass symmetrically from carbonate to iron formation to 'glaciogenic' diamictite to lavas to iron formation and back to carbonate; carbon isotope ratios pass from -0.5‰ in the carbonates to -2.5‰ in calcites of the Kuruman Iron Formation (Beukes et al. 1990) to a nadir of -8‰ in the diamictite (which includes matrix carbonate) back to -1‰ (Polteau et al. 2006).

In NW Australia $\delta^{13}C$ values in the Mount McRae Shale (2.5 Ga) rise from -7‰ to -2‰ through just 40 m as the unit shallows; $\Delta\delta$ also increases (Kaufman et al. 2007). In the terminal-Archaean Boolgeeda Iron Formation thin carbonate-rich beds record values plunging to -6.3‰ (Van Kranendonk 2010) as they pass into the deep-water shales and turbidites of the Kungarra Formation (Powell et al. 1999). In sum, Neoarchaean successions show the same isotopic variability with depth as Neoproterozoic successions.

The most positive of all carbon-isotope excursions, the Lomagundi-Jatuli, beginning after 2.3 Ga and ending around 2.06 Ga (Martin et al. 2013), coincides worldwide with the prevalence of

shallow-water dolostones, evaporites and terrestrial red beds (Melezhik et al. 1999). In the contemporaneous Tulomozero Formation isotope values range from 5 to 17‰: playa carbonates are most enriched, those from the intertidal zone less so (Melezhik et al. 2005). Recently discovered enrichment to values of 8‰ in the Wooly Dolomite of Western Australia extends the Lomagundi-Jatuli event to 2.03 Ga (Bekker et al. 2016); positive $\delta^{13}C$ is associated with high $\delta^{18}O$, indicating evaporative conditions, and the ensuing negative $\delta^{13}C$ associated with transgression. Carbonates with negative values before and after the excursion, chiefly within banded iron formations, represent deeper water. The same pattern is seen in the shales: primary, microspheroidal siderite from the more shoreward facies show higher values (0 ±2‰) than siderite from the basinward, banded facies (-5 to -2.5‰) (Winter & Knauth 1992). In the Francevillian Basin of east-central Gabon, dated to 2.1 Ga, δ_{carb} and $\Delta\delta$ both decrease from the edge to the centre of the basin (Fig. 4.15, Weber & Gauthier-Lafaye 2013). Numerous successions that show comparatively normal δ_{carb} values during the Lomagundi-Jatuli interval (Hayes & Waldbauer 2006) reinforce the point that δ_{carb} varied according to environment.

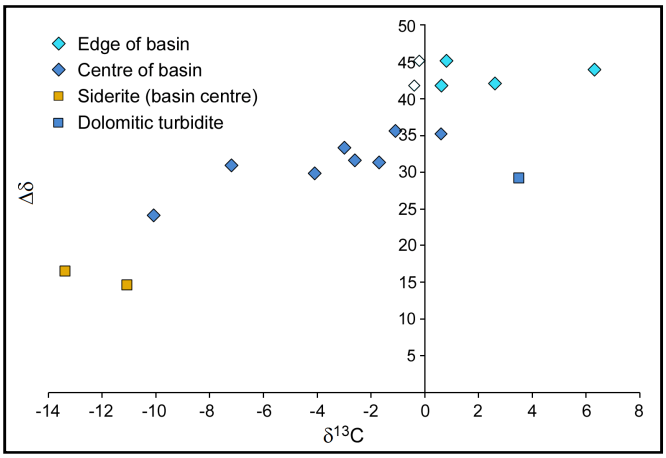

Figure 4.15. Organic fractionation as a function of carbonate $\delta^{13}C$ and independently determined water depth in the Palaeoproterozoic Francevillian Basin, Gabon. The two calcite samples (unfilled diamonds) are normalised to the dolomite by adding 1‰.

Today, most of the carbon not in the mantle is stored on the continents. Since the early Earth lacked continents, originally this carbon must have been distributed in other reservoirs, namely the atmosphere, ocean and ocean floor (Walker 1985). Over time the amount in these reservoirs decreased as the continents grew and ocean floor was subducted. Walker calculated an approximately one hundred-fold decrease. Ongoing hydrothermal alteration of ocean-crust basalt stripped the primordial carbon from the seawater, and eventually this carbon either accreted onto the proto-continents or passed into the mantle. By the end of the Archaean, all early-Archaean DIC (at whatever isotopic value) would have been replaced by outgassing mantle carbon. Since the organic fraction of ocean crust carbon would have been negligible (though not necessarily the absolute amount), the $\delta^{13}C$ of the ocean would have been much lower than on the continents.

Negligible OC burial in ocean crust throughout the Precambrian left the $\delta^{13}C$ of the CO_2 from island and continental arcs the same as that outgassed from mid-ocean ridges. This largely explains why – despite subduction of ocean crust carbon supposedly close to 0‰ – upper mantle carbon through most of history has stayed around -6‰. Over time, the amount of DIC decreased, the ocean became isotopically more homogenised, and average δ_{DIC} increased towards 0‰. The net $\delta^{13}C$ of subducting ocean crust therefore rose, and that of the CO_2 outgassed from island and continental arcs, much of it originating from the slab, likewise rose. Given that, today, a large fraction of the total input comes from arc volcanism, $\delta^{13}C_{in}$ in equation (1) cannot be assumed to approximate the ratio of the upper mantle. Measurements of volcanic $\delta^{13}C$ on land are beginning to confirm this inference (Chiodini et al. 2011, Fischer & Lopez 2016).

4.9.3. *Implications for the history of atmospheric oxygen*

Great 'oxygenation events' are inferred partly on the basis that positive excursions in $\delta^{13}C$ reflect periods of elevated organic carbon burial, allowing more oxygen to accumulate in the atmosphere (Karhu & Holland 1996). In the 'Great Oxidation Event' (GOE) of the Palaeoproterozoic, atmospheric oxygen is calculated to have risen from less than 2% of present level to 10–20%, or even modern levels (Des Marais 1997). Unfortunately for the theory, the evidence of mass-independent fractionation of sulphur isotopes has trumped the evidence of carbon isotopes (Holland 2006), so that the event must be put back to no later than 2.32 Ga, possibly lasting < 10 Ma (Luo et al. 2016) and oxygen levels put even lower (<0.001%). The 'Great Oxidation Event' thus predates the Lomagundi-Jatuli excursion, maximally dated to 2.31–2.06 Ga, and coincides instead with the last of the three Palaeoproterozoic 'glaciations' dated earlier than 2.3 Ga (Rasmussen et al. 2013). The first occurred at the Archaean-Proterozoic boundary, dated to c. 2.45 Ga (Van Kranendonk 2010, Brasier et al. 2013). As the carbon-isotope record accompanying the newly defined GOE is not well known, the possibility of episodic positive excursions cannot be excluded (Bekker & Holland 2012), but a link with the GOE appears tenuous (Lyons et al. 2014). The synchroneity of the perceived glaciations worldwide is also problematic (Hoffman 2013, Young 2014).

There is no geological evidence for enhanced OC burial in the Proterozoic earlier than 2.15 Ga, long after carbonate $\delta^{13}C$ reached record levels. The burial flux climaxed as the positive excursions petered out and sea-levels rose (Melezhik & Fallick 1996, Mossman et al. 2005, Martin et al. 2015). Elevated productivity was a consequence of intensified erosion, weathering and silicate dissolution. Most OC was therefore buried in deep-water shales (Condie et al. 2001). Successions with positive $\delta^{13}C$ were deposited in shallow, relatively well-oxygenated waters and were extremely lean in organic carbon (refs. in Aharon 2005, Bekker et al. 2008).

Throughout the Archaean, the small, but growing, continental crust was mostly under water – possibly as much as 97% by area (Arndt 1998, Flament et al. 2008). In such circumstances, the sedimentary burial of planktonic OC and the amount of reduced minerals exposed to oxidative weathering would have been much lower, with minimal net effect on the atmospheric budget. Evidence that the surface layer of the ocean was oxygenated goes back to 3.2 Ga, supported by the precipitation of calcium carbonate rather than siderite in shallow waters (Fralick & Riding 2015) and elevated U concentrations derived from oxidative weathering of granitic crust (Satkoski et al. 2015, cf. Crowe et al. 2013). Detrital uraninite – traditionally indicating minimal levels of oxygen – formed in tectonically active settings marked by faults and basal unconformities, where the circulating water was acidic because of high pCO_2 and oxygen-poor because it was hot (Kojima et al. 1994, Mukhopadhyay et al. 2016). Throughout the Precambrian concentrations of U were low because submarine environments were alkaline, uraninite being more soluble above pH 5 (Langmuir 1978). In the Palaeoproterozoic they were highest during the Lomagundi-Jatuli period – higher, indeed, than in the Ediacaran (Fig. 4.8).

A second GOE in the Neoproterozoic is also inferred partly on the grounds of carbon isotope stratigraphy (Des Marais et al. 1992, Och & Shields-Zhou 2012). Positive excursions in this era show TOC no higher than when δ_{carb} is normal (Figs. 4.6, 4.8), and other proxies suggest that major oxygenation did not take place until the Ediacaran, when in some regions δ_{carb} fell. In a case of having one's cake and eating it, the most extreme of all negative excursions, the Late Ediacaran Shuram-Wonoka event, is interpreted as reflecting global-scale oxidation of dissolved OC and therefore also as evidencing step-wise oxygenation (Fike et al. 2006, McFadden et al. 2008). Had that been what happened, the huge amounts of carbon dioxide produced would have been accompanied by dramatic climatic warming, ocean acidification, a rise in carbonate $\delta^{18}O$, de-oxygenation of the atmosphere (Bristow & Kennedy 2008) and mass extinction. Such consequences are not seen. Indeed, in China the excursion is accompanied by increasing anoxia (Zhou et al. 2012). The problems dwindle if the negative excursions reflected sea-level rise and were confined to the platforms, and the oxidation of suspended OC was primarily anaerobic. Increasing oxygenation of the water column resulted in higher concentrations of marine sulphate (Halverson & Hurtgen 2007), which promoted the microbial reduction of sulphate and oxidation of OC. The OC was mostly converted into mineral carbonate, not carbon dioxide, and δ_{carb} fell far below mantle values (Fig. 4.12) because more OC was being remineralised than was being produced.

There was some increase in the level of atmospheric oxygen. Shale TOC record cannot be interpreted simply as a proxy for production, because TOC tended to increase with water depth. For

instance, the shallow and mid-depth shales that dominate the Tonian, must have been complemented by more distal shales, which probably had more OC. That said, during the Ediacaran-Cambrian transition cyanobacterial-algal production appears to have more than doubled (Fig. 4.8), stimulated, perhaps, by upwelling of nutrient-rich waters during transgression. Elsewhere, it is likely to have surged in response to nutrients released from sediments shed during the Gondwanan orogenies (Squire et al. 2006, Ganade de Araujo et al. 2014). The Ediacaran and early Palaeozoic also saw a major increase in phytoplankton diversity (Servais et al. 2008). With the area of epicontinental seas itself expanding, more OC was being buried and more oxygen produced, sufficient to overcome the reductive power of seawater rich in Fe^{2+}, sulphide and OC itself. Oxygen partial pressure could have been greater then than it is today.

Aquatic ecosystems tend to exist in one of two states: a turbid low-diversity state dominated by cyanobacteria and characterised by high levels of suspended OC and a redox-stratified water column, or a clear high-diversity state dominated by eukaryotic phytoplankton and characterised by low suspended OC and an aerated, well-mixed water column (Butterfield 2009b). The greater depth of oxygenation can be attributed to eukaryotic particles sinking more rapidly, so that less oxygen is consumed by aerobic remineralisation at the surface. The late Ediacaran-Cambrian may have involved a transition from one state to the other (Lenton et al. 2014), at least close to shore. It may be no coincidence that the incidence of dolomite, which seems to have been favoured by a largely anoxic low-diversity ecosystem (§2.6.4), fell off during the transition.

4.10. Conclusions

Proterozoic epicontinental seas were normally oxic only through the uppermost tens of metres, where cyanobacteria were active. Warm ocean temperatures, high concentrations of carbon and an abundance of nutrients supplied by intense chemical weathering enhanced organic production. Consequent ^{13}C-enrichment of the upper water column was reversed as bacteria remineralised the carbon. Vertically and laterally, the isotopic value of DIC depended on productivity, the proportion of ^{12}C extracted from the water, the balance between HCO_3^- into CO_3^{2-}, and the degree to which remineralised carbon was mixed back into the water. Most remineralisation appears to have occurred above the level at which carbonate precipitated.

In the anoxic zone, carbon was recycled as HCO_3^- rather than CO_2. Coupled with the subaqueous dissolution of alkali feldspars, which released K^+ and Na^+ and converted HCO_3^- into CO_3^{2-}, remineralisation produced an alkalinity gradient. Offshore, pH was high, and DIC consisted mostly of bicarbonate and carbonate. In the absence of CO_2, a species 7‰ lighter than HCO_3^-,

cyanobacteria were obliged to synthesise their carbon from bicarbonate. Organic carbon was heavier and DIC consequently lighter. Nearer to shore, waters were supersaturated in CO_2 and the difference between organic and inorganic $\delta^{13}C$ at a maximum. Although atmospheric pCO_2 was much higher in the Proterozoic, the prevalence of these lateral gradients shows that marine [CO_2] was lower than today and pH higher (> 9).

Calcium carbonate precipitated from the ^{13}C-depleted lower water column and/or pore water and in offshore settings was typically up to 10‰ lighter than in proximal settings. Negative carbon-isotope anomalies were episodes of deepening, positive anomalies episodes of shallowing. Beyond the zone of deep-water shale deposition, productivity was increasingly nutrient-limited and the proportion of organic to inorganic carbon in the sediment decreased. DIC in the open ocean was close to unfractionated, -6‰ marking the normal lower limit. Carbonate $\delta^{13}C$ fell below -6‰ only where OC remineralisation exceeded OC production (as in the Shuram-Wonoka anomaly) or where carbonate formed within OC-rich shale.

Above about +4‰, waters were typically peritidal. DIC became heavier as a consequence of evaporative conditions, which promoted the evasion of lighter forms of CO_2 in preference to heavier forms. Except where dilution by isotopically depleted rain, river water or high-temperature crustal fluids disturbed the pattern, the same effect was reflected in carbonate $\delta^{18}O$.

These being the drivers of carbon-isotope change, models of isotopic mass balance in the Proterozoic need to be re-evaluated. Carbonate $\delta^{13}C$ was not constant from shore to basin and provides no basis for generalisation to the global ocean. On mass balance grounds, average DIC must have been controlled by average organic fractionation and organic carbon burial flux, but particular sediments did not express average DIC. Burial flux was not a major factor in short-term, large-amplitude $\delta^{13}C$ deviations. By the same token, carbon-isotope anomalies cannot be a basis for inferring large fluctuations in levels of atmospheric oxygen.

Possibly enough organic carbon has been measured in carbonate rocks to indicate that the burial flux rose in the lead-up to the Sturtian and the Marinoan diamictite intervals. During the diamictite intervals, the flux fell, but was still comparable with that in the late Tonian Period. Productivity was only moderately disrupted. It varied little in the Ediacaran, when carbonate $\delta^{13}C$ was generally lower. Through the Cambrian and Ordovician, $\delta^{13}C$ became less erratic and the influence of sea-level diminished, as oxygenation progressed downwards through the water column and the redox divide between shallow and deep broke down. Excursions below -4‰ were never to return.

References

Abell, P.I., McClory, J., Martin, A., Nisbet, E.G., 1985. Archaean stromatolites from the Ngesi Group, Belingwe greenstone belt, Zimbabwe; preservation and stable isotopes – preliminary results. *Precambrian Res*. 27, 357--383.

Ader, M. et al., 2009. A multilayered water column in the Ediacaran Yangtze platform? Insights from carbonate and organic matter paired $\delta^{13}C$. *Earth Planet. Sci. Lett.* 213–227.

Agawin, N.S.R., Duarte, C.M., Agustí , S., 2000. Nutrient and temperature control of the contribution of picoplankton to phytoplankton biomass and production. *Limnol. Oceanogr.* 45, 591–600.

Aharon, P., 2005. Redox stratification and anoxia of the early Precambrian oceans: Implications for carbon isotope excursions and oxidation events. *Precambrian Res.* 137, 207–222.

Algeo, T.J., Seslavinsky, K.B., 1995. Reconstructing eustatic and epeirogenic trends from Paleozoic continental flooding records. In: B.U. Haq (ed.), *Sequence Stratigraphy and Depositional Response to Eustatic, Tectonic and Climatic Forcing*, Kluwer Academic Publishers, Dordrecht, pp 209–246.

Allmon, W.D., Martin, R.E., 2014. Seafood through time revisited: the Phanerozoic increase in marine trophic resources and its macroevolutionary consequences. *Paleobiol.* 40, 256–287.

Alvarenga, C.J.S., Figueiredo, M.F., Babinski, M., Pinho, F.E.C., 2007. Glacial diamictites of Serra Azul Formation (Ediacaran, Paraguay Belt): evidence of the Gaskiers glacial event in Brazil. *J. South Am. Earth Sci.* 23, 236–241.

Anagnostou, E. et al., 2016. Changing atmospheric CO_2 concentration was the primary driver of early Cenozoic climate. *Nature* 533, 380–384.

Anderson, L.D., Delaney, M.L., Faul, K.L., 2001. Carbon to phosphorus ratios in sediments: implications for nutrient cycling. *Global Biogeochem. Cycles* 15, 65–79.

Arietta, J.M. et al., 2015. Dilution limits dissolved organic carbon utilization in the deep ocean. *Science* 348, 331–333.

Arndt, N.T., 1998. Why was flood volcanism on submerged continental platforms so common in the Precambrian? *Precambrian Res*. 97, 155–164.

Arndt, S. et al., 2013. Quantifying the degradation of organic matter in marine sediments: A review and synthesis. *Earth-Sci. Rev*. 123, 53–86.

Bambach, R.K., 1993. Seafood through time: changes in biomass, energetics, and productivity in the marine ecosystem. *Paleobiol*. 19, 372–397.

Baode, G., Ruitang, W., Hambrey, M.J., Wuchen, G., 1986. Glacial sediments and erosional pavements near the Cambrian-Precambrian boundary in western Henan Province, China. *J. Geol. Soc. Lond.* 143, 311–323.

Beauchamp, B., Oldershaw, A.E., Krouse, R., 1987. Upper Carboniferous to Upper Permian ^{13}C-enriched primary carbonates in the Sverdrup Basin, Canadian Arctic: comparisons to coeval western North American ocean margins. *Chem. Geol. (Isotope Geosci. Sect.)* 65, 391–413.

Bekker, A., Holland, H.D., 2012. Oxygen overshoot and recovery during the early Paleoproterozoic. *Earth Planet. Sci. Lett.* 317–318, 295–304.

Bekker, A., Krapež, B., Müller, S.G., Karhu, J.A., 2016. A short-term, post-Lomagundi positive C isotope excursion at *c*. 2.03 Ga recorded by the Wooly Dolomite, Western Australia. *J. Geol. Soc. Lond.* 173, 689–700.

Bekker, A. et al., 2008. Fractionation between inorganic and organic carbon during the Lomagundi (2.22–2.1 Ga) carbon isotope excursion. *Earth Planet. Sci. Lett.* 271, 278–291.

Bergmann, K.D., Zentmyer, R.A., Fischer, W.W., 2011. The stratigraphic expression of a large negative carbon isotope excursion from the Ediacaran Johnnie Formation, Death Valley. *Precambrian Res.* 188, 45–56.

Berner, R.A., 1982. Burial of organic carbon and pyrite sulphur in the modern ocean: its geochemical and environmental significance. *Am. J. Sci.* 282, 451–473.

Beukes, N.J., Klein, C., Kaufman, A.J., Hayes, J.M., 1990. Carbonate petrography, kerogen distribution, and carbon and oxygen isotope variation in an early Proterozoic transition from limestone to iron-formation deposition, Transvaal Supergroup, South Africa. *Econ. Geol.* 85, 663–690.

Bidigare, R.R. et al., 1999. Iron-stimulated changes in ^{13}C fractionation and export by equatorial Pacific phytoplankton: Toward a paleogrowth rate proxy. *Paleoceanog.* 14, 589–595.

Bissinger, J.E., Montagnes, D.J.S., Sharples, J., Atkinson, D., 2008. Predicting marine phytoplankton maximum growth rates from temperature: Improving on the Eppley curve using quantile regression. *Limnol. Oceanogr*. 53, 487–493

Bjerrum, C.J., Canfield, D.E., 2004. New insights into the burial history of organic carbon on the early Earth. *Geochem. Geophys. Geosyst.* 5, Q08001.

Blake, R.E., Chang, S.J., Lepland, A., 2010. Phosphate oxygen isotopic evidence for a temperate and biologically active Archaean ocean. *Nature* 464, 1029–1033.

Bold, U. et al., 2016. Neoproterozoic stratigraphy of the Zavkhan Terrane of Mongolia: the backbone for Cryogenian and early Ediacaran chemostratigraphic records. *Am. J. Sci.* 316, 1–63.

Brasier, A.T. et al., 2013. Earth's earliest global glaciation? Carbonate geochemistry and geochronology of the Polisarka Sedimentary Formation, Kola Peninsula, Russia. *Precambrian Res*. 235, 278–294.

Bristow, T.F., Kennedy, M.J., 2008. Carbon isotope excursions and the oxidant budget of the Ediacaran atmosphere and ocean. *Geology* 36, 863–866.

Butterfield, N.J., 2007. Macroevolution and macroecology through deep time. *Palaeontology* 50, 41–55.

Butterfield, N.J., 2009a. Macroevolutionary turnover through the Ediacaran transition: ecological and biogeochemical implications. *Geol. Soc. Lond. Spec. Pub.* 326, 55–66.

Butterfield, N.J., 2009b. Oxygen, animals and oceanic ventilation: an alternative view. *Geobiology* 7, 1–7.

Calver, C.R., 2000. Isotope stratigraphy of the Ediacaran (Neoproterozoic III) of the Adelaide Rift Complex, Australia, and the overprint of water column stratification. *Precambrian Res.* 100, 121–150.

Calvert, S.E. et al., 1991. Low organic carbon accumulation rates in Black Sea sediments. *Nature* 350, 692–695.

Canfield, D.E., Thamdrup, B., Hansen, J.W., 1993. The anaerobic degradation of organic matter in Danish coastal sediments: Iron reduction, manganese reduction, and sulfate reduction. *Geochim. Cosmochim. Acta* 57, 3867–3883.

Cartigny, P. et al., 2001. Volatile (C, N, Ar) variability in MORB and the respective roles of mantle source heterogeneity and degassing: The case of the southwest Indian. *Earth Planet. Sci. Lett*. 194, 241–257.

Carto, S.L., Eyles, N., 2011. The deep-marine glaciogenic Gaskiers Formation, Newfoundland, Canada. In: E. Arnaud, G.P. Halverson, G. Shields-Zhou (eds), *The Geological Record of Neoproterozoic Glaciations*, Geol. Soc. Lond. Mem. 36, 467–473.

Chiodini, G. et al., 2011. First $^{13}C/^{12}C$ isotopic characterisation of volcanic plume CO_2. *Bulletin of Volcanology* 73, 531–542.

Chumakov, N.M., 2011. Glacial deposits of the Bokson Group, East Sayan Mountains, Buryatian Republic, Russian Federation. In: E. Arnaud, G.P. Halverson, G. Shields-Zhou (eds), *The Geological Record of Neoproterozoic Glaciations*, Geol. Soc. Lond. Mem. 36, 285–288.

Clarkson, M.O. et al., 2015. Ocean acidification and the Permo-Triassic mass extinction. *Science* 348, 229–232.

Coltice, N., Simon, L., Lécuyer, C., 2004. Carbon isotype cycle and mantle structure. *Geophys. Res. Lett.* 32, L05603.

Condie, K.C., Des Marais, D.J., Abbott, D., 2001. Precambrian superplumes and supercontinents: a record in black shales, carbon isotopes, and paleoclimates? *Precambrian Res.* 106, 239–260.

Corkeron, M.L., George, A.D. 2001. Glacial incursion on a Neoproterozoic carbonate platform in the Kimberley region, Australia. *GSA Bull*. 113, 1121–1132.

Cox, G.M. et al., 2016. Continental flood basalt weathering as a trigger for Neoproterozoic Snowball Earth. *Earth Planet. Sci. Lett.* 446, 89–99.

Craddock, P.R., Dauphas, N., 2011. Iron and carbon isotope evidence for microbial iron respiration throughout the Archean. *Earth Planet. Sci. Lett.* 303, 121–132.

Crowe, S.A. et al., 2013. Atmospheric oxygenation three billion years ago. *Nature* 501, 535–539.

Cui, H. et al., 2015. Redox architecture of an Ediacaran ocean margin: Integrated chemostratigraphic ($\delta^{13}C$–$\delta^{34}S$–$^{87}Sr/^{86}Sr$–Ce/Ce*) correlation of the Doushantuo Formation, South China. *Chem. Geol.* 405, 48–62.

Cullen, J.J., 2015. Subsurface chlorophyll maximum layers: enduring enigma or mystery solved? *Annu. Rev. Mar. Sci.* 7, 207–239.

Dahl, T.W. et al., 2010. Devonian rise in atmospheric oxygen correlated to the radiations of terrestrial plants and large predatory fish. *Proc. Nat. Acad. Sci. USA* 107, 17911–17915.

Day, E.S., James, N.P., Narbonne, G.M., Dalrymple, R.W., 2004. A sedimentary prelude to Marinoan glaciation, Cryogenian (Middle Neoproterozoic) Keele Formation, Mackenzie Mountains, northwestern Canada. *Precambrian Res*. 133, 223–247.

De Boyer Montégut, C., Madec, G., Fischer, A.S., Lazar, A., Ludicone, D., 2004. Mixed layer depth over the global ocean: An examination of profile data and a profile-based climatology. *J. Geophys. Res.,* 109, C12003.

Deines, P., 2002. The carbon isotope geochemistry of mantle xenoliths. *Earth-Sci. Rev.* 58, 247–278.

Derry, L.A., 2010. A burial diagenesis origin for the Ediacaran Shuram-Wonoka carbon isotope anomaly. *Earth Planet. Sci. Lett*. 294, 152–162.

Des Marais, D.J., 1997. Isotopic evolution of the biogeochemical carbon cycle during the Proterozoic Eon. *Org. Geochem*. 27, 185–193.

Des Marais, D.J., Strauss, H., Summons, R.E., Hayes, J.M., 1992. Carbon isotope evidence for the stepwise oxidation of the Proterozoic environment. *Nature* 359, 605–609.

Deuser, W.G., Degens, E.T., Guillard, R.R.L., 1968. Carbon isotope relationships between plankton and sea water. *Geochim. Cosmochim. Acta* 32, 657–660.

Estep, M.L.F., 1984. Carbon and hydrogen isotopic compositions of algae and bacteria from hydrothermal environments, Yellowstone National Park. *Geochim. Cosmochim. Acta* 48, 591–599.

Fairchild, I.J., Hambrey, M.J., 1995. Vendian basin evolution in East Greenland and NE Svalbard. *Precambrian Res.* 73, 217–233.

Feather, J., Allen, P.A., Brazier, M.D., Cozzi, A., 2002. Neoproterozoic snowball Earth under scrutiny: Evidence from the Fiq glaciation of Oman. *Geology* 30, 891–894.

Fike, D.A., Grotzinger, J.P., Pratt, L.M., Summons, R.E., 2006. Oxidation of the Ediacaran Ocean. *Nature* 444, 744–747.

Fischer, T.P., Lopez, T.M., 2016. First airborne samples of a volcanic plume for $\delta^{13}C$ of CO_2 determinations. *Geophys. Res. Lett.* 43, doi:10.1002/2016GL068499.

Fischer, W.W. et al., 2009. Isotopic constraints on the Late Archean carbon cycle from the Transvaal Supergroup along the western margin of the Kaapvaal Craton, South Africa. *Precambrian Res.* 169, 15–27.

Flament, N., Coltice, N., Rey, P.F., 2008. A case for late-Archaean continental emergence from thermal evolution models and hypsometry. *Earth Planet. Sci. Lett.* 275, 326–336.

Fralick, P., Riding, R., 2015. Steep Rock Lake: Sedimentology and geochemistry of an Archean carbonate platform. *Earth-Sci. Rev.* 151, 132–175.

Frimmel, H.E., 2010. On the reliability of stable carbon isotopes for Neoproterozoic chemostratigraphic correlation. *Precambrian Res.* 182, 239–253.

Froelich, P.N. et al., 1979. Early oxidation of organic matter in pelagic sediments of the eastern equatorial Atlantic: suboxic diagenesis. *Geochim. Cosmochim. Acta* 43, 1075–1090.

Fu, F.X. et al., 2008. Interactions between changing pCO_2, N_2 fixation, and Fe limitation in the marine unicellular cyanobacterium *Crocosphaera*. *Limnol. Oceanogr*. 53, 2472–2484.

Ganade de Araujo, C.E. et al., 2014. Ediacaran 2,500-km-long synchronous deep continental subduction in the West Gondwana Orogen. *Nature Comm.* 5:5198, doi: 10.1038/ncomms6198.

Garrels, R.M., Thompson, M.E., 1962. A chemical model for sea water at 25°C and one atmosphere total pressure. *Am. J. Sci.* 260, 57–66.

Giddings, J.A., Wallace, M.W., 2009a. Sedimentology and C-isotope geochemistry of the 'Sturtian' cap carbonate, South Australia. *Sediment. Geol.* 216, 1–14.

Giddings, J.A., Wallace, M.W., 2009b. Facies-dependent $\delta^{13}C$ variation from a Cryogenian platform margin, South Australia: Evidence for stratified Neoproterozoic oceans? *Palaeogeogr. Palaeocl.* 271, 196–214.

Giddings, J.A., Wallace, M.W., Haines, P.W., Mornane, K., 2010. Submarine origin for the Neoproterozoic Wonoka canyons, South Australia. *Sed. Geol.* 223, 35–50.

Gieskes, W.W.C., Laane, R.W.P.M, Ruardij, P., 2015. Photo-oxidation: Major sink of oxygen in the ocean surface layer. *Mar. Chem.* 177, 472–475.

Gillis, K.M., Coogan, L.A., 2011. Secular variation in carbon uptake into the ocean crust. *Earth Planet. Sci. Lett.* 302, 385–392.

Gischler, E., Swart, P.K., Lomando, A.J., 2009. Stable isotopes of carbon and oxygen in modern sediments of carbonate platforms, barrier reefs, atolls and ramps: patterns and implications. *Int. Assoc. Sedimentol. Spec. Publ.* 41, 61–74.

Given, R.K., Lohmann, K.C., 1985. Derivation of the original isotopic composition of Permian marine cements. *J. Sediment. Petrol.* 55, 430–439.

Goericke, R., Fry, B., 1994. Variations of marine plankton $\delta^{13}C$ with latitude, temperature, and dissolved CO_2 in the world ocean. *Global Biogeochem. Cy.* 8, 85–90.

Green, J., 1959. Geochemical table of the elements for 1959. *GSA Bulletin* 70, 1127–1184.

Grotzinger, J.P., Fike, D.A., Fischer, W.W., 2011. Enigmatic origin of the largest-known carbon isotope excursion in Earth's history. *Nature Geosci*. 4, 285–292.

Grotzinger, J.P., Knoll, A.H., 1995. Anomalous carbonate precipitates: is the Precambrian the key to the Permian? *Palaios* 10, 578–596.

Halverson, G.P., Hoffman, P.F., Schrag, D.P., Kaufman, A.J., 2002. A major perturbation of the carbon cycle before the Ghaub glaciation (Neoproterozoic) in Namibia: Prelude to snowball Earth? *Geochem., Geophys., Geosyst.* 3, 10.1029/2001GC000244.

Halverson, G.P., Hoffman, P.F., Schrag, D.P., Maloof, A.C., Rice, A.H.N., 2005. Towards a Neoproterozoic composite carbon isotope record. *GSA Bull*. 117, 1181–1207.

Halverson, G.P., Hurtgen, M.T., 2007. Ediacaran growth of the marine sulfate reservoir. *Earth Planet. Sci. Lett.* 263, 32–44.

Halverson, G.P., Maloof, A.C., Hoffman, P.F., 2004. The Marinoan glaciation (Neoproterozoic) in northeast Svalbard. *Basin Res.* 16, 297–324.

Halverson, G.P., Dudás, F.Ö., Maloof, A.C., Bowring, S.A., 2007. Evolution of the $^{87}Sr/^{86}Sr$ composition of Neoproterozoic seawater. *Palaeogeogr. Palaeocl*. 256, 103–129.

Halverson, G.P., Wade, B.P., Hurtgen, M.T., Barovich, K.M. 2010. Neoproterozoic chemostratigraphy. *Precambrian Res*. 182, 337–350.

Hayes, J.M., Strauss, H., Kaufmann, A.J., 1999. The abundance of ^{13}C in marine organic matter and isotopic fractionation in the global biogeochemical cycle of carbon during the past 800 Ma. *Chem. Geol.* 161, 103–125.

Hayes, J.M., Waldbauer, J.R., 2006. The carbon cycle and associated redox processes through time. *Phil. Trans. R. Soc. B* 361, 931–950.

Higgins, J.A., Fischer, W.W., Schrag, D.P., 2009. Oxygenation of the ocean and sediments: Consequences for the seafloor carbonate factory. *Earth Plan. Sci. Lett.* 284, 25–33.

Hinga, K.R., Arthur, M.A., Pilson, M.E.Q., Whitaker, D., 1994. Carbon isotope fractionation by marine phytoplankton in culture: The effects of CO_2 concentration, pH, temperature, and species. *Global Biogeochem. Cy.* 8, 91–102.

Hoffman, P.F., 2011. Strange bedfellows: glacial diamictite and cap carbonate from the Marinoan (635 Ma) glaciation in Namibia. *Sedimentology* 58, 57–119.

Hoffman, P.F., 2013. The Great Oxidation and a Siderian snowball Earth: MIF-S based correlation of Paleoproterozoic glacial epochs. *Chem. Geol.* 362, 143–156.

Hoffman, P.F., Halverson, G.P., 2008. Otavi Group of the western Northern Platform, the eastern Kaoko Zone and the western Northern Margin Zone. In: R.M. Miller (ed.), *The Geology of Namibia, Vol. 2*, Ministry of Mines and Energy, Windhoek, pp 13-69–13-135.

Hoffman, P.F., Schrag, D.P., 2002. The Snowball Earth hypothesis: testing the limits of global change. *Terra Nova* 14, 129–155.

Hoffman, P.F. et al., 2012. Cryogenian glaciations on the southern tropical paleomargin of Laurentia (NE Svalbard and East Greenland), and a primary origin for the upper Russøya (Islay) carbon isotope excursion. *Precambrian Res.* 206–207, 137–158.

Hofmann, A., Dirks, P.H.G.M., Jelsma, H.A., 2001. Late Archaean foreland basin deposits, Belingwe greenstone belt, Zimbabwe. *Sed. Geol.* 141–142, 131–168.

Holland, H.D., 2006. The oxygenation of the atmosphere and oceans. *Phil. Trans. R. Soc. B* 361, 903–915.

Hollander, D.J., Smith, M.A., 2001. Microbially mediated carbon cycling as a control on the $\delta^{13}C$ of sedimentary carbon in eutrophic Lake Mendota (USA): new models for interpreting isotopic excursions in the sedimentary record. *Geochim. Cosmochim. Acta* 65, 4321–4337.

Holmden, C., Creaser, R.A., Muehlenbachs, K., Leslie, S.A., Bergström, S.M., 1998. Isotopic evidence for geochemical decoupling between ancient epeiric seas and bordering oceans: implications for secular curves. *Geology* 26, 567–570.

Horita, J., 2014. Oxygen and carbon isotope fractionation in the system dolomite–water–CO_2 to elevated temperatures. *Geochim. Cosmochim. Acta*, 129, 111–124.

Huang, J. et al., 2013. The sulfur isotope signatures of Marinoan deglaciation captured in Neoproterozoic shallow-to-deep cap carbonate from South China. *Precambrian Res*. 238, 42–51.

Hunt, J.M., 1972. Distribution of carbon in crust of Earth: geological notes. *AAPG Bull*. 56, 2273–2277.

Husson, J.M., Maloof, A.C., Schoene, B., 2012. A syn-depositional age for Earth's deepest $\delta^{13}C$ excursion required by isotope conglomerate tests. *Terra Nova* 24, 318–325.

Husson, J.M., Maloof, A.C., Schoene, B., Chen, C.Y., Higgins, J.A., 2015. Stratigraphic expression of Earth's deepest $\delta^{13}C$ excursion in the Wonoka Formation of South Australia. *Am. J. Sci*. 315, 1–45.

Jarvis, I., Lignum, J.S., Gröcke, D.R., Jenkyns, H.C., Pearce, M.A., 2011. Black shale deposition, atmospheric CO_2 drawdown, and cooling during the Cenomanian-Turonian Oceanic Anoxic Event. *Paleoceanog*. 26, PA3201.

Jenkins, R.J.F., 2011. Billy Springs glaciation, South Australia. In: E. Arnaud, G.P. Halverson, G. Shields-Zhou (eds), *The Geological Record of Neoproterozoic Glaciations*, Geol. Soc. Lond. Mem. 36, 693–699.

Jiang, G., Kaufman, A.J., Christie-Blick, N.J., Zhang, S., Wu, H., 2007. Carbon isotope variability across the Ediacaran Yangtze platform in South China: implications for a large surface-to-deep ocean $\delta^{13}C$ gradient. *Earth Planet. Sci. Lett*. 361, 303–320.

Jiang, G. et al., 2010. Organic carbon isotope constraints on the dissolved organic carbon (DOC) reservoir at the Cryogenian–Ediacaran transition. *Earth Planet. Sci. Lett*. 299, 159–168.

Jiao, N. et al., 2010. Microbial production of recalcitrant dissolved organic matter: long-term carbon storage in the global ocean. *Nature Rev. Microbiol.* 8, 593–599.

John, E. H., Wilson, J.D., Pearson, P.N., Ridgwell, A., 2014. Temperature-dependent remineralization and carbon cycling in the warm Eocene oceans. *Palaeogeogr. Palaeocl*. 413, 158–166.

Johnston, D.T., Wolfe-Simon, F., Pearson, A., Knoll, A.H., 2009. Anoxygenic photosynthesis modulated Proterozoic oxygen and sustained Earth's middle age. *Proc. Nat. Acad. Sci. USA* 106, 16925–16929.

Johnston, D.T., Macdonald, F.A., Gill, B.C., Hoffman, P.F., Schrag, D.P., 2012. Uncovering the Neoproterozoic carbon cycle. *Nature* 483, 320–324.

Kah, L.C., Bartley, J.K., Teal, D.A., 2012. Chemostratigraphy of the Late Mesoproterozoic Atar Group, Taoudeni Basin, Mauritania: Muted isotopic variability, facies correlation, and global isotopic trends. *Precambrian Res*. 200–203, 82–103.

Kano, A. et al., 2011. Evolution of animal multicellularity stimulated by dissolved organic carbon in early Ediacaran ocean: DOXAM hypothesis. *Island Arc* 20, 280–293.

Karhu, J.A., Holland, H.D., 1996. Carbon isotopes and the rise of atmospheric oxygen. *Geology* 24, 867–870.

Kaufman, A.J., Hayes, J.M., Knoll, A.H., Germs, G.J.B., 1991. Isotopic compositions of carbonates and organic carbon from upper Proterozoic successions in Namibia: stratigraphic variation and the effects of diagenesis and metamorphism. *Precambrian Res.* 49, 301–327.

Kaufman, A.J., Knoll, A.H., 1995. Neoproterozoic variation in the *C*-isotopic compositions of seawater: stratigraphic and biogeochemical implications. *Precambrian Res.* 73, 27–49.

Kaufman, A.J., Knoll, A.H., Narbonne, G.M., 1997. Isotopes, ice ages, and terminal Proterozoic earth history. *Proc. Nat. Acad. Sci. USA* 94, 6600–6605.

Kaufman, A.J. et al., 2007. Late Archean biospheric oxygenation and atmospheric evolution. *Science* 317, 1900–1903.

Kennedy, M.J., Christie-Blick, N., Prave, A.R., 2001. Carbon isotopic composition of Neoproterozoic glacial carbonates as a test of paleoceanographic models for snowball Earth phenomena. *Geology* 29, 1135–1138.

Klemme, H.D., Ulmishek, G.F. 1991. Effective petroleum source rocks of the world: stratigraphic distribution and controlling distributional factors. *AAPG Bull.* 75, 1809–1851.

Knauth, L.P., 2005. Temperature and salinity history of the Precambrian ocean: implications for the course of microbial evolution. *Palaeogeogr. Palaeocl*. 219, 53–69.

Knoll, A.H., Hayes, J.M., Kaufman, A.J., Swett, K., Lambert, I.B., 1986. Secular variation in carbon isotope ratios from Upper Proterozoic successions in Svalbard and East Greenland. *Nature* 321, 832–838.

Kojima, S., Takeda, S., Kogita, S., 1994. Chemical factors controlling the solubility of uraninite and their significance in the genesis of unconformity-related uranium deposits. *Mineral. Deposita* 29, 353–360.

Konhauser, K.O., Kappler, A., Roden, E.E., 2011. Iron in microbial metabolisms. *Elements* 7, 89–93.

Könitzer, S.F., Leng, M.J., Davies, S.J., Stephenson, M.H., 2012. An assessment of geochemical preparation methods prior to organic carbon concentration and carbon isotope ratio analyses of fine-grained sedimentary rocks. *Geochem. Geophys. Geosys.* 13, Q0AI02.

Kouchinsky, A. et al., 2007. Carbon isotope stratigraphy of the Precambrian-Cambrian Sukharikha River section, northwestern Siberian platform. *Geol. Mag.* 144, 1–10.

Kroopnick, P.M., 1985. The distribution of ^{13}C in ΣCO_2 in the world oceans. *Deep-Sea Res.* 32, 57–84.

Langmuir, D., 1978. Uranium mineral-solution equilibria at low temperatures with applications to sedimentary ore deposits. *Geochim. Cosmochim. Acta* 42, 547–569.

Le Guerroué, E., Allen, P.A., Cozzi, A., 2006. Chemostratigraphic and sedimentological framework of the largest negative carbon isotopic excursion in Earth history: The Neoproterozoic Shuram Formation (Nafun Group, Oman). *Precambrian Res.* 146, 68–92.

Le Guerroué, Cozzi, A., 2010. Veracity of Neoproterozoic negative C-isotope values: The termination of the Shuram negative excursion. *Gondwana Res.* 17, 653–661.

Lécuyer, C. et al., 2012. Carbon and oxygen isotope fractionations between aragonite and calcite of shells from modern molluscs. *Chem. Geol.* 332-333, 92–101.

Lee, C., 1992. Controls on organic carbon preservation: The use of stratified water bodies to compare intrinsic rates of decomposition in oxic and anoxic systems. *Geochim. Cosmochim. Acta* 56, 3323–3335.

Lenton, T.M., Boyle, R.A., Poulton, S.W., Shields-Zhou, G.A., Butterfield, N.J., 2014. Co-evolution of eukaryotes and ocean oxygenation in the Neoproterozoic era. *Nature Geosci.* 7, 257–255.

Lewan, M.D., 1986. Stable carbon isotopes of amorphous kerogens from Phanerozoic sedimentary rocks. *Geochim. Cosmochim. Acta* 50, 1583–1591.

Liang, J.H. et al., 2013. Parameterizing bubble-mediated air-sea gas exchange and its effect on ocean ventilation. *Global Biogeochem. Cy.* 27, 894–905.

Liu, Y., Peltier, W.R., 2013. Sea level variations during snowball Earth formation: 1. A preliminary analysis. *J. Geophys. Res. Solid Earth* 118, 4410–4425.

Logan, G.A., Hayes, J.M., Hieshima, G.B., Summons, R.E., 1995. Terminal Proterozoic reorganization of biogeochemical cycles. *Nature* 376, 53–56.

Lovell, B., 2010. A pulse in the planet: regional control of high-frequency changes in relative sea by mantle convection. *J. Geol. Soc., Lond*. 167, 637–648.

Lu, M. et al., 2013. The DOUNCE event at the top of the Ediacaran Doushantuo Formation, South China: Broad stratigraphic occurrence and non-diagenetic origin. *Precambrian Res.* 225, 86–109.

Luo, G. et al., 2014. Shallow stratification prevailed for ~1700 to ~1300 Ma ocean: Evidence from organic carbon isotopes in the North China Craton. *Earth Planet. Sci. Lett.* 400, 219–232.

Luo, G. et al., 2016. Rapid oxygenation of Earth's atmosphere 2.33 billion years ago. *Sci. Adv*. 2, e1600134.

Lyons, T.W., Reinhard, C.T., Planavsky, N.J., 2014. The rise of oxygen in Earth's early ocean and atmosphere. *Nature* 506, 307–315.

Lynch-Stieglitz, J., Stocker, T.F., Broecker, W.S., Fairbanks, R.G., 1995. The influence of air-sea exchange on the isotopic composition of oceanic carbon: Observations and modelling. *Global Biogeochem. Cy.* 9, 653–665.

Macdonald, F.A., Jones, D.S., Schrag, D.P., 2009. Stratigraphic and tectonic implications of a newly discovered glacial diamictite–cap carbonate couplet in southwestern Mongolia. *Geology* 37, 123–126.

Macdonald, F.A., Strauss, J.V., Rose, C.V., Dudas, F.O., Schrag, D.P., 2010. Stratigraphy of the Port Nolloth Group of Namibia and South Africa and implications for the age of Neoproterozoic iron formations. *Am. J. Sci.* 310, 862–888.

Macdonald, F.A. et al., 2013. The stratigraphic relationship between the Shuram carbon isotope excursion, the oxygenation of Neoproterozoic oceans, and the first appearance of the Ediacara biota and bilaterian trace fossils in northwestern Canada. *Chem. Geol.* 362, 250–272.

Martin, A.P., Condon, D.J., Prave, A.R., Lepland, A., 2013. A review of temporal constraints for the Palaeoproterozoic large, positive carbonate carbon isotope excursion (the Lomagundi–Jatuli Event). *Earth-Sci. Rev.* 127, 242–261.

Martin, A.P. et al., 2015. Multiple Palaeoproterozoic carbon burial episodes and excursions. *Earth Planet. Sci. Lett.* 424, 226–236.

Mattey, D.P., Carr, R.H., Wright, I.P., Pillinger, C.T., 1984. Carbon isotopes in submarine basalts. *Earth Planet. Sci. Lett.* 70, 196–206.

McFadden, K.A et al., 2008. Pulsed oxidation and biological evolution in the Ediacaran Doushantuo Formation. *Proc. Nat. Acad. Sci. USA* 105, 3197–3202.

McKirdy, D.M. et al., 2001. A chemostratigraphic overview of the late Cryogenian interglacial sequence in the Adelaide Fold-Thrust Belt, South Australia. *Precambrian Res.* 106, 149–186.

Melezhik, V.A., Fallick, A.E., 1996. A widespread positive $d^{13}C_{carb}$ anomaly at around 2.33–2.06 Ga on the Fennoscandian Shield: a paradox? *Terra Nova* 8, 141–157.

Melezhik, V.A., Fallick, A.E., Medvedev, P.V. et al., 1999. Extreme $^{13}C_{carb}$ enrichment in ca. 2.0 Ga magnesite-stromatolite-dolomite-'red beds' association in a global context: a case for the world-wide signal enhanced by a local environment. *Earth-Sci. Rev*. 48, 71–120.

Melezhik, V.A., Fallick, A.E., Rychanchik, D.V., Kuznetsov, A.B., 2005. Palaeoproterozoic evaporites in Fennoscandia: Implications for seawater sulphate, $\delta^{13}C$ excursions and the rise of atmospheric oxygen. *Terra Nova* 17, 141–148.

Melezhik, V.A., Pokrovsky, B.G., Fallick, A.E., Kuznetsov, A.B., Bujakaite, M.I., 2009. Constraints on $^{87}Sr/^{86}Sr$ of Late Ediacaran seawater: insight from Siberian high-Sr limestones. *J. Geol. Soc. Lond.* 166, 183–191.

Meng, F. et al., 2011. Ediacaran seawater temperature: Evidence from inclusions of Sinian halite. *Precambrian Res.* 184, 63–69.

Meyers, P.A., 2014. Why are the ^{13}Corg values in Phanerozoic black shales more negative than in modern marine organic matter? *Geochem. Geophys. Geosys.* 15, 3085–3106.

Milliman, J.D., 1992. Production and accumulation of calcium carbonate in the ocean: Budget of a nonsteady state. *Global Biogeochem. Cy.* 7, 927–957.

Montañez, I.P., Osleger, D.A., Banner, J.L., Mack, L.E., Musgrove, M., 2000. Evolution of the Sr and C isotope composition of Cambrian oceans. *GSA Today* 10, 1–7.

Mook, W.G., Bommerson, J.C., Staverman, W.H., 1974. Carbon isotope fractionation between dissolved bicarbonate and gaseous carbon dioxide. *Earth Planet. Sci. Lett.* 22, 169–172.

Mossman, D.J., Gauthier-Lafaye, F., Jackson, S.E., 2005. Black shales, organic matter, ore genesis and hydrocarbon generation in the Paleoproterozoic Franceville Series, Gabon. *Precambrian Res.* 137, 253–272.

Moucha, R. et al., 2008. Dynamic topography and long-term sea-level variations: There is no such thing as a stable continental platform. *Earth Planet. Sci. Lett.* 271, 101–108.

Mukhopadhyay, J., Mishra, B., Chakrabarti, K., De, S., Ghosh, G., 2016. Uraniferous paleoplacers of the Mesoarchean Mahagiri Quartzite, Singhbhum craton, India: Depositional controls, nature and source of > 3.0 Ga detrital uraninites. *Ore Geol. Rev.* 72, 1290–1306.

Nakamura, K., Kato, Y., 2007. Carbonatization of oceanic crust by the seafloor hydrothermal activity and its significance as a CO_2 sink in the Early Archean. *Geochim. Cosmochim. Acta* 68, 595-4618.

Och, L.M., Shields-Zhou, G.A., 2012. The Neoproterozoic oxygenation event: Environmental perturbations and biogeochemical cycling. *Earth-Sci. Rev.* 110, 26–57.

Oehlert, A.M. et al., 2011. The stable carbon isotopic composition of organic material in platform derived sediments: implications for reconstructing the global carbon cycle. *Sedimentology* 59, 319–335.

Opdyke, B.N., Wilkinson, B.H., 1993. Carbonate mineral saturation state and cratonic limestone accumulation. *Am. J. Sci.* 293, 217–234.

Patterson, W.P., Walter, L.M., 1994. Depletion of ^{13}C in seawater $\sum CO_2$ on modern carbonate platforms: Significance for the carbon isotopic record of carbonates. *Geology* 22, 885–888.

Pawlowska, M.M., Butterfield, N.J., Brocks, J.J., 2013. Lipid taphonomy in the Proterozoic and the effect of microbial mats on biomarker preservation. *Geology* 41, 103–106.

Pelechaty, S. M., 1998. Integrated chronostratigraphy of the Vendian System of Siberia: implications for a global stratigraphy. *J. Geol. Soc. Lond.* 155, 957–973.

Peters, S.E., Gaines, R.R., 2012. Formation of the 'Great Unconformity' as a trigger for the Cambrian explosion. *Nature* 484, 363–366.

Pimenov, N.V., Lunina, O.N., Prusakova, T.S., Rusanov, I.I., Ivanov, M.V., 2008. Biological fractionation of stable carbon isotopes at the aerobic/anaerobic water interface of meromictic water bodies. *Microbiology* 77, 751–759.

Planavsky, N.J. et al., 2010. The evolution of the marine phosphate reservoir. *Nature* 467, 1088–1090.

Pokrovskii, B.G., Melezhik, V.A., Bujakaite, M.I., 2006. Carbon, oxygen, strontium, and sulfur isotopic compositions in Late Precambrian rocks of the Patom Complex, Central Siberia: Communication 1. Results, isotope stratigraphy, and dating problems. *Lithol. Min. Resources* 41, 450–474.

Polteau, S., Moore, J.M., Tsikos, H., 2006. The geology and geochemistry of the Palaeoproterozoic Makganyene diamictite. *Precambrian Res.* 148, 257–274.

Popp, B.N., Takigiku, R., Hayes, J.M., Louda, J.W., Baker, E.W., 1989. The post-Paleozoic chronology and mechanism of ^{13}C-depletion in primary marine organic matter. *Am. J. Sci.* 289, 436–454.

Popp, B.N. et al., 1998. Effect of phytoplankton cell geometry on carbon isotopic fractionation. *Geochim. Cosmochim. Acta* 62, 69–77.

Porter, S.M., Knoll, A.H., Affaton, P., 2004. Chemostratigraphy of Neoproterozoic cap carbonates from the Volta Basin, West Africa. *Precambrian Res.* 130, 99–112.

Potter, J., Siermann, M.G., Tsypukov, M., 2004. Large-scale carbon isotope fractionation in evaporites and the generation of extremely ^{13}C-enriched methane. *Geology* 32, 533–536.

Powell, C.M., Oliver, N.H.S., Li, Z.X., Martin, D.M., Ronaszeki, J., 1999. Synorogenic hydrothermal origin for giant Hamersley iron oxide ore bodies. *Geology* 27, 175–178.

Preto, N. et al., 2015. Primary dolomite in the Late Triassic Travenanzes Formation, Dolomites, Northern Italy: Facies control and possible bacterial influence. *Sedimentology* 62, 697–716.

Price, G.D., 2011. Inorganic carbon transporters of the cyanobacterial CO_2-concentrating mechanism. *Photosynth Res*. 109, 47–57.

Prokoph, A., Shields, G.A., Veizer, J., 2008. Compilation and time-series analysis of a marine carbonate $\delta^{18}O$, $\delta^{13}C$, $^{87}Sr/^{86}Sr$ and $\delta^{34}S$ database through Earth history. *Earth-Sci. Rev.* 87, 113–133.

Pruss, S.B., Bosak, T., Macdonald, F.A., McLane, M., Hoffman, P.F., 2010. Microbial facies in a Sturtian cap carbonate, the Rasthof Formation, Otavi Group, northern Namibia. *Precambrian Res.* 181, 187–198.

Quay, P. Stutsman, P., 2003. Surface layer carbon budget for the subtropical N. Pacific: $\delta^{13}C$ constraints at station ALOHA. *Deep-Sea Res.* I 50, 1045–1061.

Quay, P. Stutsman, P., Feely, R.A., Juranek, L.W., 2009. Net community production rates across the subtropical and equatorial Pacific Ocean estimated from air-sea $\delta^{13}C$ disequilibrium. *Global Biogeochem. Cy.* 23, GB2006.

Rasmussen, B., Bekker, A., Fletcher, I.R., 2013. Correlation of Paleoproterozoic glaciations based on U–Pb zircon ages for tuff beds in the Transvaal and Huronian Supergroups. *Earth Planet. Sci. Lett.* 382, 173–180.

Rau, G.H., Riebesell, U., Wolf-Gladrow, D., 1997. CO_2aq-dependent photosynthetic ^{13}C fractionation in the ocean: a model versus measurements. *Global Biogeochem. Cy.* 11, 267–278.

Rigo, M., Preto, N., Roghi, G., Tateo, F., Mietto, P., 2007. A rise in the Carbonate Compensation Depth of western Tethys in the Carnian (Late Triassic): Deep-water evidence for the Carnian Pluvial Event. *Palaeogeogr. Palaeocl.* 246, 188–205.

Rivkin, R.B., Legendre, L., 2001. Biogenic carbon cycling in the upper ocean: effects of microbial respiration. *Science* 2398–2400.

Romanek, C.S., Grossman, E.L., Morse, J.W., 1992. Carbon isotopic fractionation in synthetic aragonite and calcite: Effects of temperature and precipitation rate. *Geochim. Cosmochim. Acta* 56, 419–430.

Ronov, A.B., 1993. *Stratisfera – Iii Osadochnaya Obolochka Zemli (Kolichestvennoe Issledovanie)*. Moscow, Nauka, 1–144.

Ronov, A.B., Yaroshevsky, A.A., 1969. Chemical composition of the Earth's crust. In: P.J. Hart (ed.), *The Earth's Crust and Upper Mantle*, American Geophysical Union, Washington, D.C.

Rothman, D.H., Hayes, J.M., Summons, R.E., 2003. Dynamics of the Neoproterozoic carbon cycle. *Proc. Nat. Acad. Sci. USA* 100, 8124–8129.

Saltzman, M.R. et al., 2000. A global carbon isotope excursion (SPICE) during the Late Cambrian: relation to trilobite extinctions, organic-matter burial and sea level. *Palaeogeogr. Palaeocl*. 162, 211–223.

Saltzman, M.R. et al., 2004. The Late Cambrian SPICE ($\delta^{13}C$) event and the Sauk II-SAUK III regression: new evidence from Laurentian basins in Utah, Iowa and Newfoundland. *J. Sedim. Res*. 74, 366–377.

Santelli, C.M. et al., 2008. Abundance and diversity of microbial life in ocean crust. *Nature* 453, 653–657.

Satkoski, A.M., Beukes, N.J., Li, W., Beard, B.L., Johnson, C.M., 2015. A redox-stratified ocean 3.2 billion years ago. *Earth Planet. Sci. Lett.* 430, 33–53.

Schieber, J., Bose, P.K., Eriksson, P.G., Sarkar, S., 2007. Paleogeography of microbial mats in terrigenous clastics – environmental distribution of associated sedimentary features and the role of geologic time. In: J. Schieber et al. (eds), *Atlas of Microbial Mat Features Preserved within the Clastic Rock Record*, Elsevier, Amsterdam, pp 267–275.

Servais, T. et al., 2008. The Ordovician Biodiversification: revolution in the oceanic trophic chain. *Lethaia* 41, 99–109.

Shen, B. et al., 2008. Stratification and mixing of a post-glacial Neoproterozoic ocean: Evidence from carbon and sulfur isotopes in a cap dolostone from northwest China. *Earth Planet. Sci. Lett.* 265, 209–228.

Shen, B. et al., 2011. Carbon, sulfur, and oxygen isotope evidence for a strong depth gradient and oceanic oxidation after the Ediacaran Hankalchough glaciation. *Geochim. Cosmochim. Acta* 75, 1357–1373.

Sheppard, S.M.F., Schwarcz, H.P., 1970. Fractionation of carbon and oxygen isotopes and magnesium between coexisting metamorphic calcite and dolomite. *Contrib. Mineral. Petrol*. 26, 161–198.

Shields, G.A., 2005. Neoproterozoic cap carbonates: a critical appraisal of existing models and the *plumeworld* hypothesis. *Terra Nova* 17, 299–310.

Siegenthaler, U., Münnich, K.O., 1981.$^{13}C/^{12}C$ fractionation during CO_2 transfer from air to sea. In: B. Bolin (ed.), *Carbon Cycle Modelling*, John Wiley, New York, pp 249–257.

Sluijs, A., Dickens, G.R., 2012. Assessing offsets between the $\delta^{13}C$ of sedimentary components and the global exogenic carbon pool across early Paleogene carbon cycle perturbations. *Global Biogeochem. Cy.* 26, GB4005.

Squire, R.J., Campbell, I.H., Allen, C.M., Wilson, C.J.L., 2006. Did the Transgondwanan Supermountain trigger the explosive radiation of animals on Earth? *Earth Planet. Sci. Lett*. 250, 116–133.

Stanley, S.M., 2010. Relation of Phanerozoic stable isotope excursions to climate, bacterial metabolism, and major extinctions. *Proc. Natl. Acad. Sci. USA* 107, 19185–19189.

Stiller, M., Rounick, J.S., Shasha, S., 1985. Extreme carbon-isotope enrichments in evaporating brines. *Nature* 316, 434–435.

Strauss, H., Beukes, N.J., 1996. Carbon and sulfur isotopic compositions of organic carbon and pyrite in sediments from the Transvaal Supergroup, South Africa. *Precambrian Res*. 79, 57–71.

Swanson-Hysell, N.L. et al., 2010. Cryogenian glaciation and the onset of carbon-isotope decoupling. *Science* 328, 608–610.

Swart, P.K., 2008. Global synchronous changes in the carbon isotopic composition of carbonate sediments unrelated to changes in the global carbon cycle. *Proc. Nat. Acad. Sci. USA* 105, 13741–13745.

Tartèse, R., Chaussidon, M., Gurenko, A., Delarue, F., Robert, F., 2017. Warm Archean oceans reconstructed from oxygen isotope composition of early-life remnants. *Geochem. Persp. Let.* 3, 55–65.

Thomazo, C., Nisbet, E.G., Grassineau, N.V., Peters, M., Strauss, H., 2013. Multiple sulfur and carbon isotope composition of sediments from the Belingwe Greenstone Belt (Zimbabwe): A biogenic methane regulation on mass independent fractionation of sulfur during the Neoarchean? *Geochim. Cosmochim. Acta* 121, 120–138.

Towe, K.M., 1982. Anomalous ^{13}C depletion in Precambrian organic carbon. *Nature* 295, 171.

Van Breugel, Y., Schouten, S., Paetzel, M., Nordeide, R., Sinninghe Damsté, J.S., 2005. The impact of recycling of organic carbon on the stable carbon isotopic composition of dissolved inorganic carbon in a stratified marine system (Kyllaren fjord, Norway). *Org. Geochem.* 36, 1163–1173.

Van Kranendonk, M.J. 2010. Three and a half billion years of life on Earth: a transect back into deep time. Geological Survey of Western Australia, Record 2010/21.

Veizer, J., Hoefs, J., Lowe, D.R., Thurston, P.C., 1989a. Geochemistry of Precambrian carbonates: II. Archean greenstone belts and Archean sea water. *Geochim. Cosmochim. Acta* 53, 859–871.

Veizer, J., Hoefs, J., Ridler, R.H., Jensen, L.S., Lowe, D.R., 1989b. Geochemistry of Precambrian carbonates: I. Archean hydrothermal systems. *Geochim. Cosmochim. Acta* 53, 845–857.

Verdel, C., Wernicke, B.P., Bowring, S.A., 2011. The Shuram and subsequent Ediacaran carbon isotope excursions from southwest Laurentia, and implications for environmental stability during the metazoan radiation. *GSA Bull*. 123, 1359–1559.

Villinski, J.C., Dunbar, R.B., Mucciarone, D.A., 2000. Carbon 13/Carbon 12 ratios of sedimentary organic matter from the Ross Sea, Antarctica: A record of phytoplankton bloom dynamics. *J. Geophys. Res.* C6, 14163–14172.

Wakeham, S.G. et al., 2007. Microbial ecology of the stratified water column of the Black Sea as revealed by a comprehensive biomarker study. *Org. Chem.* 38, 2070–2097.

Walker, J.C.G., 1985. Carbon dioxide of the early Earth. *Origins of Life* 16, 117–127.

Walker, J.C.G., Lohmann, K.C, 1989. Why the oxygen isotope composition of sea water changes with time. *Geophys. Res. Lett*. 16, 323–326.

Weber, F., Gauthier-Lafaye, F., 2013. No proof from carbon isotopes in the Francevillian (Gabon) and Onega (Fennoscandian shield) basins of a global oxidation event at 1980–2090 Ma following the Great Oxidation Event (GOE). *C. R. Geosci*. 345, 28–35.

Winter, B.L., Knauth, L.P., 1992. Stable isotope geochemistry of cherts and carbonates from the 2.0 Ga Gunflint Iron Formation: implications for the depositional setting, and the effects of diagenesis and metamorphism. *Precambrian Res*. 59, 283–313.

Wolf-Gladrow, D.A., Riebesell, U., Burckhardt, S., Bijma, J., 1999. Direct effects of CO_2 concentration on growth and isotopic composition of marine plankton. *Tellus* 51B, 461–476.

Wright, J.D., Schaller, M.F., 2013. Evidence for a rapid release of carbon at the Paleocene-Eocene thermal maximum. *Proc. Nat. Acad. Sci. USA* 110, 15908–15913.

Xiao, S. et al., 2004. The Neoproterozoic Quruqtagh Group in eastern Chinese Tianshan: evidence for a post-Marinoan glaciation. *Precambrian Res.* 130, 1–26.

Xiao, S. et al., 2012. Integrated chemostratigraphy of the Doushantuo Formation at the northern Xiaofenghe section (Yangtze Gorges, South China) and its implication for Ediacaran stratigraphic correlation and ocean redox models. *Precambrian Res*. 192–195, 125–141.

Yamaguchi, K., 2002. Geochemistry of Archean Paleoproterozoic black shales: the early evolution of the atmosphere, oceans, and biosphere. Ph.D. thesis, Pennsylvania State University.

Yashioka, H., Asahara, Y., Tojo, B., Kawakami, S., 2003. Systematic variations in C, O, and Sr isotopes and elemental concentrations in Neoproterozoic carbonates in Namibia: implications for a glacial to interglacial transition. *Precambrian Res*. 124, 69–85.

Young, G.M., 2014. Contradictory correlations of Paleoproterozoic glacial deposits: Local, regional or global controls? *Precambrian Res*. 247, 33–44.

Zeebe, R.E., 2007. An expression for the overall oxygen isotope fractionation between the sum of dissolved inorganic carbon and water. *Geochem. Geophys. Geosys.* 8, Q09002, doi:10.1029/2007GC001663.

Zhang, J., Quay, P.D., Wilbur, D.O., 1995. Carbon isotope fractionation during gas–water exchange and dissolution of CO_2. *Geochim. Cosmochim. Acta* 59, 107–114.

Zhou, C.M., Jiang, S.Y., Xiao, S.H., Yuan, X.L., 2012. Rare earth elements and carbon isotope geochemistry of the Doushantuo Formation in South China: Implication for middle Ediacaran shallow marine redox conditions. *Chi. Sci. Bull.* 57, 1998–2006.

Zhu, M.Y., Babcock, L.E., Peng, S.C., 2006. Advances in Cambrian stratigraphy and paleontology: Integrating correlation techniques, paleobiology, taphonomy and paleoenvironmental reconstruction. *Palaeoworld* 15, 217–222.

CHAPTER FIVE

Silicate weathering in the Neoproterozoic as evidenced by strontium isotopes

Abstract

The strontium isotope ratios of marine carbonates over the Neoproterozoic increased much more rapidly than can be accounted for solely by the increase in ^{87}Sr due to Rb decay. Vigorous silicate weathering is implied, driven by high levels of atmospheric CO_2. An emphasis on the utility of strontium ratios for chronostratigraphy has led to a distinction between low-value samples that, by definition, are 'least altered' and the remainder that are rejected. But it remains to be demonstrated that the carbonates with higher values are more altered; they could simply include a greater-than-average continental component and as such be informative of local weathering and/or contamination by fluids of subsurface origin. This chapter offers a more inclusive compilation for the period 1060–620 Ma. The compilation affords insight into the interplay between continental weathering and tectonic perturbations and a crucial test of the Snowball hypothesis, which predicts extremely low levels of CO_2 in the run-up to glaciations, extremely low levels of weathering during the glaciations themselves, and extremely high levels of weathering in their aftermath. The intervals of greatest weathering according to the Sr-isotope record were 820–790, 660–650 and 630–620 Ma, possibly also 1000–960 Ma. Continents appear to have undergone lower than average weathering in the period 780–720 Ma leading up to the Sturtian interval and moderate weathering during the Sturtian itself. Multi-regional spikes punctuate the Tonian and Cryogenian periods, most prominently at c.740, 720 and 645–635 Ma: events when the upper crust was deeply fractured and penetrated by hydrothermal fluids rich in ^{87}Sr.

5.1. Introduction

On land, chemical weathering occurs as carbonates and silicates react with acid rain. Dissolved carbon dioxide releases the cations from the minerals and forms bicarbonate, the products washing as solutes into the sea. Under high pCO_2 weathering is intense, and will remain so if the CO_2 consumed by weathering is replenished by mantle degassing. To the extent it is not replenished, pCO_2 will fall and weathering diminish until a balance between inputs and outputs is restored. Mantle degassing has decreased as the Earth has cooled. Consequently the intensity of chemical

weathering has also decreased. Most studies indicate that in the Archaean weathering was aggressive (Table 1 in Hessler & Lowe 2006). The dynamics of continent aggregation, uplift, mountain erosion and disaggregation complicate the secular trend. Supercontinents undergo less weathering because their interiors are dry. Conversely, disaggregating landmasses become exposed to wetter conditions and weathering increases. Because the disaggregation is driven by the opening up of new areas of ocean volcanism, mantle degassing may also increase.

Another factor is temperature, which controls reaction rates and is controlled by pCO_2. Once continents are above water, weathering prevents concentrations of the gas from indefinitely rising. Conversely, as weathering consumes more CO_2, temperatures fall, weathering decreases and pCO_2 recovers. In a world where CO_2 is continually entering the exosphere, the feedback sets limits on how far glaciation can proceed, and indeed is reinforced as ice sheets isolate bedrock from the atmosphere. Fluctuations may be quite small. During the late Pleistocene, Earth went through several glacial and interglacial periods, in the course of which CO_2 levels oscillated between 180 and 300 ppm (Zeebe and Caldeira 2008). The imbalance between supply and uptake was never more than 2%. Marine beryllium sediment records suggest that silicate weathering fluctuated little throughout the Pleistocene (von Blanckenburg et al. 2015).

The main index of global chemical weathering is the marine carbonate $^{87}Sr/^{86}Sr$ signal, the ratio of the Sr derived from decay of ^{87}Rb to the non-radiogenic Sr isotope most similar in abundance to radiogenic Sr. Over time, continental crust accumulates a higher proportion of ^{87}Sr relative to ocean crust because it is enriched in Rb and much older. By the same token, older layers of the continental crust are more radiogenic than younger. Seawater reflects a balance between the Sr weathered from the continent and Sr entering the ocean through hydrothermal exchange with depleted juvenile crust at mid-ocean ridges. As continental crust ages, the isotopic ratio in seawater tends to increase. Thus variation in continental weathering can be gauged, to a first order, according to whether the ratio rises faster or more slowly than the long-term trend. As with the CO_2 flux, tectonics affects both the terrestrial and oceanic sides of the equation. When landmasses disaggregate, ridge length, hydrothermal circulation and hence input from the ocean increase.

5.2. Seawater $^{87}Sr/^{86}Sr$ in the Precambrian

As originally proposed (Wickman 1948), the strontium ratio was expected to be useful chiefly as a tool for dating and correlation. Strontium has a long residence time in the ocean, 0.7–3.3 Ma according to Jacobsen & Kaufman (1999), and its isotopes are well mixed. The modern ocean therefore has a fairly uniform ratio of around 0.7092, representing the balance between the flux

from rivers (~ 0.7120) and the flux from ocean basalt (~ 0.7035). In the Precambrian the ocean is also assumed to have been well mixed, but the assumption may not be so straightforward. Nearly all carbonate samples come from epicontinental environments, at some distance from the open ocean. To the extent that mixing was not perfect, nearshore locations might have reflected a greater proportion of continental input than offshore locations. Carbonates are purest (and thus most suitable for strontium analysis) where siliciclastic weathering, and hence the continental contribution, is at a minimum. Also, because residence time is the amount in the reservoir divided

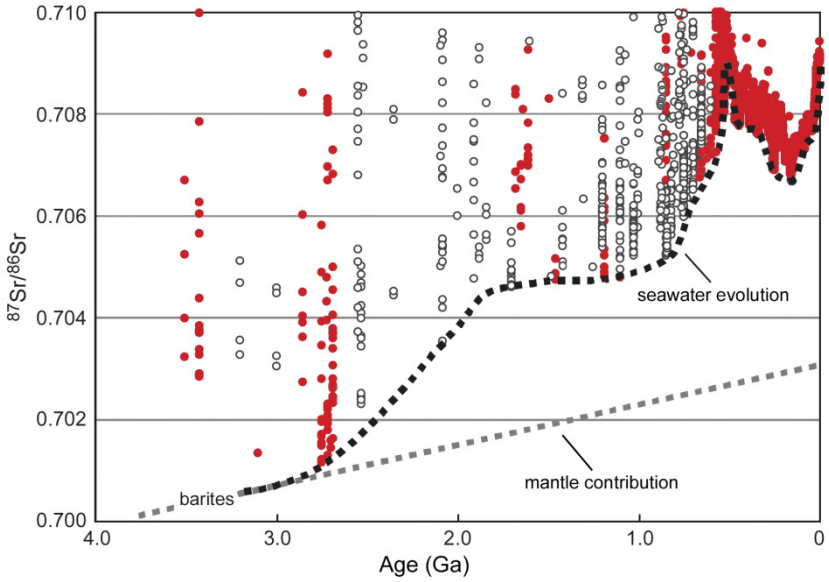

Figure 5.1a. Compilation of strontium isotope data (redrawn from Shields & Veizer 2002). Open symbols: poorly dated, e.g. values from the Lower Vindhyan Supergroup assigned to c.1100 Ma are now dated c.1600 Ma.

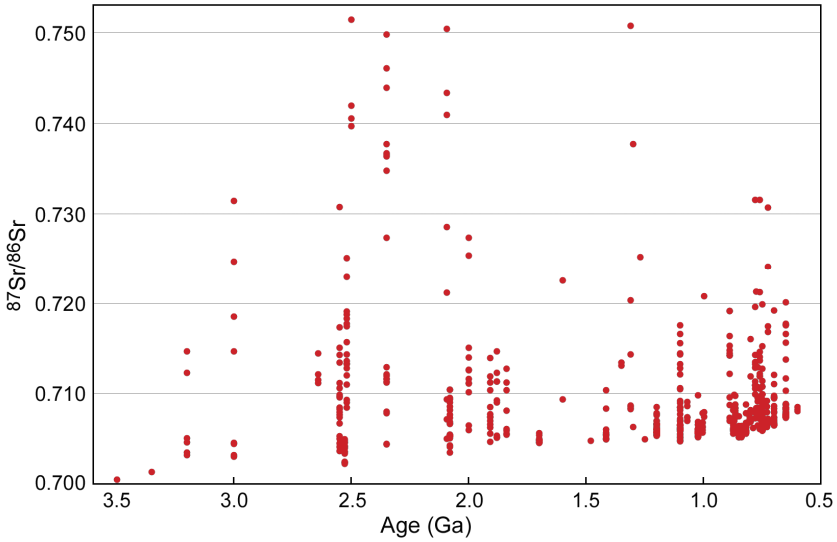

Figure 5.1b. The same data as in Figure 5.1a but with the y-axis extended. Numerous values far exceed that of modern river-water (0.7124) or river sediment (0.7178). At 3.0 Ga, river sediment is estimated to have been 0.7030, though it could have been higher (Shields 2007).

by the input rate, the intense weathering that accompanied higher levels of CO_2 would have reduced the residence time. Ultimately, whether the oceans were well mixed is a question of fact.

Going back in time, strontium-isotope data show an enormous increase in scatter (Shields & Veizer 2002; Fig. 5.1). This could be due to increasing alteration or to variability in the original signal. Over short stratigraphic intervals, the variation can be surprisingly systematic, and unrelated to secular change (e.g. Gorokhov et al. 1998, Kah et al. 2001). In general, the assumption of ocean homogeneity is buttressed by the further assumption that most Precambrian samples are too altered to provide a reliable, systematic signal. Normal criteria for determining whether a sample is altered – for example, petrographic or oxygen-isotope evidence of late recrystallisation – are replaced by *a priori* geochemical rules, notably a certain Mn/Sr threshold (which, as Dehler et al. (2005) note, may be anything from > 2 to > 10). After the sifted samples have been analysed, the results provide further occasion for imputing alteration. If there is a spread of values, the lowest are deemed to be the 'least altered' and the remainder discarded.

Although widely consented to, the approach overlooks two crucial distinctions. One is that the Precambrian ocean was predominantly anoxic below the photic zone. Since unoxidised Mn is soluble, the ocean was rich in the metal, and carbonates precipitating in deeper water contained more Mn than those precipitating in shallow water (Fig. 4.10). Thus high-Mn carbonates might be more representative of the open ocean than low-Mn carbonates. The other distinction is that contamination, from whatever source, is not necessarily alteration. Anything abnormal is in effect outlawed. As noted by Huang et al. (2011), many cap carbonates are Mn-rich and thus fail the Mn/Sr test, but they also reveal above-average concentrations of other redox-sensitive elements; the imputation of diagenesis is unwarranted. As in the Majiatun Formation, where Mn concentrations vary systematically with $\delta^{13}C$ but, below -1‰, in the direction opposite to that normally observed (Fig. 3.14d), the enrichments are *prima facie* evidence of hydrothermal influence, and the elevated $^{87}Sr/^{86}Sr$ evidence that the source of the low-Eh fluids was continental rather than oceanic, radiogenic Sr being assimilated from fractured wallrock. Mn and $^{87}Sr/^{86}Sr$ usually do not correlate. In cases where they do, such as the Little Dal Group (above 60 ppm, Halverson et al. 2007), the Maieberg Formation (above 80 ppm, *ibid*.) and the Virgin Spring Limestone (no threshold, Macdonald et al. 2013), the common cause is likely to be contemporaneous contamination of seawater by subsurface fluids, not systematic alteration, though in regions affected by orogenesis post-depositional fracturing may also play a role (e.g. Bartley et al. 2007). Much the same applies to the other short-cuts for detecting diagenesis.

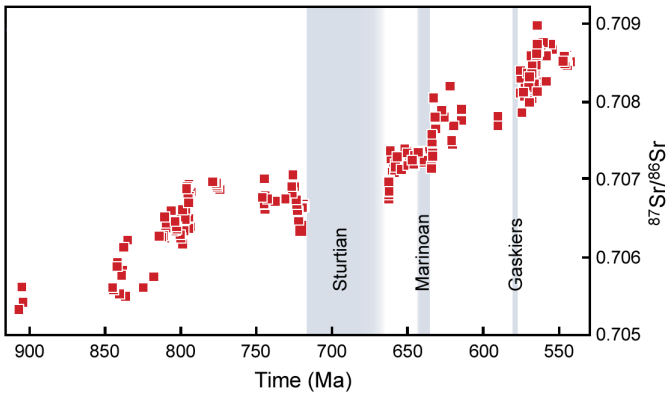

Figure 5.2. Selective compilation of strontium isotope ratios for the Neoproterozoic (from Cox et al. 2016, updated from Halverson et al. 2007). Shaded bands identify putative glaciations.

In brief, once samples have passed empirical tests of diagenetic alteration, all data are data. At a minimum, an important implication of the decreasing scatter resulting from abnormally high values is that there was a marked decrease in intensity of silicate weathering over the Precambrian. In addition, the eruption of hydrothermal fluids may have been much more frequent in the past.

5.3. Strontium isotope variation in the Neoproterozoic

The most widely cited version of strontium isotope variation through the Neoproterozoic is that of Halverson et al. (2007), modified in Cox et al. (2016, Fig. 5.2). Constructed from single localities on the basis that they are globally representative and filtered to exclude samples with low Sr content (a procedure Macdonald et al. (2010) found unreliable), the record still fails to yield an evolutionary path without scatter. Chemical weathering appears at times to have been intense. The pattern is stepped. The influx of radiogenic Sr rose steeply through the period 820–780 Ma, fell through the period 780–720 Ma leading up to the Cryogenian, rose steeply again immediately after the Sturtian interval, remained steady through the rest of the Cryogenian, and rose steeply again in the immediately post-Marinoan and post-Gaskiers intervals, reaching an all-time high in the late Ediacaran.

Purportedly, the profile includes all data ‘of the highest quality’ and excludes those that are suspect. Efforts by previous workers to be discriminating are implicitly discounted and their results rejected. How reasonable this is can be gauged by comparing the 2007 compilation with the 2016 version. There are two significant changes: one, the addition of data that help fill the gap after the Marinoan interval; the second, the omission of previously published data (with high Sr and low Mn/Sr) from the Blueflower and Sheepbed Formations (~600 Ma). The omission is not explained.

Another instance of omitted data is the post-Sturtian Rasthof Formation (Yashioka et al. 2003). The full data show a systematic trend of plummeting $^{87}Sr/^{86}Sr$ through the first 4 m after the diamictite, from 0.7173 to 0.7070 (Fig. 5.3g), but the trend is excluded on the grounds that dolostones are necessarily altered and give higher values than limestones; only the samples with the highest Sr are included. Again, such rules about what to include and what not are dubious. Although dolostones often do have higher ratios, this might be for reasons unrelated to alteration. The progressiveness of the trend, and continuity with the calcite samples, suggests that the signal is authentic. The correlative cap carbonate overlying the Numees Formation is limestone and records descending values of 0.7291 and 0.7286, dropping to 0.7138 in the Holgat Formation (Macdonald et al. 2010).

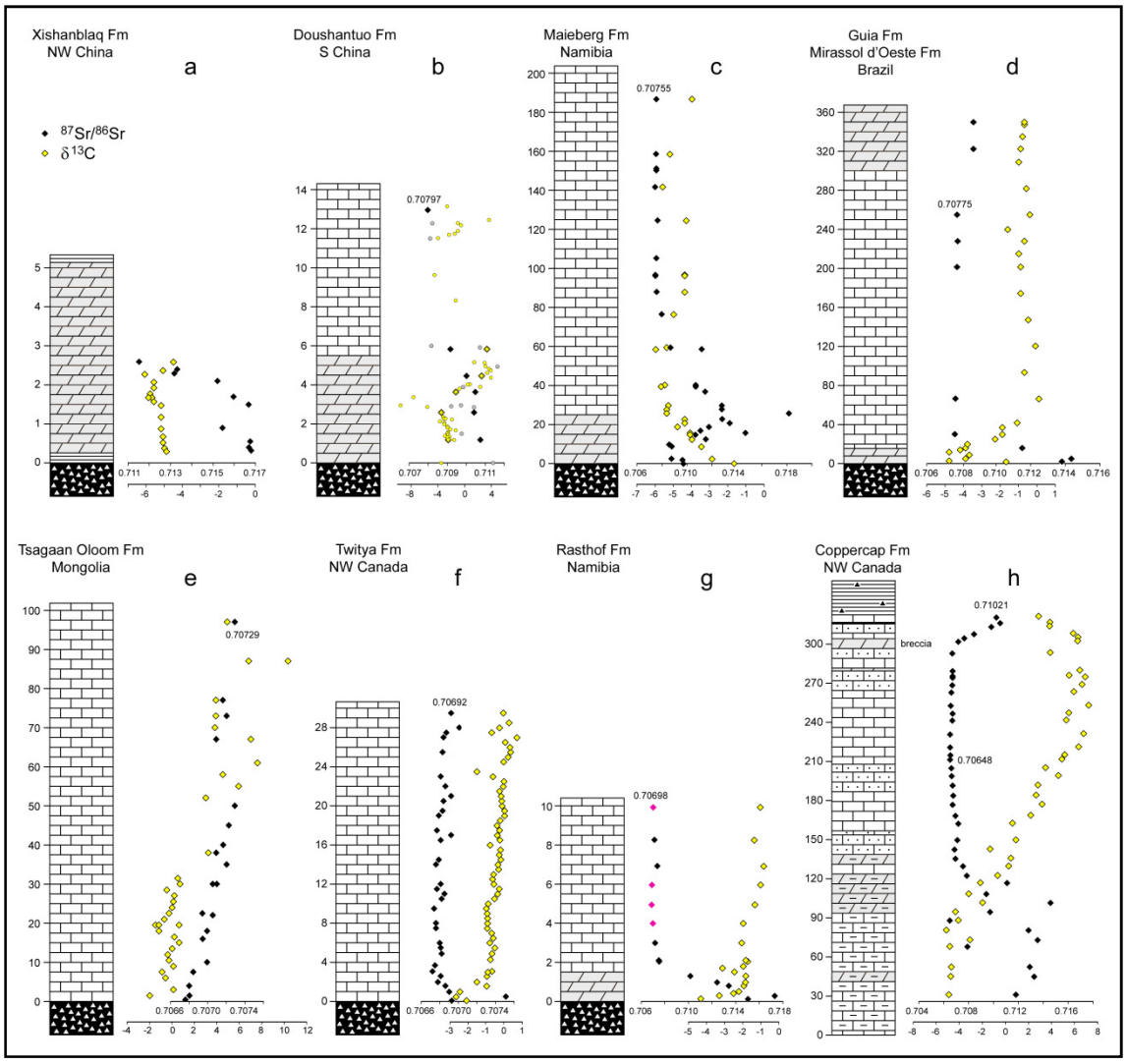

Figure 5.3. Chemostratigraphic logs: $^{87}Sr/^{86}Sr$ in black (upper scale), $\delta^{13}C$ in yellow (lower scale). (**a**) mid Ediacaran, (**b–d**) earliest Ediacaran = post-Marinoan, (**e–g**) mid Cryogenian = post-Sturtian, (**h**) latest Tonian. Data from Xiao et al. (2004), Ohno et al. (2008), Halverson et al. (2007), de Alvarenga et al. (2008), Brasier et al. (1996), Shields et al. (2002), Yashioka et al. (2003) and Rooney et al. (2014). Smaller symbols in (b) denote data from Sawaki et al. (2010a). Pink symbols in (g) denote data included in the Halverson et al. compilation.

Accompanying such redaction is an interpretation which sees 'abrupt increases following deglaciation, ... a predictable result of extremely high CO_2 levels and corresponding elevated silicate weathering rates' (Halverson & Shields-Zhou 2011). However, more often than not $^{87}Sr/^{86}Sr$ fell, as through the post-Sturtian Twitya Formation, the three post-Marinoan sequences and the mid-Ediacaran sequence from NW China (Fig. 5.3). The post-Sturtian Tsagaan Oloom Formation goes the other way, but is not enriched relative to lowest values of the period. The contemporaneous cap dolostone above the Altungol Formation, NW China, also goes the other way; here strong correlation between $^{87}Sr/^{86}Sr$, Mn and Fe (the latter reaching 87,000 ppm) suggests hydrothermal influence, increasing through the sequence (Feng et al. 2016).

In the 13 years since the compilation of Shields and Veizer many more $^{87}Sr/^{86}Sr$ determinations have been published and the chronology of already documented successions refined (e.g. Rooney et al. 2015). Figures 5.4 and 5.5, accordingly, present a new digest for the period 1060–620 Ma. Stratigraphic heights are converted to ages on the basis that sedimentation rates through a formation were constant. Strontium isotope values from different formations are integrated primarily in accordance with the best fit of lowest values, thereafter in accordance with the best fit of all values. The result is an inter-regional time-anchored correlation of all formations for which there are adequate data. In general, chronological constraints are weaker early in the sequence, largely because the preserved formations then are fewer.

Two aspects stand out. One is the preponderance of low values that, at least from 800 Ma, trail along the bottom and provide some support for the view that these come close to the well-mixed ocean. From 810 to 785 Ma there is a strongly rising trend, possibly steeper than through any commensurate time in Earth history. Thereafter the trend came to a halt and reversed: between 790 and 720 Ma there is no net change. Arguably the rising trend was tempered by the weathering of penecontemporaneous continental flood basalts, which were less radiogenic. However, such magmas were erupting over a much longer period, from at least 850 Ma to as late as 712 Ma. They would also have expelled large volumes of CO_2 (Ernst & Bell 2010), thereby promoting the weathering of all rock types until non-equilibrium consumption of CO_2 restored the position (§1.2). Lowest values at 660 Ma were higher than at the end of the Tonian, then rose steeply, flattened in the run-up to the Marinoan episode, rose steeply immediately after the Marinoan, briefly dropped, and resumed a rising trend soon after 630 Ma.

The other salient aspect is the occurrence of multi-regional spikes, notably at c. 980 Ma, at the beginning and end of the Sturtian interval, 720–660 Ma, and at the end of the Marinoan interval, 635 Ma. The reality of the spike at c. 980 Ma is uncertain; it assumes that the Little Dal Group

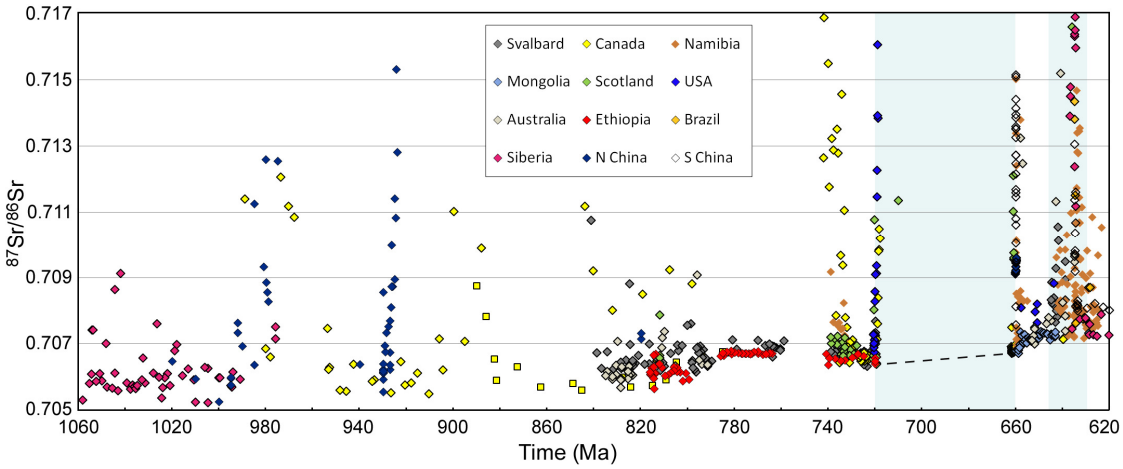

Figure 5.4. Compilation of reasonably well-dated strontium isotope data published since 1989 for the period 1060–620 Ma (Svalbard including Greenland, N China the Tarim Block). Interpolation between dated horizons assumes constant sedimentation rates. Dotted line connects lowest values at beginning and end of the Sturtian, suggesting more silicate weathering during that interval (ignoring carbonate weathering) than in the preceding 60 Ma.

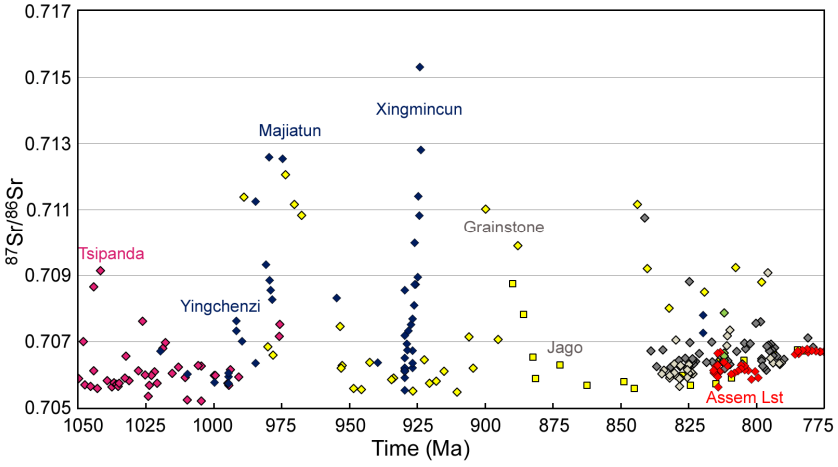

Figure 5.5a. Expanded view of the period 1050–775 Ma, with some names. Ages for North China's Jinxian Group pre-930 Ma are tentative. Symbols as for Fig. 5.4.

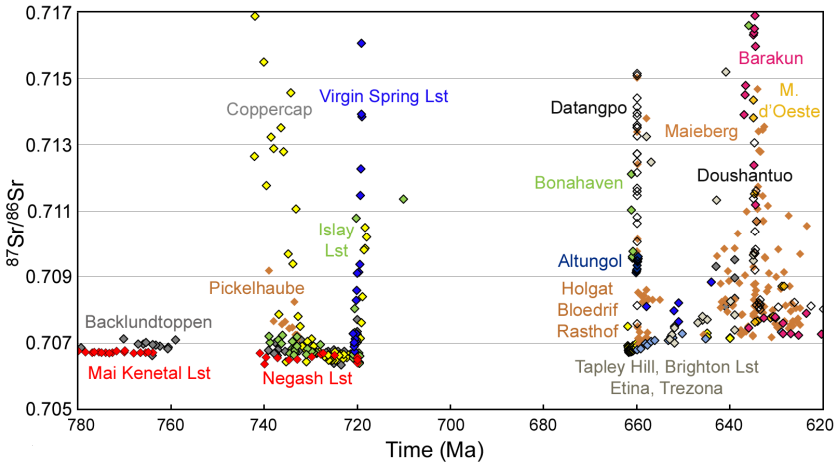

Figure 5.5b. Expanded view of the period 780–620 Ma.

began c. 995 Ma and the Majiatun Formation c. 985 Ma. The spike at c. 925 Ma, recorded by the Xingmincun Formation, North China, stands alone. A spike at c. 740 Ma at the base of the Coppercap Formation coincides with an abrupt transgression and with the deposition of carbonates increasingly depleted in ^{13}C and rich in Mn and ^{87}Sr – not to mention the basal copper deposits. Over the following 250 m (Fig. 5.3h), $\delta^{13}C$ rose to +7, then declined, until over the last 7 m (including a thin debrite) Mn shot up to 4500 ppm. At the boundary with the Sayunei Formation re-activation of major faults gave rise to iron-rich mudstones, turbiditic siltstones, sandstones and occasional debrites. Sediments at the footwall end accumulated to a depth of 900 m (Eisbacher 1981). Hydrothermal iron formation dominated towards the top, then coarser diamictite. Canada, the USA, Scotland and Svalbard all record surges in the approach to the Sturtian. Namibia, the Tarim Block, South China, and Scotland all record surges at the end of the Sturtian.

Although discrete carbonate beds occur within the diamictite-bearing intervals (Table 1.2), only one of Sturtian age has been analysed for $^{87}Sr/^{86}Sr$, giving a ratio of 0.7114 (Sawaki et al. 2010b). Values through the Marinoan-age Ghaub Formation range from 0.7073 to 0.7089 (Kennedy et al. 1998), the highest coming from dolostones immediately after the diamictites. Limestone horizons within the coeval Bol'shoi Patom Formation, another diamictite unit, range up to 0.7148 (Pokrovsky et al. 2010). The entire Marinoan – including, it is proposed, the non-diamictite-bearing Trezona and Ombaatjie Formations – is a time of unusually high values symmetrically climaxing around the end of the Cryogenian (Fig. 5.5b).

Coincident surges across more than one region suggest global-scale influxes of ^{87}Sr-enriched fluids from the lower crust in the course of catastrophic fracturing and graben subsidence. Fluids, accordingly, were anoxic, depleted in ^{18}O and rich in Mg, redox metals and C, as well as ^{87}Sr. Lowest values immediately after the spikes, particularly after the Sturtian and Marinoan, were elevated because of these surges.

5.4. Atmospheric pCO_2 in the Neoproterozoic

The Snowball Earth hypothesis has always been reticent about what triggered pole-to-equator glaciation, but the key idea is that climate cooled as landmasses flocked to low latitudes and global albedo rose. Substantial discussion has been left to modellers. To compensate for lower solar luminosity in the Neoproterozoic, atmospheric CO_2 would have had to be around 3360 ppm if the world had the same average temperature as today, with ice at high latitudes (Pierrehumbert et al. 2011). Another calculation puts pCO_2 around 10,000 ppm (Kasting 1993). Assuming pre-industrial modern concentrations of ~280 ppm (close to the all-time low of the Pleistocene ice age) along

with modern geography and topography, Yang et al. (2012) concluded that runaway ice-albedo feedback might have caused global freezing if ice albedo was at least 0.60 and snow albedo 0.78. At lower and probably more realistic values (Voigt & Abbot 2012), pCO_2 would have had to fall much lower than 280 ppm. Benn et al. (2015) assumed ice albedo of 0.60, snow albedo of 0.55–0.90 and initial CO_2 concentrations of 100 ppm.

Concentrations in the Neoproterozoic are not well constrained, but we can get some idea. Towards the end of the Archaean they are variously modelled from 9000 ppm (Wolf & Toon 2014) to a few tenths of a bar (0.1 bar ≈ 100,000 ppm) (Kasting 2014, Kanzaki & Murakami 2015). The smaller estimates assume low oxygen concentrations and relatively high amounts of methane and/or nitrogen. A mean surface temperature higher than today's 15° C would require higher pCO_2 (Charnay et al. 2013). Since the oceans were warmer in the Precambrian – by how much is debated (Marin-Carbonne et al. 2012) – an estimate of 50,000 ppm would appear conservative. This accords with the minimum 40,000 ppm inferred from the occurrence of massive siderite beds before 1.8 Ga, though again some of the arguments are debatable (Ohmoto et al. 2004), and with the two orders of magnitude greater flux than present conservatively estimated from the carbonate content of ocean crust in the Mesoarchaean (Shibuya et al. 2012). Methane is unlikely to have been abundant, regardless of how much oxygen was in the atmosphere (Halevy 2009, Dasgupta 2013, Kasting 2014).

Evidence of extreme calcium carbonate supersaturation in the ocean shows that pCO_2 in the Archaean was high, declined over time, but was still elevated in the Neoproterozoic (Grotzinger & James 2000, Shields 2002). The occurrence of diamictites above in-situ carbonates in many parts of the world indicates a chemistry and climate favourable to carbonate precipitation until the very moment that erosion and diamictite generation produced the unconformities. That is, the time occupied by the unconformities was probably no greater than that occupied by the eroded sediments.

Most important is the evidence of the strontium isotope signal itself, reflecting the balance between subaerial weathering and subocean hydrothermal alteration. Throughout the Proterozoic isotope ratios rose, both as a result of the growth in continental landmass, since more land was subject to weathering (Flament et al. 2013), and as a result of the igneous differentiation which accompanied growth, enriching the crust in radioactive ^{87}Rb. Initially the oceanic contribution far outweighed the continental. Secular mantle cooling slowed everything down: seafloor spreading, hydrothermal alteration, continental growth, volcanic outgassing (Dasgupta 2013). The almost linear trend of isotope ratios from 2.8 to 1.9 Ga (Figs. 5.1a, 5.6a) supports a model of progressive continental

growth through the period (e.g. Roberts & Spencer 2015), intense weathering (since exposed land area was small) and no major swings in submarine magmatism (Pehrsson et al. 2014). Apparently events around the Archaean/Proterozoic boundary did not further intensify global weathering rates. Subaqueous silicate dissolution will have contributed to the signal. The much gentler slope from 1.9 Ga to 0.9 Ga (the 'boring billion' of Holland 2006) corresponds with a time when, generally, tectonic activity was subdued, and continental growth sluggish. Surprisingly, ordinary processes of weathering had little effect on the isotope ratio. So did the tectonic processes which created Rodinia, notably the Grenville Orogeny.

In order to sustain levels > 50,000 ppm and the chemical weathering that went with them, CO_2 outgassing in the Archaean must have been high. Carbon was precipitated principally as calcite in ocean crust. Eventually it was subducted back into the mantle and part of the subducted carbon re-gassed via metamorphism into the atmosphere. During the later Palaeoproterozoic erosion declined as topographic gradients diminished. To some extent the reduction in freeboard was counterbalanced by thickening of the crust, hence greater buoyancy, as the mantle cooled. Thickening may have reached its maximum towards the end of the Mesoproterozoic (Dhuime et al. 2015). Generally enriched strontium isotope values show that the early Neoproterozoic was not uneventful. Around 820 Ma erosion and weathering intensified, with consequences for atmospheric CO_2. Apart from in the period 780–740 Ma, erosion and weathering continued to be intense, apparently, all the way into the Cambrian. This ties in with the crustal extension and disintegration that characterised much of the mid to late Neoproterozoic (Evans & Mitchell 2011). Rodinia began to fracture around 825 Ma, in a long process that merged, towards the end of the era, with the

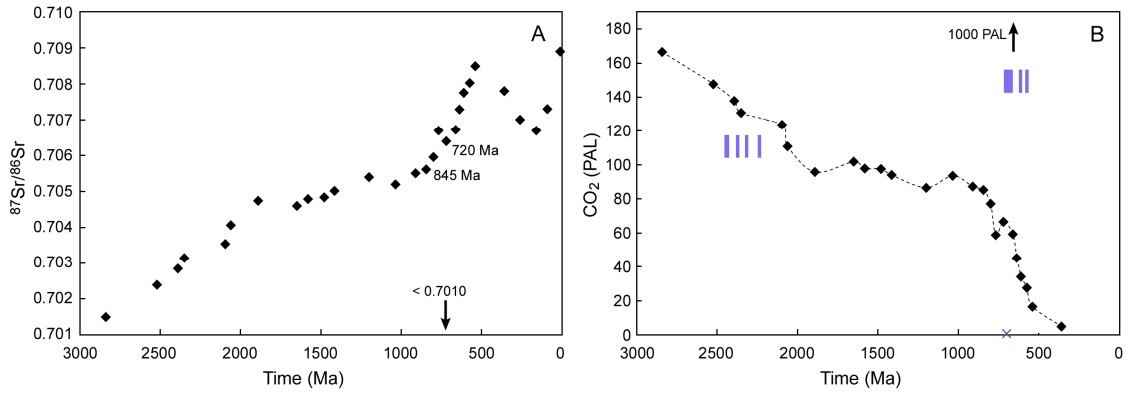

Figure 5.6. (**a**) Lowest strontium isotope values for the late Archaean and Proterozoic, together with a few sketching out the Phanerozoic. The almost linear slope in the Neoproterozoic is steeper than at any previous time. The arrow marks the calculated fall during Sturtian glaciation. (**b**) The same curve calibrated to CO_2, allowing for a 0.001 rise in mantle $^{87}Sr/^{86}Sr$, on the footing that levels were 50,000 ppm at 2800 Ma and 5000 at 520 Ma. Vertical bars mark the putative ice ages of the Palaeoproterozoic and Neoproterozoic. The cross near the x-axis marks 1 PAL (300 ppm), the maximum level of CO_2 compatible with Sturtian glaciation; the arrow refers to the postulated rise in CO_2 at the end of the Marinoan (off the scale).

amalgamation of Gondwana (Li et al. 2008). A mid-Neoproterozoic shift to lower latitudes and hotter climes (*ibid.*) would also have accelerated weathering.

Somehow, one has to get from 50,000 ppm at 2839 ±33 Ma (the date of the first strontium isotope datum, Kamber & Webb 2001) to an estimated 5000 ppm at 520 Ma (Berner 2006). Accepting that there is a close connection between $^{87}Sr/^{86}Sr$ and silicate weathering, Figure 5.6b translates the lowest isotope values – adjusted for a small increase in mantle $^{87}Sr/^{86}Sr$ – into atmospheric CO_2 levels by straight calibration. The linear rise in $^{87}Sr/^{86}Sr$ through the early Palaeoproterozoic suggests that weathering continued unabated, contrary to the 10° C cooling expected to have attended the 'Great Oxidation Event' and concomitant fall in atmospheric methane (Haqq-Misra et al. 2008). Rather, a subdued decline through the Palaeoproterozoic steepens around 2100 Ma, coincident with the tail end of the Lomagundi-Jatuli Event. Rapid transgression at this time (§4.9.3) induced a temporary increase in erosion, seen, for example, in a greater incidence of shales, and a rise in $^{87}Sr/^{86}Sr$, before the consequent reduction in land area reversed the effect. Overall, from the mid Palaeoproterozoic to early Neoproterozoic, pCO_2 is likely to have remained high. Most of the fall leading to the low levels of the Phanerozoic must have taken place after 820 Ma. It is difficult to see how levels at 820 Ma can have been much below 20,000 ppm.

We can also consider the question working back from the Cambrian, when $^{87}Sr/^{86}Sr$ started to decline (Maloof et al. 2010). The 'Great Unconformity' underlying Cambrian sequences on Laurentia marks an interval of massive erosion, during which vast areas were planed off to below sea-level. The rate of carbonate deposition rose exponentially, from 18 to 180 $km^3\ Ma^{-1}$ (Peters & Gaines 2012). In Siberia great volumes of carbonate were already being deposited in the late Ediacaran (Melizhek et al. 2009), capturing, in part, the recycling of dissolved organic carbon (§4.9.1). Possibly the most widespread detrital sequence ever deposited on continental crust are the quartz-rich sandstones of North Africa and Arabia. Their mineralogical maturity implies intense chemical weathering (Avigad et al. 2005). While most abundant in the Precambrian, quartz-rich sandstones are also abundant in the Cambro-Ordovician (Chandler 1988, Soegaard & Eriksson 1989, Dott 2003). The substantial drawdown of CO_2 represented by the carbonates and sandstones implies that pCO_2 in the late Neoproterozoic was higher than in the Cambrian. Some of the drawdown would have been offset by higher outgassing as Rodinia rifted and ocean spreading centres lengthened (Lee et al. 2016).

The crucial question for modellers of Snowball Earth therefore is how, towards the end of the Tonian (~720 Ma), concentrations came to fall from ~20,000 ppm to < 300 ppm in the brief period represented by the pre-diamictite unconformities. During the glaciations themselves, ice isolated

the continents from the atmosphere, preventing the consumption of CO_2, while sub-zero temperatures reduced the rate of weathering in the places where dissolution still occurred. According to one calculation (Jacobsen & Kaufman 1999), seawater $^{87}Sr/^{86}Sr$ would have declined by about 0.0003 Ma^{-1}; according to another (Higgins & Schrag 2003), by about 0.00016 Ma^{-1}. Within 24 Ma – less than half the duration attributed to the Sturtian glaciation – the ratio would have fallen below the then mantle value. Conversely, during the cap-carbonate interval, $^{87}Sr/^{86}Sr$ is expected to have risen, in total by an estimated 0.0009 (*ibid.*). Actual records in most cases show or imply the opposite: static or declining values in the run-up to the Sturtian interval, rising values during it, and a sharp decline from high values through deposition of the cap carbonates.

During the Sturtian and Marinoan, strontium ratios would have been the outcome of three factors: silicate weathering, carbonate weathering, and injection of fault-mediated crustal fluids. The increase in lowest values from 0.7067 to 0.7069 (Fig. 5.4) was the effect of silicate dissolution net of carbonate dissolution – potentially a significant counteraction, to the extent that uplift initially exposed preceding carbonate formations. These being far younger and less radiogenic than average continental crust, their dissolution would have damped the signal from silicate dissolution (Shields 2007). Possibly more significant was hydrothermal fluid injection, though it had no long-term effect.

Through most of the illustrated sections strontium and carbon isotope ratios anti-correlate, suggesting that waters became richer in ^{87}Sr as they deepened (Fig. 5.3). Some of the relationship may reflect the shallowing-up pattern of carbonate cycles. Sediment accumulated in low-erosion systems as sea-level fell; at the beginning of cycles sea-level rise tended to be more rapid and, in the hinterland, more erosive. A specifically hydrothermal influence may show up in relation to the stable-isotope trends (Fig. 5.7). Deeper water, too, might have been richer in ^{87}Sr because this was where most shales accumulated and underwent dissolution – hence the association between ^{87}Sr enrichment and marly facies in the Coppercap Formation (Fig. 5.3). A strong anti-correlation between $\delta^{13}C$ and $^{87}Sr/^{86}Sr$ is seen in the calcites of the 2.5-Ga Gamohaan and Kuruman Formations of South Africa (Heimann et al. 2010). The Xishanblaq Formation, a mid-Ediacaran cap dolostone, likewise shows enrichment in the offshore direction, the highest values exceeding 0.7200 (Fig. 5.3a, Xiao et al. 2004). A strong correlation between $\delta^{13}C$ and $^{87}Sr/^{86}Sr$ in the Gariep and Saldania Belts of Namibia and South Africa is linked, in part, to a trend of declining $^{87}Sr/^{86}Sr$ in the wake of the diamictite Numees and Kaigas Formations (Fölling & Frimmel 2002). Sea-level trends immediately after the diamictites were mostly regressive, not transgressive. The signals also anti-correlate through the Shuram-Wonoka interval in the Doushantuo Formation (Cui et al. 2015).

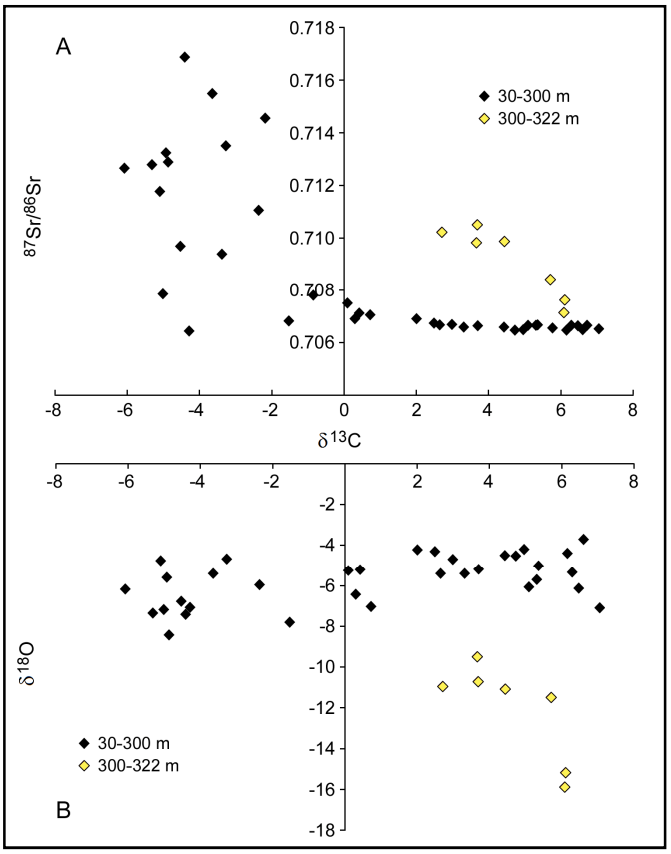

Figure 5.7. Strontium (**a**) and oxygen (**b**) isotope values of the Coppercap Formation plotted against $\delta^{13}C$, showing the distinct geochemistry of the interval affected by hydrothermal fluids (cf. Fig. 5.3h; data from Rooney et al. 2013). Note the characteristic fall in $\delta^{18}O$ as $\delta^{13}C$ falls.

The pattern through the Palaeozoic is oscillatory (Veizer et al. 1999) but overall shows an unprecedented fall in $^{87}Sr/^{86}Sr$, as (1) the era of high outgassing of CO_2 and consumption by weathering came to an end, (2) a series of marine transgressions reduced the area of exposed continent, with first-order peaks in sea-level until the Carboniferous roughly correlating with peaks in $^{87}Sr/^{86}Sr$, (3) the transgressions left a legacy of carbonate cover that was less radiogenic than silicate rock and (4) the ocean became less alkaline, so that dissolution of sedimentary silicates diminished. Notwithstanding the calculated present residence time of 0.7–3.3 Ma, the long-term fall in $^{87}Sr/^{86}Sr$ (Fig. 5.6) suggests that excess ^{87}Sr from the Neoproterozoic remained in the oceans throughout the Palaeozoic and early Mesozoic, and a long-lasting equilibrium between continents and oceans was never reached. Transgressions during the Palaeozoic were rapid enough to be erosive, more so than regressions. Periods from the Jurassic onwards saw a first-order anti-correlation between $^{87}Sr/^{86}Sr$ and sea-level.

5.5. Strontium isotopes and dolomite

The dolostones of the cap carbonate sequences tend to record higher values (Fig. 5.3). Whatever

conditions led to raised $^{87}Sr/^{86}Sr$ also favoured dolomite formation. The explanation cannot be proximity to land, for in these sequences limestone superseded dolomite as the environment shallowed. A better scenario may be that dolomite was promoted by an influx of Mg from supersaturated fault fluids and by above-normal production of organic matter, which nutrients in the fluids stimulated. The greater incidence of dolomite in the Marinoan cap carbonates than in the Sturtian may have been due to higher levels of organic production generally in the Ediacaran (Fig. 4.7).

5.6. Correlations based on the new strontium isotope stratigraphy

Applying *a priori* rules of exclusion and notions of normality produces a filtered version of the record that risks being a misrepresentation of it. Ironically, another result is that in practice strontium isotopes are rarely used for fine-scale correlation and dating in the Proterozoic. Despite hundreds of values having been published over recent decades, the Neoproterozoic isotope curve remains ambiguous and in places threadbare. Most values register above that which can be plausibly imputed to the well-mixed ocean, and large tracts of time fail to show the consistently rising trend that would make lowest values chronologically distinctive.

According to U-Pb dating, the oldest negative carbon-isotope anomaly in the Tonian period was the Majiatun excursion of North China, some time before 940 Ma and possibly coeval with others in India and Siberia around 1000–900 Ma. Two other sets of anomalies occurred c. 810 Ma and towards the end of the Tonian. Anomalous carbon and strontium isotope values, the sharp increase in lowest $^{87}Sr/^{86}Sr$ from 0.7055 to 0.7066 and the stratigraphic evidence of shifting freeboard tell a consistent story. Continental crust was fracturing and isostatically adjusting to the release of thermal pressure. Weathering and hydrothermal input consequently increased.

The compilation assumes that the diamict-generating episodes of the Cryogenian began and ended at the same time everywhere. The presumption of synchroneity is parsimonious but not everywhere proved, and is certainly not valid in relation to the Marinoan episode. In places along the Otavi Platform carbonate sedimentation continued into the Ediacaran (Fig. 5.6) and in Australia there is too much stratigraphy for the Trezona Formation to be squeezed into the maximum 15 Ma between the Sturtian and Marinoan, if the latter began no later than 645 Ma. In addition to confirming the approximate synchroneity of the ‘Bitter Springs’ anomalies, the new chemostratigraphy suggests synchroneity between the lower Coppercap Formation and the Pickelhaube Formation, the latter following the Kaigas diamictite, and confirmation of the revised stratigraphy for the Port Nolloth Group, Namibia, proposed by Macdonald et al. (2010).

Research into the strontium-isotope evolution of North China seas is work in progress. Six samples from the Majiatun Formation (analysed by Ying Shields-Zhou) range from 0.70828 (QPM 42) to 0.72015 (QPM 1), all to varying degrees affected by hydrothermal fluids. One sample from the upper Yingchenzi Formation (LH 3), just before the tectonic ructions, was lower (0.70637). Also of interest is the uppermost Xingmincun Formation (Fairchild et al. 2000) two formations above the Majiatun, where $^{87}Sr/^{86}Sr$ systematically rises (Fig. 5.5a) and there are strong correlations between $^{87}Sr/^{86}Sr$, Fe and Mn, again supporting a hydrothermal control. Soon afterwards (~925 Ma), the region was dissected by mafic sills and dikes and apparently lifted above sea-level.

5.7. Conclusions

Strontium isotope values are useful not only as a tool for correlation but as an index of weathering and tectonic activity. The steep rise in lowest values after 820 Ma implies that weathering and erosion were extreme, coupled, during times of extension, with more radiogenic fluxes from the lower crust. Atmospheric CO_2 levels, very high in the early Neoproterozoic, were falling. Carbon removal by subduction and carbonate deposition on the continents was greater than the input from CO_2 outgassing. Nonetheless, even at the end of the Neoproterozoic, levels are unlikely to have been less than 5000 ppm; in the Tonian they were probably several times higher. Repeated plunges to below the 300 ppm threshold at which global freezing might have become possible are difficult to conceive and have never been modelled. Contrary to predictions based on Snowball Earth, $^{87}Sr/^{86}Sr$ appears to have been high during the Sturtian and Marinoan intervals and to have declined, in systematic fashion, immediately after them. Anomalous enrichment in ^{87}Sr was principally due to the injection of hydrothermal fluids at times of crustal-scale faulting. Negative carbon-isotope anomalies, occurring at the same time as steep rises in $^{87}Sr/^{86}Sr$, also reflect the instability.

Unfiltered strontium isotope ratios provide a basis for inter-regional correlation that complement carbon-isotope ratios. Along with absolute dates, they provide a chronological framework for the whole of the Neoproterozoic. How the records of Siberia, North China and Northwest Canada in the early Tonian integrate with each other remains uncertain.

References

Avigad, D. et al., 2005. Mass-production of Cambro–Ordovician quartz-rich sandstone as a consequence of chemical weathering of Pan-African terranes: Environmental implications. *Earth Planet. Sci. Lett.* 240, 818–826.

Bartley, J.K., Kah, L.C., McWilliams, J.L., Stagner, A.F., 2007. Carbon isotope chemostratigraphy of the Middle Riphean type section (Avzyan Formation, Southern Urals, Russia): Signal recovery in a fold-and-thrust belt. *Chem. Geol.* 237, 211–232.

Benn, D.I. et al., 2015. Orbitally forced ice sheet fluctuations during the Marinoan Snowball Earth glaciation. *Nature Geosci.* 8, 704–708.

Berner, R.A., 2006, Inclusion of the weathering of volcanic rocks in the GEOCARBSULF model. *Am. J. Sci*. 306, 295–302.

Brasier, M.D., Shields, G., Kuleshov, V.N., Zhegallo, E.A., 1996. Integrated chemo- and biostratigraphic calibration of early animal evolution: Neoproterozoic–Early Cambrian of southwest Mongolia. *Geol. Mag*. 133, 445–485.

Chandler, F.W., 1988. Quartz arenites: review and interpretation. *Sediment. Geol*. 58, 105–126.

Charnay, B. et al., 2013. Exploring the faint young Sun problem and the possible climates of the Archean Earth with a 3-D GCM. *J. Geophys. Res. Atmos.* 118, 1–18.

Cox, G.M. et al., 2016. Continental flood basalt weathering as a trigger for Neoproterozoic Snowball Earth. *Earth Planet. Sci. Lett.* 446, 89–99.

Cui, H. et al., 2015. Redox architecture of an Ediacaran ocean margin: Integrated chemostratigraphic ($\delta^{13}C$–$\delta^{34}S$–$^{87}Sr/^{86}Sr$–Ce/Ce*) correlation of the Doushantuo Formation, South China. *Chem. Geol.* 405, 48–62.

Dasgupta, R., 2013. Ingassing, storage, and outgassing of terrestrial carbon through geologic time. *Rev. Min. Geochem.* 75, 183–229.

De Alvarenga, C.J.S. et al., 2008. Isotope stratigraphy of Neoproterozoic cap carbonates in the Araras Group, Brazil. *Gondwana Res.* 13, 469–479.

Dehler, C.M. et al., 2005. High-resolution $\delta^{13}C$ stratigraphy of the Chuar Group (ca. 770–742 Ma), Grand Canyon: Implications for mid-Neoproterozoic climate change. *GSA Bull.* 117, 32–45.

Dhuime, B., Wuestefeld, A., Hawkesworth, C.J., 2015. Emergence of modern continental crust about 3 billion years ago. *Nature Geosci.* 8, 552–555.

Dott, R.H., 2003. The importance of eolian abrasion in supermature quartz sandstones and the paradox of weathering on vegetation-free landscapes. *J. Geol.* 111, 387–405.

Eisbacher, G.H., 1981. Late Precambrian tillites of the northern Yukon–Northwest Territories region, Canada. In: M.J. Hambrey, W.B. Harland (eds), *Earth's Pre-Pleistocene Glacial Record*, Cambridge University Press, Cambridge, pp 724–727.

Ernst, R.E., Bell, K., 2010. Large igneous provinces (LIPs) and carbonatites. *Miner. Petrol.* 98, 55–76.

Evans, D.A.D., Mitchell, R.N., 2011. Assembly and breakup of the core of Paleoproterozoic–Mesoproterozoic supercontinent Nuna. *Geology* 39, 443–446.

Fairchild, I.J., Spiro, B., Herrington, P.M., Song, T., 2000. Controls on Sr and C isotope compositions of Neoproterozoic Sr-rich limestones of East Greenland and North China. In: J.P. Grotzinger & N.P. James (eds), *Carbonate Sedimentation in the Evolving Precambrian World*, SEPM Spec. Publ. 67, 297–313.

Feng, F. et al., 2016. Geochemistry of Altungol cap dolostones from the Tarim Basin, NW China. *Arab J. Geosci.* 9:715.

Flament, N., Coltice, N., Rey, P.F., 2013. The evolution of the $^{87}Sr/^{86}Sr$ of marine carbonates does not constrain continental growth. *Precambrian Res.* 229, 177–188.

Foden, J. Barovich, K., Jane, M., O'Halloran, G., 2001. Sr-isotopic evidence for Late Neoproterozoic rifting in the Adelaide Geosyncline at 586 Ma: implications for a Cu ore forming fluid flux. *Precambrian Res.* 106, 291–308.

Fölling, P.G., Frimmel, H.E., 2002. Chemostratigraphic correlation of carbonate successions in the Gariep and Saldania Belts, Namibia and South Africa. *Basin Res.* 14, 69–68.

Gorokhov, I.M., Kuznetsov, A.B., Melezhik, V.A., Konstantinova, G.V., Melnikov, N.N., 1998. Sr isotopic composition in the Upper Jatulian (Early Paleoproterozoic) dolomites of the Tulomozero Formation, southeastern Karelia. *Doklady Earth Sci*. 360, 609–612.

Grotzinger, J.P., James, N.P., 2000. Precambrian carbonates: evolution of understanding. In: N.P. James (ed.), *Carbonate Sedimentation and Diagenesis in the Evolving Precambrian World*, SEPM Spec. Pub. 67, 3–20.

Halevy, I., Pierrehumbert, R.T., Schrag, D.P., 2009. Radiative transfer in CO_2-rich paleoatmospheres. *J. Geophys. Res.* 114, D18112.

Halverson, G.P., Dudas, F.O., Maloof, A.C., Bowring, S.A., 2007. Evolution of the $^{87}Sr/^{86}Sr$ composition of Neoproterozoic seawater. *Palaeogeogr. Palaeocl*. 256, 103–129.

Halverson, G.P., Shields-Zhou, G.A., 2011. Chemostratigraphy and the Neoproterozoic glaciations. In: E. Arnaud, G.P. Halverson, G. Shields-Zhou (eds), *The Geological Record of Neoproterozoic Glaciations*, Geol. Soc. Lond. Mem. 36, 51–66.

Haqq-Misra, J.D., Domagal-Goldman, S.D., Kasting, P.J., Kasting, J.F., 2008. A revised, hazy methane greenhouse for the Archean Earth. *Astrobiol.* 8, 1127–1137.

Heimann, A. et al., 2010. Fe, C, and O isotope compositions of banded iron formation carbonates demonstrate a major role for dissimilatory iron reduction in ~2.5 Ga marine environments. *Earth Planet. Sci. Lett.* 294, 8–18.

Hessler, A.M., Lowe, D.R., 2006. Weathering and sediment generation in the Archean: An integrated study of the evolution of siliciclastic sedimentary rocks of the 3.2 Ga Moodies Group, Barberton Greenstone Belt, South Africa. *Precambrian Res.* 151, 185–210.

Higgins, J.A., Schrag, A.P., 2003. Aftermath of a snowball Earth. *Geochem., Geophys., Geosys*. 4, 1028.

Holland, H.D., 2006. The oxygenation of the atmosphere and oceans. *Phil. Trans. R. Soc. B* 361, 903–915.

Huang, J., Chu, X., Jiang, G., Feng, L., Chang, H., 2011. Hydrothermal origin of elevated iron, manganese and redox-sensitive trace elements in the c. 635 Ma Doushantuo cap carbonate. *J. Geol. Soc. Lond.* 168, 805–811.

Jacobsen, S.B., Kaufman, A.J., 1999. The Sr, C and O isotopic evolution of Neoproterozoic seawater. *Chem. Geol*. 161, 37–57.

Kah, L.C., Lyons, T.W., Chesley, J.T., 2001. Geochemistry of a 1.2 Ga carbonate-evaporite succession, northern Baffin and Bylot Islands: implications for Mesoproterozoic marine evolution. *Precambrian Res.* 111, 203–234.

Kamber, B.S., Webb, G.E., 2001. The geochemistry of late Archaean microbial carbonate: Implications for ocean chemistry and continental erosion history. *Geochim. Cosmochim. Acta* 65, 2509–2525.

Kanzaki, Y., Murakai, T., 2015. Estimates of atmospheric CO_2 in the Neoarchean–Paleoproterozoic from paleosols. *Geochim. Cosmochim. Acta* 159, 190–219.

Kasting, J.F., 1993. Earth's early atmosphere. *Science* 259, 920–926.

Kasting, J.F., 2014. Modeling the Archean atmosphere and climate. In: H. Holland, K. Turekian (eds), *Treatise in Geochemistry Vol. 6*, *The Atmosphere – History*, pp 157–175.

Lee, H. et al., 2016. Massive and prolonged deep carbon emissions associated with continental rifting. *Nature Geosci.* 9, 145–150.

Li, Z.X. et al., 2008. Assembly, configuration, and break-up history of Rodinia: a synthesis. *Precambrian Res*. 160, 179–210.

Macdonald, F.A., Strauss, J.V., Rose, C.V., Dudás, F.O., Schrag, D.P., 2010. Stratigraphy of the Port Nolloth Group of Namibia and South Africa and implications for the age of Neoproterozoic Iron Formations. *Am. J. Sci.* 310, 862–888.

Macdonald, F.A. et al., 2013. The Laurentian record of Neoproterozoic glaciation, tectonism, and eukaryotic evolution in Death Valley, California. *GSA Bull.* 125, 1203–1223.

Maloof, A.C. et al., 2010. The earliest Cambrian record of animals and ocean geochemical change. *Geol. Soc. Am. Bull*. 122, 1731–1774.

Marin-Carbonne, J., Chaussidon, M., Robert, F., 2012. Micrometer-scale chemical and isotopic criteria (O and Si) on the origin and history of Precambrian cherts: Implications for paleo-temperature reconstructions. *Geochim. Cosmochim. Acta* 92, 129–147.

Melezhik, V.A., Pokrovsky, B.G., Fallick, A.E., Kuznetsov, A.B., Bujakaite, M.I., 2009. Constraints on $^{87}Sr/^{86}Sr$ of Late Ediacaran seawater: insight from Siberian high-Sr limestones. *J. Geol. Soc. Lond.* 166, 183–191.

Ohmoto, H., Watanabe, Y., Kumazawa, K., 2004. Evidence from massive siderite beds for a CO_2-rich atmosphere before ~1.8 billion years ago. *Nature* 429, 395–399.

Ohno, T., Komiya, T., Ueno, Y., Hirata, T., Maruyama, S., 2008. Determination of $^{88}Sr/^{86}Sr$ mass-dependent isotopic fractionation and radiogenic isotope variation of $^{87}Sr/^{86}Sr$ in the Neoproterozoic Doushantuo Formation. *Gondwana Res.* 14, 126–133.

Pehrsson, S.J., Buchan, K.L., Eglington, B.M., Berman, R.M., Rainbird, R.H., 2014. Did plate tectonics shutdown in the Palaeoproterozoic? A view from the Siderian geologic record. *Gondwana Res.* 26, 803–815.

Peters, S.E., Gaines, R.R., 2012. Formation of the 'Great Unconformity' as a trigger for the Cambrian explosion. *Nature* 484, 363–366.

Pierrehumbert, R.T., Abbot, D.S., Voigt, A., Koll, D., 2011. Climate of the Neoproterozoic. *Ann. Rev. Earth Planet. Sci*. 39, 417–60.

Pokrovsky, B.G., Chumakov, N.M., Melezhik, V.A., Bujakaite, M.I., 2010. Geochemical properties of Neoproterozoic "cap dolomites" in the Patom paleobasin and problem of their genesis. *Lithol. Min. Resources* 45, 577–592.

Roberts, N.M.W., Spencer, C.J., 2015. The zircon archive of continent formation through time. In: N.M.W. Roberts et al. (eds), *Continent Formation Through Time*, Geol. Soc. Lond. Spec. Pub. 389, 197–225.

Rooney, A.D. et al., 2014. Re-Os geochronology and coupled Os-Sr isotope constraints on the Sturtian snowball. *Proc. Nat. Acad. Sci.* 111, 51–56.

Rooney, A.D., Strauss, J.V., Brandon, A.D., Macdonald, F.A., 2015. A Cryogenian chronology: Two long-lasting synchronous Neoproterozoic glaciations. *Geology* 43, 459–462.

Sawaki, Y. et al., 2010a. The Ediacaran radiogenic Sr isotope excursion in the Doushantuo Formation in the Three Gorges area, South China. *Precambrian Res.* 176, 46–64.

Sawaki, Y. et al., 2010b. $^{87}Sr/^{86}Sr$ chemostratigraphy of Neoproterozoic Dalradian carbonates below the Port Askaig glaciogenic formation, Scotland. *Precambrian Res.* 179, 150–164.

Schaller, M.F., Wright, J.D., Kent, D.V., 2015. A 30 Myr record of Late Triassic atmospheric pCO_2 variation reflects a fundamental control of the carbon cycle by changes in continental weathering. *GSA Bull.* 127, 661–671.

Shibuya, T. et al., 2012. Depth variation of carbon and oxygen isotopes of calcites in Archean altered upper oceanic crust: Implications for the CO_2 flux from ocean to oceanic crust in the Archean. *Earth Planet. Sci. Lett.* 321–322, 64–73.

Shields, G.A., 2002. 'Molar-tooth microspar': a chemical explanation for its disappearance ~ 750 Ma. *Terra Nova* 14, 108–113.

Shields, G.A., 2007. A normalised seawater strontium isotope curve: possible implications for Neoproterozoic-Cambrian weathering rates and the further oxygenation of the Earth. *eEarth* 2, 35–42.

Shields, G., Veizer, J., 2002. Precambrian marine carbonate isotope database: Version 1.1. *Geochem*. *Geophys. Geosys.* 3, 10.1029/2001GC000266.

Shields, G.A., Brasier, M.D., Stille, P., Dorjnamjaa, D., 2002. Factors contributing to high $\delta^{13}C$ values in Cryogenian limestones of western Mongolia. *Earth Planet. Sci. Lett*. 196, 99–111.

Soegaard, K., Eriksson, K.A., 1989. Origin of thick, first-cycle quartz arenite successions: evidence from the 1.7 Ga Ortega Group, northern New Mexico. *Precambrian Res*. 43, 129–141.

Veizer, J. et al., 1999. $^{87}Sr/^{86}Sr$, $\delta^{13}C$ and $\delta^{18}O$ evolution of Phanerozoic seawater. *Chem. Geol.* 161, 59–88.

Von Blanckenburg, F., Bouchez, J., Ibarra, D.E., Maher, K., 2015. Stable runoff and weathering fluxes into the oceans over Quaternary climate cycles. *Nature Geosci.* 8, 538–542.

Voigt, A., Abbot, D.S., 2012. Sea-ice dynamics strongly promote Snowball Earth initiation and destabilize tropical sea-ice margins. *Clim. Past* 8, 2079–2092.

Wickman, J., 1948. Isotope ratios: a clue to the age of certain marine sediments. *J. Geol.* 56, 61–66.

Wolf, E.T., Toon, O.B., 2014. Controls on the Archean climate system investigated with a global climate model. *Astrobiol.* 14, 241–253.

Yang, J., Peltier, W.R., Hu, Y., 2012. The initiation of modern “soft snowball” and “hard snowball” Climates in CCSM3. Part I: the influences of solar luminosity, CO_2 concentration, and the sea ice/snow albedo parameterization. *J. Clim.* 25, 2711–2736.

Xiao, S. et al., 2004. The Neoproterozoic Quruqtagh Group in eastern Chinese Tianshan: evidence for a post-Marinoan glaciation. *Precambrian Res*. 130, 1–26.

Yashioka, H., Asahara, Y., Tojo, B., Kawakami, S., 2003. Systematic variations in C, O, and Sr isotopes and elemental concentrations in Neoproterozoic carbonates in Namibia: implications for a glacial to interglacial transition. *Precambrian Res*. 124, 69–85.

Zeebe, R.E., Caldeira, K., 2008. Close mass balance of long-term carbon fluxes from ice-core CO2 and ocean chemistry records. *Nature Geosci.* 1, 312–315.

CHAPTER SIX

Causes of sedimentation in the Nanhua Rift Basin, South China, during the mid Neoproterozoic: a critical review

Abstract

The Nanhua Basin, running SW-NE through the middle of the South China Block, preserves a continuous sequence of Neoproterozoic sediments from at least 860 Ma onward. This chapter presents an overview of the chronology, stratigraphy and sedimentology of the later Tonian and Cryogenian record. As in other parts of the world, the dominant control on sedimentation was rifting, beginning soon after 820 Ma and continuing to at least 663 Ma. Formations mark tectonic shifts in provenance in the course of basin infilling. At the base of the Chang'an Formation, not long after the start of the Cryogenian Period (as currently defined), sediment became slightly coarser but remained subaqueous, as throughout the period. The Datangpo Formation represents a relatively short (c. 663–648 Ma) interval when rifting was in abeyance. By the start of the Ediacaran the entire craton was flooded. The pattern of sedimentation seems incompatible with the hypothesis of global glaciation, which predicts a eustatic rise of > 500 m at the end of the Fulu Formation (c. 663 Ma) and a 700-m fall around the end of the Datangpo before the diamictites of the Nantuo Formation. Globally, zircons record lower $\delta^{18}O$ values during the Cryogenian than at any other time in the Proterozoic, consistent with unusually hot asthenosphere. In South China values were initially higher and began falling earlier, c. 820 Ma, about the same time as a peak in zircon frequency, suggesting that both the heating and the rifting were plume-related, distinct from the build-up of heat that drove the supercontinent's disaggregation in the Cryogenian.

6.1. The formation of the South China Block

The South China Block or Craton consists of two major terranes, the Yangtze Block to the north west and the Cathaysia Block to the south east (Fig. 6.1). During the Mesoproterozoic, Cathaysia was part of Laurentia, possibly separated from the Yangtze Block by a small bay-like expanse of ocean (Li et al. 2008b). According to most workers, the blocks began to converge in the late Mesoproterozoic, about the same time as other land masses are thought to have aggregated into the supercontinent Rodinia. The eastern ends finally amalgamated in the early Neoproterozoic. Although the suture is obscured by a second collision during the Palaeozoic (He et al. 2013), there

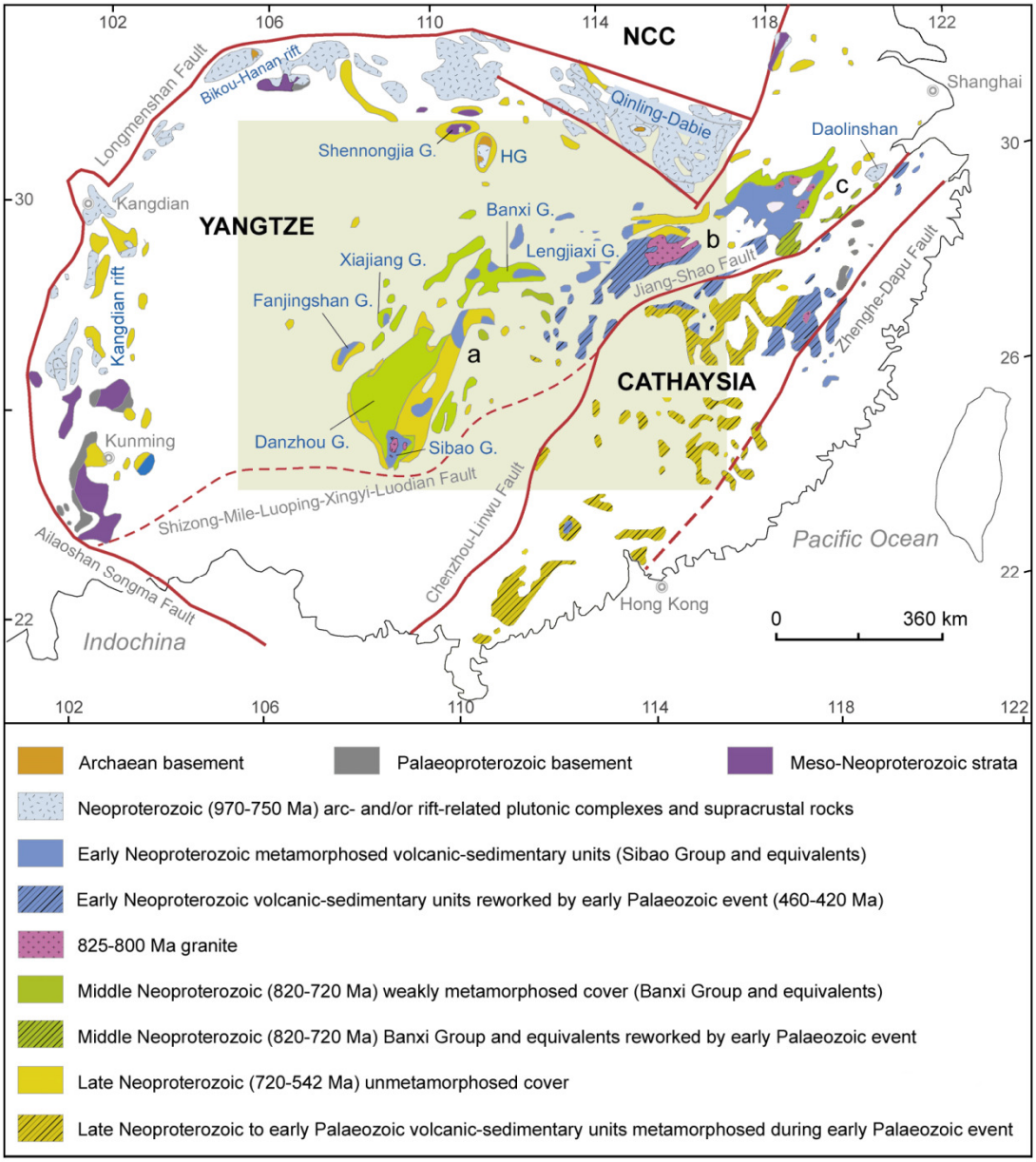

Figure 6.1. Precambrian outcrops in South China (after Zhao & Cawood 2012). The Nanhua Rift Basin comprises (a) the Hunan-Guangxi, (b) Jiagnan Ridge and (c) Northern Zhengjiang sub-basins, as shown. HG: Huangling Granite (837 ±7 and 819 ±7 Ma). Most granite outcrops in the Nanhua basin date to 825-800 Ma. A satellite map of the shaded area, with locations, is given in Figure 6.3.

is evidence of subduction under the Yangtze Block, with volcanism along its south-eastern margin; there may also have been subduction under Cathaysia (Wang et al. 2015). Mafic-ultramafic complexes identified as back-arc ophilolites occur in NE Jiangxi and South Anhui Provinces, dated to c. 990 and 840-820 Ma respectively (*ibid*., Zhang, C. et al. 2013).

The Sibao, Fanjingshan and Lengjiaxi groups, laterally equivalent siliciclastic sequences, accumulated on the Yangtze Block in the course of the inferred convergence (Wang et al. 2012b) and

constitute the region's upper basement. The Sibao Group, a representative sequence not far from the suture zone, consists of mudstones, siltstones and sandstones interpreted as mostly turbiditic, with occasional pillow lavas, tuffs and volcaniclastic breccias. If we ignore (as throughout) the unknown lag between crystallisation and sedimentary age, youngest zircon ages of c. 820 Ma give the date of the amalgamation. Folding and uplift along the suture is termed the Sibao or Jiangnan Orogen. 'Orogen' is something of a misnomer, for sedimentation across the unconformity marking the collapse of the fold belt was almost continuous and only weakly metamorphosed, and, within the Yangtze Block, rifting immediately undid the crustal thickening (Yang et al. 2015). Above the unconformity lie the laterally equivalent Danzhou, Xiajiang (Fig. 6.2) and Banxi groups, amongst others, dating from soon after 820 Ma (*ibid*., X.C. Wang et al. 2012). These are also siliciclastic, beginning with conglomerates and including high proportions of volcanic clasts. Gold and manganese deposits suggest some hydrothermal influence (Fig. 6.2d).

For want of sufficient data, palaeogeographic reconstructions for the Neoproterozoic are still in flux. According to one scheme, South China at 825 Ma was nestled within the supercontinent at the relatively high latitude of 50° N, with Laurentia to its SW and North Australia to its NE (Li et al. 2013, revised in Niu et al. 2016). According to another, South China lay on the periphery, adjoining Tarim and India (Evans 2009). Palaeogeography affects tectonic scenarios, and the tectonic evolution of South China is variously interpreted (Zhao & Cawood 2012). According to the 'plume-rift' model, the granitoids, uplift and subsequent rifting along the northern, western and south-eastern margins were caused by an ascending mantle plume (Li et al. 2003). The 'slab-arc' model attributes the magmatism to ocean crust subduction. After the Yangtze and Cathaysia Blocks amalgamated, subduction continued along the northern and western margins while the former orogen became a back-arc basin (Zhao et al. 2011). A third model, termed 'plate-rift', has the main phase of arc magmatism in the late Mesoproterozoic rather than mid Neoproterozoic, attributing the magmatism of 830–800 Ma (granites, gabbros, komatiites) to decompression-induced melting of the mantle during orogenic collapse. Subsequent upwelling of the asthenosphere caused lithospheric extension and intracontinental rifting. A fourth model argues that South China formed in the early Neoproterozoic by north-westward accretion of successive arc-backarc terranes, with subduction directed to the SE and the craton located adjacent to Western Australia and northern India on the periphery of Rodinia (Cawood et al. 2013). Whatever the precise tectonic setting, the crust received substantial additions of juvenile material in the Tonian period (Liu et al. 2008, X.C. Wang et al. 2012). Indeed, on the Cathaysian side an estimated 90% of the Precambrian basement consists of Neoproterozoic rock (Zhao & Cawood 2012). There, however, Phanerozoic orogenesis and magmatism have obscured much of the early record, leaving the Neoproterozoic more difficult

Figure 6.2a. Tectonic rippling in the Fanzhao Formation, Xiajiang Group (= Banxi Group) near Taijiang, E Guizhou. The formation is dated to ~800-770 Ma. Foreground field of view approximately 9 m.

Figure 6.2b. Flute casts in the Fanzhao Formation, same location. Foreground field of view approximately 9 m.

Figure 6.2c. Turbidites, Fanzhao Formation, same location.

Figure 6.2d. Rhodochrosite nodules in the Fanzhao Formation, same location – evidence of rift-related hydrothermal fluids.

to decipher. Diamictite units correlatable with the Sturtian and Marinoan intervals have been reported (Feng & Zhang 2016).

In the plume-rift model South China emerged as an entity near the centre of Rodinia and its early history was therefore intimately linked with the supercontinent. Around 825 Ma a superplume beneath the lithosphere initiated widespread rifting (Li et al. 2013). Cited evidence for the superplume comes partly from South China itself, the proposed centre of the plume, but also includes (Huang et al. 2015):

- the 827±6 Ma Gairdner Dyke Swarm of South Australia and 824±4 Ma Amata Dyke Swarm of Central Australia (feeding continental flood basalts of which the Wooltana Volcanics, for example, are remnants)
- the Boucaut Volcanics of South Australia, now dated older than 800 Ma (Preiss et al. 2009)
- the Richtersveld Igneous Complex in South Africa 800–770 Ma, followed by rifting, mafic dikes and other volcanism climaxing around 740 Ma
- a mafic dike complex along the western margin of Laurentia dated to 780 Ma
- granitoid bodies along the western margin of Laurentia that underlie rift successions and appear unrelated to plate convergence, poorly dated to around 760–740 Ma
- the 770–740 Ma granitoids of southeastern Laurentia.

About the same time (from c. 810 Ma) Rodinia is inferred to have rotated 90° and shifted rapidly southwards (Li et al. 2013). By 780 Ma it had centred itself about the equator, putting South China in the subtropical zone. By 720 Ma a widening ocean between East Antarctica and South China was pushing South China out of its internal position toward Rodinia's periphery.

This reconstruction of plate-tectonic evolution through the Neoproterozoic is uncertain, as are all others (e.g. Scotese 2009, Piper 2013); in particular, some workers question whether South China occupied a central position in Rodinia (Li, Z.X. et al. 2009, Zhao et al. 2011, Cawood et al. 2013, Du et al. 2014). Although the Yangtze Block appears to extend further to the west than previously supposed, beneath eastern Tibet (Guo et al. 2013), the age of the underthrust terrane is unknown, and does not exclude the possibility that the Bikou-Hanan magmatic arc formed above a subduction zone (as advocated by Du et al. 2014). In contrast to North China, which has a carbonate record extending from the Tonian back into the Mesoproterozoic, carbonate platforms did not develop on the Yangtze Block until the Ediacaran, although carbonate within the rift basin does occur in the upper Baizhu and Hetong Formations (lower Danzhou Group).

6.2. Rifting in relation to sediment generation

As well as being subject to intermittent volcanism, the rift basins were places where thick successions of mudstones, siltstones, sandstones and conglomerates accumulated. The Nanhua Basin has been divided into three sub-basins. This chapter focuses on the largest, the 'Hunan-Guangxi sub-basin' which occupies eastern Guizhou, northern Guangxi and western Hunan Province and trends SW-NE (Wang & Li 2003). Most transects have been constructed either N to S (Jiang et al. 2006, Bahlburg & Dobrzinski 2007, Zhang et al. 2008a) or E to W (Jiang et al. 2006, Bahlburg & Dobrzinski 2007), tracing the progression from shallow margins to deep trough. Although the N-S transect of Jiang et al. (Fig. 6.4) infers a simple and relatively smooth progression, published logged sections indicate that the basin was segmented by rift-parallel faults. Between Tianping and Maopingdong, for example, the Wuqiangxi Formation (upper part of the Banxi Group) beneath the pre-diamictite unconformity decreases in thickness from 1200 m to 150 m. The equivalent interval between Maopingdong and Zhijiang thickens from 150 m to 2200 m (Fig. 6.5). These disparities suggest at least two half grabens across the region, sinking in response to synsedimentary faulting, loading and crustal thinning, and filling up as material was shed from eroding footwalls (cf. Wang & Li 2003). As sedimentation progressed, the rift basin widened to encompass Yangjiaping and even more northerly regions.

Correlation of stratigraphic units across the mountainous terrain of the Nanhua rift is not straightforward (Zhang et al. 2003). In the centre of the basin there are multiple diamictite horizons, with interleaved finer sediments; on the margins there are rarely more than two. The current consensus is that the diamictites represent the same two periods of glaciation as are attested on other cratons in the Cryogenian, with an interglacial period represented in most places by the Datangpo Formation. Where several diamictite units occur beneath the Datangpo these are ascribed to the Sturtian glaciation; where only one, the unit is ascribed to the upper Sturtian. In some places there are none, as for example above the Liantuo Formation of northern Hunan and Hubei or above the Xiajiang Group in northeastern Guizhou, and the relationship with units further south has to be determined principally through geochronology. Most researchers now put the Liantuo before the oldest diamictites, placing the latest of several zircon age determinations, 728 ±5 Ma (Table 1), close to the onset of the erosional unconformity. The formation comprises two tectonic cycles (Fig. 8.4), the older one correlating with the Madiyi Formation, the younger with the Wuqiangxi Formation (Fig. 8.5, Zhang et al. 2008a). In northern Hubei the lower part of the Liantuo stratigraphically overlies the Huangling Granite, with polymict conglomerate. The upper part has a radically different zircon-age profile (unrelated to the Huangling Granite) and appears to be substantially older.

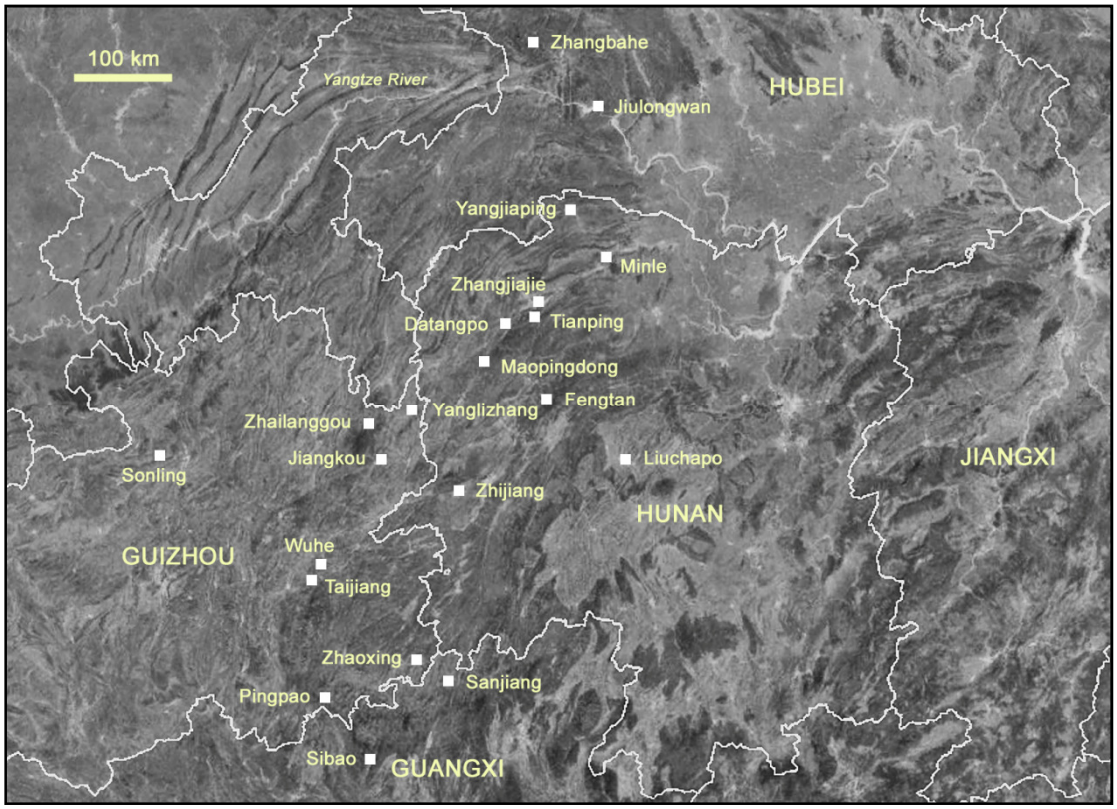

Figure 6.3. Locations of geological sections referred to in figures and text. Liantuo is 10 km east of Jiulongwan (Yangtze Gorges area), the Huangling Granite immediately to their north, and Li(ao)jiapo adjacent to Pingpao.

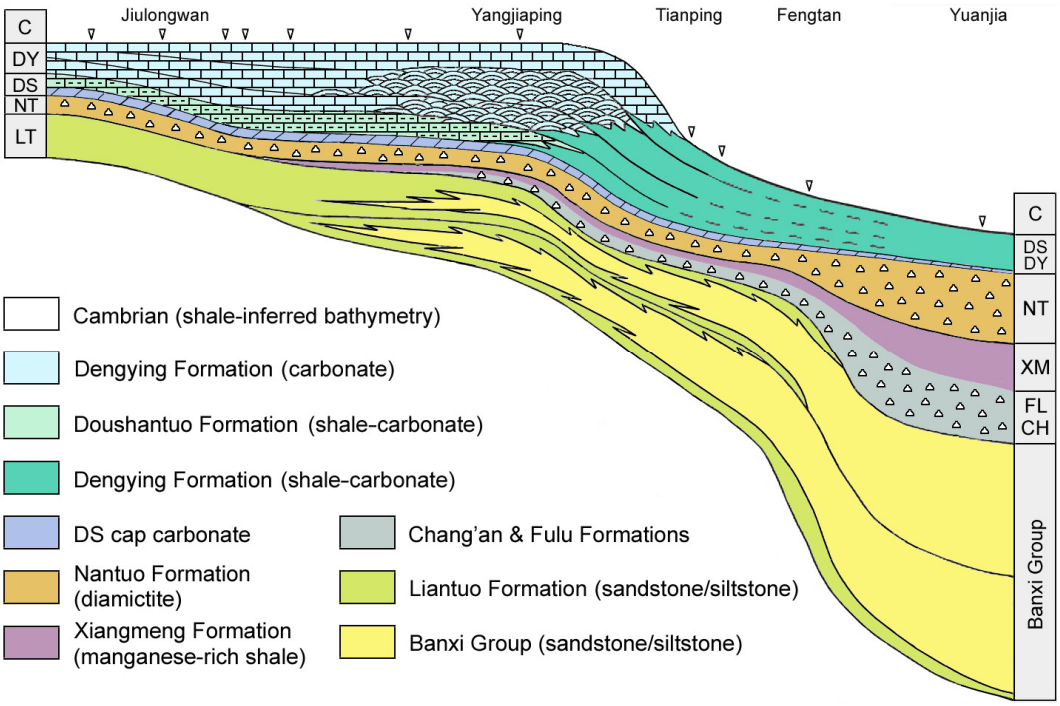

Figure 6.4. Transect inferred by Jiang et al. (2006) from 11 sections running N-S through the Nanhua Basin. See Figure 6.3 for the locations indicated and compare with Figure 6.5. The Xiangmeng Formation (western Hunan Province) is equivalent to the Datangpo Formation.

Formation	Province	Date (Ma)	Material	Context	Source
Xieshuihe	Hunan	692 ±8	Tuffaceous siltstone	Underlies Dongshanfeng Fm	Lan et al. 2015a
Xieshuihe	Hunan	758 ±23	Tuffaceous sandstone & slate	Underlies Dongshanfeng Fm	Yin et al. 2003
Chang'an	SE Guizhou	710 ±6.5	Diamictite	Underlies Fulu Fm	Hofmann et al. 2011
Chang'an	C Hunan	751 ±3.6	Tuffaceous siltstone	Lower part of formation	X.C. Wang et al. 2012
Niuguping (Banxi Gp)	W Hunan	725 ±10	Tuffaceous siltstone	300 m below top of formation.	Zhang et al. 2008
Liantuo (upper)	SW Hubei	714 ±8	Tuffaceous siltstone	Top of formation, overlain by Nantuo	Lan et al. 2015b
Liantuo (upper)	SW Hubei	724 ±12	Tuff bed	Same horizon	Gao & Zhang 2009
Liantuo	SW Hubei	728 ±5	Sandstone	Underlies Gucheng Mb	Hofmann et al. 2011
Liantuo (upper)	SW Hubei	734 ±8.1	Tuff		Pi & Jiang 2016
Liantuo (upper)	N Hubei	736 ±5.8	Tuff	Underlies Nantuo Fm	Du et al. 2013
Liantuo	Hubei	766 ±18	Tuff	Underlies Nantuo Fm	Zheng 2003
Liantuo (lower)	N Hubei	779 ±12	Tuff	Underlies Nantuo Fm	Du et al. 2013
Gongdong (Danzhou Gp)	SE Guizhou	716 ±3.4 716 ±2.8	Tuffaceous siltstone	Upper part of Gongdong, underlies Chang'an Fm	Lan et al. 2014
Gongdong	N Guangxi	734 ±4.3	Siltstone	Upper part of Gongdong	Wang & Zhou 2012
Gongdong	N Guangxi	787 ±5.6	Tuffaceous	Upper part of Gongdong	Gao et al. 2013
Gongdong	N Guangxi	731 ±4.4	Siltstone	Lower part of Gongdong	X.C. Wang et al. 2012
Sanmenjie (Danzhou Gp)	W Hunan	765 ±14	Volcanics	Lower part of >200-m-thick unit, underlies Gongdong	Zhou et al. 2007

Table 6.1. U-Pb zircon ages relevant to the dating of the lowermost diamictites in the Nanhua Basin. Some zircons are probably detrital. All formations other than the Chang'an itself immediately underlie the first diamictites in their vicinity. The Xieshuihe Formation is equivalent to lower Fulu.

Ages from the upper Banxi Group and correlatives constrain the age of the overlying Chang'an Formation (Jiangkou Group), the oldest diamictite-bearing unit. At Lijiapo the successive Qingshuijiang, Pinglue and Longli Formations span 2250 m of stratigraphy (Huang et al. 2014). Although one group of zircons from a tuff bed near the top of the Qingshuijiang Formation provided a concordia age of 772 ±5 Ma (X.C. Wang et al. 2012), numerous zircons were younger, including seven all dating to 750 Ma (surely more likely to be igneous) and two younger than 750 Ma. Another study yielded ages of similar distribution, with four zircons younger than 750 Ma (Wang et al. 2010). No data have been published for the Pinglue or Longli Formations, accounting for 1640 m of the stratigraphy. The Gongdong Formation, correlative with the Longli, yielded two concordia ages of 716 ±3 Ma.

Tuffaceous deposits are dated on the basis that clusters of zircons from the ash deposit can be distinguished from the detrital zircons mixed in with it. However, the identification of clusters by means of histograms can be misleading. The youngest reported $^{206}Pb/^{238}U$ age of the Liantuo

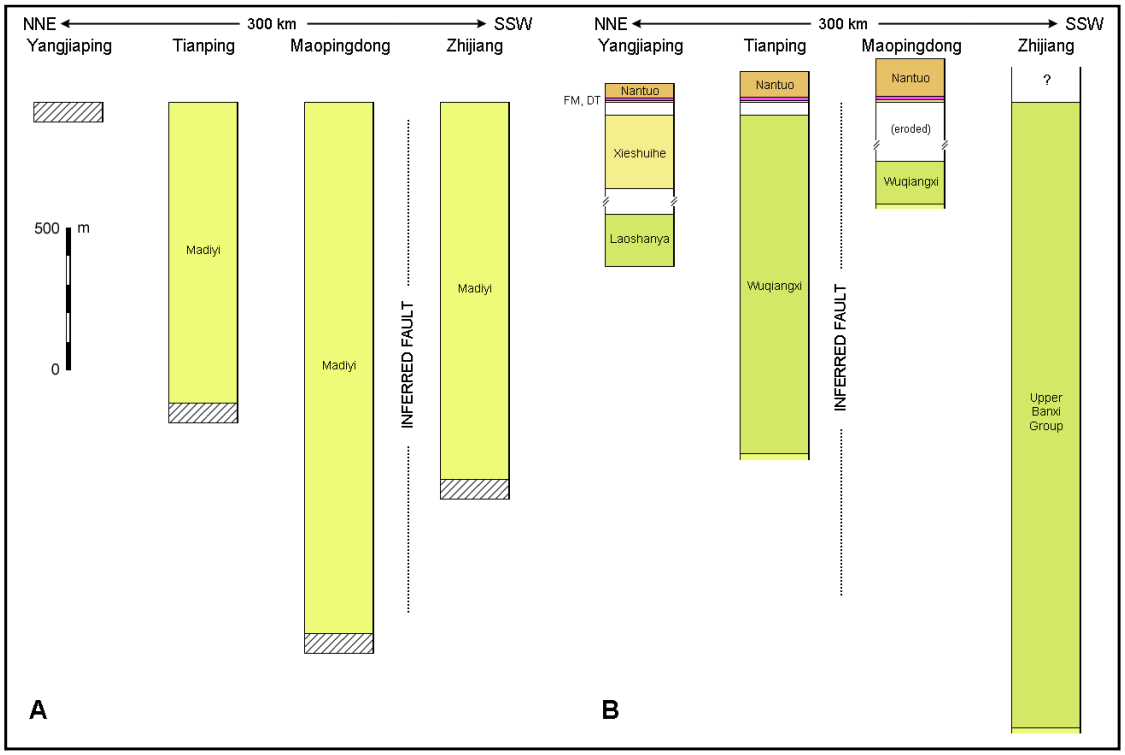

Figure 6.5. (a) Formation thicknesses of the lower Banxi Group along a 300-km transect running NNE-SSW through W Hunan (Fig. 6.3). The transect is that of Zhang et al. (2008a), where Dayong is the old name for Zhangjiehe, referring to the Tianping section, and Guzhang presumably the Maopingdong section. **(b)** Formation thicknesses of the upper Banxi Group at the same locations, along with thicknesses of the Fulu and Datangpo Formations (or equivalents).

Formation, for example, comprises 7 zircons ranging from 726 ±10 (1σ) to 705 ±10 Ma, and in reality these do not form a cluster (Fig. 6). With the ambiguous exception of the 3 youngest, having ages of 704.5 ±10, 705 ±12, and 706.1 ±10, there is no increase in frequency; the next oldest is 711.9 ±10 Ma, after that 722 ±10 Ma. Identification of which zircons to lump together is critical, for the more extensive the group, the older its mean age. In this case, the zircons are too few to identify a statistically meaningful group. While a substantial gap precedes the 7 selected, the gap is filled by a sample 2.5 m lower, improbably dated to 24 Ma earlier. It should also be mentioned that only 4 of the $^{206}Pb/^{238}U$ ages are < 10% discordant (however defined) with the corresponding $^{207}Pb/^{206}U$ ages. In the particular case this is not material, but it could be in other cases.

Another example is the age of 725 ±10 Ma given to a purportedly tuffaceous siltstone in the Niuguping Formation (Danzhou Group). The bed lies 300 m below the top of the 720-m-thick formation, and the zircons making up the mean age range from 741 ±22 to 702 ±22 Ma. They do not form a cluster. The penultimate 6 zircons, ranging from 714 ±24 to 709 ±36 Ma, may do, as evidenced by frequency somewhat above average. The weighted mean of these is 712.4 ±9.8.

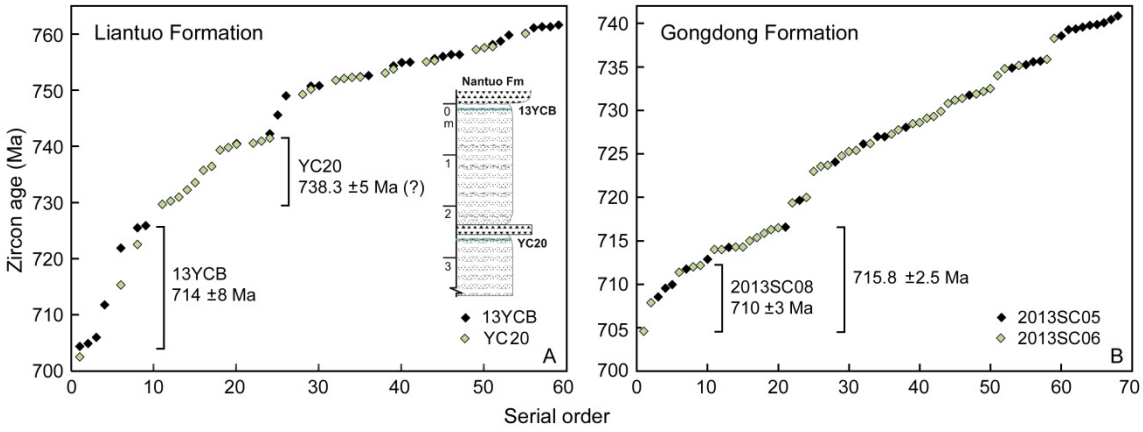

Figure 6. (**a**) Age-frequency of youngest zircons in tuffaceous beds near top of the Liantuo Formation (data from Lan et al. 2015b). Frequency drops off after 740 and again after 728 Ma. (**b**) Age-frequency of youngest zircons in tuffaceous beds near top of Gongdong Formation (data from Lan et al. 2014).

The Gongdong Formation provides one further example. Two tuffaceous samples were analysed, one from 60 m below the contact with the Chang'an Formation, where the Gongdong is > 350 m thick, the other 25 m below where it is > 850 m thick. Ages in the older sample (2013SC05) were seen as falling into three groups, peaking at c. 716 (actually skewed towards c. 710, but with n only 8), c. 739 (n = ~18) and c. 753 Ma (n = ~15). At best, only the youngest can represent the ash fall, and evidently a group may not represent an ash fall at all. Ages in the sample from 25 m below the boundary fell into two overlapping groups, one thought to peak at c. 715, the other at c. 728 Ma. Again, since the older cannot represent an ash fall, the younger also may not. Furthermore, the younger group in this sample is indistinguishable from the youngest in the sample from 60 m. If we combine the samples (Fig. 8.6), a continuous group of normally distributed ages follows a clear gap. Logically, it is difficult to attribute a single cluster from two samples 35 m apart to two separate ash falls. Since the great majority of zircons in the Nanhua basin come from granitoids, the 20 zircons composing the cluster more probably represent, not a single datable event, but the variable crystallisation ages of a cooling pluton. In other words, the zircons are detrital.

Age-frequency has to be interpreted against the background of detrital zircons decreasing through the period 800–700 Ma and petering out after 720 Ma (e.g. Figs. 8.11, 8.12). Any argument that zircons represent an ash fall must therefore be able to show an increase in frequency above background. Without such evidence, a group of zircons cannot confidently be attributed to a penecontemporaneous ash fall. Unfortunately, tuffaceous deposits in the Chang'an and Fulu Formations are rare, if they occur at all. One possibly tuffaceous bed near the base of the Chang'an Formation yielded an age of 778 ±5 (Gao et al. 2013), older than the 765 ±14 Ma obtained from volcanics of the underlying Samenjie Formation. Another such horizon in the middle of the

Chang'an 250 km to the NW yielded an age of 752 ±4 Ma (X.C. Wang et al. 2012). Neither age agrees with those obtained from the upper Gongdong Formation.

As things stand, the maximum age of the Chang'an Formation is constrained only by the age of the formations directly or indirectly underlying it. As discussed, the relevant constraints are: (1) 300 m below the top of the Niuguping Formation, 712.4 ±10 Ma, possibly dating an ash bed, (2) detrital zircons from the top of the Liantuo, 714 ±8 Ma, and (3) detrital zircons from 25 m below the top of the Gongdong, the 5 youngest having a mean age of 710 ±3 Ma. Accordingly, the base of the Chang'an is unlikely to be older than 710 Ma.

The only tight constraint on the end of the Sturtian diamictite interval comes from a tuffaceous bed within a 3-m-thick rhodochrosite (manganese carbonate) unit 1 m above the base of the Datangpo Formation, which yielded a concordia $^{207}Pb/^{206}Pb$ age of 663 ±4 Ma (Zhou et al. 2004). A table of all zircon ages obtained was not reported.

The upslope unconformity at the base of the Cryogenian, coincident with the appearance of clasts in the deeper parts of the basin, marks a shift in tectonics. To the north, Chang'an or Chang'an-equivalent sediments are absent, and diamictites and conglomerates attributable to the later Fulu Formation and equivalents almost absent (typically <10 m). The high-energy character of the sediments above the hiatus suggests that the surface was erosional. Where Fulu-age sediments are absent, the unconformity may mark a palaeo-high, along a profile less regular than commonly assumed. To the south, where the basin profile deepens, sections become more complete. At Zhaoxing (Fig. 6.7) the Chang'an abruptly reaches 1900 m in thickness and the contact with the underlying formation is conformable (Zhang et al 2011). Sedimentation here went on continuously and sediment supply, in part at least, was unrelated to glacial erosion.

Whatever the nature of the underlying, pre-Cryogenian surface, thickness variations above it show that depocentres continued to be generated by fault movements. Grabens developed and filled up in different places at different times. At Sanjiang the Chang'an Formation is only a fifth of its thickness at Zhaoxing, 36 km to the NW. By contrast, the Fulu Formation is relatively thick, and, unusually, thicker than the Chang'an (Fig. 6.7a).

Higher up in the succession the trend of thickening distally is maintained. The Chang'an and Fulu Formations, both generally interpreted as glaciogenic, are overlain by the Datangpo Formation and correlatives (the Xiangmeng and Heling Formations). Previously regarded as the middle member of the succeeding Nantuo Formation (e.g. Liao 1981), the Datangpo is a fine-grained unit of shales and siltstones. It oversteps the unconformity as far as the middle shelf (e.g. Fig. 3 in Zhang et al.

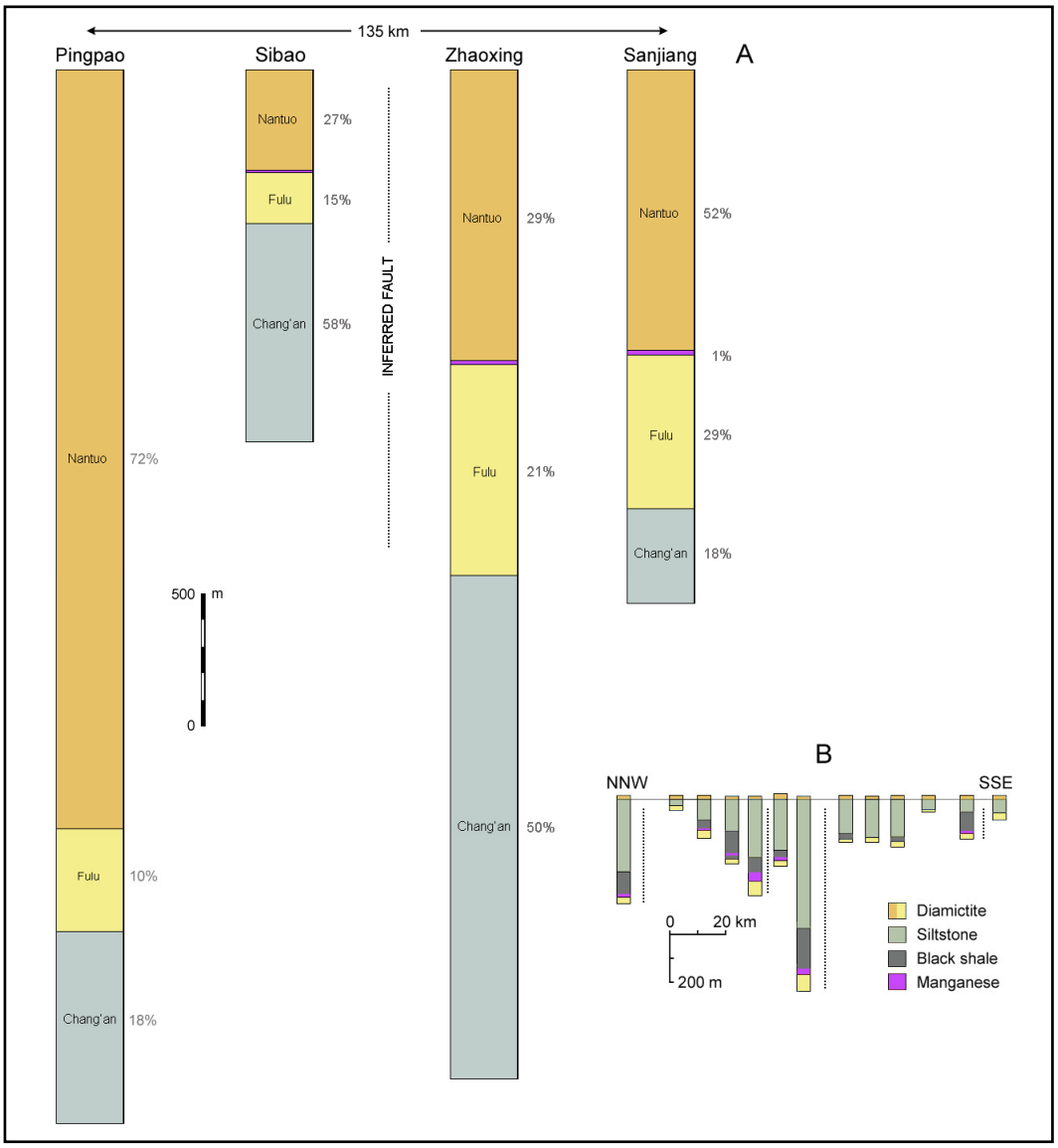

Figure 6.7. (a) Thicknesses of the Cryogenian formations in SE Guizhou and N Guangxi from W to E, except that Sibao is 78 km SE of Pingpao. Relative proportions differ greatly from place to place. Data from Liao (1981), Zhang et al. (2011) and Lan et al. (2015). See Fig. 6.3 for locations. (**b**) Log transect through the Mn mining area of NE Guizhou (after Yu et al. 2016).

2011). At the type section near Yanglizhang, Songtao county, it is around 180 m thick; at Minle, 120 km to the NE, it exceeds 200 m (Li et al. 2012). At Jiangkou, to the south, it is 60 m, at Zhaoxing and Sanjiang 12–16 m, and absent from Pingpao. The trend is one of downslope thinning related to low-energy sedimentation. Published logs do not substantiate the downslope thickening portrayed in the Jiang et al. transect (Fig. 6.4). A fence diagram of 13 logs across a 115 km NNW-SSE transect in the same area (Fig. 6.7b) suggests the presence of further (half-)grabens.

Only the Nantuo Formation extends across the whole basin. Together with the Datangpo and the upper member of the Fulu Formation, the Nantuo also occurs in the Shennongjia region in the north of the craton, where diamictites can exceed 300 m in thickness (Lu & Qu 1987). While generally

the Nantuo thins landward, thicknesses both in absolute terms and relative to other formations in the same section vary enormously (Figs. 6.5, 6.7). At Maopingdong the formation is 130 m thick; at Jiangkou, which, assuming a single 'Hunan-Guangxi sub-basin', would be located in a similar position along the profile, the formation is almost 1200 m. At Pingpao, Congjiang county, it is a staggering 2900 m, dominantly diamictite; at Zhaoxing, 100 km away, it is less than half that thickness. In Northern Guangxi there are similar disparities, with the Nantuo in one place representing less than 10% of the total diamictite-bounded interval (Wang & Li 2003) and in another 52% (Fig. 6.7). As with the Chang'an Formation, such variations are incompatible with a gradational increase in palaeo-depth from margin to basin. While the thick accumulations of Chang'an and Fulu sediments in the central basin must have flattened the gradient for a time, the effect was soon reversed. Renewed faulting around the beginning of Nantuo time greatly increased the initial accommodation space. Overall, the Datangpo-Nantuo sequence was transgressive, the net effect of basin subsidence, basin infill and hinterland subsidence. The erosion producing the diamict was tectonic rather than glacial.

The youngest date from the Datangpo Formation comes from Maopingdong and constrains the onset of Nantuo deposition to after 654 ±4 Ma (Table 6.2). An eroded tuff 5.4 m higher, in the Nantuo itself, gave a date of 636 ±5 Ma. Within the Datangpo a tuff synchronous with that at Maopingdong occurs at Wangjiapeng half way up the formation, showing that much of the Datangpo at Maopingdong has been eroded away (cf. Fig. 4 in Wu et al. 2016). Assuming constant sedimentation and little erosion at the top of the more complete section, we get a youngest date around 648 Ma.

Formation	Province	Date (Ma)	Material	Context	Source
Doushantuo	W Hubei	628 ±5.8	Ash bed	2 m above Nantuo Fm. Same locality as 621 Ma date.	Yin et al. 2005
Doushantuo	W Hubei	635 ±0.6	Ash bed	Cap carbonate 2.3 m above Nantuo Fm, Wuhe	Condon et al. 2005
Leilongwu/ Nantuo	Jiangxi	635 ±5.4	Tuff	Immediately above diamictite	Chu et al. 2005
Nantuo	W Hubei	600 ±6	Diamictite	Lower part (detrital)	Liu et al. 2008
Nantuo	W Hunan	636 ±4.9	Tuffaceous	4.8 m above base of Nantuo Fm	Zhang et al. 2008b
Nantuo	W Hubei	644 ±6.8	Diamictite	(Detrital)	Hoffman et al. 2011
Datangpo	W Hunan	654 ±3.8	Ash bed	0.6 m below top of Datangpo Fm	Zhang et al. 2008b
Datangpo	W Hubei	654 ±2.7	Tuff	Half way up formation	Liu et al. 2015
Datangpo	E Guizhou	663 ±4	Tuffaceous	Within basal rhodochrosite	Zhou et al. 2004

Table 6.2. U-Pb zircon ages relevant to the dating of the uppermost diamictites in the Nanhua Basin.

At Yangjiaping the transition from the Datangpo into the Nantuo is geochemically continuous (Feng et al. 2004) and therefore probably conformable, as it is in some other places (Wu et al.

2016). At Liuchapo the transition appears to be from siltstone into sandstone, the latter punctuated by dropstones; alternatively, but less probably, the sandstones are assigned to the Sturtian glaciation (Dobrzinski & Bahlburg 2007). The earliest date for the end of Nantuo deposition is given by an ash bed within the cap carbonate at the base of the Doushantuo Formation, at 635 ±1 Ma. An ash bed directly overlying the Nantuo Formation yields the same date (635 ±5 Ma). Unlike the preceding diamictites, the cap carbonate tends to be thicker where water depth was shallower, but similarly extends into deep-water settings (Huang et al. 2011), though not everywhere. The lowermost part of the cap is characterised by tepee structures, breccias and sheet cracks (Jiang et al. 2006, Fig. 6.8d), suggesting that the environment was wave-agitated and tectonically disturbed. A virtually identical age has been obtained from an ash bed 30 m below the top of the Ghaub Formation in Namibia, thought to be equivalent to the Nantuo Formation (Hoffmann et al. 2004).

6.3. Lithological change through the Cryogenian Period

The stratigraphic record is thickest and, except for the Datangpo, most complete in the basinal sections of eastern Guizhou and northern Guangxi. Salient details of the lithostratigraphy are described below.

Gongdong Formation

The Gongdong Formation (upper Danzhou Group, pre-Sturtian age) rests on the Sanmenjie Formation, the latter consisting of pillow basalt and basaltic andesite (Wang & Zhou 2012). Where the Sanmenjie is absent, it rests on dolomites and shales of the Hetong Formation, separated by a time gap. In the lowermost strata conglomerates are common, after which the succession progresses from greywackes with finer interlayers, mudstones and siltstones with coarser interlayers to mudstone, slate and siltstone with thin sandstone and siltstone interlayers. The sequence is interpreted as background basinal sedimentation punctuated by distal turbidites (BGMRGX 1987). Total thickness varies from 843 to 1164 m. In the section sampled for geochemical analysis (upper 500 m, Chapter 8) the dominant lithology is thin-bedded pale blue-green siltstone, sometimes laminated, with minor slump structures (cm- to m-scale). Laminar, slightly less fine-grained, white stringers are frequent at various levels.

Chang'an Formation

At Zhaoxing the Chang'an Formation attains a thickness of 1900 m, a low-resolution log of which is reproduced in Zhang et al. (2011). The contact with the Gongdong Formation is conformable, marked by a change in texture from siltstone to pebbly silt or grit and the first appearance of clasts, up to boulder size (Fig. 6.7a). Within a few metres clasts larger than ~1 cm disappear and after a

Figure 6.8a. Distal turbidites near base of Chang'an Formation, Zhaoxing. The arrow marks a solitary clast in blue-grey siltstone.

Figure 6.8b. Close-up of clast (just above centre of photograph) indicated in Fig. 6.7a.

Figure 6.8c. Laminated calcareous shale in Fulu Formation, Wuhe, penetrated by fractures and fluids rich in iron. Coin for scale.

Figure 6.8d. Convolute bedding at the base of the purplish dark-grey Doushantuo cap carbonate in the Wuhe River, indicating continuing instability after the high-energy deposits of the Nantuo Formation.

further 50 m the texture reverts to mudstone/siltstone. Occasional dropstones and striated clasts are reported. Clast-poor, gritty, non-bedded textures return at 450 m and again at 625 m, from which point they are prevalent, interrupted only by an interval of mudstone/siltstone 110 m thick around 1000 m. Clast size is generally less than 5 cm in the lower part, up to 80 cm in the upper part (*ibid*.). A few clasts are striated. The sandstones of the lower part appear to be turbidites, some massive, some graded. Massive turbidites immediately overlie the formation.

At Gaoyou, 25 km north of Sanjiang, the formation is ~550 m and consists of pebbly muddy sandstone or sandy mudstone (Lan et al. 2014). Clasts are generally small (1–3 mm) and infrequent (1–2%). The middle part includes sandy conglomerate lenses with clasts up to 13 cm.

At Pingpao, 130 km to the west, the Chang'an is 720 m thick (Liao 1981). The lower third of the unit is mostly pebble-bearing slate with occasional lenses of sandstone and conglomerate. The remaining two-thirds are somewhat coarser. As at Gaoyou, the contact with the Gongdong Formation is conformable.

Fulu Formation

At Pingpao, the 390-m-thick sequence consists mainly of sandstone, but includes intervals of pebbly and cobbly slate (Liao 1981). At Zhaoxing, where the Fulu approaches maximum thickness, it reaches 800 m. It is divided into two members, the Liangjiehe and Gucheng; in some of the literature these units still have formation status. In the area around Guzhang the lower member consists of muddy siltstone, the upper of diamictite (70 m), becoming reddish brown through the final 10 m (Zhu et al. 2006). Dolomite lenses are known, as are lenses of rhodochrosite (Zhang et al. 2011).

In more proximal locations the Liangjiehe Member and equivalents (e.g. Xieshuihe Formation at Yangjiaping) rest dis- or unconformably on pre-Sturtian (Banxi Group) deposits. At Zhaoxing the Langjiehe is 510 m thick and rests disconformably on the Chang'an Formation. Along much of the rift basin iron minerals characterise the basal strata, overlain in some areas by manganese ores (Tang et al. 1987). The dominant lithology is sandstone, with occasional stringers (granule trains) and beds or lenses of diamictite. Cross-stratification, ripples and graded bedding (*ibid*.) suggest deposition by turbidites. Lonestones also occur.

Where it overlies the Liangjiehe Member, the Gucheng Member or its equivalent is generally much thinner (e.g. Zhou et al. 2004). At Zhaoxing, where it is 217 m thick, diamictites occur at the base and middle, but half of the member is mudstone. The thinner the stratigraphy, the less clear the chronostratigraphy. At Wuhe the unit underlying the Datangpo Formation is designated the Tiesiao

Formation and about 55 m in thickness. Most of it is siltstone and mudstone, succeeded by 12 m of coarser material. According to one interpretation the Tiesiao equates with the whole of the Fulu Formation and the lower diamictite unit with the Chang'an Formation (Lan et al. 2015a); alternatively, only the upper Fulu may be present. Often the contact between diamictite and underlying sandstone is gradational (Dobrzinski & Bahlburg 2007). In places sandstones are graded and/or coarsely laminar, suggestive of turbidites. Some lonestones are randomly dispersed within the sandstones (*ibid*.) and may have been entrained with them. Like the turbidites, carbonate filling the pores of some diamictites indicates a marine environment. Although the carbonate has been described as 'secondary' (*ibid*.), the occurrence of detrital dolomite at Minle well within the Fulu-equivalent Chunmu Formation (Li et al. 1999) suggests it is synsedimentary. At Zhaoxing, a deep-water section, the diamictites are safely interpreted as mass flow deposits. The section also includes mudstones, which in contrast to the fine-grained but here highly condensed Datangpo Formation are voluminous and presumably a more distal expression of high-energy events.

Datangpo (Xiangmeng) Formation

Extending over 600 km along strike and 200 km down dip, the Datangpo Formation marks a dramatic change of lithology and environment. At most localities the basal contact is with diamictite (Dobrzinski & Bahlburg 2007) and usually conformable. Above the contact, laminae of pyritic carbonaceous shale, a few metres in total thickness, interleave with laminae of rhodochrosite. Further up, the rhodochrosite becomes lenticular, pillow-shaped or nodular, with fractures and pores filled by fibrous quartz and granular barite (Xu et al. 1990). Organic matter derives mostly from planktonic algae, decomposition of which generated gas, leaving holes, diapirs and mud volcanoes in the rhodochrosite (Zhang et al. 2011). Evidently the hydrothermal influx of nutrients (C, Mn, Fe, P, Mo) stimulated productivity.

In some places – generally where the palaeo-environment was deeper (Fig. 6.7b) – manganese is abundant and rich enough (MnO 20–35 wt %) to be mined, notably at Daotuo, Minle and Datangpo itself. The largest ore deposits cluster in the NE corner of Guizhou Province near Yanglizhang (Fig. 6.3), and all are located above NE-SW trending faults (Wu et al. 2016), the source of the enrichments. The Mn-rich organic-rich fine-grained deposits also have a high proportion of dolomite, quartz (22–40%) and clay, mostly illite (14–43%). They grade upwards into grey shales and siltstones.

The Datangpo Formation reaches a maximum thickness of 700 m (Yu et al. 2016) but is much thinner in distal locations, if present at all. At Zhaoxing it is around 10 m, the first 1.7 m of which are manganese-rich, the rest carbonaceous shale. At nearby Lijiapo it is logged as 57 m of carbona-

ceous shale according to Laio (1981) but is absent according to Huang et al. (2014). At Zhailangou the formation is 200 m thick, at Yangjiaping only 12 m thick and highly condensed (Li et al. 2012).

Nantuo Formation

The final diamictite interval extends across the entire Nanhua Basin and beyond, to a maximum thickness of over 2000 m. The matrix is of variable grade, including clay (Liao 1981). Clasts tend to be bigger and more numerous than in the Chang'an and Fulu Formations, lithologically more variable, sometimes striated and/or bullet-shaped. At Gaoqiaohe, in the Shennongjia region to the north, the formation comprises three members: a lower diamictite 87 m thick, purplish or grey-green siltstones with minor conglomerate and limestone lenses in the middle, 76 m thick, and an upper diamictite 48 m thick (Lu & Qu 1987). Clasts are more abundant in the lower member (30–50%) than in the upper (< 10%). At the Zhangbahe section, further east (Fig. 6.3), the Nantuo is thicker (306 m) and dominantly black diamictite, punctuated by thinner intervals of greyish-black to black mudstones, siltstones and fine sandstones; some of these intervals contain conglomerate and dropstones. The black of the diamictite is attributed to fine-grained magnetite. Major-element analysis of three diamictite samples indicates that 23% of the matrix is dolomite. Although low in relation to some units sampled, levels of 0.01 to 0.13% organic carbon found in the Nantuo (Wang et al. 2008) are typical of many non-glacial carbonates in the Neoproterozoic (e.g. Kaufman et al. 1991, Swanson-Hysell et al. 2010, Fig. 3.11).

More direct evidence of marine life at this time comes from a section at Songluo, not far from Zhangbahe (Ye et al. 2015). Here the 230-m-thick Nantuo consists mainly of massive diamictite. In places the diamictite is laminated, with pebbles deflecting the laminae interpreted as glacial dropstones. Occasionally finer sediments interrupt the diamictite. Two horizons, a 3-m-thick black shale 62 m from the base and a lens of silty shale 73 m from the base, preserve compressions of macroalgae. The assemblage includes at least eight morphotypes. Some are complex and suggest adaptation to muddy substrates within the photic zone. The environment was open water.

In the deepest parts of the Nanhua Basin the formation is dominantly massive diamictite (Liao 1981). Thicknesses in SE Guizhou/N Guangxi Province vary from 130 m to 2860 m (Figs. 6.5, 6.7), with the maximum difference spanning a distance of only 40 km. In central Guizhou Province (27° 01.427' N, 107° 23.338' E) the thickness is 4 m, divided by a 5-cm Mn-rich layer (Zhu et al. 2006). At Shayi, Sanjiang county, interbeds are rich in pyrite and reduced carbon. At Pingpao, the uppermost beds of the 2860-m-thick formation are pyritic; the lowest 430 m are purplish (Liao 1981). At Jiulongwan in the Three Gorges area, 80 km SE of Zhangbahe, the formation is mostly massive or weakly stratified diamictite (Hu et al. 2012), 120 m thick. Single diamictite units are 5–

25 m, within which clasts commonly become less frequent upwards. Intervening sandstones are laminated or massive, the laminated sandstones including silt stringers, the massive ones including minor amounts of gravel. Greenish-black siltstones also occur. In other places, clasts in massive diamictites tend to increase in size and frequency (Dobrzinski & Bahlburg 2007), possibly reflecting basin infilling. The occurrence of carbonate clasts (*ibid*.) suggests that carbonate was being precipitated in shallow locations contemporaneously with diamict deposition. Carbonate-rich shales and concretions occur even at Wuhe, an outer shelf location.

The boundary with the Doushantuo cap carbonate is sharp but conformable. In several places, including where the Nantuo Formation is thin (6 m), the diamictite is draped by a 8-to-20-cm-thick claystone (Zhang et al. 2008b). Most of this sediment is illite and kaolinite, with 10–20% silty quartz and thin laminae of pyrite. In other places, e.g. at Wuhe, the terminal layer is cross-bedded (Wang et al. 1981; pers. obs.). In both shelf and basinal sections sporadic pebble-sized conglomerate occurs in the basal 0.5 m of the cap carbonate (Jiang et al. 2006, 2011). Brecciation and bed disruption are also widespread at this level. Although normally regarded as the first expression of global warming, the cap carbonates were preceded in places by strong chemical weathering (evidenced by the clay), in other places penetrated by exotic clasts that would usually be regarded as ice-rafted. An alternative interpretation is that the climate was stable and the clasts introduced by currents, waning as debris flow deposition ceased. An anomalously high $^{87}Sr/^{86}Sr$ ratio in the lowermost cap carbonate, decreasing through the unit toward normal values (Ohno et al. 2008), conflicts with the Snowball Earth expectation that $^{87}Sr/^{86}Sr$ should have risen through the unit (Higgins & Schrag 2003).

6.4. Regional sea-level change

In addition to factors operating on a global scale, such as global climate and average age of the ocean crust, sea-level is also affected by changes in buoyancy of the continental crust and changes in regional tectonics. Rifting in the Nanhua Basin, in particular, was repeatedly creating accommodation space and filling it up, overprinting any movements due to eustatic change.

The restriction of Chang'an-age sediments to the deepest parts of the basin contrasts with the much wider extent of the pre-Sturtian units and indicates a fall in sea-level and/or greater distance of transport (owing to steeper slopes and/or greater energy). Since outsize clasts, including dropstones, appear at the same juncture, the shift could be ascribed to the growth of continental ice-sheets. In the snowball scenario, the Earth is calculated to have reached isostatic equilibrium within 0.5 Ma of glaciation, at which point sea-level fell by some 525 m (Liu & Peltier 2013). However,

whereas the advance of ice would have brought about a dramatic change in environment, the Chang'an Formation represents only a coarser continuation of sedimentation already going on, without stratigraphic break. The glaciation hypothesis requires, in effect, that one agent of erosion and deposition (rifting) stopped just at the point when another (ice-sheet movement) began. If such a coincidence is improbable, it is also contradicted by the cross-basin disparities in unit thickness, showing that rifting continued throughout the Sturtian (Fig. 6.7). Turbidite deposition also continued (Fig. 6.8a). Thus the coarsening of sediment more probably reflects a tectonic shift.

The extent of the Fulu Formation and equivalents is much greater than that of the Chang'an (Zhang et al. 2011), consistent with overall shallowing as the basin filled. In relation to the shoreline, however, sea-level was high. Glaciation at this time should have left the sea-level extremely low. Deglaciation, if it occurred, would not have set in until the basal Datangpo, where the cap dolostone occurs.

The Datangpo Formation transgressed further onto the continent. The undisturbed lamination of the shales in its lower part suggests that the environment was relatively deep. As this was a low-energy deposit, part of the transgression may have been simply an effect of quieter conditions causing terrigenous sediment to settle out more proximally. Large-scale rifting was in abeyance.

The Nantuo Formation is generally attributed to a second period of global glaciation, at which time sea-level is calculated to have fallen by about 720 m (Liu & Peltier 2013). However, sediments now extended further onto the continent than even Datangpo sediments. There are two situations in which this inconsistency might be mitigated. One is if the more proximal diamictites were terrestrial: not a likely possibility in view of the occurrence of matrix dolomite as far north as Shennongjia and the stratiform nature of some deposits. The second is if the extensiveness of the Nantuo was due to late-stage deglaciation (e.g. Zhang et al. 2008a). This too is problematic. Ice-sheet melting models and Quaternary analogues suggest that deglaciation would have been rapid, lasting less than 10,000 years and much less if deglaciation began only once atmospheric CO_2 had reached a critical concentration (Hoffman et al. 1998, 2007). The primary evidence for deglaciation in the snowball hypothesis – the diamictites being tillites – is the cap carbonates. If one includes the up to 2000-m-thick Nantuo Formation within the deglaciation interval, the problem of disproportionate rates of sedimentation is hugely aggravated. Although there are Quaternary analogues for large accumulations of diamictites and turbidites beyond the continental shelf, in locations where water depths increased sharply from 200 to 2000 m, these were deposited when ice sheets were at their greatest extent. The Nanhua Basin, moreover, had a different bathymetry. As in Pre-Marinoan periods, disparities in unit thickness suggest that the diamictites were primarily the

product of renewed rifting rather than ice streams and slope failures along a simple gradient from shore to abyssal plain. The rise in relative sea-level through the Datangpo and Nantuo appears to have been a consequence of craton-wide subsidence, not deglaciation. The conformable contact between the formations in places shows that there was not always a time-gap between them, and the unconformities in other places are likely to be erosive rather than hiatuses of non-deposition.

The base of the Doushantuo Formation is approximately co-extensive with the diamictites beneath it. The horizon does not mark the onset of a major transgression. Rather, the succeeding shales and carbonates represent a period of further deepening – continuing the trend of Nantuo deposition – until almost the whole Yangtze Block was under water (Wang & Li 2003, Jiang et al. 2011). Abrupt facies changes, turbidites, slump folds, olistostromes and slide blocks speak of continuing instability, partly because the seafloor continued to be disturbed by faulting along grabens that had formed in the Tonian and Cryogenian (Vernhet 2007). The fundamental topography, including the steep break of slope from platform to basin that arc-ed from SW to NE, was inherited. Lessened now by the build-up of shallow-water carbonate, water depths on the platform were in the order of tens rather than hundreds of metres.

6.5. The evidence for glaciation

Despite general acceptance that the Nanhua Basin was subject to persistent rifting during the early to mid Neoproterozoic, all Cryogenian deposits except the Datangpo are thought to have been laid down in glacial conditions. No systematic case – at least in English – has ever been made for such an origin. Almost the only evidence adduced is the occurrence of diamictite, striated clasts and outsize clasts (lonestones), evidence that is open to question.

Ice sheets as they thaw leave behind tillites, deposits of ill-sorted clasts in a fine-grained matrix. Mass-flow deposits (debrites) also commonly have such a texture and may or may not have formed in a glacial environment. While glacial attrition can generate large amounts of coarse sediment and thereby form steep depositional slopes, so can other mechanisms. In the absence of additional characters such as foreset stacking and clinoforms steeper than 20° (Lønne 1995), it is impossible to distinguish. Indeed, the non-prejudicial term ‘diamictite’ was introduced because sedimentological criteria by themselves are rarely decisive (Flint et al. 1960). South China provides a good illustration of why caution is needed.

The Nantuo Formation was first interpreted as glaciogenic in 1907, by Bailey Willis and others, long before debrites were acknowledged to mimic tillites. Hence for many years the terms ‘Nantuo Formation’ and ‘Nantuo Tillite’ were used interchangeably (e.g. Wang et al. 1981, Liao 1981). The

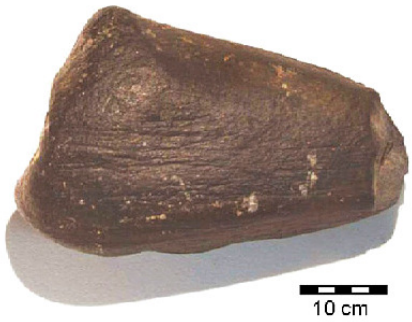

Figure 6.9. Striated bullet-shaped clast from the Nantuo Formation, Wuhe section (Dobrzinski & Bahlburg 2007).

Figure 6.10. Small 'dropstone' from sample DJ 5, upper Nantuo Formation. The gritty laminated matrix suggests high-energy flow.

consensus now is that most of the diamictites are marine and represent mass flow. Dobrzinski and Bahlburg (2007) regard the more proximal diamictites as lodgement deposits, as do Wang et al. (2008) and S. Zhang et al. (2013) in their illustrations of the extent of the Nantuo horizon (which differ from each other). However, at least some of the proximal diamictites are aqueous – hence the shales and the macroalgae (Ye et al. 2015) – and the deeper-water deposits are debrites. The Sturtian diamictites are also mass-flow deposits.

Lonestones – isolate clasts in a fine-grained matrix – necessarily drop out of the water column by gravity. Where the matrix is laminated and the laminae deflected (Fig. 6.10), they are attributed to icebergs and termed dropstones, the enclosing sediments having accumulated in still conditions. Planar laminae also form in the course of turbidite deposition, and these will be deflected as the stones fall out, increasingly as the sediment is compacted. In the Nanhua Basin, lonestones and dropstones are quite common in the Sturtian units. Except where the Nantuo Formation is very thick (Zhang et al. 2011), dropstones are rare in most of the Marinoan units (Dobrzinski and Bahlburg 2007), as are turbidites. Typically they occur in the more distal environments.

Could the dropstones have been entrained by turbidity currents? In the downslope direction, mass-flow deposits not infrequently grade into turbidites (Alvarenga & Trompette 1992, Ross et al. 1995, Amy & Talling 2006, Ito 2008). Which of the two types materialises depends on flow density (Lowe 1982) and the energy of the event initiating the flow. The lateral and/or vertical 'facies association' of debrites, turbidites and dropstones – here (e.g. Fig. 6.8b) as in many other Cryo-

genian localities (e.g. Harland 1964, Young & Gostin 1989, Feather et al. 2002, Hoffman 2011, McGee et al. 2012) – suggests that the clasts were borne along by turbulent flow. The Paraguay Belt (Alvarenga & Trompette 1992) and the northern Flinders Range (fig. 2 in Giddings & Wallace 2009, Rose et al. 2013) are two regions where diamictites can be traced laterally into dropstone-bearing units. Dropstones are admitted to occur within turbidite beds themselves (Le Heron et al. 2014), although still interpreted as iceberg debris. Further documentation of dropstones within turbidites is given in Chapter 1.

Consideration should also be given to when ice-rafted clasts most probably impinged on the glacial record. If the whole of the Nantuo Formation consists of deglaciation debris, it must have followed a period of glaciation that is not represented, except negatively in the basal unconformity. In relation to the thicker units this hardly seems tenable, and in some places the boundary with the Datangpo Formation is conformable. The base of the Chang'an Formation (and subsequent Fulu Formation) is also conformable, and there is no evidence of a hydrological cycle shutdown (Dobrzinski and Bahlburg 2007). Snowball Earth nonetheless virtually necessitates that these formations be assigned to the deglacial phase, since at a latitude some 30° from the equator (Zhang, S. et al. 2013) the craton would have been frozen over, with consequently little deposition until sea ice ceased to buttress terrestrial ice-sheets (supposing that the Yangtze Block faced open ocean at the time) and the ice-sheets began to melt. 'Snowball Earth is a state in which ice-shelves are mutually continuous and no calving-line exists; their dynamics are governed by sublimation and basal melting, not by calving' (Hoffman 2011). Ice-rafted clasts should therefore preponderate in the upper part of glacial sequences. This is not the case, not at least as regards the Chang'an Formation (Liao 1981, Zhang et al. 2011). The Nantuo Formation is dominated by conglomerate/ diamictite.

Finally, there is the question of striated clasts. These are potential evidence of glaciation because bedrock can be striated by stones on the underside of a moving glacier and subsequently plucked, or the stones themselves can become striated during glacial abrasion. However, striations formed by landslides, mudflows and debris flow can have the same appearance. The features are not therefore diagnostic of glacial action (Judson & Barks 1961, Harrington 1971, Schermerhorn 1974, references therein).

Clasts with rounded striated surfaces are common in pre-Pleistocene contexts, including the Nantuo Formation (Liao 1981). Within subaqueous debrites, they are difficult to interpret as glacial, because the rocks must have been rounded first, subsequently striated, and the striations then preserved over 100s to 1000s of metres of transport in abrasive mass-flow deposits. The difficulty

increases with size: large originally angular boulders entail more rounding and higher energy of transport than cobbles do. In Sturtian deposits striated clasts are generally rare and most visible on siltstones and fine-grained sandstones; they are not often seen on carbonate clasts (Le Heron 2015). In the Marinoan diamictites of NE Svalbard, which are friable enough for the clasts to be extracted intact and analysed statistically and at least some of which are subaqueous, striations are frequent (Dowdeswell et al. 1985). Most of the striated clasts consist of limestone and dolostone, lithologies quite easily abraded but also easily marked; granite and granite-gneiss clasts are unmarked. A strong correlation with hardness is also seen in striated clasts from marine settings along the Antarctic margin (Kuhn et al. 1993). In all Neoproterozoic contexts striated clasts tend to be streamlined and scored on one surface only, as if they had protruded above a bedding plane and subsequently been sculpted, smoothed and striated by shear from the overlying bed (e.g. Fig. 6.9, Le Heron 2015). The most parsimonious explanation of these observations is that striation mostly occurred after deposition, but before redeposition, in the basin. This might also apply to clasts in deep-water Pleistocene deposits. Because striations are prone to erasure during debris flows, the 'only plausible explanation' in the Snowball scenario is that the clasts dropped into the diamictite from icebergs (Le Heron 2015) – the same *deus ex machina* as is invoked for dropstones within turbidites.

In both glacial and non-glacial settings, striations on bedrock surfaces may be unidirectional or multidirectional, as stress vectors shift. They may be narrow scratches or wide mullion-like grooves (e.g. Fig. 1.1, Bradwell 2005, Rhys et al. 2015). 'Fault grooves are deeply furrowed slickensided features that look exactly like bedrock surfaces that have been polished and grooved by glacial flow' (Davis & Reynolds 1996, cf. Fig. 1.1). Chattermarks, often associated with glacial abrasion, may also form on fault surfaces (*ibid*., Rhys et al. 2015). Likewise, intraformational, interstratal shear can produce surfaces indistinguishable from striated bedrock (López-Gamundí & Martínez 2000, Deynoux & Ghienne 2004, Le Heron et al. 2005, Le Heron & Craig 2008, Mory et al. 2008, Le Heron et al. 2013). Whether the shearing was caused by an overriding ice sheet or by sudden increases in slope is an open question. The immediate agent of striation are clasts in the overlying sediment, typically diamictite.

No striated pavements of Neoproterozoic age have been reported from South China, but they do occur elsewhere, including instances where they are directly overlain by diamictite. Notable examples are the pavement at the base of the Luoquan Formation, in North China (Fig. 1.1), that in the Smalfjord Formation, Bigganjargga, Norway, the polished and striated pavement at the base of the Blaini Formation, NW India (Etienne et al. 2011), the coeval striated pavements of the

Kimberley region, NW Australia (Corkeron 2007) and the boulder pavements within the Storeelv Formation of East Greenland (Moncrieff & Hambrey 1988). Again, the obvious agent of striation is the moving body of the diamict itself – as in the Bigganjargga case (Harland 1964, 2011). In Greenland two of the erosional horizons occur within the diamictite. In the better preserved upper horizon (preceded, tellingly, by climbing ripples) the striations occur on the upper surfaces of the boulders. Many of the boulders are elongated (cf. Flinn 1956). Most of them are partially planed off parallel or sub-parallel to the bedding and, where they project above the bedding surface, show faceting similar to that on the downstream side of ice-plucked boulders embedded in tills. More recent work has identified up to nine 'pavements' (planar erosion surfaces) in the Storeelv Formation (Hoffman et al. 2012). Repeated cycles of glacial melt-back and re-advance over accumulating tillite without bulldozing away the pavements seem improbable.

Diamictites, dropstones and striated surfaces also occur together in localities dated to the Ediacaran, including at tropical/equatorial palaeolatitudes just before the Cambrian (§1.2, Fig. 1.3, Hambrey & Harland 1981). If the phenomena are considered diagnostic of glacial influence, the whole planet must have been under ice then too, not least in South China, where there was continuous carbonate sedimentation during the terminal Ediacaran (Chen et al. 2015), animal activity (Chen et al. 2013) and no trace of ice sheets. It is not tenable to treat the same types of sedimentological evidence as diagnostic in one period and not in another.

6.6. Magmatism and lithospheric extension as inferred from zircons

If diamictites in the Nanhua Basin were a product of rifting, it remains to be explained why rifting, which had been going on since at least 815 Ma, did not produce diamictites earlier than c. 710 Ma. The question needs qualification. 'Diamictite' – a very broad term – barely applies to the relatively fine siliciclastics with rare outsize clasts that characterise most of the Chang'an Formation. Some of the pre-Sturtian sediments are coarser: conglomerates at the base of the Gongdong Formation, for example, or gravelly sandstones in the upper Wuqiangxi Formation. What is most striking about the transition is the apparent fall in base-level, accounting for the contrast between the wide extent of upper Banxi Group sedimentation across the Nanhua Basin and the narrow extent of Chang'an sedimentation (Figs. 6.5 and 6.7). Preceded by a general increase in sand/shale ratios (Gu et al. 2002), the sporadic occurrence of clast-rich sediments in the Cryogenian units may be primarily a consequence of steeper gradients.

Magmatism on the South China Block has been attributed to a superplume (Li et al. 2003), possibly caused by the heating of slabs subducted around the margins of Rodinia. Alternatively, heat may

have increased beneath the supercontinent as a result of thermal insulation (Rolf et al. 2012), as postulated for the break-up of Pangaea in the Permian, Triassic and early Jurassic (Anderson 1982). Modelling of the factors involved is ongoing, and it remains to be determined which scenario is preferable (Nance et al. 2014). In either case, heating of the lithosphere causes uplift, extension and eventually disaggregation, in the course of which accelerated ocean-crust production causes global sea-level to rise. Rifting of the supercontinent in the late Tonian and early Cryogenian provides an explanation for the changes in relative sea-level. Initial uplift caused by hotter, more buoyant mantle was accompanied by continental magmatism, faulting and crustal thinning. Much of the evidence for a plume at this time is simply evidence for extension and an anomalously hot upper mantle (e.g. Ling et al. 2003, Wang et al. 2009). The cooling involved was the release of excess heat – one reason why pan-glaciation is unlikely during supercontinental break-up. Indeed, during the eruption of the end-Permian Siberian Traps and their aftermath, ocean temperatures are believed to have been 'lethally hot' (Song et al. 2014).

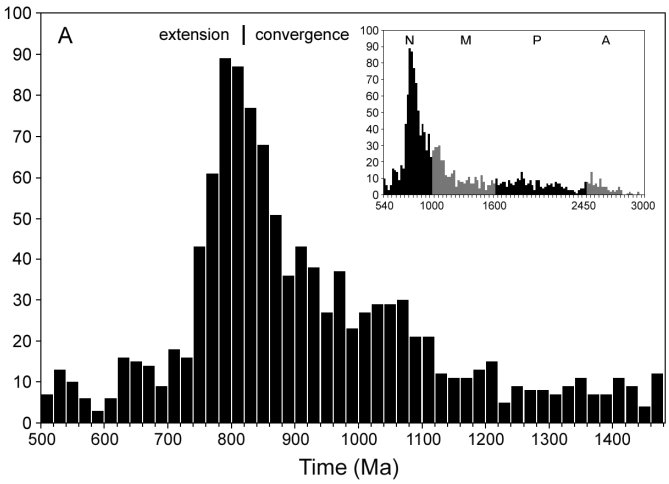

Figure 6.11. (**a**) Age-frequency of Meso- and Neoproterozoic detrital zircons extracted from Palaeozoic sandstones of the Yangtze Block. Data from Duan et al. (2011), Wang et al. (2012), Yao et al. (2012), Xu et al. (2012), Wang et al. (2013), Cui et al. (2014) and Okada et al. (2014). Inset: same dataset for 3000–540 Ma.

In sufficient quantity, detrital zircon dates can be used to track the interplay between magmatism, erosion of magmatic product and preservation of eroded product, all of which vary over time. Dates from Yangtze-Block Ediacaran and Palaeozoic sandstones cluster in the period 1120–750 Ma (Fig. 6.11). Because zircons preponderate in felsic rocks, the pattern mainly reflects granitoid magmatism, in the form of plutons and remelted basement in the Neoproterozoic and Mesoproterozoic eras and primordial basement in the Palaeoproterozoic and Archaean. Frequency increases from about 1200 Ma, peaking during deposition of the Sibao Group and lower Danzhou Group. It plummets after 750 Ma.

Major volcanic units are older than 750 Ma (Wang & Li 2003). Basalt and rhyodacite from the lower half of the more than 200-m-thick Sanmenjie Formation were dated to 765 ±14 and 768 ±28 Ma respectively (Zhou et al. 2007); an unpublished age of ~780 Ma from where the volcanics are

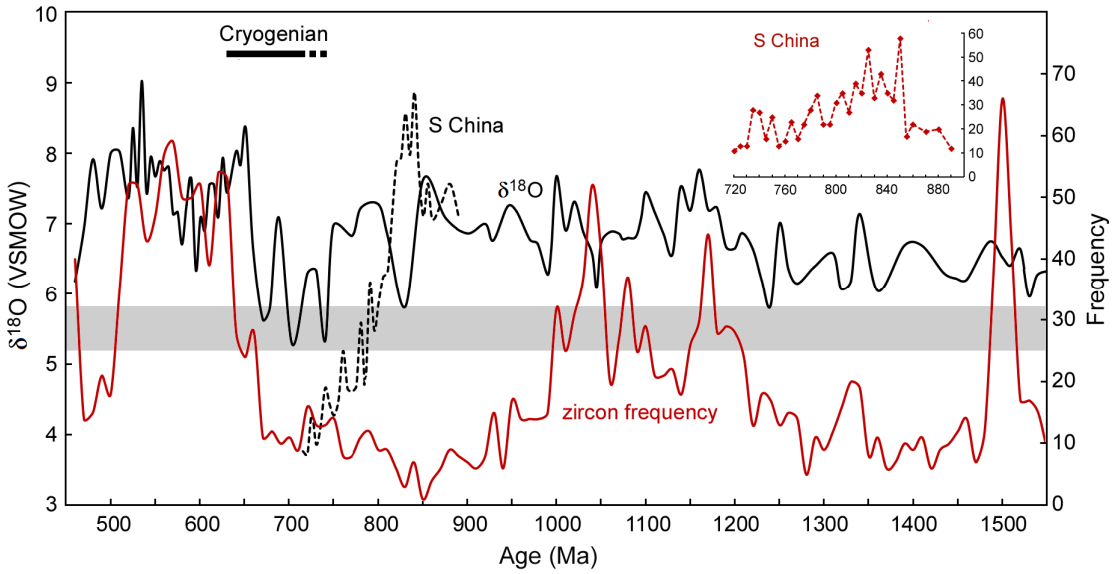

Figure 6.12. Black line: zircon $\delta^{18}O$ from a global compilation (Spencer et al. 2014), corrected for mis-assigned dates, supplemented by more recent data and excluding South China zircons in the period 870-700 Ma, which figure disproportionately and are shown separately. Global frequency curve based on 10 Ma bins, South China's curve 5 Ma bins. Grey band: $\delta^{18}O$ values typical of the mantle. The start of the Cryogenian is defined according to the first appearance of diamictites, which appear earlier in some regions than c. 720 Ma.

up to 850 m thick accords with the age of the underlying Hetong Formation (Wang & Li 2003). Other evidence of volcanism includes occasional tuffaceous horizons (Tables 6.1 and 6.2). The lower half of the Qingshuijiang Formation, slightly younger than the upper Sanmenjie, is represented as at least 50% tuffaceous (Wang et al. 2011, Huang et al. 2014). Much later, in southern Sichuan Province, in the west of the Yangtze Block, Nantuo-equivalent purplish diamictite is followed by volcaniclastic conglomerate and tuffaceous pebbly sandstone (Sun et al. 2009, Wang et al. 2012a). In southern Anhui and Jiangxi, in the NE, Nantuo-equivalent diamictites include tuffs and andesites (Wang et al. 1981), overlain in the Wuwu section by 7 m of tuff (Chu et al. 2004). Occasional ash beds punctuate the record after 630 Ma (Zhang et al. 2004).

Increasingly, zircons are being analysed for oxygen isotope composition. The isotope signal enables differentiation between magmas derived solely from the upper mantle ($\delta^{18}O$ 5.7 ±0.4‰, including 0.2‰ fractionation) and magmas incorporating melt from continental crust ($\delta^{18}O$ generally > 6.1‰). Higher values result from interaction (through weathering or remelting) with supracrustal material, of any age, that has been modified by low-temperature processes on or near the surface where oxygen isotope fractionations are large (Valley et al. 2005). Low values indicate little interaction with the crust. While more data can be expected to refine the picture, widespread diamict deposition in the Sturtian interval coincided with a fall to values lower than at any previous time in the Proterozoic (Fig. 6.12). Thereafter, at the start of the Marinoan, $\delta^{18}O$ rose to an all-time

Proterozoic high. The pattern suggests extension during most of the Sturtian and Marinoan intervals and compression inbetween. The preceding period, back to 1200 Ma, was when most cratons formed a supercontinent and the crust was thick. The Cryogenian signal is fundamentally tectonic, not climatic.

Unlike for the rest of the world, zircon data for South China in the period 850–700 Ma are abundant, owing to prolific granite production as well as preponderance in the literature. Ages can therefore be binned at 5 Ma intervals with an average n of 26. South China also records a minimum in the Cryogenian. However, it differs from the general pattern in starting from much higher values, plunging to even lower ones, and tracing an earlier, steeper and more regular decline. An extraordinary surge at 850–840 Ma contrasts with a global trough. The rifting which immediately followed collision correlates with the fall in $\delta^{18}O$. The magnitude of the drop accords with the lateral and vertical extent of the rifting, driven by anomalously hot mantle (Wang et al. 2009). Increasing input direct from the mantle is also indicated by the inverse correlation between $\delta^{18}O$ and $\varepsilon_{Nd}(t)$ (Wang et al. 2013). Zircon frequency fell because there was a decrease in granitoid magmatism. As thinning of the lithosphere and the introduction of magma heated up the crust, the crust became more ductile, less susceptible to fracture and hence less penetrable by magma. Hence, indeed, the general scarcity of magmatic rocks in the Cryogenian.

Although the Yangtze and Cathaysia Blocks were united by 820 Ma if not long before, renewed compression in the mid Palaeozoic caused a second collision, resulting in partial overthrusting of Cathaysia over the Yangtze Block and final closure of the Nanhua Basin (Xu et al. 2012, Yao et al. 2014). Whether in the Ediacaran or earlier in the Neoproterozoic, extensional tectonics must have caused some separation.

6.7. Chemical deposits

Hydrothermal influence episodically punctuated the Cryogenian, as seen in the iron-rich sediments of the lower Fulu Formation (Tang et al. 1987), sporadic rhodochrosite in the upper Fulu and thick rhodochrosite in the lower Datangpo Formation (Tan 2009). Maximal correlation between Mn+Ca+Mg and LOI (data in Wu et al. 2016, Yu et al. 2016) suggests that the ‘rhodochrosite’ in the Datangpo, and hence possibly other formations, is actually kutnahorite, $(Mn,Ca)CO_3$, with some substitution of Mg for Mn; the mineral co-occurs with rhodochrosite and is found in rift settings, among others (Johnson et al. 2016). In places, dilution by clastic sedimentation was sufficiently low for the concentration of chemical precipitates to reach mineable levels. Elevated concentrations of Mg, Fe, Mn, Ba and heavy REE suggest that the dolomite at the base of the

Doushantuo, often precipitating in relatively deep-water (Jiang et al. 2006, Huang et al. 2011), was also in essence a hydrothermal deposit. Renewed enrichment is seen in the abundant nodules of manganese-rich carbonate just above the cap at Wuhe and manganese ore above the Nantuo near Doujiang. Yet another feature indicating hydrothermal influence, at the start of both the Datangpo and Doushantuo Formations (Fig. 5.3), is a surge in $^{87}Sr/^{86}Sr$ (Yu et al. 2016).

Horizons rich in magnesium, iron and/or manganese coincide with the base of the respective formations, immediately above intervals dominated by debris flows (also in Cathaysia – Feng & Zhang 2016). Their episodic occurrence reflects large-scale deep-crustal faulting, followed either by further high-energy deposition, as in the Fulu Formation, or a remission of tectonic activity, as in the Datangpo. Volcaniclastics are associated with manganese in places and may constitute up to 50% of the deposit (Zhang et al. 2011, citing a Chinese source).

6.8. Summary

Following the amalgamation of the Yangtze and Cathaysia Blocks (a diachronous process completed by 820 Ma), the South China superterrane was subject to extensional tectonics. The collapsed 'orogen' at the suture zone subsided, and rifting within the basin created a number of grabens or half grabens. Shed from segmented basement, which was both augmented and ruptured by the development of voluminous granitoid plutons, siliciclastic material filled the rapidly created accommodation space. Sediment delivery was chiefly turbiditic, as it was through the early Cryogenian. With the Chang'an Formation, subsidence brought about a steepening of depositional slope and generated more pebbly, sometimes gritty, sediment; much of the background sedimentation remained fine-grained. With the Fulu Formation, graben formation and infilling were renewed. The Datangpo represents a lull in tectonic activity, the Nantuo a resumption of it, dominated this time by debris rather than turbidity flows. The South China Block was now almost all under water.

Chemical deposits – iron oxide at the start of the Fulu Formation and manganese carbonate at the start of the Datangpo – indicate episodes of crustal-scale faulting and injection of hot metalliferous fluids. The proposition that this same period of thermal subsidence was accompanied by pole-to-pole glaciation is logically problematic and not supported by the stratigraphic evidence, which shows that relative sea-level was high through most of the Cryogenian. In context, the diamictites, dropstones and striated clasts documented in South China suggest a tectonic rather than glacial origin.

The start of Sturtian-age sedimentation in South China is constrained to c. 710 Ma, its end to 663 ±4 Ma. The start of Marinoan-age sedimentation is constrained to c. 648 Ma, its end to 635 Ma.

References

Alvarenga, C.J.S., Trompette, R., 1992. Glacially influenced sedimentation in the later Proterozoic of the Paraguay belt (Mato Grosso, Brazil). *Palaeogeogr. Palaeocl*. 92, 85–105.

Amy, L.A., Talling, P.J., 2006. Anatomy of turbidites and linked debrites based on long distance (120 x 30 km) bed correlation, Marnoso Arenacea Formation, Northern Apennines, Italy. *Sedimentology* 53, 161–212.

Anderson, D.L., 1982. Hotspots, polar wander, Mesozoic convection and the geoid. *Nature* 297, 391–393.

BGMRGX 1987. Bureau of Geology and Mineral Resources of Guangxi Province Regional Geological Survey Report (Baotan area, 1:50000), Geological Publishing House, Beijing (in Chinese).

Bradwell, T., 2005. Bedrock megagrooves in Assynt, NW Scotland. *Geomorphology* 65, 195-204.

Cawood, P.A., Wang, Y., Xu, Y., Zhao, G. 2013. Locating South China in Rodinia and Gondwana: A fragment of greater India lithosphere? *Geology* 41, 903–906.

Chen, D., Zhou, X., Fu, Y., Wang, J., Yan, D., 2015. New U–Pb zircon ages of the Ediacaran–Cambrian boundary strata in South China. *Terra Nova* 27, 62–68.

Chen, Z. et al., 2013. Trace fossil evidence for Ediacaran bilaterian animals with complex behaviours. *Precambrian Res.* 224, 690–701.

Chu, X.L., Todt, W., Zhang, Q.R., Chen, F.K., Huang, J., 2005. U–Pb zircon age for the Nanhua–Sinian boundary. *Chin. Sci. Bull*. 50, 716–718.

Condon, D. et al., 2005. U-Pb ages from the Neoproterozoic Doushantuo Formation, China. *Science* 308, 95–98.

Corkeron, M., 2007. 'Cap carbonates' and Neoproterozoic glacigenic successions from the Kimberley region, north-west Australia. *Sedimentology* 54, 871–903.

Cui, Z., Zhu, W.B., Ge, R.F., 2014. Provenance and crustal evolution of the Northern Yangtze Block revealed by detrital zircons from Neoproterozoic–Early Paleozoic sedimentary rocks in the Yangtze Gorges Area, South China. *J. Geol*. 122, 217–235.

Davis, G.H., Reynolds, S.J., 1996. *Structural Geology of Rocks and Regions*, John Wiley & Sons, New York.

Deynoux, M., Ghienne, J.F., 2004. Late Ordovician glacial pavements revisited: a reappraisal of the origin of striated surfaces. *Terra Nova*, 16, 95–101.

Dobrzinski, N., Bahlburg, H., 2007. Sedimentology and environmental significance of the Cryogenian successions of the Yangtze platform, South China block. *Palaeogeogr. Palaeocl*. 254, 100–122.

Dowdeswell, J.A., Hambrey, M.J., Wu, R., 1985. A comparison of clast fabric and shape in late Precambrian and modern glacigenic sediments. *J. Sed. Petrol.* 55, 691–704.

Du, Q. et al., 2013. Geochronology and paleoenvironment of the pre-Sturtian glacial strata: Evidence from the Liantuo Formation in the Nanhua rift basin of the Yangtze Block, South China. *Precambrian Res*. 233, 118–131.

Du, L. et al., 2014. Implications for Rodinia reconstructions for the initiation of Neoproterozoic subduction at ~860 Ma on the western margin of the Yangtze Block: Evidence from the Guandaoshan Pluton. *Lithos* 196–197, 67–82.

Duan, L., Meng, Q.R., Zhang, C.L., Liu, X.M., 2011. Tracing the position of the South China block in Gondwana: U–Pb ages and Hf isotopes of Devonian detrital zircons. *Gondwana Res*. 19, 141–149.

Etienne, J.L. et al., 2011. The Blaini Formation of the Lesser Himalaya, NW India. In: E. Arnaud, G.P. Halverson, G. Shields-Zhou (eds), *The Geological Record of Neoproterozoic Glaciations*, Geol. Soc. Lond. Mem. 36, 347–355.

Evans, D.A.D., 2009. The palaeomagnetically viable, long-lived and all-inclusive Rodinia supercontinent reconstruction. *Geol. Soc. Lond. Spec. Pub.* 327, 371–404.

Feather, J., Allen, P.A., Brazier, M.D., Cozzi, A., 2002. Neoproterozoic snowball Earth under scrutiny: Evidence from the Fiq glaciation of Oman. *Geology* 30, 891–894.

Feng, L., Zhang, Q., 2016. The pre-Sturtian negative $\delta^{13}C$ excursion of the Dajiangbian Formation deposited on the western margin of Cathaysia Block in South China. *J. Earth Sci.* 27, 225–232.

Feng, L.J. et al., 2004. New evidence of deposition under cold climate for the Xieshuihe Formation of the Nanhua System in northwestern Hunan, China. *Chin. Sci. Bull.* 49, 1420–1427.

Flinn, D., 1956. On the deformation of the Funzie Conglomerate, Fetlar, Shetland. *J. Geol*. 64, 480–505.

Flint, R.F., Sanders, J.E., Rodgers, J., 1960. Diamictite, a substitute term for symmictite. *Geol. Soc. Am. Bull.* 71, 1809–1810.

Gao, L., Ding, X., Ying, C., Zhang, C., Ettensohn, F.R., 2013. Qingbaikouan and Cryogenian in South China: constraints by SHRIMP zircon U-Pb dating. *Acta Geologica Sinica* 87, 1540–1553.

Gao, W., Zhang, C.H., 2009. Zircon SHRIMP U–Pb ages of the Huangling granite and the tuff beds from Liantuo Formation in the Three Gorges area of Yangtze River, China and its geological significance. *Geol. Bull. China* 28, 45–50 (in Chinese with English abstract).

Giddings, J.A., Wallace, M.W., 2009. Sedimentology and C-isotope geochemistry of the 'Sturtian' cap carbonate, South Australia. *Sediment. Geol.* 216, 1–14.

Gu, X.X., Liu, J.M., Zheng, M.H., Tang, J.X., Qi, L., 2002. Provenance and tectonic setting of the Proterozoic turbidites in Hunan, South China: geochemical evidence. *J. Sed. Res*. 72, 393–407.

Guo, X. et al., 2013. Imaging the crustal structure beneath the eastern Tibetan Plateau and implications for the uplift of the Longmen Shan range. *Earth Planet. Sci. Lett.* 379, 72–80.

Hambrey, M.J., Harland, W.B. (eds), 1981. *Earth's Pre-Pleistocene Glacial Record*, Cambridge University Press, Cambridge.

Harland, W.B., 1964. Critical evidence for a great infra-Cambrian glaciation. *Geologische Rundschau* 54, 45–61.

Harland, W.B., Herod, K.N., Krinsley, D.H., 1966. The definition and identification of tills and tillites. *Earth-Sci. Rev.* 2, 225–256.

Harland, W.B., 2011. Origins and assessment of snowball Earth hypotheses. *Geol. Mag.* 144, 633–642.

Harrington, H.J., 1971. Glacial-like "striated floor" originated by debris-laden torrential water flows. *AAPG Bull.* 55, 1344–1347.

He, C., Dong, S., Santosh, M., Chen, X., 2013. Seismic evidence for a geosuture between the Yangtze and Cathaysia Blocks, South China. *Scientific Reports* 3, 2200.

Higgins, J.A., Schrag, D.P., 2003. Aftermath of a Snowball Earth. *Geochem., Geophys., Geosyst.* 4, 1028.

Hoffman, P.F., 2005. On Cryogenian (Neoproterozoic) ice-sheet dynamics and the limitations of the glacial sedimentary record. *S. Afr. J. Geol*., 108, 557–577.

Hoffman, P.F., 2011. Strange bedfellows: glacial diamictite and cap carbonate from the Marinoan (635 Ma) glaciation in Namibia. *Sedimentology* 58, 57–119.

Hoffman, P.F., Kaufman, A.J., Halverson, G.P., Schrag, D.P., 1998. A Neoproterozoic snowball Earth: *Science* 281, 1342–1346.

Hoffman, P.F. et al., 2012. Cryogenian glaciations on the southern tropical paleomargin of Laurentia (NE Svalbard and East Greenland), and a primary origin for the upper Russøya (Islay) carbon isotope excursion. *Precambrian Res*. 206–207, 137–158.

Hoffmann, K.H., Condon, D.J., Bowring, S.A., Crowley, J.L., 2004. U-Pb zircon date from the Neoproterozoic Ghaub Formation, Namibia: Constraints on Marinoan glaciation. *Geology* 32, 817–820.

Hofmann, M. et al., 2011. The India and South China cratons at the margin of Rodinia – Synchronous Neoproterozoic magmatism revealed by LA-ICP-MS zircon analyses. *Lithos* 123, 176–187.

Hu, J. et al., 2012. Multiple cycles of glacier advance and retreat during the Nantuo (Marinoan) glacial termination in the Three Gorges area. *Front. Earth Sci.* 6, 101–108.

Huang, J., Chu, X., Jiang, G., Feng, L., Chang, H., 2011. Hydrothermal origin of elevated iron, manganese and redox-sensitive trace elements in the c. 635 Ma Doushantuo cap carbonate. *J. Geol. Soc. Lond.* 168, 805–811.

Huang, J. et al., 2014. Multiple climate cooling prior to Sturtian glaciations: Evidence from chemical index of alteration of sediments in South China. *Sci. Reports*. 4, 6868, DOI: 10.1038/srep06868.

Huang, Q. et al. 2015. Neoproterozoic (ca. 820–830 Ma) mafic dykes at Olympic Dam, South Australia: Links with the Gairdner Large Igneous Province. *Precambrian Res.* 271, 160–172.

Ito, M., 2008. Downfan transformation from turbidity currents to debris flows at a channel-to-lobe transitional zone: the Lower Pleistocene Otadai Formation, Boso Peninsula, Japan. *J. Sed. Res.* 78, 668–682.

Jiang, G., Kennedy, M.J., Christie-Blick, M., Wu, H., Shang, S., 2006. Stratigraphy, sedimentary structures, and textures of the Late Neoproterozoic Doushantuo cap carbonate in South China. *J. Sed. Res.* 76, 978–995.

Jiang, G., Shi, X., Zhang, S., Wang, Y., Xiao, S., 2011. Stratigraphy and paleogeography of the Ediacaran Doushantuo Formation (ca. 635–551 Ma) in South China. *Gondwana Res.* 19, 831–849.

Johnson, J.E., Webb, S.M., Ma, C., Fischer, W.W., 2016. Manganese mineralogy and diagenesis in the sedimentary rock record. *Chem. Geol.* 173, 210–231.

Judson, S., Barks, R.E., 1961. Microstriations on polished pebbles. *Am. J. Sci.* 259, 371–381.

Kaufman, A.J., Hayes, J.M., Knoll, A.H., Germs, G.J.B., 1991. Isotopic compositions of carbonates and organic carbon from upper Proterozoic successions in Namibia: stratigraphic variation and the effects of diagenesis and metamorphism. *Precambrian Res.* 49, 301–327.

Kuhn, G., Melles, M., Ehrmann, W.U., Hambrey, M.J., 1985. Character of clasts in glaciomarine sediments as an indicator of transport and depositional processes, Weddell and Lazarev Seas, Antarctica. *J. Sed. Petrol.* 63, 477–487.

Lan, Z. et al., 2014. A rapid and synchronous initiation of the wide spread Cryogenian glaciations. *Precambrian Res.* 255, 401–411.

Lan, Z., Li, X.H., Zhang, Q., Li, Q.L., 2015a. Global synchronous initiation of the 2nd episode of Sturtian glaciation: SIMS zircon U–Pb and O isotope evidence from the Jiangkou Group, South China. *Precambrian Res.* 267, 28–38.

Lan, Z.H., Li, X.H., Zhu, M., Zhang, Q., Li, Q.L., 2015b. Revisiting the Liantuo Formation in Yangtze Block, South China: SIMSU–Pb zircon age constraints and regional and global significance. *Precambrian Res.* 263, 123–141.

Le Heron, D.P., 2015. The significance of ice-rafted debris in Sturtian glacial successions. *Sed. Geol.* 322, 19–33.

Le Heron, D.P., Busfield, M.E., Collins, A.S., 2014. Bolla Bollana boulder beds: A Neoproterozoic trough mouth fan in South Australia? *Sedimentology* 61, 978–995.

Le Heron, D.P., Busfield, M.E., Kamona, A.F., 2013. Neoproterozoic ironstones in northern Namibia: Biogenic precipitation and Cryogenian glaciation. *Palaeogeogr. Palaeocl*. 369, 48–57.

Le Heron, D.P., Craig, J., 2008. First-order reconstructions of a Late Ordovician Saharan ice sheet. *J. Geol. Soc. Lond.* 165, 19–29.

Le Heron, D.P., Sutcliffe, O.E., Whittington, R.J., Craig, J., 2005. The origins of glacially related soft-sediment deformation structures in Upper Ordovician glaciogenic rocks: implication for ice-sheet dynamics. *Palaeogeogr. Palaeocl*. 218, 75–103.

Li, C. et al., 2012. Evidence for a redox stratified Cryogenian marine basin, Datangpo Formation, South China. *Earth Planet. Sci. Lett.* 331–332, 246–256.

Li, R. et al., 1999. Spatial and temporal variations in carbon and sulfur isotopic compositions of Sinian sedimentary rocks in the Yangtze platform, South China, *Precambrian Res*. 97, 59–75.

Li, W.X., Li, X.H., Li, Z.X., Lou, F.S., 2008a. Obduction-type granites within the NE Jiangxi Ophiolite: implications for the final amalgamation between the Yangtze and Cathaysia blocks. *Gondwana Res.* 13, 288–301.

Li, Z.X. et al., 2003. Geochronology of Neoproterozoic syn-rift magmatism in the Yangtze Craton, South China and correlations with other continents: evidence for a mantle superplume that broke up Rodinia. *Precambrian Res.* 122, 85–109.

Li, Z.X. et al., 2008b. Assembly, configuration, and break-up history of Rodinia: a synthesis. *Precambrian Res*. 160, 179–210.

Liao, S.F., 1981. Sinian glacial deposits of Guizhou Province, China. In: M.J. Hambrey, W.B. Harland (eds), *Earth's Pre-Pleistocene Glacial Record*, Cambridge University Press, Cambridge, pp 414–423.

Ling, W. et al., 2003. Neoproterozoic tectonic evolution of the northwestern Yangtze craton, South China: implications for amalgamation and break-up of the Rodinia Supercontinent. *Precambrian Res*. 122, 111–140.

Liu, P. et al., 2015. New SIMS U–Pb zircon age and its constraint on the beginning of the Nantuo glaciation. *Sci. Bull.* 60, 958–963.

Liu, X., Goa, S., Diwu, G., Ling, W., 2008. Precambrian crustal growth of Yangtze craton as revealed by detrital zircon studies. *Am. J. Sci.* 308, 421–468.

Liu, Y., Peltier, W.R., 2013. Sea level variations during snowball Earth formation: 1. A preliminary analysis. *J. Geophys. Res. Solid Earth* 118, 4410–4425.

Lønne, I., 1995. Sedimentary facies and depositional architecture of ice-contact glaciomarine systems. *Sediment. Geol.* 98, 13–43.

López-Gamundí, O., Martínez, M., 2000. Evidence of glacial abrasion in the Calingasta–Uspallata and western Paganzo basins, mid-Carboniferous of western Argentina. *Palaeogeogr. Palaeocl*. 159, 145–165.

Lowe, D.R., 1982. Sediment gravity flows: II. Depositional models with special reference to the deposits of high-density turbidity currents. *J. Sed. Petrol.* 52, 279–297.

Lu, S., Qu, L., 1987. Characteristics of the Sinian glaciogenic rocks of the Shennongjia region, Hubei Province, China. *Precambrian Res*. 36, 127–142.

Maruyama, S., Santosh, M., Zhao, D., 2007. Superplume, supercontinent, and post-perovskite: mantle dynamics and anti-plate tectonics on the core–mantle boundary. *Gondwana Res*. 11, 7–37.

McGee, B., Halverson, G.P., Collins, A.S., 2012. Cryogenian rift-related magmatism and sedimentation: South-western Congo Craton, Namibia. *J. Afr. Earth Sci* 76, 34–49.

Moncrieff, A.C.M., Hambrey, M.J., 1988. Late Precambrian glacially-related grooved and striated surfaces in the tillite group of central East Greenland. *Palaeogeogr. Palaeocl*. 65, 183-200.

Mory, A.J., Redfern, J., Martin, J.R., 2008. A review of Permian–Carboniferous glacial deposits in Western Australia. In: C.R Fielding et al. (eds), *Resolving the Late Paleozoic Ice Age in Time and Space*. GSA Spec. Pap. 441, pp 29–40.

Nance, R.D., Murphy, J.B., Santosh, M., 2014. The supercontinent cycle: A retrospective essay. *Gondwana Res.* 25, 4–29.

Niu, J., Li, Z.X., Zhu, W., 2016. Palaeomagnetism and geochronology of mid-Neoproterozoic Yanbian dykes, South China: implications for a c. 820–800 Ma true polar wander event and the reconstruction of Rodinia. In: Z.X. Li et al. (eds), *Supercontinent Cycles through Earth History*, Geol. Soc. Lond. Spec. Pub. 424, 191–211.

Ohno, T., Komiya, T., Ueno, Y., Hirata, T., Maruyama, S., 2008. Determination of $^{88}Sr/^{86}Sr$ mass-dependent isotopic fractionation and radiogenic isotope variation of $^{87}Sr/^{86}Sr$ in the Neoproterozoic Doushantuo Formation. *Gondwana Res.* 14, 126–133.

Okada, Y. et al., 2014. New chronological constraints for Cryogenian to Cambrian rocks in the Three Gorges, Weng'an and Chengjiang areas, South China. *Gondwana Res*. 25, 1027–1044.

Pi, D.H., Jiang, S.Y., 2016. U–Pb dating of zircons from tuff layer, sandstone and tillite samples in the uppermost Liantuo Formation and the lowermost Nantuo Formation in Three Gorges area, South China. *Chemie der Erde* 76, 103–109.

Piper, J.D.A., 2013. Continental velocity through Precambrian times: The link to magmatism, crustal accretion and episodes of global cooling. *Geosci. Front.* 4, 7–36.

Preiss, W.V., Drexel, J.F., Reid, A.J. 2009. Definition and age of the Kooringa Member of the Skillogalee Dolomite: host for Neoproterozoic (c.790 Ma) porphyry-related copper mineralisation at Burra. *MESA Journal* 55, 19-33.

Roberts, N.J., Evans, S.G., 2013. The gigantic Seymareh (Saidmarreh) rock avalanche, Zagros Fold-Thrust Belt, Iran. *J. of Geol. Soc. Lond.* 170, 685–700.

Rhys, D. et al., 2015. Controls of fault and fold geometry on the distribution of gold mineralization on the Carlin Trend. In: W.M. Pennell, L.J. Garside (eds), *New Concepts and Discoveries: Geological Society of Nevada 2015 Symposium*. DEStech Publications, Lancaster, Penn., pp 333–389.

Rolf, T., Coltice, N., Tackley, P.J., 2012. Linking continental drift, plate tectonics and the thermal state of the Earth's mantle. *Earth Planet. Sci. Lett.* 351–352, 134–146.

Rose, C.V. et al., 2013. The end-Cryogenian glaciation of South Australia. *Geosci. Can.* 40, 256-293.

Ross, G.M., Bloch, J.D., Krouse, H.R., 1995. Neoproterozoic strata of the southern Canadian Cordillera and the isotopic evolution of seawater sulphate. *Precambrian Res.* 73, 71–99.

Schermerhorn, L.J.G., 1974. Late Precambrian mixtites: glacial and/or nonglacial? *Am. J. Sci*. 274, 673–824.

Scotese, C.R., 2009. Late Proterozoic plate tectonics and palaeogeography: a tale of two supercontinents, Rodinia and Pannotia. *Geol. Soc. Lond. Spec. Pub.* 326, 67–83.

Song, H. et al., 2014. Anoxia/high temperature double whammy during the Permian-Triassic marine crisis and its aftermath. *Sci. Rep.* 4, 4132, DOI: 10.1038/srep04132.

Spencer, C.J. et al., 2014. Proterozoic onset of crustal reworking and collisional tectonics: Reappraisal of the zircon oxygen isotope record. *Geology* 42, 451–454.

Swanson-Hysell, N.L. et al., 2010. Cryogenian glaciation and the onset of carbon-isotope decoupling. *Science* 328, 608–611.

Sun, W.H. et al., 2009. Detrital zircon U–Pb geochronological and Lu–Hf isotopic constraints on the Precambrian magmatic and crustal evolution of the western Yangtze Block, SW China. *Precambrian Res.* 172, 99–126.

Tan, M., Lu, Z., Zhang, Y., 2009. Preliminary analysis on genesis of manganese deposit in Datangpo Formation, Western Hubei Province. *Resources Environment & Engineering* 23, 108–113.

Tang, J., Fu, H., Yu, Z., 1987. Stratigraphy, type and formation conditions of the Late Precambrian banded iron ores in South China. *Geochemistry* 6, 331–341.

Valley, J.W. et al., 2005. 4.4 billion years of crustal maturation: oxygen isotope ratios of magmatic zircon. *Contrib. Mineral. Petrol*. 150, 561–580.

Vernhet, E., 2007. Paleobathymetric influence on the development of the late Ediacaran Yangtze platform (Hubei, Hunan, and Guizhou provinces, China). *Sediment. Geol.* 197, 29–46.

Wang, J., Li, Z.X., 2003. History of Neoproterozoic rift basins in South China: implications for Rodinia break-up. *Precambrian Res*. 122, 141–158.

Wang, L.J., Griffin, W.L., Yu, J.H., O'Reilly, S.Y., 2013. U–Pb and Lu–Hf isotopes in detrital zircon from Neoproterozoic sedimentary rocks in the northern Yangtze Block: Implications for Precambrian crustal evolution. *Gondwana Res*. 23, 1261–1272.

Wang, P.M. et al. 2013. Composition variations of the Sinian-Cambrian sedimentary rocks in Hunan and Guangxi provinces and their tectonic significance. *Sci. China Earth Sci*. 56, 1899–1917.

Wang, T.G. et al., 2008. Organic molecular evidence in the Late Neoproterozoic tillites for a palaeo-oceanic environment during the snowball Earth era in the Yangtze region, southern China. *Precambrian Res*. 162, 317–326.

Wang, W., Zhou, C., Yuan, X., Chen, Z., Xiao, S., 2012a. A pronounced negative $\delta^{13}C$ excursion in an Ediacaran succession of western Yangtze Platform: A possible equivalent to the Shuram event and its implication for chemostratigraphic correlation in South China. *Gondwana Res.* 22, 1091–1101.

Wang, W., Zhou, M.F., 2012. Sedimentary records of the Yangtze Block (South China) and their correlation with equivalent Neoproterozoic sequences on adjacent continents. *Sed. Geol*. 265–266, 126–142.

Wang, W., Zhou, M.F., Yan, D.P., Li, J.W., 2012b. Depositional age, provenance, and tectonic setting of the Neoproterozoic Sibao Group, southeastern Yangtze Block, South China. *Precambrian Res*. 192–195, 107–124.

Wang, X.C., Li, X.H., Li, W.X., Li, Z.X., 2009. Variable involvements of mantle plumes in the genesis of mid-Neoproterozoic basaltic rocks in South China: A review. *Gondwana Res.* 15, 381–395.

Wang, X.C., Li, Z.X., Li, X.H., Li, Q.L., Zhang, Q.R., 2011. Geochemical and Hf–Nd isotope data of Nanhua rift sedimentary and volcaniclastic rocks indicate a Neoproterozoic continental flood basalt provenance. *Lithos* 127, 427–440.

Wang, X.C., et al., 2012. Episodic Precambrian crust growth: Evidence from U–Pb ages and Hf–O isotopes of zircon in the Nanhua Basin, central South China. *Precambrian Res*. 222–223, 386–403.

Wang, X.L. et al., 2013. Magmatic evolution and crustal recycling for Neoproterozoic strongly peraluminous granitoids from southern China: Hf and O isotopes in zircon. *Earth Planet. Sci. Lett.* 366, 71–82.

Wang, X.S. et al., 2015. Early Neoproterozoic multiple arc–back-arc system formation during subduction–accretion processes between the Yangtze and Cathaysia blocks: New constraints from the supra-subduction zone NE Jiangxi ophiolite (South China). *Lithos* 236–237, 90–105.

Wang, Y., Lu, S., Gao, Z., Lin, W., Ma, G., 1981. Sinian tillites of China. In: M.J. Hambrey, W.B. Harland (eds), *Earth's Pre-Pleistocene Glacial Record*, Cambridge University Press, Cambridge, pp 386–401.

Willis, B., Blackwelder, E., Sargeant, R.H., 1907. *Research in China, 1*. Carnegie Institute, Washington.

Wu, C. et al., 2016. Nanhuan manganese deposits within restricted basins of the southeastern Yangtze Platform, China: Constraints from geological and geochemical evidence. *Ore Geol. Rev.* 75, 76–99.

Xu, X., Huang, H., Liu, B., 1990. Manganese deposits of the Proterozoic Datangpo Formation, South China: genesis and palaeogeography. In: J. Parnell, Y. Lianjun, C. Changming (eds), *Sediment-hosted Mineral Deposits*, IAS Spec. Pub. 11, pp 39–50.

Xu, Y. et al., 2012. Detrital zircon provenance of Upper Ordovician and Silurian strata in the northeastern Yangtze Block: Response to orogenesis in South China. *Sediment. Geol*. 267-268, 63–72.

Yang, C., Li, X.H., Wang, X.C., Lan, Z., 2015. Mid-Neoproterozoic angular unconformity in the Yangtze Block revisited: Insights from detrital zircon U–Pb age and Hf–O isotopes. *Precambrian Res*. 266, 165–178.

Yang, S.X., Pang, K.T., 2006. Mineralization model for the manganese deposits in northwestern Hunan – an example from Minle manganese deposit in Huayuan, Hunan. *Sediment. Geol. Tethyan Geol.* 26, 72–80 (in Chinese).

Yao, J., Shu, L., Santosh, M., Li, J., 2012. Precambrian crustal evolution of the South China Block and its relation to supercontinent history: Constraints from U–Pb ages, Lu–Hf isotopes and REE geochemistry of zircons from sandstones and granodiorite. *Precambrian Res.* 208–211, 19–48.

Yao, J., Shu, L., Santosh, M., Xu, Z., 2014. Palaeozoic metamorphism of the Neoproterozoic basement in NE Cathaysia: zircon U–Pb ages, Hf isotope and whole-rock geochemistry from the Chencai Group. *J. Geol. Soc. Lond.* 171, 281–298.

Ye, Q. et al., 2015. The survival of benthic macroscopic phototrophs on a Neoproterozoic snowball Earth. *Geology* 53, 507–510.

Yin, C. et al., 2005. U-Pb zircon age from the base of the Ediacaran Doushantuo Formation in the Yangtze Gorges, South China: constraint on the age of Marinoan Glaciation. *Episodes* 28, 48–49.

Young, G.M., Gostin, V.A., 1989. An exceptionally thick upper Proterozoic (Sturtian) glacial successsion in the Mount Painter area, South Australia. *Geol. Soc. Am. Bull*. 101, 834–845.

Yu, W. et al. 2016. Genesis of Cryogenian Datangpo manganese deposit: Hydrothermal influence and episodic post-glacial ventilation of Nanhua Basin, South China. *Palaeogeogr. Palaeocl*. 459, 321–337.

Zhang, C.L., Li, H.K., Santosh, M., 2013. Revisiting the tectonic evolution of South China: interaction between the Rodinia superplume and plate subduction? *Terra Nova* 25, 212–220.

Zhang, C.L., Santosh, M., Zou, H.B., Li, H.K., Huang, W.C., 2013a. The Fuchuan ophiolite in Jiangnan Orogen: Geochemistry, zircon U–Pb geochronology, Hf isotope and implications for the Neoproterozoic assembly of South China. *Lithos* 179, 263–274.

Zhang, J. et al., 2004. Stratigraphic implications of Sinian-Early Cambrian volcanic ash beds on the Yangtze Platform. *Progress in Natural Science* 14, 71–76.

Zhang, Q.R. et al., 2003. Stratigraphic architecture of the Neoproterozoic glacial rocks in the "Xiang-Qian-Gui" region of the central Yangtze Block, South China. *Progress in Natural Science* 13, 783–787.

Zhang, Q.R., Li, X.H., Feng, L.J., Huang, J., Song, B., 2008. A new age constraint on the onset of the Neoproterozoic glaciations in the Yangtze Platform, South China. *J. Geol.* 116, 423–429.

Zhang, Q.R. Chu, X.L., Feng, L.J., 2011. Neoproterozoic glacial records in the Yangtze Region, China. In: E. Arnaud, G.P. Halverson, G. Shields-Zhou (eds), *The Geological Record of Neoproterozoic Glaciations*, Geol. Soc. Lond. Mem. 36, 357–366.

Zhang, S. et al., 2005. U-Pb sensitive high-resolution ion microprobe ages from the Doushantuo Formation in south China: Constraints on late Neoproterozoic glaciations. *Geology* 33, 473–476.

Zhang, S., Jiang, G.Q., Dong, J., Han, Y.G., Wu, H.C., 2008a. New SHRIMP U-Pb age from the Wuqiangxi Formation of Banxi Group: Implications for rifting and stratigraphic erosion associated with the early Cryogenian (Sturtian) glaciation in South China. *Sci China Ser D-Earth Sci* 51, 1537–1544.

Zhang, S., Jiang, G.Q., Han, Y.G., 2008b. The age of the Nantuo Formation and Nantuo glaciation in South China. *Terra Nova* 20, 289–294.

Zhang, S. et al., 2013. Paleomagnetism of the late Cryogenian Nantuo Formation and paleogeographic implications for the South China Block. *J. Asian Earth Sci.* 72, 164–177.

Zhao, J.H., Zhou, M.F., Yan, D.P., Zheng, J.P., Li, J.W., 2011. Reappraisal of the ages of Neoproterozoic strata in South China: No connection with the Grenvillian orogeny. *Geology* 39, 299–302.

Zhao, G., Cawood, P.A., 2012. The Precambrian geology of China. *Precambrian Res*. 222–223, 13–54.

Zheng, Y.F., 2003. Neoproterozoic magmatic activity and global change. *Chin. Sci. Bull*. 48:1639–1656.

Zhou, C., et al. 2004. New constraints on the ages of Neoproterozoic glaciations in south China. *Geology* 32, 437–440.

Zhou, J., Li, X.H., Ge, W., Li, Z.X., 2007. Age and origin of middle Neoproterozoic mafic magmatism in southern Yangtze Block and relevance to the break-up of Rodinia. *Gondwana Res.* 12, 184–197.

Zhu, M., Xiao, S., Yin., C., 2006. The Cryogenian and Ediacaran of South China: Ice Ages, Animal Embryos, Acritarchs, and Algae. Field excursion guide book A8. 2nd International Palaeontological Congress, 17–21 June 2006, Beijing.

CHAPTER SEVEN

The chemical index of alteration: issues of interpretation, and secular differences in weathering style

Abstract

The chemical alteration of igneous rocks during weathering is the first phase of the rock cycle, accompanied and usually accelerated by various processes of physical degradation. Rocks weather faster where the climate is warmer and wetter. Chemical weathering is most often quantified as the ratio of aluminium, the immobile element characteristic of clays, to the sum of sodium, calcium and potassium, the mobile elements characteristic of feldspars. Here I review the effect of sedimentation rate, grain size, igneous source, intracrustal recycling and secondary Ca minerals on the index. The frequent enrichment in potassium seen in shales and muds is not, in most cases, an effect of metasomatism but a true weathering trend where accelerated dissolution of plagioclase under high pCO_2 decreased the solubility of K-feldspar. Illite as a proportion of clay minerals correlates well with inferred pCO_2.

7.1. Major element composition as a function of weathering

In carbonate contexts, the most direct clue to silicate weathering is the ratio of strontium isotopes, reflecting the balance between subaerial weathering of continental crust and hydrothermal alteration of oceanic crust. In siliciclastic contexts, the most direct clue comes from the ratios of major elements. Rocks weather as primary igneous minerals react with acidic rainwater. In the modern environment rainwater is acidic because of root respiration and the decay of vegetable matter in soils; in the Proterozoic it was acidic because of high concentrations of carbon dioxide in the atmosphere.

Since the end of the Archaean, the upper crust has had a bulk composition approximating that of granodiorite, with 20% quartz and roughly equal proportions of plagioclase and alkali feldspar. Where the basement is exposed, the mobile cations Ca^{2+}, Na^{+}, Mg^{2+} and K^{+} leach out of the feldspars to leave minerals rich in Al. In the end-member case, the clay product is a pure aluminium silicate:

$$\underset{\text{plagioclase}}{2NaAlSi_3O_8} + H_2O + 2H^+ \rightarrow \underset{\text{kaolinite}}{Al_2Si_2O_5(OH)_4} + 4SiO_{2(aq)} + 2Na^+ \qquad (1)$$

$$\underset{\text{orthoclase}}{2KAlSi_3O_8} + H_2O + 2H^+ \rightarrow \underset{\text{kaolinite}}{Al_2Si_2O_5(OH)_4} + 4SiO_{2(aq)} + 2K^+ \quad (2)$$

Or taking carbon into account:

$$2NaAlSi_3O_8 + H_2O + 2H_2CO_3 \rightarrow Al_2Si_2O_5(OH)_4 + 4SiO_{2(aq)} + 2Na^+ + 2HCO_3^- \quad (3)$$

The reactions as presented are condensed; normally, kaolinite forms from plagioclase via dissolution (Blum & Stillings 1995). Ignoring silicon, the molar ratio of mobile to total cations in the primary minerals is 1:2, in the weathered products 1:1. From this starting point the chemical index of alteration (or 'CIA', referring usually to specific values) quantifies the degree of weathering on a scale of 50 (no feldspar weathering) to 100 (complete loss of mobile ions). Average upper continental crust ('UCC') on this scale is around 50.8 (Rudnick & Gao 2003). Rates of reaction depend on activation energy and accelerate with temperature. Higher CIAs are expected in warmer climates. Sediments produced by glacial erosion typically have CIAs no higher than the eroded bedrock (Nesbitt & Young 1996). Proglacial mudstones may record higher values, but they are not straightforward analogues for the Precambrian, since they are affected by vegetation, which also promotes silicate weathering (Anderson et al. 2000).

The CIA was first proposed as a means of tracing extreme weathering change through the Palaeoproterozoic Huronian Supergroup, interpreted on other grounds as recording the coming and going of several ice ages (Fig. 7.1). Diamictite matrix from the Gowganda Formation has an average value of 56; laminated argillites in the same formation, interpreted as glaciogenic varved deposits (Grant 2002), have averages up to 73. Formations lacking diamictite range from 62, a surprisingly low number, to 91, an extraordinarily high one (Fedo et al. 1997, Young 2013). Values from the Gordon Lake Formation, around 70, are also surprisingly low, for conditions were wet enough to have transported large volumes of sediment and hot enough to have left evaporitic nodules.

7.2. Sedimentation rates

As these numbers illustrate, interpreting CIA data is not straightforward. One issue is the sedimentological context. Dated to 2450–2350 Ma (Rasmussen et al. 2013), the Huronian succession has a maximum thickness of 12,000 m, of which the Gowganda Formation occupies over 1000 m. About 31% of the unit consists of diamictite and conglomerate, 29% laminated argillite, and 33% siltstones and sandstones (Young 1981). Laminar mudstones occur at intervals throughout and include contorted bedding, slump structures, lenticular and wavy bedding, ripple cross-lamination and lonestones (Fralick & Miall 1989). Many of the structures suggest turbidites. Sandstones occur mostly in the upper half of the formation and include trough cross-bedding, lenticular and wavy

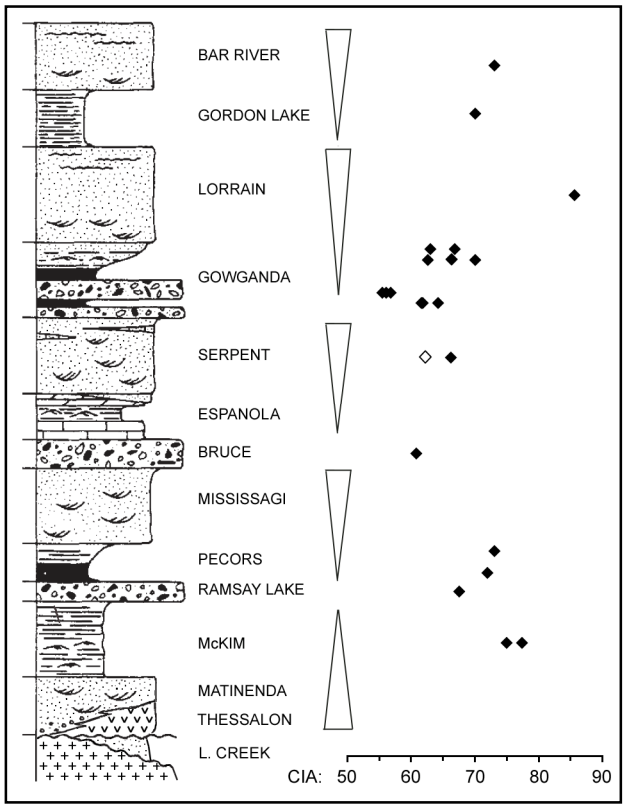

Figure 7.1. Summary of the Huronian Supergroup, Canada (Nesbitt & Young 1982), with average CIA values. The Ramsay Lake, Bruce and Lower Gowganda Formations represent supposed glaciations. Note the relatively high average of 67 from the Ramsay Lake diamictite and low average (open diamond) from Serpent Formation mudstones (Fedo et al. 1997). While most diamictite units are associated with deepening, the deepening accompanying the Bruce Formation was minor – hence the cap carbonate. The Gordon Lake Formation includes gypsum and anhydrite nodules (Wood 1973), indicating evaporation; the upper three formations are dominated by red beds.

bedding, ripple cross-lamination, and ball-and-pillow structures. In other words, the environment was subaqueous, tectonically active and subject to strong currents. Sedimentation was often rapid, with abrupt changes in thickness and facies controlled by movement along the Murray Fault (McLennan et al. 1979, Zolnai et al. 1984). In such circumstances, erosion dominated over weathering, and climatic inferences, if any, should be drawn with this in mind (Johnsson 1993, Hofmann 2006, Lowe 2007). Compositionally mature sediments characterise tectonically quiescent settings. Where sedimentation rates are ill-constrained, warm humid climates can be inferred from high CIAs much more confidently than arid climates, warm or cold, can be inferred from low CIAs.

7.3. Grain size

Clays are generally finer-grained than unweathered sediments, and sorting during transport results in a compositional gradient along which the coarser and least weathered products are deposited upstream, the finer and more weathered products downstream (von Eynatten et al. 2012). Because of their greater porosity, sandstones may contain authigenic clay minerals (Weaver 1989). While the CIA of average Proterozoic shale is 72.4, that of average Proterozoic sandstone is 60.4 (Condie 1993). Since CIA studies are fundamentally a comparative exercise and intended to assess chemical weathering under comparable conditions, analysis should be restricted to fine-grained samples, i.e. siltstones or finer (Bahlburg & Dobrzinski 2011). In the Gowganda case, the matrix material is a

poorly-sorted, muddy sandstone, the finer material having been pulverised in the course of physical erosion (Young 1981). That the matrix yields a lower average CIA than the argillites is unsurprising. The same applies to the sandstones of the Livingstone Creek and Matinenda Formations (Young et al. 2001): the low values of the former reflect rapid erosion at the start of rifting. The presence of diamictite in the latter formation (Zolnai et al. 1984) also suggests rapid erosion. On the other hand, sandstones of the Lorrain Formation, increasing in mineralogical maturity from 44% feldspar to more than 95% quartz (Hadley 1970), can have CIAs up to 91.

Distinguishing between siltstone and fine sandstone is not always easy, but trace elements offer a complementary sieve. In first-cycle, granite-derived sediments ranging from very coarse sand to clay, Zr tends to be most abundant in the very-fine sand to very-coarse silt fractions (von Eynatten et al. 2012). Zinc becomes enriched towards finer grades, peaking with clay. Thus Zr/Zn ratios can discriminate between grain sizes, with values for coarse silt or finer typically < 5.

7.4. The composition of the precursor rock

Weathering indices measure the degree of alteration by reference to the weathered source. For simplicity, often the source is assumed to have the composition of average UCC, which is adequately defined in terms of Al, Ca, Na and K. However, UCC is a composite of granite, basalt, andesite and greywacke. Siliciclastics do not arise from the erosion of bulk crust but from specific lithologies, and over time compositions change.

Commonly the source rock is a type of granite, but granitoids do not all have CIAs close to 50 (*pace* Fedo et al. 1995). Values can be as high as 60. Some of the variation relates to origin. Granites derived from partial melting of sedimentary (supracrustal) rocks are usually richer in Al than those derived from igneous rocks (Chappell & White 2001). There is also secular change. In the Archaean, average granite had a CIA of 54.2, falling to 51.7 in the Proterozoic and 50.9 in the Phanerozoic; average shale fell from 76.5 in the Archaean to 72.4 in the Proterozoic to 69.0 in the Phanerozoic (Condie 1993) – a greater drop than for granite that presumably reflected a secular decline in pCO_2 and weathering intensity. According to one dataset, the average CIA of diamictites fell from 76 in the Archaean to 67.7 in the Palaeoproterozoic to 62.2 in the Neoproterozoic (Gaschnig et al. 2014) – partly, one supposes, because the CIA of the source rocks declined, partly because the intensity of weathering did. Archaean weathering conditions, insofar as they were subaerial, are thought to have been extreme (Hessler & Lowe 2006, Lowe 2007).

Average CIA for the mudstone matrix of Neoproterozoic diamictites in Oman is 73.4, as against 76.3 for the non-diamictite mudstones (Rieu et al. 2007) – a trivial difference, given that equally

weathered soils can vary by ± 3 units (Schoenborn & Fedo 2011). The CIA of the source rock is unknown, leaving it unclear whether a CIA of 73 represents strong or only moderate weathering. Although the extant basement of the Huronian Supergroup has a CIA of 51 (Rainbird et al. 1990), the sediments trace the erosion of basement that was increasingly mafic back in time (McLennan et al. 1979): the CIA of the rocks supplying the younger formations would therefore have been progressively lower (in the range 45–49) and that of the sediments weathered and eroded from them, assuming no climate change, correspondingly lower. The dominant clay mineral in the Gowganda Formation, in particular, is chlorite (Lindsey 1966), indicating a mafic origin.

7.5. Recycling

A fourth issue concerns the degree of weathering already undergone by the source. If the source rock was not igneous, deposits resulting from renewed erosion and transport will reflect the weathering of that earlier time. Where extreme and relatively short-term changes in climate are in mind, the point can be especially relevant. Faced with diamictites that show significant chemical weathering, some have concluded that the weathering was inherited from the rocks over which the glaciers traversed – that bedrock below the first few metres of regolith was sedimentary rather than igneous (Panahi & Young 1997, Young 2002, Rieu et al. 2007, Gaschnig et al. 2014). While inheritance may be an acceptable explanation in some cases, albeit *ad hoc*, most bedrock will have been granitic, if for no other reason than that ice sheets preferentially erode higher elevations, and sediments accumulate in depressions. The mid Neoproterozoic was a time of rifting, erosion and sometimes intense weathering (Fig. 5.6). Little collisional tectonics had gone on since the Grenville orogeny (1100–980 Ma), topography was subdued, and higher land mostly denuded of sedimentary cover.

The extent to which sediments were recycled is commonly assessed by plotting Zr/Sc against Th/Sc (McLennan et al. 1993, Bahlburg & Dobrzinski 2011). Since zirconium and thorium are incompatible and scandium compatible, the Zr/Sc and Th/Sc ratios increase with igneous differentiation, the latter in particular being used to distinguish between mafic and felsic provenance (Th/Sc < 0.2 mafic, > 0.4 felsic). Since, in all igneous rock types, the parameters co-vary, non-covariation, whereby Zr/Sc goes on increasing while Th/Sc flattens, is attributed to recycling: Zr increases because it is heavier and more resistant to dissolution.

In reality, the relationships are not so simple. In the few weathering profiles analysed for the relevant elements (in granodiorites on Flagstaff Mountain, Colorado, and at Toorongo, Australia), both Zr/Sc and Th/Sc show as much covariation, over the same range, as they do in transported

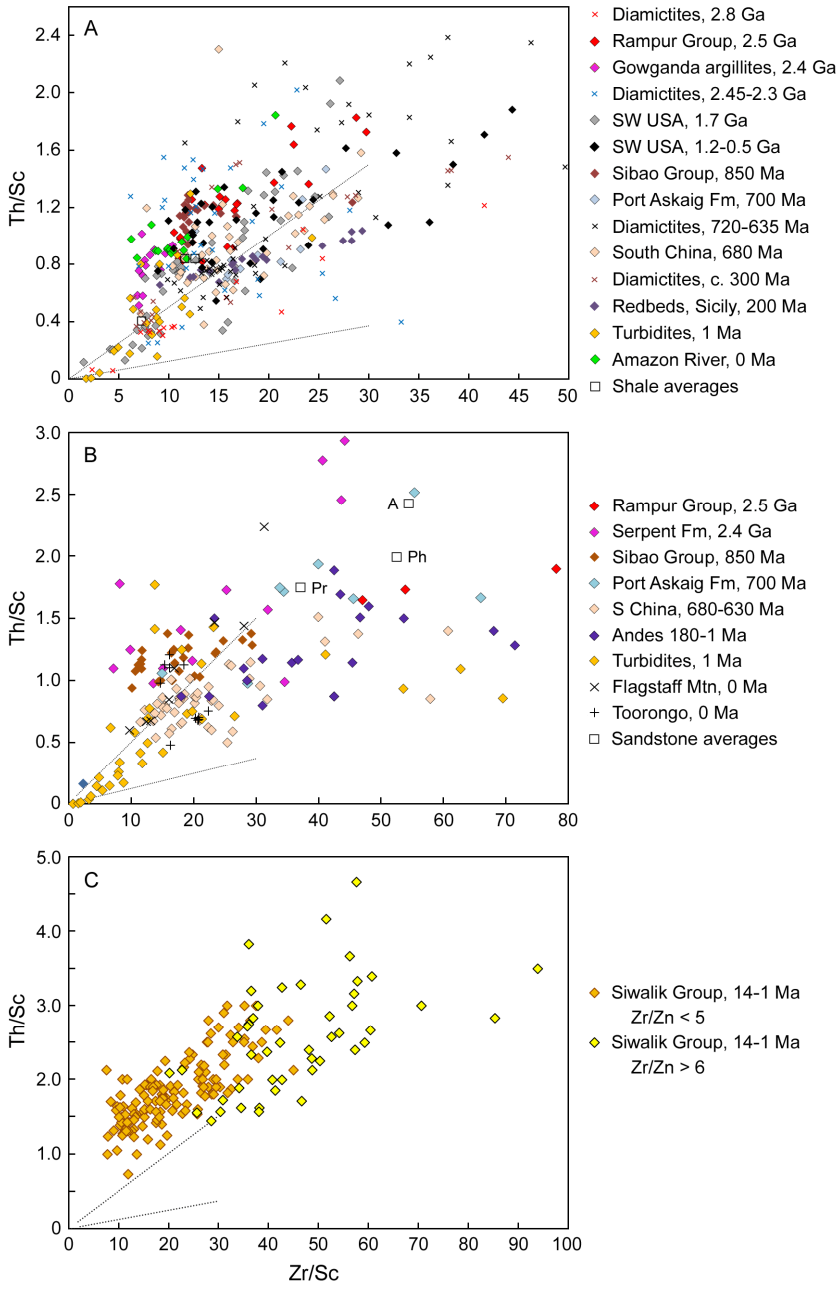

Figure 7.2. Zr/Sc versus Th/Sc for (**a**) mudstones and fine diamictite matrix, (**b**) sandstones, (**c**) samples from the Siwalik Group. Dotted lines mark the upper and lower bounds of most igneous compositions. Averages from Condie (1993): A = Archaean, Pr = Proterozoic, Ph = Phanerozoic. Other data from Bhat & Ghosh (2001), Young (2000), Cox et al. (1995), Wang et al. (2012), Panahi & Young (1997), Dobrzinski & Bahlburg (2007), Mongelli et al. (2006), McLennan et al. (1990), Gaillardet et al. (1995), Basu et al. (1990), Faúndez et al. (2002), Condie et al. (1995), Nesbitt & Markovics (1997), Ulak et al. (2008) and Gaschnig et al. (2016). Modern granite weathering profiles included in (b). The Th/Sc of most sediments is felsic (> 0.4).

sediments. In the Toorongo profile Zr decreases as weathering intensifies, Sc rises slightly as far as CIA 75, then decreases, Th doubles in concentration to the same point, then decreases. In Portugal, over most profiles Zr/Sc and Th/Sc also strongly co-vary, with Th/Sc going from 1.3 to 5.9 (Middelburg et al. 1988, data courtesy of J. B. Maynard). Although all three elements are deemed

immobile, this is only if concentrations are normalised to Ti; why they are normalised is not clear. If the concentrations in the Toorongo and Flagstaff Mountain profiles are so normalised, the Zr and Sc patterns change radically.

In some sediments (e.g. those from South China, Chapter 8), Zr shows no co-variation with CIA, Sc co-varies throughout, and Th co-varies up to CIA 72. Generally, Th is enriched in sediments relative to their igneous sources. Mudstones contain rather less Zr than sandstones (Fig. 7.2a,b), since zircon is heavier than most minerals and therefore less easily transported. By the same token, the higher Zr/Sc in sandstones is not necessarily evidence of more recycling than mudstones; indeed, being coarser, they are less likely to have undergone recycling. Coarse sandstones have less Zr than fine sandstones (von Eynatten et al. 2012). The vertical grading from coarse to fine which occurs *in situ* when turbidites form is quite different from the lateral grading that occurs downslope in fluvio-deltaic sequences. Most turbidites are re-deposited and to that extent re-cycled sediments, notwithstanding low Zr/Sc values.

Over time one would expect sediments to show greater recycling, but it is difficult to infer this from trends in Zr/Sc. Nor, as originally suggested by McLennan et al. (1993), is recycling indicated by flattening of Th/Sc around 1.0 (Fig. 7.2a). In the mid-to-late Proterozoic shales of the United States, Th/Sc continually rises as a function of Zr/Sc. Perhaps most telling are the diverse sediments from the mid-Miocene to Pleistocene Siwalik Group, Nepal. Sorted visually, the fine sediments have Zr/Zn ranges almost indistinguishable from those of the coarse sediments. Sorted on the basis of Zr/Zn, fine sediments have significantly lower Zr/Sc (Fig. 7.2c): Zr increases with grain size and Sc decreases (Zn and Sc strongly correlate). Th/Sc rises in the fine sediments as far as 3.0, with no obvious flattening. It also rises continually in the coarser sediments, where the lowest Zr/Sc ratio is 20. Averages for shales (Condie 1993) show no difference between Proterozoic and Phanerozoic; those for sandstones hint at the possibility of significant recycling in the Phanerozoic, but while there is some increase in Zr (from 89 to 105 ppm), the more striking statistic is the difference, irrespective of time, between shales and sandstones as regards Sc (17 and 1.6 ppm for Proterozoic shales and sandstones respectively, 16 and 2.4 for Phanerozoic). As with the Nepalese data, sandstones are depleted in Sc, as has been established in other studies (Mielke 1979, von Eynatten et al. 2012). They are also depleted in Th. In short, sandstones are not a reliable basis for inferring recycling, certainly below Zr/Sc 50, while mudstone trends show little flattening.

Analyses of detrital zircons for the purpose of constraining age or provenance commonly show a mixture of ages, although peaks do decrease with age of deposition (Condie et al. 2009). If feasible, recycling should be evaluated by reference to the tectonic and stratigraphic context. The Merinjina

Tillite, South Australia, for example, cuts progressively deeper into underlying units and presumably derived from those units. The CIA of 68 obtained for one finely laminated siltstone sample (own data) probably largely reflects the weathering which generated the original sediment; it tells us nothing about the climate during erosion and re-deposition. Most deposits construed as glaciogenic occur in rift basins, where faulting exposed and eroded sedimentary rocks to a considerable depth and in that way produced the texturally and lithologically mixed sediment known as diamictite. Indeed, recycling (re-deposition) may have occurred more often in such contexts than in more normal times.

7.6. Non-silicate CaO

Another question is what to do with the calcium component. Using molar proportions, CIA values are computed as:

$$\frac{Al_2O_3}{Al_2O_3 + CaO^* + Na_2O + K_2O} \times 100$$

where CaO* is the amount of CaO incorporated in the silicate fraction. Non-silicate CaO is that contained in calcite, dolomite and apatite. Since bulk element analysis does not distinguish between silicate and non-silicate CaO, some adjustment may be required. Using measured P_2O_5, Condie (1993) adjusted only for apatite, on the basis that carbonate in shale was negligible. If the carbonate fraction is significant, one alternative is to dissolve the sample in acid and measure the evolved CO_2 (Rieu et al. 2007). Another is to assume that the molar ratio of CaO to Na_2O after correction for apatite should be ≤ 1 in the igneous source rocks and check that it is ≤ 1 in the sediment; if it is not, treat molar Na_2O as equivalent to CaO*, since Ca typically leaches more rapidly than Na (McLennan 1993). Failure to adjust for non-silicate CaO can invalidate climatic inferences. For example, the low CIAs of diamictites in the putatively glacial Pakhuis Formation, of Ordovician age, are entirely due to this error (Young et al. 2004); properly adjusted, they are only slightly lower (72–76) than the overlying mudstones (75–77).

Studies of plagioclase weathering show that granites (*s.l.*) release Ca in preference to Na, regardless of climatic conditions (Nesbitt et al. 1996). Since Ca and Na are mainly present in plagioclase, the anorthite component must be more reactive to weathering solutions than the albite – hence the correction for non-silicate CaO proposed by McLennan. Experimental studies support this conclusion (Gudbrandsson et al. 2014). The observation applies to soils and fluvial environments where water is continually flowing through the system. However, average shale compositions show greater loss of Na than Ca: Proterozoic shale, for example, has 57% as much Ca as Proterozoic

granite, but only 35% Na (data from Condie 1993). North American shale composite (Gromet et al. 1984), mostly of Palaeozoic age, shows a substantial gain in Ca. A large rise in shale Ca through the Phanerozoic is in fact a general phenomenon (Hower et al. 1976). It appears that in the place of final deposition a considerable proportion of Ca re-enters the system as calcite and dolomite, even in non-marine environments (Young 2000, Ulak et al. 2008).

7.7. The possibility of K metasomatism

Weathering trends are commonly plotted on A-CN-K triplots and interpreted in relation to a 'predicted weathering trend' running parallel to the A-CN axis (Nesbitt & Young 1984). Calcium and sodium are lumped together because both are components of plagioclase, and they vary in inverse proportion. The predicted trend is on the footing that granites in the Precambrian weathered in the same manner as they do today (Nesbitt & Young 1989), whereby Ca and Na decline but K – a component of orthoclase, biotite and muscovite – remains essentially constant. Orthoclase, the main K-bearing mineral, has about the same solubility as albite but is orders of magnitude less soluble than anorthite (Brantley 2008).

One of the most common trends in the compositional variation of Precambrian weathering profiles and sedimentary successions is the apparent enrichment in K (as in the Livingstone Creek and Matinenda Formations, Fig. 7.1). This almost universal peculiarity, affecting granite and basalt alteration alike, is put down to almost universal metasomatism (metamorphism by interaction with aqueous fluids), although the absence of land plants, which extract potassium, may also have been

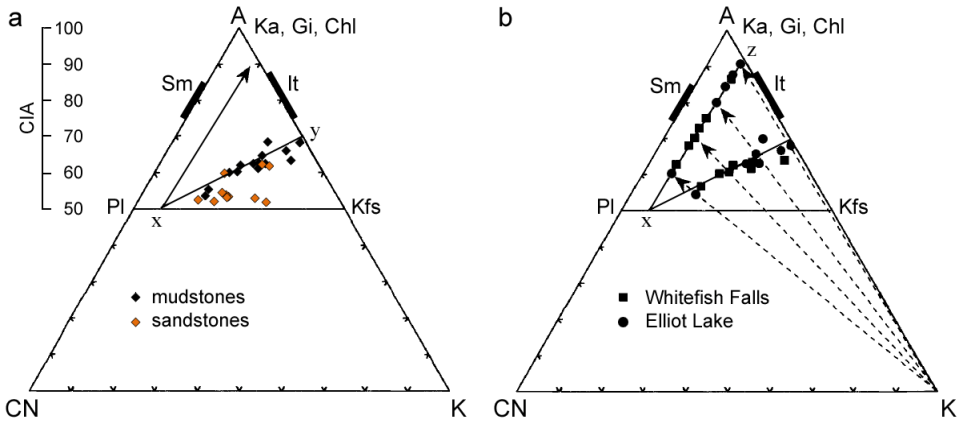

Figure 7.3. Trilateral proportions of molar Al_2O_3, $CaO+Na_2O$ and K_2O in samples from the Serpent Formation, Huronian Supergroup, at Whitefish Falls and Elliot Lake (after Fedo et al. 1995, 1997). Sandstones are omitted from the original diagrams. Straight arrow in (**a**) indicates the 'predicted' weathering trend, from which the authors infer metasomatic enrichment in K, reversed in (**b**), although there is no indication that kaolinite regressed to illite. Line x-y is slightly shorter than line x-z and corrected values therefore increase the spread. Ka = kaolinite, Gi = gibbsite, Chl = chlorite, Pl = plagioclase, It = illite, Kfs = K-feldspar. The non-quartz fraction of a sample plotting in the same place as smectite or illite will not necessarily consist of smectite or illite.

a factor (Knoll & James 1987). In most cases, plagioclase is understood to have weathered to kaolinite and subsequently regressed to illite, with K being adjusted downwards and the CIA upwards; the higher the CIA, the greater the adjustment (Fig. 7.3; Fedo et al. 1995). Metasomatism is routinely invoked whenever triplots indicate enrichment of K, in Phanerozoic contexts as well as Proterozoic. However, triplots rarely indicate kaolinite-to-illite regression, and petrographic evidence of metasomatism, or an explanation of how the pervading fluids came to be K-enriched and other rocks dehydrated and depleted, is rarely offered. Trends of depletion to balance out the enrichment are also not documented.

A very early example of deep in-situ weathering is the uppermost Ville Marie granite at the base of the Huronian succession (Rainbird et al. 1990). Plagioclase is here almost entirely altered to sericite, an illite mica with a K:Al ratio of 1:3. Rinds on some clasts in the overlying breccias also consist of sericite. In the whole-rock analysis, consequently, Na through the palaeosol dwindles to zero, and K presents its mirror image (Fig. 7.4). Although invoked, metasomatism is hardly the appropriate concept, since, along with dissolution of quartz and minor degradation of K-feldspar, the alteration to sericite went on at the same time as the weathering, possibly earlier; there is no evidence that it formed via kaolinite, a mineral not reported in the samples (*pace* Fedo et al. 1995).

K-metasomatism is rarely observed in modern weathering profiles, so the expectation of modern-style weathering is rescued only by a postulate that is non-uniformitarian. The frequent association

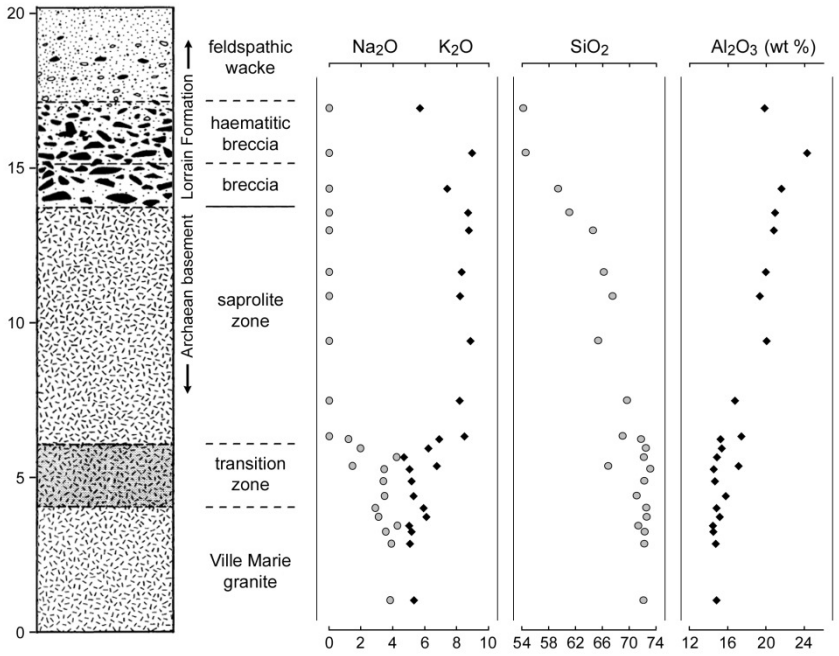

Figure 7.4. Chemostratigraphic profile of the 10-m thick 'palaeosol' beneath the Lorrain Formation, Huronian Supergroup, which here unconformably overlies Archaean basement (Rainbird et al. 1990). The breccia is a mass flow deposit. The section also provides the CIA data for the study by Fedo et al. (1995), who imply that the rocks devoid of Na contain illite; this is not the case.

of sericite with the phenomenon in Archaean and Palaeoproterozoic contexts (Chandler 1988, Prasad & Roscoe 1991, Macfarlane et al. 1994, Crowe et al. 2013) is another clue that conditions were different. The aluminous products of modern weathering tend to be smectite (from mafic precursors), vermiculite (from biotite) and kaolinite (from feldspar). Sericite usually arises when plagioclase or K-feldspar comes into contact with hydrothermal fluids and as such requires moderately high temperatures – perhaps down to 150° C (Grandstaff et al. 1986). Weathering, here indistinguishable from hydrothermal alteration, apparently took place while the igneous bodies were still warm. Hydrothermal alteration has also been inferred for an Archaean sericite-rich weathering profile beneath the Black Reef, Witwatersrand Basin (Maynard et al. 1995). Smectite, on the A-CN limb, is favoured by relatively dry conditions and cool climates (Weaver 1989) and hardly ever occurs in Precambrian weathering profiles (Retallack & Mindszenty 1994). Interestingly, correlation between both Mg and Fe and increasing LOI in the upper 3–4 m suggests the formation of ferromagnesite, $(Fe,Mg)CO_3$, and a switch towards alkaline conditions.

If the Ville Marie granite is a poor exemplar for the proposition that ancient weathering was like modern weathering, one may also question whether modern weathering itself is adequately described by the proposed trend. The Panola regolith in Georgia, USA, is a thick soil-saprolite sequence on granitic bedrock whose long-term steady-state conditions are considered optimal for characterising chemical weathering (White et al. 2001). It does not follow the predicted trend of Nesbitt and Young. Rather, the trend is almost identical to that of the Ville Marie granite (Fig. 7.5). Ca is lost and K and Al proportionally gained as kaolinite replaces plagioclase. K-feldspar begins to alter to kaolinite only at the bedrock-saprolite interface, by which point plagioclase is almost totally consumed. Note, too, that the Panola samples which plot on the A-K limb above 75% Al – like those of the profile through the gneiss at Morton, Minnesota (Goldich 1938) – consist of quartz, K-feldspar and kaolinite, not illite. Triplots that show samples close to the proportions of illite are in this respect misleading: they may not have any illite.

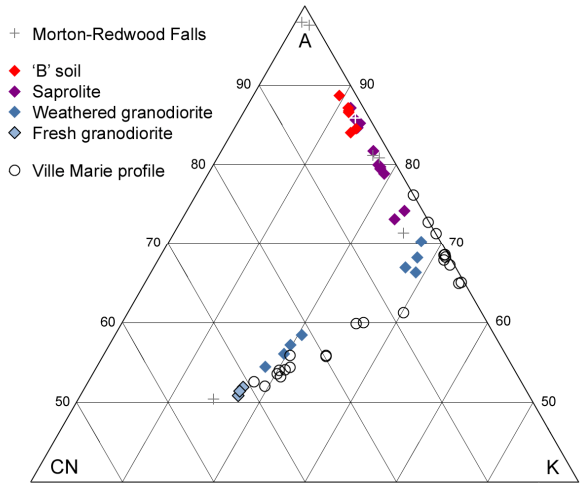

Figure 7.5. Al, Ca-Na and K proportions of the present-day Morton and Panola regoliths, compared with those of the Palaeoproterozoic Ville Marie saprolite (Fig. 7.4).

Whether weathering proceeds as far as the alteration of K-feldspar and complex clay minerals to kaolinite and gibbsite depends, *inter alia*, on the depth and longevity of the weathering profile. In erosive and/or tectonically active regions profiles may remain shallow. Turbidite muds and sands in modern tectonic settings show K enrichment, the sands more than the muds (Fig. 7.6). The percentage of clay minerals in the sands is low, the weathering trends being due to the alteration of plagioclase (McLennan et al. 1990). A similar difference is seen in the mudstones and sandstones of the Serpent Formation (Fig. 7.3). There is no suggestion that metasomatism altered the sandstones, let alone to a greater degree than the finer-grained sediments. Muds and sands from the Amazon River, by contrast, run parallel to the A-CN limb (Vital & Stattegger 2000).

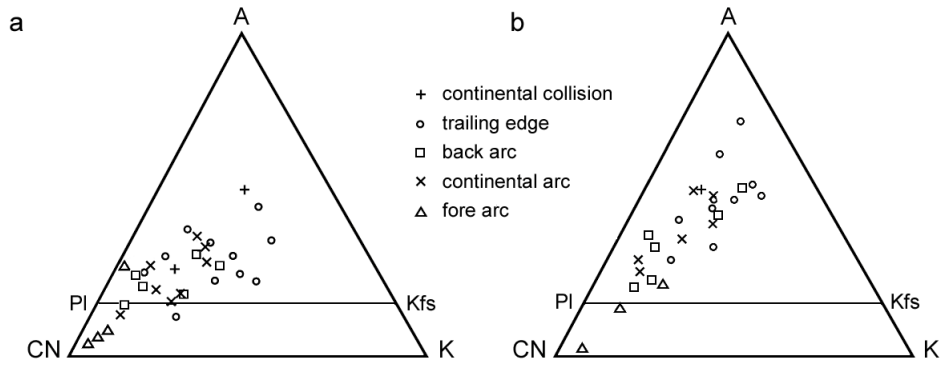

Figure 7.6. Trilateral proportions of molar Al_2O_3, $CaO+Na_2O$ and K_2O in deep-sea turbidite sands (**a**) and muds (**b**) (McLennan et al. 1990). Lower part of the triplot omitted. As in Fig. 7.3, sands have proportionally more K than muds because they have more K-feldspar.

In some circumstances plagioclase may dissolve without residue. If only quartz, K-feldspar and illite are left – largely the case with the Jiuliqiao and Sidingshan Formations – the data will plot all on the A-K axis, with higher CIAs reflecting progressive alteration of feldspar to quartz and/or illite.

In some instances only quartz is left, other granite components having been winnowed in high-energy environments and completely dissolved. Presumably the minerals taking up the dissolved Al were deposited in offshore shales. Pure quartzites, many of them first-cycle, are characteristic especially of the Precambrian and Cambro-Ordovician (Chandler 1988, Soegaard & Eriksson 1989, Dott 2003, Avigad et al. 2005). Quartzite is also abundant in much of the Huronian Supergroup, namely, the Mississagi, Serpent, Gowganda, Lorrain and Bar River Formations, as are arkoses – sandstones consisting almost entirely of quartz and K-feldspar, thus one stage less mature than quartz arenites. On a A-CN-K triplot their compositions (ignoring caveats about grain size) would plot on the A-K limb, reflecting the Al:K ratio of the feldspar. Although there would be no

adjustment for K metasomatism and CIA values would be extremely low, they would in fact be examples of extreme weathering.

At the highest level of generality, the imputation of metasomatism rests partly on the proposition that average Palaeoproterozoic shale originated from average Archaean UCC (Fedo et al. 1995). Archaean UCC has less K than Archaean shale. Although the authors cite Condie (1993), he gives the average shale composition only for the whole of the Proterozoic, which is less enriched than the shale illustrated and has a higher CIA (72, not 68). Archaean shale has a CIA of 76. If Proterozoic shale on average originated from Palaeoproterozoic UCC, there would be less of an anomaly. It is also worth mentioning that the granite plutons that intruded into the upper crust towards the end of the Archaean and were exhumed and eroded in the Palaeoproterozoic were unusually rich in potassium (McLennan et al. 1983).

An element can be considered immobile if its percentage weight in the sediment is greater than in the igneous source, and mobile if its weight is less. When average Proterozoic shale is compared with average Proterozoic UCC, Al, Fe and K go up; the other elements either remain approximately constant (Si, Ti, Mg) or go down (Ca, Na). Fe is problematic in Proterozoic environments because precipitation of pyrite, siderite and haematite could have added Fe to the sediment (along with Ca) from the Fe dissolved in seawater. If we ignore Fe and model Proterozoic weathering on the basis that Al increases in inverse proportion to Ca and Na while Al, Ca, Na and K in total remain constant (simulating dissolution of plagioclase but non-alteration of orthoclase), potassium necessarily increases (Table 7.1) since all quantities are proportions of 100%. Critically, the proportional increase in K is greater than that of Al. This is because the initial percentage is smaller: 4.76% less 3.05% represents an increase of 56% on 3.05%, whereas Al increases by only 22%. On a trilateral plot K appears to become progressively enriched.

Mass balance calculations are sometimes performed (e.g. Grandstaff et al. 1986, Driese et al. 2007). One element, usually Al, is treated as immobile, and the ratio between Al in the non- or little-weathered sample and Al in weathered samples then compared to that of all other elements. Relative to Al, mobile elements (including Si) in Proterozoic palaeosols show a loss; only K shows an increase. However, the gain is illusory, as may be seen when Table 7.1 is plotted in this way and increases in Al and K are calculated by reference to the composition of the least weathered sample in each dataset (Fig. 7.7). The fact that most data plot below the predicted evolution of UCC to shale suggests that, in most samples, K decreases. Nonetheless, the loss recorded by modern sediments is typically much greater, and the loss in weathering profiles enormous (Fig. 7.7a). Somehow, in the Proterozoic K-feldspar was less prone to dissolution than plagioclase was.

	Al	Ca	Na	K	Total	CIA
UCC:	14.95	3.50	3.30	3.05	24.8	49.8
	15.31	3.19	3.06	3.24	24.8	51.6
	15.67	2.88	2.82	3.43	24.8	53.6
	16.03	2.57	2.58	3.62	24.8	55.5
	16.39	2.26	2.34	3.81	24.8	57.6
	16.75	1.95	2.10	4.00	24.8	59.6
	17.11	1.64	1.86	4.19	24.8	61.8
	17.47	1.33	1.62	4.38	24.8	64.0
	17.83	1.02	1.38	4.57	24.8	66.3
	18.19	**0.71**	**1.14**	**4.76**	**24.8**	68.6
shale:	17.50	0.71	1.06	3.62	22.9	71.6
shale:	**18.20**	**0.74**	**1.10**	**3.76**	**23.8**	71.6

Table 7.1. Modelled weathering of average Proterozoic UCC to shale (end-member percentages from Condie 1993). Al increases, and Ca and Na decrease, towards their respective shale totals by arbitrary increments; K increases if total ACNK is constant. The final numbers in bold are for actual shale grossed up for lower major-element totals (UCC 98.37%, shale 94.6%). Average shale composition has less K than the modelled composition.

K-metasomatism (which may have occurred in some instances) should not be the default explanation of apparent trends of enrichment, and, where advanced, supportive evidence needs to be sound. In one study, alteration of K-feldspar to albite is mistakenly described as alteration of albite to K-feldspar (Wang & Zhou 2013); in another, alteration of K-feldspar to quartz (as in the Jiuliqiao Formation) is mistaken for K-rich overgrowths (Rieu et al. 2007, Fig. S2); in a third, alteration of K-feldspar to adularia (a low-temperature form of K-feldspar) is presented as evidence of K being added (Driese et al. 2007).

Fundamentally, the CIA is an analysis tool based on granite weathering where both plagioclase and K-feldspar alter to kaolinite. The weathering trend depends on the relative contributions of the two minerals: the slope being gentle where only plagioclase alters to kaolinite, steepening towards the A-CN limb to the extent that K-feldspar also degrades. In both cases there are usually two vectors, one moving towards the A-K limb, the other along the limb (Fig. 7.5). If only plagioclase weathers, the two vectors are of similar length; to the extent that K-feldspar also weathers, the first vector becomes longer and the second shorter.

Illite is something of a special case. The idea that it forms abundantly today during granite weathering owes more to theoretical interpretations of A-CN-K triplots than to actual detection. The frequency distribution of modern soil CIAs shows a minimum around 75–85 (Maynard 1993), precisely the range of illite. Despite being illustrated as constituting up to 15% of the Stone Mountain Granite saprolite (Nesbitt & Young 1989), illite is not even mentioned in the source

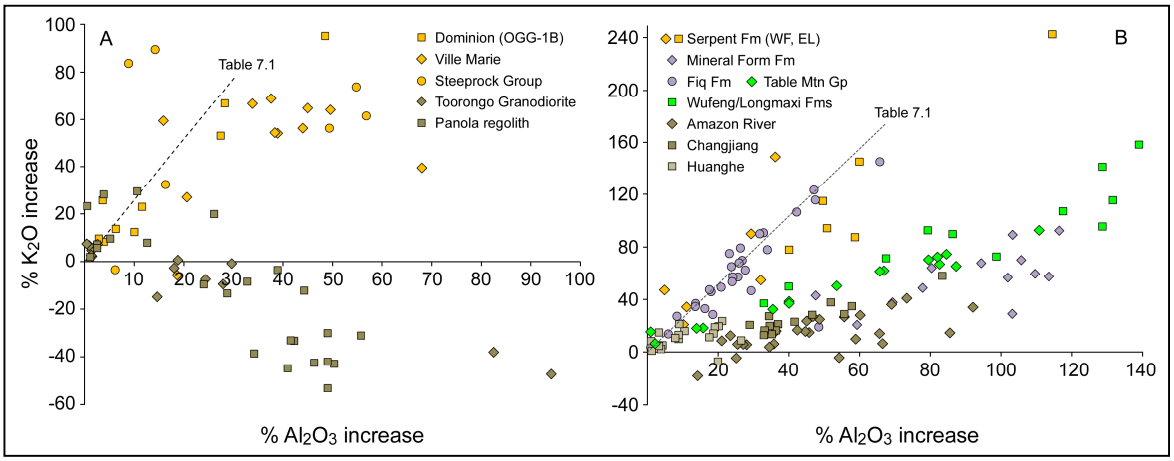

Figure 7.7. (**a**) Variation in Al and K oxide ratios as the respective palaeosols weather and thereby increase in Al content (light brown, Archaean and Palaeoproterozoic; dark brown, Quaternary). Data for Steeprock Group from Schau & Henderson 1983. (**b**) Variation of Al and K oxides in sediments (light brown, Palaeoproterozoic; mauve, Neoproterozoic; green, Ordovician; other shades of brown, Quaternary). Only compositions well to the left of the dotted line are possibly K-enriched, but in the literature the Serpent Formation, Fiq Formation and Ordovician units are all tainted with K metasomatism; apparent enrichment in the Mineral Fork Formation is attributed to a previous cycle (but Zr/Sc ratios are mostly low). Data sources not elsewhere cited: Yan et al. 2010, Vital & Stattegger 2000, Yang et al. 2004.

study (Grant 1963). In the Toorongo Granodiorite (Nesbitt & Markovics 1997) it was detected in small amounts (0–5%) and interpreted as deriving from K-feldspar (Nesbitt & Young 1989), consistent with another study of granodiorite weathering (Eggleton & Buseck 1980). Neither of these paradigm examples establishes that illite is a significant product of modern weathering.

Typically, illite is a component of mudstones that have undergone low-grade metamorphism (shales) and is diagnostic of such alteration (Verdel et al. 2011). It forms via smectite, the proportion of illite (I/S) increasing from the diagenesis zone into the anchizone and metamorphic epizone, the potassium so added coming from K-feldspar. The mineral has three common polytypes, 1M*d*, 1M and 2M. The initial phase is 1M*d*, which changes to 1M and then 2M as burial depth increases. Muscovite, which may be metamorphic or detrital (from the breakdown of granite), has the same structure as 2M illite and under XRD is indistinguishable from it.

Illite formation may be studied through the Mesoproterozoic Belt Supergroup of western Montana and northern Idaho. In a 1400-m-thick section representing the shallow eastern part of the series the dominant polymorph is 1M*d*; 2M is absent (Maxwell & Hower 1967). At the opposite extreme, through an almost 12,000-m-thick section to the west, 2M is the dominant polymorph, increasing with depth; K-feldspar decreases with depth. Smectite is also absent (Eslinger & Sellars 1981) and, since the source of the sediments was granitic, is unlikely to have generated the illite. Residual smectite is absent even from the shales unaffected by burial. Pre-metamorphic (1M*d*) illite

therefore must have derived direct from K-feldspar, altering to illite, possibly after deposition. Unweathered K-feldspar in the deep-water section altered to 1M and 2M illite during burial, a reaction observed at burial temperatures in experiments (Divis & McKenzie 1975).

The alteration of smectite to illite is not a significant weathering reaction. Like other complex clay minerals (Weaver 1989), smectite tends to weather to the simpler kaolinite group. It can change to illite at Earth-surface temperatures in alkaline lakes (Eberl et al. 1993) and in the shallow-buried volcanic sediments of accretionary complexes (Tribble & Yeh 1994). The absence of smectite in all but the latest Precambrian assemblages suggests that, on the calcium side, kaolinite originated direct from plagioclase. On the potassium side, kaolinite originated either direct from K-feldspar or from illite.

Through the geological record as a whole the proportion of illite in the clay fraction decreases as sediments get younger, from around 75% in the Cambrian and earlier to 25% in the Pliocene (Weaver 1989). Proportions were largely flat until the Carboniferous when they plunged to 45%; during the Permo-Triassic they rose from 40 to 55%, then gradually declined towards the present. Weaver linked the large mid-Palaeozoic fall to the rise of land plants, which increased soil acidity and accelerated leaching. However, the effect of humic acids on weathering is controversial (Drever & Stillings 1997) and much of the vegetation at this time grew in swamps, so that the effect on muds sourced from higher ground and settling offshore may have been minor. Other workers have interpreted the pattern as reflecting orogenic episodes, which generated more volcanic material, hence more smectite and hence, following burial, more illite (Eslinger & Sellars 1981). While this also may have been a factor, the problem is the sheer volume of illite in the lower Palaeozoic, implying that the original clays consisted predominantly of smectite. Perhaps a better correlation would be with pCO_2, which overall declined substantially and, like the proportion of illite, temporarily plunged in the late Devonian and early Carboniferous, though perhaps not as much as currently believed (Fig. 7.8, Berner 2006). The relationship would also accord with the generation of voluminous illite in the Precambrian – a product of subaerial or subaqueous weathering as much as metamorphism.

Another question is whether the K taken up in younger successions by smectite-illite alteration originated from within or outside the system. A well-researched example is that of the Cenozoic shales off the coast of Texas. Although K_2O increased from 2.3% at 1850 m to 3.7% at 4300 m, Hower et al. (1976) ascribed this to loss of calcite and redistribution of the K already present in K-feldspar. In one of several ensuing discussions, Bloch et al. (1998) pointed out that most of the

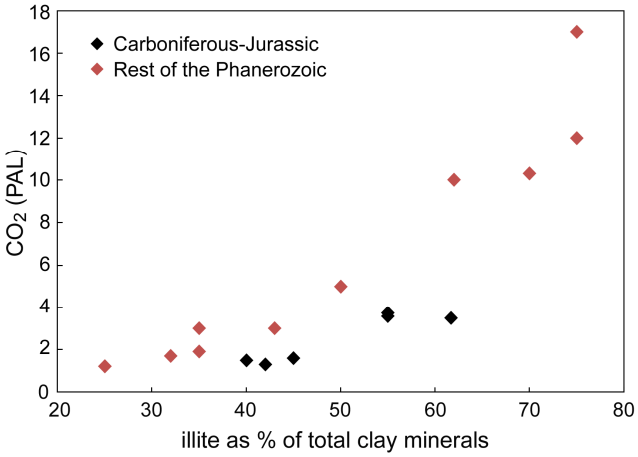

Figure 7.8. The proportion of illite in North American shales through successive periods/epochs of the Phanerozoic (estimated by Weaver 1989) compared with pCO_2 (Berner 2006). Modelling of pCO_2 does not take account of large flood basalt events (e.g. Siberian Traps, CAMP), and some of the mid-to-late Palaeozoic estimates may be too low (cf. Leavitt et al. 2013). Estimates based on plant fossils and palaeosols show a much weaker correlation.

volcanics supplying the smectite were alkaline, and argued that the greater K content of the older shales was attributable primarily to variation in the source composition.

In short, K metasomatism is largely a fiction, and without strong evidence to the contrary, correction of CIAs unwarranted. Chemical alteration is a response to at least four factors:

1. *climate* (temperature and rainfall)
2. *tectonics*, inasmuch as a large spread in values through a sequence is likely to reflect variation in the length of time a surface is exposed to weathering before erosion
3. *pCO_2*, inasmuch as silicate minerals have different solubilities at a given pH and respond to changes in pH in different ways; and
4. *burial diagenesis*, which changes both the element and the mineralogical composition.

The trends revealed in A-CN-K triplots trace such alteration well, but not without ambiguity. The index measures weathering on the basis that it is reflected in increasing Al. Only the distance travelled from the CN-K parallel towards A is therefore measured. Whether a direct path towards A signifies the same degree of weathering as an indirect path is debatable and needs to be informed by an understanding of the reactions involved. While the decrease in Ca and Na recorded in weathering profiles is a real phenomenon, the increase in K is not – it arises from their decrease – and may mask some real decrease in K. If Al becomes mobile, the loss of K will be understated. The trends of regoliths and saprolites that preserve a record of the whole journey will often be multilinear. Those of sediments – transported material that has undergone a degree of mineralogical sorting – will usually be both shorter and unilinear.

CIAs cannot be compared across the aeons without some recognition that the controls on weathering of feldspars change through time (*pace* Nesbitt & Young 1984), the main differences between Precambrian and Phanerozoic weathering being:

1. K-feldspar more commonly altered to illite in the Precambrian
2. Less potassium leached out of Precambrian systems
3. Precambrian siliciclastics, on the whole, contained less CaO
4. Significant chemical weathering went on subaqueously after transport

Most of these differences are the consequence of higher pCO_2 in the past. The paucity of CaO in Precambrian shales and mudstones could be due to the absence of biomineralisers. Although higher pCO_2 in the Palaeo- than in the Neoproterozoic would have made for more intense weathering, the apparent failure of the Huronian Supergroup to show this, except in the form of quartzites, is due to higher sedimentation rates: 100 m Ma^{-1} (10,000 m over 2450–2350 Ma) as against, say, 25 m Ma^{-1} for the Cryogenian formations of South China. The Mesoproterozoic Belt Supergroup suggests even higher rates.

A remaining question is why K-feldspar degraded less readily in the Precambrian. One factor was the absence of plants and microbes, which take up K (e.g. Ullman et al. 1996, Drever & Stillings 1997, Oelkers & Schott 1998). On the other hand, experiments under high pCO_2 suggest that K is mobile even in abiotic settings (Fabre et al. 2011). What the experiments neglect to simulate is evaporation (the reactor bottles were sealed). In natural conditions, rapid dissolution of plagioclase coupled with high rates of evaporation may have led to supersaturation in respect of alkali feldspar, owing to high concentrations of Na and Al. Under such conditions the degradation of K-feldspar may have been inhibited (Oelkers & Schott 1995, Brantley & Stillings 1996, White 2001, Zhu & Lu 2009). At neutral-to-high pH modern seawater is also supersaturated with respect to K-feldspar, undersaturated with respect to anorthite and albite (Stefánsson & Arnórsson 2000). Evidence of K-feldspar dissolution in Neoproterozoic seawater (Chapter 2) suggests that seawater then was undersaturated in respect of all three minerals. The degree of K leaching from minerals in Neoproterozoic environments was variable, owing to other controls.

7.8. Conclusions

Analysing siliciclastic sediments for trends in weathering is an exercise beset with pitfalls. The most widely used weathering index is the ‘chemical index of alteration’, molar Al divided by the sum of molar Al, Ca, Na and K. The index is not well understood. Although the almost ubiquitous tendency of K to rise as a proportion of Ca+Na in the Proterozoic is generally interpreted to reflect

'K metasomatism', in reality it was the consequence of K-feldspar being less soluble than plagioclase. CIA values do not need adjusting upward for apparent enrichment.

In order to compare like with like, the CIA should be restricted to analysis of mudstones. Sandstones usually retain more K-feldspar and record lower values than mudstones, irrespective of climate. The index assumes that Al is immobile. Under extreme conditions, sands may lose aluminous phases so that only quartz is left. The Zr/Zn ratio is useful for ensuring that samples are similar in grain size (preferably < 6). Mobility of Zr and Sc during weathering and transport make Zr/Sc an unreliable index of recycling. Precambrian sediments exhibiting a degree of weathering difficult to reconcile with glacial conditions may have derived from fault-exposed sedimentary successions eroded and redeposited as a result of rifting.

References

Anderson, S.P., Drever, J.I., Frost, C.D., Holden, P., 2000. Chemical weathering in the foreland of a retreating glacier. *Geochim. Cosmochim. Acta* 64, 1173–1189.

Avigad, D. et al., 2005. Mass-production of Cambro–Ordovician quartz-rich sandstone as a consequence of chemical weathering of Pan-African terranes: Environmental implications. *Earth Planet. Sci. Lett.* 240, 818–826.

Bahlburg, H., Dobrzinski, N., 2011. A review of the Chemical Index of Alteration (CIA) and its application to the study of Neoproterozoic glacial deposits and climate transitions. In: E. Arnaud, G.P. Halverson, G. Shields-Zhou (eds), *The Geological Record of Neoproterozoic Glaciations*, Geol. Soc. Lond. Mem. 36, 81–92.

Basu, A.R., Sharma, M., DeCelles, P.G., 1990. Nd, Sr-isotopic provenance and trace element geochemistry of Amazonian foreland basin fluvial sands, Bolivia and Peru: implications for ensialic Andean orogeny. *Earth Planet. Sci. Lett*. 100, 1–17.

Berner, R.A., 2006. GEOCARBSULF: A combined model for Phanerozoic atmospheric O_2 and CO_2. *Geochim. Cosmochim. Acta* 70, 5653–5664.

Bhat, M.I., Ghosh, S.K., 2001. Geochemistry of the 2.51 Ga old Rampur group pelites, western Himalayas: implications for their provenance and weathering. *Precambrian Res*. 108, 1–16.

Bloch, J., Hutcheon, I.E., de Caritat, P., 1998. Tertiary volcanics and the potassium content of Gulf Coast shales – The smoking gun. *Geology* 26, 527–530.

Blum, A.E., Stillings, L.L., 1995. Feldspar dissolution kinetics. *Rev. Miner.* 31, 291–351.

Brantley, S.L., 2008. Kinetics of water-rock interaction. In: S.L. Brantley, J.D. Kubicki, A.F White (eds), *Kinetics of Water Rock Interactions*, Springer, New York, pp 151–210.

Brantley, S.L., Stillings, L., 1996. Feldspar dissolution at 25°C and low pH. *Am. J. Sci.* 296, 101–127.

Chandler, F.W., 1988. Quartz arenites: review and interpretation. *Sediment. Geol*. 58, 105–126.

Chappell, B.W., White, A.J.R., 2001. Two contrasting granite types: 25 years later. *Aus. J. Earth Sci.* 48, 489–499.

Condie, K.C. 1993. Chemical composition and evolution of the upper continental crust: contrasting results from surface samples and shales. *Chem. Geol*. 104, 1–37.

Condie, K.C., Dengate, J., Cullers, R.L., 1995. Behavior of rare earth elements in a paleoweathering profile on granodiorite in the Front Range, Colorado, USA. *Geochim. Cosmochim. Acta* 59, 279–294

Condie, K.C., Belousova, E., Griffin, W.L., Sircombe, K.N., 2009. Granitoid events in space and time: Constraints from igneous and detrital zircon age spectra. *Gondwana Res*. 15, 228–242.

Cox, R., Lowe, D.R., Cullers, R.L., 1995. The influence of sediment recycling and basement composition on evolution of mudrock chemistry in the southwestern United States. *Geochim. Cosmochim. Acta* 59, 2919–2940.

Crowe, S.A. et al., 2013. Atmospheric oxygenation three billion years ago. *Nature* 501, 535–539.

Divis, A.F., McKenzie, J.A., 1975. Experimental authigenesis of phyllosilicates from feldspathic sands. *Sedimentology* 22, 147–155.

Dobrzinski, N., Bahlburg, H. 2007. Sedimentology and environmental significance of the Cryogenian successions of the Yangtze platform, South China block. *Palaeogeogr. Palaeocl*. 254, 100–122.

Dott, R.H., 2003. The importance of eolian abrasion in supermature quartz sandstones and the paradox of weathering on vegetation-free landscapes. *J. Geol.* 111, 387–405.

Drever, J.I., Stillings, L.L., 1997. The role of organic acids in mineral weathering. *Colloid Surface A* 120, 167–181.

Driese, S.G., Medaris, L.G., Ren, M., Runkel, A.C., Langford, R.P., 2007. Differentiating pedogenesis from diagenesis in early terrestrial paleoweathering surfaces formed on granitic composition parent materials. *J. Geol.* 115, 387–405.

Eberl, D.D., Velde, B., McCormick, T., 1993. Synthesis of illite-smectite from smectite at Earth surface temperatures and high pH. *Clay Min.* 28, 49–60.

Eggleton, R.A., Buseck, P.R., 1980. High resolution electron microscopy of feldspar weathering. *Clays Clay Min.* 28, 173–178.

Eslinger, E.V., Sellars, B., 1981. Evidence for the formation of illite from smectite during burial metamorphism in the Belt Supergroup, Clark Fork, Idaho. *J. Sed. Petrol*. 51, 203–216.

Fabre, S., Berger, G., Nédélec, A., 2011. Modeling of continental weathering under high-CO_2 atmospheres during Precambrian times. *Geochem. Geophys. Geosyst*. 12, Q10001.

Faúndez, V., Hervé, F., Lacassie, J.P., 2002. Provenance and depositional setting of pre-Late Jurassic turbidite complexes in Patagonia, Chile. *New Zeal. J. Geol. Geop*. 45, 411–425.

Fedo, C.M., Nesbitt, H.W., Young, G.M., 1995. Unraveling the effects of potassium metasomatism in sedimentary rocks and paleosols, with implications for paleoweathering conditions and provenance. *Geology* 93, 921–924.

Fedo, C.M., Young, G.M., Nesbitt, H.W., Hanchar, J.M., 1997. Potassic and sodic metasomatism in the Southern Province of the Canadian Shield: Evidence from the Paleoproterozoic Serpent Formation, Huronian Supergroup, Canada. *Precambrian Res.* 84, 17–36.

Fralick, P.W., Miall, A.D., 1989. Sedimentology of the Lower Huronian Supergroup (Early Proterozoic), Elliot Lake area, Ontario, Canada. *Sediment. Geol.* 63, 127–153.

Gaillardet, J., Dupré, B., Allègre, C.J., Négrel, P., 1995. Chemical and physical denudation in the Amazon River Basin. *Chem. Geol*. 142, 141-173.

Gaschnig, R.M. et al., 2014. Onset of oxidative weathering of continents recorded in the geochemistry of ancient glacial diamictites. *Earth Planet. Sci. Lett.* 408, 87–99.

Gaschnig, R.M. et al., 2016. Compositional evolution of the upper continental crust through time, as constrained by ancient glacial diamictites. *Geochim. Cosmochim. Acta* 186, 316–343.

Goldich, S.S., 1938. A study of rock weathering. *J. Geol.* 46, 17–58.

Grandstaff, D.E. et al., 1986. Chemistry and mineralogy of Precambrian paleosols at the base of the Dominion and Pongola groups (Transvaal, South Africa). *Precambrian Res.* 32, 97–131.

Grant, W.H., 1963, Weathering of Stone Mountain Granite. *Clay. Clay Miner*. 11, 65–73.

Gromet, L.P., Dymek, R.F., Haskin, L.A., Korotev, R.L., 1984. The "North American shale composite": Its compilation, major and trace element characteristics. *Geochim. Cosmochim. Acta* 48, 2469–2482.

Gudbrandsson, S., Wolff-Boenisch, D., Gislason, S.R., Oelkers, E.H., 2014. Experimental determination of plagioclase dissolution rates as a function of its composition and pH at 22 °C. *Geochim. Cosmochim. Acta* 139, 154–172.

Hadley, D.G., 1970. Paleocurrents and origin of Huronian Lorrain Formation, Ontario and Quebec. *AAPG Bull.* 54, 850.

Hessler, A., Lowe, D.R., 2006. Weathering and sediment generation in the Archean: An integrated study of the evolution of siliciclastic sedimentary rocks of the 3.2 Ga Moodies Group, Barberton Greenstone Belt, South Africa. *Precambrian Res.* 151, 185–210.

Hofmann, A., 2006. The geochemistry of sedimentary rocks from the Fig Tree Group, Barberton greenstone belt: Implications for tectonic, hydrothermal and surface processes during mid-Archaean times. *Precambrian Res.* 143, 23–49.

Hower, J., Eslinger, E.V., Hower, M.E., Perry, E.A., 1976. Mechanism of burial metamorphism of argillaceous sediments I. Mineralogical and chemical evidence. *GSA Bull*. 87, 725–737.

Johnsson, M.J., 1993. The system controlling the composition of clastic sediments. In: M.J. Johnsson, A. Basu (eds), *Processes Controlling the Composition of Clastic Sediments*. Geol. Soc. Am. Spec. Pap. 284, 1–20.

Knoll, M.A., James, W.C., 1987. Effect of the advent and diversification of vascular land plants on mineral weathering through geologic time. *Geology* 15, 1099–1102.

Leavitt, W.D., Halevy, I., Bradley, A.S., Johnston, D.T., 2013. Influence of sulfate reduction rates on the Phanerozoic sulfur isotope record. *Proc. Nat. Acad. Sci.* 110, 11244–11249.

Lindsey, D.A., 1966. Sediment transport in a Precambrian ice age: the Huronian Gowganda Formation. *Science* 154, 1442–1443.

Lowe, D.R., 2007. A comment on "Weathering of quartz as an Archean climatic indicator". *Earth Planet. Sci. Lett.* 253, 530–533.

Macfarlane, A.W., Danielson, A., Holland, H.D., 1994. Geology and major and trace element chemistry of late Archean weathering profiles in the Fortescue Group, Western Australia: implications for atmospheric $P_{O2.}$ *Precambrian Res*. 65, 297–317.

Maynard, J.B., 1993. Chemistry of modern soils as a guide to interpreting Precambrian paleosols. *J. Geol.* 100, 279–289.

Maynard, J.B., Sutton, S.J., Robb, L.J., Ferraz, M.F., Meyer, F.M., 1995. A paleosol developed on hydrothermally altered granite from the hinterland of the Witwatersrand Basin: characteristics of a source of basin fill. *J. Geol.* 103, 357–377.

Maxwell, D.T., Hower, J., 1967. High-grade diagenesis and low-grade metamorphism of illite in the Precambrian Belt Series. *Am. Mineral*. 52, 843–857.

McLennan, S.M., 1993. Weathering and global denudation. *J. Geol*. 101, 295–303.

McLennan, S.M., Fryer, B.J., Young, G.M., 1979. Rare earth elements in Huronian (Lower Proterozoic) sedimentary rocks: composition and evolution of the post-Kenoran upper crust. *Geochim. Cosmochim. Acta* 43, 376–388.

McLennan, S.M., Hemming, S., McDaniel, D.K., Hanson, G.N., 1993. Geochemical approaches to sedimentation, provenance, and tectonics. In: M.J. Johnsson, A. Basu (eds), *Processes Controlling the Composition of Clastic Sediments*. Geol. Soc. Am. Spec. Pap. 284, 21–40.

McLennan, S.M., Taylor, S.R., Kröner, A., 1983. Geochemical evolution of Archean shales from South Africa. I. The Swaziland and Pongola Supergroups. *Precambrian Res*. 22, 93–124.

McLennan, S.M., Taylor, S.R., McCulloch, M.T., Maynard, J.B., 1990. Geochemical and Nd–Sr isotopic composition of deep-sea turbidites: crustal evolution and plate tectonic associations. *Geochim. Cosmochim. Acta* 54, 2015–2050.

Mielke, J.E., 1979. Composition of the Earth's crust and distribution of the elements. In: F.R. Siegel (ed.), *Reviews of Research on Modern Problems in Geochemistry*. Int. Assoc. Geochem. Cosmochem. and UNESCO, Paris, 13–37.

Middelburg, J.J., van der Weijden, C.H., Woittiez, J.R.W., 1988. Chemical processes affecting the mobility of major, minor and trace elements during weathering of granitic rocks. *Chem. Geol.* 68, 253–273.

Mongelli, G., Critelli, S., Perri, F., Sonnino, M., Perrone, V., 2006. Sedimentary recycling, provenance and paleoweathering from chemistry and mineralogy of Mesozoic continental redbed mudrocks, Peloritani mountains, southern Italy. *Geochem. J*. 40, 197-209.

Nesbitt, H.W., Markovics, G., 1997. Weathering of granodioritic crust, long-term storage of elements in weathering profiles, and petrogenesis of siliciclastic sediments. *Geochim. Cosmochim. Acta* 61, 1653–1670.

Nesbitt, H.W., Young, G.M., 1982. Early Proterozoic climates and plate motions inferred from major element chemistry of lutites. *Nature* 299, 715–717.

Nesbitt, H.W., Young, G.M., 1984, Prediction of some weathering trends of plutonic and volcanic rocks based on thermodynamic and kinetic considerations. *Geochim. Cosmochim. Acta* 48, 1523–1534.

Nesbitt, H.W., Young, G.M., 1996. Petrogenesis of sediments in the absence of chemical weathering: effects of abrasion and sorting on bulk composition and mineralogy. *Sedimentology* 43, 341–358.

Nesbitt, H.W., Young, G.M., 1989. Formation and diagenesis of weathering profiles. *J. Geol.* 97, 129–147.

Nesbitt, H.W., Young, G.M., McLennan, S.M., Keays, R.R., 1996. Effects of chemical weathering and sorting on the petrogenesis of siliciclastic sediments, with implications for provenance studies. *J. Geol.* 104, 525–542.

Oelkers, E.H., Schott, J., 1995. Experimental study of anorthite dissolution: the relative mechanism of feldspar hydrolysis. *Geochim. Cosmochim. Acta* 59, 5039–5053.

Oelkers, E.H., Schott, J., 1998. Does organic acid adsorption affect alkali-feldspar dissolution rates? *Chem. Geol*. 151, 235–245.

Panahi, A., Young, G.M., 1997. A geochemical investigation into the provenance of the Neoproterozoic Port Askaig Tillite, Dalradian Supergroup, western Scotland. *Precambrian Res*. 85, 81–96.

Prasad, N., Roscoe, S.M., 1991. Profiles of altered zones at ca 2.45 Ga unconformities beneath Huronian strata, Elliot Lake, Ontario: evidence for early Aphebian weathering under anoxic conditions. *Geol. Surv. Can. Pap.* 91-1C, 43-54.

Rainbird, R.H., Nesbitt, H.W., Donaldson, J.A., 1990. Formation and diagenesis of a sub-Huronian saprolith: comparison with a modern weathering profile. *J. Geol*. 98, 801–82.

Rasmussen, B., Bekker, A., Fletcher, I.R., 2013. Correlation of Paleoproterozoic glaciations based on U–Pb zircon ages for tuff beds in the Transvaal and Huronian Supergroups. *Earth Planet. Sci. Lett.* 382, 173–180.

Retallack, G.J., Mindszenty, A. 1994. Well preserved late Precambrian paleosols from northwest Scotland. *J. Sed. Res.* A64, 264–281.

Rieu, R., Allen, P.A., Plötze, M., Pettke, T., 2007. Climatic cycles during a Neoproterozoic "snowball" glacial epoch. *Geology* 35, 299–302.

Rudnick R.L., Gao, S., 2003. Composition of the continental crust. In: R.L. Rudnick (ed.), *The Crust*, vol. 3, Elsevier, Amsterdam, pp 1–64.

Schau, M., Henderson, J.B., 1983. Archean chemical weathering at three localities on the Canadian Shield. *Precambrian Res*. 20, 189–224.

Schoenborn, W.A., Fedo, C.M., 2011. Provenance and paleoweathering reconstruction of the Neoproterozoic Johnnie Formation, southeastern California. *Chem. Geol.* 285, 231–255.

Soegaard, K., Eriksson, K.A., 1989. Origin of thick, first-cycle quartz arenite successions: evidence from the 1.7 Ga Ortega Group, northern New Mexico. *Precambrian Res*. 43, 129–141.

Stefánsson, A., Arnórsson, S., 2000. Feldspar saturation state in natural waters. *Geochim. Cosmochim. Acta* 64, 2567–2584.

Tribble, J.S., Yeh, H.W., 1994. Origin of smectite and illite-smectite in the Barbados accretionary complex: Oxygen isotopic evidence. *Geology* 22, 219–222.

Ulak, P.D., Roser, B., Hossain, H.M.Z., 2008. Major and trace element analyses of sandstones and mudstones from the Siwalik Group, Bakiya Khola, central Nepal. *Geosci. Rep. Shimane Univ*. 27, 43–51.

Ullman, W.J., Kirchman, D.L., Welch, S.A., Vandevivere, P., 1996. Laboratory evidence for microbially mediated silicate mineral. *Chem. Geol.* 132, 11–17.

Verdel, C., Niemi, N., van der Pluijm, B.A., 2011. Variations in the illite to muscovite transition related to metamorphic conditions and detrital muscovite content: insight from the Paleozoic passive margin of the Southwestern United States. *J. Geol.* 119, 419–437.

Vital, H., Stattegger, K., 2000. Major and trace elements of stream sediments from the lowermost Amazon River. *Chem. Geol*. 168, 151–168.

Von Eynatten, H., Tolosana-Delgado, R., Karius, V., 2012. Sediment generation in modern glacial settings: Grain-size and source-rock control on sediment composition. *Sediment. Geol.* 280, 80–92.

Wang, W., Zhou, M.F., 2013. Petrological and geochemical constraints on provenance, paleoweathering, and tectonic setting of the Neoproterozoic sedimentary basin in the eastern Jiangnan Orogen, South China. *J. Sed. Res.* 83, 974–993.

Wang, W., Zhou, M.F., Yan, D.P., Li, J.W., 2012. Depositional age, provenance, and tectonic setting of the Neoproterozoic Sibao Group, southeastern Yangtze Block, South China. *Precambrian Res*. 192–195, 107–124.

Weaver, C.E., 1989. *Clays, Muds, and Shales*, Elsevier, New York.

White, A.F. et al., 2001. Differential rates of feldspar weathering in granitic regoliths. *Geochim. Cosmochim. Acta* 65, 847–869.

Wood, J., 1973. Stratigraphy and depositional environment of Upper Huronian rocks of the Rawhide Lake-Flat Lake area, Ontario. In: G.M. Young (ed.), *Huronian Stratigraphy and Sedimentation*, Geol. Assoc. Canada. Spec. Pap. 12, 73–95.

Yan, D., Chen, D., Wang, Q., Wang, J., 2010. Large-scale climatic fluctuations in the latest Ordovician on the Yangtze block, south China. *Geology* 38, 599–601.

Yang, S., Jung, H.S., Li, C., 2004. Two unique weathering regimes in the Changjiang and Huanghe drainage basins: geochemical evidence from river sediments. *Sediment. Geol*. 164, 19–34.

Young, G.M., 1981. The Early Proterozoic Gowganda Formation, Ontario, Canada. In: M.J. Hambrey, W.B. Harland (eds), *Earth's Pre-Pleistocene Glacial Record*, Cambridge University Press, Cambridge, pp 807–812.

Young, G.M., 2000. Comparative geochemistry of Pleistocene and Paleoproterozoic (Huronian) glaciogenic laminated deposits: relevance to crustal and atmospheric composition in the last 2.3 Ga. *J. Geol.* 109, 463–477.

Young, G.M., 2002. Geochemical investigation of a Neoproterozoic glacial unit: The Mineral Fork Formation in the Wasatch Range, Utah. *GSA Bull.* 114, 387–399.

Young, G.M., 2013. Precambrian supercontinents, glaciations, atmospheric oxygenation, metazoan evolution and an impact that may have changed the second half of Earth history. *Geosci. Front.* 4, 247–261.

Young, G.M., Long, D.G.F., Fedo, C.M., Nesbitt, H.W., 2001. Paleoproterozoic Huronian basin: product of a Wilson cycle punctuated by glaciations and a meteorite impact. *Sediment. Geol.* 141–142, 233–254.

Young, G.M., Minter, W.E.L., Theron, G.N., 2004. Geochemistry and palaeogeography of upper Ordovician glaciogenic sedimentary rocks in the Table Mountain Group, South Africa. *Palaeogeogr. Palaeocl*. 214, 323–345.

Zhu, C., Lu, P., 2009. Alkali feldspar dissolution and secondary mineral precipitation in batch systems: 3. Saturation states of product minerals and reaction paths. *Geochim. Cosmochim. Acta.* 73, 3171–3200.

Zolnai, A.I., Price, R.A., Helmstaedt, H., 1984. Regional cross section of the Southern Province adjacent to Lake Huron, Ontario: implications for the tectonic significance of the Murray Fault Zone. *Can. J. Earth Sci.* 21, 447–456.

CHAPTER EIGHT

Major and trace element analysis of sedimentary rocks of the Nanhua Rift Basin in the period 820–620 Ma

Abstract

The Nanhua Rift Basin of South China preserves an essentially continuous sequence of siliciclastic sedimentation from the mid Tonian to the end of the Proterozoic and beyond. Samples of fine-grained sediments from the late Tonian to the end of the Cryogenian periods are here analysed for major and trace elements. Since mobile elements are lost during weathering, changes in composition potentially reflect changes in climate and can be used to evaluate (i) the transition from warm to cold across the period boundary, (ii) the transition into the following warm interval and (iii) the transition into the second supposed icehouse interval at the end of the Cryogenian. Extreme swings in temperature are not evidenced. Weathering ranged from negligible to strong, increased across the Tonian/Cryogenian boundary, and was controlled primarily by tectonics, which affected grain size, rate of erosion and distance of transport. Iron ore resulted from the injection of metal-rich fluids at the Chang'an/Fulu Formation boundary. Cap carbonates precipitated as seawater mixed with metal- and carbonate-rich fluids at the Fulu/Datangpo and Nantuo/Doushantuo Formation boundaries.

If we consider the Neoproterozoic as a whole, the fine-grained clastics thought to have formed under snowball conditions are indistinguishable, in terms of weathering, from those that formed in non-glacial contexts. The same is true of Palaeoproterozoic sediments interpreted as glaciogenic. Since it is improbable that glaciers would not have mainly eroded igneous basement, with minimal chemical weathering, sediments characterised by moderate to strong weathering are more plausibly ascribed to large-scale faulting and downcutting through sediments weathered in a previous cycle. In the case of South China, however, the source rock appears to have been overwhelmingly crystalline. Such weathering as occurred took place in the environment of deposition, under water.

8.1. The geological context of the samples

The sedimentology and tectonic conditions of the Nanhua Rift Basin, South China, were described in Chapter 6. Samples visually identified as mudstone or fine siltstone were taken from six formations with a view to quantifying changes in chemical weathering towards the end of the Tonian and into the Cryogenian and during subsequent intervals in the Cryogenian (Table 8.1).

Samples	Unit	Age (Ma)	Location	Coordinates
Fanzhao 1–2	Fanzhao Fm.	770	Shangjiaomeng village	26°40'27.42"N 108°22'3.54"E
NW 1–3	Qingshuijiang Fm.	750	Nanwan village	26°40'26.75"N 108°12'16.84"E
	Pinglue Fm Longli Fm ≈ Gongdong Fm			
CX 1–27	Upper Gongdong Fm.	725–710	Cenxin village	25°54'24.67"N 109°15'27.15"E
CX 28–33	Chang'an Fm.*	710–690		
FM 1–9	Lowermost Fulu Fm.*	690	Fengmu village	25°57'29.10"N 109°38'15.06"E
WH 10–32	Tiesiao Fm. (= upper Fulu Fm.)*	665	Wuhe river	26°46'36.57"N 108°25'9.06"E
Dat 1–3	Datangpo Fm.	655	Wuhe river	
NT 1–4	Nantuo Fm.*	648–635	Wuhe river	
DJ 1–7	Lowermost Doushantuo Fm.*	635	Doujiang village	25°44'22.80"N 109°41'55.86"E

Table 8.1. Location, approximate age and stratigraphic order of the formations sampled. Asterisks denote formations usually interpreted as glaciogenic.

8.2. Analytical method

Major element composition was determined by X-ray fluorescence spectrometry. Samples were cleaned to remove modern weathering surfaces, broken into smaller pieces and pulverised in a tungsten-carbide TEMA mill. At Royal Holloway University of London powders were weighed, pre-heated for 8 hours at 450 °C to drive off water and organic carbon. On cooling, samples were re-weighed, mixed with a flux of lithium tetraborate, heated to 1100 °C and fused discs analysed in a 2010 PANalytical Axios sequential XRF spectrometer with 4kW Rh-anode X-ray tube. Pellets for trace-element analysis were prepared using the procedure of Watson (1996).

The degree of weathering reflected in the sediments is assessed by means of the 'chemical index of alteration' (CIA, an acronym also used for individual values). The index measures changes in the relative proportions of Al, Ca, Na and K as minerals, chiefly feldspars, lose the more mobile elements and turn into clay minerals (Nesbitt & Young 1982). The underlying theory is discussed in Chapter 7. No adjustment is made for non-silicate CaO, on the grounds that calcite, dolomite and apatite in the sediments are generally negligible.

8.3. Geochemical results and associated lithologies

8.3.1. *The extent of recycling*

Zr/Sc is often plotted against Th/Sc to assess whether sediments had undergone a previous cycle of weathering, erosion and deposition (Bahlburg & Dobrzinski 2011). During igneous differentiation, the parameters co-vary, with Th/Sc > 0.4 indicating a felsic origin. Recycling is predicted to result in enrichment of Zr but this is questionable (§7.5). Mudstones show much the same positive correlation whether they are products of primary or secondary erosion, and such preferential enrichment of Zr as occurs tends to be minor. In the present sample set there is no flattening of Th/Sc at higher Zr/Sc (Fig. 8.1).

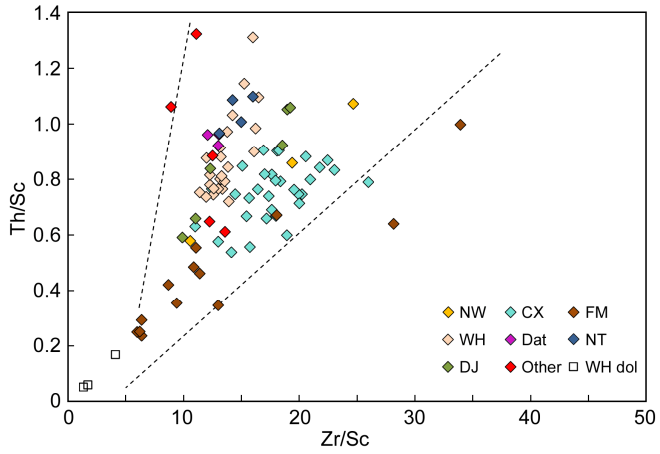

Figure 8.1. Zr/Sc versus Th/Sc for the samples investigated; dotted lines delimit the field typical of mudstones (Fig. 7.2). The low Th/Sc of some of the FM samples indicates mafic/hydrothermal influence.

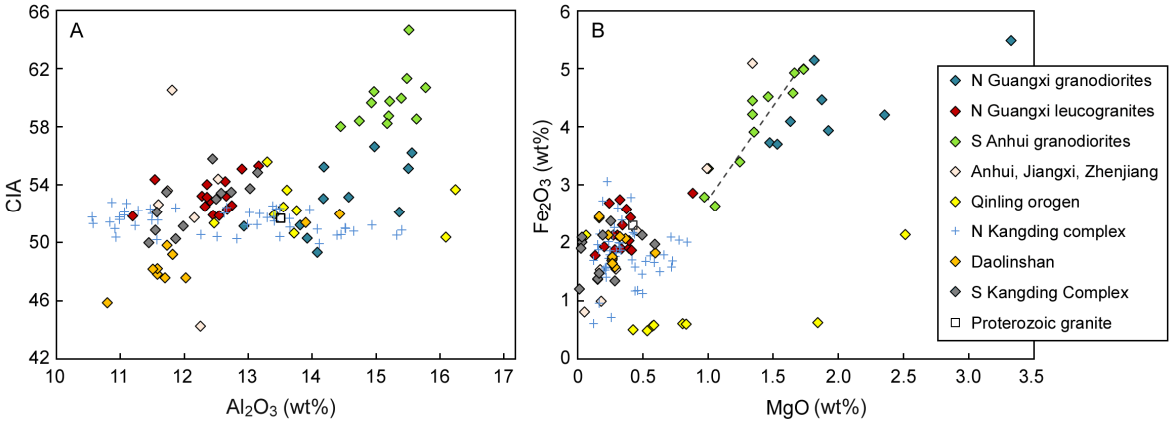

Figure 8.2. Composition of granite bodies in south China, varying both by region and sample: (**a**) Al in relation to mobile elements, (**b**) ratio of Mg to Fe, becoming more regular as percentages increase. Anhui and N Guangxi plutons are rich in Mg and Fe relative to the Proterozoic average. Dotted line for reference (Fig. 8.16). Data from Li et al. (2003), Chen et al. (2006), Wu et al. (2006), Zheng et al. (2008), Huang et al. (2008), Zhao et al. (2008), Q. Wang et al. (2010).

8.3.2. *Composition of the source rocks*

Granitoid compositions vary, so it is important to attempt some characterisation of the ultimate source rock. Figure 8.2 compares Tonian granites in South China from a range of tectonic settings. The simplest system is that of the North Kangdian complex, in the far west of the Yangtze Block

(Fig. 6.1). Although Al content varies widely, CIAs do not. By contrast, the CIAs of granites geographically closest to the samples studied – those of northern Guangxi Province, in the south-west of the rift basin – range from 49.9 to 56.6. Granodiorites in northern Guangxi are much richer in Ca (2–5 % oxide) than the leucogranites (< 1%), the leucogranites richer in K (3.5–5.5%) than the granodiorites (2.6–4.5%). Inevitably such variation will be inherited by the weathering indices of the sediments derived from them. The high CIAs of the S-type (supracrustal) granodiorites from southern Anhui Province, at the north-eastern end of the basin, are ascribed to melting of sedimentary rock (Wu et al. 2006) – a case of weathering inherited by igneous rock.

Dating to 826–819 Ma, the northern Guangxi granitoids outcrop over 1500 km^2, intrude the Sibao Group (c. 860–815 Ma) and are overlain by the Danzhou Group (younger than 815 Ma). Unroofing of the sediments originally overlying them must have taken place during the 'Jiangnan Orogen', immediately after the intrusion.

The Cryogenian Chang'an and Fulu Formations and correlatives had a depositional area extending SW-NE across the entire Nanhua Rift Basin, totalling some 500,000 km^2 (Zhang et al. 2011). Most of the extant granitoids in the basin date to 825–820 Ma (Li et al. 2003). They are much smaller in total area and widely distributed.

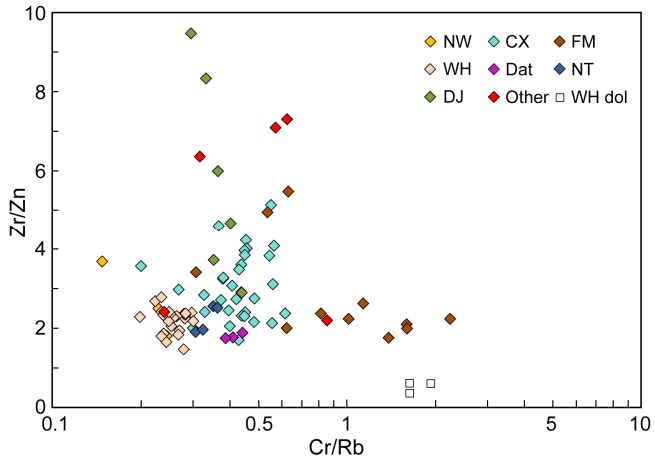

Figure 8.3. Zr/Zn as a discriminator of grain size. Falling below Zr/Zn = 6, most samples are confirmed to be of silt or finer grade.

8.3.3. *Grain size*

In first-cycle granite-derived sediments Zr concentrations tend to peak in the very coarse silt to very fine sand fractions, whereas Zn becomes enriched towards still finer grades and peaks in the clay fraction (von Eynatten et al. 2012). Hence Zr/Zn ratios discriminate between grain sizes, with coarse silt or finer typically having values < 5. Most values in the present dataset range between 1.5 and 4.0 (Fig. 8.3). The highest come from samples DJ 4–7, from around the Nantuo/Doushantuo boundary, which exceptionally contain very small clasts, two samples from the Nantuo Formation

near Machong village and one from 10 m below the top of the Nantuo at Tuanjie. The 'glacial' samples of Dobrzinski & Bahlburg (2007) have an average Zr/Zn of 6.6; paradoxically, the 'interglacial' samples have a higher average of > 10.

Like Th/Sc, the Cr/Rb ratio broadly distinguishes between felsic (< 0.8) and mafic (> 0.5). FM samples span the full range, with two recording extremely low concentrations of Rb (< 1 ppm) that push Cr/Rb values off the scale. All other series fall within a narrow Cr/Rb range and are consistent with a felsic origin.

8.3.4. *Loss on ignition and carbonate content*

Loss on ignition (LOI) quantifies the amount combusted during heating of samples in the furnace. At 450° C heating chiefly vaporises water and organic carbon; at 1100° C it vaporises the carbonate in calcite and/or dolomite and the lattice-bound water in clay (Murray & White 1955). Thus LOI at low temperature is a crude proxy for organic C content. The difference between the measurements, 'net LOI', is a proxy for the carbonate content, assuming that lattice-bound water is proportional. The actual amount of carbonate mineral can be estimated by reference to total CaO (net of apatite) and MgO. Except in the upper Nantuo Formation (DJ series), CaO and MgO show little correlation.

Na_2O strongly anti-correlates with LOI in all large datasets, and consequently there is a strong correlation between LOI and CIA, especially in the Huang et al. (2014) and Wang et al. (2011) datasets. When compared with CaO and MgO, samples with high Na do not appear to have low carbonate. Perhaps the explanation is that Na decreases as the clay component (namely, kaolinite) increases, and LOI contains a significant amount of clay-bound OH. LOI also correlates with F, Cl, Rb and Th. Rb is preferentially taken into the lattice of clay minerals (Nesbitt et al. 1980).

In nearly all the sediments analysed CaO is less than NaO and mostly below 0.9%. An adjustment just for calcium apatite, on the basis that this was the form taken by P_2O_5, often gives rise to negative CaO, and P_2O_5 does not correlate significantly with either F or Cl. Non-silicate CaO is therefore not adjusted for except in explicit circumstances, and unadjusted CIAs are conservative. For comparison, a calcium-free index of weathering, termed 'ANK', is also used, calculated as:

$$\frac{Al_2O_3}{Al_2O_3 + Na_2O + K_2O} \times 100$$

The resultant values are of course somewhat higher than those of the CIA, as are those of the source. A similar index, $(Na_2O+K_2O)/ Al_2O_3$, has been used in Cenozoic contexts as a proxy for weathering temperature (Passchier & Krissek 2008).

8.3.5. *Loss on ignition and organic carbon*

In providing an index of relative OC content, LOI at 450° C can be calibrated to measured TOC (Heiri et al. 2001) and the results compared with TOC preservation and, by inference, productivity across the succession. TOC was directly measured for the four Nantuo samples NT 1–4. The amounts are similar to those reported in other studies (Table 8.2).

Formation	TOC (%)	Average TOC (%)	n	Reference
Marinoan:				
Doushantuo cap		0.18	5	Wang et al. 2008, Ader et al. 2009
		0.21	5	Xiao et al. 2012
Nantuo (NT)	0.11			
	0.13			
	0.10			
	0.14	0.12	4	This study
Nantuo (DJ)		0.01	6	This study
Nantuo		0.12	13	Wang et al. 2008
		0.31	3	Guo et al. 2007
		0.08	4	Gaschnig et al. 2014
		0.56	2	Yu et al. 2016
Ghaub		0.11	3	Gaschnig et al. 2014
Elatina		0.16		McKirdy & Watson 1983
Sturtian:				
Tiesiao		0.09	19	This study
Fulu		0.03	6	This study
Chang'an		0.02	6	This study
Chang'an		0.01	3	Wang et al. 2008
Chang'an		0.05	5	Partin et al. 2013
Pocatello		0.07	6	Gaschnig et al. 2014
Numees		0.08	4	Gaschnig et al. 2014
Rapitan Iron		0.21	9	Klein & Beukes 1993
Pre-Sturtian:				
Gongdong		0.02	26	This study
Gongdong		0.02	4	Partin et al. 2013

Table 8.2. Average TOC per geological unit, supposedly deposited in glacial conditions. The Ghaub, Numees and Pocatello Formations are diamictite-bearing units in Namibia and the USA.

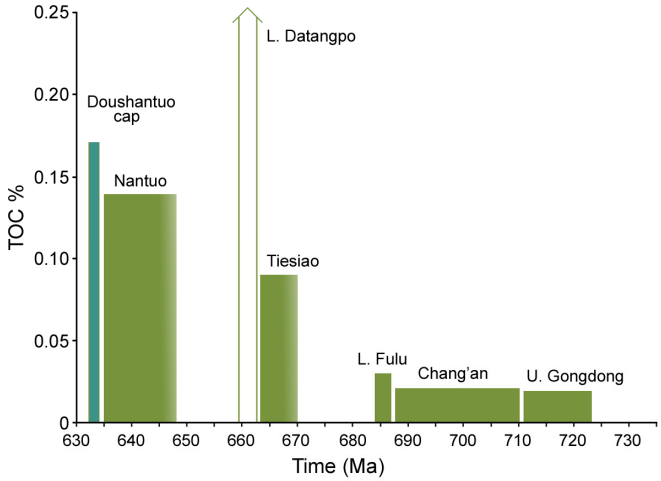

Figure 8.4. Estimated organic carbon content 725–630 Ma. All formations except the lower Doushantuo are siliciclastic. TOC content is in part a function of sedimentation rate.

Results for South China are given in Figure 8.4. Production in the lowermost Datangpo Formation was anomalously high, up to 4.8% (Ader et al. 2009, Feng et al. 2010), stimulated by nutrient-rich hydrothermal fluids. That aside, levels in the Cryogenian were low. Organic carbon rose from an average 0.03% in the early Chang'an Formation to 0.14% in the Nantuo, not unlike the trend of the carbonate record (Fig. 4.7). Percentages were low chiefly because of dilution by high rates of sedimentation – some 30–60 m/Ma through the Gongdong and Chang'an Formations. Given that the whole basin became glaciated around the end of the Tonian, the most significant finding is that there was any production at all, continuing unabated as the Cryogenian approached. Organic molecules deriving from chlorophyll-*a* indicate that the organisms inhabiting the ice-beset Chang'an and Nantuo environments were photosynthesisers (Wang et al. 2008).

8.4. Geochemical results and associated sedimentology

Fanzhao Formation (Xiajiang Group)

The formation consists of fine-grained turbidites. In the Huang et al. dataset the entire 600 m of this formation are described as slate. Two samples were taken, both with CIAs of 70. As that study sampled the unit far more comprehensively, the samples are not further discussed.

Qingshuijiang Formation

The Qingshuijiang Formation overlies the Fanzhao. Beds are silicified mudstone roughly 0.5 m thick, with some iron-staining, minor soft-sediment deformation, and occasional bentonite layers. Upsection the sediment becomes more shaly. The CIA of the three samples ranges from 61 to 65. Huang et al. describe the formation as slate, often tuffaceous, with a thickness of 600 m.

Gongdong and Chang'an Formations

The Qingshuijiang Formation is followed by a further 1700 m of distal turbidites (slate). According to Wang & Li (2003) the thickness of the Gongdong Formation is 880 m. If this is representative, our sampling began about half way up (Fig. 8.5). The lithology is thin-bedded, pale blue-green siltstone, sometimes laminated, with minor cm-scale slump structures and a few larger-scale folds. Ripples at various levels between CX 11 and CX 12 suggest turbidites. Thin rhodochrosite beds – associated at 270 m with pyrite – indicate episodes of minor hydrothermal influence and pauses between turbidity flows sufficient to capture high concentrations of the mineral.

The boundary with the overlying Chang'an Formation is conformable and marked by a gradational coarsening of sediment to pebbly silt, gritty in places. The bedding is thin and slightly wavy. A displaced boulder around this level consists of faint laminae enclosing mostly subangular clasts smaller than 6 cm, plus a larger clast 15 cm across. Generally small and never frequent, clasts seem most common near the base of the formation. Upsection, sediment continues to be pale blue-green and mainly gritty, although siltstone also occurs. Turbidite beds comprise both lithologies (Fig. 6.7a). In places, weathering accentuates the elevated Mn content. Pyrite cubes are up to 1 cm.

The final sample, CX 33, is from the top of the Chang'an: pale blue-green, gritty-to-fine matrix, with very small (< 1 cm) clasts. The overlying Fulu Formation consists of well-sorted, massive sandstone beds fining upwards from coarse to medium, interpreted as turbidites. There is no cap carbonate. Turbidites are also seen in a quarry not far away.

CIA ratios are surprisingly variable, fluctuating between extremes of 60.7 to 73.4. ANK reduces the variation to between 64.4 and 73.7. The difference between the two indices increases as CIA decreases, the two coinciding where the CIA is at a maximum, i.e. Ca is minimal. Maximum weathering is reached at two points: at 278 m and 1000 m, the latter in the middle of the Chang'an Formation.

Much of the variation appears linked to changes in grain size. Contrary to the expected trend, a sharp drop in CIA at 100 m coincides with the deposition of finer sediment, reversed at 135 m as the sediment slightly coarsens. Zr/Zn shows no clear trends. A progressive fall in CIA, from 73 to 61, begins after the thin rhodochrosite beds at 270 m. The index rises sharply in the final 10 m of the formation. No samples from the Chang'an are less than 65. All things considered, the variation probably relates to how long sediments were exposed to weathering rather than to changes in climate assuming constant exposure.

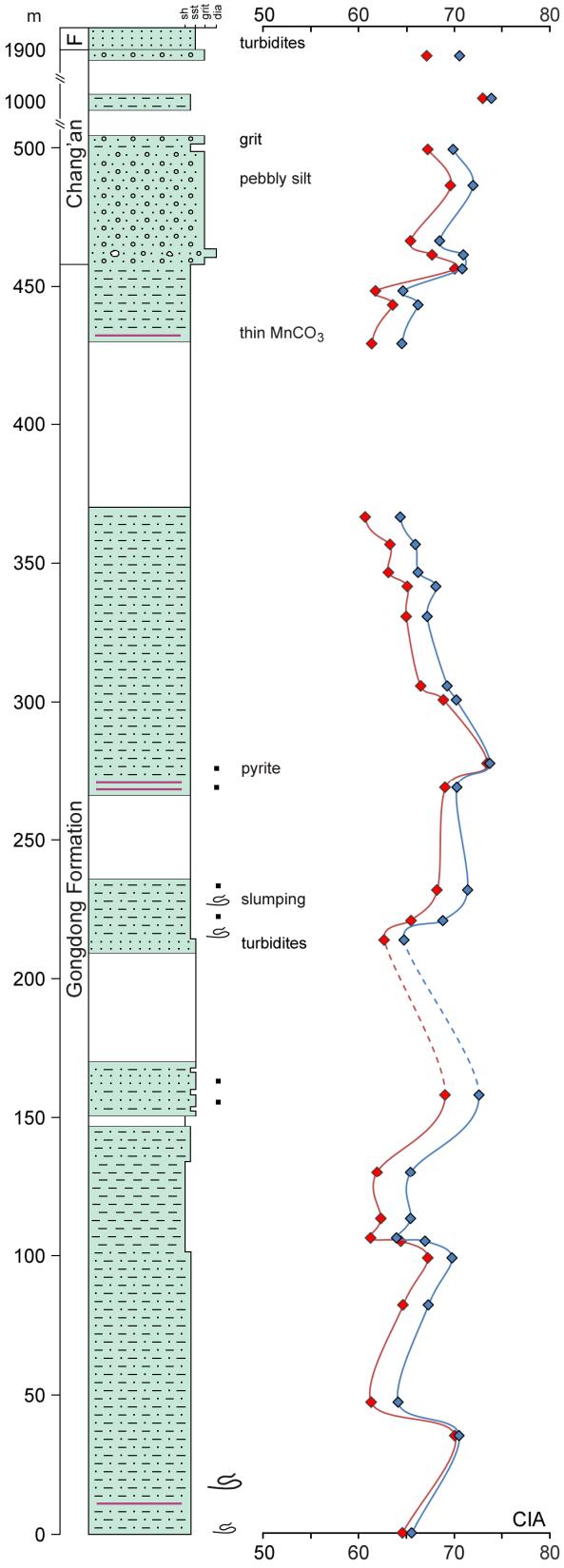

Figure 8.5. The upper Gondong Formation and Chang'an Formation (truncated) near Cenxin: CIA in blue, ANK in red.

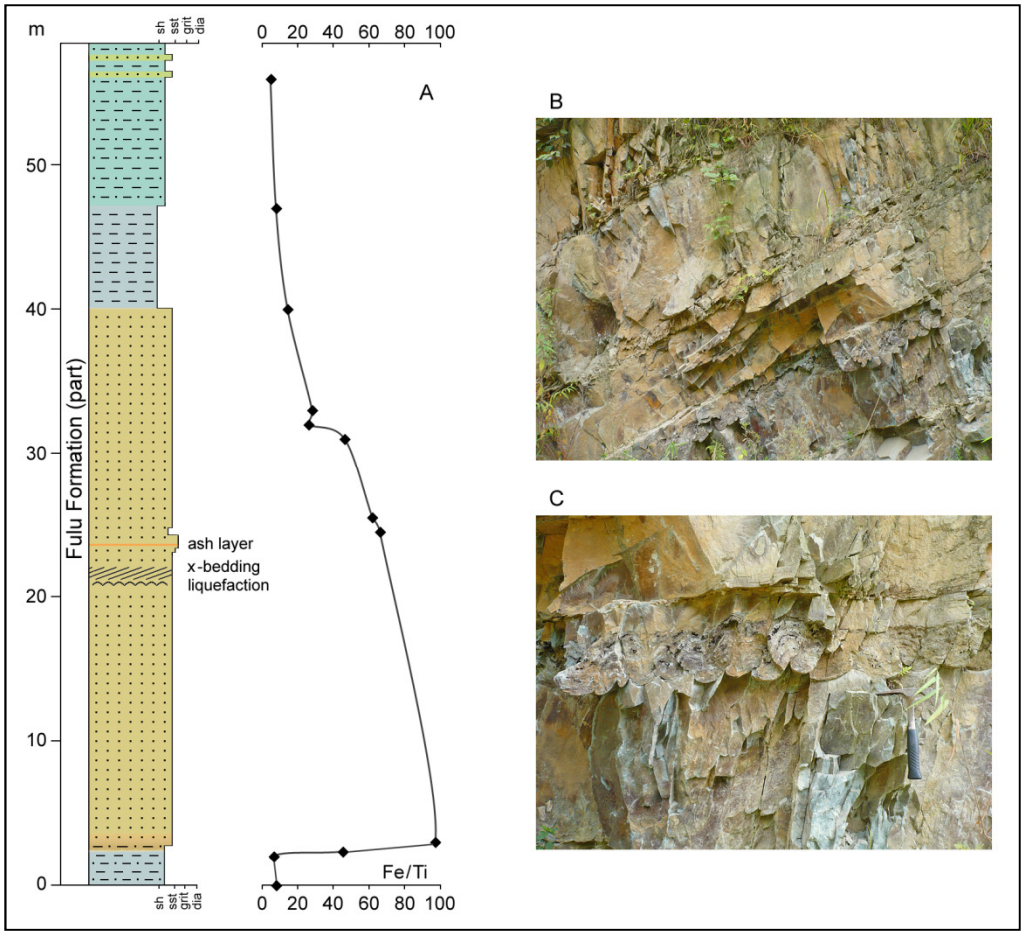

Figure 8.6. (**a**) Lowermost Fulu Formation, Fengmu section. (**b**) Turbidites above the seismic liquefaction layer, visible lower right. (**c**) Closer view of the liquefaction layer.

Iron content (total Fe_2O_3) ranges from 2.6 to 6.4%. Proportions fall sharply at 100 m and rise sharply just after the turbidites, after which they are fairly steady. The maximum value is in the Chang'an, at 1000 m. Potassium variation is cyclical, declining from an initial peak of 3.8% to a low of 1.5% at 278 m, rising to a second maximum of 4% at 367 m and falling to a second low of 1.7% at 487 m. Sodium content is high (1.5–4%) and also cyclical, varying inversely with K (as in Fig. 7.4).

Lowermost Fulu Formation

Beds at the Fengmu section are thin to massive, ranging from mudstone to fine sandstone, sometimes laminar, iron-rich especially near the base. The fine sandstone is turbiditic. At 21 m a laminated, strongly crumpled bed 17cm thick records an episode of seismic liquefaction (Fig. 8.6c). Although care was taken to sample nothing coarser than siltstone, CIA or ANK values as a measure

of chemical weathering in the iron-rich sediments are not meaningful. The log in Figure 8.6 traces the change in iron content (which the CIA largely follows), normalised to titanium.

At 3 m height, Fe_2O_3 surges to an immediate peak of 44%. MnO peaks at 2.2 m. Together, the coarser grain size, turbidite sedimentation, liquefaction layer and iron enrichment suggest an episode of region-wide deep-rooted seismically induced faulting. As iron formation is a common feature of the Sturtian interval (§1.2), the ore deposits at this level (Tang et al. 1987) assume the significance of the global context.

Fe and V here do not correlate, as they do where the relationship is governed by igneous differentiation, and as in the rest of the succession. Elements that anti-correlate with Fe through the enriched interval (2.3–35 m) are Ca, Na, K, Sr, Rb and Ta. From background levels around 36 ppm Cr surges to 144 ppm.

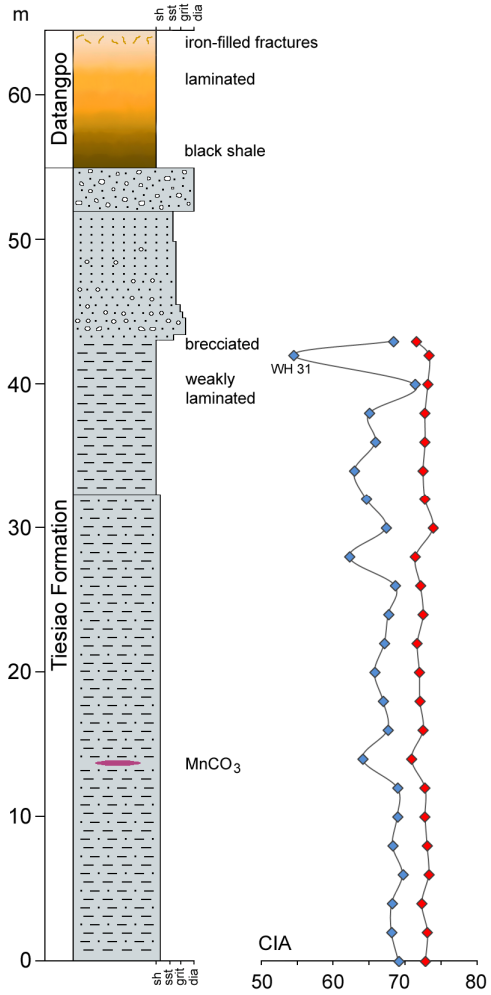

Figure 8.7. Tiesiao Formation, Wuhe river section. CIA in blue, ANK in red.

Tiesiao Formation = (upper?) Fulu Formation

At Wuhe the lowest diamictite unit is interpreted to equate with the Chang'an Formation and the middle diamictite unit with the Fulu Formation (Lan et al. 2015). Alternatively, as assumed here, the sampled interval is upper Fulu. Its 43 m of siltstone and mudstone suggest remarkably quiet conditions. Thereafter the lithology abruptly coarsens into grit with thin discontinuous layers of poorly sorted, small, elongate, mostly angular clasts. It then fines up, terminating at 52 m with a 3-m-thick sandy diamictite (Fig. 8.7). The diamictite is followed by the iron-rich base of the Datangpo Formation.

Lenses of rhodochrosite/kutnahorite, occurring sporadically as far back as the Fanzhao Formation, suggest eruptions of anoxic fluids rich in Mn^{2+}. There are several such horizons in the Tiesiao Formation (not all illustrated), closely associated with iron-rich laminae and dolomite/calcite. A few samples were analysed for stable isotopes. Carbon-isotope ratios range from -7.8 to -10.3‰, reflecting a substantial contribution of organic carbon, and oxygen-isotope ratios from -11.1 to -16.3‰, suggesting elevated temperatures. The samples are fine-grained (Fig. 8.1) and rich in phosphate, Ba, Sr and volatile trace elements. Mn is somewhat enriched throughout the sequence; Ca shows a rising trend. Sulphur surges around 32–34 m. Many element patterns are oscillatory, notably Na, Cr, V, Sc and Rb.

CIAs are depressed by significant amounts of carbonate, increasingly from 25 m. For this reason, combined with the coarsening after 43 m, the sequence is interpreted as shallowing up. The sudden drop in CIA just below the brecciated horizon results from a substantial increase in CaO (to 4.2%, LOI = 6.5%), while background MnO doubles. The ANK signal is steady.

Datangpo Formation

As elsewhere, the formation is Mn-rich in its lowermost part, in which respect there is some continuity with the horizon just below the diamictite with which the Fulu Formation terminates. The basal shale suggests a sudden deepening at the boundary, triggered by faulting. Fe-rich fluids flowed through the faults. Three samples were taken at Wuhe, from mudstones in the lower, middle and upper parts of the formation. They are very alike. CIA is ~72, ANK ~73, the latter not materially different from the average of the upper Tiesiao Formation.

Nantuo Formation

Samples NT 1–4 were taken at Wuhe from mudstone horizons varying in thickness from 50 cm to 4 m. CIA varies from 65 to 71, ANK from 67 to 72. Samples DJ 1–7 were slightly coarser samples

from the last 20 m of the formation near Doujiang, below a quarry that worked the lower Doushantuo for manganese. The unit here is well-bedded, with sub-cm laminae. DJ 4, 5 and 7 contain very small clasts that, dropstone-like, deflect the laminae. CIA varies from 71.5 (DJ 1, stratigraphically the lowest sample) down to 56 (DJ 4). Because some of the samples include appreciable dolomite, ANK, at 68–73, is much less erratic and even in this narrow range anti-correlates well with the grain-size proxy Zr/Zn. Taking Dat 3 and the NT and DJ series as successive, there is a systematic rise in K from 3.2 to 6.6%, some of which presumably relates to source composition. Na rises to 2.2% (NT 3), then plunges to levels around 0.1% in the DJ series. Fe plunges from a high of 6.5% in DJ 1 to < 1% at the top of the formation. Mn, Cr and Zn also show a mostly falling trend.

Two samples from near Machong also come from the uppermost Nantuo. Here the lithology is dominantly siltstone, sandier towards the top, with occasional pyritic nodules and pebbles. A final sample, from Tuanjie, comes from mudstone several metres thick, 10 m below the top. At the top a few small clasts and pyritic nodules were seen. The samples are rich in Fe, K and V. CIA is 66–71, ANK are both 69–72. Despite extensive searching, a cap carbonate unit was observed only at Wuhe.

8.5. Iron as an index of hydrothermal input

As briefly reviewed in the Introduction (§1.2), iron formation – rock containing more than 15 wt% Fe_2O_3 – is not an uncommon occurrence in the Cryogenian. Concentrations can be as high as 73% (Breitkopf 1988). Iron formation is *prima facie* evidence of hydrothermal input, where erupting low-eH fluids from the mafic interior introduced large quantities of dissolved Fe^{2+}. The metal precipitated as it was oxidised in the upper water column. Although most discussions assume that fluid escape was through oceanic crust, the context of iron formation in the Neoproterozoic – rift systems within continental crust – makes this unlikely. A few authors propose eruption through major faults in the continental crust, possibly with volcanic admixture (Breitkopf 1988, Volkert et al. 2010, Freitas et al. 2011).

What constitutes iron formation is a matter of definition. Fe content can be below 15% yet still be far above the 1.3% of average Proterozoic sandstones or the 5.6% of average Proterozoic shales (Condie 1993). Since hydrothermal influence need not have been restricted to iron formation, the question is whether geochemistry can be used to detect it in rocks whose Fe content falls below the definitional threshold.

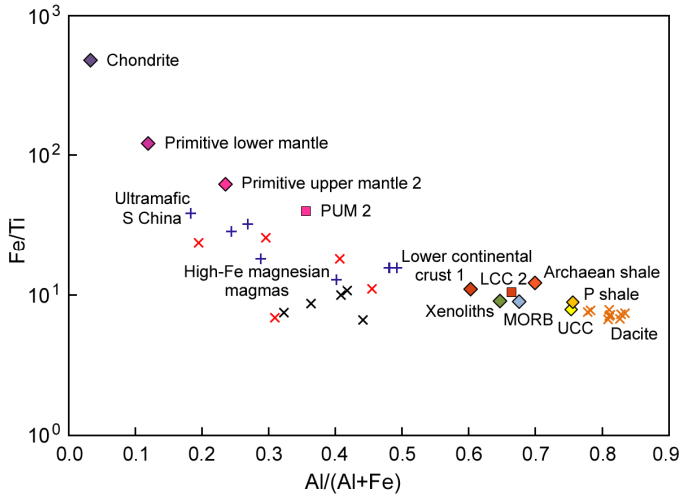

Figure 8.8a. Magmatic rocks show a broadly linear relationship between Fe and Al (oxide ratios); with crust-mantle differentiation Fe increases exponentially. The high-Fe, high-Mg magmas are attributed to mantle plumes (Gibson 2002). Archaean magmatic rocks shown in red. South China data from Lin et al. (2016).

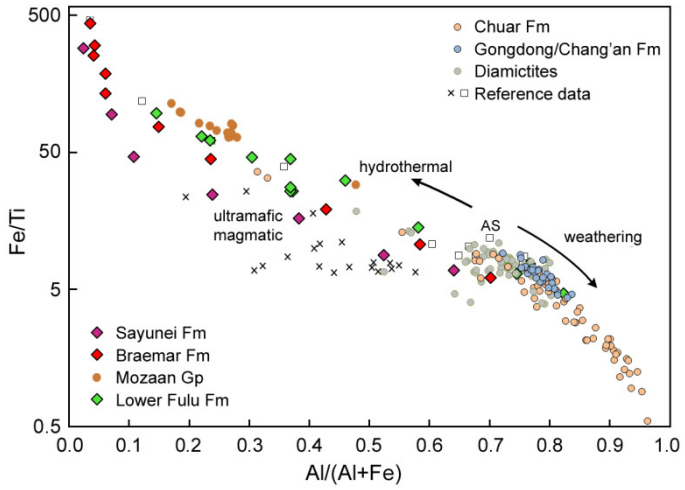

Figure 8.8b. Same plot as for Fig. 8.8a but with y-axis expanded. Iron formation (e.g. Braemar, Sayunei Formations) plots to the left of Archaean shale (AS) and accords with the primitive trend of crust-mantle differentiation. The Chuar Group is late Tonian. The Mozaan Group represents diamictites and mudstones from the ~2.9 Ga Archaean 'glaciation'.

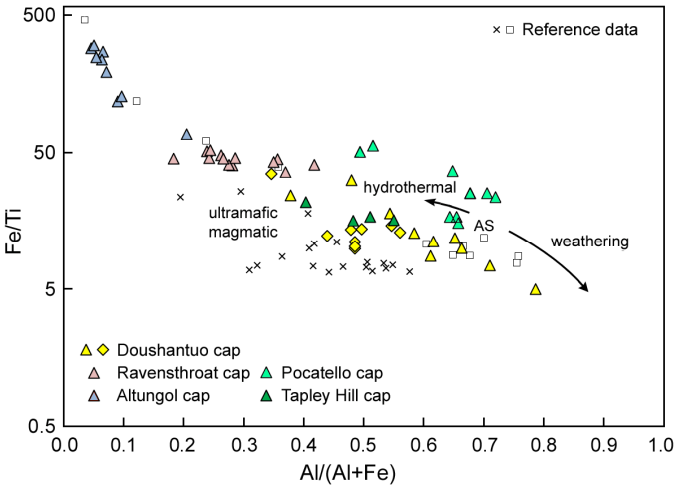

Figure 8.8c. As for Fig. 8.8b, but focusing on the whole-rock composition of cap carbonates, nearly all of which evince hydrothermal addition of Fe. Doushantuo Formation triangles denote shallow-water, diamonds deep.

Normalised to Ti (an insoluble element not enriched in hydrothermal fluids), Fe tends to increase as rocks become more mafic. The upper continental crust has the lowest Fe, chondrites, representing the primeval composition, the highest (Fig. 8.8a). Variation of Fe resulting from crust-mantle differentiation follows an exponential trend. Magmas show little variation, generally remaining below 10, while Al/(Al+Fe) varies between 0.6 (the value of lower continental crust) and 1.0 as a

consequence of igneous differentiation. Mineralogical evolution via erosion, chemical alteration and re-deposition is a third process, whereby weathering follows the Bowen reaction series towards more felsic compositions and Fe/Ti decreases because Ti is less mobile than Fe. Shales, the most evolved product of weathering, have a composition close to UCC, with the secular trend – as igneous differentiation itself increases – evolving towards the low-Fe end-member (Cox et al. 1995). In principle, then, the relation of Fe/Ti to Al can distinguish between the three types of control. Rocks of primitive composition, including, by extension, terrestrial hydrothermal deposits, should follow an exponential trend, starting from an Fe/Ti ratio greater than 10; variably differentiated magmas, no trend but below primitive values; and sediments derived from igneous rocks, an exponential trend going in the reverse direction from rocks of primitive composition.

Iron formation derived from hydrothermal fluids has a metal content partly controlled by its origin and partly by the degree of dilution from ongoing siliciclastic sedimentation. In deeply rifted environments iron formation can be heavily diluted by sediment. In other places, rifting is less penetrative and Fe metasomatism not a significant factor. Shales and other such sediments tend to plot in the field Fe/Ti < 10 and Al/(Al+Fe) > 0.65 (Fig. 8.9b), where the sedimentary component is represented by Ti and Al.

Archaean shale represents an end-member for normal siliciclastic composition because the parent rock was more mafic than in later times. Iron formation sediments are richer in Fe than Archaean shale, with variable proportions of Al (Fig. 8.8b). In their alignment with primitive mantle compositions they suggest that the crustal fractures which provided passage for dissolved iron went deep. Neoproterozoic shales and comparable siliciclastics are typically poorer in Fe. Most of the Fulu Formation samples plot in the field characteristic of iron formation. So do the cap carbonates that terminate the Cryogenian in South China, rich also in Mg and Mn (Huang et al. 2011, Och et al. 2016), and so do the Mn-rich levels of the Datangpo Formation, the carbonate-siliciclastic unit overlying the Fulu (Wu et al. 2016, Yu et al. 2016). Enrichment in Fe, Mg and Mn seems to be a general feature of cap carbonates (Meyer et al. 2012, Peucker-Ehrenbrink et al. 2016, Feng et al. 2016, own data, Fig. 8.8c). The metals became concentrated in the carbonates for the same reason that carbonate took over from diamict sedimentation: catastrophic rifting was no longer generating high volumes of clastic sediment.

8.6. Secular trends

8.6.1. *Data integration*

I now offer an overview of the succession, integrating the new dataset with others published. These include:

- the Jialu to Nantuo Formations at Lijiapo/Liaojiapo, Guizhou Province (Huang et al. 2014)
- siltstones from the Langjiehe Member, lower Fulu Formation, at Liuchapo, Hunan Province (Dobrzinski & Bahlburg 2007)
- shales and siltstones from the Datangpo Formation at Xiangtan and Tanganshan, Hunan Province (Liu et al. 2006), and at Zhailangou, Guizhou Province (Dobrzinski & Bahlburg 2007)
- fine-grained sediments from the Nantuo Formation at Wuhe, Guizhou Province (*ibid.*)
- three siltstone samples from the Doushantuo Formation at Tianping and three from the formation at Jiangkou, both in Hunan Province (*ibid.*)
- dolomitic black shales from the lower part of Member II of the Doushantuo Formation (Och et al. 2016).

Where data include trace elements, values with Zr/Sc > 25 are excluded from weathering indices. Cryogenian ages are interpolated proportional to stratigraphic height between the following fixed points:

- base of the Chang'an Formation, 710 Ma
- base of the Fulu Formation, 685 Ma
- base of the Datangpo Formation, 663 Ma
- base of the Nantuo Formation, 645 Ma
- base of the Doushantuo Formation, 635 Ma

The dates are estimates constrained by the absolute dates summarised in Chapter 6. The condensed Tiesiao (Fulu) Formation at Wuhe is allocated 7 Ma. In several places the base of the Nantuo Formation is unconformable, so is likely to vary in age. The top 20 m of the Nantuo at Doujiang, Machong and Tuanjie are most parsimoniously integrated with the record at Wuhe on the basis that they formed about the same time as the cap carbonate at Wuhe. In total the integrated data span almost 200 Ma, from the mid Tonian to the start of the Ediacaran. There is scope to extend them further into the early Cambrian (Och et al. 2016).

8.6.2. *ANK variation 815–630 Ma*

ANK is somewhat more regular than CIA variation (Fig. 8.9); scatter is reduced further if data are filtered for Zr/Sc < 25 (Fig. 8.10). Some of the ratios from the Pinglue, Longli and Chang'an Formations at Lijiapo are surprisingly high. In the smaller dataset of Wang et al. (2011), CIAs

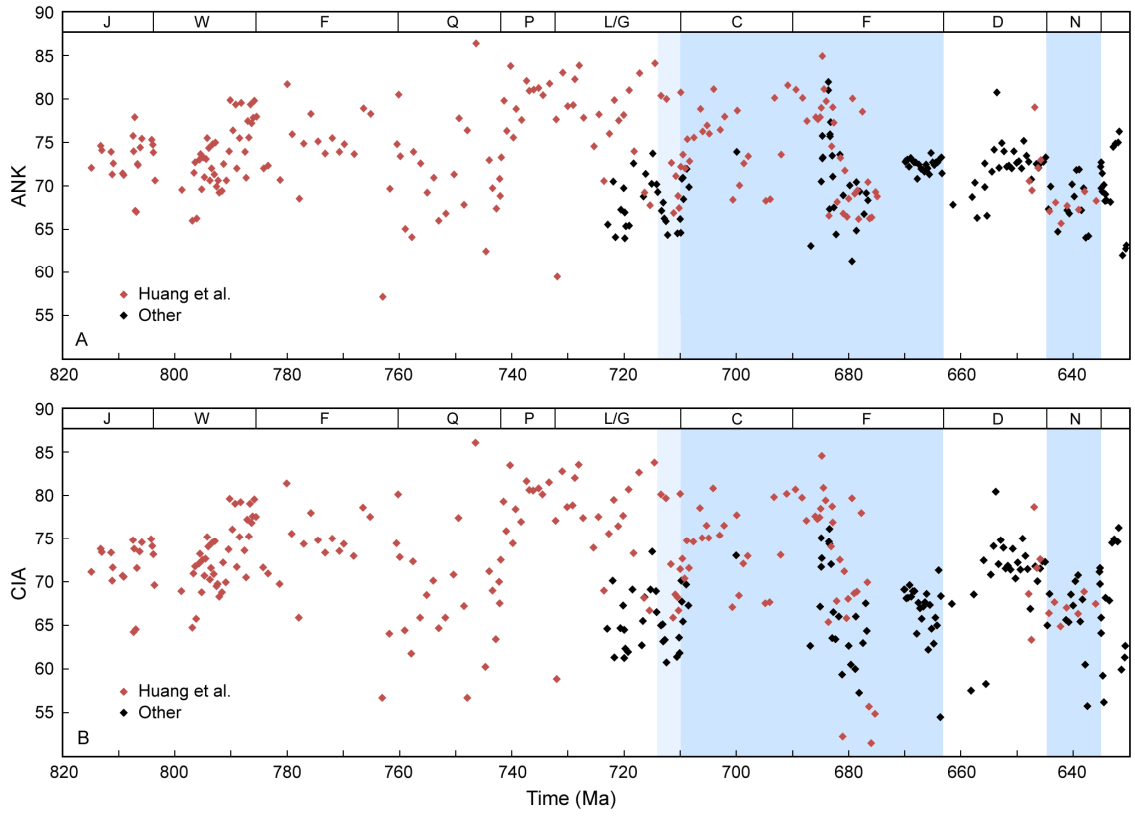

Figure 8.9. (**a**) ANK variation and (**b**) CIA variation in the Nanhua Rift Basin, 815–630 Ma. Formation names initialised. Shaded areas denote the Sturtian and Marinoan intervals. 'Other' excludes data of Liu et al. (2006) and Zr/Sc > 25.

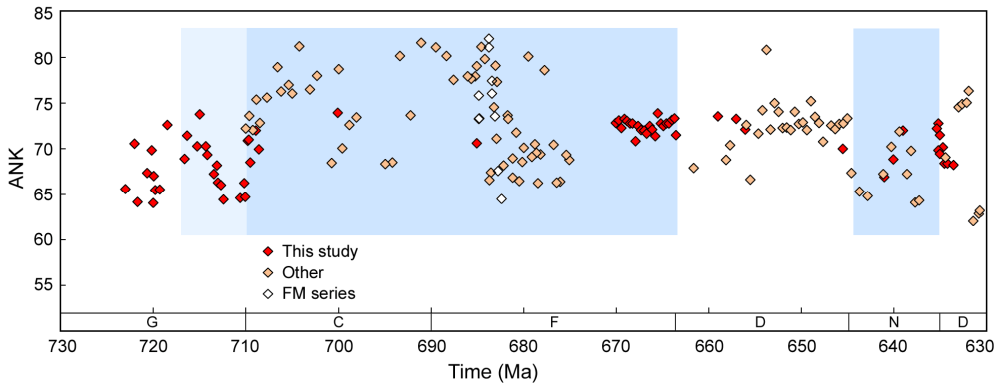

Figure 8.10. ANK variation through the period 723–630 Ma, samples restricted to Zr/Sc < 25 except the Chang'an and lower Fulu Formations (no Zr/Sc data). Shaded areas denote the Sturtian and Marinoan intervals.

through the Qingshuijiang, Pinglue and Longli Formation are all below 75 except two anomalous sandstones from the Longli; two siltstones from the Gongdong Formation yield 63 and 64; three from the Chang'an Formation in Hunan Province range from 54 to 62, contrasting with two from the same formation in Guizhou Province, which are 76 and 80. Some of the disparity may be due to regional variation.

ANK through the upper Gongdong and Chang'an Formations is oscillatory, rising across the formation boundary (Figs. 8.5, 8.10). It continues to rise, at least at Lijiapo, through the first 150 m of the Chang'an, here 650 m thick in total, from 72 to 81; similarly high ratios (> 77.5) are recorded in the final 220 m. They are lower in the middle. Through the upper Fulu (Tiesiao) Formation ratios are fairly steady, and similar to those in the Datangpo apart from a dip at the beginning of the latter. The pattern is oscillatory through the Nantuo Formation, similar in range and amplitude to that of the upper Gongdong, and suggests a tripartite division equivalent to the three members discerned in the Shennongjia region (§6.3). The highest values occur at the top (DJ 1–3), perhaps equivalent to the 8-to-20-cm-thick claystone reported by Zhang et al. (2008). The lowest occur in the Doushantuo Formation, at Tianping, well after the Cryogenian.

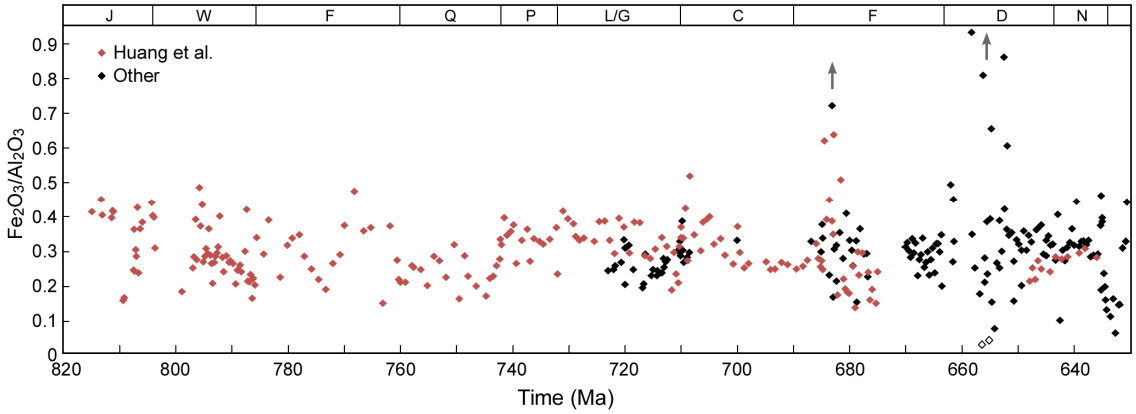

Figure 8.11. Fe variation through the period. Unfilled symbols in Datangpo Formation: Al_2O_3 > 27%.

8.6.3. *Fe variation 815–630 Ma*

Unusual enrichments or depletions in Fe are traced by normalising to Al (Fig. 8.11). Through the early part of the sequence variation is considerable (0.15–0.45), with ratios above 0.4 (Fe/Al 0.3) probably reflecting some basalt contribution. The Longli Formation at Liuchapo is more enriched than the coeval Gongdong at Cenxin. The Chang'an is depleted relative to the other formations. After c. 795 Ma there is no evidence that erosion of mafic rock contributed much to the mix. The greatest perturbations were (1) at the start of the Fulu Formation, where an influx of Fe was reversed somewhat higher in the sequence, and (2) at the start of the Datangpo Formation, which saw a second influx of Fe. There is also a sharp dip around the Nantuo/ Doushantuo boundary (DJ series). Fe and Mg generally co-vary through the sequence, as discussed below.

8.6.4. *Trace elements 730–620 Ma*

Trace elements tend to be better conserved than major elements during weathering and transport (Taylor & McLennan 1985). They are also likely to be more abundant in crustal fluids, which if

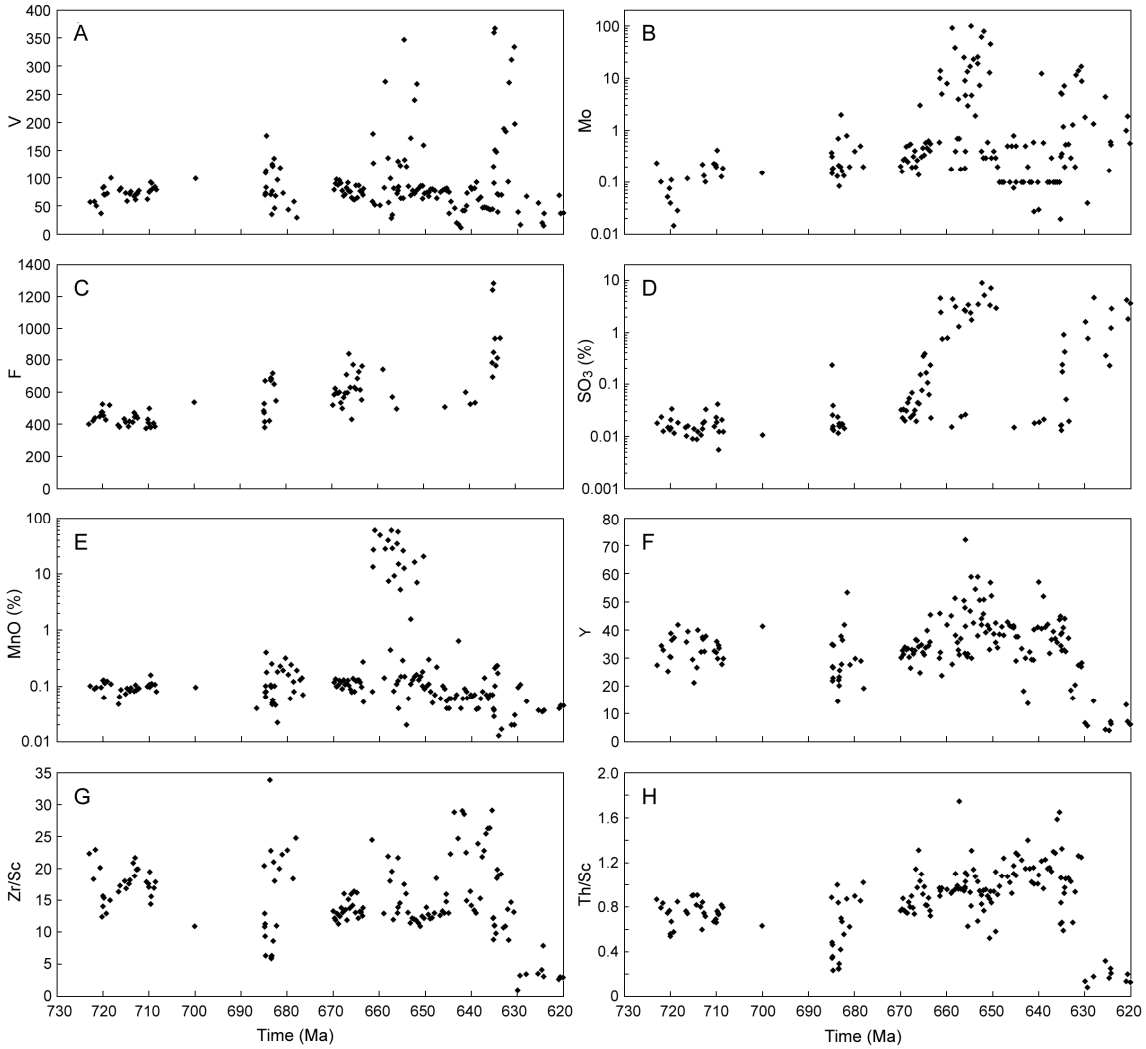

Figure 8.12. Selected trace elements for the late Tonian to early Cryogenian. Quantities in ppm except (d) and (e). Logarithmic scales in (b), (d) and (e).

they reach the surface then mix with the sediments. Concentrations of some trace elements as they varied through time are highlighted in Figure 8.12.

Like Cr, trivalent V readily substitutes for Fe^{3+}, and is enriched in mafic and ultramafic rocks. Of itself, correlation with MgO is not considered indicative of mafic provenance (*pace* Wang et al. 2011). Like Cr and Fe^{2+}, V can also be a sign of anoxia. Its abundance near the base of the Fulu Formation c. 690 Ma accords with the eruption of mafic fluids at this juncture (Fig. 8.12). That is, V arrived in the depositional environment already concentrated (relative to oxic conditions) by anoxia in the source; the environment apart from these fluids may not have been anoxic. There is a second spike in the terminal Nantuo, continuing for a short while into the Doushantuo Formation (Sahoo et al. 2016). In the late Doushantuo, about the time of the Shuram-Wonoka $\delta^{13}C$ excursion, levels commonly exceed 1000 ppm (Och et al. 2016).

Mo rises through the period by an order of magnitude quite steadily, is very high through most of the Datangpo (up to 100 ppm) and moderately elevated in the early Doushantuo (0.5–15 ppm). Again, extreme enrichment is associated with hydrothermal input and does not necessarily represent the open ocean. In the late Doushantuo, levels commonly exceed those of the Datangpo.

Sulphur rises exponentially from about 670 Ma, through the later part of the Fulu and throughout the Datangpo Formation. Concentrations return to pre-Chang'an levels in the Nantuo, then surge to persistently high levels in the Doushantuo. S correlates with Fe (pyrite) beyond about 2% Fe. Since the surge was hydrothermal, the euxinic conditions inferred for shale-dominated environments through the Doushantuo were not necessarily representative of the open ocean. Data for Cl and F are more limited. Cl is generally elevated through the Tiesiao Formation (36–84 ppm, as against 21-47 in the Gongdong), declining through the Datangpo (lower part not sampled) and Nantuo. F is similar, except that it surges at the end of the Nantuo. In the lower Datangpo one of the F-bearing minerals is bastnaesite (Ce, La,Y)CO_3 (Wu et al. 2016). After water and carbon dioxide, SO_2, HF and HCl are the most abundant gases in volcanic emissions. The high concentrations of these barely magma-soluble volatiles imply ejection of hydrous mantle fluids before they could degas and diffuse into the rockwall.

Manganese content rises abruptly by orders of magnitude in the lowermost Datangpo, then falls to below pre-Chang'an levels. Sr content is also lower than in the Cryogenian, typically 60–100 ppm. It falls at the base of the Fulu, includes some high values in the lower Datangpo, and climbs to 900 ppm in the Doushantuo. The patterns of Y, Sm and Nd are similar to each other, with depletion apparent near the base of the Fulu and in the lower Doushantuo, and a steady rise through the Fulu and Datangpo.

The following trace elements correlate strongly with CIA and ANK: V, Sc, Ga (which substitutes for Al especially well), Th and Rb. Hence Cr/Rb (Fig. 8.3) anti-correlates to some extent. Strontium also anti-correlates. In principle, these trends can therefore be extrapolated back to the initial CIA, if known, and used to characterise the source rock. Zr/Sc, a proxy for distance of transport (Fig. 8.1), shows an oscillatory pattern and also very low in the Doushantuo. Peaks occur twice through the Gongdong Formation, twice in the Fulu Formation, once in the early part of the Datangpo Formation and twice through the Nantuo Formation. Probably they reflect tectonic pulses of enhanced sediment generation. Th/Sc, partly reflecting the degree of igneous differentiation, is low in the Chang'an, highest in the Nantuo, and plunges to low levels at the base of the Fulu and end of the Nantuo. It remains at low levels until the late Doushantuo.

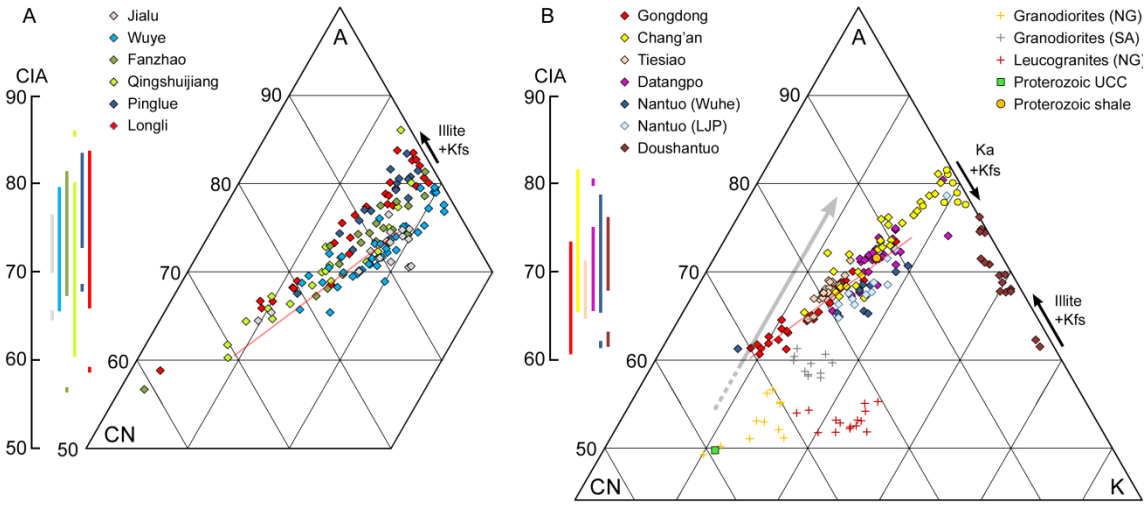

Figure 8.13. (**a**) Weathering trends of the formations at Lijiapo, 815–710 Ma (data from Huang et al. 2014). Red line: trend of the Gongdong Formation in (b) for reference. The CaO of four calcareous samples from the upper Jialu Formation has been conservatively adjusted down to 0.25%, increasing the linearity of the arrays. (**b**) Weathering trends of the formations analysed in this and comparable studies, 720–620 Ma, Zr/Sc < 25. Compositions of the Northern Guangxi granodiorites and leucogranites also shown (Li et al. 2003). CaO in the several calcareous samples from the Nantuo Formation is adjusted down to 0.3%. The Doushantuo includes samples from the lowermost part at Doujiang, Machong, Tuanjie (this study), Liuchapo and Jiangkou (Dobrzinski & Bahlburg 2007); where these are inferred to be calcareous, CaO is adjusted down to 0.1%. Grey arrow is the 'predicted weathering trend' of Fedo et al. (1995). Yellow circles near A-K axis: K enrichment associated with high CIA through the upper 260 m of the Chang'an Formation at Lijiapo.

8.7. Evaluation of CIA

Formation-specific trends are seen on a triplot of Al, Ca+Na and K (Fig. 8.13). Unless there was an initial, unrecorded weathering trend that went parallel to the A-CN limb, whereby plagioclase and the more soluble K-bearing minerals (biotite, muscovite) dissolved in concert, the trends do not point to any of the obvious candidate sources, compositionally various though they were. Trends are generally steeper through the Tonian succession than through the Cryogenian, but all point towards a composition more aluminous than average Proterozoic upper continental crust and less potassic. On a total alkali (Na_2O+K_2O) versus SiO_2 diagram, the least weathered representatives of the Fanzhao, Qingshuijiang and Longli Formations plot in the granite field, the Gongdong Formation in the granodiorite field; all are peraluminous. On the whole, weathering was greater in the Tonian than in the Cryogenian.

The Gongdong, Chang'an, Tiesiao and Nantuo arrays are strongly linear, the Datangpo somewhat less so. Linearity is an indication of uniform composition, presumably homogenised by erosional downcutting and sedimentary reworking. Initial CIAs are unlikely to have been much below 60. Sediments close to 60 are therefore essentially unweathered. Progressive breakdown of plagioclase

and its replacement by kaolinite resulted in K proportionally increasing as a consequence of Ca and Na loss. The steeper slopes of the Pinglue, Longli and Gongdong Formations suggest that K-bearing minerals, especially K-feldspar, were barely dissolving at all. The Chang'an Formation does suggest some such dissolution. However, through the upper part of the formation, where the array approaches the A-K axis, the vector switched, converging on the point where continuation of the Gongdong array would have intersected the axis. After nearly all plagioclase had been converted to kaolinite, K-feldspar apparently began to crystallise *de novo*, drawing on the K previously leached into solution. CIAs consequently fell, even though this represented a further stage of alteration. The 'prediction' that plagioclase and K-feldspar would have weathered in equal proportions (Nesbitt & Young 1984, Fedo et al. 1995) is not borne out and cannot be treated as a finding of what actually happened, in relation to which the apparent enrichment of K is attributable to metasomatism (through the entire 4500 m of the Xiajiang Group per Huang et al. 2014, to say nothing of all the sediments represented by average Proterozoic shale). As seen in the anti-correlation between Na and K through the Gongdong, Datangpo and Nantuo Formations, plagioclase was simply dissolving faster than K-feldspar, if K-feldspar was dissolving at all.

The one formation that might seem to justify an imputation of potassium metasomatism is the Doushantuo. Adjusted for non-silicate CaO, all samples run close to the A-K axis towards K, indicating that almost no plagioclase remained. However, if these constitute a vector trending towards the K axis, the origin of the apparently excess K is unexplained. More probably, the array represents a radical switch in provenance to a granite poor in plagioclase but rich in K-feldspar. The little plagioclase present rapidly weathered to kaolinite, the K-feldspar, to varying degrees, then weathered to illite. Stratigraphic variability in source composition may have increased the spread in Al/K ratios. If we take the N Guangxi leucogranites as illustrative (Fig. 8.2, Li et al. 2003) and model weathering of the end-member compositions on the basis that Al and K increased in weight % proportional to the loss of Ca and Na, the final products span a range very similar to that encountered (Fig. 8.13). Note that the respective CIAs are understated relative to the formations deriving from more aluminous sources.

The transition from the Gongdong to the Chang'an is particularly significant because it tests the prediction that chemical weathering would have fallen as the land became glaciated. During the middle to late Eocene lead-up to the growth of ice sheets on Antarctica, CIAs fell from 72 to around 61 (Dingle et al. 1998). During the Oligocene they fell further to 44–55 (Passchier & Krissek 2008). No such fall is seen in the record of Neoproterozoic South China. At Liajiapo, values in the Chang'an Formation rise through the first 150 m from 71 to 81, drop to 67, erratically

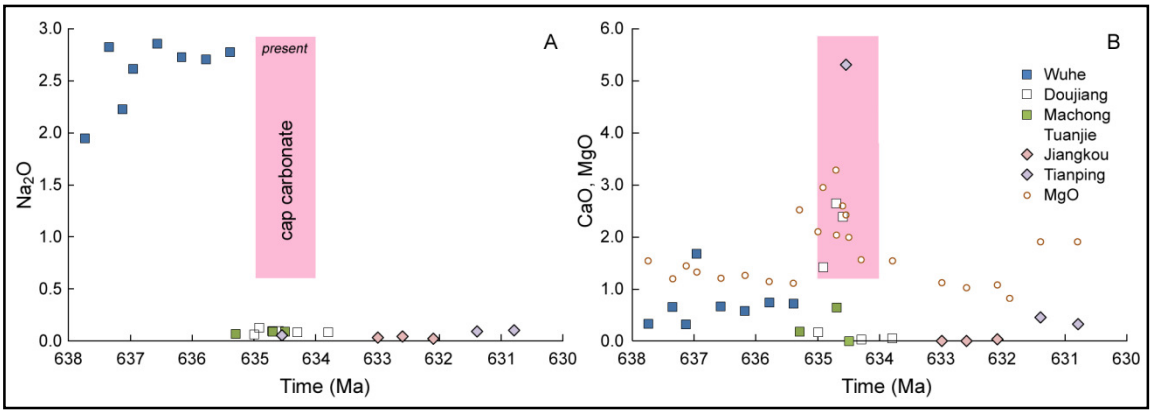

Figure 8.14. Chemostratigraphic correlation through the Cryogenian-Ediacaran transition. (**a**) The dramatic fall in Na at the end of the Cryogenian suggests that some of the samples from the Nantuo Formation (squares) at Doujiang, and others from Machong and Tuanjie, were coeval with the cap dolostone present but not sampled at Wuhe. Diamonds represent the Doushantuo Formation. (**b**) The spike in Ca and Mg in these same siliciclastic deposits supports correlation with the dolomite.

rise to 81, finally abate to around 78. The six samples analysed in this study average 68, peaking in the middle of the unit at 73. The range of the Nantuo Formation is almost as wide as that of the Chang'an. CIAs fall from 72 to 61 through the first third, a carbonate horizon marks a pause, in the second third CIAs climb to 71 and in the last third fall again to 62. At Lijiapo, ratios early on touch 79. The claim, based on elevated δ^{26}Mg (Huang et al. 2016), that an episode of intense weathering preceded the end of the Nantuo seems doubtful: Al is not enriched in any of the relevant samples.

The record takes us continuously from the diamictite, through the cap carbonate interval and into the less disturbed Ediacaran proper. According to the snowball hypothesis, Earth switched from an icehouse to a greenhouse state and air temperature soared by 100°, from -50° C (Feulner et al. 2015) to something like +50° during deglaciation, as pCO_2 rose to 300,000 ppm (Pierrehumbert et al. 2011). Lack of weathering should have left CIAs close to the source value, followed by extreme weathering and CIAs above 90. Again, the geochemistry hardly supports such a scenario. Some ratios in the Nantuo Formation are close to the inferred source value, others over 70; at the beginning of the cap carbonate they rise to 72, returning to Nantuo levels (though the source was probably less aluminous) later in the Doushantuo.

8.8. Mg, Ca, Na and K through time

Element proportions vary according to source composition, degree of weathering and hydrothermal influence (if any).

One of the most striking features is a sudden fall in Na at the end of the period (Fig. 8.14). Apparently there was a switch to a source depleted in Na. In view of the steepness of the fall,

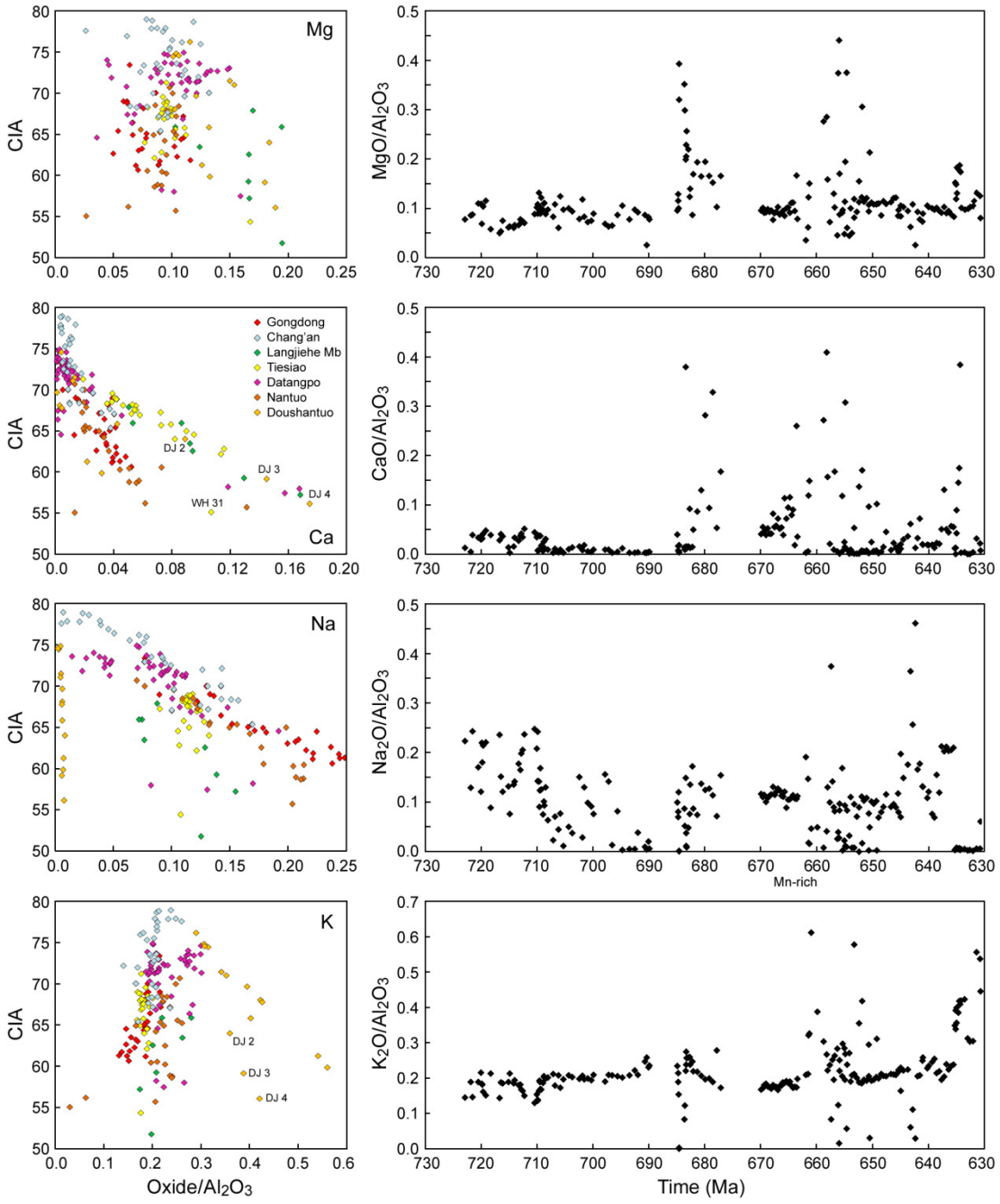

Figure 8.15. Major element proportions as they varied with weathering (CIA, unadjusted) and over time. DJ 2–DJ 4 (cf. Fig. 8.14), many of the Tiesiao and Datangpo and some of the Nantuo samples are calcareous.

parsimony requires that the low-Na samples from the terminal Nantuo Formation (as identified on sedimentological grounds) be coeval with the low-Na samples from the basal Doushantuo. Elevated Ca and Mg in the earlier of the low-Na Nantuo samples also suggest correlation with the dolostone. Deposition of gritty siltstone ('diamictite' *s.l.*) was occurring in some places at the same time as dolomite was precipitating in others, and at the same time as dolomite was precipitating here within the siltstone. In the top 2 m of the Nantuo Formation 25 km east of Jiangkou Na also fell abruptly (Huang et al. 2016); at the same time, diamictite gave place to siltstone, then ^{13}C-

depleted dolostone. The question of what kind of sedimentation was going on in parts of the basin where cap carbonate was not precipitating, or precipitated later than in other places, can thus be answered: it was gritty siltstone, such as occurs at various levels in the Nantuo (*ibid*.).

Magnesium during weathering remained immobile. Depletions in the upper Gongdong and lower Datangpo Formations (Fig. 8.15) are therefore attributable to shifts in area and/or depth of erosion. Elevated weight ratios through the lower Fulu, the whole of the Datangpo and at the start of the Doushantuo show that hydrothermal fluids were commonly enriched in the element – a point of importance for understanding the genesis of cap carbonates. Indeed, the dominance of smectite through the lower Doushantuo and of dolomite through the upper (Bristow et al. 2009) suggests that, in shallow settings, hydrothermal fluids were the main source of Mg throughout the Ediacaran. Suitable Mg-rich rocks are lacking.

Calcium decreases as Al is enriched. Weathering shows two main trends, that of the Fulu Formation and lowermost Doushantuo (DJ 2–4), from a starting CaO/Al_2O_3 ratio in excess of 0.18, and that of the Gongdong and Nantuo Formations, from a starting CaO/Al_2O_3 ratio in excess of 0.08. The greater the initial concentration, the greater the loss, so that both trends converge around CIA = 75. As evidenced by lenses of rhodochrosite, higher Ca content in the upper Fulu and lowermost Doushantuo reflects a calcitic component, promoted by low sedimentation rates and proximity to hydrothermal inflow. The same enrichment occurs through an equivalent section at Liuchapo (data from H. Bahlburg). Adjusting CaO downwards increases the CIA but does not alter the slope materially. At Wuhe, the most calcareous sample is WH 31; if aligned with the respective trend and thereby adjusted for carbonate CaO, its CIA would be around 64.

Although less mobile than Ca, sodium also decreases as Al is enriched. The most regular trends are those of the Gongdong and Chang'an Formations, which both extrapolate to an initial Na_2O/Al_2O_3 beyond 0.25. The trend of the Datangpo steepens beyond 0.10, pointing to a source less rich in Na but not unlike that of the Nantuo Formation. Plotted against time, sodium content through the upper Gongdong rises, then falls. It is more regular through the Cryogenian, but drops in places affected by hydrothermal activity (hence the bimodal CIA trend), notably in the Mn-rich, ore-grade sediments of the Datangpo. In the lower Nantuo, and again towards the end of the formation, levels surge. Minimal levels through the Doushantuo indicate a switch of source, with some hydrothermal influence.

In most units potassium appears to be immobile. Any loss during weathering was neutralised by the greater loss of Ca and Na. Only the Gongdong Formation correlates with CIA. Most lower

Doushantuo samples display a strong negative trend, indicating prolonged metasomatic enrichment. Generally, there is remarkably little scatter in the ratio.

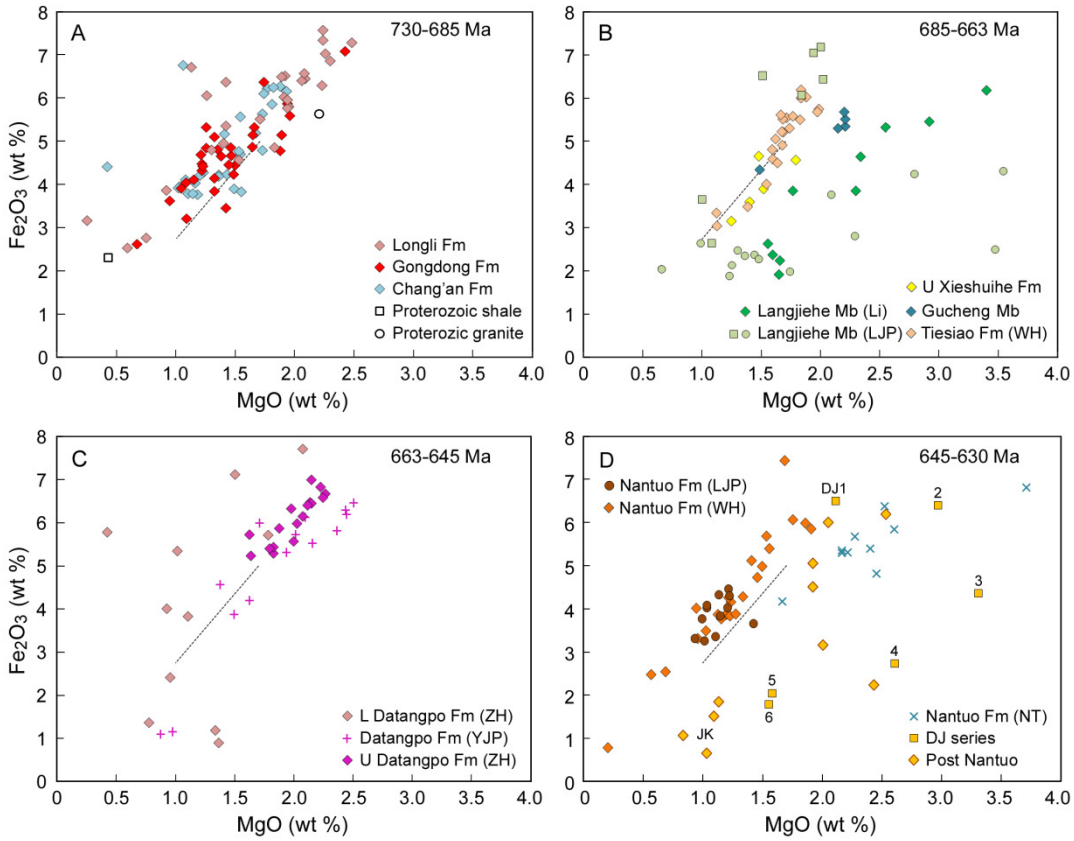

Figure 8.16. Mg v. Fe in the Nanhua basin from 730–630 Ma. Xieshuihe Formation data from Feng et al. (2004), NT series from Gaschnig et al. (2014), dotted line as in Fig. 8.2. Squares and circles in (**b**) differentiate the lower 100 m and remaining 180 m of the Langjiehe Mb at Liujapo respectively; the Fe_2O_3 of two samples from the former exceed 8%.

8.9. Mg v. Fe

Like those of S Anhui Province, the granodiorites of N Guangxi are relatively rich in Mg and Fe (Fig. 8.2). Beyond Mg = 1% the elements increase roughly in proportion; in the mafic rocks there is no such relationship (Zhou et al. 2007). Weathering may have decreased Mg relative to Fe, Mg being more mobile (Fabre et al. 2011). However, this would imply a higher original Fe/Mg ratio in the source rock than in the sediments, something the analogues do not corroborate.

The trends of the Longli, Gongdong and Chang'an Formations (c. 730–690 Ma) constitute a single array and show considerable variability, especially in the Longli. As with most of the samples, they come closest to the Nanhua Basin granodiorites of S Anhui, though the Fe/Mg ratio is slightly higher. Data in the upper Sturtian (c. 690–660 Ma) are more diverse. The most linear trend is that of the lower Langjiehe Member at Liujiapo, the upper Xieshuihe Formation and the Tiesiao

Formation. The trend is somewhat steeper than in the earlier interval and to that extent suggests a switch in provenance. The upper Langjiehe Member is less regular, with the trend at Lijiapo differing from that at Liuchapo; the distribution most resembles that of the N Guangxi granodiorites.

Through the lower part of the Datangpo Formation, ratios are dispersed, reflecting irregular hydrothermal input; further up they co-vary. The Nantuo at Wuhe and Lijiapo shows the same trend as that of the Longli–Chang'an sequence, possibly reflecting a return to the same source. The provenance of the Doushantuo Formation was clearly different. In particular, the DJ series at the bottom of the formation becomes progressively less mafic after DJ 2, a trend continued by the samples from Jiangkou.

8.10. Precambrian ice ages or catastrophic rifting?

CIAs were first used to measure the degree of weathering undergone by putatively glaciogenic sediments in the Palaeoproterozoic (§7.1–7.2). Indeed, the Palaeoproterozoic Huronian basin is not unlike the Nanhua: both were rift basins that widened over time and accommodated high-energy sedimentation. In the older basin the lower Gowganda Formation is predominantly diamictite and therefore thought to have accumulated in a cold climate. Fine-grained sediments of the Serpent Formation immediately below it average 62 (n = 27), the argillites composing much of the lower Gowganda average 62 (n = 148), and the argillites of the upper Gowganda average 63 (n = 27). This is so far from what the glaciation hypothesis predicts that the lower Gowganda samples are further hypothesised to include material from surfaces weathered in temperate climates (Young & Nesbitt 1999) – presumably, since some sediment would have been first-cycle, material more weathered than that of the Serpent Formation. Zr/Sc ratios ranging from 7.3 to 15.6, however, suggest that recycling was minimal. Given that the sedimentology is, at best, equivocal (Miall 1985), one might well conclude that the hypothesis – taking the term at face value – is disproven.

A number of Cryogenian successions have been analysed in respect of their CIA (Fig. 8.17). Northeast Svalbard (Kunzmann et al. 2015) encompasses the pre-Sturtian Svanbergfjellet and Russøya Formations (average CIA 77), the post-Sturtian Arena Formation and Macdonaldryggen Member (average 61), and the post-Marinoan Dracoisen Formation (average 62), deposited in non-glacial conditions. Since the inferred latitude was subequatorial and pCO_2 many times higher than now, conditions in the post-Sturtian and post-Marinoan intervals were apparently too disturbed to have permitted much weathering. Average CIAs are almost identical to that of the lower Gowganda (64), which in relation to a source CIA of ~48 suggests moderate weathering. The non-carbonate

diamictite matrix of the Ghaub Formation has an average of 61 (Bahlburg & Dobrzinski 2011). The siliciclastic fraction of the putatively glaciogenic Port Askaig Formation, filtered for low Zr/Sc and Zr/Zn, has an average of 71 (Panahi & Young 1997). Mudstones of the Sturtian-age Mineral Fork Formation, also screened for recycling and grain size, has an average of 72. The argillite matrix below the top of the eponymous Sturt Tillite consists mainly of muscovite (metamorphosed illite), chlorite and quartz, and does not materially differ from the overlying Tindelpina Shale (data from Sumartojo 1974). Excluding carbonate-rich samples, its average CIA (n = 21) is 68, that of the Tindelpina Shale ~70. The pre-Sturtian Gongdong Formation has an average of 66, the Sturtian-age upper Fulu Formation (WH series) 68, the post-Sturtian Datangpo Formation 72, the Marinoan Nantuo Formation (at Wuhe) 64. Overall, the CIAs of diamictites are no lower than those of non-diamictite sediments.

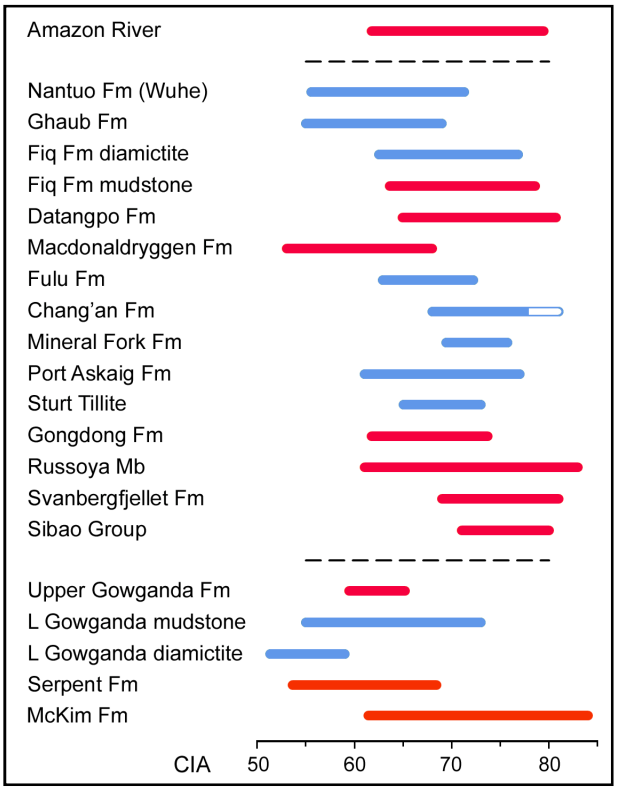

Figure 8.17. CIA ranges of fine-grained samples from a variety of geological units, some considered glaciogenic (blue), others not (red). Rieu et al. (2007) interpret low-CIA mudstones of the Fiq Formation to reflect cold temperatures. One value of 76 omitted from the Sturt Tillite data.

Typically, formations vary by 15 units or more. Huge variability in CIA, irrespective of facies, suggests that temperature was not the dominant control on weathering. Rather, the dominant control was exposure to weathering, itself a function of erosion rate and hence of variable tectonic activity. Warm, wet conditions generate high values; cold conditions are not required to generate low values. Moderate to high CIAs may have been due to recycling. However, if glaciers were the agents of erosion, sediments are most likely to have been eroded from crystalline bedrock (§7.5). In the Fiq Formation diamictite, CIAs are continuous with the CIAs of preceding or succeeding

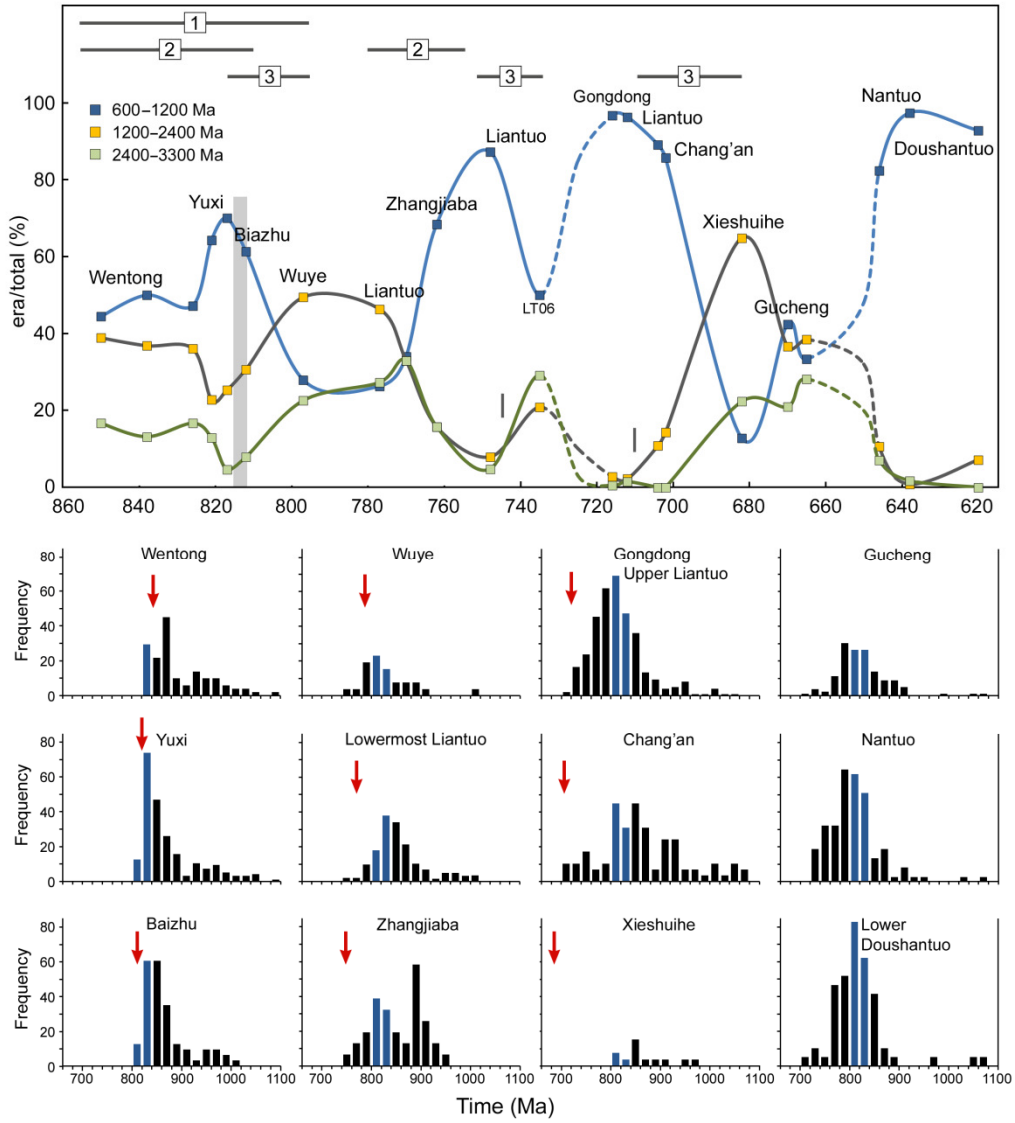

Figure 8.18. (**a**) Detrital zircon percentages of Hunan-Guangxi sediments grouped by $^{206}Pb/^{238}U$ age. Data from Wang et al. (2007), Liu et al. (2008), L.J. Wang et al. (2010), Wang et al. (2011), Hofmann et al. (2011), X.C. Wang et al. (2012), W. Wang et al. (2012a), W. Wang et al. (2012b), Wang et al. (2013), Cui et al. (2014), Okada et al. (2014), Yang et al. (2015) and Pi & Jiang (2016), sifted for discordance <10%. Unit ages are based on the zircons themselves combined with stratigraphic position. The Yuxi, upper Fulu (Gucheng Member) and Nantuo Formation are differentiated between lower and upper, the Wentong and Liantuo Formations between lowermost, lower/middle and upper. Sample LT 06 (Liu et al. 2008) is understood to come from the thick sandstone at the base of the upper Liantuo. Boxed numbers: (1) period of greatest felsic magmatism, (2) periods of greatest mafic volcanism, (3) periods of greatest extension. Grey band: the 'Jiangnan Orogen' (post-Yuxi unconformity) relative to the formations as dated. Vertical bars: estimated base of upper Liantuo (745 Ma) and Chang'an Formation (710 Ma).

(**b**) Age-frequency distribution of zircons per formation (frequency normalised to size of largest sample, all ages). Blue columns: frequency at 840-800 Ma highlighted for reference. Arrows: inferred approximate medial age of formation.

mudstones. Zr/Sc ratios are low throughout, the highest coming from a mudstone with one of the lowest CIAs (65). In the thickest diamictite unit CIAs start at 77 and fall, more or less progressively, to a minimum of 62 near the top – all this during 'Snowball Earth'. As has been remarked, 'CIA values in glacially influenced deposits are never as low as would be expected for sediments produced solely by mechanical erosion' (Rieu et al. 2007).

The chronology and nature of the 'Jiangnan Orogen' is not entirely resolved. While the Yuxi Formation beneath the angular unconformity contains numerous zircons younger than 820 Ma, it is intruded by granites dating to 825–820 Ma. Volcanics immediately above the unconformity date to c. 819 Ma (Yang et al. 2015), although one date has been revised down to 797 ±4 Ma (Wang et al. 2007). In places the boundary is conformable (Yang et al. 2015). At any rate, if the deformation associated with the unconformity does mark the collision of two plates, it was the only major compressional event to affect the Yangtze Block in the Neoproterozoic post 860 Ma and it left no lasting topography. Since the block was nearly all under water during the Ediacaran, during the earlier Neoproterozoic it must have been largely flat, low-elevation and, apart from regolith, devoid of sedimentary cover. Sediment generation from subaerial weathering and fluvial erosion would have been limited. The main agent of erosion and topography was the rifting that, from soon after 820 Ma segmented the Nanhua region into grabens. Sediment originated, initially, from fault scarps.

Detrital zircons from the Nanhua Basin can be divided into three groups (Fig. 6.11): older than 2400 Ma, 2400–1200 Ma, and post 1200 Ma. Most of the basement constituting the Yangtze Block is Palaeoproterozoic in age, underlain by Archaean rock whose extent is unknown (Zhang & Zheng 2013). Most zircons younger than 1200 Ma derived from plutons intruding Palaeoproterozoic basement beneath the Nanhua basin; a small proportion derived from basaltic magmatism. The rise in frequency 880–820 Ma reflects increasing plutonism. In the final 30 Ma of that period, 50–70% of the sediment came from the juvenile crust so generated, at the same time as magmatism peaked. Melt bodies reached shallow levels and included large proportions of weathered sediment, producing granite and granodiorite rich in aluminium. Intrusion, solidification, exhumation, erosion and transport all took place within a few Ma (Fig. 8.18, Yuxi Formation). Immediately thereafter, if not already before the unconformity (Figs. 6.12, 8.18), the tectonic regime was extensional: the collision zone became the rifting zone.

After c. 780 Ma, as the crust thinned and the rift deepened, the contribution from Palaeoproterozoic basement – chiefly that lying beyond the Hunan-Guangxi basin – dwindled, from 70 to 15%. From 760 to 700 Ma at least 70% of the sediment consisted of eroded plutons, as continuing extension

exposed and fragmented the plutons and sinking of the basin redistributed the detritus from shallow to deep. Again, much of the eroded rock was not much older than the date of deposition. Around 745 Ma, coincident with a major unconformity half way up the Banxi Group (Fig. 6.4) and the steep drop in zircon frequency, lateral incision of basement resumed, but only briefly, with the late Mesoproterozoic/Neoproterozic proportion reaching a new peak c. 720 Ma. Lateral incision resumed again soon after the start of the Cryogenian, with detritus older than 1200 Ma accounting for more than 85% of sediment by 685 Ma (though, of course, more data are still desirable). In the Datangpo interval, apart from intermittent volcanism, conditions were comparatively quiet and erosion rates low. Rates increased again in the Nantuo interval. However, in contrast to the early Cryogenian, the contribution from Palaeoproterozoic basement continued to fall; most sediment now came from within the rift basin itself.

Thus the most dramatic shift in zircon provenance began not at the start of the Sturtian interval, but after 780 Ma, when the input from juvenile crust rose from 25% to, eventually, almost 90%. A similar shift took place at the start of the Marinoan. Extension was accommodated by basin deepening. Conversely, the rifting which resulted in widening of the basin took place predominantly in the periods 815–780 Ma and 710–660 Ma. Widening does not seem to have occurred significantly during the Marinoan interval. Note that, while the lowermost Nantuo sample (Pi & Jiang et al. 2016) may be biased by proximity to the Huangling batholith, this is not an issue with the younger sample (Wang et al. 2010). Moreover, many of the Nantuo zircons from this area yield positive $\varepsilon_{Hf}(t)$ values, distinct from those of the batholiths (Cui et al. 2014).

Based on the compiled zircon data, 58% of the pre-rift sediment, 59% of the Baizhu-to-Liantuo sediment and 54% of the Chang'an-to-Nantuo sediment derived from juvenile sources. Much the same peak in frequency, and preponderance of Meso/Neoproterozoic ages, appears in Palaeozoic sandstones, sampling by erosion the record as it stood long after the rifting, without bias towards younger samples (Fig. 6.11). By contrast, no granitoids with ages of 1000–900 Ma have been found in the Hunan-Guangxi sub-basin and, with few exceptions, none in the Nanhua basin as a whole (Wang et al. 2007). Most plutons in the basin date to 825–800 Ma (Li et al. 2003). In comparison with the detrital record, the age profile is skewed towards the later Tonian and, in comparison with the total area of the basin, extant plutons represent only a small fraction of Neoproterozoic magmatism. Apparently, plutons older than 840 Ma were intruded higher up in the crust.

The thickness of the sediments and dominantly turbiditic style of sedimentation down to 665 Ma show that the basin was deep. Since all but the most proximal parts of the basin were under water and all identifiable sources of sediment apart from rock thrust up during the Jiangnan Orogen were

igneous, nearly all weathering (*s.l.*) must have been subaqueous. Weathering chiefly consisted of the dissolution of plagioclase in pore waters that, insofar as they derived from ocean water, were alkaline and, by virtue of hyperextension, hot. High pH and temperature promoted silicate dissolution. In addition, neoformation of K-feldspar in the upper Chang'an Formation was the consequence of slower rates of sedimentation, which allowed more K to leach from K-feldspar; supersaturation of the mineral increased as decreasing permeability prevented equilibration with open water. Possibly the Datangpo Formation did not reach the high CIAs of the Chang'an because its sediments were generally finer and porosity lower.

The start of the Ediacaran marks the end of large-scale rifting. Sedimentation rates during the Ediacaran were lower than at any time in the Cryogenian, partly because of the reduction in tectonism and partly because little land was above water. To what extent weathering was now subaerial in these circumstances is unclear. On the platform of the Yangtze Gorges area the dominant clay mineral of the lower Doushantuo was saponite, forming subaqueously at pH > 9 (Bristow et al. 2009).

8.11. Conclusions

Most of the source rocks in the northern Guangxi region of the Nanhua Rift Basin consisted of peraluminous granite and granodiorite. They included granitoids crystallising in the period 1120–720 Ma and subsequently unroofed, plus material from Palaeoproterozoic and Archaean basement. Input from mafic rock appears to have been minimal. An abrupt shift in source age took place around 780 Ma. Another such shift, along with a change in source composition, took place c. 685 Ma at the start of the Fulu Formation, and another, from granodiorite to alkali feldspar granite, around 635 Ma. Although transport distances could be considerable and sediments repeatedly reworked along their journey, weathering was essentially first-cycle. Throughout the Cryogenian, sediments were often fine-grained, even – as in the upper Fulu, much of the Datangpo and parts of the Nantuo Formation – calcareous. Chemical alteration was variable, from slight to strong; most of it took place after deposition. Stronger weathering during the Datangpo may be attributed to sedimentation rates three to four times lower than during the early and late Cryogenian.

Snowball Earth posits a catastrophic fall in atmospheric pCO_2 in the approach to glaciation, whereupon isolation from the atmosphere and extreme cold all but halted chemical weathering. Evidence of this is lacking. Sedimentation across the transition from the Gongdong to the Chang'an Formation was continuous, powered by rifting rather than glacial erosion, and CIA values, on average, increased. Conversely, as the region emerged from the hypothesised glaciation, during the

transition from the Fulu to the Datangpo Formation, weathering did not increase. It declined in the transition from the Datangpo to the 'glaciogenic' Nantuo Formation, briefly returning to Datangpo levels in the middle of the Nantuo. Levels seem to have been moderately high at the beginning of the Ediacaran.

Consistent patterns in trace and major element variation enable correlation with other datasets. In total the data constitute the most comprehensive and high-resolution sampling of a region through the Cryogenian period ever undertaken. One outcome is that sediments characteristic of the uppermost Nantuo Formation, where the cap carbonate is absent, properly correlate with the lowermost Doushantuo. Diamictite, *sensu lato*, was being deposited in one place at the same time as carbonate in another. As earlier, climate does not appear to have been a major control on lithological and sedimentological change.

The trace element record is punctuated by spikes, notably in abundance of metals (including redox-sensitive metals) and volatiles (including S). The spikes represent episodes of heightened hydrothermal input from deep extensional faults, typically at or near formation boundaries. Some are negative (e.g. Na, Ti, Th). The biggest, at the base of the Fulu, coincides with a surge in Fe. No spikes occur at the start of the Cryogenian for the same reason that the Tonian/Cryogenian boundary is conformable. Rifting had been proceeding apace for some time, and the tectonic shift that caused a slight coarsening of sediment at that juncture was relatively minor. The cap dolomite at the start of the Doushantuo Formation reflects a further episode of hydrothermal enrichment, not least in Mg.

The organic carbon record also does not support panglaciation. Inferred or actual TOC was no lower in the Sturtian-age Chang'an and Fulu Formations than in the Gongdong and comparatively high in the Nantuo Formation. Had surface temperatures been tens of degrees below zero, organic production would be expected to have shut down. Nutrients introduced by hydrothermal fluids, as in the ^{12}C-enriched rhodochrosite and black shales of the lowermost Datangpo, stimulated production.

A finding that the glaciation hypothesis fails in one region naturally prompts a review of successions elsewhere. Cessation of chemical weathering in the Sturtian and Marinoan intervals, or a marked decline in chemical weathering immediately before these intervals, is no more evident in other parts of the world than in China, or indeed at other times in the Proterozoic. The Huronian Supergroup – presenting the classic evidence for snowball conditions in the Palaeoproterozoic – has four things in common with the South China succession: large-scale sedimentation was going

on anyway, the sedimentation was rift-related, CIAs were well above those of the inferred source rocks, and the CIAs of units interpreted as glaciogenic were not materially lower than those of non-glaciogenic units. The fundamental control on weathering intensity was tectonics, not climate.

References

Ader, M. et al., 2009. A multilayered water column in the Ediacaran Yangtze platform? Insights from carbonate and organic matter paired $\delta^{13}C$. *Earth Planet. Sci. Lett.* 288, 213–227.

Bahlburg, H., Dobrzinski, N., 2011. A review of the Chemical Index of Alteration (CIA) and its application to the study of Neoproterozoic glacial deposits and climate transitions. In: E. Arnaud, G.P. Halverson, G. Shields-Zhou (eds), *The Geological Record of Neoproterozoic Glaciations*, Geol. Soc. Lond. Mem. 36, 81–92.

Breitkopf, J.H., 1988. Iron formations related to mafic volcanism and ensialic rifting in the southern margin zone of the Damara Orogen, Namibia. *Precambrian Res*. 38, 111–130.

Bristow, T.F. et al., 2009. Mineralogical constraints on the paleoenvironments of the Ediacaran Doushantuo Formation. *Proc. Nat. Acad. Sci. USA* 106, 13190–13195.

Chen, Z. et al., 2006. Constraining the role of the Qinling orogen in the assembly and break-up of Rodinia: Tectonic implications for Neoproterozoic granite occurrences. *J. Asian Earth Sci.* 28, 99–115.

Condie, K.C. 1993. Chemical composition and evolution of the upper continental crust: contrasting results from surface samples and shales. *Chem. Geol*. 104, 1–37.

Cox, R., Lowe, D.R., Cullers, R.L., 1995. The influence of sediment recycling and basement composition on evolution of mudrock chemistry in the southwestern United States. *Geochim. Cosmochim. Acta* 59, 2919–2940.

Cui, Z., Zhu, W.B., Ge, R.F., 2014. Provenance and crustal evolution of the Northern Yangtze Block revealed by detrital zircons from Neoproterozoic–Early Paleozoic sedimentary rocks in the Yangtze Gorges Area, South China. *J. Geol*. 122, 217–235.

Dingle, R., Marenssi, S.A., Lavelle, M., 1998. High latitude Eocene climatic deterioration: evidence from the northern Antarctic Peninsula. *J. S. Am. Earth Sci*. 11, 571–579.

Dobrzinski, N., Bahlburg, H. 2007. Sedimentology and environmental significance of the Cryogenian successions of the Yangtze platform, South China block. *Palaeogeog., Palaeocl*. 254, 100–122.

Fabre, S., Berger, G., Nédélec, A., 2011. Modeling of continental weathering under high-CO_2 atmospheres during Precambrian times. *Geochem. Geophys. Geosyst*. 12, Q10001.

Fedo, C.M., Nesbitt, H.W., Young, G.M., 1995. Unraveling the effects of potassium metasomatism in sedimentary rocks and paleosols, with implications for paleoweathering conditions and provenance. *Geology* 93, 921–924.

Feng, F. et al., 2016. Geochemistry of Altungol cap dolostones from the Tarim Basin, NW China. *Arab. J. Geosci.* 9, 715.

Feng, L.J. et al., 2004. New evidence of deposition under cold climate for the Xieshuihe Formation of the Nanhua System in northwestern Hunan, China. *Chin. Sci. Bull.* 49, 1420–1427.

Feng, L.J., Chu, X.L., Huang, J., Zhang, Q.R., Chang, H.J., 2010. Reconstruction of paleo-redox conditions and early sulfur cycling during deposition of the Cryogenian Datangpo Formation in South China. *Gondwana Res*. 18, 632–637.

Feulner, G., Hallmann, C., Kienert, H., 2015. Snowball cooling after algal rise. *Nature Geosci*. 8, 659–662.

Freitas, B.T., Warren, L.V., Boggiani, P.C., De Almeida, R.P., Piacentini, T., 2011. Tectono-sedimentary evolution of the Neoproterozoic BIF-bearing Jacadigo Group, SW-Brazil. *Sediment. Geol.* 238, 48–70.

Gaschnig, R.M. et al., 2014. Onset of oxidative weathering of continents recorded in the geochemistry of ancient glacial diamictites. *Earth Planet. Sci. Lett.* 408, 87–99.

Gibson, S.A., 2002. Major element heterogeneity in Archean to Recent mantle plume starting-heads. *Earth Planet. Sci. Lett.* 195, 59–74.

Guo, Q. et al., 2007. Carbon isotopic evolution of the terminal Neoproterozoic and early Cambrian: Evidence from the Yangtze Platform, South China. *Palaeogeog., Palaeocl*. 254, 140–157.

Heiri, O., Lotter, A.F., Lemcke, G., 2001. Loss-on-ignition as a method for estimating organic and carbonate content in sediments: reproducibility and comparability of results. *J. Paleolimn*. 25, 101–110.

Hofmann, M. et al., 2011. The India and South China cratons at the margin of Rodinia – Synchronous Neoproterozoic magmatism revealed by LA-ICP-MS zircon analyses. *Lithos* 123, 176–187.

Huang, K.J. et al., 2016. Episode of intense chemical weathering during the termination of the 635 Ma Marinoan glaciation. *Proc. Nat. Acad. Sci. USA* 113, 14904–14909.

Huang, J., Chu, X., Jiang, G., Feng, L., Chang, H., 2011. Hydrothermal origin of elevated iron, manganese and redox-sensitive trace elements in the c. 635 Ma Doushantuo cap carbonate. *J. Geol. Soc. Lond.* 168, 805–811.

Huang, J. et al., 2014. Multiple climate cooling prior to Sturtian glaciations: Evidence from chemical index of alteration of sediments in South China. *Sci. Reports*. 4, 6868, DOI: 10.1038/srep06868.

Huang, X. L. et al., 2008. Petrogenesis and tectonic implications of Neoproterozoic, highly fractionated A-type granites from Mianning, South China. *Precambrian Res*. 165, 190–204.

Kunzmann, M., Halverson, G.P., Scott, C., Minarik, W.G., Wing, B.A., 2015. Geochemistry of Neoproterozoic black shales from Svalbard: Implications for oceanic redox conditions spanning Cryogenian glaciations. *Chem. Geol.* 417, 383–393.

Lan, Z., Li, X.H., Zhang, Q., Li, Q.L., 2015. Global synchronous initiation of the 2nd episode of Sturtian glaciation: SIMS zircon U–Pb and O isotope evidence from the Jiangkou Group, South China. *Precambrian Res.* 267, 28–38.

Li, X.H. et al., 2003. Neoproterozoic granitoids in South China: crustal melting above a mantle plume at ca. 825 Ma? *Precambrian Res*. 122, 45–83.

Lin, M. et al., 2016. Geochemistry, petrogenesis and tectonic setting of Neoproterozoic mafic–ultramafic rocks from the western Jiangnan orogen, South China. *Gondwana Res*. 35, 338–356.

Liu, T.B., Maynard, J.B., Alten, J., 2006. Superheavy S isotopes from glacier-associated sediments of the Neoproterozoic of south China: Oceanic anoxia or sulfate limitation? In: S.E. Kesler, H. Ohmoto (eds), *Evolution of Early Earth's Atmosphere, Hydrosphere, and Biosphere—Constraints from Ore Deposits*, Geol. Soc. Am. Mem. 198, pp 205–202.

Liu, X., Goa, S., Diwu, G., Ling, W., 2008. Precambrian crustal growth of Yangtze craton as revealed by detrital zircon studies. *Am. J. Sci.* 308, 421–468.

McKirdy, D.M., Watson, B.L., 1983. Moorowie 1. Total organic carbon; Rock-Eval pyrolysis; organic petrology; interpretation. Amdel report F5638/84. *South Australia. Department of Primary Industries and Resources.* Open file Envelope, 5084 (unpublished).

Meyer, E.E., Quicksall, A.N., Landis, J.D., Link, P.K., Bostick, B.C., 2012. Trace and rare earth elemental investigation of a Sturtian cap carbonate, Pocatello, Idaho: Evidence for ocean redox conditions before and during carbonate deposition. *Precambrian Res.* 192–195, 89–106.

Miall, A.D., 1985. Sedimentation on an early Proterozoic continental margin under glacial influence: the Gowganda Formation (Huronian), Elliot Lake area, Ontario, Canada. *Sedimentology* 32, 763–788.

Murray, P., White, J., 1955. Kinetics of clay dehydration. *Clay Miner.* 2, 255–264.

Nesbitt, H.W., Markovics, G., Price, R.C., 1980. Chemical processes affecting alkalis and alkaline earths during continental weathering. *Geochim. Cosmochim. Acta* 44, 1659–1666.

Nesbitt, H.W., Young, G.M., 1982. Early Proterozoic climates and plate motions inferred from major element chemistry of lutites. *Nature* 299, 715–717.

Nesbitt, H.W., Young, G.M., 1984, Prediction of some weathering trends of plutonic and volcanic rocks based on thermodynamic and kinetic considerations. *Geochim. Cosmochim. Acta* 48, 1523–1534.

Och, L. et al., 2016. Palaeoceanographic controls on spatial redox distribution over the Yangtze Platform during the Ediacaran–Cambrian transition. *Sedimentology* 63, 378–410.

Okada, Y. et al. 2014. New chronological constraints for Cryogenian to Cambrian rocks in the Three Gorges, Weng'an and Chengjiang areas, South China. *Gondwana Res*. 25, 1027–1044.

Panahi, A., Young, G.M., 1997. A geochemical investigation into the provenance of the Neoproterozoic Port Askaig Tillite, Dalradian Supergroup, western Scotland. *Precambrian Res*. 85, 81–96.

Partin, C.A. et al., 2013. Large-scale fluctuations in Precambrian atmospheric and oceanic oxygen levels from the record of U in shales. *Earth Planet. Sci. Lett.* 339–370, 284–293.

Passchier, S., Krissek, L.A., 2008. Oligocene–Miocene Antarctic continental weathering record and paleoclimatic implications, Cape Roberts drilling Project, Ross Sea, Antarctica. *Palaeogeog., Palaeoclim., Palaeoecol*. 260, 30–40.

Peucker-Ehrenbrink, B., Waters, C.A., Kurz, M.D., Hoffman, P.F., 2016. No evidence of extraterrestrial noble metal and helium anomalies at Marinoan glacial termination. *Earth Planet. Sci. Lett.* 437, 76–88.

Pi, D.H., Jiang, S.Y., 2016. U–Pb dating of zircons from tuff layer, sandstone and tillite samples in the uppermost Liantuo Formation and the lowermost Nantuo Formation in Three Gorges area, South China. *Chemie der Erde* 76, 103–109.

Pierrehumbert, R.T., Abbot, D.S., Voigt, A., Koll, D., 2011. Climate of the Neoproterozoic. *Annu. Rev. Earth Planet. Sci*. 39, 417–60.

Rieu, R., Allen, P.A., Plötze, M., Pettke, T., 2007. Climatic cycles during a Neoproterozoic "snowball" glacial epoch. *Geology* 35, 299–302.

Sahoo, S.K. et al., 2016. Oceanic oxygenation events in the anoxic Ediacaran ocean. *Geobiology* 10.1111/gbi.12182.

Sumartojo, J., 1974. A Study of the Mineralogy and Geochemistry of the Tindelpina Shale (Upper Proterozoic), Adelaide Geosyncline, South Australia. PhD thesis, Univ. of Cincinnati, Ohio.

Tang, J., Fu, H., Yu, Z., 1987. Stratigraphy, type and formation conditions of the Late Precambrian banded iron ores in South China. *Geochemistry* 6, 331–341.

Taylor, R.S., McLennan, S.M. 1985. *The Continental Crust: Its Composition and Evolution*, Blackwell, Oxford.

Volkert, R.A. et al., 2010. Geochemistry and origin of Neoproterozoic ironstone deposits in the New Jersey Highlands and implications for the eastern Laurentian rifted margin in the north-central Appalachians, USA. *Geol. Soc. Am. Mem*. 206, 283–306.

Von Eynatten, H., Tolosana-Delgado, R., Karius, V., 2012. Sediment generation in modern glacial settings: Grain-size and source-rock control on sediment composition. *Sediment. Geol.* 280, 80–92.

Wang, J., Li, Z.X., 2003. History of Neoproterozoic rift basins in South China: implications for Rodinia break-up. *Precambrian Res*. 122, 141–158.

Wang, L.J., Griffin, W.L., Ju, J.H., O'Reilly, S.Y., 2010. Precambrian crustal evolution of the Yangtze Block tracked by detrital zircons from Neoproterozoic sedimentary rocks. *Precambrian Res.* 177, 131–144.

Wang, L.J., Griffin, W.L., Yu, J.H., O'Reilly, S.Y., 2013. U–Pb and Lu–Hf isotopes in detrital zircon from Neoproterozoic sedimentary rocks in the northern Yangtze Block: Implications for Precambrian crustal evolution. *Gondwana Res*. 23, 1261–1272.

Wang, Q. et al., 2010. Petrology, geochronology and geochemistry of ca. 780 Ma A-type granites in South China: Petrogenesis and implications for crustal growth during the breakup of the supercontinent Rodinia. *Precambrian Res.* 178, 185–208.

Wang, T.G. et al., 2008. Organic molecular evidence in the Late Neoproterozoic Tillites for a palaeo-oceanic environment during the snowball Earth era in the Yangtze region, southern China. *Precambrian Res*. 162, 318–326.

Wang, W., Chen, F., Hu, R., Chu, Y., Yang, Y.Z., 2012a. Provenance and tectonic setting of Neoproterozoic sedimentary sequences in the South China Block: evidence from detrital zircon ages and Hf–Nd isotopes. *Int. J. Earth Sci. (Geol. Rundsch.)* 101, 1723–1744

Wang, W., Zhou, M.F., Yan, D.P., Li, J.W., 2012b. Depositional age, provenance, and tectonic setting of the Neoproterozoic Sibao Group, southeastern Yangtze Block, South China. *Precambrian Res*. 192–195, 107–124.

Wang, X.C., Li, Z.X., Li, X.H., Li, Q.L., Zhang, Q.R., 2011. Geochemical and Hf–Nd isotope data of Nanhua rift sedimentary and volcaniclastic rocks indicate a Neoproterozoic continental flood basalt provenance. *Lithos* 127, 427–440.

Wang, X.C. et al., 2012. Episodic Precambrian crust growth: Evidence from U–Pb ages and Hf–O isotopes of zircon in the Nanhua Basin, central South China. *Precambrian Res*. 222–223, 386–403.

Wang, X.L. et al., 2007. Detrital zircon geochronology of Precambrian basement sequences in the Jiangnan orogen: Dating the assembly of the Yangtze and Cathaysia Blocks. *Precambrian Res*. 159, 117–131

Watson, J.S., 1996. Fast, simple method of powder pellet preparation for x-ray fluorescence analysis. *X-Ray Spectrometry* 25, 173–175.

Wu, C. et al., 2016. Nanhuan manganese deposits within restricted basins of the southeastern Yangtze Platform, China: Constraints from geological and geochemical evidence. *Ore Geol. Rev.* 75, 76–99.

Wu, R.X. et al., 2006. Reworking of juvenile crust: Element and isotope evidence from Neoproterozoic granodiorite in South China. *Precambrian Res*. 146, 179–212.

Xiao, S. et al., 2012. Integrated chemostratigraphy of the Doushantuo Formation at the northern Xiaofenghe section (Yangtze Gorges, South China) and its implication for Ediacaran stratigraphic correlation and ocean redox models. *Precambrian Res.* 192–195,125–141.

Yang, C., Li, X.H., Wang, X.C., Lan, Z., 2015. Mid-Neoproterozoic angular unconformity in the Yangtze Block revisited: Insights from detrital zircon U–Pb age and Hf–O isotopes. Precambrian Res. 266, 165-178.

Young, G.M., Nesbitt, H.W., 1999. Paleoclimatology and provenance of the glaciogenic Gowganda Formation (Paleoproterozoic), Ontario, Canada: A chemostratigraphic approach. *GSA Bull.* 11, 264–274.

Yu, W. et al. 2016. Genesis of Cryogenian Datangpo manganese deposit: Hydrothermal influence and episodic post-glacial ventilation of Nanhua Basin, South China. *Palaeogeogr. Palaeocl*. 459, 321–337.

Zhang, Q.R. Chu, X.L., Feng, L.J., 2011. Neoproterozoic glacial records in the Yangtze Region, China. In: E. Arnaud, G.P. Halverson, G. Shields-Zhou (eds), *The Geological Record of Neoproterozoic Glaciations*, Geological Society, London, Memoir 36, 357–366.

Zhang, S., Jiang, G.Q., Han, Y.G., 2008. The age of the Nantuo Formation and Nantuo glaciation in South China. *Terra Nova* 20, 289–294.

Zhang, S.B., Zheng, Y.F., 2013. Formation and evolution of Precambrian continental lithosphere in South China. *Gondwana Res*. 23, 1241–1260.

Zhao, X.F., Zhou, M.F., Li, J.W., Wu, F.W., 2008. Association of Neoproterozoic A- and I-type granites in South China: Implications for generation of A-type granites in a subduction-related environment. *Chem. Geol*. 257, 1–15.

Zhou, J., Li, S.H., Ge, W., Li, Z.X., 2007. Age and origin of middle Neoproterozoic mafic magmatism in southern Yangtze Block and relevance to the break-up of Rodinia. *Gondwana Res.* 12, 184–197.

CHAPTER NINE

Sedimentary systems under high atmospheric CO_2

Abstract

Carbon dioxide is Earth's principal greenhouse gas. Lower solar radiation combined with planetary degassing entails that CO_2 was much more abundant in the Precambrian, with consequently faster rates of seafloor spreading. Other consequences in the marine realm include the dissolution of silicates, higher pH, a nearshore gradient in pH and higher calcium carbonate supersaturation. Over time the degree of supersaturation declined. Carbonate-secreting animals, overriding the kinetic and chemical inhibitors, arrived at a time when spontaneous precipitation was waning; they increased the efficiency of carbonate production, accelerated the decline in pCO_2 and lowered seawater alkalinity.

Dolomite, the most common carbonate mineral in the Precambrian, was promoted by high Mg and CO_3^{2-} concentrations, high seawater temperatures and subsurface anoxia. The ocean crust was not, as now, a sink of Mg. Anoxia promoted the activity of Mg^{2+} through the microbial reduction of sulphate. Most sulphate reduction took place in, rather than under, the water column; dolomite precipitation likewise.

The history of CO_2 is linked via photosynthesis to the history of atmospheric O_2. Anoxia in the Proterozoic ocean does not entail anoxia above the ocean because the increase in density with depth, due to increasing concentrations of dissolved Fe, inhibited downward circulation of the oxygen-producing surface layer. Alongside trace fossils of microbes plausibly interpreted as cyanobacteria, geochemical proxies indicate substantial quantities of free oxygen from as early as 3.7 Ga. Recently discovered micrometeorites suggest that the Late Archaean atmosphere had as much oxygen as the modern. Mass-independent fractionation of sulphur does not necessitate atmospheric anoxia because rain-out from sulphate-rich ash clouds could have delivered the signal intact. Several of the element and isotopic proxies for atmospheric oxygen (U, Mo, $\delta^{53}Cr$) assume that substrate pH was low, which is probably not correct.

Finally, there is the question of whether the Neoproterozoic was punctuated by long periods of pole-to-equator glaciation. The evidence of high pCO_2 in the Precambrian, combined with the

negative feedback which limits consumption of CO_2 by silicate weathering – in the sea (Coogan & Dosso 2015) as well as on land – renders the snowball state improbable. If weathering was high in the mid Neoproterozoic, so was the rate of CO_2 production. In specific contexts rift-related diastrophism adequately accounts for the sedimentation, leaving glaciation causally redundant. In South China, sedimentation continued unabated across the Tonian-Cryogenian boundary, as did silicate weathering, while sea-level was higher during the Marinoan episode than at any previous time in the Cryogenian. Globally, carbon-isotope excursions, strontium-isotope spikes, mass-flow deposits and iron formation are closely linked to the zircon oxygen-isotope signal, which fluctuated as terrestrial lithosphere thinned or thickened. Sedimentary systems during the Sturtian and Marinoan remained fluid and, as indicated by the prevalence of turbidites, relative sea-level rose.

9.1. Carbon dioxide, marine carbon isotope ratios and carbonate mineral formation

Carbonates in the Precambrian formed where seas were warm and shallow. Cyanobacteria flourished there because nutrients from continental erosion were abundant and levels of dissolved carbon high. Via rivers and flood plains silicate weathering delivered bicarbonate, Na, K, Ca and Mg, while subaqueous dissolution of detrital silicate converted bicarbonate to carbonate and released more ions (§2.4.1, Figs. 9.2, 9.3).

Thin sections of samples from the Jiuliqiao Formation suggest that the relationship between carbonate and siliciclastic deposition was intimate. Tiny grains of a creamy greenish mineral speckle the calcite. Under SEM they turn out to be feldspar crystals half altered to quartz (Fig. 9.1). Feldspar was losing its cations. Driven by high pH, silicate dissolution was taking place under the sea as well as on land. At the same time, calcium carbonate included extraordinarily high amounts of dissolved Si, K, and even Al. Calcium carbonate formed in amongst the silicate crystals and precipitated as spheres of metastable vaterite, a phase typical of pH > 9. As the silicate dissolved, amorphous calcium carbonate also formed within the crystals.

In addition, the carbonate minerals of the Jiuliqiao Formation and overlying Sidingshan Formation were rich in Mg. Geochemistry's 'dolomite problem' is essentially twofold: how does sedimentary dolomite form when under simulated natural conditions it is so difficult to synthesise, and why was dolomite much more common in the Proterozoic than in the Phanerozoic? Although not entirely free of controversy, the first aspect is largely solved. Dolomite formation is inhibited by ionic complexing of Mg^{2+} with SO_4^{2-} and CO_3^{2-} and promoted by the microbes that overcome it, whether by sulphate-reduction or the electronegative attraction exerted by cell walls and exopolymeric substances. The second aspect, less well understood, has to do with the lower-water-column anoxia

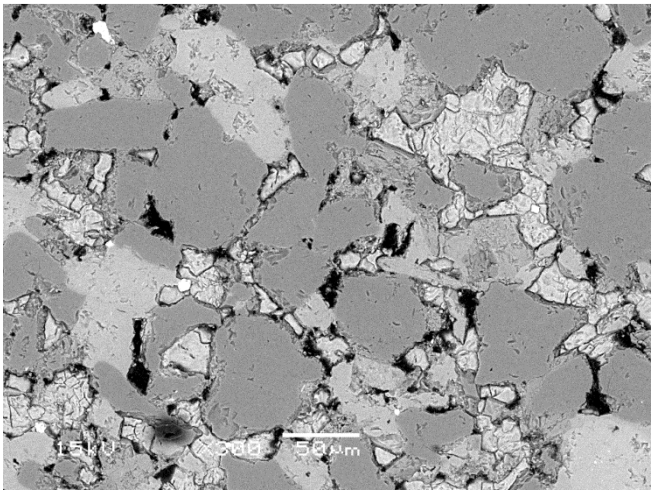

Figure 9.1. Partially altered K-feldspar near the base of the Jiuliqiao Formation. Dark grey patches: quartz. Medium grey: feldspar. Light grey: compacted calcite grains. Black: organic carbon.

that characterised Proterozoic seas. Where there was sufficient sulphate, as there was close to the shore, SRM were the principal means by which suspended organic matter was recycled: voracious anaerobic microbes of the ocean's digestive tract.

The mineralogies of the two formations differ markedly. As preserved, carbonate in the Jiuliqiao Formation consists of high and very-high magnesian calcite, the former granular, the latter an altered amorphous phase. Being metastable, VHMC is not expected in rocks of this age. Virtually none of the carbonate has a Mg/Ca ratio greater than 0.40. By contrast, the Sidingshan Formation consists entirely of unimodal, substoichiometric, largely microcrystalline dolomite, and its Mg/Ca is not less than 0.40. Phases of intermediate Mg/Ca such as might have supported a diagenetic path to dolomite are lacking.

The dolomite precipitated direct from seawater. The stratigraphic transition from calcite (originally vaterite) to dolomite was sharp, triggered by a switch in ecology as the water shallowed and essential nutrients such as Fe became scarce. The oxygenated layer was squeezed. Although organic productivity cannot be gauged, the high $\Delta^{34}S$ and fall in carbonate-included sulphur are consistent with high sulphate consumption in the water column and raised Mg^{2+} activity, as anaerobic microbes remineralised organic carbon.

Dating to the early Tonian, North China's Majiatun Formation is appreciably older than the Jiuliqiao. It too is worth detailed study because it preserves an exceptionally systematic example of a negative carbon-isotope excursion. Because of the water's high temperature the original mineralogy at all depths was aragonite (Morse et al. 1997), supplemented by extant rhombs of VHMC. As in other regions where $\delta^{13}C$ went negative – in the Cryogenian and Ediacaran as well as the Tonian – DIC became less fractionated as the environment deepened.

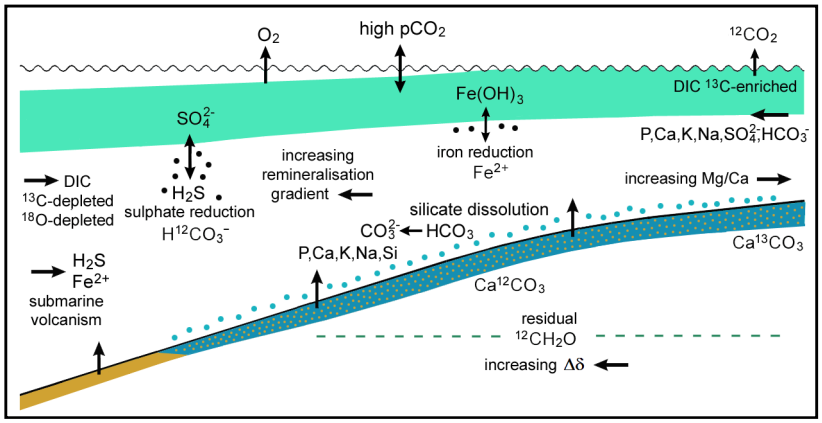

Figure 9.3. Vertical and lateral gradients in the Precambrian ocean. Nearshore waters were supersaturated in respect of CO_2. Evasion of CO_2 in these environments enriched seawater in ^{13}C. Continental weathering, intensified by high pCO_2 and runoff, supplied an abundance of nutrients, which stimulated organic production. Subaqueous silicate dissolution also supplied nutrients. Offshore, sulphate was recycled through microbial and inorganic oxidation of H_2S at the redox boundary. Microbial sulphate reduction oxidised organic carbon (black dots) to HCO_3^- rather than CO_2 while silicate dissolution converted HCO_3^- to CO_3^{2-}, thereby increasing carbonate alkalinity. Residual organic carbon in deeper environments was isotopically lighter because cyanobacteria compensated for low dissolved CO_2 by synthesising it partly from HCO_3^-. Incoming water from the open ocean was also isotopically depleted. $CaCO_3$ (blue dots) precipitated from DIC close to the seafloor. Along with moderate rates of organic carbon burial, high rates of organic production imply a well oxygenated atmosphere.

Shifts in $\delta^{13}C$ that would be considered extraordinary in the Phanerozoic were common in the Neoproterozoic. After the Majiatun event, the first major negative excursions occurred around 820–805 Ma, when South Australia, Ethiopia, northwest Canada, Svalbard and Scotland recorded falls down to -4‰ or more. Further negative excursions cluster at the end of the Tonian. The incorporating sedimentology (§3.7) shows that they were accompanied by rises in sea-level. Major shifts in $\delta^{13}C$, positive and negative, were associated generally with changes in sea-level (§4.2). Even the Sidingshan Formation illustrates the relationship. Forming predominantly in a shallow, probably evaporitic environment, its carbonates record $\delta^{13}C$ values mostly in the range 3–4‰. A 3‰ fall over 15 m in the upper part coincides with sedimentological evidence of rapid deepening.

Phototrophs' preference for ^{12}C created a vertical gradient. Seawater was isotopically heaviest at the surface, the zone of organic production; as organic matter sank, it was processed back into the water, with most remineralisation taking place above the sediment. The extent of the gradient depended on mixing. In shallow environments DIC at the seafloor would have been well-mixed; as environments deepened, DIC at the seafloor became lighter than at the surface (thereby resulting also in a lateral gradient). In addition, the CO_2 component of total dissolved carbon at the surface decreased seaward as agitation by waves decreased. Cyanobacteria, forced by starvation into producing CO_2 of their own, produced it from bicarbonate, and since bicarbonate is isotopically heavier than CO_2, the organisms extracted less ^{12}C, thereby lowering $\delta^{13}C_{DIC}$. However, the total

concentration of dissolved carbon was many times greater than today. Therefore, to account for the (inferred) activation of their carbon-concentrating mechanisms, pH offshore had to have been significantly higher than today, probably higher than 9 (§4.7).

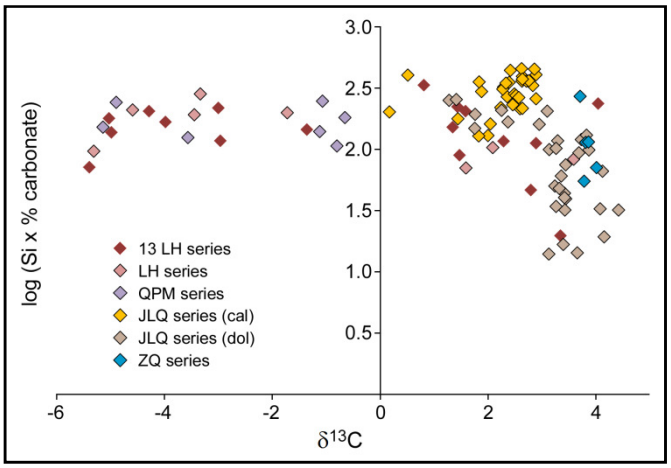

Figure 9.2. Within-carbonate silicon as a function of $\delta^{13}C$ (proxy for depth) in the Shisanlitai, Majiatun, Jiuliqiao, Sidingshan and Zhaowei Formations. Concentrations are lowest in the CO_2-saturated environments close to shore, rising steeply as the water deepens.

Meanwhile, seawater became more depleted from the coast oceanward as production declined and shelf sediments gave way to carbonate-rich crust. Nearshore DIC was enriched because of evaporation; open-ocean DIC was close to the unfractionated mantle value. In short, Neoproterozoic seas were not isotopically homogeneous, and the $\delta^{13}C$ of shallow-water carbonates did not reflect the isotopic composition of the ocean beyond those seas.

Finally, in the alkaline bottom waters characteristic of the Neoproterozoic, calcium carbonate formed as cations bonded with ionic carbonate rather than bicarbonate. Since CO_3^{2-} is 16‰ lighter than HCO_3^-, the $\delta^{18}O$ of the mineral was significantly lighter than in the modern world, regardless of temperature and possibly different values for the seawater with which the carbonate was equilibrated.

9.2. Great oxygenation events

If all this represents a major challenge to the way we think about the carbon cycle in the Neoproterozoic, there are also implications for the rest of the Precambrian, concerning the history of oxygen as well as the carbon cycle. Generated by the photosynthetic oxidation of water, oxygen enters the atmosphere to the extent not consumed by ferrous iron, sulphide and organic carbon. In anoxic conditions consumption by organic carbon is indirect: remineralisation is anaerobic, involving nitrate, iron oxide and sulphate (§4.7), which are themselves products of oxidation. Directly or indirectly, remineralisation of organic carbon implies – though does not necessitate – free oxygen. The oldest isotopic evidence of microbial sulphate reduction goes back to 3.5 Ga (Ueno et al. 2008); trace fossils associated with the process go back to 3.4 Ga (Wacey et al. 2011a).

There is wide acceptance that pCO_2 must have been high in the Precambrian, if only because CO_2 is the most likely gas to have kept Earth warm when less heat came from the Sun. Today, with solar radiation 7% greater than in the Neoproterozoic, there is concern about global warming as concentrations rise past 400 ppm. In the Archaean, the ocean would have been frozen at present concentrations. Estimates of how much CO_2 was needed to sustain a warm climate vary, and usually include a contribution from methane, a more effective greenhouse gas, though less effective than formerly supposed (Byrne & Goldblatt 2014). Archaea generate methane as they decompose organic matter. Aerobic bacteria and anaerobic archaea – the latter via sulphate reduction – convert the gas into CO_2 and HCO_3^-. The microbial world, it might be said, is biased against methane. Since methane breaks down in an oxic atmosphere, estimates of CO_2 levels include an assumption about the amount of free O_2.

The atmosphere is thought to have become oxygenated in two steps, one in the early Palaeoproterozoic, the other in the Ediacaran. Initially, the atmosphere was devoid of free oxygen. Regions of Archaean ocean where concentrations of oxygen do not appear to have been minimal are therefore characterised as 'oases', much as regions unaffected by glaciation in the early and late Cryogenian are characterised as oases. Nonetheless, their number is growing (Fralick & Riding 2015).

One line of evidence for oxygenated water is the occurrence of limestone in the Archaean, since anoxic water was rich in Fe^{2+} and would have precipitated $FeCO_3$ rather than $CaCO_3$ (Tice & Lowe 2004, Riding et al. 2014). The reaction of shallow-water basalt with Archaean seawater also produced $CaCO_3$ (Veizer et al. 1989a, Nakamura & Kato 2004). Fe-poor carbonates occur in contexts as early as the Isua Supracrustal Belt (Craddock & Dauphas 2011).

Sedimentary carbonate rocks before 2.8 Ga are rare and appear to cluster around 3.5–3.3 Ga, the age of hydrothermally influenced ferroan dolomites from Australia's Warrawoona Group and South Africa's Onverwacht and Fig Tree Groups (Veizer et al. 1989b). Typically, the units are thinner than 20 m and represent quiet interludes between episodes of volcanism (Siahi et al. 2016). Perhaps not coincidentally, primary haematite (ferric iron oxide) in jasper rocks also dates to this period (Hoashi et al. 2009). By contrast, Late Archaean, originally aragonite carbonates (Sumner & Grotzinger 2000) are comparatively widespread. Amongst the oldest such deposits of any bulk is the Mosher Carbonate Formation of central Canada, dated to 2.8 Ga (Fralick & Riding 2015). In the Transvaal, iron speciation data indicate oxic conditions during deposition of the 2.65-Ga-old dolomite-rich Lokamonna and Monteville Formations (Zerkle et al. 2012).

The succeeding shales of the Nauga Formation also formed in oxic conditions, the water becoming anoxic as it deepened (Kendall et al. 2010). The same is true in the Proterozoic; hardly any of the datasets analysing iron species attest unmitigated anoxia. Iron, rhenium and molybdenum isotopes and other redox-sensitive elements provide further evidence of an oxygenated surface, some going back to 3.7 Ga (Rosing & Frei 2004, Crowe et al. 2013, Planavsky et al., 2014, Satkoski et al. 2015). Uranium/TOC ratios in shale are not much lower during some intervals of the Precambrian, including the Archaean, than through much of the Phanerozoic and do not corroborate a quantum leap in atmospheric oxygen in the early Proterozoic (*pace* Partin et al. 2013). Low concentrations of U and Mo are consistent with anoxic bottom waters that were alkaline, the respective compounds being relatively soluble in these conditions (UO_2, MoO_4^{2-}). Chromium solubility also increases with pH as well as eH (Saputro et al. 2014): Cr/Ti ratios are low in the interval 1750–750 Ma but before then equal to those in the Phanerozoic (Reinhard et al. 2013). Inferences of low pO_2 from Cr isotope ratios assume pH < 7.5 and are therefore questionable. Low $\delta^{53}Cr$ in shales throughout the Precambrian is consistent with pH > 7.5 (Cole et al. 2016), with the single exception of a late-Tonian unit anomalously rich in organic C, V, Mo and U.

Under an oxic atmosphere, marine sulphate mostly comes from the continental weathering of sulphide minerals, mediated by microbes (Wacey et al. 2011b). Significant volumes of sulphate and the large isotope fractionations characteristic of sulphate reduction are not expected until the 'Great Oxidation Event' (GOE) of the early Proterozoic. The expectation is borne out, but this may have been because through most of the Archaean most continental crust lay under water, so was not exposed to subaerial weathering. Where it was, the only substantial occurrences of sulphate were barite deposits: for example, barite up to 2.4 m thick in the Fig Tree Group (Heinrichs & Reimer 1977, cf. Bao et al. 2007) and lenses of barite up to 10 m thick in evaporitic settings in the Warrawoona Group (Shen et al. 2009). In the latter case, as also in Palaeoarchaean sulphides (Ohmoto & Felder 1987) and Palaeoarchaean barites (Roerdink et al. 2012), microbial sulphate reduction is evidenced by significant $\delta^{34}S$ fractionation between sulphate and pyrite. Barite

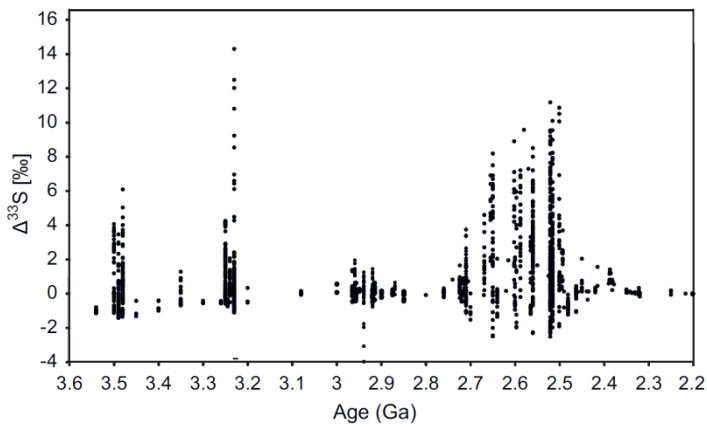

Figure 9.4. Compilation of MIFS data from the Archaean (from Kurzweil et al. 2013). After 2.2 Ga $\Delta^{33}S$ is close to zero.

deposits are relatively common in the period 3.5–3.2 Ga but uncommon through the rest of the Archaean (Huston & Logan 2004). Massive deposits occur as late as 2.7 Ga (Cameron & Hettori 1987), associated with felsic volcanoclastics and cherty sandstones.

The degree to which isotopes of sulphur fractionate, as with any element, usually correlates with mass. Mass-independent fractionation (MIF) is where differences in $\delta^{34}S$ and $\delta^{33}S$, normalised to mass and expressed as $\Delta^{33}S$, are non-zero. Large deviations, mostly positive, are characteristic exclusively of Archaean sediments (Fig. 9.4). The only mechanism known to produce MIFS is ultraviolet photolysis of SO_2, a major constituent of volcanic gas. Ozone – and to a lesser extent oxygen – would have absorbed ultraviolet radiation at wavelengths less than 300 nm, as would a methane-induced organic haze (Farquhar & Wing 2003), thereby preventing photolysis at lower altitudes. In an oxygen-free atmosphere, photolysis could have occurred at all altitudes, with the degree of MIF depending on the length of time volcanic gases were exposed to UV radiation and the ratio of SO_2 to H_2S in these gases (Halevy et al. 2010). The various sulphur phases thereby generated (SO_2, S_8, H_2S) would have entered the ocean unoxidised and maintained their respective fractionations, with aerosol S forming H_2S and SO_4^{2-}, and H_2S forming pyrite. MIFS is thus deemed the strongest evidence for an anoxic atmosphere in the Archaean.

The explanation has its problems, however. These include:

- $\Delta^{33}S$ data through the Archaean are surprisingly spikey, with the highest deviations occurring at the end of the era. Spikes even then are episodic (Williford et al. 2011). Some Archaean intervals record little deviation (e.g. Ohmoto et al. 2006), although a MIFS signal is still detectible (Farquhar et al. 2007).
- Most deviations are positive, a 'puzzling asymmetry' (Claire et al. 2014) which requires the existence of an unknown reservoir of sulphur with negative $\Delta^{33}S$. As per the previous point, the asymmetry is greatest in the late Archaean.

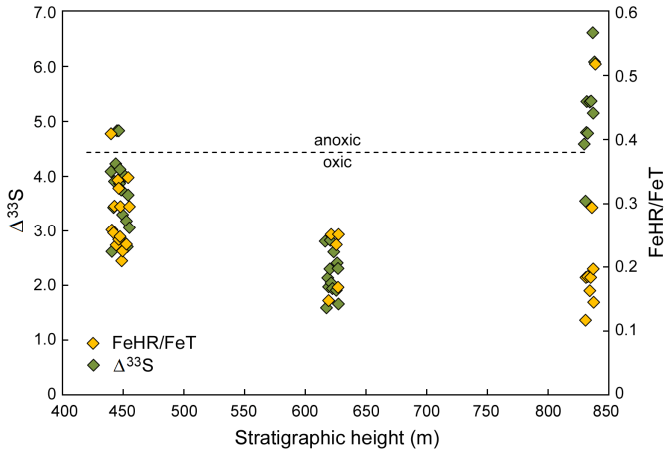

Figure 9.5. The $\Delta^{33}S$ and iron redox signal (dotted line: FeHR/FeT = 0.38) through three intervals in the Nauga Formation, Campbellrand-Malmani platform margin (GKF01 core), South Africa. The water seems to have been fully oxic, notwithstanding the non-zero $\Delta^{33}S$ signal (data from Kendall et al. 2010).

- In the Mount McRae Shale, a unit claimed to capture 'the widespread and possibly permanent activation of the oxidative sulfur cycle for perhaps the first time in Earth's history', $\Delta^{33}S$ varies between -1.5 and +9‰ (close to the Archaean maximum) in the course of just 80 metres, with peaks in $\Delta^{33}S$ coinciding with minima in $\delta^{13}C$ and maxima in Fe (Kaufman et al. 2007). It is difficult to take these swings as a global signal.
- In the same locality high TOC is suggested to indicate 'high rates of primary productivity that released oxidants [oxygen] into the shallow marine environment' at the same time as positive $\Delta^{33}S$, consistent with FeHR/FeT > 0.38 (Reinhard et al. 2009), is thought to indicate an anoxic environment. Lower in the section the FeHR/FeT values fall comfortably below the 0.38 oxic/anoxic threshold. All samples show a MIFS signal.
- In the only other study that includes FeHR/FeT data, one core shows FeHR/FeT values below the 0.38 oxic/anoxic threshold, yet non-zero $\Delta^{33}S$ (Fig. 9.5, Kendall et al. 2009). As with the Mount McRae Shale, if MIFS is linked to redox, the signals are mutually contradictory.
- Neoarchaean Fe-rich micrometeorites were oxidised while passing through the upper atmosphere, consistent with oxygen concentrations similar to today's (Tomkins et al. 2016). An oxic upper atmosphere would have shielded the lower atmosphere from UV radiation and thereby reduced the routine incidence of SO_2 photolysis. The finding also bears on the argument that it was photolysis rather than free oxygen that depleted the surface ocean of Fe (Braterman et al. 1983).

Barites are among the sediments exhibiting MIFS (Farquhar et al. 2000, Claire et al. 2014). These precipitated in hydrothermal settings, as reducing fluids rich in Ba mixed with seawater rich in sulphate. Barite solubility decreases with pressure and temperature (Hanor 2000). Sulphur dioxide, a highly soluble gas, reacts with water to produce H_2SO_3 and H_2SO_4, so part of the sulphate probably had the same origin as the Ba, namely SO_2-bearing fault fluids (Nijman et al. 1999). On the other hand, low $\Delta^{33}S$ values in hydrothermal veins do not support an association of MIFS with mantle outgassing (Grosch & McLoughlin 2013). Despite the problems outlined above, it seems inescapable that most of the sulphate in the pre-Neoarchaean ocean originated via photolysis (scenario 1 in Bao et al. 2007).

Nonetheless, it does not follow that the atmosphere was anoxic. Large injections of volcanic SO_2 and H_2O vapour into the stratosphere can reduce ozone levels, thereby increase photolytic reactions and, via the adsorption of SO_2 onto falling ash particles, result in large MIFS preserved as sulphate at the present Earth's surface (Ohmoto et al. 2006, Whitehill et al. 2015). Widespread MIFS could

simply reflect a greater intensity of volcanism than now. Non-volcanic sediments in the Archaean (including those analysed for S isotopes) are far and few between; most of the record consists of thick accumulations of igneous material produced by 'submarine eruptions, with greenstone belts characterized by submarine basalt–komatiite successions and dominantly submarine island-arc-like volcanic complexes' (Kump & Barley 2007). Submergence would have suppressed the mobilisation of continental sulphide, so that nearly all sulphur showed MIFS. After 2.75 Ga, also at 3.47–3.24 Ga, the record includes a significant non-MIFS component, as seen in the loss of correlation between $\Delta^{33}S$ and $\delta^{34}S$ and many $\Delta^{33}S$ values close to zero (Reinhard et al. 2009, Kurzweil et al. 2013, Grosch & McLoughlin 2013, Galic 2015). The increase in MIFS in the Neoarchaean is explicable as a consequence of cratons colliding and emerging (Flament et al. 2008, Gaillard et al. 2011), leading to subduction and explosive, dominantly subaerial continental arc volcanism (Condie & Kröner 2008). The precipitous drop after the Archaean-Proterozoic boundary marks a rapid cooling of the upper mantle (Condie & O'Neill 2010), craton stabilisation and a permanent drop in the intensity of explosive volcanism. The chert record also reflects rapid cooling (Knauth 2005).

On the strength of marine carbon isotope ratios the first GOE was previously dated to 2.31–2.06 Ga. The discovery of MIFS forced the event to be detached from the evidence that should have explained it and pushed it back to 2.45–2.32 Ga. Carbon isotopes fractionate and oxygen is liberated in excess of that required for remineralisation to the extent that organic carbon is removed from the exosphere. At the start of the Archaean there was presumably no fractionation, because any previous life would have been obliterated by the Late Heavy Bombardment (Sleep et al. 1989). Nonetheless, as early as 3.8–3.7 Ga, Fe-poor carbonates in the Isua Supracrustal Belt were 5‰ heavier than mantle carbon ($\delta^{13}C$ = -1‰, Craddock & Dauphas 2011) and by 3.5–3.4 Ga epicratonic marine carbonates around 8‰ heavier ($\delta^{13}C$ = 1.5‰, Veizer et al. 1989b). If one assumes global isotopic homogeneity and organic fractionation ($\Delta\delta$) of around 33‰ (Eigenbrode & Freeman 2006), carbonate values of +1‰ imply a burial fraction (*f*) of 0.25, higher than that inferred for the present day. Carbonate production, mostly in altered ocean crust, was many times greater than today (Shibuya et al. 2012). At steady state, organic productivity would have been greater by the same factor.

Organic carbon would have included the remains of thermophilic archaea, notably methanogens, as well as aerobic phototrophs and methanotrophs. While burial of all such organisms would have fractionated the marine carbon reservoir, only burial of cyanobacteria would have liberated oxygen. Whether cyanobacteria mostly flourished on and around the submerged cratons rather than in the

open ocean is unknown. Given that epicratonic environments were often steaming hot, production may have been more evenly distributed than in the modern world. The fallout of ash plumes rich in Fe and P could have stimulated production far from cratonic nutrient sources (Frogner et al. 2001, Mills et al. 2004).

Another unknown is when oxygenic photosynthesis 'evolved' (as with SRM, it was not a simple matter). The biomarker evidence for the existence of cyanobacteria at 2.7 Ga has been retracted, and possibly no such evidence exists, because almost all Archaean rocks lie above the maturity window in which it could have survived (French et al. 2015), the lithosphere having been hotter in the Archaean. Nonetheless, fossils of siphonous algae – oxygenic, aerobic organisms – have been recovered from rocks dated to 2.8–2.7 Ma (Kaźmierczak et al. 2016), and biomarker remains are not crucial. Isotopic evidence suggests that sulphate reducers, sulphide oxidisers, iron reducers, nitrogen fixers (excluding cyanobacteria themselves, whose ability to fix nitrogen is ancient (Zehr et al. 2003)), denitrifiers, manganese oxidisers (Crowe et al. 2013), methanogens and methanotrophs were all in existence before the late Archaean, and on the strength of U abundances and δ^{56}Fe values, the existence of oxygenic phototrophs has been proposed as early as 3.2 Ga (Satkoski et al. 2015). Where there is evidence of free O_2, it is difficult not to infer the presence of cyanobacteria. Fossils, such as the microbial mats in tidal-flat facies of the 3.2-Ga Moodies Group (Noffke et al. 2006) or the 3.4-Ga Buck Reef Chert (Tice & Lowe 2004), or the distinctively cyanobacterial tufted mats and coniform stromatolites of the 2.7-Ga Tumbiana Formation (Flannery & Walter 2012, Coffey et al. 2013), furnish, alongside carbon isotope fractionations typical of photosynthesis, complementary evidence. The sea was redox-stratified, and although the pO_2 of the surface layer was low, this may have been because in hot, saline water oxygen was virtually insoluble (Knauth 2005). The same point applies to other indicators of low pO_2, such as detrital uraninite. High temperatures do not necessarily inhibit cyanobacterial growth. Some organisms are thermophilic (42–75° C), just as some have been found to thrive under high pCO_2 (50,000 ppm, Ono & Cuello 2007). Several studies show strong increases in photosynthesis and nitrogen fixation under high pCO_2 (Kranz et al. 2009).

Temperature may be part of the reason why the ocean was redox-stratified. Negative correlations with δ^{13}C suggest that seawater temperature (reflected in δ^{18}O), density (related to $[Fe^{2+}]$) and degree of anoxia (ditto) all increased with depth (Figs. 4.12, 4.11). In contrast to the modern ocean, the subsurface was warmer rather than colder. In addition, high atmospheric pCO_2 and pH_2O, combined with lower solar luminosity, reduced ultraviolet radiation at the surface and thereby

reduced the extent to which oxygen was consumed by photochemical reactions (Gieskes et al. 2015). Since production did not necessarily decline, more oxygen escaped into the atmosphere.

Once cyanobacteria were in existence, they must have proliferated, for there was nothing to hold them back: it is the purpose of microbes to proliferate (Fenchel 2002). 'Because the ubiquitous H_2O molecule is the electron donor for oxygenic photosynthesis, it is reasonable to expect that the initiation of oxygenic photosynthesis would [have] "supercharge[d]" carbon fluxes' (Lyons et al. 2014). Moreover, their trace metal preferences suggest that oxic and sulphidic environments were not mutually exclusive (Saito et al. 2003): their world included both. Indeed, in the presence of sulphide, some species have the ability to switch to anoxygenic photosynthesis (Johnston et al. 2009). Iron, like manganese an important constituent of the photosynthetic apparatus, was abundant. While it might have scavenged free oxygen, it would not have suppressed its production. Phosphorus was generally not a limiting nutrient, since carbonate fluorapatite, the main phosphate mineral in ocean sediments, was more soluble in alkaline water (Jahnke 1984). Iron oxide is a phosphorus sink, but little oxide was deposited except, secondarily, in BIFs (Planavsky et al. 2010); normally ferric iron was reduced back to ferrous iron (cf. Satkoski et al. 2015). Adapted to a wide range of salinity (Knauth 2005), oxygen concentrations, alkalinity (Sorokin et al. 2014), light wavelengths (Stomp et al. 2007), temperature and nutrient availability (Mackey et al. 2008), cyanobacteria may have dominated primary production from very early on. Lyons et al. (2014) reached the same conclusion. After assessing the various anoxygenic possibilities (photosynthesis via oxidation of Fe^{2+}, H_2 and H_2S), they found that the most likely source of the carbon in Archaean organic-rich shales was oxygenic photosynthesis; this, despite accepting that MIFS indicated an anoxic atmosphere.

The oldest organic-rich deposits (at 4–10%) go back to 3.2 Ga (Rasmussen 2005, Buick 2008). As measured by percentage TOC, the burial flux in the Neoarchaean was generally as high as in the Palaeoproterozoic and about half that in the Phanerozoic (Fig. 9.7) – before allowing for greater loss of OC due to metamorphism (Watanabe et al. 1997) and faster rates of sedimentation. But spikes punctuating long periods of low TOC make generalisation hazardous. The amount of organic carbon thought to have been buried by the Lomagundi-Jatuli Event of < 2.30–2.03 Ga, the most positive of all carbon-isotope excursions, was sufficient to supply the present inventories of SO_4^{2-} and O_2 and more (Hayes & Waldbauer 2006), and the flux was higher in the period 2.1–1.8 Ga (Martin et al. 2015) than during the MIFS-identified GOE. That modern levels of O_2 were not sustained in the subsequent billion years (Partin et al. 2013, Cole et al. 2016) when average

carbonate $\delta^{13}C$ was still around 0‰ encapsulates the failure of current theory to turn the facts into a coherent story.

Subsequent facts do not mitigate the inconsistencies. Some 200 Ma before the second 'Great Oxygenation Event', evaporation in several regions produced sulphate deposits up to 500 m thick. Since the atmosphere must have been 'strongly and persistently oxidizing' (Turner & Bekker 2016), the phenomenon is characterised as another event, temporally restricted much as Archaean 'oases' were spatially restricted. Halite crystals from Australia's Browne Formation, about the same age, include atmospheric bubbles with an average oxygen content of 10.9% (Blamey et al. 2016). Although 10.9% is comparable with Phanerozoic levels, the reporting authors judiciously refrain from speaking of an 'event' or inferring that the anomaly was reversed during the Bitter Springs anomaly, when supposedly less OC was buried (Turner & Bekker 2016). Indeed, the Browne Formation is thought to have been contemporaneous with the Bitter Springs Group.

Carbon isotope ratios went negative several times during the Neoproterozoic, sometimes down to the level of mantle carbon. If marine $\delta^{13}C$ was the same everywhere, each of these events should have represented a great de-oxygenation event. With little to no OC being buried, atmospheric oxygen would have reverted to supposed Archaean levels. Why, then, are these not part of the story?

The second GOE took place towards the end of the Ediacaran, about the time of the Shuram-Wonoka anomaly. Carbonate $\delta^{13}C$ fell – the opposite of what occurred during the Lomagundi-Jatuli Event, and ostensibly implying that less OC was buried and less O_2 released to the atmosphere (§4.6). Indeed, the signal plunged to its lowest level ever.

Iron speciation data do not indicate a permanent shift in redox structure at any time in the Proterozoic. What can be affirmed is that epicontinental seas expanded (Fig. 9.6), erosion caused by the transgression increased the supply of nutrients, and cyanobacterial and algal production

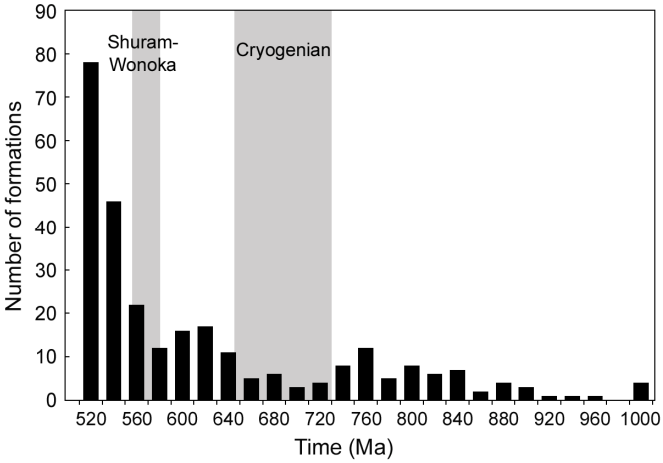

Figure 9.6. Number of epicontinental carbonate formations through the Neoproterozoic. Low frequency in the Precambrian is interpreted as reflecting rift grabens within generally elevated continents. The exponential rise from 580 Ma onwards reflects multi-regional transgression and increasing drawdown of CO_2 (§5.4).

continued to rise (Leavitt et al. 2013): TOC data suggest a fairly steady rise from ~810 Ma, with a surge near the end of the Proterozoic. Shales – increasingly common in the Ediacaran because of intensified erosion – increased the rate of OC burial and thereby released more O_2 to the atmosphere, which in turn pushed down the redox boundary, oxidising more H_2S to sulphate. An increase in sulphate stimulated the anaerobic oxidation of dissolved organic carbon, as seen after 600 Ma in the unusually high $\delta^{34}S$ of sulphate (Shields et al. 2004). Carbon isotope ratios fell far below -6‰ because remineralisation was no longer in equilibrium with the supply of sinking organic matter: the turbid, iron-rich water column was being cleared. Thereafter sinking organic carbon was remineralised increasingly by aerobic oxidation. Sulphate $\delta^{34}S$, accordingly, declined (Kampschulte & Strauss 2004). A general rise in carbonate $\delta^{18}O$ suggests that alkalinity also did.

Oxygenated, albeit fleetingly, the seafloor became habitable – first the nearshore, then to greater depths. Appearing as if from nowhere, animals, epifaunal and infaunal, began to colonise the new ecospace. Zooplankton began to graze phytoplankton; benthic animals fed on both. As trophic levels multiplied, cyanobacterial production declined, the slack taken up by new types of phytoplankton. Warm, CO_2-saturated, shallow seas, ever prone to algal and cyanobacterial blooms, were gradually de-toxified (Paerl & Hulsman 2009).

Over the long term, the percentage of OC buried in Phanerozoic shales was not very different from that in the Proterozoic. However, shales themselves were more frequent (Fig. 9.7): the equivalent period 1390–820 Ma, not to mention 1640–1480 Ma and most of the Archaean, preserves very few shales. As microbes were continually reducing Fe and S, atmospheric oxygen may have been little affected. The long-term average of shallow-marine $\delta^{13}C$ through the Archaean and Mesoprot-

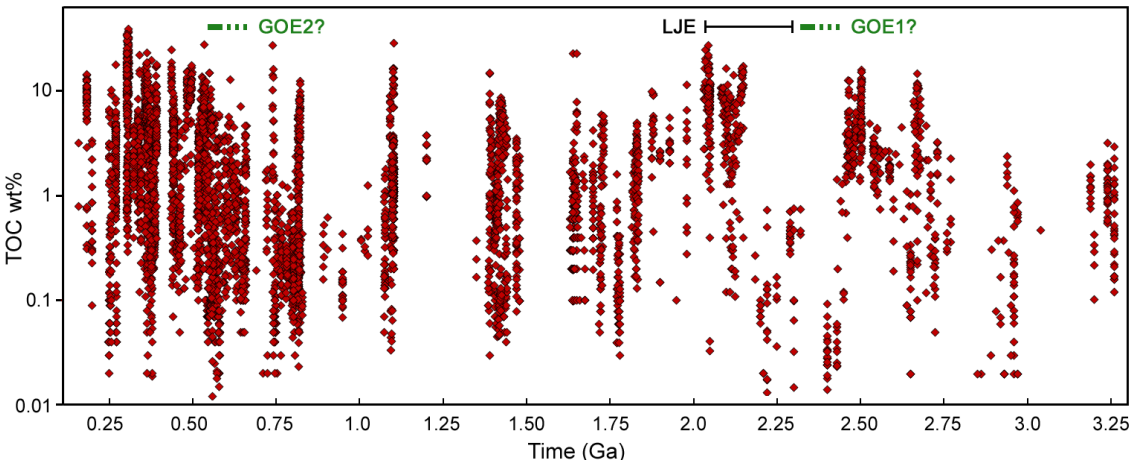

Figure 9.7. TOC buried in shales over time (compilation of published data). The hypothesised 'Great Oxygenation Event' of 2.45-2.32 Ga (maximum range) coincides with a paucity of shales and with the lowest percentages in the whole Proterozoic. LJE = 'Lomagundi-Jatuli Event'. In contrast to carbon isotope trends, the TOC record supports a (non-unique) rise in oxygen production at the end of the Neoproterozoic.

erozoic was 0‰, somewhat higher through the Palaeoproterozoic, most of the Neoproterozoic and the Phanerozoic – at variance with the notion that pO_2 underwent orders-of-magnitude increases (Schidlowski 1984). Epicontinental seas, where most oxygen production took place, reached their maximum extent in the late Ordovician (Haq & Schutter 2008). Embryophytes – land plants – hit the fossil record in the mid Ordovician (Edwards et al. 2015). If marine oxygen production ever fell, it was more or less counterbalanced by the rise of terrestrial photosynthesisers.

9.3. Silicate weathering, outgassing, seafloor spreading rates, ocean pH, degree of carbonate saturation, dolomite

Estimates of CO_2 levels in the Late Archaean depend, *inter alia*, on an assessment of how warm the Archaean world was and whether the atmosphere could have tolerated significant quantities of methane. Also influential is whether the diamictites, dropstones and striated clasts of South African's Mozaan Group (2.9 Ga) signify the Earth's first glaciation and thus a catastrophic fall in greenhouse gases. To the present author the high temperature of the mantle, the high degree of ocean-crust alteration (Shibuya et al. 2012), the predominance of surface and subsurface magmatism in continental successions, the evaporitic and/or hydrothermal nature of chemical sediments before 2.8 Ga, the low $\delta^{18}O$ of marine cherts and carbonates thereafter (uninterrupted by glaciations), the ubiquity of sericite in Precambrian granite palaeosols and the intense chemical weathering suggest a world that was relatively hot. Nonetheless, as much of the heat appears to have come from below rather than above, a fairly conservative estimate of 50,000 ppm (0.05 bar) for the Late Archaean is adopted (§5.4). The figure is intended only to be illustrative.

The essential point is that high pCO_2 has geological consequences, the most important of which is that volcanic outgassing had to be at a rate which sustained pCO_2 at the postulated level, net of consumption by silicate weathering. Cratons were submerged through most of the Archaean and their total area small, so weathering must have been minimal, as the $^{87}Sr/^{86}Sr$ record confirms (Fig. 5.1a, Veizer et al. 1982). Since the Hadean world was not necessarily as hot, nor submerged (Valley 2005, Hopkins et al. 2008), pCO_2 may even have risen for a time – the implication, too, if the influx was proportional to the global rate of crust production and degassing depth (Zahnle & Sleep 2002). Weathering – enhanced by exposure of a dominantly mafic upper crust and large quantities of aerosol H_2SO_4 – would have consumed CO_2 in appreciable quantities only from the Late Archaean, when cratons emerged and arguably plate tectonics kicked in (Condie & Kröner 2008, Tang et al. 2016). If pCO_2 rose through the Archaean, it had to have been high enough at the end of the aeon for the Earth to have been warm 1.0 Ga earlier, when both pCO_2 and solar radiation were lower.

Silicate weathering is a weak function of pCO_2. A widely adopted approximation is that of Walker et al. (1981) whereby the weathering flux increases as $pCO_2^{0.3}$. In their attempt to account for snowball glaciation, Le Hir et al. (2009) argued that weathering was limited by runoff, and long-term run-off cannot exceed the present rate by more than 22% because atmospheric circulation becomes sluggish as temperature rises and inhibits precipitation. Evidence of greatly enhanced weathering rates during past pCO_2 spikes (e.g. Cohen et al. 2004, Dal Corso et al. 2015) is not supportive. Nor is modern experience (Donat et al. 2016): annual precipitation and extreme precipitation are currently each increasing by 1–2% per decade in dry regions as pCO_2 rises by 20 ppm per decade. A term describing the inhibiting effect of aqueous species on mineral dissolution also seems unjustified, since an increase in runoff would tend to flush weathering systems. In addition, chemical weathering critically depends on tectonics, viz. the active physical denudation of continental rock to refresh mineral surfaces (Gaillardet et al. 1999, West et al. 2005) – the reason why the rise in $^{87}Sr/^{86}Sr$ was subdued over the period 1900–900 Ma but steep in the period 820–540 Ma.

If we adopt an exponent of 0.3 for the relation between weathering and pCO_2, then at 50,000 ppm the input from volcanism and metamorphism would have been 4.6 times greater than pre-industrial. If, as argued by Lee et al. (2013), it scales approximately with the square root of pCO_2, then 50,000 ppm would correspond with an input 13 times higher. In a plate-tectonics world, the implication is higher volcanic outgassing coupled with higher rates of seafloor spreading (fivefold higher according to Phipps Morgan 1998) and, at the opposite end, higher rates of subduction. Volcanism, in turn, was more intense because the mantle was hotter (by up to 600°, Sossi et al. 2016) and contained more CO_2, which lowered melting temperatures (Wyllie & Huang 1975) and increased explosivity (vesiculation). For the same reason, metamorphic devolatisation of subducted carbonate would also have been more vigorous (Santosh & Omori 2008). Although shorter-term factors such as the rise of vascular plants will have played a role, the secular decline in pCO_2 was ultimately due to secular mantle cooling.

There are also consequences for ocean pH. High pCO_2 does not, as sometimes assumed, entail that oceans were acidic (Lee & Morse 2010). At the same temperature and salinity, carbonate alkalinity – the balance between the aqueous carbon species – at a given pH remains the same. The present rise in pCO_2 has lowered pH because the rise has been occurring faster than the rate at which deep-sea calcium carbonate, which generates CO_3^{2-} and HCO_3^-, dissolves to buffer the system. Eventually, as in times past (Penman et al. 2016), greater consumption of atmospheric CO_2 by silicate weathering will counteract carbonate dissolution. Even today, river-water is significantly

more alkaline than sea-water (Spivack & Staudigel 1994), requiring that the flux of HCO_3^- be balanced by acidity from the hydrothermal alteration of ocean crust.

Greater degassing in the Proterozoic caused coastal waters to be more alkaline and abyssal waters in the immediate vicinity of outgassing CO_2 to be more acidic; pH would have been highest when silicate weathering was highest. Beyond the axial zone, it was sufficient for plagioclase to alter to calcite. On the continental shelf, greater runoff coupled with subaqueous silicate dissolution increased the flux of Na, K, Ca and bicarbonate. Greater concentrations of dissolved silica are another aspect of higher pH (Maliva et al. 2005).

There would also have been consequences for carbonate mineral saturation state. According to Henry's law, the amount of CO_2 dissolved in water is proportional to the partial pressure of the gas in equilibrium with the water. Hence, at equivalent temperature, the concentration of CO_3^{2-} and the saturation state in respect of carbonate minerals would have been much higher than now. Seawater was at least 20 times oversaturated in respect of both calcite and aragonite (Lee & Morse 2010). As a consequence of high concentrations of CO_3^{2-} and Mg^{2+}, Ca^{2+} concentrations in the Neoproterozoic were lower than at any later time before the Cenozoic (Fig. 9.8). That the oceans became less saturated in respect of calcium carbonate over time is well established (Grotzinger 1989, Sumner & Grotzinger 2000).

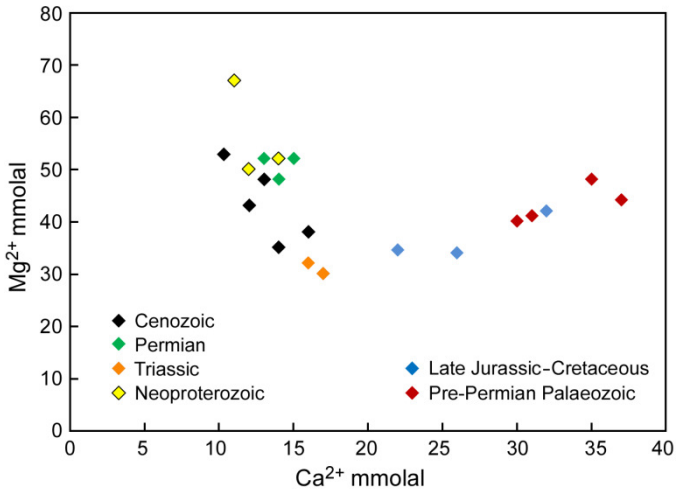

Figure 9.8. Seawater concentrations of Ca and Mg ions based on fluid inclusion data, Neoproterozoic onwards.

Complexing of the cations with sulphate would have been another control on saturation state. The concentration of sulphate, in turn, depended on the availability of oxygen. Although calcium sulphate was rare before 1.6 Ga, this was partly because $CaCO_3$ precipitation exhausted Ca^{2+} before saturation in respect of $CaSO_3$ was reached (Grotzinger 1989). Higher $[CO_3^{2-}]$ promoted the precipitation of $CaCO_3$ and inhibited the precipitation of $CaSO_3$. High pCO_2 might therefore have

masked absolute sulphate concentrations. Over time, as pCO_2 fell, gypsum deposits became more common irrespective of pO_2.

The advent of biomineralisation towards the end of the Proterozoic (with *Cloudina* and other small shelly fossils) marks a turning point in ocean chemistry. Calcium carbonate precipitation became increasingly organic. Carbonate skeletons evolved at least 28 times among eukaryotes (Knoll 2003) and were a permanent, globally important source of carbonate sediment from the Ordovician onwards (Pruss et al. 2010), albeit, in the Ordovician, still a very minor component. After the Palaeozoic (with the rise of calcareous nannoplankton, foraminifera and coralline algae) carbonate sediments were almost entirely organic. In other words, saturation state fell below the level at which calcium carbonate spontaneously precipitated, and atmospheric CO_2 was drawn down to a greater extent than CO_2 outgassing was declining. Muds produced by blooms of cyanobacteria in the modern Bahamas (Swart et al. 2014) are exceptions that prove the rule.

Saturation state depends on pH as well as the concentration of DIC. Because the commonly cited reaction

$$Ca^{2+} + 2HCO_3^- \rightarrow CaCO_3 + H_2O + CO_2$$

is an abbreviation of:

$$2HCO_3^- \rightarrow H_2O + CO_2 + CO_3^{2-}$$
$$Ca^{2+} + CO_3^{2-} \rightarrow CaCO_3$$

$CaCO_3$ will form more readily as the water becomes more basic and alkaline. At pH 8, the ratio of HCO_3^- to CO_3^{2-} is 9:1; at pH 10, it is 10^2 times less: the propensity to precipitate calcium carbonate proportionally rises. Thus, the fall in alkalinity to present values over time must have counteracted the fall in DIC and atmospheric pCO_2. Biomineralising organisms, on the other hand, extracted more carbonate from the system.

DIC being proportional to atmospheric pCO_2, in the early Precambrian nearly all deposited carbonate consisted of secondary calcite in ocean crust (Bjerrum & Canfield 2004), at volumes many times greater than now. In a transect of mid-Archaean greenstone, carbonate content decreased from 31% wt through the first 500 m to 2% at 2500–3000 m (Shibuya et al. 2012). For comparison, in the much thinner oceanic crust of the late Miocene, at Hole 504B, carbonate content through the first 500 m was 0.4% wt (Alt & Teagle 1999). Taking thickness into account but not spreading rate, the difference is more than a hundredfold. The long-term constancy of shallow-marine carbonate $\delta^{13}C$ at ≥ 0‰ requires that the long-term ratio of deposited organic to total carbon be approximately 1:5 ($f = 0.20$). If the system so represented was the whole ocean, 100–200 times greater deep-sea deposition of calcium carbonate in the early Precambrian plus a small amount of

epicratonic deposition is irreconcilable with the isotope signal and the constancy of *f* indicated by TOC wt %. The system must have been restricted to the cratons, leaving the isotopic value of open-ocean DIC, to balance, substantially lower than -1‰ (adjusting 0‰ for 1‰ carbonate-DIC fractionation), even if some OC ended up buried in ocean sediment. The ocean-crust carbon recycled partly into the mantle and partly, through outgassing above subduction zones, into the atmosphere, must also have been substantially lower than -1‰. Over time, the balance changed, as (1) the mass of both dissolved and ocean-crust carbon declined, (2) calcareous biogenic ooze began to compensate for the decrease in ocean-crust carbonation, and (3) the divide between the oceanic and epicontinental systems broke down, owing to the declining bicarbonate flux from runoff. Today DIC is orders-of-magnitude lower than in the Archaean and isotopically near homogeneous.

It should be noted that an OC burial fraction of 0.20 at a time of higher sedimentation rates (driven by higher seafloor spreading rates) represents a correspondingly greater absolute biomass, and it is absolute mass that matters as regards oxygen generation. Per unit time possibly more O_2 was being produced in the early Precambrian than today. Since the redox state of the mantle appears to have changed little, the possibility that nearly all oxygen was consumed by H_2, H_2S and Fe^{2+} is unlikely. On the other hand, before 2.7 Ga, degassing at higher pressure may have entailed a higher proportion of reductive gases entering the exosphere (Gaillard et al. 2011) and thus a higher rate of oxygen consumption.

Most dolomite in the Precambrian probably precipitated direct from seawater (§2.7.6), promoted by higher concentrations of CO_3^{2-} and Mg^{2+}, subsurface anoxia and higher temperatures. In very shallow environments [Mg^{2+}] was raised by evaporation, while the downslope precipitation of calcium carbonate raised Mg/Ca in shallow environments. Mg concentration was generally higher because much of the plagioclase in the upper ocean crust reacted with DIC to produce calcite, so that there was no loss of Ca to permit a corresponding gain in Mg (Nakamura & Kato 2004). Mg^{2+} concentrations in the Neoproterozoic were higher than at any later time before the Cenozoic (Fig. 9.8). Ocean crust was neither a sink for Mg nor a source of Ca. Anoxia promoted dolomite, because anaerobic microbes converted sulphate to sulphide, and sulphide raised the activity of Mg^{2+} by countering hydration. Higher temperatures meanwhile helped to overcome the kinetic barrier. Dolomite became less common in the Palaeozoic and less commonly a primary mineral as ocean-crust carbonation decreased, as the subsurface water column became oxygenated, and as [CO_3^{2-}] and temperature decreased.

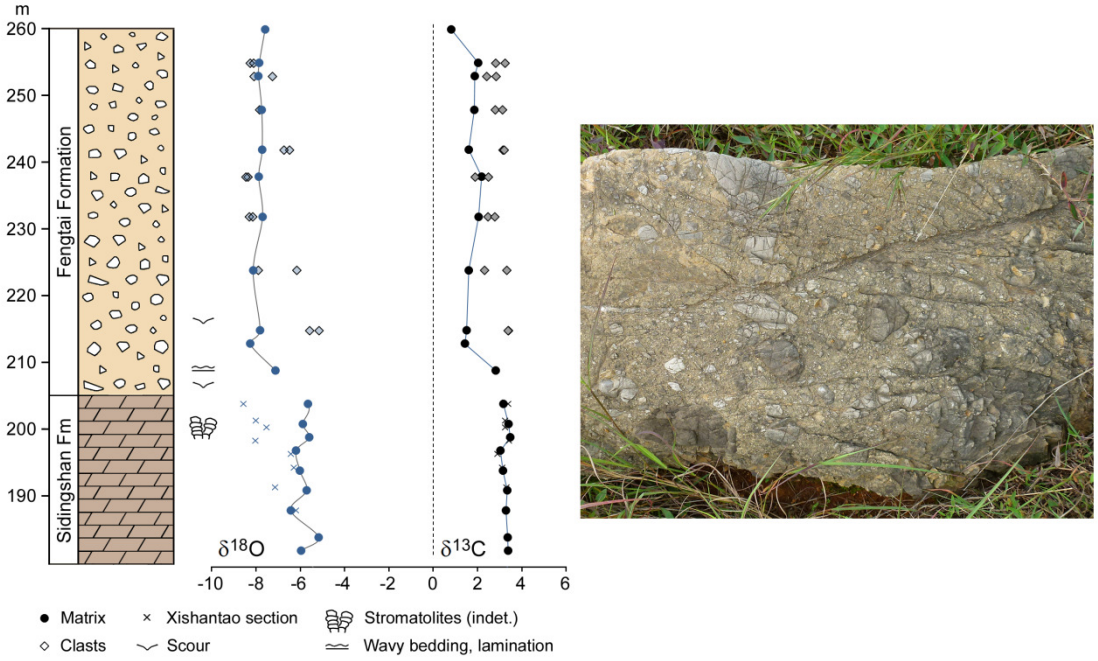

Figure 9.9. The Fengtai Formation as logged and sampled at Yangdengshan, 7.5 km NNW of the Xishantao section (Fig. 2.2), which is here correlated. Matrix and clasts are dolomite, the latter derived from the underlying Sidingshan Formation. The matrix records lower $\delta^{13}C$ values, reflecting a combination of eroded Sidingshan carbonate plus dolomite newly precipitating in the deeper water. Oxygen isotopes normalised to calcite are also lower. Those of the uppermost Sidingshan Formation were altered by rainwater before deposition of the Fengtai. The photograph illustrates scoured bedding in the lower part of the diamictite.

9.4. Climate change in the Neoproterozoic – an alternative view

There are no diamictite units of Marinoan age on the North China craton, possibly because the craton was on the periphery of Rodinia, if connected at all, and did not undergo major rifting. Probably none is of Sturtian age either. The only contender is the Fengtai Formation, overlying the Sidingshan Formation (Fig. 9.9). Since there is isotopic continuity across the unconformity and the latter appears to be mid Tonian in age, the Fengtai is more likely to correlate with the Bitter Springs events, c. 810 Ma. The one other diamictite horizon on the North China Craton – the Luoquan Formation – is late Ediacaran, complete with dropstones, striated clasts and striated pavements (Figs. 1.1, 1.2). Although several other such deposits at low palaeolatitudes date to this interval (§1.2), few geologists are willing to conclude that ice once again covered the Earth from tip to toe. The closer in time the diamictites are to the appearance of animals, the more difficult the interpretation becomes. Somehow diamictites, striated clasts and spectacular striated pavements lose their diagnostic power.

Another instructive region is the Nanhua Basin of South China. Most of the Tonian succession consists of rift-generated turbidites. The transition into the Cryogenian is conformable, marked by a

slight coarsening of sediment. Did rifting stop and glacial erosion seamlessly take over, producing turbidites at the same rate and from the same source? That faulting continued to segment the basin is evident from the huge, irregular variations in formation thickness across the basin. The Cryogenian deposits are subaqueous – there is no evidence that ice impeded sediment flow – and the pattern as a whole is one of transgression, as the basin widened and became open to the sea. Despite calculations that global sea-level should have fallen by 700 m, Marinoan sediments extended further onto the continent than sediments of the 'interglacial' period.

Chemical weathering did not fall in the approach to the Cryogenian. Through the last 20 m of the pre-Sturtian Gongdong Formation the weathering index rose; it continued to rise through the first 30 m of the Chang'an Formation, when the region was supposedly under ice. The highest value comes from about half way through the Chang'an. Similar levels, though not high in absolute terms, are recorded near the top of the Fulu Formation at the other end of the Sturtian, and cyclically in the Nantuo Formation during the Marinoan.

During the early Tonian lowest strontium isotope values were almost flat. They started to rise around 840 Ma. It was a pivotal moment. Soon afterwards South China began to rift, marine $\delta^{13}C$ plunged, shale formations became common (Fig. 9.7), and Svalbard (Maloof et al. 2006), Ethiopia (Swanson-Hysell et al. 2012) and South China (Li et al. 2013) all left evidence of true polar wander. The whole supercontinent shifted to low latitudes centred on the equator. Tectonic instability – the lithosphere spasmodically doming and, by consequence, undergoing increased erosion and weathering – was the ultimate driver of high levels of ^{87}Sr and variability in carbonate $\delta^{13}C$, as it was of high alkalinity and high rates of sedimentation. The periods of greatest rise in lowest $^{87}Sr/^{86}Sr$ values were 820–790, 660–650 and 560–545 Ma, all coinciding with major carbon-isotope anomalies and rapid changes in sea-level. Just below the Sturtian diamictites values surged far above background levels. They also rose during the Sturtian interval itself. There was no suspension of silicate weathering driving $^{87}Sr/^{86}Sr$ back to its mantle value, as the glaciation scenario predicts, nor a reversal of the predicted descent straight after the Sturtian: following another spike at that juncture, ratios fell. At the end of the Marinoan they also fell.

Snowball Earth requires a lowering of atmospheric pCO_2, most realistically to below 300 ppm. Taking into account the weaker luminosity of the Sun, pre-glacial levels can hardly have been less than 3400 ppm – the modelled concentration needed to sustain today's relatively cool temperatures – and probably were much higher. Consumption of CO_2 was counteracted by increased outgassing as the lithosphere rifted and disaggregated (Lee et al. 2016) and as subducted ocean crust was decarbonated. In the Cambrian, concentrations are estimated around 5000 ppm, some 18 times pre-

industrial levels. Back in time the uncertainties increase, but strontium isotope ratios indicate that during the mid to late Neoproterozoic the influx of radiogenic Sr – at least partly due to weathering – was greater than at any time before or since. Since weathering consumed CO_2, concentrations in the early Tonian must have been many times higher than 5000 ppm, consistent with the large amounts consumed by carbonate deposition in the Ediacaran (Fig. 9.6). Modelling studies fail to demonstrate how pCO_2 could have plunged catastrophically to 300 ppm or less.

Insofar as ice isolated the continents, silicate weathering should have been minimal. For the same reason, the curtailed supply of Na, K and Ca, coupled with the unremitting build-up of dissolved CO_2 from submarine volcanism, would have acidified the ocean, probably never fully buffered by the dissolution of ocean-crust carbonate and basalt. Marine diamictites ought to have contained almost no carbonate, whether detrital or precipitated (contrary to Table 1.2). If small areas of water remained unfrozen, the ocean would have been further acidified by exchange with increasing CO_2 in the atmosphere (Goddéris et al. 2011).

How warm, then, was the Neoproterozoic ocean? The most direct evidence of temperature is carbonate oxygen isotope ratios, which rise as temperature falls. Shallow-water, low-latitude carbonates in the late Cenozoic are around 1 ±1.5‰, ratios in the Neoproterozoic around -8 ±2‰, decreasing as $\delta^{13}C$ becomes more negative (Fig. 4.11). While interpretation depends critically on the $\delta^{18}O$ of seawater (Jaffrés et al. 2007), it seems inescapable that some of the difference relates to temperature. As we have seen from the carbonates of North China where isotopic differences between calcium carbonate and dolomite are preserved and $\delta^{18}O$ in the Majiatun Formation declines just at the point where $\delta^{13}C$ reaches its nadir, the record is not homogenised: values were not materially affected by pervasive diagenesis. Chert oxygen isotope ratios (Tartèse et al. 2016), inferred pCO_2 well above Cambrian levels, the absence of organic calcifiers that would have suppressed pCO_2, the common occurrence of aragonite, VHMC and dolomite, the susceptibility of shallow-marine DIC to evaporative isotopic enrichment, the efficiency of organic carbon remineralisation and the high concentrations of precipitated SiO_2 all suggest an ocean still much warmer than today's. Given that the atmosphere was oxic, the ocean's subsurface anoxia itself suggests high temperatures, for oxygen is less soluble in warm water. The Phanerozoic includes many instances of anoxia caused by concurrent rises in pCO_2 and temperature (Meyer & Kump 2008), to say nothing about the present-day expansion of anoxia.

With the recent concession that dropstone clasts occur in turbidites and that striations would not have survived the abrasion of debris flows (§§1.3, 6.5), the classic evidence for Cryogenian glaciation is itself crumbling. Since, to reiterate, climate models cannot generate Snowball Earth

from realistic initial pCO_2 levels and struggle to explain, assuming it did happen, how it was reversed, a bystander might well ask what is left to lend it credibility – why anyone would want to defend this most extreme of geological hypotheses.

The alternative mooted here is simply a more integrated recognition of what is already acknowledged. The continents prior to 750 Ma comprised a single landmass (Li et al. 2013). Unlike heat beneath the ocean crust, which continued to be dissipated through submarine volcanism, mantle heat under the much thicker continental crust was trapped. Thermal pressure caused the supercontinent to rift, eventually on a catastrophic scale. Seismic erosion off fault scarps triggered sediment-laden debris and turbidity flows. Steepening of depositional slopes led to striation of embedded clasts as one bed sheared against another. Occasionally entire bedding surfaces were striated (§6.5). Sediments were of mixed composition and rich in clasts because the vertically eroded formations consisted of various lithologies, of varying hardness. The weathering recorded in the matrix was not significantly less than at other times because the crumbling rock faces already consisted of weathered material; it was not significantly more because the erosion was primarily physical. While no ocean crust survives from the new margins to fix the chronology, palaeomagnetic data (*ibid*.) suggest that post-rift disaggregation of the supercontinent began in earnest soon after 720 Ma, even if some regions were still rifting.

In any one place, carbon-isotope ratios fluctuated in response to the up-and-down oscillations of the lithosphere. Positive excursions signified uplift, negative excursions deepening episodes, not the eustatic draining of platforms by terrestrial ice sheets. Prior to both the Sturtian and Marinoan episodes, carbonate – typically a product of shallow, low-energy conditions – was the most common lithology (Fig. 5.4), in places including brief descents into deeper water. Uplift was the prelude to rifting (cf. Esedo et al. 2012). That many of these events occurred synchronously across the globe reflects the fact that at the end of the Tonian most continents were still aggregated and all were subject to thermal pressure.

Continental flood volcanism, also symptomatic of an overheated asthenosphere, was frequent and voluminous from about 920 Ma, ceasing soon after the start of the Cryogenian (Fig. 9.10). In the Permian, Triassic and Jurassic periods, when Pangaea was rifting, terrestrial volcanism occurred on a similar scale. Contemporaneous negative swings in carbonate $\delta^{13}C$ suggest that the eruptions triggered massive influxes of magmatic CO_2 (§4.9.1). That negative excursions in the Tonian did not coincide with large-scale eruptions is due to three factors: the primacy of water depth in controlling carbonate $\delta^{13}C$, the much higher level of pCO_2, diluting the impact of surges in volcanism, and atmospheric CO_2 being isotopically lighter than the injected CO_2 (§4.7); in the

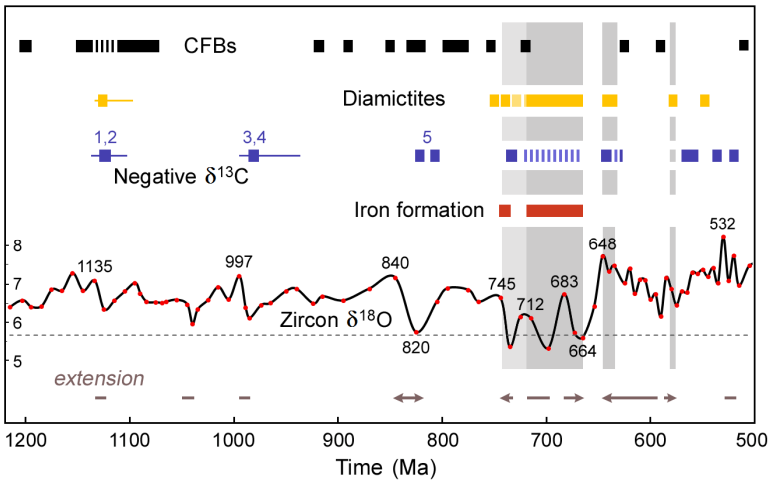

Figure 9.10. Continental flood basalts > 100,000 km^2, diamictites, the carbon isotope signal of marine carbonates, iron formation, the oxygen isotope signal of zircons (data as per Fig. 6.9, averaged) and inferred episodes of tectonic extension. Large-amplitude negative C-isotope excursions: (1, 2) Atar Group and Lapa Formation, the latter excursion immediately above diamictite, (3, 4) Majiatun and Shorikha Formations, poorly dated (horizontal lines: probable age range), (5) multiple 'Bitter Springs' excursions. Dotted line: $\delta^{18}O$ of the mantle. Grey bands denote the Sturtian, Marinoan and Gaskiers intervals.

Mesozoic, atmospheric $\delta^{13}C$ was heavier. Rapid weathering of basalt in the Tonian consumed the excess CO_2 and may have contributed to the rise in carbonate production (Fig. 9.6). There is no indication that it drew down CO_2 sufficiently to produce icehouse conditions, and there is no succour for such a hypothesis (Cox et al. 2016) in Mesozoic analogues.

Most magmas incorporate a certain amount of continental crust and/or buried sediment as they ascend from the mantle; hence the $\delta^{18}O$ of their zircons tends to be enriched (§6.6, Fig. 9.10). On only two occasions after the Archaean do they show no mixing: one around 740–660 Ma, the other around the end of the Triassic with the break-up of Pangaea (Spencer et al. 2014). By contrast, the peak just after this trough (c. 648 Ma) is the highest in the Precambrian. The very highest occurs at the onset of the Cambrian transgression and, perhaps not coincidentally, at the onset of another postulated episode of true polar wander (Kirschvink et al. 1997, Mitchell et al. 2010). The paucity of data between 980 and 660 Ma (Fig. 6.10) reflects low levels of granitic magmatism, but by the same token makes inferences less robust. In general, published zircon data are of a piece with the crustal thinning, iron formation and other hydrothermal influxes characteristic of the Cryogenian.

Iron formation in the Neoproterozoic was primarily a Sturtian phenomenon (§1.2, Cox et al. 2013). Some units are early Sturtian (e.g. Sayunei Formation), some are late (e.g. Surprise Member, Kingston Peak Formation). Older units include those in Egypt and Saudi Arabia, dated between 759 ±17 and 710 ±5 Ma, and the Erzin BIF of Russia and northern Mongolia, above volcanics dated to 767 ±15 Ma (Gaucher et al. 2015). Thus iron enrichment occurred at the same time as the

drop in zircon $\delta^{18}O$, a consequence of hyperextension, not glaciation. It did not occur in all Sturtian sequences, so its absence in the Marinoan should be interpreted with caution. That said, the rise in $\delta^{18}O$ after 665 Ma suggests that thickening of the crust inhibited the large-scale leakage of iron-rich hydrothermal fluids.

Through a link with sea-level change, the zircon record has the potential to increase the resolution of Neoproterozoic chronostratigraphy. With average $\delta^{18}O$ plunging 840–820 Ma, then climbing to above the long-term average of ~6.5‰ soon after 810 Ma, it may not be fortuitous that the Akademikerbreen Group (Svalbard), Eleanor Bay Group (Greenland), Callanna Group (South Australia) and Bitter Springs Group (Central Australia) all date about that time. The ductile lower crust was stretched; faulting subsequently affected the upper crust and grabens deepened, shallowing as sediments filled the grabens and/or the faults reversed. In carbonate rocks, sea-level rise c. 820 Ma is traced through the carbon-isotope signal. A steep drop in $\delta^{18}O$ c. 990 Ma suggests another such link with the initiation, in Canada, of the Reynolds Point Group (Victoria Island), Little Dal Group (Mackenzie Mountains) and Fifteen Mile Group (Ogilvie Mountains) and with the Majiatun and Shorikha carbon-isotope excursions. At the other end of the Tonian, the oldest 'Islay' anomaly begins soon after a region-wide unconformity at the base of the Callison Lake Formation and the deposition of shales with a Re-Os age of 753 ±5.5 (Rooney et al. 2015). The correlative unconformity at the top of Arizona's Chuar Group dates to c. 742 ±6 Ma (Dehler et al. 2010). If the start of the Cryogenian Period is to be defined by the first appearance of diamictites (Shields-Zhou et al. 2016), it might be placed there rather than at 720 Ma, aligning it with the diamictites of Utah's Big Cottonwood Formation (Dehler et al. 2010), NW China's Bayisi Formation (Xu et al. 2009), South Australia's Fitton Formation (Preiss et al. 1998), Namibia's Kaigas Formation (Macdonald et al. 2010a) and the diamictites of the Arabian Nubian Shield (Stern et al 2011). In Canada the Cryogenian would then start with the fault-triggered up-to-1100-m-thick debris-flow conglomerates immediately above the Callison Lake Formation (Mustard 1991). While more data are requisite, the zircon $\delta^{18}O$ record potentially fixes the boundary on a more objective basis than the 'first appearance of widespread glaciation' – widespread but not necessarily global, and taking glaciation as self-evident. Of the two dates thought to constrain the start of the Cryogenian, one is 716.5 Ma from 20 m above the contact with the pre-Sturtian unit (Macdonald et al. 2010b), the other 715.8 ±2.5 Ma from 25 m below the contact (Lan et al. 2014), which should now be revised to a detrital age of 710 ±3 Ma (§6.2). The two boundaries were not synchronous.

Zircon $\delta^{18}O$ dips twice through the Sturtian interval. The corresponding stratigraphy is often bipartite. Examples include the stratigraphy of Mongolia (Maikhan-Uul Formation, comprising two

Figure 9.11. The Sturtian diamictite-cap carbonate boundary in the Flinders Ranges, Australia: enriched in hydrothermal carbonate, iron and magnesium, depleted in ^{13}C, chock-full of clasts. (Penknife for scale.)

Figure 9.12. One of several outcropping tepees in the Nucca-leena Formation, Flinders Ranges, South Australia, above Marinoan diamictite and the GSSP for the base of the Ediacaran Period.

massive diamictite units separated by clast-poor sediments), Canada (Sayunei/Shezal Formations) and Australia (Pualco Tillite/Wilyerpa Formations). A case that we have examined in some detail is that of the Hunan-Guangxi basin, South China, where the oldest diamictites, those of the Chang'an Formation, date c. 710 Ma, followed by the as yet poorly dated Fulu Formation. The base of the overlying post-Sturtian Datangpo Formation is dated to ~663 ±4 Ma, coinciding with the final nadir of zircon $\delta^{18}O$. The other constraints on the end of the Sturtian are a Re-Os date of 662.4 ±4 Ma from 2 m above the Shezal Formation (Rooney et al. 2014) and a Re-Os date of 659 ±4 from 1 m above the Maikhan-Uul Formation (Rooney et al. 2015).

Finally, another major drop in $\delta^{18}O$ coincides with the diamictite horizons clustered around 584–581 Ma, notably the eponymous Gaskiers Formation (McGee et al. 2013, Fig. 1.1b). Some workers regard the Shuram-Wonoka carbon-isotope anomalies as synchronous with the Gaskiers episode. Others – in my view, more convincingly – link the latter with an earlier negative excursion (e.g. Macdonald et al. 2013).

Most of the cap carbonates that succeeded the diamictites were dolostone; the carbonates following the Marinoan episode all were (Fig. 5.3, Shields 2005). The transition was sharp, not a gradual progression from marl to limestone to dolostone as climate warmed, and no Missoula Floods gouged out canyons and scablands. Deeply penetrating faults injected hydrothermal fluids rich in Mg, Fe, DIC, ^{87}Sr, Ba and trace-metal nutrients (Mn, Cd, Cu, Zn, Ni, Co). Except in a few places where there is a slight overlap with carbonate precipitation (Fig. 9.11, Trompette 1981, Giddings & Wallace 2009, Fairchild et al. 2016), coarse-clastic sedimentation stopped and fine-clastic sedimentation plummeted. As the waters calmed, cyanobacteria proliferated (though the only evidence is TOC net of remineralisation), their sulphate-reducing auxiliaries proliferated (hence high $\delta^{34}S$), and for a short time conditions for dolomite precipitation were ideal.

Carbonate $\delta^{13}C$ was nearly always negative at the end of the Sturtian and usually negative at the end of the Marinoan. The Snowball Earth hypothesis proposes that, deprived of light and warmth, phototrophs perished, organic carbon ceased to be extracted from the ocean and $\delta^{13}C$ consequently fell: by the time the glaciers started to melt, DIC was close to unfractionated (Hoffman et al. 1998). However, $\delta^{13}C$ at the base of the carbonates is typically well above the mantle value, the underlying sequences preserve significant amounts of organic carbon, and, with pCO_2 rising to 300,000 ppm, the acidity of the water should have inhibited precipitation. Other workers, notwithstanding, suggest that the carbonate precipitated from upwelling deep-water rendered alkaline and ^{13}C-depleted by remineralisation. While this seems closer to the truth, the preceding sediments do not record the ocean's withdrawing to the craton margins and welling back up, and an explanation is needed which recognises that cap carbonates are not the only sequences to capture low $\delta^{13}C$. The present analysis suggests that, here as elsewhere, $\delta^{13}C$ was a function of sea-level. Dolomite, briefly and unusually, was now forming in comparatively deep water.

Marinoan cap carbonates differ from Sturtian ones. They are thicker, richer in Mg, sometimes contain stromatolitic tube structure (Corsetti & Grotzinger 2005) and their facies are more disturbed (Fig. 6.7d). Commonly the upper dolostones form giant tepees suggestive of oscillatory flow (Fig. 9.12). In Namibia, where the tepees have been studied through many sections (Hoffman et al. 2007), they occur near the top of a deepening sequence in which facies pass from peloidal to swaley, and $\delta^{13}C$ becomes increasingly negative. One interpretation attributes them to hurricane-force winds blowing over fetch-unlimited seas during deglaciation (Allen & Hoffman 2005); they could equally well reflect oscillation within fault-bounded basins as the faults slipped.

Immediately after the tepees, the dolomite factory shut down and aragonite took over, with spectacular crystal fans growing up from the floor as micrite rained down (Corsetti et al. 2004, Hoffman et al. 2007, Sansjofre et al. 2011). Identical structures characterise carbonate precipitation in the Neoarchaean. Although the influx of Mg stopped at the same time as the tepees, saturation state was still exceptionally high and precipitation on and above the seafloor very rapid (Sumner & Grotzinger 2000, Corsetti & Grotzinger 2005).

The contrasting isotopic profiles of the two intervals – Sturtian $\delta^{13}C$ typically becoming less depleted, Marinoan more (Kennedy et al. 1998) – reflect, respectively, regressions and transgressions. In the Sturtian rift basins diamictite sedimentation ceased at the point that zircon $\delta^{18}O$ began to rise. The tectonic regime during the brief post-Sturtian interval ceased to be extensional (Fig. 9.10) and in many places $\delta^{13}C$ rose. As in siliciclastic-dominated successions (e.g. the Mackenzie Mountains), environments shallowed. Chronologically, the negative excursion known as the 'Trezona anomaly' is Marinoan. It precedes diamictites in regions where they are thin (Australia, Namibia, Canada) and represents the deepening that generated diamictites elsewhere. The zircon $\delta^{18}O$ evidence suggests that the thickest sequences began c. 648 Ma.

Geochemistry and tectonics are best not interpreted in isolation. Nor are carbonates and siliciclastics: tectonics influenced the geochemistry of both. Deep fractures penetrated the crust repeatedly in the Neoproterozoic, causing element abundances to surge. Examples from North China include the spike in Mn at the base of the Shishanlitai Formation, coincident precipitation of calcian dolomite, and subsequent deposition of iron-rich mudstones in the Cuijiatun and Xingmincun Formations. Examples from South China include sporadic nodules, lenses and beds of rhodochrosite/ kutnahorite in the Fanzhao, Fulu, Datangpo and lower Doushantuo Formations, spikes in Fe at the base of the Fulu and Datangpo Formations, and spikes in Cr, V, F, Cl and S at the base of the Fulu, Datangpo and Doushantuo Formations. Near the base of the Doushantuo at numerous localities barite precipitated (Jiang et al. 2006). Although comparisons have been made with the barite found in cold methane seeps, they might equally be made with the barite and closely associated aragonite crystal fans that characterise Neoarchaean carbonates. The strongest evidence for methane is a horizon of black limestone lenses near the top of the cap, where $\delta^{13}C$ dropped momentarily from -4 to -48 ‰ (Wang et al. 2008), along with similarly depleted fills of calcite a little lower down (Jiang et al. 2006). Since in the Snowball scenario dolomite started to precipitate after mean surface temperatures had reached 60° C, cold methane 'seeps' within the dolostones and presumably generated after glaciation do not meet the case.

This work has called into question four of the fundamental ideas that shape our understanding of the Precambrian: that dolomite has always been a secondary mineral; that marine carbonates reflected the carbon-isotope composition of the global ocean; that atmospheric oxygen levels were very low and rose in quantum steps; and that the Palaeoproterozoic and mid Neoproterozoic (not to venture further) were characterised by multiple world-wide glaciations. Linking the discussions is the role played by carbon dioxide and the many ways in which, supplied by a hotter mantle, higher concentrations in the atmosphere affected both marine and terrestrial systems. The effects, I submit, were profound.

References

Allen, P.A., Hoffman, P.F., 2005. Extreme winds and waves in the aftermath of a Neoproterozoic glaciation. *Nature* 433, 123–127.

Alt, J.C., Teagle, D.A.H., 1999. The uptake of carbon during alteration of oceanic crust. *Geochim. Cosmochim. Acta* 63, 1527–1535.

Bao, H., Rumble, D., Lowe, D.R., 2007. The five stable isotope compositions of Fig Tree barites: Implications on sulfur cycle in ca. 3.2 Ga oceans. *Geochim. Cosmochim. Acta* 71, 4868–4879.

Bjerrum, C.J., Canfield, D.E., 2004. New insights into the burial history of organic carbon on the early Earth. *Geochem. Geophys. Geosyst.* 5, Q08001.

Blamey, N.J.F. et al., 2016. Paradigm shift in determining Neoproterozoic atmospheric oxygen. *Geology* 44, 651–654.

Braterman, P.S., Cairns-Smith, A.G., Sloper, R.W., 1983. Photo-oxidation of hydrated Fe^{2+} – significance for banded iron formations. *Nature* 303, 163–164.

Buick, R., 2008. When did oxygenic photosynthesis evolve? *Phil. Trans. R. Soc. B* 363, 2731–2743.

Byrne, B., Goldblatt, C., 2014. Radiative forcings for 28 potential Archean greenhouse gases. *Clim. Past* 10, 1779–1801.

Cameron, E.M., Hattori, K., 1987. Archean sulphur cycle: evidence from sulphate minerals and isotopically fractionated sulphides in Superior Province, Canada. *Chem. Geol.* 65, 341–358.

Claire, M.W. et al, 2014. Modeling the signature of sulfur mass-independent fractionation produced in the Archean atmosphere. *Geochim. Cosmochim. Acta* 141, 365–380.

Coffey, J.M., Flannery, D.T., Walter, M.R., George, S.C., 2013. Sedimentology, stratigraphy and geochemistry of a stromatolite biofacies in the 2.72 Ga Tumbiana Formation, Fortescue Group, Western Australia. *Precambrian Res.* 236, 282–296.

Cohen, A.S., Coe, A.L., Harding, S.M., Schwark, L., 2004. Osmium isotope evidence for the regulation of atmospheric CO_2 by continental weathering. *Geology* 32, 157–160.

Cole, D.B. et al., 2016. A shale-hosted Cr isotope record of low atmospheric oxygen during the Proterozoic. *Geology* 44, 555–558.

Condie, K.C., Kröner, A., 2008. When did plate tectonics begin? Evidence from the geologic record. In: K.C. Condie, V. Pease (eds), *When did Plate Tectonics Begin on Planet Earth?* GSA Spec. Pap. 440, 281–294.

Condie, K.C., O'Neill, C., 2010. The Archean-Proterozoic boundary: 500 my of tectonic transition in Earth history. *Am. J. Sci.* 310, 775–790.

Coogan, L.A., Dosso, S.E., 2015. Alteration of ocean crust provides a strong temperature dependent feedback on the geological carbon cycle and is a primary driver of the Sr-isotopic composition of seawater. *Earth Planet. Sci. Lett.* 415, 38–46.

Corsetti, F.A., Grotzinger, J.P., 2005. Origin and significance of tube structures in Neoproterozoic post-glacial cap carbonates: example from Noonday Dolomite, Death Valley, United States. *Palaios* 20, 348–362.

Corsetti, F.A., Lorentz, N.J., Pruss, S.B, 2004. Formerly-aragonite seafloor fans from the Neoproterozoic strata, Death Valley and southeastern Idaho, United States: Implications for 'cap carbonate' formation and Snowball Earth. In: G.S. Jenkins et al. (eds), *The Extreme Proterozoic: Geology, Geochemistry, and Climate*, Geophys. Monogr. Ser. 146, 33–44.

Cox, G.M. et al., 2013. Neoproterozoic iron formation: An evaluation of its temporal, environmental and tectonic significance. *Chem. Geol.* 362, 232–249.

Cox, G.M. et al., 2016. Continental flood basalt weathering as a trigger for Neoproterozoic Snowball Earth. *Earth Planet. Sci. Lett.* 446, 89–99.

Craddock, P.R., Dauphas, N., 2011. Iron and carbon isotope evidence for microbial iron respiration throughout the Archean. *Earth Planet. Sci. Lett.* 303, 121–132.

Crowe, S.A. et al., 2013. Atmospheric oxygenation three billion years ago. *Nature* 501, 535–539.

Dal Corso, J. et al., 2015. Carbon isotope records reveal synchronicity between carbon cycle perturbation and the "Carnian Pluvial Event" in the Tethys realm (Late Triassic). *Global Planet. Change* 127, 79–90.

Dehler, C.M., Fanning, C.M., Link, P.K., Kingsbury, E.M., Rybczynski, D., 2010. Maximum depositional age and provenance of the Uinta Mountain Group and Big Cottonwood Formation, northern Utah: Paleogeography of rifting western Laurentia. *GSA Bull.* 122, 1686–1699.

Donat, M.G., Lowry, A.L, Alexander, L.V., O'Gorman, P.A., Maher, N., 2016. More extreme precipitation in the world's dry and wet regions. *Nat. Clim. Change* 6, 508–513.

Edwards, D., Chern, L., Raen, J.A., 2015. Could land-based early photosynthesizing ecosystems have bioengineered the planet in mid-Palaeozoic times? *Palaeontology* 58, 803–837.

Eigenbrode, J.L., Freeman, K.H., 2006. Late Archean rise of aerobic microbial ecosystems. *Proc. Nat. Acad. Sci. USA* 103, 15759–15764.

Esedo, R., van Wijk, J., Coblentz, D., Meyer, R., 2012. Uplift prior to continental breakup: Indication for removal of mantle lithosphere? *Geosphere* 8, 1078-1085.

Fairchild, I.J. et al., 2016. The Late Cryogenian Warm Interval, NE Svalbard: Chemostratigraphy and genesis. *Precambrian Res.* 281, 128–154.

Farquhar, J., Bao, H., Thiemens, M., 2000. Atmospheric influence of Earth's earliest sulphur cycle. *Science* 289, 756–758.

Farquhar, J., Wing, B.A., 2003. Multiple sulfur isotopes and the evolution of the atmosphere. *Earth Planet. Sci. Lett.* 213, 1–13.

Farquhar, J. et al., 2007. Isotopic evidence for Mesoarchaean anoxia and changing atmospheric sulphur chemistry. *Nature* 449, 706–709.

Fenchel, T., 2002. *The Origin and Early Evolution of Life*, Oxford University Press, Oxford.

Flament, N., Coltice, N., Rey, P.F., 2008. A case for late-Archaean continental emergence from thermal evolution models and hypsometry. *Earth Planet. Sci. Lett.* 275, 326–336.

Flannery, D.T., Walter, M.R., 2012. Archean tufted microbial mats and the Great Oxidation Event: new insights into an ancient problem. *Aus. J. Earth Sci*. 59, 1–11.

Fralick, P., Riding, R., 2015. Steep Rock Lake: Sedimentology and geochemistry of an Archean carbonate platform. *Earth-Sci. Rev.* 151, 132–175.

French, K.L. et al., 2015. Reappraisal of hydrocarbon biomarkers in Archean rocks. *Proc. Nat. Acad. Sci. USA* 112, 5915–1920.

Frogner, P., Gíslason, S.R., Óskarsson, N., 2001. Fertilizing potential of volcanic ash in surface water. *Geology* 29, 487–490.

Gaillard, F., Scaillet, B., Arndt, N.T., 2011. Atmospheric oxygenation caused by a change in volcanic degassing pressure. *Nature* 478, 229–232.

Gaillardet, J., Dupré, B., Louvat, P., Allègre, C.J., 1999. Global silicate weathering and CO_2 consumption rates deduced from the chemistry of large rivers. *Chem. Geol.* 159, 3–30.

Galic, A., 2015. Unravelling atmospheric photolysis and ocean redox chemistry from Paleoarchean pyrite: a multiple sulfur and iron stable isotope study. PhD thesis, Utrecht University.

Gaucher, C., Sial, A.N., Frei, R.F., 2015. Chemostratigraphy of Neoproterozoic banded iron formation (BIF): types, age and origin. In: M. Ramkumar (ed.), *Chemostratigraphy: Concepts, Techniques, and Applications*, Elsevier, Amsterdam, pp 443–449.

Giddings, J.A., Wallace, M.W., 2009. Sedimentology and C-isotope geochemistry of the 'Sturtian' cap carbonate, South Australia. *Sediment. Geol.* 216, 1–14.

Gieskes, W.W.C., Laane, R.W.P.M, Ruardij, P., 2015. Photo-oxidation: Major sink of oxygen in the ocean surface layer. *Mar. Chem.* 177, 472–475.

Goddéris, Y., Le Hir, G., Donnadieu, Y., 2011. Modelling the Snowball Earth. In: E. Arnaud, G.P. Halverson, G. Shields-Zhou (eds), *The Geological Record of Neoproterozoic Glaciations*, Geol. Soc. Lond. Mem. 36, 151–161.

Grosch, E.G., McLoughlin, N., 2013. Paleoarchean sulphur cycle and biogeochemical surface conditions on the early Earth, Barberton, South Africa. *Earth Planet. Sci. Lett.* 377–378, 142–154.

Grotzinger, J., 1989. Facies and evolution of Precambrian carbonate depositional systems: emergence of the modern platform archetype. In: P.D. Crevello et al. (eds), *Controls on Carbonate Platform and Basin Development*, SEPM Spec. Pub. 44, 79–106.

Halevy, I., Johnston, D.T., Schrag, D.P., 2010. Explaining the structure of the Archean mass-independent sulphur isotope record. *Science* 309, 204–207.

Hanor, J.S., 2000. Barite-celestine geochemistry and environments of formation. *Rev. Min. Geochem*., 40, 193–275.

Haq, B.U., Schutter, S.R., 2008. A chronology of Paleozoic sea-level changes. *Science* 322, 64–68.

Hayes, J.M., Waldbauer, J.R., 2006. The carbon cycle and associated redox processes through time. *Phil. Trans. R. Soc. B* 361, 931–950.

Heinrichs, T.K., Reimer, T.O., 1977. A sedimentary barite deposit from the Archean Fig Tree Group of the Barberton Mountain Land (South Africa). *Econ. Geol*. 72, 1426–1441.

Hoashi, M. et al., 2009. Primary haematite formation in an oxygenated sea 3.46 billion years ago. *Nature Geosci.* 2, 301–306.

Hoffman, P.F., Kaufman, A.J., Halverson, G.P., Schrag, D.P., 1998. A Neoproterozoic Snowball Earth. *Science* 281, 1342–1346.

Hoffman, P.F. et al., 2007. Are basal Ediacaran (635 Ma) post-glacial "cap dolostones" diachronous? *Earth Planet. Sci. Lett*. 258, 114–131.

Hopkins, M., Harrison, T.M., Manning, C.E., 2008. Low heat flow inferred from >4 Gyr zircons suggests Hadean plate boundary interactions. *Nature* 456, 493–496.

Huston, D.L., Logan, G.A., 2004. Barite, BIFs and bugs: evidence for the evolution of the Earth's early hydrosphere. *Earth Planet. Sci. Lett.* 220, 41–55.

Jaffrés, J.B.D., Shields, G.A., Wallmann, K., 2007. The oxygen isotope evolution of seawater: A critical review of a long-standing controversy and an improved geological water cycle model for the past 3.4 billion years. *Earth-Sci. Rev.* 83, 83–122.

Jahnke, R.A., 1984. The synthesis and solubility of carbonate fluorapatite. *Am. J. Sci.* 284**,** 58–78.

Jiang, G., Kennedy, M.J., Christie-Blick, M., Wu, H., Shang, S., 2006. Stratigraphy, sedimentary structures, and textures of the Late Neoproterozoic Doushantuo cap carbonate in South China. *J. Sed. Res.* 76, 978–995.

Johnston, D.T., Wolfe-Simon, F., Pearson, A., Knoll, A.H., 2009. Anoxygenic photosynthesis modulated Proterozoic oxygen and sustained Earth's middle age. *Proc. Nat. Acad. Sci. USA* 106, 16925–16929.

Kampschulte, A., Strauss, H., 2004. The sulfur isotopic evolution of Phanerozoic seawater based on the analysis of structurally substituted sulfate in carbonates. *Chem. Geol*. 204, 255–286.

Kaufman, A.J. et al., 2007. Late Archean biospheric oxygenation and atmospheric evolution. *Science* 317, 1900–1903.

Kaźmierczak, J., Kremer, B., Altermann, W., Franchi, I., 2016. Tubular microfossils from ~2.8 to 2.7 Ga-old lacustrine deposits of South Africa: A sign for early origin of eukaryotes? *Precambrian Res.* 286, 180–194.

Kendall, B. et al., 2010. Pervasive oxygenation along late Archaean ocean margins. *Nature Geosci.* 3, 647–652.

Kennedy, M.J., Runnegar, B., Prave, A.R., Hoffmann, K.-H., Arthur, M.A., 1998. Two or four Neoproterozoic glaciations? *Geology* 26, 1059–1063.

Kirschvink, J.L., Ripperdan, R.L., Evans, D.A., 1997. Evidence for a large-scale reorganization of Early Cambrian continental masses by inertial interchange true polar wander. *Science* 277, 541–545.

Knauth, L.P., 2005. Temperature and salinity history of the Precambrian ocean: implications for the course of microbial evolution. *Palaeogeog. Palaeocl*. 219, 53–69.

Knoll, A. H., 2003. Biomineralization and evolutionary history. *Rev. Min. Geochem.* 54, 329–356.

Kranz, S.A., Sültemeyer, D., Richter, K.U, Rost, B., 2009. Carbon acquisition by Trichodesmium: The effect of pCO2 and diurnal changes. *Limnol. Oceanogr*. 54, 548–559.

Kurzweil, F. et al., 2013. Atmospheric sulfur rearrangement 2.7 billion years ago: Evidence for oxygenic photosynthesis. *Earth Planet. Sci Lett.* 366, 17–26.

Kump, L.R., Barley, M.E., 2007. Increased subaerial volcanism and the rise of atmospheric oxygen 2.5 billion years ago. *Nature* 448, 1033–1036.

Lan, Z. et al., 2014. A rapid and synchronous initiation of the wide spread Cryogenian glaciations. *Precambrian Res.* 255, 401–411.

Le Hir, G. et al., 2009. The snowball Earth aftermath: Exploring the limits of continental weathering processes. *Earth Planet. Sci. Lett.* 277, 453–463.

Leavitt, W.D., Halevy, I., Bradley, A.S., Johnston, D.T., 2013. Influence of sulfate reduction rates on the Phanerozoic sulfur isotope record. *Proc. Nat. Acad. Sci. USA* 110, 11244–11249.

Lee, C.T.A. et al., 2013. Continental arc–island arc fluctuations, growth of crustal carbonates, and long-term climate change. *Geosphere* 9, 1–36.

Lee, H. et al., 2016. Massive and prolonged deep carbon emissions associated with continental rifting. *Nature Geosci.* 9, 145–150.

Lee, J., Morse, J.W., 2010. Influences of alkalinity and *p*CO2 on CaCO3 nucleation from estimated Cretaceous composition seawater representative of “calcite seas”. *Geology* 38, 115–118.

Li, Z.X., Evans, D.A.D., Halverson, G.P., 2013. Neoproterozoic glaciations in a revised global palaeogeography from the breakup of Rodinia to the assembly of Gondwanaland. *Sed. Geol.* 294, 219–232.

Lyons, T.W., Reinhard, C.T., Planavsky, N.J., 2014. The rise of oxygen in Earth’s early ocean and atmosphere. *Nature* 506, 307–315.

Macdonald, F.A., Strauss, J.V., Rose, C.V., Dudas, F.O., Schrag, D.P., 2010a. Stratigraphy of the Port Nolloth Group of Namibia and South Africa and implications for the age of Neoproterozoic iron formations. *Am. J. Sci.* 310, 862–888.

Macdonald, F.A. et al., 2010b. Calibrating the Cryogenian. *Science* 327, 1241–1243.

Macdonald, F.A. et al., 2013. The stratigraphic relationship between the Shuram carbon isotope excursion, the oxygenation of Neoproterozoic oceans, and the first appearance of the Ediacara biota and bilaterian trace fossils in northwestern Canada. *Chem. Geol.* 362, 250–272.

Mackey, K., Paytan, A. Grossman, A.R., Bailey, S., 2008. A photosynthetic strategy for coping in a high-light, low-nutrient environment. *Limnol. Oceanogr*. 53, 900–913.

Maliva, R.G., Knoll, A.H., Simonson, B.M., 2005. Secular change in the Precambrian silica cycle: insights from chert petrology. *GSA Bull*. 117, 835–845.

Maloof, A.C. et al., 2006. Combined paleomagnetic, isotopic, and stratigraphic evidence for true polar wander from the Neoproterozoic Akademikerbreen Group, Svalbard, Norway. *GSA Bull.* 118, 1099–1124.

Martin, A.P. et al., 2015. Multiple Palaeoproterozoic carbon burial episodes and excursions. *Earth Planet. Sci. Lett.* 424, 226–236.

McGee, B., Collins, A.S., Ricardo, I.F., Trindade, R.I.F., 2013. A glacially incised canyon in Brazil: Further evidence for mid-Ediacaran glaciation? *J. Geol.* 121, 275–287.

Meyer, K.M., Kump, L.R., 2008. Ocean euxinia in Earth history: causes and consequences. *Annu. Rev. Earth Planet. Sci.* 36, 251–88.

Mills, M.M., Ridame, C., Davey, M., La Roche, J., Geider, R.J., 2004. Iron and phosphorus co-limit nitrogen fixation in the eastern tropical North Atlantic. *Nature* 429, 292–294.

Mitchell, R.N., Evans, D.A.D., Kilian, T.M., 2010. Rapid Early Cambrian rotation of Gondwana. *Geology* 38, 755–758.

Morse, J.W., Wang, Q., Tsio, M.Y., 1997. Influences of temperature and Mg:Ca ratio on the mineralogy of $CaCO_3$ precipitates from seawater. *Geology* 25, 85–87.

Mustard, P.S., 1991. Normal faulting and alluvial-fan deposition, basal Windermere Tectonic Assemblage, Yukon, Canada. *GSA Bull.* 103, 1346-1364.

Nakamura, K., Kato, Y., 2004. Carbonatization of oceanic crust by the seafloor hydrothermal activity and its significance as a CO_2 sink in the Early Archean. *Geochim. Cosmochim. Acta* 68, 595-4618.

Nijman, W., de Bruijne, K.C.H., Valkering, M.E., 1999. Growth fault control of early Archaean cherts, barite mounds and chert-barite veins, North Pole Dome, eastern Pilbara, Western Australia. *Precambrian Res*. 88, 25–52.

Noffke, N., Eriksson, K.A., Hazen, R.M., Simpson, E.L., 2006. A new window into Early Archean life: Microbial mats in Earth's oldest siliciclastic tidal deposits (3.2 Ga Moodies Group, South Africa). *Geology* 34, 253–256.

Ohmoto, H., Felder, R.P., 1987. Bacterial activity in the warmer, sulphate-bearing, Archaean oceans. *Nature* 328, 244–246.

Ohmoto, H., Watanabe, Y., Ikemi, H., Poulson, S.R., Taylor, B.E., 2006. Sulphur isotope evidence for an oxic Archaean. *Nature* 442, 908–911.

Ono, E., Cuello, J.L., 2007. Carbon dioxide mitigation using thermophilic cyanobacteria. *Biosys. Eng.* 96, 129–134.

Paerl, H.W., Hulsman, J., 2007. Climate change: a catalyst for global expansion of harmful cyanobacterial blooms. *Environ. Microbiol. Rep*. 1, 27–37.

Partin, C.A. et al., 2013. Large-scale fluctuations in Precambrian atmospheric and oceanic oxygen levels from the record of U in shales. *Earth Planet. Sci. Lett.* 339–370, 284–293.

Penman, D.E. et al., 2016. An abyssal carbonate compensation depth overshoot in the aftermath of the Palaeocene–Eocene Thermal Maximum. *Nature Geosci*. 9, 575–580.

Planavsky, N.J. et al. 2010. The evolution of the marine phosphate reservoir. *Nature* 467, 1088–1090.

Planavsky, N.J. et al., 2014. Evidence for oxygenic photosynthesis half a billion years before the Great Oxidation Event. *Nature Geosci*. 7, 283–286.

Phipps Morgan, J., 1998. Thermal and rare gas evolution of the mantle. *Chem. Geol*. 145, 431–445.

Preiss, W.V., Dyson, I.A., Reid, P.W., Cowley, W.M. 1998. Revision of lithostratigraphic classification of the Umberatana Group. *MESA (Mines and Energy South Australia) Journal* 9, 36–42.

Pruss, S.B., Finnegan, S., Fischer, W.W., Knoll, A.H., 2010. Carbonates in skeleton-poor seas: new insights from Cambrian and Ordovician strata of Laurentia. *Palaios* 25, 73–84.

Rasmussen, B., 2005. Evidence for pervasive petroleum generation and migration in 3.2 and 2.63 Ga shales. *Geology* 33, 497–500.

Reinhard, C.T., Raiswell, R., Scott, C., Anbar, A.D., Lyons, T.W., 2009. A late Archean sulfidic sea stimulated by early oxidative weathering of the continents. *Science* 326, 713–716.

Reinhard, C.T. et al., 2013. Proterozoic ocean redox and biogeochemical stasis, *Proc. Nat. Acad. Sci. USA* 110, 5357–5362.

Riding, R., Fralick, P., Liang, L., 2014. Identification of an Archean marine oxygen oasis. *Precambrian Res.* 252, 232–237.

Roerdink, D.L., Mason, P.R.D., Farquhar, J., Reimer, T., 2012. Multiple sulfur isotopes in Paleoarchean barites identify an important role for microbial sulfate reduction in the early marine environment. *Earth Planet. Sci. Lett.* 331–332, 177–186.

Rooney, A.D. et al., 2014. Re-Os geochronology and coupled Os-Sr isotope constraints on the Sturtian snowball. *Proc. Nat. Acad. Sci. USA* 111, 51–56.

Rooney, A.D., Strauss, J.V., Brandon, A.D., Macdonald, F.A., 2015. A Cryogenian chronology: Two long-lasting synchronous Neoproterozoic glaciations. *Geology* 43, 459–462.

Rosing, M.T., Frei, R., 2004. U-rich Archaean sea-floor sediments from Greenland – indications of > 3700 Ma oxygenic photosynthesis. *Earth Planet. Sci. Lett.* 217, 237–244.

Saito, M.A., Sigman, D.M., Morel, F.M.M., 2003. The bioinorganic chemistry of the ancient ocean: the co-evolution of cyanobacterial metal requirements and biogeochemical cycles at the Archean–Proterozoic boundary? *Inorg. Chim. Acta* 356, 308–318.

Sansjofre, P. et al., 2011. A carbon isotope challenge to the snowball Earth. *Nature* 478, 93–97.

Santosh, M., Omori, S., 2008. CO_2 flushing: A plate tectonic perspective. *Gondwana Res*. 13, 86–102.

Saputro, S. Et al., 2014. Speciation of dissolved chromium and the mechanisms controlling its concentration in natural water. *Chem. Geol.* 364, 33–41.

Satkoski, A.M., Beukes, N.J., Li, W., Beard, B.L., Johnson, C.M., 2015. A redox-stratified ocean 3.2 billion years ago. *Earth Planet. Sci. Lett.* 430, 33–53.

Schidlowski, M., 1984. Early atmospheric oxygen levels: constraints from Archaean photoautotrophy. *J. Geol. Soc. Lond.* 141, 243–250.

Shen, Y., Farquhar, J., Masterson, A., Kaufman, A.J., Buick, R., 2009. Evaluating the role of microbial sulfate reduction in the early Archean using quadruple isotope systematics. *Earth Planet. Sci. Lett.* 279, 383–391.

Shibuya, T. et al., 2012. Depth variation of carbon and oxygen isotopes of calcites in Archean altered upper oceanic crust: Implications for the CO_2 flux from ocean to oceanic crust in the Archean. *Earth Planet. Sci. Lett.* 321–322, 64–73.

Shields, G.A., 2005. Neoproterozoic cap carbonates: a critical appraisal of existing models and the *plumeworld* hypothesis. *Terra Nova* 17, 299–310.

Shields, G.A., Kimura, H., Yang, J., Gammon, P., 2004. Sulphur isotopic evolution of Neoproterozoic-Cambrian seawater: new francolite-bound sulphate $\delta^{34}S$ data and a critical appraisal of the existing record. *Chem. Geol.* 204, 163–182.

Shields-Zhou, G.A., Porter, S., Halverson, G.P., 2016. A new rock-based definition for the Cryogenian Period (circa 720 – 635 Ma). *Episodes* 39, 3–8.

Siahi, M., Hofmann, A., Hegner, E., Master, S., 2016. Sedimentology and facies analysis of Mesoarchaean stromatolitic carbonate rocks of the Pongola Supergroup, South Africa. *Precambrian Res.* 278, 244–264.

Sleep, N.H., Zahnle, K.J., Kastling, J.F., Morowitz, H.J., 1989. Annihilation of ecosystems by large asteroid impacts on the Early Earth. *Nature* 342, 139–142.

Sorokin D.Y. et al., 2014. Microbial diversity and biogeochemical cycling in soda lakes. *Extremophiles* 18, 791–809.

Sossi, P. et al., 2016. Petrogenesis and geochemistry of Archean komatiites. *J. Petrol.* 57, 147–184.

Spencer, C.J. et al., 2014. Proterozoic onset of crustal reworking and collisional tectonics: Reappraisal of the zircon oxygen isotope record. *Geology* 42, 451–454.

Spivack, A.J., Staudigel, H., 1994. Low-temperature alteration of the upper oceanic crust and the alkalinity budget of seawater. *Chem. Geol.* 115, 239–247.

Stern, R.S., Johnson, P.R., Ali, K.A., Mukherjee, S.K., 2011. Evidence for Early and Mid-Cryogenian glaciation in the Northern Arabian -Nubian Shield (Egypt, Sudan, and western Arabia). In: E. Arnaud, G.P. Halverson, G. Shields-Zhou (eds), *The Geological Record of Neoproterozoic Glaciations*, Geol. Soc. Lond. Mem. 36, 277–284.

Stomp, M. et al., 2007. Colourful coexistence of red and green picocyanobacteria in lakes and seas. *Ecol. Lett.* 10, 290–298.

Sumner, D.Y., Grotzinger, J.P., 2000. Late Archean aragonite precipitation: petrography, facies associations, and environmental significance. In: J.P. Grotzinger, N.P. James (eds), *Carbonate Sedimentation and Diagenesis in the Evolving Precambrian World*, SEPM Spec. Pub. 67, 123–144.

Swanson-Hysell, N.L. et al., 2012. Constraints on Neoproterozoic paleogeography and Paleozoic orogenesis from paleomagnetic records of the Bitter Springs Formation, Amadeus Basin, central Australia. *Am. J. Sci.* 312, 817–884.

Swart, P.K., Oehlert, A.M., Mackenzie, G.J., Eberli, G.P., Reijmer, J.J.G., 2014. The fertilization of the Bahamas by Saharan dust: A trigger for carbonate precipitation? *Geology* 42, 671–674.

Tang, M., Chen, K., Rudnick, R.L., 2016. Archean upper crust transition from mafic to felsic marks the onset of plate tectonics. *Science* 351, 372–375.

Tartèse, R., Chaussidon, M., Gurenko, A., Delarue, F., Robert, F., 2017. Warm Archean oceans reconstructed from oxygen isotope composition of early-life remnants. *Geochem. Persp. Let.* 3, 55–65.

Tice, M.M., Lowe, D.R., 2004. Photosynthetic microbial mats in the 3,416-Myr-old ocean. *Nature* 431, 549–552.

Tomkins, A.G. et al., 2016. Ancient micrometeorites suggestive of an oxygen-rich Archaean upper atmosphere. *Nature* 533, 235–238.

Trompette, R., 1981. Late Precambrian tillites of the Volta Basin and the Dahomeyides Orogenic Belt (Benin, Ghana, Niger, Togo and Upper Volta). In: M.J. Hambrey, W.B. Harland (eds), *Earth's Pre-Pleistocene Glacial Record*, Cambridge University Press, Cambridge, pp 135–139.

Turner, E.C., Bekker, A., 2016. Thick sulfate evaporite accumulations marking a mid-Neoproterozoic oxygenation event (Ten Stone Formation, Northwest Territories, Canada). *GSA Bull.* 128, 203-222.

Ueno, Y., Ono, S., Rumble, D., Maruyama, S., 2008. Quadruple sulfur isotope analysis of ca. 3.5 Ga Dresser Formation: New evidence for microbial sulfate reduction in the early Archean. *Geochim. Cosmochim. Acta* 72, 5675–5691.

Valley, J.W., 2005. A cool early Earth? *Sci. Am.* (Oct) 293, 58–65.

Veizer, J., Compston, W., Hoefs, J., Nielsen, H., 1982. Mantle buffering of the early oceans. *Naturwissenschaften* 69, 173–180.

Veizer, J., Hoefs, J., Ridler, R.H., Jensen, L.S., Lowe, D.R., 1989a. Geochemistry of Precambrian carbonates: I. Archean hydrothermal systems. *Geochim. Cosmochim. Acta* 53, 845–857.

Veizer, J., Hoefs, J., Lowe, D.R., Thurston, P.C., 1989b. Geochemistry of Precambrian carbonates: II. Archean greenstone belts and Archean seawater. *Geochim. Cosmochim. Acta* 53, 859–871.

Wacey, D., Kilburn, M.R., Saunders, M., Cliff, J., Brasier, M.D., 2011a. Microfossils of sulphur-metabolizing cells in 3.4-billion-year-old rocks of Western Australia. *Nature Geosci.* 4, 698–702.

Wacey, D., Saunders, M., Brasier, M.D., Kilburn, M.R., 2011b. Earliest microbially mediated pyrite oxidation in ~3.4 billion-year-old sediments. *Earth Planet. Sci. Lett.* 301, 393–402.

Walker, J.C., Hays, P., Kasting, J.F., 1981. A negative feedback mechanism for the longterm stabilization of Earth's surface temperature. *J Geophys Res* 86, 9776–9782.

Wang, J., Jiang, J., Xiao, S., Li, Q., Wei, Q., 2008. Carbon isotope evidence for widespread methane seeps in the ca. 635 Ma Doushantuo cap carbonate in south China. *Geology* 36, 347–350.

Watanabe, Y., Naraoka, H., Wronkiewicz, D.J., Condie, K.C., Ohmoto, H., 1997. Carbon, nitrogen, and sulfur geochemistry of Archean and Proterozoic shales from the Kaapvaal Craton, South Africa. *Geochim. Cosmochim. Acta* 61, 3441–3459.

West, A.J., Galy, A., Bickle, M., 2005. Tectonic and climatic controls on silicate weathering. *Earth Planet. Sci. Lett.* 235, 211 –228.

Whitehill, A.R., Jiang, B., Guo, H., Ono, S., 2015. SO_2 photolysis as a source for sulfur mass-independent isotope signatures in stratospheric aerosols. *Atmos. Chem. Phys*. 15, 1843–1864.

Williford, K.H., Van Kranendonk, M.J., Ushikubo, T., Kozdon, R., Valley, J.W., 2011. Constraining atmospheric oxygen and seawater sulfate concentrations during Paleoproterozoic glaciation: In situ sulfur three-isotope

microanalysis of pyrite from the Turee Creek Group, Western Australia. *Geochim. Cosmochim. Acta* 75, 5686–5705.

Wyllie, P.J., Huang, W.L., 1975. Influence of mantle CO_2 in the generation of carbonatites and kimberlites. *Nature* 257, 297–299.

Xu, B. et al., 2009. SHRIMP zircon U–Pb age constraints on Neoproterozoic Quruqtagh diamictites in NW China. *Precambrian Res.* 168, 247–258.

Zahnle, K., Sleep, N.H., 2002. Carbon dioxide cycling through the mantle and implications for the climate of ancient Earth. In: C.M.R. Fowler, C.J. Ebinger, C.J. Hawkesworth (eds), *The Early Earth: Physical, Chemical and Biological Development.* Geol. Soc. Lond. Spec. Pub. 199, 231–257.

Zehr, J.P., Jenkins, B.D., Short, S.M., Steward, G.F., 2003. Nitrogenase gene diversity and microbial community structure: a cross-system comparison. *Environ. Microbiol.* 5, 539–554.

Zerkle, A.L., Claire, M.W., Domagal-Goldman, S.D., Farquhar, J., Poulton, S.W., 2012. A bistable organic-rich atmosphere on the Neoarchaean Earth. *Nature Geosci.* 5, 359–363.

Acknowledgements

I am indebted to the National Environment Research Council, who sponsored my research as part of a 4-year multi-disciplinary program entitled 'The Long-term Co-evolution of Life and the Planet'. The program encompassed four areas, one of which was 'The Neoproterozoic revolution in oxygenation, biogeochemistry and biological complexity'. My studentship fell broadly under this heading. The project gave me exposure to some of the most significant questions that geochemistry can address in relation to that critical time, and I felt very privileged.

I am indebted to my supervisor, Graham Shields-Zhou, for being brave enough to take me on as a research student, bearing in mind that I was advanced in years and something of an unknown quantity. While there were times when he may have regretted the decision, I never regretted mine. For all our differences of opinion, he gave me a lot of latitude, and for that I am grateful.

This work would also not have been possible without the expert assistance of staff in the laboratories, namely Jim Davy, Gary Tarbuck and Anne-Lise Jourdan at UCL, and Christina Manning and Matthew Thirlwall at Royal Holloway. To them I am also indebted. Lastly, I thank Heinrich Bahlburg for making available the major and trace element data underlying the two papers published by him and Nicole Dobrzinski (Chapter 8).

Appendix 1. Data for Jiuliqiao, Sidingshan and Zhaowei Formations

Sample	Height	Fe	Mg	Ca	K	Mn	Sr	%carb	$\delta^{13}C$	$\delta^{18}O$	TOC	$\delta^{13}C_{org}$
					ICP-OES				IRMS		Org C	
Jiuliqiao Formation												
JLQ 1	0	8507	1.3	16.25	4544	165	93	45.22	2.35	-5.7	0.11	-28.59
Ji 2	1								2.38	-5.86	0.03	
Ji3	3								2.50	-5.72	0.03	
Ji 4	4								2.56	-5.62	0.04	-27.85
Ji 5	5.5								2.26	-6.25	0.04	-28.55
JLQ 2	10.1	9356			824	266	206		2.62	-5.01		
JLQ 3	11.3	5491	1.5	17.73	6067	134	145	49.54	2.47	-6.15		
JLQ 4	12.5	4086	0.8	30.89	748	151	365	79.95	1.98	-5.58		
JLQ 5	13.7	5918	2.0	32.54		197	267	88.29	2.40	-5.55		
JLQ 6	14.9	3665	1.0	28.64	1515	145	203	75.14	2.58	-5.89	0.04	
JLQ 7	16.1	3644	0.7	23.90	1372	145	168	62.34	1.87	-4.93		
JLQ 8	17.3	5285	0.8	11.32		106	65	31.21	2.28	-6.7		
JLQ 9	19.1	2384	0.2	21.92	2190	126	102	55.50	1.82	-6.18	0.05	-28.29
JLQ 10	20.4	5184	1.0	22.90	2314	140	149	60.71	2.62	-5.42	0.03	
Ji 9	21.5								2.65	-4.71		
Ji 10	22.52											
JLQ 11	22.4	8103	1.9	20.32	2638	171	132	57.57	2.87	-4.73	0.14	-29.04
JLQ 12	23.6	7364			3564	211	170		2.82	-5.33	0.17	-29.10
JLQ 13	24.8	6560	1.7	20.42	2660	151	133	56.99	2.88	-6.04	0.06	-27.84
JLQ 14	26	6812	1.7	21.06	3119	154	139	58.42	2.85	-5.44		
JLQ 15	27.1	3382	0.9	26.59	1563	137	195	69.64	2.38	-5.54	0.05	-27.31
JLQ 16	28.4	3607	0.7	26.88	1421	166	283	69.58	2.26	-4.99		
JLQ 17	29.8	5266	1.4	18.59	2044	125	165	51.46	2.61	-5.34	0.07	
JLQ 18	31.57	3925	0.8	26.38	1500	182	259	68.92	2.32	-4.75	0.07	-28.16
JLQ 19	32.8	4085	1.0	29.45	1160	145	221	76.96	2.44	-4.92		
JLQ 20	34	3020	0.9	23.95	1234	106	198	63.13	2.51	-5.14		
JLQ 21	35	2727	1.2	30.78	989	151	265	81.02	2.56	-5.18	0.05	-26.71
JLQ 22	36	4150	1.9	**21.02**	1620	128	190	59.10	2.70	-5.25		
JLQ 23	38	948	0.2	**23.10**	1912	83	163	58.35	0.50	-7.47		
JLQ 24	39	1012	0.1	30.97	928	92	173	77.94	0.16	-7.37	0.03	-28.45
JLQ 25	40.5	3102	0.8	31.35	616	142	150	81.28	2.03	-6.38	0.08	-28.19
Si 1	42								2.48	-3.91	0.11	-28.25
Si 2	44								2.73	-4.89	0.05	-27.38
Si 3	47								2.49	-5.05	0.05	
Si 4	49								2.75	-4.45	0.05	-27.10
Si 5	51								2.81	-3.95	0.03	-28.75
JLQ 26	53	3155	0.6	29.95	1145	173	345	77.15	2.22	-4.3	0.05	-29.14
JLQ 27	58	4248	1.1	22.46	1814	104	136	59.82	2.75	-5.09	0.08	-29.32
JLQ 28	62.5	5487	1.4	17.79	4074	97	107	49.35	2.62	-5.86	0.05	-29.26
JLQ 29	69.5	5036	2.0	17.13	4373	113	117	49.79	2.62	-5.68	0.02	-28.70
JLQ 30	73.5	2122	0.4	32.18	587	108	304	81.99	1.81	-5.79	0.02	-28.92
JLQ 31	88.5	1150	1.1	31.93	560	88	87	83.71	1.43	-8.01		
Sidingshan Formation												
JLQ 32	96.5	3483			1823	113	50		2.36	-6.14	0.03	-28.78
JLQ 33	101.5	3283			1901	67	34		3.09	-5.08	0.01	-27.96
JLQ 34	106.5	576			235	49	21		3.28	-4.37		
JLQ 35	112.5	2292			986	61	26		3.72	-3.63	0.02	-25.81
JLQ 36	118.5	1201			573	27	27		3.43	-2.58	0.01	-25.17
JLQ 37	119.5	1347			142	76	28		3.40	-3.67	0.01	-26.44
JLQ 38	121.5	1171			371	33	28		3.35	-3.19		-27.71
JLQ 39	124.5	1202			224	41	27		3.31	-3.31	0.01	-26.02
JLQ 40	126.5	588			116	19	28		3.42	-2.94	0.02	-28.79

Mg	Ca	Si	Al	K	Fe	S	%carb	Mg	Si	Ca	K	Fe	S	Al
Bulk ion probe mapping								Carbonate spot ion probe analysis						
1.02	7.74	30.99	5.42	3.26	1.07	0.07	22.11	1.15	12.24	25.78	1.11	0.85	0.075	2.56
3.20	18.96	17.88	3.84	2.82	1.93	0.12	54.20	3.87	7.29	26.50	1.24	1.35	0.073	1.86
1.43	15.19	24.51	3.49	3.18	0.88		40.51	3.99	7.02	26.40	0.93	1.36	0.102	1.45
0.87	36.13	7.43	1.84	1.52	0.73	0.09	81.04	3.61	1.61	32.53	0.47	0.83	0.061	0.62
1.78	25.74	15.64	2.76	2.03	0.92	0.12	62.95	2.58	7.08	28.66	0.87	0.95	0.065	1.52
1.23	36.68	7.47	1.87	1.07	0.66	0.09	82.08	5.64	2.63	28.80	0.42	0.87	0.071	0.67
0.92	35.88	8.65	1.55	1.24	0.63	0.03	80.13	2.84	3.73	31.70	0.60	0.74	0.052	0.87
0.80	10.31	30.68	3.71	3.23	0.75	0.15	27.10	2.33	11.94	24.82	1.18	0.71	0.096	1.71
0.39	25.82	15.49	3.34	2.22	0.94	0.05	60.83	0.24	5.85	33.37	0.86	0.55	0.030	1.33
1.18	29.20	11.03	3.98	1.71	0.94	0.07	69.61	2.77	5.22	29.41	0.80	1.04	0.057	2.81
1.36	35.40	8.81	1.66	1.34	0.69	0.08	79.66	3.55	3.27	30.78	0.54	1.23	0.063	0.76
2.37	25.32	12.44	3.12	2.27	1.48	0.10	66.80	3.80	5.01	28.89	0.92	1.17	0.051	1.36
2.09	24.85	15.10	2.94	2.64	1.06	0.04	62.60	3.74	6.51	27.34	1.16	1.07	0.082	1.44
2.13	24.48	14.84	3.51	2.73	1.35	0.08	62.05	3.36	7.29	26.71	1.35	1.33	0.093	1.94
1.25	30.53	10.93	2.43	1.81	0.75	0.04	72.62	2.60	4.89	30.72	0.81	0.76	0.087	1.43
0.76	35.09	8.45	1.65	1.38	0.81	0.04	79.69	2.09	3.91	32.54	0.63	0.81	0.068	0.81
2.08	22.31	16.28	3.50	2.65	1.50	0.11	58.32	3.68	7.88	25.86	1.32	1.24	0.075	1.92
1.21	32.19	10.24	2.25	1.62	1.01	0.03	74.98	3.00	4.66	30.36	0.72	0.97	0.051	1.10
1.22	37.26	6.21	2.17	1.06	0.83	0.09	83.85	3.35	2.77	31.86	0.54	0.86	0.064	0.90
1.32	33.09	8.77	1.85	1.36	0.65	0.11	78.39	3.31	3.52	31.24	0.60	0.73	0.086	0.87
1.49	36.96	5.43	1.78	1.22	0.61	0.06	85.46	2.95	3.11	32.01	0.70	0.64	0.064	1.15
2.46	27.04	11.91	4.58	1.97	0.88	0.09	67.46	4.07	5.36	27.56	0.89	1.00	0.095	2.66
0.32	26.98	14.13	3.44	2.49	1.16	0.04	63.20	0.31	6.44	32.42	1.06	0.68	0.050	1.72
0.21	39.16	5.18	1.38	0.79	0.45	0.03	86.97	0.21	2.33	37.06	0.38	0.31	0.036	0.73
0.90	42.42	3.85	1.22	0.64	0.43	0.09	90.54	3.50	1.80	32.90	0.27	0.57	0.063	0.42
0.94	38.14	5.35	1.99	0.97	0.62	0.04	85.64	3.37	2.58	32.11	0.43	0.56	0.057	1.01
1.49	28.51	11.65	2.94	2.06	1.27	0.11	69.74	3.45	5.25	29.17	0.90	1.03	0.073	1.60
1.38	17.38	21.33	6.06	4.17	1.29	0.07	43.54	4.59	5.01	27.10	0.92	1.53	0.050	1.61
1.89	19.23	19.50	4.14	3.78	1.36	0.04	50.21	3.68	7.50	26.12	1.50	1.24	0.049	1.89
0.69	38.11	5.70	1.20	1.21	0.48	0.04	85.88	4.41	1.51	31.48	0.46	0.95	0.044	0.42
2.26	37.47	5.36	1.46	1.23	0.53	0.06	85.11	5.16	2.10	30.14	0.44	0.58	0.041	0.68
12.15	23.37	6.95	2.55	1.97	0.82	0.03	81.78	11.57	2.06	21.21	0.60	0.41	0.026	1.05
12.05	24.27	6.17	1.80	1.68	0.59	0.06	84.56	11.27	2.44	21.25	0.69	0.53	0.039	0.82
13.84	25.89	2.74	1.05	0.78	0.35	0.05	92.71	11.85	1.28	21.81	0.31	0.38	0.051	0.58
13.38	25.88	3.06	0.67	0.68	0.37	0.02	92.74	11.71	1.28	21.89	0.26	0.53	0.043	0.59
14.41	27.07	1.68	0.82	0.46	0.31	0.02	95.34	12.03	0.79	22.02	0.19	0.21	0.050	0.39
14.40	27.81	0.89	0.62	0.22	0.25	0.04	97.25	11.98	0.45	22.63	0.11	0.25	0.044	0.34
13.90	26.63	1.40	1.67	0.43	0.30	0.01	94.49	12.03	0.64	22.01	0.18	0.17	0.023	0.88
14.35	29.68	1.36	0.53	0.31	0.34	0.04	96.60	11.61	0.87	22.77	0.11	0.29	0.040	0.28
								11.57	0.61	22.91	0.11	0.20	0.090	0.81

Sample	Height	Fe	Mg	Ca	K	Mn	Sr	%carb	$\delta^{13}C$	$\delta^{18}O$	TOC	$\delta^{13}C_{org}$
		ICP-OES							IRMS		Org C	
Sidingshan Formation (cont.)												
JLQ 41	128.5	413			171	13	34		3.43	-2.74	0.002	-26.34
JLQ 42	130.5	919			621	25	25		3.40	-3.66	0.03	-27.22
JLQ 43	133	815			639	28	34		3.13	-3.22	0.02	-26.80
JLQ 44	137	824			393	51	24		3.23	-3.63	0.01	-26.22
JLQ 45	143	306			100	29	20		3.37	-5.73	0.06	-25.21
JLQ 46	145	355			183		34		4.11	-2.78	0.03	-26.51
JLQ 47	147	524			714	19	114		4.14	-2.75	0.05	-26.21
JLQ 48	149	345			75	9	35		4.41	-3.12	0.05	-26.01
JLQ 49	160	550			355	16	44		4.07	-2.97	0.05	-25.92
JLQ 50	162.5	825			188	32	37		3.86	-3.88	0.04	-25.58
JLQ 51	164.5	766			129	33	37		3.81	-3.53	0.03	-25.79
2M-1	165.3	603	10.94	21.32	227		55	91.3	2.87	-3.34		
2M-2	167.2								3.09	-3.26		
JLQ 52	169	471			278	15	71		2.94	-2.11	0.03	-25.85
2M-3	169.7	1153	8.98	17.53	1868		50	75.1	2.49	-2.87		
2M-4	169.95	580	8.32	16.69	2022		47	70.6	2.57	-4.70		
2M-5	170.55								2.49	-2.58		
2M-6	170.95	759	10.55	20.76	341		52	88.6	2.64	-2.77		
2M-7	171.55								2.69	-2.31		
2M-8	171.9	894	9.66	19.17	547		49	81.5	2.64	-3.14		
2M-8a	172.55	742	8.04	16.18	1411		38	68.4	2.61	-3.57		
2M-9	172.6	1226	11.21	22.63	90		55	95.6	2.71	-3.15		
2M-10	173.1								2.60	-3.19		
JLQ 53	174.5	951			1219	83	55		1.27	-3.65	0.02	-26.34
JLQ 54	178.5	1575			821	75	38		1.40	-3.58	0.02	-27.39
JLQ 55	180	2468			732	104	27		1.75	-4.19	0.02	-27.00
JLQ 56	182.5	1443			535	94	32		1.75	-3.32	0.03	-26.83
JLQ 57	183.5	763			139	43	39		3.67	-3.85	0.01	-27.20
JLQ 58	188	1632			504	77	43		2.24	-3.95	0.02	-26.43
JLQ 59	191.5	464			113	45	21		3.31	-4.77	0.04	-27.20
JLQ 60	194.5						32		3.11	-3.98	0.02	-26.98
JLQ 61	196.5	441			96	53	19		3.64	-3.99	0.04	-27.70
JLQ 62	198.5	318			148	36	24		3.41	-5.52	0.02	-26.79
JLQ 63	200.5	471			412	32	32		3.25	-5.23	0.04	-26.95
JLQ 64	201.5	558			173	34			3.25	-5.55	0.02	-27.18
JLQ 65	204	330			111	42	20		3.38	-6.06	0.03	-26.74
Zhaowei Formation												
ZW 12									3.80	-8.19		
ZW 22									3.77	-7.47		
ZW 45									3.69	-6.89		
ZW 51									3.85	-7.48		
ZW 61									4.00	-8.37		

Mg	Ca	Si	Al	K	Fe	S	%carb	Mg	Si	Ca	K	Fe	S	Al
			Bulk ion probe mapping							Carbonate spot ion probe analysis				
14.57	28.05	1.22	0.61	0.42	0.17	0.02	96.57	11.71	0.41	23.12	0.15	0.16	0.029	0.29
14.25	26.57	1.92	0.98	0.59	0.25	0.03	94.53	12.18	0.43	22.38	0.12	0.16	0.024	0.55
13.93	27.23	2.55	1.30	0.55	0.30	0.03	93.13	11.21	1.08	23.09	0.19	0.16	0.050	0.59
14.71	27.18	0.77	0.60	0.21	0.21	0.01	97.44	12.14	0.52	22.17	0.13	0.16	0.044	0.32
								11.66	0.19	23.47	0.04	0.09	0.041	0.32
14.25	27.28	1.66	1.58	0.29	0.08	0.04	94.44	11.83	0.71	22.50	0.12	0.08	0.034	0.97
14.40	26.83	1.56	0.76	0.16	0.15	0.09	95.93	12.25	0.20	22.66	0.05	0.11	0.028	0.20
15.27	27.85	0.49	0.14	0.08	0.12	0.04	98.81	11.99	0.33	22.92	0.04	0.13	0.037	0.19
15.09	29.30	0.54	0.33	0.08	0.08	0.02	98.50	11.71	0.33	23.02	0.06	0.10	0.037	0.50
14.52	27.26	1.90	0.28	0.05	0.19	0.03	96.19	12.11	1.03	21.98	0.11	0.16	0.031	0.21
14.37	27.25	2.75	0.35	0.12	0.12	0.02	94.64	11.76	1.39	22.06	0.04	0.12	0.034	0.21
13.80	25.41	3.39	0.47	0.15	0.12	0.004	93.02	11.83	1.74	21.81	0.12	0.16	0.062	0.29
11.94	22.11	8.61	0.89	0.76	0.28	0.02	82.11	11.73	3.09	20.65	0.20	0.21	0.022	0.36
12.62	24.48	5.88	1.52	0.62	0.27	0.04	86.63	11.24	2.98	21.27	0.28	0.28	0.049	0.68
13.58	25.97	3.35	1.27	0.42	0.53	0.015	91.75	11.40	1.58	22.04	0.18	0.46	0.048	0.92
							89	11.38	2.19	21.59	0.29	0.37	0.055	0.88
14.19	26.35	2.96	0.31	0.10	0.16	0.04	94.23	12.05	1.00	22.04	0.04	0.13	0.030	0.28
12.00	24.00	5.66	0.97	0.84	0.53	0.03	87.10	11.48	2.32	21.53	0.30	0.38	0.036	0.37
14.26	28.01	1.51	0.69	0.11	0.17	0.05	96.24	12.12	0.50	22.38	0.07	0.20	0.042	0.53
14.58	29.01	0.36	0.51	0.04	0.14	0.05	98.55	12.29	0.14	22.55	0.03	0.21	0.042	0.29
15.18	28.02	0.23	0.22	0.08	0.11	0.03	99.18	12.30	0.15	22.55	0.03	0.10	0.032	0.09
							97	12.42	0.33	22.26	0.07	0.10	0.026	0.36
							94	11.54	1.09	22.72	0.11	0.22	0.067	0.32
							97	12.27	0.35	22.42	0.05	0.18	0.041	0.28
15.32	27.40	0.36	0.24	0.05	0.09	0.02	98.94	12.71	0.17	21.96	0.04	0.06	0.015	0.14
5.60	36.75	2.30	0.64	0.23	0.30	0.02	94.55	5.74	1.22	30.58	0.15	0.27	0.020	0.40
							97	7.78	0.57	28.53	0.07	0.13	0.025	0.21
7.53	28.85	6.13	1.93	1.29	0.58	0.01	84.18	6.43	3.26	27.23	0.76	0.42	0.026	1.13
12.45	27.73	2.96	1.28	0.71	0.62	0.03	92.11	9.10	1.26	25.71	0.31	0.29	0.048	0.64
							98	5.36	0.73	31.67	0.14	0.20	0.033	0.22

Appendix 2. Data for Yingchenzi, Shisanlitai and Majiatun Formations

Sample	Height	Ca	Mg	Sr	Mn	K	Fe	% carb	$\delta^{13}C$	$\delta^{18}O$
		ICP-OES							IRMS	
Yingchenzi Formation										
13LH 1	0	36.4	0.18	145	206	84	379	91.67	2.09	-10.94
13LH 2	1	28.0	1.70	216	322	822	469	76.12	2.88	-9.36
13LH 3	3	35.1	0.24	269	274	290	432	88.73	2.78	-9.53
13LH 4	5	36.1	0.16	205	234	184	303	90.96	2.64	-9.64
13LH 5	7	33.4	0.88	244	306	809	985	86.72	3.05	-9.49
13LH 6	9	35.5	0.19	167	258	213	352	89.38	3.33	-9.97
13LH 7	11.5	34.7	0.42	169	326	324	773	88.39	2.66	-10.04
13LH 8 (d)	13.5	14.7	5.45	279	754	3493	14361	56.37	4.03	-5.66
13LH 9	15.5	19.3	0.92	133	575	2606	1966	52.04	1.43	-8.03
Shisanlitai Formation										
13LH 10	26.5	9.6	0.98	43	900	3652	1009	28.21	1.57	-5.60
13LH 11	28.5	30.2	0.19	254	1530	769	1401	76.70	1.33	-9.79
13LH 12	31	11.1	0.46	23	678	3751	646	30.05	1.74	-6.48
13LH 13	33	26.6	0.18	138	751	1485	2038	67.60	0.80	-9.31
13LH 14	36.5	33.4	0.17	171	1117	405	1461	84.39	2.28	-9.70
13LH 15	38	34.1	0.16	235	536	312	1411	86.04	2.25	-10.24
13LH 16	42									
13LH 17	47	0.3	0.04	8	56	3805	687	1.42		
13LH 18	53	32.7	0.15	134	890	448	677	82.52	1.46	-9.14
13LH 19	63									
Majiatun Formation										
13LH 20	64	27.6	0.18	107	533	768	791	69.90	-1.38	-9.37
13LH 21	68	30.2	0.38	412	308	604	1386	77.03	-1.90	-11.12
13LH 21c									-2.44	-15.51
13LH 22	71.5	18.3	0.10	52	147	788	244	46.23	-3.0	-9.3
13LH 22 (d)										
13LH 23	76.2	33.3	0.17	201	216	717	953	84.01	-4.1	-10.2
13LH 24	80.3	32.4	0.13	168	194	988	1549	81.65	-4.3	-9.1
13LH 25	83.4	29.9	1.79	193	316	909	6983	81.13	-4.4	-8.7
13LH 26	86.5	30.8	0.52	321	202	1289	1988	79.13	-5.0	-9.1
13LH 26 (d)										
13LH 27	89.6	29.4	2.04	232	221	1048	6333	80.69	-5.0	-8.9
13LH 28	92.7	19.0	2.00	89	293	2029	970	54.71	-3.0	-7.4
13LH 28 (d)										
13LH 29	93.7	28.8	1.54	220	346	1002	7723	77.47	-4.4	-9.1
13LH 30	95.8	21.9	4.17	154	651	848	16744	69.39	-4.0	-8.0
13LH 30 (d)										
13LH 31	97.8	32.4	0.17	243	170	832	1524	81.70	-5.3	-9.2
13LH 32	100.9	31.0	0.61	246	236	860	3801	79.85	-5.0	-8.8
13LH 33	102	32.4	0.16	227	154	624	1107	81.76	-5.4	-9.3
13LH 34	104	32.3	0.18	286	199	942	1750	81.61	-5.2	-8.9
13LH 35	110.2	33.6	0.15	188	835	309	3417	84.83	1.7	-9.6
Shisanlitai Formation										
LH 1	46							*85*	3.58	-9.48
LH 2	58							*84*	2.08	-9.32
LH 2 (d)								*84*		
LH 3	60							*82*	1.59	-9.97
Majiatun Formation										
LH 4	66							*77*	-1.74	-9.59
LH 5	72							*78*	-3.46	-8.14
LH 6	77							*75*	-4.60	-9.45
LH 7	80								-4.73	-8.81
LH 8	85								-4.96	-8.89
LH 9	91								-5.31	-9.25
LH 10	97							*80*	-5.33	-8.80
LH 10 (d)								*83*		
LH 11	104								-5.36	-9.10
LH 12	109								-3.93	-9.06
LH 13	114								-3.52	-9.07
LH 14	119							*66*	-3.35	-9.31

TOC %	$\delta^{13}C_{org}$	%carb	Mg	Si	Ca	Mn	K	Al	Fe	S
	Org C				Carbonate spot ion probe analysis					
			3.78	1.49	33.05	0.06	0.26	0.56	0.31	0.032
			2.17	0.53	34.97	0.06	0.05	3.65	0.20	0.077
			0.63	0.22	38.87	0.07	0.04	0.05	0.16	0.033
			9.04	4.22	22.12	0.11	0.72	1.74	1.78	0.121
			0.30	4.31	34.83	0.10	0.53	1.14	1.08	0.043
			2.92	7.29	27.09	0.34	1.22	2.90	2.30	0.028
			0.26	1.99	37.47	0.21	0.16	0.56	0.46	0.018
			0.34	4.97	33.72	0.18	0.68	1.63	1.50	0.039
			0.23	1.39	38.11	0.15	0.16	0.41	0.41	0.036
			0.26	1.09	38.05	0.13	0.16	1.19	0.29	0.035
			0.33	2.08	36.97	0.09	0.23	1.05	0.70	0.029
			1.57	1.61	35.54	0.07	0.25	1.82	0.22	
			0.79	4.72	33.56	0.10	0.62	1.30	1.27	0.028
			7.02	6.19	23.32	0.18	0.68	1.62	1.67	0.033
			0.83	2.52	36.17	0.09	0.28	0.66	0.42	0.041
			0.86	2.28	36.37	0.06	0.19	0.59	0.44	0.054
			6.86	1.69	28.57	0.04	0.18	0.44	0.50	0.046
			1.07	2.17	35.89	0.07	0.25	1.10	0.57	0.049
			7.66	1.72	26.84	0.06	0.28	0.97	1.37	0.036
			1.14	2.42	35.65	0.09	0.25	0.74	0.73	0.051
			7.13	2.05	27.39	0.11	0.16	0.52	1.71	0.045
			1.66	1.73	35.87	0.04	0.15	0.34	0.43	0.035
			0.24	0.88	38.56	0.06	0.11	0.24	0.55	0.034
0.030			0.28	0.99	38.11	0.11	0.13	0.52	1.04	0.042
0.031			1.36	1.24	35.99	0.15	0.08	0.61	2.00	0.025
			7.11	0.71	26.89	0.37	0.07	0.40	6.12	0.023
0.012			0.24	0.87	38.47	0.08	0.23	0.52	0.42	0.033
0.021			1.19	2.60	35.40	0.10	0.21	0.59	0.98	0.041
0.017			3.19	2.47	32.86	0.12	0.09	0.31	1.13	0.032
0.017			0.37	2.82	36.30	0.08	0.40	0.92	0.63	0.036
0.016										
0.027										
0.014										
0.058			0.79	1.21	37.15	0.10	0.21	0.57	1.06	0.065
			5.98	0.98	30.38	0.10	0.10	0.28	0.82	0.060
0.041										
0.040										
0.010										
0.017			0.44	4.34	34.31	0.09	0.57	1.67	1.05	0.049

Sample	Height	Ca	Mg	Sr	Mn	K	Fe	%carb	$\delta^{13}C$	$\delta^{18}O$	TOC	$\delta^{13}C_{org}$	%carb
		ICP-OES							IRMS		Org C		
Majiatun Formation													
QPM 1	0	33.3	0.26	257	646	309	883	84.30	-1.09	-10.71	0.020	-26.01	87.74
QPM 2	0.5	30.6	0.86	223	516	470	2056	79.78	-1.15	-10.65	0.023	-25.24	83.96
QPM 3	3.5	19.2	0.82	95	289	582	1025	51.09	-2.39	-9.88	0.018		70.15
QPM 4	4.2	23.3	1.04	154	331	385	2614	61.99	-2.36	-10.57	0.014		76.35
QPM 5	5.7	24.9	1.15	128	330	582	1960	66.38	-2.73	-10.25	0.020	-23.83	76.79
QPM 6	8.2	34.0	0.25	176	242	645	1158	85.98	-3.14	-10.43	0.015	-27.84	83.31
QPM 7	9.6	30.1	0.35	140	442	863	1014	76.80	-3.48	-10.34	0.011		80.40
QPM 8	10.6	32.8	0.16	179	257	613	1043	82.79	-3.87	-10.38	0.007	-25.71	90.69
QPM 9	12.2	32.3	0.14	206	201	742	1186	81.34	-3.88	-10.80	0.014		87.40
QPM 10	13.4	32.6	1.14	185	217	732	2088	85.51	-3.71	-9.78	0.006	-26.43	92.06
QPM 11	15	30.3	0.16	173	197	708	1193	76.43	-4.14	-9.87	0.006	-23.31	88.50
QPM 12	16	29.5	0.16	196	249	666	1278	74.38	-4.26	-9.57	0.014		88.12
QPM 13	17.5	32.4	0.16	205	231	679	1965	81.60	-4.19	-10.63	0.005		87.12
QPM 14	18.9	33.7	0.13	212	153	638	1164	84.73	-4.68	-10.02	0.009	-26.70	89.64
QPM 15	19.9	32.7	0.60	285	213	713	1671	83.93	-4.38	-9.86	0.006	-25.93	90.53
QPM 18	24	34.6	0.13	178	141	592	887	87.00	-5.22	-8.87	0.005	-25.22	91.40
QPM 19	25.5	32.9	0.37	273	177	429	1824	83.63	-4.91	-9.93	0.014	-26.36	87.95
QPM 20	27	32.8	0.21	238	163	702	2118	82.86	-5.02	-10.36	0.003		89.41
QPM 21	28.5	31.2	0.39	268	143	453	4540	79.51	-4.95	-11.24	0.012		86.96
QPM 25	35.4	33.3	0.08	127	156	445	417	83.60	-5.16	-8.55	0.006	-25.97	89.90
QPM 27	43	32.5	0.13	201	130	812	1330	81.74	-5.28	-9.22	0.038	-27.34	88.62
QPM 28	44.7	33.7	0.09	155	73	831	634	84.81	-5.90	-9.13	0.013	-26.07	90.52
QPM 29	45.7	25.0	0.86	175	260	1651	2086	65.76	-5.25	-9.86	0.026	-24.12	72.37
QPM 30	47.4	33.6	0.17	296	134	656	2257	84.78	-5.28	-10.25	0.002		88.45
QPM 31	50	32.9	0.41	289	234	647	2470	83.73	-5.24	-10.43	0.004	-26.48	90.17
QPM 32	51.2	32.6	0.19	294	200	701	1640	82.31	-4.76	-11.70	0.005	-28.11	90.64
QPM 33	52.2	32.9	0.21	320	233	793	1975	83.29	-4.61	-12.16	0.001	-25.87	93.22
QPM 34	53.2	34.2	0.23	349	247	699	1538	86.52	-4.56	-9.98	0.005	-26.43	92.82
QPM 35	53.7	32.3	0.24	298	187	552	2023	81.83	-4.48	-10.04			
QPM 36	54.7	33.6	0.21	311	191	593	2245	84.96	-4.67	-10.48			
QPM 37	56	31.9	0.22	283	226	726	2344	80.78	-4.68	-9.99	0.005	-25.06	91.68
QPM 38	57	33.7	0.17	260	183	458	1454	84.98	-4.48	-11.42	0.009	-25.87	92.32
QPM 39	58	33.2	0.16	248	247	700	1446	83.79	-4.23	-11.51	0.006	-25.85	90.84
QPM 40	59	38.2	0.21	303	242	471	2242	96.37	-4.04	-10.58	0.003		92.76
QPM 41	60	34.6	0.41	270	234	653	3715	88.17	-4.34	-10.26	0.003	-26.10	91.87
QPM 42	61.5	35.3	0.22	337	233	423	1750	89.08	-3.82	-10.56	0.004	-26.77	94.95
QPM 43	63	33.5	0.13	225	168	399	762	84.27	-4.50	-10.11	0.003	-27.05	93.83
QPM 44	65.2	33.7	0.17	265	197	670	1621	84.91	-4.36	-10.39	0.005	-26.88	91.42
QPM 45	67.2	34.2	0.14	234	317	618	1666	86.07	-4.13	-9.96	0.013	-26.98	90.69
QPM 46	68.2	32.8	0.19	258	286	692	1934	82.85	-3.78	-9.58	0.005	-26.77	90.36
QPM 47	69.7	31.5	0.17	297	222	957	2208	79.57	-3.84	-10.06	0.011	-27.22	88.39
QPM 48	72.7	32.3	0.17	374	358	839	2222	81.64	-3.86	-10.23	0.016	-26.69	90.26
QPM 49	74.7	28.7	0.21	249	334	900	3252	72.81	-3.59	-10.59	0.012	-25.97	87.08
QPM 50	77.7	32.6	0.22	266	317	521	2692	82.43	-3.50	-12.45	0.006	-25.64	89.18
QPM 51	80	29.6	0.18	324	351	690	2857	74.75	-0.81	-12.32	0.020	-28.02	80.66
QPM 52	82.5	28.6	0.27	394	414	663	2654	72.77	-0.68	-12.31	0.012	-27.35	85.73
QPM 53	84	28.0	0.15	226	449	669	1726	70.72	-0.79	-11.20	0.017	-29.33	84.54
QPM 54	86.4	18.3	0.12	200	275	2207	2222	46.48	-0.83	-11.84	0.021		79.86
QPM 55	88.2	28.1	0.13	241	416	762	2192	70.91	-1.14	-10.88	0.008	-26.38	83.80
QPM 57	100	25.7	0.22	311	439	723	3608	65.15	-1.38	-12.18	0.025	-22.92	77.79
QPM 58	101.5	18.4	0.16	397	352	3574	4745	47.25	-1.54	-11.84	0.036	-24.57	64.02
QPM 59	102.6	6.2	0.12	122	116	4648	2325	16.73	-1.64	-12.10	0.022	-24.10	71.47
QPM 60	103.4	7.3	0.11	212	135	5159	2863	19.34	-1.91	-12.23	0.054		41.43
QPM 61	104.4	8.0	0.09	209	140	3796	2122	20.89	-2.19	-11.76	0.091	-25.75	22.42
QPM 62	106.1	10.6	0.12	266	227	4295	3220	27.58	-1.95	-12.07	0.033	-24.24	73.27
QPM 63	108	23.0	0.21	338	488	1708	5412	58.54	-1.68	-12.59	0.076	-23.90	26.47
QPM 64	109.5	5.5	0.10	144	99	4550	2373	14.78	-1.90	-12.48	0.082	-23.93	18.20
QPM 65	112.5	22.2	0.15	439	360	1898	3545	56.41	-1.50	-12.72	0.045	-27.61	70.53
QPM 66	114.5	29.3	0.17	305	388	1180	2585	74.24	-0.95	-12.21	0.021	-29.81	82.71
QPM 67	118.9	31.3	0.17	273	339	789	1677	79.02	-1.00	-10.84	0.017	-26.39	87.21
QPM 68	120.9	28.2	0.18	314	293	1116	2537	71.37	-1.07	-11.33	0.016	-26.21	84.90
QPM 69	124.4	29.4	0.19	231	840	748	1865	74.36	-0.65	-11.16	0.013	-26.28	87.90
QPM 70	127.6	28.6	0.19	285	506	1116	3272	72.54	-0.51	-12.43	0.018	-26.37	82.37
QPM 71	129.9	28.6	0.23	263	612	854	2678	72.58	-0.41	-12.70	0.021		78.05
QPM 72	132.4	30.3	0.23	235	506	874	2460	76.86	-0.41	-11.96	0.019	-26.77	83.48
QPM 73	140	31.6	0.22	297	1231	859	3881	80.17	-0.22	-12.80	0.028	-27.40	81.93

Appendix 3. XRF data, South China

Sample	Height	Age	SiO_2	Al_2O_3	Fe_2O_3	MgO	CaO	Na_2O	K_2O	TiO_2	MnO	P_2O_5	Total
Fanzhao Formation, Shangjiaomeng village													
Fanzhao 1			66.49	17.34	6.61	1.41	0.31	2.21	3.00	0.90	0.09	0.096	98.93
Fanzhao 2			66.34	17.24	6.73	1.41	0.30	2.17	3.01	0.89	0.08	0.097	98.65
Pingue or Qingshuijiang Formation, Nanwan village													
NW 1			70.31	18.03	2.77	1.07	0.34	2.54	4.58	0.63	0.06	0.048	100.83
NW 2			80.18	11.49	1.84	0.49	0.16	3.39	1.43	0.33	0.04	0.057	101.93
NW 3			66.90	17.88	6.04	1.85	1.11	2.34	3.31	0.65	0.13	0.485	101.00
Upper Gongdong Formation, Danzhou													
CX 1	0	723	69.74	16.90	4.16	1.31	0.21	3.79	2.44	0.68	0.10	0.019	99.60
CX 2	35	722	69.85	17.11	4.25	1.47	0.08	2.21	3.24	0.67	0.09	0.085	99.35
CX 3	47	722	72.60	14.88	3.86	1.31	0.58	3.63	2.18	0.59	0.10	0.131	100.09
CX 4	82	721	76.13	12.84	3.46	1.41	0.43	2.19	2.43	0.41	0.09	0.083	99.71
CX 5	99	720	66.74	17.63	5.89	1.93	0.53	2.15	3.79	0.65	0.13	0.083	99.80
CX 6	105	720	70.93	15.66	3.22	1.08	0.60	3.45	2.89	0.71	0.06	0.094	98.99
CX 8	106	720	65.43	18.11	5.61	1.95	0.58	3.27	3.28	0.78	0.13	0.117	99.56
CX 9	113	720	69.50	15.65	4.89	1.63	0.65	3.36	2.53	0.73	0.11	0.125	99.50
CX 10	130	719	67.85	16.22	5.16	1.88	0.78	3.59	2.46	0.69	0.12	0.168	99.18
CX 11	158	718	63.30	21.43	5.34	1.25	0.83	1.91	4.58	1.01	0.11	0.224	100.30
CX 12	214	717	76.55	13.32	2.62	0.66	0.37	3.15	1.92	0.56	0.05	0.038	99.45
CX 13	221	717	69.68	17.51	3.63	0.94	0.72	2.65	3.29	0.82	0.06	0.089	99.65
CX 14	232	716	68.63	17.45	5.12	1.31	0.63	2.12	3.24	0.76	0.09	0.055	99.66
CX 15	269	715	69.78	17.51	4.06	1.08	0.24	2.32	3.32	0.84	0.07	0.046	99.52
CX 16	278	715	67.33	19.54	4.86	1.25	0.05	1.50	4.15	0.77	0.09	0.032	99.85
CX 17	301	714	71.00	16.91	3.92	1.03	0.26	2.30	3.13	0.85	0.08	0.035	99.75
CX 18	306	714	68.40	18.25	4.49	1.21	0.61	2.59	3.53	0.80	0.09	0.058	100.31
CX 19	331	713	69.74	17.22	4.12	1.14	0.47	3.07	3.11	0.80	0.08	0.097	100.12
CX 20	342	713	68.66	17.22	4.83	1.34	0.64	2.84	3.12	0.68	0.10	0.100	99.82
CX 21	347	713	68.57	16.97	4.33	1.21	0.70	3.38	2.85	0.82	0.09	0.114	99.29
CX 22	357	713	69.67	16.37	4.43	1.22	0.57	3.37	2.69	0.76	0.09	0.163	99.59
CX 23	367	712	67.76	16.97	4.71	1.20	0.88	4.03	2.54	0.82	0.09	0.189	99.47
CX 24	430	711	70.26	15.47	4.67	1.37	0.68	3.84	2.01	0.65	0.10	0.111	99.38
CX 25	444	710	68.48	16.19	5.34	1.65	0.56	3.38	2.50	0.73	0.11	0.123	99.30
CX 26	449	710	69.08	16.24	4.68	1.46	0.64	3.95	2.21	0.76	0.10	0.138	99.48
CX 27	457	710	64.50	18.33	7.10	2.41	0.15	2.60	3.02	0.76	0.16	0.075	99.44
CX 28	462	710	68.37	17.00	5.16	1.64	0.63	2.10	3.22	0.73	0.11	0.160	99.39
CX 29	467	709	70.28	16.54	4.46	1.49	0.62	2.79	2.79	0.71	0.11	0.136	100.16
CX 30	487	709	68.82	16.87	4.79	1.87	0.43	1.71	3.47	0.69	0.11	0.111	99.15
CX 31	500	709	69.51	16.37	4.87	1.45	0.51	2.14	3.26	0.66	0.08	0.114	99.23
CX 32		700	65.04	19.25	6.39	1.73	0.18	1.47	4.04	0.74	0.09	0.108	99.34
CX 33		685	71.76	14.93	4.46	1.44	0.60	1.49	3.50	0.63	0.08	0.104	99.59
Lowermost Fulu Formation, Fengmu village													
FM 1	0	684.8	66.83	18.12	6.86	2.10	0.13	1.27	3.42	0.86	0.10	0.114	100.26
FM 2	2	684.7	71.95	15.42	5.23	1.55	0.10	1.85	2.37	0.80	0.08	0.067	99.69
FM Iron 1	2.3	684.7	47.62	16.75	28.38	6.60	0.07	0.03	0.02	0.63	0.40	0.073	100.67
FM 3	3	684.7	43.52	7.56	44.77	2.42	0.14	0.01	0.02	0.46	0.18	0.097	99.30
FM 4	24.5	683.7	65.63	6.49	23.08	2.29	0.09	0.57	0.54	0.35	0.11	0.062	99.35
FM Iron 2b		684.8	69.98	10.79	12.72	1.40	0.18	0.88	2.31	0.40	0.07	0.106	99.06
FM Iron 2t	25.5	683.7	67.16	6.61	21.66	1.98	0.06	0.35	0.81	0.35	0.10	0.058	99.29
FM 5	31	683.4	64.64	9.06	20.79	1.86	0.10	0.34	2.16	0.45	0.05	0.043	99.75
FM Iron 3	32	683.4	63.23	10.57	17.87	2.42	0.17	0.12	2.90	0.68	0.05	0.117	98.42
dup.			63.01	10.53	18.11	2.43	0.17	0.13	2.91	0.69	0.05	0.116	
FM 6	33	683.3	64.01	10.57	18.18	2.72	0.12	0.09	2.71	0.65	0.06	0.084	99.48
FM 7	40	683.0	63.88	14.96	10.81	3.29	0.23	0.73	3.87	0.76	0.05	0.178	99.11
FM 8	47	682.7	70.04	16.08	4.93	2.25	0.21	2.18	3.83	0.63	0.04	0.137	100.62
FM 9	56	682.3	69.91	16.22	3.50	1.41	0.23	2.80	4.01	0.74	0.02	0.130	99.36

LOI	loi	LOI(Σ)	Ni	Co	Cr	V	Sc	Cu	Zn	As	S	F	Cl	Ga
2.81	0.18		37.1	19.1	96.1	105.7	17.9	24.5	109.9		1491	558	35	21.4
2.87	0.19	3.07	16.1	12.1	32.4	83.1	15.6	27.2	80.2		1560	630	50	23.3
2.81	0.80	2.81	9.6	16.1	19.6	53.2	14.9	11.9	78.0		1255	574	44	23.0
1.44	0.46	1.91	5.2	13.7	9.9	23.3	7.4	7.8	72.4		1347	338	43	11.4
3.44	0.49	3.44	19.1	14.1	31.7	83.7	19.5	33.1	112.8		152	644	48	23.2
2.19	0.32	2.52	13.1	8.4	30.9	58.3	12.4	15.5	85.6	0.7	8	404	25	19.8
2.80	0.41	3.22	20.3	6.7	41.6	58.8	14.3	7.1	96.7	1.2	15	423	43	21.6
1.98	0.22	1.98	14.5	10.1	42.1	51.3	11.4	13.2	84.1	0.9	2	442	24	17.9
1.83	0.11	1.94	14.1	8.3	25.2	37.6	8.1	11.4	81.6	0.8	1	451	23	17.2
2.70	0.17	2.87	39.0	17.3	56.8	83.1	15.9	15.4	115.4	0.8	0	476	24	24.4
1.79	0.16	1.95	16.1	8.1	60.0	71.2	15.5	13.7	59.4		31	528	30	19.4
2.54	0.14	2.68	25.2	10.6	55.4	84.6	17.0	17.4	110.2	1.1	3	476	27	23.4
2.10	0.11	2.21	21.7	11.2	54.5	70.2	14.3	28.6	92.5	1.9	232	457	25	18.9
2.30	0.25	2.30	21.9	10.2	49.3	73.2	16.3	20.3	98.9		15	430	27	19.8
3.30	0.41	3.30	21.7	12.1	73.5	101.2	22.3	14.9	79.3		106	521	25	27.8
1.59	0.24	1.59	9.1	8.3	37.9	50.7	10.3	6.0	51.7		227	363	22	14.9
2.23	0.25	2.23	12.5	5.5	54.1	79.4	16.0	7.0	65.1		10	398	25	22.0
2.83	0.30	2.83	17.4	10.4	51.8	82.4	15.5	13.2	91.8		107	384	21	22.0
2.59	0.42	2.59	17.2	8.3	52.2	74.1	15.4	7.3	76.9		17	435	36	21.4
4.30	0.29	4.30	11.3	7.2	29.6	59.3	17.2	6.5	80.9		13	415	25	25.0
2.58	0.26	2.58	16.2	5.9	48.5	72.3	15.6	5.8	78.9		19	389	23	20.3
2.46	0.21	2.46	16.5	7.2	47.6	76.3	14.5	6.0	80.2		13	422	26	22.8
2.17	0.16	2.17	13.2	9.3	40.6	68.4	14.7	10.5	66.9		12	415	26	21.0
2.37	0.17	2.37	11.9	11.7	29.7	62.1	14.9	8.4	94.5		24	475	26	22.8
2.07	0.07	2.14	13.5	6.1	44.8	72.3	13.0	8.0	71.1	0.9	13	447	32	20.8
2.01	0.29	2.31	12.9	14.4	42.2	73.3	13.7	14.1	70.8	1.7	35	458	28	20.4
2.09	0.39	2.49	14.2	10.7	47.9	78.5	14.9	14.5	77.6	1.0	18	443	36	21.0
2.04	0.29	2.34	17.3	12.1	31.5	63.1	12.2	16.4	91.2	0.9	2	377	22	17.9
2.19	0.19	2.38	18.5	11.6	38.7	75.7	13.4	20.9	101.2	0.8	4	432	25	20.6
2.01	0.27	2.29	17.3	11.5	38.7	77.8	14.3	14.6	88.9	0.8	8	412	25	19.5
3.04	0.31	3.36	26.9	20.8	46.8	93.2	14.7	24.1	123.8	0.7	244	501	33	22.5
2.61	0.36	2.98	18.2	11.5	44.4	91.6	15.8	14.2	92.7		93	388	47	22.0
2.33	0.23	2.57	14.7	8.7	41.0	80.7	14.5	13.5	82.8	0.6	6	382	25	20.6
2.77	0.23	3.01	18.3	11.7	41.5	84.9	13.8	17.6	97.1	1.0	12	410	23	22.6
2.36	0.18	2.54	18.6	10.7	39.2	80.0	13.4	12.7	84.5	0.9	9	390	24	21.1
3.11	0.28	3.40	34.3	17.1	62.4	100.4	19.6	32.1	104.2	0.7	9	539	27	24.1
2.64	0.19	2.84	17.3	13.5	45.2	70.6	11.9	20.6	79.1	1.8	2012	485	26	18.4
3.63			37.0	39.6	67.4	110.4	18.7	23.3	101.4	0.3	77	475	25	22.3
2.72	0.6		32.5	17.0	61.8	84.5	15.4	12.3	73.8	1.0	312	382	27	16.7
5.72			21.6	18.9	66.0	114.5	19.0	14.3	130.3		31	417	27	27.7
3.49			17.7	22.1	65.0	176.8	18.0	32.7	88.5		20	672	45	12.8
1.86	0.27	2.14	12.9	7.7	42.0	71.0	4.2	15.6	63.9	1.4	8	424	23	10.5
2.03	0.28	2.32	16.2	8.8	51.4	74.3	14.7	4.3	34.9	0.8	49	532	22	15.6
1.73	0.24	1.97	14.4	-3.9	36.6	62.7	5.8	12.6	61.5	0.7	19	391	26	12.1
2.74			20.3	10.3	110.0	77.2	17.8	26.8	50.4		20	690	39	12.5
2.40	0.38	2.79	23.2	10.6	143.9	126.2	24.8	23.9	77.0	0.7	53	676	22	15.6
2.47	0.225	2.70	22.5	12.3	115.8	123.1	23.7	29.6	85.3	0.9	3	685	23	14.8
3.11			22.4	9.2	120.8	136.8	23.4	34.5	90.6	0.5	10	719	22	20.5
3.20			14.3	9.0	35.6	68.9	13.6	16.8	71.8		35	651	33	19.3
2.61			11.9	8.9	63.8	98.0	20.2	22.5	45.2		54	550	28	21.7

Pb	Sr	Rb	Ba	Zr	Nb	Ta	Th	U	Y	La	Ce	Nd	Sm	Yb
22.2	80.5	112.0	770.3	243.0	15.6	2.5	11.0	1.9	34.8	41.4	84.1	36.4	7.2	4.3
13.6	76.8	134.9	510.2	194.3	12.4	2.0	13.8	1.4	33.0	37.0	76.5	34.6	7.1	4.3
26.3	95.8	132.4	1150.9	288.6	14.2	2.4	12.8	2.1	41.1	29.0	67.3	32.8	6.5	4.8
11.1	115.4	43.2	451.2	182.0	9.5	1.8	7.9	1.5	27.7	24.0	54.0	25.0	5.0	3.9
12.5	99.5	129.2	734.2	205.8	11.1	2.1	11.3	1.7	34.4	48.7	98.7	45.6	8.3	4.3
5.4	179.7	81.1	451.6	278.7	14.1	1.6	10.8	2.1	27.6	18.3	58.0	20.5	4.9	3.8
5.8	127.8	110.8	739.5	262.9	13.8	2.1	11.4	2.4	34.5	50.0	55.6	43.5	7.6	4.5
4.3	154.8	74.6	525.9	262.7	12.8	1.8	9.5	2.0	33.0	11.2	29.7	15.8	3.6	4.5
4.7	102.7	83.6	604.0	164.2	11.0	1.8	6.1	1.9	25.4	22.8	67.5	23.7	4.7	3.2
3.1	89.0	131.8	955.2	197.8	12.8	1.4	12.2	2.1	30.7	20.2	55.1	21.9	4.7	3.9
6.0	126.1	105.6	812.5	243.3	12.3	1.6	8.6	1.5	30.5	23.8	50.4	27.9	5.8	3.8
7.1	117.7	114.1	877.9	239.3	12.6	1.3	9.2	2.3	38.8	16.3	40.4	20.2	4.2	4.3
6.0	116.5	87.8	754.5	220.4	12.1	1.4	9.6	1.8	36.5	36.0	69.0	33.3	7.1	4.3
3.8	129.2	88.2	740.0	211.6	12.1	1.6	9.4	1.4	37.4	29.3	69.5	29.6	7.1	4.3
8.1	120.5	161.1	817.4	336.0	21.8	2.0	19.0	2.4	42.0	24.7	40.0	31.7	5.0	5.2
12.8	123.6	68.3	337.1	266.3	11.0	2.0	8.1	1.3	33.8	33.9	36.1	31.1	8.0	3.3
4.5	141.6	117.8	547.7	262.4	15.0	1.6	12.2	2.0	35.9	21.2	57.1	22.2	5.8	3.9
12.6	129.8	117.9	542.7	268.2	13.9	1.7	11.4	1.9	39.6	40.0	74.5	36.7	5.5	4.2
15.2	128.2	118.6	574.1	278.5	16.3	1.7	13.9	2.1	29.6	34.9	68.7	32.2	6.0	4.7
14.8	108.8	147.7	721.1	289.8	18.9	2.7	15.6	3.0	21.3	14.9	43.5	17.8	2.8	4.8
9.1	133.9	112.0	550.7	275.2	15.5	2.3	12.8	2.1	26.7	14.6	60.6	19.0	4.5	3.8
6.9	149.3	124.7	646.8	263.8	15.3	2.1	13.1	2.1	40.1	32.9	60.5	30.5	6.6	4.3
9.7	161.3	110.1	632.7	308.4	15.7	1.9	11.8	2.3	32.4	34.0	73.0	33.5	7.3	4.1
9.5	159.1	109.8	646.7	281.7	12.5	1.3	8.9	1.7	37.5	33.2	74.7	34.7	7.7	4.3
6.2	166.5	99.3	586.4	283.0	14.6	1.6	11.0	2.4	36.8	30.6	72.1	32.4	7.8	4.5
16.9	151.3	93.2	578.6	273.3	13.3	1.5	10.3	2.3	32.4	31.1	69.0	33.1	6.4	4.0
7.8	164.6	87.4	550.2	298.2	13.3	1.7	10.7	2.2	37.9	40.4	78.0	37.2	7.5	4.9
14.0	164.3	69.5	429.6	219.9	10.9	1.8	8.2	1.8	32.7	26.5	56.1	29.1	6.7	3.3
4.8	142.9	87.8	539.9	235.5	12.0	1.6	9.3	1.6	32.1	24.9	59.1	24.3	5.8	4.0
4.4	156.6	79.5	474.6	245.5	12.4	1.6	9.5	2.0	36.0	24.9	67.4	28.2	6.2	4.4
13.4	135.5	103.7	625.0	287.3	14.7	1.5	11.2	2.5	30.0	41.8	97.9	36.7	6.8	4.5
7.1	122.6	111.5	664.3	228.2	13.2	1.7	11.8	2.0	34.7	23.9	55.8	27.2	6.6	4.8
5.0	142.3	96.9	617.5	227.3	12.8	1.9	10.7	2.0	33.6	19.8	50.2	22.8	6.4	4.0
14.3	113.2	125.4	838.3	234.9	13.1	1.7	11.3	1.9	27.9	13.0	42.2	16.4	4.7	4.4
15.8	127.6	119.2	800.0	240.6	12.5	1.7	10.7	1.9	30.0	19.1	57.6	22.1	4.6	3.8
10.1	116.7	155.2	752.0	215.1	12.2	1.4	12.4	2.9	41.5	28.1	97.1	30.6	7.5	3.6
20.6	108.0	110.3	851.5	244.1	12.2	1.9	10.5	2.3	35.0	31.5	63.8	32.8	7.4	4.4
8.8	125.5	107.5	737.2	203.9	12.9	1.5	9.1	1.6	27.0	33.0	40.0	31.6	6.6	4.4
40.3	137.8	75.4	531.4	175.5	10.7	1.2	7.2	1.9	23.0	19.1	44.0	17.5	5.1	3.6
1.5	6.5	0.6	25.3	178.9	11.7	-	6.8	0.7	26.8	42.3	36.7	29.1	1.0	3.8
9.2	7.1	0.8	150.2	114.8	9.2	- -	4.3	0.3	34.6	37.3	50.6	35.8	4.6	1.3
7.7	18.8	18.7	186.6	143.4	5.8	- -	4.2	1.1	14.5	9.8	25.4	10.7	2.6	2.5
5.1	38.7	81.0	717.1	191.6	5.6	1.2	5.1	0.9	22.1	14.8	28.9	14.0	1.9	3.4
6.6	17.4	32.2	284.9	162.2	5.7	0.1	3.7	1.1	17.0	8.7	17.2	8.9	1.9	3.7
6.5	22.1	68.8	813.4	106.1	4.5	0.6	4.5	0.0	20.3	15.3	27.2	16.3	3.6	2.2
5.7	21.0	89.9	816.3	154.0	7.6	0.9	6.3	1.1	23.4	17.8	38.9	17.8	1.6	2.6
5.6	17.8	83.4	762.5	150.7	5.6	0.4	7.0	0.9	25.8	22.9	49.6	24.1	4.1	2.1
3.7	42.1	119.0	1018.3	203.0	13.2	1.8	9.9	1.4	37.8	35.8	70.4	38.0	6.7	4.3
4.0	57.2	115.7	719.1	245.3	11.9	1.3	9.1	1.0	36.6	35.0	66.6	33.8	6.2	4.4
25.6	91.3	118.5	1570.0	224.2	13.7	1.8	11.2	1.7	42.0	39.8	66.6	38.1	6.7	4.8

Sample	Height	Age	SiO_2	Al_2O_3	Fe_2O_3	MgO	CaO	Na_2O	K_2O	TiO_2	MnO	P_2O_5	Total
Tiesiao Formation, Wuhe													
WH 10	0	670	67.59	17.80	5.57	1.70	0.72	2.09	2.98	0.69	0.12	0.170	99.71
WH 11	2	670	65.34	18.50	6.04	1.87	1.02	2.05	3.18	0.69	0.13	0.174	99.29
WH 12	4	669	66.40	18.27	5.53	1.67	0.84	2.10	3.30	0.71	0.10	0.166	99.38
WH 13	6	669	66.06	18.81	5.32	1.73	0.73	1.90	3.46	0.73	0.10	0.235	99.36
WH 14	8	669	65.43	18.46	6.22	1.83	0.97	2.01	3.25	0.72	0.13	0.167	99.46
WH 15	10	668	65.72	18.87	5.60	1.76	0.79	2.14	3.28	0.75	0.12	0.209	99.60
WH 16	12	668	67.93	17.33	5.63	1.66	0.72	2.00	2.96	0.63	0.09	0.127	99.43
WH 17	14	668	73.86	14.54	3.36	1.12	1.19	1.91	2.63	0.53	0.13	0.108	99.64
WH 18	16	668	68.25	17.40	4.83	1.58	0.96	2.00	3.07	0.64	0.11	0.159	99.32
WH 19	18	667	67.16	18.01	5.23	1.68	1.04	2.18	3.15	0.67	0.11	0.149	99.65
WH 20	20	667	66.24	17.79	6.02	1.83	1.29	2.27	2.97	0.68	0.13	0.149	99.68
WH 21	22	667	67.83	18.03	4.61	1.59	0.94	2.23	3.20	0.63	0.10	0.148	99.59
WH 22	24	666	67.76	18.34	4.93	1.67	0.99	2.07	3.29	0.65	0.09	0.208	100.48
WH 23	26	666	69.30	16.97	5.08	1.61	0.66	1.90	3.20	0.57	0.08	0.165	99.83
WH 24	28	666	75.47	13.14	3.06	1.12	1.49	1.59	2.45	0.48	0.14	0.102	99.46
WH 25	30	665	70.27	16.26	4.52	1.63	1.17	1.46	3.12	0.56	0.08	0.468	99.90
WH 26	32	665	66.16	17.77	5.52	1.82	1.69	1.87	3.32	0.65	0.12	0.126	99.78
WH 27	34	665	68.76	16.87	4.03	1.54	1.95	1.79	3.21	0.57	0.13	0.160	99.78
WH 28	36	665	66.22	17.82	5.76	1.98	1.41	1.96	3.20	0.67	0.13	0.148	99.79
WH 29	38	664	65.95	17.59	5.69	1.97	1.58	2.01	3.03	0.64	0.12	0.421	99.42
WH 30	40	664	68.84	17.50	5.24	1.66	0.33	1.90	3.07	0.61	0.10	0.122	99.82
WH 31	42	664	64.54	16.10	5.61	2.69	4.18	1.73	2.80	0.55	0.27	0.157	99.20
WH 32	43	664	71.10	17.40	3.50	1.38	0.62	1.95	3.45	0.66	0.05	0.187	100.60
Datangpo Formation, Wuhe													
Dat 1		657	66.61	18.67	6.30	2.43	0.17	1.69	3.66	0.71	0.14	0.094	100.75
Dat 2		655	66.09	18.27	6.14	2.09	0.26	1.71	3.57	0.69	0.08	0.068	99.26
Dat 3		654	68.41	17.02	6.00	1.71	0.16	1.89	3.23	0.65	0.13	0.057	99.51
Nantuo Formation, Wuhe													
NT 1		645.5	71.50	17.90	5.69	1.53	0.29	2.11	3.89	0.69	0.05	0.099	104.00
NT 2		641.0	70.19	15.73	5.13	1.40	0.30	2.07	4.06	0.64	0.06	0.095	99.97
NT 3		640.0	65.71	18.41	5.86	1.90	0.33	2.24	4.31	0.73	0.06	0.125	100.00
NT 4		639.0	65.70	19.01	5.99	1.85	0.25	1.32	4.84	0.74	0.04	0.092	100.13
Top of Nantuo Formation, Doujiang													
DJ 1	0	635.2	70.65	14.10	6.51	2.11	0.18	0.06	4.78	0.59	0.04	0.150	99.43
DJ 2	1.5	635.0	65.05	16.14	6.41	2.96	1.44	0.13	5.76	0.84	0.21	0.181	99.75
DJ 3	5.5	634.7	61.09	18.38	4.37	3.30	2.66	0.10	7.08	1.14	0.23	0.234	100.22
DJ 4	7.5	634.5	70.19	13.79	2.75	2.60	2.41	0.10	5.76	0.59	0.23	0.097	99.30
DJ 5	11	634.2	72.79	15.41	2.05	1.58	0.04	0.09	6.45	0.64	0.01	0.079	99.50
DJ 6	13												
DJ 7	18.5	633.5	73.40	15.71	1.79	1.55	0.07	0.08	6.64	0.62	0.02	0.092	100.28
Machong 1		635.1	69.65	16.62	3.16	2.00	0.01	0.09	6.51	0.95	0.03	0.023	98.12
Machong 2		635	66.92	15.55	6.01	2.05	0.66	0.09	6.20	0.81	0.10	0.201	99.33
Tuanjie		635.3	67.16	16.50	6.19	2.53	0.20	0.07	5.77	0.76	0.04	0.204	99.77

LOI	loi	LOI(Σ)	Ni	Co	Cr	V	Sc	Cu	Zn	As	S	F	Cl	Ga
3.34	1.39	4.78	21.3	11.4	28.9	80.1	14.9	27.4	101.7	6.1	69	522	47	21.8
3.78	1.33	5.16	14.6	6.0	33.1	90.6	16.5	28.6	89.3	2.0	52	586	36	23.4
3.44	1.23	4.71	16.9	10.3	35.7	98.4	16.2	27.7	81.8	14.2	92	625	54	22.8
3.40	1.56	5.01	15.2	6.9	37.0	88.0	16.2	26.4	87.7	2.9	46	598	40	23.0
3.74	1.41	5.20	16.1	8.0	35.8	97.1	17.8	28.2	85.6	5.9	75	596	42	23.1
3.54	0.96	4.53	15.2	11.4	33.5	91.7	16.7	27.7	141.6	7.7	276	601	75	23.7
3.26	1.21	4.51	14.9	10.0	29.5	78.0	13.7	23.2	81.9	7.3	222	537	41	22.0
3.39	0.98	4.40	15.4	16.2	25.2	68.9	12.4	21.5	71.2		186	500	52	18.4
3.49	1.41	4.95	12.5	11.5	25.9	71.3	12.9	20.7	85.8	4.1	580	569	42	21.2
3.54	0.72	4.29	25.2	9.1	29.7	83.4	14.8	28.1	84.2	3.6	66	596	42	22.2
3.90	1.23	5.18	24.8	84.0	33.1	92.9	16.3	29.7	81.2	5.7	86	710	84	22.4
3.49	1.47	5.01	11.9	7.8	28.3	77.4	13.9	28.4	89.8	5.2	96	597	46	22.9
4.13	1.00	4.13	83.7		27.2	76.8	15.5	27.3	79.1		224	841	52	22.8
3.33	0.55	3.90	16.5	10.1	29.9	65.4	12.4	25.4	95.8	10.0	1186	631	51	22.4
3.30	0.37	3.68	8.7	6.3	25.7	62.6	10.5	22.1	80.4	5.5	1507	432	50	17.1
3.31	0.48	3.81	14.2	7.2	29.3	61.9	12.0	23.3	89.8	5.5	1042	774	49	21.0
4.07	1.12	5.24	15.4	11.7	33.0	87.8	14.5	26.4	78.5	9.4	2313	631	62	22.9
4.03	1.36	5.45	11.3	8.4	22.9	65.4	11.6	20.8	82.0	9.3	3441	621	50	20.7
4.10	0.91	5.05	18.5	13.0	39.2	87.5	15.8	27.0	88.3	8.3	1332	686	75	23.0
3.86	1.06	4.96	15.8	9.9	28.2	77.4	14.1	24.1	99.4	8.8	1321	728	52	22.1
4.48	1.49	4.48	21.0	12.7	29.3	75.5	14.9	26.1	118.1		368	615	47	22.3
6.50	1.18	7.76	12.4	8.7	25.3	70.2	14.0	21.6	97.1	6.8	1489	555	70	20.2
4.04	0.88	4.04	9.2	4.2	32.0	81.6	17.3	13.7	85.5		190	765	50	22.3
4.00	1.29	4.00	60.4	217.0	60.2	83.2	15.9	41.7	115.2	2.4	64	742	64	23.6
3.54	0.50	4.06	28.9	29.1	56.7	82.3	16.0	26.5	109.7	2.8	1446	573	57	24.2
3.78	1.40	3.78	19.9	17.3	56.4	78.3	15.2	20.9	103.7		121	499	51	22.1
3.76	1.97	3.76	20.2	9.1	53.0	82.1	14.7	9.1	91.8	7.0	44	510	49	23.8
3.03	0.66	3.03	28.2	25.9	59.2	73.7	15.3	13.5	91.0		128	601	110	20.6
4.14	1.46	4.14	22.5	11.3	51.7	81.0	17.5	65.6	130.6		131	527	51	27.4
4.76	1.91	4.76	21.6	5.1	55.5	93.6	19.3	19.7	127.8		146	537	45	26.6
2.67	0.17	2.84	28.3	9.0	48.2	91.6	13.6	19.4	57.7	0.8	35	695	28	19.4
4.71	0.11	4.83	27.1	28.8	45.9	152.0	17.7	17.9	52.1		1041	851	66	20.8
6.17	0.16	6.34	32.1	12.5	63.5	148.1	22.7	196.7	48.0	14.9	3923	940	36	23.9
5.30	0.13	5.44	17.6	6.5	44.8	72.3	11.8	8.9	36.3	14.7	1188	766	38	17.7
2.56	0.16	2.72	23.2	88.0	45.6	71.0	12.6	14.4	28.6	13.3	4057	815	24	19.5
2.60	0.20	2.60	7.8	7.1	41.3	70.7	12.5	6.7	25.3		222	943	29	19.1
3.51	0.45	3.98	33.9	31.6	84.0	360.4	15.7	42.4	19.0		15756	1242	24	19.4
5.81	0.14	5.96	41.6	58.3	87.6	368.4	14.3	51.1	22.3	28.2	16830	1286	31	21.8
2.96	0.28	3.25	38.6	29.3	45.3	122.4	19.5	39.2	37.4	13.1	225	785	37	20.8

Pb	Sr	Rb	Ba	Zr	Nb	Ta	Th	U	Y	La	Ce	Nd	Sm	Yb
17.0	77.4	106.7	537.8	198.8	12.2	1.8	11.4	1.9	30.4	35.5	74.6	32.5	5.8	4.2
17.3	72.2	117.4	541.1	201.7	12.6	1.6	12.9	2.0	32.9	39.1	84.8	36.9	6.4	3.7
18.0	66.8	127.2	542.1	194.2	12.4	2.2	14.2	1.9	31.5	41.4	77.0	34.6	6.1	4.5
18.1	74.7	124.0	601.8	211.0	12.8	2.3	12.5	2.1	34.0	41.8	84.4	36.6	7.1	3.4
13.1	66.5	126.4	558.3	202.1	12.4	1.9	13.4	2.2	33.1	37.7	81.0	36.4	6.5	4.0
15.6	80.9	119.4	929.4	209.9	13.1	2.1	12.5	2.4	33.5	37.8	81.4	36.2	6.4	3.7
16.7	93.5	111.4	968.5	190.0	11.9	2.0	11.6	2.1	30.5	36.5	77.0	34.2	4.4	3.3
18.1	78.2	97.4	508.1	162.3	9.8	2.1	9.9	1.6	26.6	38.7	84.5	35.3	6.0	4.1
18.0	78.1	110.1	499.7	208.0	12.2	2.3	11.7	2.3	33.2	35.0	72.9	33.4	7.1	4.2
20.5	77.8	118.0	533.7	199.8	11.8	2.2	11.7	2.1	31.6	35.2	73.9	31.9	6.2	3.9
20.3	71.8	116.6	619.1	193.9	11.5	1.8	12.0	2.4	32.8	35.8	76.6	34.3	6.7	3.9
22.1	76.1	118.7	556.4	210.8	15.4	2.2	15.9	3.2	36.7	39.2	85.4	38.2	6.3	4.7
20.0	81.0	121.5	813.7	213.0	14.9	0.1	15.1	1.9	36.4	40.9	82.5	35.7	8.3	3.3
22.1	73.1	117.4	570.8	197.8	15.6	2.8	16.3	2.9	34.3	42.0	87.1	37.4	7.4	4.2
20.8	69.7	95.7	464.0	148.7	9.5	2.6	10.8	2.2	24.9	35.4	74.7	28.8	6.4	3.6
26.0	63.6	117.6	630.4	197.2	13.8	2.1	13.1	2.4	34.8	23.8	53.7	27.6	7.8	3.8
13.3	74.5	132.2	531.2	190.2	12.0	1.8	13.3	2.3	32.2	37.6	81.0	38.1	7.4	3.8
17.5	85.6	115.6	543.7	188.0	12.4	1.9	11.4	2.2	31.4	35.1	74.4	31.5	6.4	4.0
17.5	77.8	129.8	588.3	193.2	12.6	2.0	12.9	2.1	33.8	39.4	82.2	36.0	8.1	4.1
16.3	85.9	117.8	602.7	187.1	11.7	2.1	11.5	2.4	39.9	43.4	96.2	48.4	11.0	4.0
18.7	88.2	119.6	1668.7	196.8	13.3	2.5	13.2	1.9	34.6	41.3	81.7	40.7	8.2	4.7
13.3	99.3	107.6	499.7	176.0	11.4	2.3	10.7	2.6	35.9	33.6	71.7	33.3	8.1	4.2
22.4	85.7	136.0	568.5	239.4	15.7	2.6	12.4	2.1	45.6	59.2	119.7	48.0	8.6	5.1
27.0	62.2	146.2	554.0	205.6	15.1	1.5	14.6	2.2	45.2	43.0	88.3	43.4	6.8	5.4
21.3	82.3	145.9	446.8	192.9	15.2	2.5	15.4	2.7	37.0	42.5	86.7	39.4	6.8	4.6
16.1	51.9	126.9	404.7	197.4	15.3	2.8	14.6	1.6	31.8	33.8	65.0	28.7	4.3	3.8
9.6	53.3	150.0	539.7	235.8	17.5	2.0	16.2	2.6	40.9	46.0	92.4	44.4	8.0	5.4
8.2	56.5	162.2	588.1	230.0	14.8	2.1	15.5	2.2	40.3	42.0	80.2	41.1	8.6	4.5
10.7	55.5	168.2	676.9	249.3	20.5	3.0	19.0	3.5	57.1	66.4	104.8	59.0	13.8	6.9
30.8	50.5	170.2	594.0	252.3	20.3	2.5	18.7	3.0	52.2	55.7	101.8	53.3	11.4	5.7
2.0	55.9	109.5	577.3	167.3	13.3	1.8	11.4	2.0	38.6	24.2	55.9	27.9	6.1	4.1
3.2	122.9	129.4	666.3	194.6	15.6	2.2	11.7	1.4	32.9	28.2	59.0	28.1	5.4	4.4
8.4	213.8	157.2	652.5	224.2	19.6	2.1	13.5	2.2	41.0	30.3	65.1	33.4	7.8	4.4
7.5	138.1	122.5	633.0	217.8	12.6	1.7	10.9	1.6	32.9	25.8	57.1	25.5	4.7	4.9
11.3	40.7	136.5	688.0	238.2	15.4	1.7	13.2	2.1	32.6	25.1	54.8	25.1	6.0	3.8
6.8	43.4	139.4	667.6	240.2	15.1	2.5	13.3	1.7	37.3	28.6	61.1	29.1	6.1	4.2
31.8	38.5	133.6	924.0	139.3	14.3	2.9	16.7	8.6	34.5	49.1	120.4	41.9	9.0	3.7
36.8	43.9	152.3	950.1	158.7	16.5	2.2	19.0	9.7	39.1	73.3	124.9	45.2	8.3	4.0
2.8	39.2	142.6	956.3	237.9	30.7	3.3	12.6	2.2	45.0	43.1	88.0	41.2	8.3	5.5

Notes

1. ICP-OES data are in ppm except Ca and Mg, which are per cent; EDS data and TOC are per cent.
2. Spot ion probe data are averages of 30–50 analyses per sample.
3. Isotope values are calibrated to the PDB standard.
4. Carbonate percentage was calculated both from acetic acid and HCl dissolution, as described in the Methods sections.
5. Data in grey (Appendix 1) were collected and analysed by Romain Guilbaud (*Nature Geosci.* 8, 466–470).
6. Ages are interpolations between the absolute dates cited in Chapter 6, pro rata to stratigraphic height.
7. LOI is loss on ignition at 1100 °C, loi the prior loss at 450 °C, LOI(Σ) the total loss on ignition.
8. Major and minor elements are per cent, trace elements in ppm.

Appendix 4. Backscattered electron photomicrographs of samples from the Jiuliqiao and Sidingshan Formations.

JLQ 1

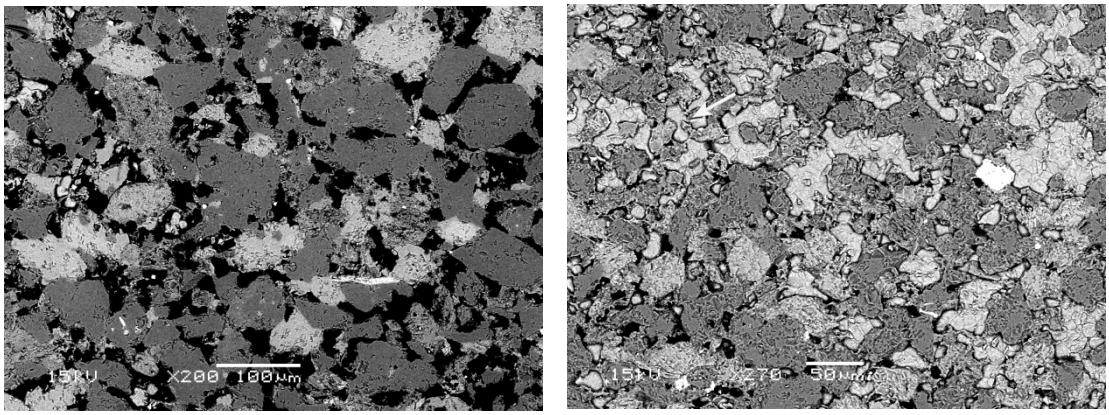

Figure 1. Light grey = partly dissolved K-feldspar crystals, dark grey = quartz, black = OM.

Figure 2. Partly dissolved K-feldspar crystals. Arrow highlights evidence that the carbonate grains (pale grey) filled voids left by dissolution and were authigenic. Large bright crystal is titanium oxide, Ti_2O_5.

JLQ 2, 4

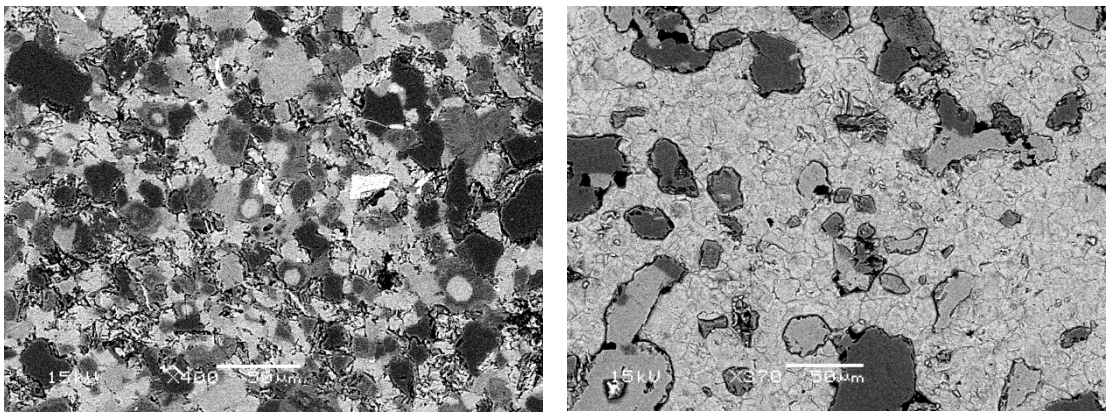

Figure 3. Recrystallised partly dissolved feldspar, calcite and silica-rich matrix. Circular patches are remains of calcite grains, typically 10–15 μm across. Note darker rhombs at centre of some VHMC patches.

Figure 4. Partly dissolved K-feldspar crystals (light grey = feldspar, dark grey = quartz) in a pale-grey matrix of granular calcite. Some grains are rimmed by calcite cement. Discrete medium-grey crystals, some rhombohedral, are VHMC.

JLQ 4, 6

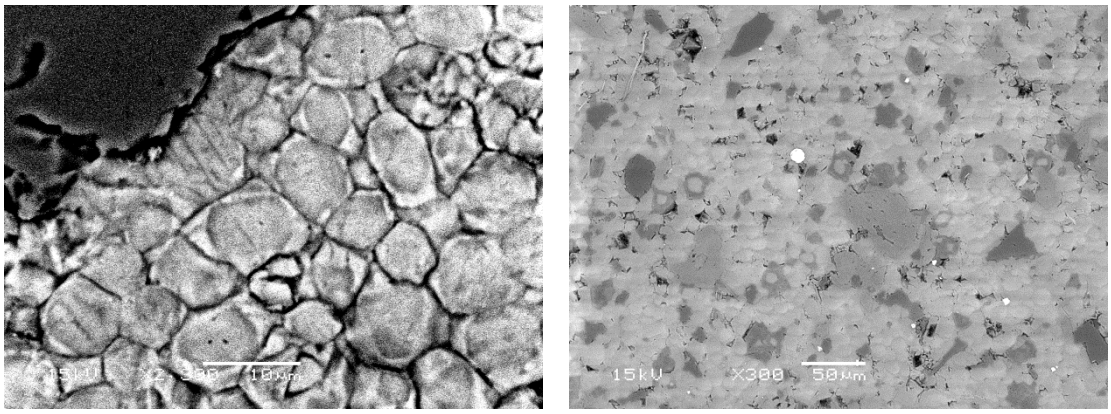

Figure 5. Molar tooth microspar. Calcite grains (5–10 μm across) are somewhat smaller than elsewhere in the sample or in other samples. The lighter hue of the surrounds comes from enrichment in iron.

Figure 6. Amorphous recrystallised feldspar and partly recrystallised calcite. Outlines of grains still visible. Medium-grey pools around some of the grains are VHMC and in several cases rhombohedral. Dark grey is quartz, large medium-grey patches K-feldspar. Bright crystal is FeS_2.

JLQ 8, 9

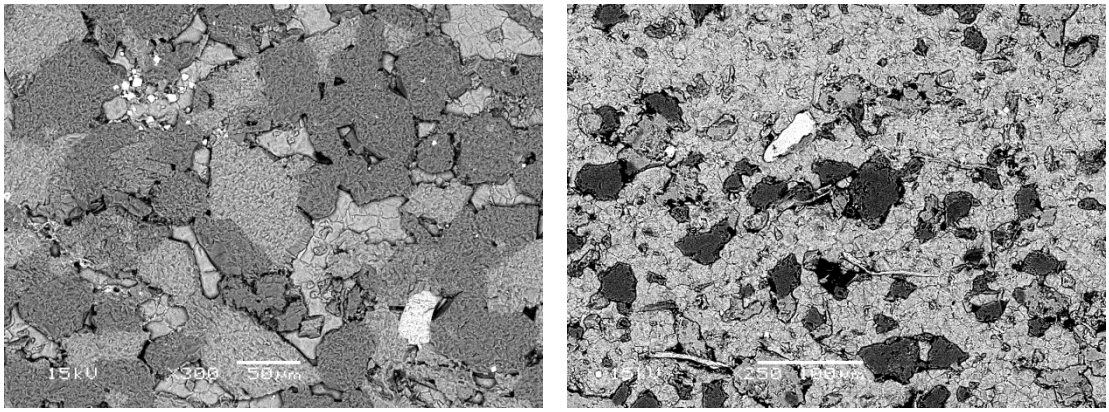

Figure 7. Partly dissolved K-feldspar crystals with etched surfaces, authigenic calcite grains filling voids. Later-formed crystal lower right is apatite, bright crystals top left are $FeS_{1.6}$.

Figure 8. Partly dissolved K-feldspar crystals in granular calcite matrix. Minor biotite.

JLQ 16

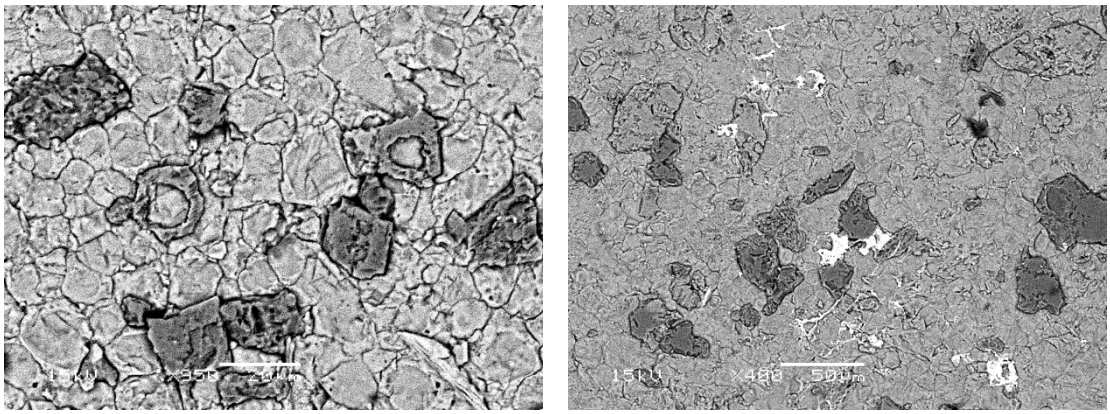

Figure 9. Rimmed calcite grains, VHMC (Mg/Ca 0.18–0.20 wt) and quartz, scale-bar 20 μm.

Figure 10. Siderite filling between-grain interstices.

JLQ 17

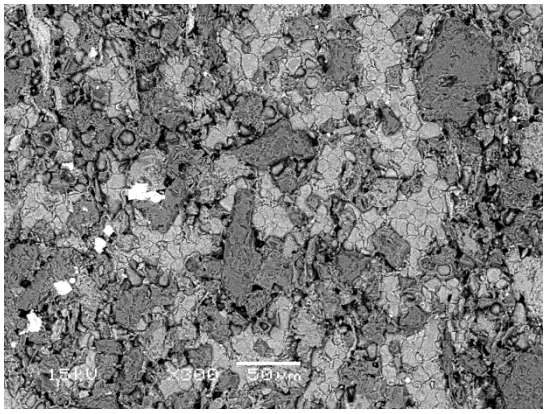

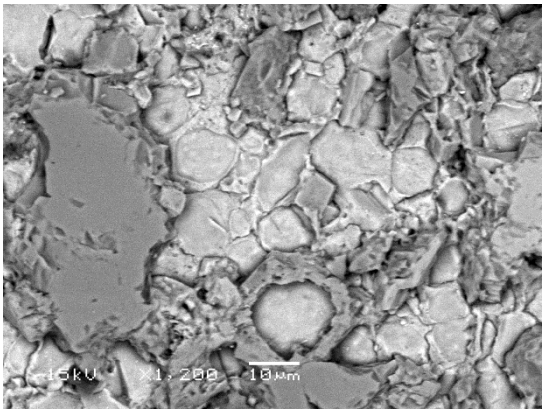

Figure 11. Partly dissolved K-feldspar amid grains of calcite, some grains surrounded by pools of VHMC (Mg/Ca 0.19–0.34 wt). Bright crystals are later-formed $FeS_{1.7}$.

Figure 12. VHMC (Mg/Ca 0.36) surrounds grain of LMC (Mg/Ca 0.028), lower centre of image. Centre: a VHMC rhombohedron (Mg/Ca 0.28). Quartz on the left, K-feldspar far right and top right.

JLQ 24, 25

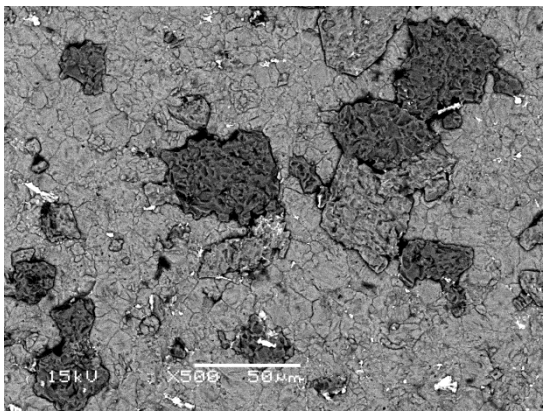

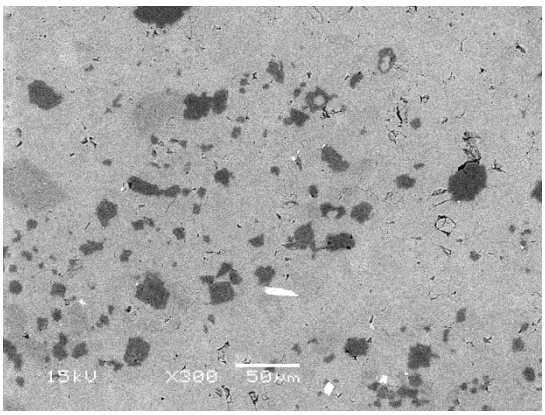

Figure 13. Partly dissolved K-feldspar amid grains of calcite (originally aragonite). The bright streaks on the central crystal and elsewhere are mainly ankerite, $(Ca,Fe)CO_3$.

Figure 14. Recrystallised quartz (dark), feldspar (faint), VHMC (slightly less dark than the quartz, some rhombic) and calcite. Bright crystals at bottom are $FeS_{1.7}$.

JLQ 27, 28

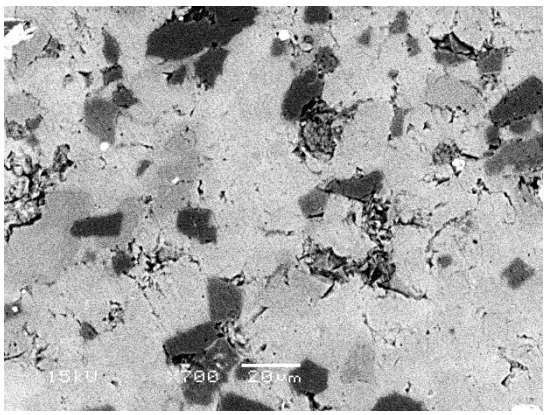

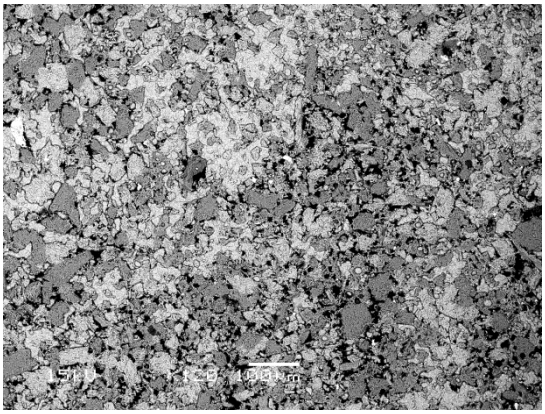

Figure 15. As for Figure 14.

Figure 16. Similar to JLQ 1 and 17.

JLQ 29, 30

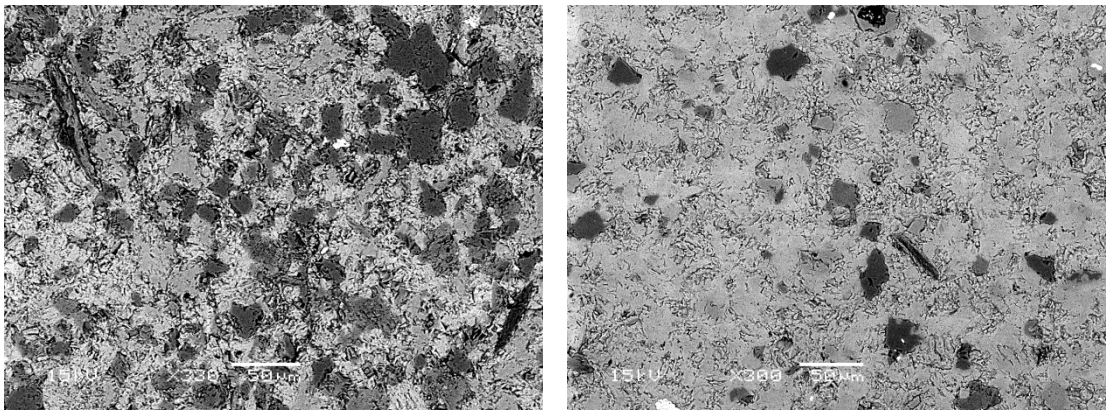

Figure 17. Pseudocubic quartz crystals (dark), presumably precipitated from water column, and largely recrystallised VHMC and calcite matrix. Darker lath top right is probably $Al_2Si_2O_7$, halloysite.

Figure 18. Similar to Figure 17. Small pseudocubic quartz crystal near centre is 45.8 wt% Si, 23.5 wt% Ca.

JLQ 30, 31

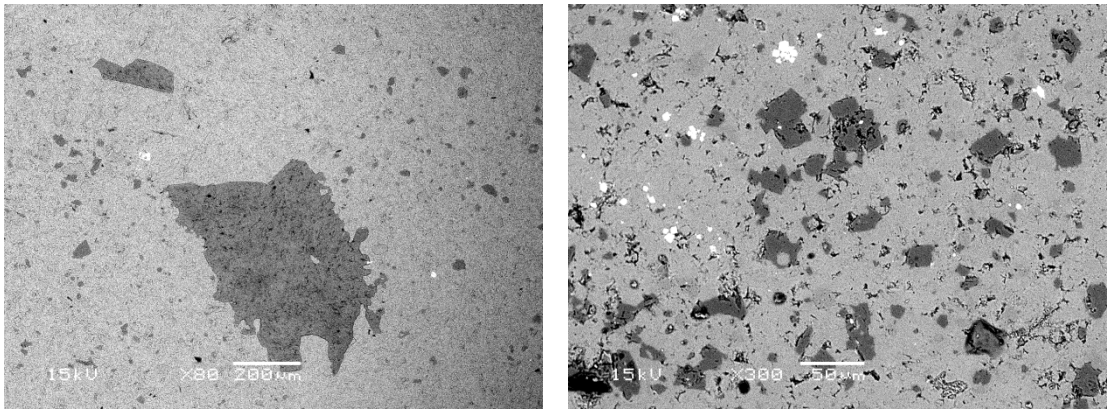

Figure 19. Patches of secondary VHMC (Mg/Ca 0.23–0.31 wt).

Figure 20. The medium-grey crystals, including the rhombs, are mostly VHMC, the bright grains ankerite, $(Ca,Fe)CO_3$. The medium-grey area under the '15' is quartz (40.7 wt% Si, 15.3 wt% Ca).

JLQ 31

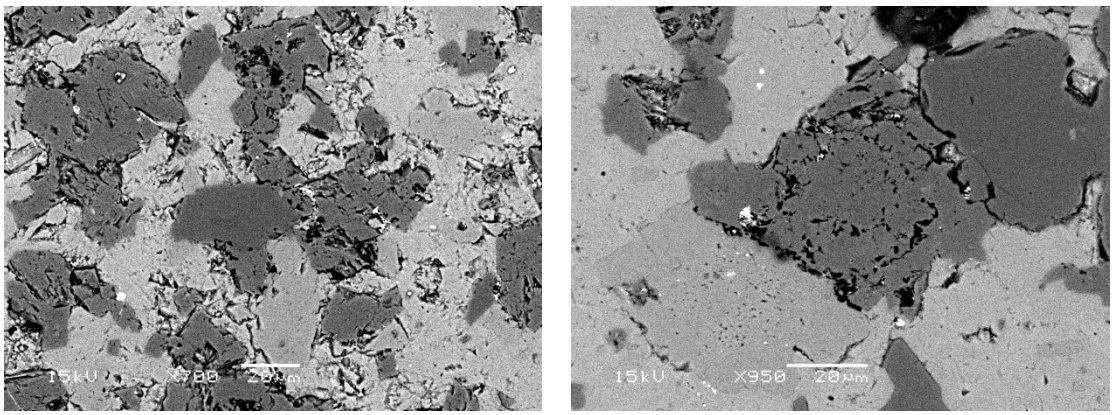

Figure 21. Partly dissolved K-feldspar in recrystallised calcite matrix. Quartz (Ca-rich) has smooth texture, VHMC marked by flecks of OC.

Figure 22. K-feldspar (pale) on left, VHMC (Mg/Ca 0.27–0.29 wt) with flecks of OC in the middle, quartz on right (59.7 wt% Si, 20.0 wt% Ca).

JLQ 32

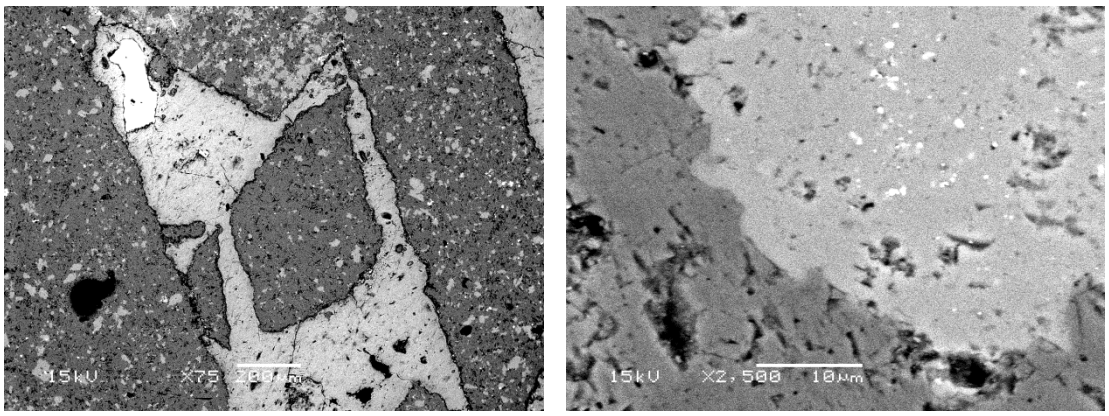

Figure 23. Low-Mg calcite vein with dolomite intraclasts in dolomite matrix. Light-grey fragments are K-feldspar, bright crystal mainly barite.

Figure 24. High-magnification detail of K-feldspar, showing inclusions of barite.

JLQ 32, 39

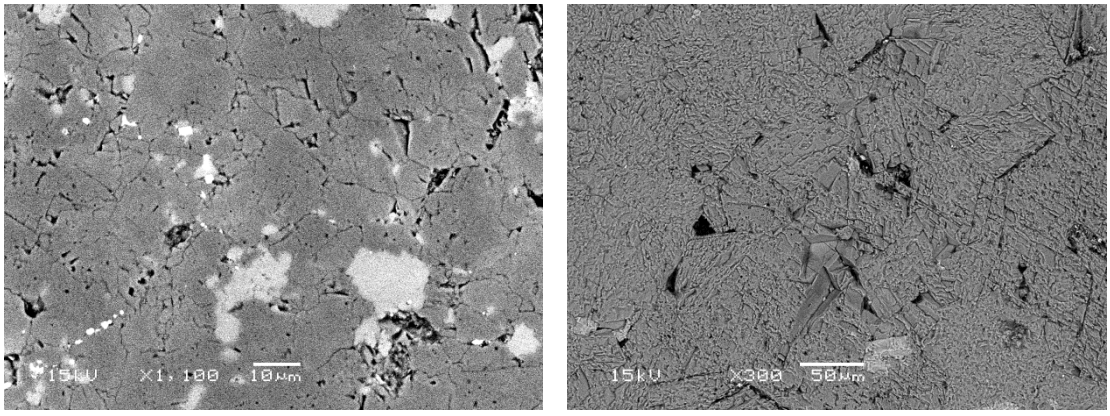

Figure 25. Boundaries of variously-sized dolomite crystals still visible (down to 2 μm across). Feldspar re-crystallised within the dolomite.

Figure 26. Dolomite crystals.

JLQ 40, 42

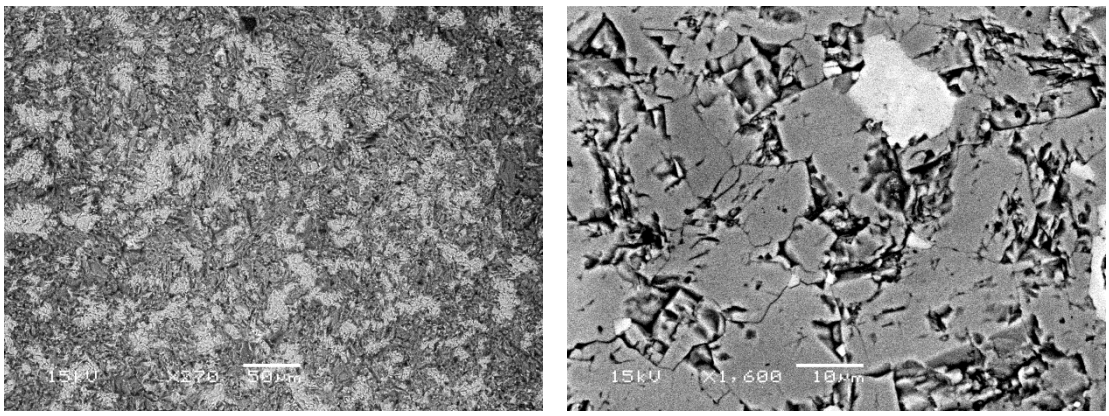

Figure 27. Dark/light dichotomy correlates with differences in OC content. There is no difference in Mg/Ca. The sample is stromatolitic and also distinguished by high carbonate-associated sulphur. The OC is inferred to have been synthesised by stromatolitic bacteria, with no impact on dolomite composition or bulk $\delta^{13}C$.

Figure 28. As for Figure 25.

JLQ 48, 49

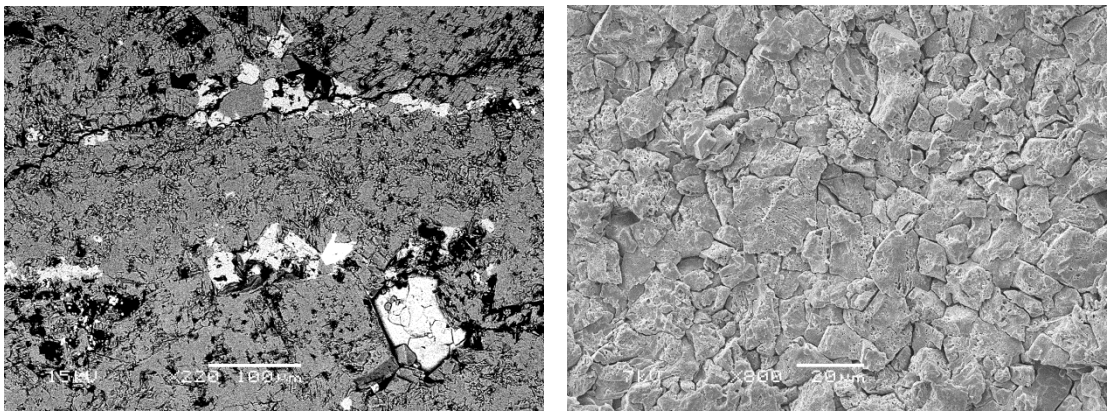

Figure 29. K-feldspar and quartz in dolomite matrix. Bright crystal = ankerite. Void bottom right filled by calcite.

Figure 30. Dolomite crystals (gold-coated).

ZW 22, 51

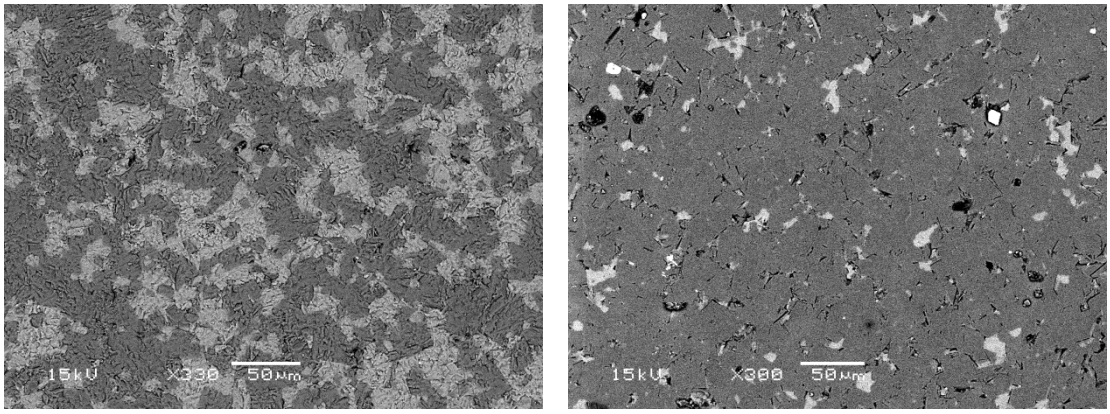

Figure 31. Light and grey patches similar to JLQ 40 (Fig. 4.27) but here corresponding to differences in Mg content (0.11–0.14 Mg/Ca and 0.31–0.39 respectively), suggesting that HMC was turning to VHMC in the substrate.

Figure 32. VHMC (light grey) appears to occlude pore space after precipitation of calcitic dolomite. Relict crystal boundaries suggest rhombs typically 20–30 μm across.

Appendix 5. Transmitted light photomicrographs of samples from the Jiuliqiao and Sidingshan Formations.

JLQ 4, 5

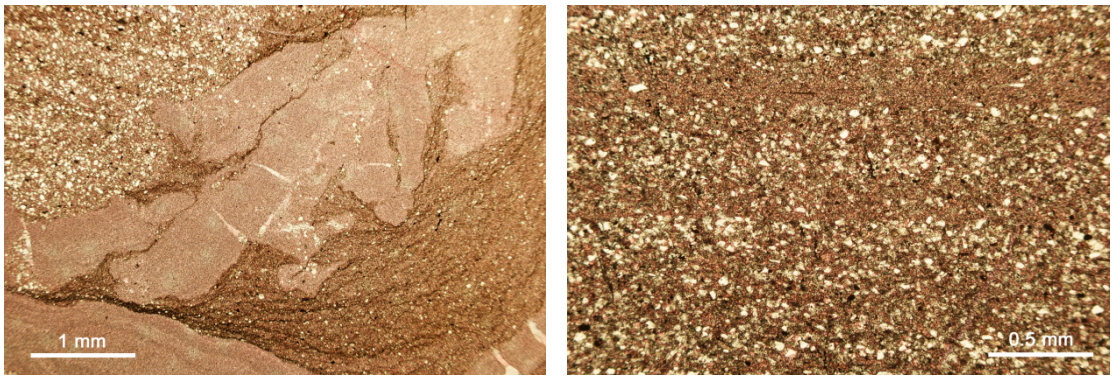

Figure 1. Dendritic molar tooth structure, composed of calcite granules; quartz crystals upper left, microbial lamination lower right. (Slides *passim* stained with Alizarin red S.)

Figure 2. Laminar alternations of quartz-rich, quartz-poor calcite.

JLQ 24, 25

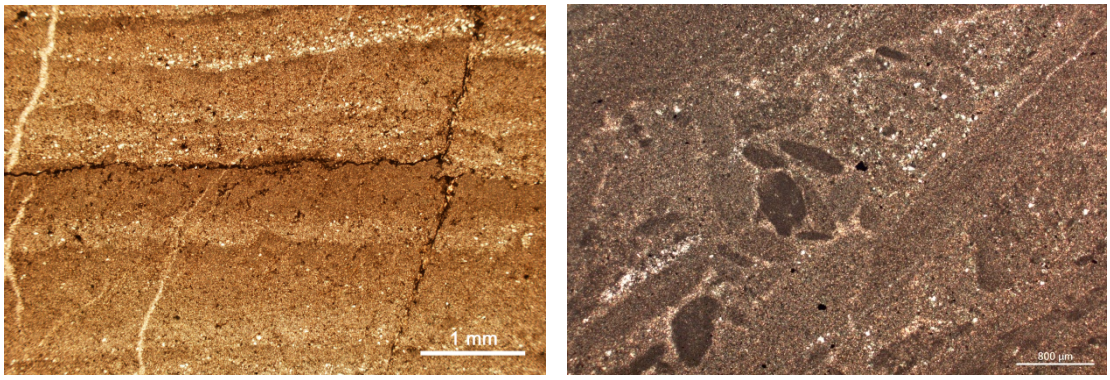

Figure 3. Stromatolitic laminae. Layering is the effect of variation in organic content, accentuated by dense quartz particles. More organic carbon entered post-lithification through a micro-fault that displaced the upper laminae vertically and horizontally.

Figure 4. Piled-up stromatolite fragments (oblique view, no staining).

JLQ 27, 30

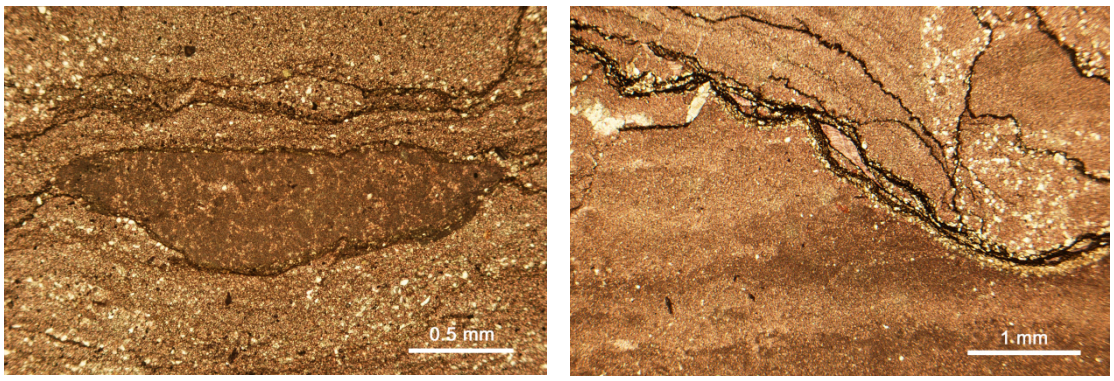

Figure 5. Early-lithified microlaminae separated by OM; small intraclast showing microbial clotting.

Figure 6. Lower part stromatolitic, upper part intraclastic and laminar.

JLQ 31

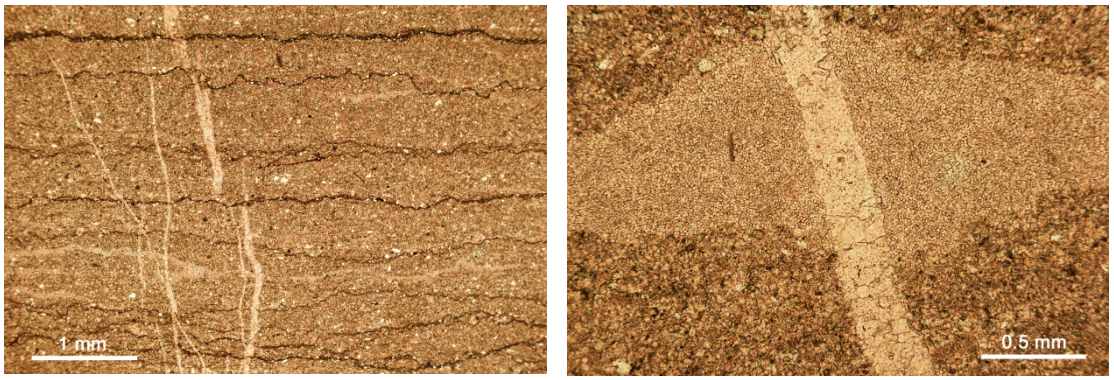

Figure 7. Last limestone sample. Microbial lamination, contrasting with OM-poor calcite veins and incipient fenestrae.

Figure 8. Partly recrystallised matrix, granule-filled fenestra, cross-cutting coarse-crystalline vein.

JLQ 32

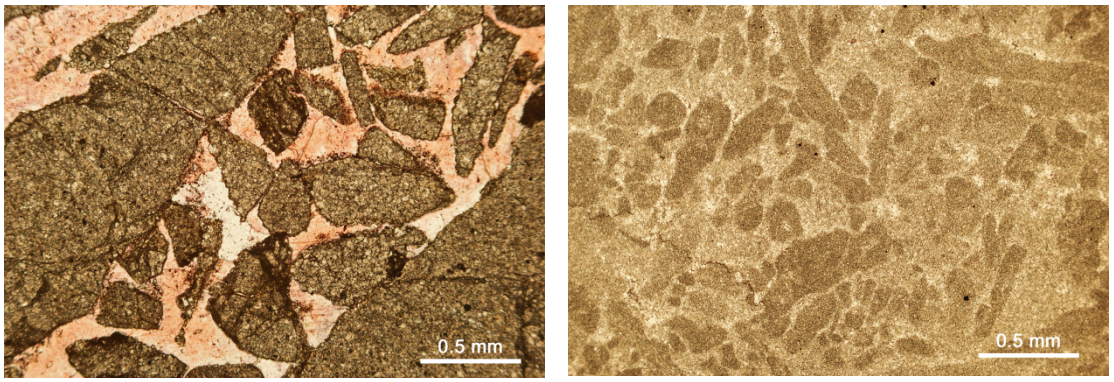

Figure 9. Dolomite matrix and fragments (some organic-rich), stained coarse-crystalline calcite vein.

Figure 10. Diverse algal forms in coarser-crystalline dolomite matrix.

JLQ 32, 36

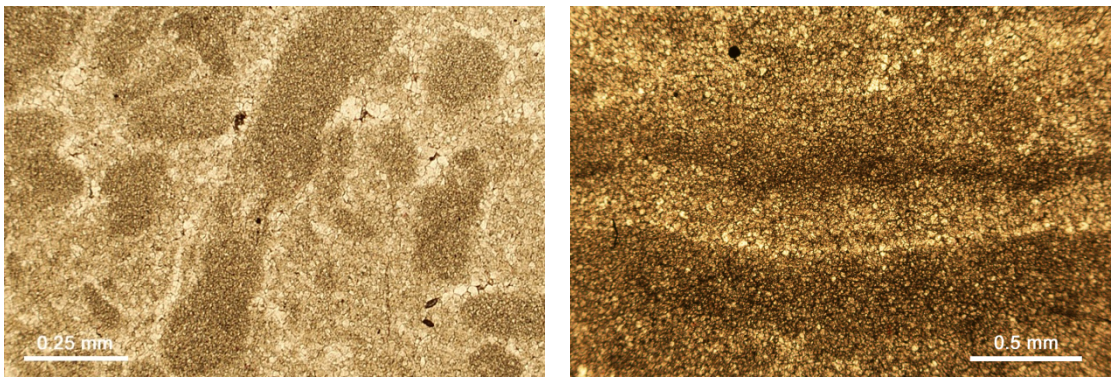

Figure 11. Detail: coarser dolomite crystals – paler crystals lacking organic carbon – developed in spaces between the algae.

Figure 12. Stromatolitic laminae.

JLQ 37

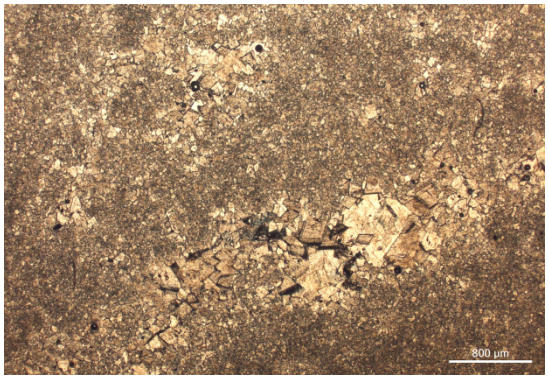

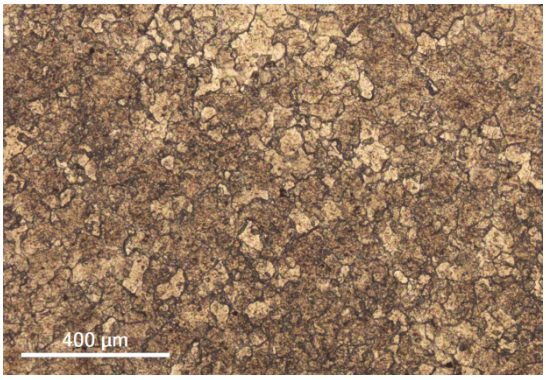

Figure 13. Stromatolitic laminae: fine dolomite crystals in the organic-rich layers, coarser inbetween.

Figure 14. Detail: the smallest crystals, barely visible, appear granular.

JLQ 38, 42

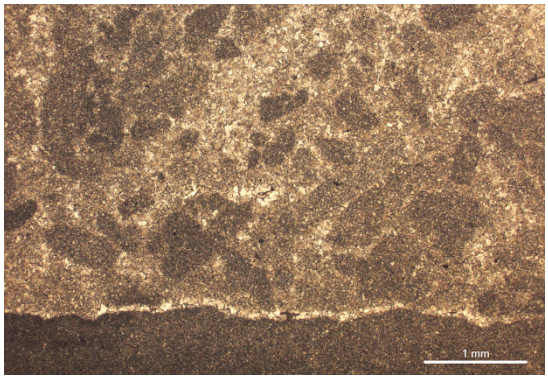

Figure 15. Remains of algae above an organic-rich intraclast rimmed by coarse crystals.

Figure 16. Coarse rhombohedral dolomite spar – calcite spar stained red.

JLQ 43, 56

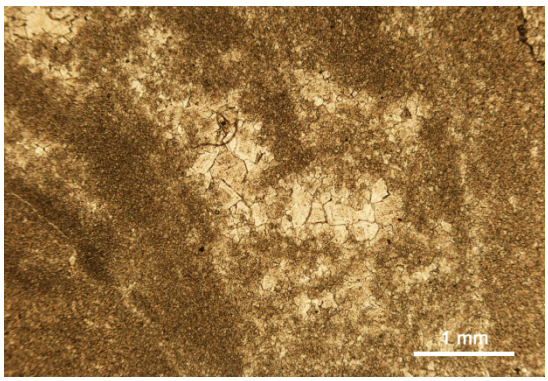

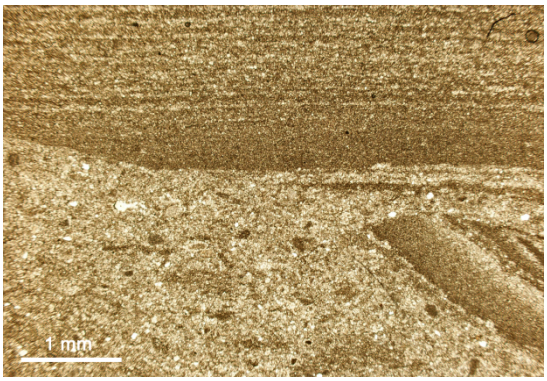

Figure 17. Edge of microdigitate stromatolite (left), spar filling void.

Figure 18. Laminar intraclasts, matrix poorer in OM, with organic remains and siliciclastic material.

JLQ 56, 59

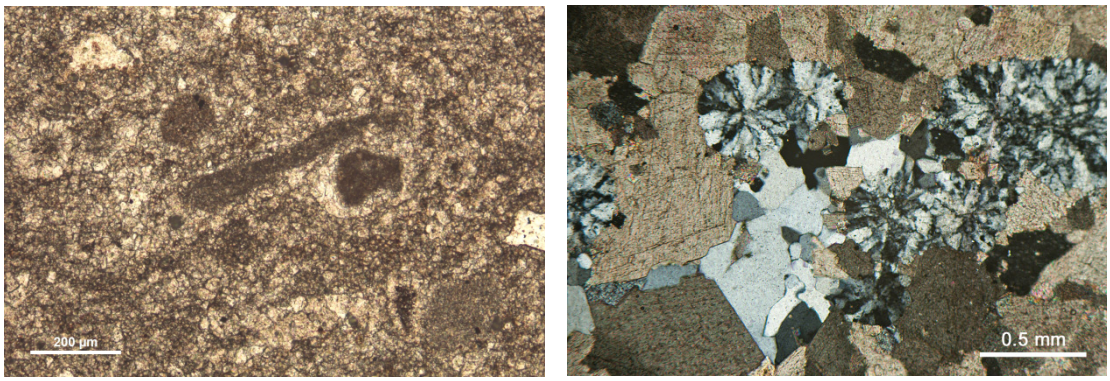

Figure 19. Detail of organic-rich matrix.

Figure 20. Quartz rosettes and spar in dolomite matrix (cross-polarised light).

JLQ 59, 60

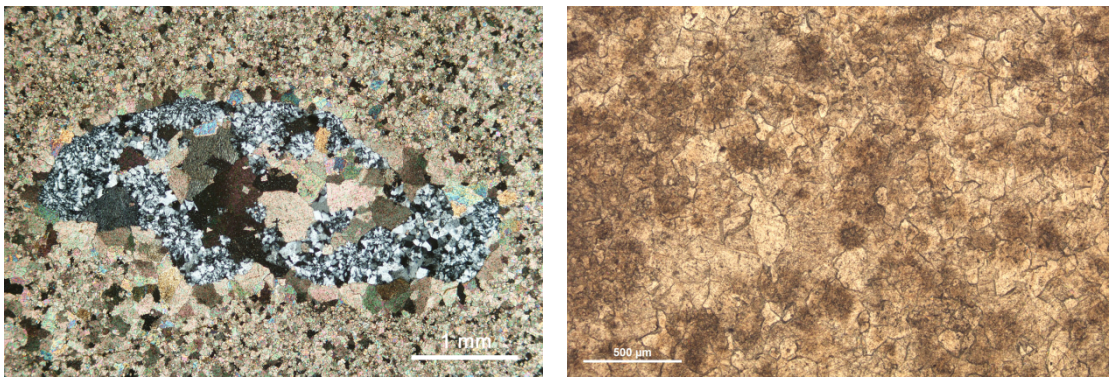

Figure 21. Dolomite matrix and quartz inflling void (cross-polarised light).

Figure 22. Algal matter in recrystallised dolomite.

JLQ 61

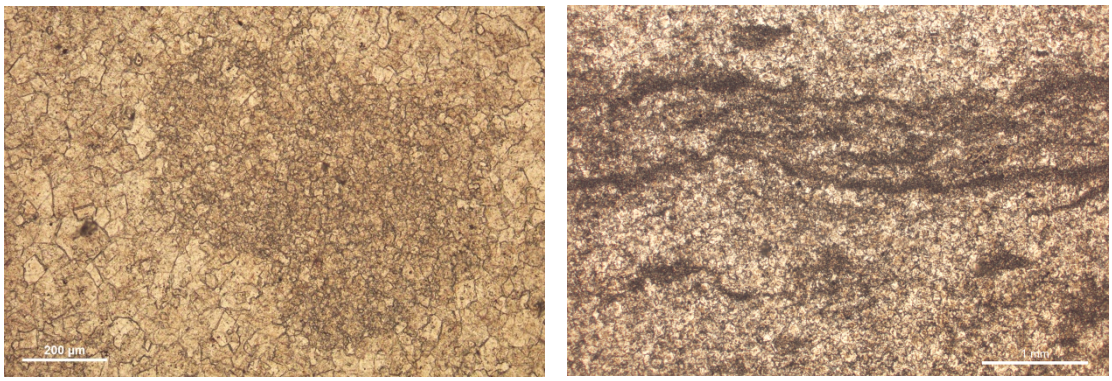

Figure 23. Dolomite crystals, generally smaller within organic matter stain than outside.

Figure 24. Microbial mats (thicker than in, say, Figure 7).